

Dissertation zur Erlangung des Doktorgrades
der Fakultät für Chemie und Pharmazie
der Ludwig-Maximilians-Universität München

Metal oxide nanomorphologies for electrocatalysis and battery materials

Daniel Benjamin Böhm

aus

München, Deutschland

2020

Erklärung

Diese Dissertation wurde im Sinne von § 7 der Promotionsordnung vom 28. November 2011 von Frau Prof. Dr. Dina Fattakhova-Rohlfing betreut.

Eidesstattliche Versicherung

Diese Dissertation wurde eigenständig und ohne unerlaubte Hilfe bearbeitet.

München, den 26.05.2020

Böhm D.

Daniel Böhm

Dissertation eingereicht am: 29.04.2020

1. Gutachter: Prof. Dr. Dina Fattakhova-Rohlfing
2. Gutachter: Prof. Dr. Thomas Bein

Mündliche Prüfung am: 15.05.2020

Abstract

The ongoing replacement of fossil fuels by renewable energy sources induces changes of the existing infrastructure and usage behavior of energy in general and demands for novel and efficient storage, transmittance and utilization concepts. Research in the field of physics and chemistry of the last decades only made this possible by energy saving technologies such as light emitting diodes or silicon based integrated circuits, Si- and non-Si based photovoltaics for electricity generation or highly efficient novel generators with superconducting coils being developed for wind power harvesting. For the conversion of sustainable electrical energy, electrocatalysts were developed for hydrogen generation by water splitting or for CO₂ reduction. Finally, for storage of sustainable electrical energy, among other mainly stationary technologies, batteries became increasingly important. Although all of the aforementioned concepts are not fundamentally new, the efficiency and thus the economic value of the respective devices still can and needs to be increased by optimizing the composition and morphology of the used materials. Nanosized- and nanostructured materials are particularly beneficial for the energy conversion and storage applications. The high surface-to-volume ratio significantly improves the performance of surface-related heterogeneous catalytic reactions relevant for diverse energy conversion processes such as the hydrogen evolution and reduction reactions (HER, HRR), oxygen evolution and reduction reactions (OER, ORR) or CO₂ reduction. It furthermore enhances the electrode kinetics of energy storage materials due to an increased electrode/electrolyte interface area, which allows for rapid ion diffusion. In addition, nanostructuring allows for the fabrication of novel mixed metal oxide meta-stable phases with unique electrochemical and catalytic properties that are not accessible in the bulk. It can furthermore stabilize known bulk phase compositions and enable the fabrication of advanced composite materials for durable and high-performance electrochemical applications.

In this thesis, the most relevant approaches for the synthesis of nanosized- and nano-structured materials are introduced (Chapter 1) together with examples of selected materials used as oxygen evolution reaction catalysts required for efficient hydrogen generation, and transition metal oxides used in battery negative electrodes (anodes) for electrochemical energy storage. Relevant analytical techniques to characterize and describe the synthesized structures are discussed in Chapter 2.

The first part of the work (Chapters 3 and 4) is composed of literature overviews of current developments in the field of novel nanostructured transition metal chalcogenides with a focus on tin oxide-based materials employed as anodes for secondary alkali metal batteries. Chapter 3 is based on a book chapter contribution with the title “Ceramic anodes for Li and Na-ion batteries” in *Advanced Ceramics for Energy Conversion and Storage*” and specifically discusses ceramic anodes for Li and Na-ion batteries. From the overwhelming variety of materials classes and compositions cumulated in the class of ceramics, a selection of the most prominent and promising materials for future energy storage materials in secondary battery negative electrodes is discussed. The first section introduces transition metal oxide-based insertion type materials such as titanate-based anodes, garnet type ceramics ($\text{Li}_3\text{Nd}_3\text{W}_2\text{O}_{12}$) and the prominent class of phosphate-based Na-Super-Ionic-CONductor (NASICON)-type anodes with a short overview of polymer-derived SiOC and SiON ceramics as negative electrodes. A further section is dedicated to conversion and alloying-type ceramic anodes mainly originating from the class of transition metal oxides and chalcogenides, with prominent examples such as Fe_3O_4 , SnO_x and SnO_2 . Key properties of the aforementioned materials are discussed together with examples of their electrochemical performance as anodes in Li and Na secondary batteries and overarching strategies such as nanostructuring and (carbon) composite formation are highlighted to finally obtain electrodes with an increased reversibility (cyclability), energy density and reaction kinetics (rate capability).

In Chapter 4, a brief literature overview of recent progress in the field of tin oxide-based nanosized and nanostructured materials as conversion and alloying/dealloying-type anodes in lithium-, sodium- and potassium-ion batteries is given. The first section addresses the importance of the initial SnO₂ micro- and nanostructure on the conversion and alloying/dealloying reaction upon lithiation and its impact on the microstructure and cyclability of the anodes. A further section is dedicated to recent advances in the fabrication of diverse 0D to 3D nanostructures to overcome stability issues induced by large volume changes during cycling. Additionally, the role of doping on conductivity and synergistic effects of redox-active and -inactive dopants on the reversible lithium-storage capacity and rate capability are discussed. Furthermore, the synthesis and electrochemical properties of nanostructured SnO₂/C composites are reviewed. The broad research spectrum of SnO₂ anode materials is finally reflected in a brief overview of recent work published on Na- and K-ion batteries.

The second main part of this thesis from Chapter 5-8 is dedicated to (doped) nanostructured or nanosized transition metal oxides for energy conversion applications in form of electrochemical and photoelectrochemical water oxidation by assistance of respective catalysts.

In Chapter 5, the synthesis and structural properties of dispersible akaganéite (β -FeOOH) nanocrystals doped with various elements in different oxidation states such as Co(II), Ni(II), V(III), Ti(IV), Sn(IV), Si(IV), and Nb(V) synthesized by a microwave-assisted solvothermal synthesis in *tert*-butanol are discussed. Rod-like nanocrystals with a thickness of ≈ 4 nm and a length depending on the doping element ranging from ≈ 4 nm, resulting in an almost-spherical shape, to 90 nm are described. In-depth characterization of the structure and composition on the particle scale by electron microscopy revealed that concentrations of up to 20 at% of the respective doping elements could be incorporated. This is attributed to the kinetic control of the phase formation during the solvothermal reaction, together with the extremely small crystal

size, which can stabilize the unusual structural compositions. Due to the perfect dispersibility, the particles can be deposited on different substrates to produce thin films of 35 – 250 nm thickness. By means of an in situ microwave-assisted film growth synthesis, mesoporous films of up to 30 μm thickness could be obtained. The nanostructured and doped $\beta\text{-FeOOH}$ films could then be thermally oxidized at temperatures between 480 – 600 $^{\circ}\text{C}$ to form morphologically similar hematite ($\alpha\text{-Fe}_2\text{O}_3$) films. Thereby, tin-doped $\alpha\text{-Fe}_2\text{O}_3$ films displayed a photoelectrochemical activity towards the water oxidation reaction under basic conditions that exhibited a scaling relation with the electrode layer thickness.

In Chapter 6, time dependent phase transitions of vanadium-doped nanosized nickel-oxide based catalysts are discussed and related to their properties as oxygen evolution reaction (OER) catalysts under basic conditions. To achieve this aim, a synthesis procedure for the controllable formation of vanadium (III) doped nanosized nickel hydroxide and nickel oxide polymorphs was introduced. The complex dynamic character of the α to β -phase $\text{Ni}(\text{OH})_2$ phase transitions and resulting structure-activity correlation was investigated by electron microscopy and electron energy loss spectroscopy to confirm a homogeneous incorporation of V(III) ions in the initially synthesized $\alpha\text{-Ni}(\text{OH})_2$ structure. Depending on the concentration, V(III)-doping was thereby shown to retard or prevent a spontaneous structural rearrangement known as chemical ageing process. The difference in electrocatalytic activity of different doping levels could be mainly attributed to the inhibited conversion of highly active $\alpha\text{-Ni}(\text{OH})_2$ to a less active, but more stable β -polymorph by vanadium ions, which is important for understanding the mechanisms of electrocatalytic activity of nickel oxide-based compounds.

In the further sections (Chapter 7 and 8) of this thesis the rational design of highly active and stable transition metal oxide supported nanosized noble metal oxide OER catalysts for electrochemical water splitting under acidic conditions and potential application in proton-exchange membrane electrolyzers was explored.

In Chapter 7 the fabrication of a highly active TiO₂ supported Ir-based OER catalyst for the application in proton exchange membrane (PEM) electrolyzers with reduced noble metal content is described. Commercially available P25 titania employed as a high surface area corrosion resistant catalyst support was homogeneously coated with a 1 – 2 nm thin layer of amorphous IrOOH_x resulting in a theoretical iridium density of only 0.05 – 0.08 g_{Ir} cm⁻³. Oxidation in molten NaNO₃ between 350 – 375 °C enabled a controllable phase transformation and crystallization to form a layer of interconnected IrO₂ nanoparticles of around 1 – 2 nm on the surface of the TiO₂ support. The increase in crystallinity is thereby accompanied by a significant increase in conductivity and stability under OER conditions with an electrocatalytic activity maintained at the level of the highly active amorphous IrOOH_x phase used as a precursor.

In the final chapter, a multistep synthesis procedure for the homogeneous coating of a complex porous conductive oxide with small Ir nanoparticles is introduced to obtain a highly active electrocatalyst for water oxidation under acidic conditions. At first, inverse opal macroporous Sb-doped SnO₂ (ATO) microparticles with defined pore size, composition, and open-porous morphology were synthesized that were further used as conductive catalyst support. ATO-supported iridium nanoparticle catalysts with a controlled amount of active material were prepared by solvothermal reduction of an IrO_x colloid in the presence of the porous ATO particles, whereby homogeneous coating of the complete outer and inner surface of the particles with nanodispersed metallic Ir was achieved. By means of thermal oxidation ATO-supported IrO₂ nanoparticles were obtained that exhibit a calculated void volume fraction of about 89%. A resulting remarkably low Ir bulk density of ≈0.08 g cm⁻³ for this supported oxide catalyst architecture with 25 wt% Ir was determined, allowing for a significant reduction of the noble metal content for the application as OER catalyst in proton exchange membrane electrolyzers (PEM). The highly efficient catalyst reaches a current density of 63 A g_{Ir}⁻¹ at an

overpotential of 300 mV versus reversible hydrogen electrode, thereby significantly exceeding a commercial TiO₂-supported IrO₂ reference catalyst under the same measurement conditions.

In conclusion, the nanostructuring concepts discussed in this thesis may guide a way for the fabrication of novel highly efficient transition metal oxide-based electrodes for next-generation energy storage devices. The introduced synthesis approaches for ultra-small and doped metal oxide particles as well as complex porous composite nanostructures may further deepen our understanding of the structure-activity relation of electrocatalytically active nanosized compounds in general. The application of the developed synthesis procedures with a possible control over the nanomorphology, phase and crystallinity as well as doping ion concentration thereby allows for the preparation of highly efficient electrocatalysts for future energy conversion processes.

Table of contents

1.	Introduction	1
1.1	Catalytic properties of nanoscale transition metal oxides.....	1
1.2	Nanoscale transition metal oxide electrocatalysts for energy conversion applications	7
1.2.1	Water electrolysis.....	7
1.2.2	Photoelectrochemical water splitting	11
1.2.3	Fuel cell and oxygen reduction reaction catalysts.....	14
1.3	Nanomorphology and particle size control	17
1.3.1	Synthesis of metal oxide nanoparticles	17
1.3.2	Fabrication of 1D - 3D metal oxide nanostructures	23
1.4	Nanosized transition metal oxide catalysts for water electrolysis	28
1.4.1	Oxygen evolution reaction catalysis with earth abundant transition metals	31
1.4.2	Oxygen evolution reaction catalysis with Ir-based catalysts	36
1.5	Electrochemical energy storage by transition metal oxides in secondary alkali metal ion batteries.....	51
1.6	References	56
2.	Characterization.....	69
2.1	X-ray diffraction (XRD)	70
2.2	Raman spectroscopy	75
2.3	Thermogravimetric analysis (TGA) and differential scanning calorimetry (DSC)..	79
2.4	Dynamic light scattering (DLS)	80
2.5	Inductively coupled plasma optical emission spectroscopy	82
2.6	Nitrogen sorption.....	84
2.7	Electron microscopy	87
2.7.1	Transmission electron microscopy	89
2.7.2	Scanning electron microscopy (SEM).....	92
2.8	Quartz crystal microbalance (QCM)	95
2.9	4-Point probe (Van-der-Pauw) and 2-point direct current (DC) conductivity measurements.....	97
2.10	Electrochemical characterization.....	100
2.10.1	Redox activity probed by cyclic voltammetry	105
2.10.2	Characterization of oxygen evolution reaction kinetics by linear sweep voltammetry	108
2.10.3	Characterization of oxygen evolution reaction kinetics by chronopotentiometry	110
2.10.4	Cyclic voltammetry on rotating disc electrode	111
2.10.5	Impedance spectroscopy	113
2.11	References	117
3.	Ceramic anodes for Li and Na-ion batteries	
3.1	Introduction	121

3.2	Insertion-type ceramic anodes	125
3.2.1	Titanate-related battery anodes - Structure and key properties	125
3.2.2	Other transition metal oxides: $\text{Li}_3\text{Nd}_3\text{W}_2\text{O}_{12}$ -A garnet-type ceramic anode	139
3.2.3	Silicon (SiON , SiCN , SiOC and related)-based ceramic anodes	141
3.2.4	Na-Super-Ionic-CONductor (NASICON)-type battery anodes	143
3.3	Conversion-type ceramic anode materials.....	148
3.4	Protective ceramic coating of alkali metal anodes	157
3.5	References	160
4.	Tin Oxide Based Nanomaterials and Their Application as Anodes in Lithium-Ion Batteries and Beyond.....	167
4.1	Cover and profile	168
4.2	Introduction	170
4.3	Nanostructured Phase-Pure SnO_2 LIB Anodes	176
4.3.1	Nanoparticles	177
4.3.2	Nanorods.....	181
4.3.3	Nanowires and -tubes	183
4.3.4	Nanosheets.....	185
4.3.5	3D hollow nanostructures.....	186
4.4	Doped SnO_2 LIB Anodes	188
4.5	SnO_2 -Based Composite LIB Anodes.....	193
4.5.1	Amorphous carbon (SnO_2/C composites).....	193
4.5.2	CNTs (SnO_2/C composites).....	194
4.5.3	Graphene (SnO_2/C composites).....	195
4.5.4	SnO_2 /non-carbonaceous composites.....	199
4.6	Full LIB Cell Performance with SnO_2 -Based Anodes	203
4.7	SnO_2 -Based Anodes for NIBs and KIBs	205
4.7.1	SnO_2 -based NIB anodes	205
4.7.2	SnO_2 -based KIB anodes	207
4.8	Summary and Outlook.....	211
4.9	References	214
5.	Non-agglomerated iron oxyhydroxide akaganeite nanocrystals incorporating extraordinary high amounts of different dopants.....	225
5.1	Introduction	226
5.2	Results and discussion	228
5.3	Conclusion.....	245
5.4	Experimental.....	246
5.5	Supporting Information	251
5.6	References	261
6.	V(III) Doped Nickel Oxide-Based Nano-Catalysts for Electrochemical Water Splitting: Influence of Phase Composition and Doping on the Electrocatalytic Activity	265
6.1	Introduction	266

6.2	Results and discussion	269
6.3	Conclusion	287
6.4	Experimental.....	289
6.5	Supporting Information	294
6.6	References	305
7.	Core-shell titania/iridium oxide nanoarchitectures with ultrathin Ir shells are highly efficient OER catalysts for massively scalable PEM.....	309
7.1	Introduction	310
7.2	Results and discussion	314
7.3	Conclusion	334
7.4	Experimental.....	336
7.5	Supporting Information	342
7.6	References	353
8.	Efficient OER catalyst with low Ir volume density obtained by homogeneous deposition of iridium oxide nanoparticles on macroporous antimony-doped tin oxide support.....	359
8.1	Cover	360
8.2	Introduction	361
8.3	Results and discussion	364
8.4	Conclusion	390
8.5	Experimental.....	392
8.6	Supporting Information	400
8.7	References	428
9.	Conclusion and outlook	433

1. Introduction

1.1 Catalytic properties of nanoscale transition metal oxides

Among the different families of property-sharing elements in the periodic system of elements the transition metals located in groups 3-12 (d-block elements) and the so-called inner transition metals of the f-block (lanthanoid and actinoid) of the periodic system of elements exhibit an outstanding value for catalytic and energy related chemical processes today.^[1]

The common element in this set is their electronic configuration with a partial occupancy of their 3d, 4d or 5d and/or 4s, 5s, 6s orbitals which results in a variety of different possible oxidation states. The band structure of these elements causes metallic properties such as electrical and heat conductivity, ductility, malleability and metallic gloss with diverse possible applications in construction, electronics, catalysis and more.

An even higher variety of properties, structures and therefore possible applications are given by the formation of transition metal oxides (TMOs) with metal-oxygen bonds ranging between nearly ionic to highly covalent or metallic.^[2]

The diverse electronic and magnetic properties of transition metal oxides are related to the unique nature of their d-electrons which discriminate them from metallic elements and alloys as well covalent semiconductors or ionic insulators. At first, many of them possess narrow electronic bands of $\approx 1-2$ eV due to the small overlap of metal d- and oxygen p-orbitals that lead to an enhanced electron correlation with a local electronic structure which can be described in terms of atomic-like states. A last decisive factor influencing the properties of transition metal oxides is their variation in the structural dimensionality with numerous examples of layered 2-D structures as well as 3-D structures.^[2]

This leads to a broad variety of electrical conductivities ranging from metallic RuO_2 , IrO_2 , ReO_3 etc., over semi-conducting TMOs like TiO_2 , V_2O_3 to insulators such as BaTiO_3 . Beyond conductivity, TMOs may also exhibit more complex electronic phenomena such as charge

density waves, charge ordering, defect ordering or high temperature superconductivity as observed in certain complex copper oxides. Due to the partial occupancy of d-orbitals (especially 4d and 5d resulting in a high magnetic momentum) various types of magnetism and related phenomena such as ferro- and anti-ferromagnetism, ferroelectric or ferroelastic properties can be observed.^[2] The origin of some unforeseen physical behavior in 4d and 5d transition metal oxides can be associated with the existence of several overlapping energy scales and competing interactions present in these oxides with spin-orbital coupling as well as Coulomb and exchange interactions.^[3]

In general transition metal oxides span a wide range of technological applications in microelectronic circuits, sensors, piezoelectric devices, surface passivating and functional coatings, heterogeneous catalysts for industrial scale synthesis and refinement, battery materials as well as electrocatalysts for fuel cells and electrolyzers.^[4] During the last decades of research in the field it became apparent that novel (mixed or structured) transition metal oxides often exhibited surprising or even revolutionary physical properties which led to great advances in various fields of technology affecting everybody's life.^[3]

In this thesis we focus on two important applications of transition metal oxides, namely heterogeneous catalysis (more specifically, the oxygen evolution reaction (OER) of the electrochemical water splitting reaction) and electrochemical energy storage (specifically, insertion, conversion and alloying-type negative electrodes in secondary alkali metal ion batteries) which both rely on the existence of multiple oxidation states of the applied transition metal.

In practical applications the transition metals are often either present as oxides or the surface may be oxidized by reaction with atmospheric oxygen or oxygen from the reaction gas mixture. The oxides of the respective transition metals represent entirely different chemical compounds as their parent metals with significantly altered surface chemical properties employed in

heterogeneous catalysis.^[5] Concerning the catalytic properties, the surface of transition metals and their oxides are of great interest. Especially late transition metals such as Ru, Rh, Ir, Pd and Pt are well-known catalysts to promote general or selective oxidation reactions with widespread application in exhaust gas treatment, catalytic combustion of natural gas, selective oxidation of organic compounds and fuel cell as well as electrolyzer catalysts.^[5]

As an example, Figure 1 shows a schematic representation of a $\text{RuO}_2(110)$ surface with highly active coordinatively unsaturated Ru atoms (Ru_{cus}), fully coordinated Ru atoms (violet) as well as bridge-bonded (O_{br}) and three-fold coordinated oxygen atoms ($\text{O}_{3\text{f}}$). The $\text{RuO}_2(110)$ surface exhibits an array of bridging oxygens (O_{br}) along the $[001]$ direction which forms a plane 1.15 Å above the outmost Ru atoms. The coordinatively unsaturated Ru atoms located in between the array of bridging oxygens expose a kind of dangling bond which explains their high reactivity. For the example of CO adsorption which can be observed on the atomic level by STM, the CO was shown to adsorb on the Ru_{cus} sites.

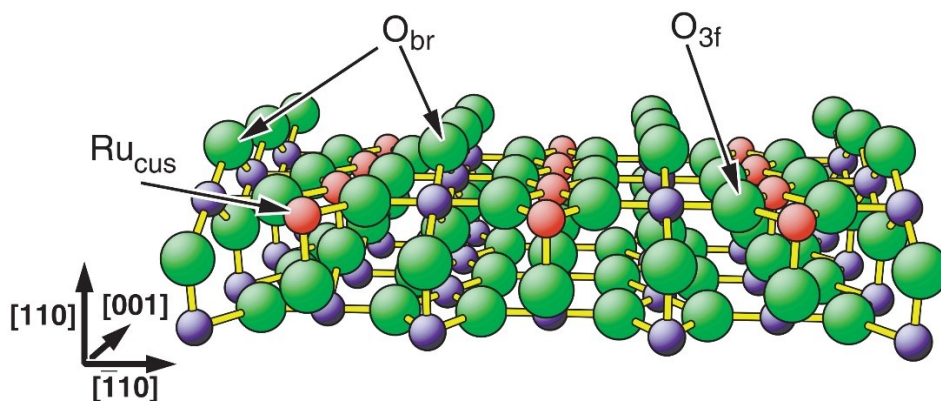


Figure 1 Schematic representation (ball-and-stick) of the $\text{RuO}_2(110)$ surface with empty Ru_{cus} sites. Large (green) balls represent O, and small (blue, red) balls represent Ru atoms of $\text{RuO}_2(110)$.^[6]

Reproduced with permission from Ref. [6]. Copyright 2000, The American Association for the Advancement of Science.

According to DFT calculations, a coupling of the CO 5s orbital with the Ru_{cus} surface atoms and back-donation of d-electrons from the substrate to a $2\pi^*$ orbital of CO is expected.^[6]

The Ru_{cus} sites of $\text{RuO}_2(110)$ exhibit an even stronger Lewis acidity than metallic sites on Ru(0001), which leads to an enhanced dative bond with the lone pair of NH_3 for the example

of ammonia adsorption. Additional hydrogen bonding of NH₃-hydrogen and O_{br} oxygen further increases the adsorption.^[5]

Beyond the adsorption of CO or NH₃ there are numerous reactions catalytically accelerated or even enabled by transition metal oxide surfaces with their unique electronic structure of coordinatively unsaturated d-metals and surrounding oxygen atoms.

In the last decades, with an advancement of analytical and synthesis techniques, nanosized transition metal oxides became ever more present in fundamental science and technological applications. Nanosizing- and structuring of TMOs can serve several purposes from simply decreased dimensions of functional components in silicon-based integrated circuits, over a significant increase of the exposed surface area for catalytically active material towards the formation of transition metal oxides with altered physicochemical properties with respect to those of bulk or single crystalline compounds.^[4]

The decrease in the particles size down to the nanometer regime significantly increases the surface area which scales quadratically with the radius (equation 1)^[7], which has a great impact on the surface-related catalytic applications:

$$S = 4\pi R^2 \quad (1)$$

With this strategy the electrochemical surface area can be increased by up to three orders of magnitude from below 1 m² g⁻¹ to several hundreds of m² g⁻¹.^[8]

Besides the physical increase in surface area, the decrease in nanoparticle sizes well below 10 nm increases the number of corner and edge surface sites and hence significantly changes the ratio of terminal crystal facets.^[4, 9] The latter can have a significant effect on the catalytic properties. Thus, edge sites have been identified as active sites for various catalytic compounds such as Fe-doped NiOOH or CoFe-layered double hydroxide (LDH) graphene composites for the electrocatalytic oxygen evolution reaction, therefore the morphology-controlled facet ratio can change the total catalytic activity of the material.^[10-11]

Distinct crystal facets are furthermore associated with varying catalytic activities under given operation conditions due to different adsorption energies of reactants and/or reaction intermediates. As an example, for IrO_2 and RuO_2 shown in Figure 2, the (100) surface is reported to show the highest OER activity in alkaline media opposed to the thermodynamic most stable (110) surface present from synthesis.^[12] The size of nanoparticles furthermore influences the surface free energy and thus the thermodynamic stability, which can result in a change of cell lattice parameters and structural transformations. Nanoparticles with a negative surface free energy are thereby unstable and prone to dissolution and re-precipitation under given conditions, which can be observed as Ostwald-ripening and growth of particles on the expense of smaller ones.

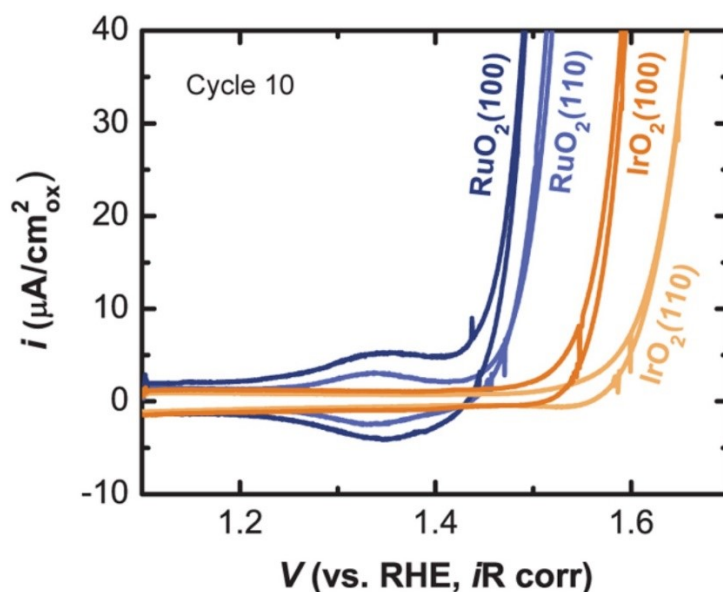


Figure 2 Cyclic voltammetry at a scan rate of 10 mV s^{-1} in O_2 -saturated 0.1 M KOH of the (100) and (110) orientation of RuO_2 (blue) and IrO_2 (orange) employed as oxygen evolution reaction catalyst.^[12]

Reproduced with permission from Ref. [12]. Copyright 2014, American Chemical Society.

A further consequence of the increased surface free energy in nanostructured materials is a possible stabilization of phases that are metastable or instable in bulk materials. This phenomenon was reported in the literature for TiO_2 , VO_x , Al_2O_3 or MoO_x .^[4] Furthermore, nanosizing provides the possibility to access metastable mixed oxide phases with unusual high

ratios of constituent that are not stable in the bulk phase, as for example shown for nanosized transition metal doped β -FeOOH^[13] or V-doped Ni(OH)₂ (Chapter 6).

In addition to aforementioned change of physicochemical properties, the quantum confinement effects^[14] in nanosized transition metal oxides can alter their electronic structure and thereby significantly affect their performance in photocatalytic and/or photoabsorber applications.^{[4, 15-}

16]

Resulting discrete, atomic-like electronic states upon nanosizing can be considered as being a superposition of bulk-like states with an increase in the oscillator strength, which may lead to an energy shift of exciton levels and the optical bandgap E_g . The change of the bandgap can thereby significantly influence the conductivity and chemical reactivity of nanosized transition metal oxides.^[4]

1.2 Nanoscale transition metal oxide electrocatalysts for energy conversion applications

In the following section examples of nanoscale transition metal oxides for energy conversion applications are presented with focus on water electrolysis, photoelectrochemical water splitting and fuel cell applications. The preparation of various nanoarchitectures for MO_x ranging from nanoparticles (0D) over nanorods (1D) and nanosheets (2D) or complex hierarchical 3D networks with electronic features differing from their bulk counterparts guides the way towards novel applications or at least a significantly increased performance.

1.2.1 Water electrolysis

The development of novel catalysts for water electrolysis is mainly focused on the oxygen evolution reaction (OER) at the anode, as it represents a kinetically demanding four electron process. Besides the traditionally employed precious transition metals of the Pt-group, various non-noble (mixed) transition metal oxides were evaluated as OER and/or hydrogen evolution reaction catalysts in recent years.

To increase the activity of heterogeneous surface area-dependent catalysis reactions, nanosizing is a valid approach as it can significantly increase the available surface area from well below $1 \text{ m}^2 \text{ g}^{-1}$ for bulk material to several hundred $\text{m}^2 \text{ g}^{-1}$ for ultra-small nanoparticles. For the preparation of functional electrode layers with efficient charge transport and mass transport characteristic for high catalyst loading per electrode area, the formation of more complex porous three-dimensional (3D) nanostructures is preferred. These structures maintain a high surface area but typically exhibit an increased conductivity across the electrode layer as the number of grain boundaries is significantly reduced versus a random assembly of nanoparticles. The porosity furthermore influences the electrocatalytic performance by restricting (e.g. by pore clogging of gaseous products) or facilitating the mass transport of liquid and gaseous educts and products. Nanosizing can further be used to synthesize

metastable mixed oxide phases with mixing ratios that are not accessible in the bulk but exhibit an increased catalytic performance.^[17-18] A phase separation is thereby inhibited as the formation of a second phase within the nanosized particle is energetically not favorable due to a large interfacial energy.^[19] A further strategy to increase the catalytic performance of transition metal oxides is the formation of defect rich phases (e.g. structural defects with transition metals in differing oxidation state and oxygen vacancies) which can exhibit an increased amount of active sites.^[20] Nanoparticles with defect rich phases may thereby be obtained by rapid kinetically controlled synthesis approaches that do not lead to the formation of the respective phase predicted by thermodynamic equilibrium.

A prominent example of nanosized 0D transition metal oxide structures for OER catalysis are nickel oxide-based nanoparticles. Dispersible NiO^[21] and NiFeO_x^[18] particles of ≈ 2 nm were prepared by Fominykh *et al.* as shown in Figure 3 for Ni_{0.9}Fe_{0.1}O_x with an exceptionally high OER activity of 59 ± 5 mA cm⁻² at an overpotential of 350 mV for the electrode with 10% Fe-doped NiO.

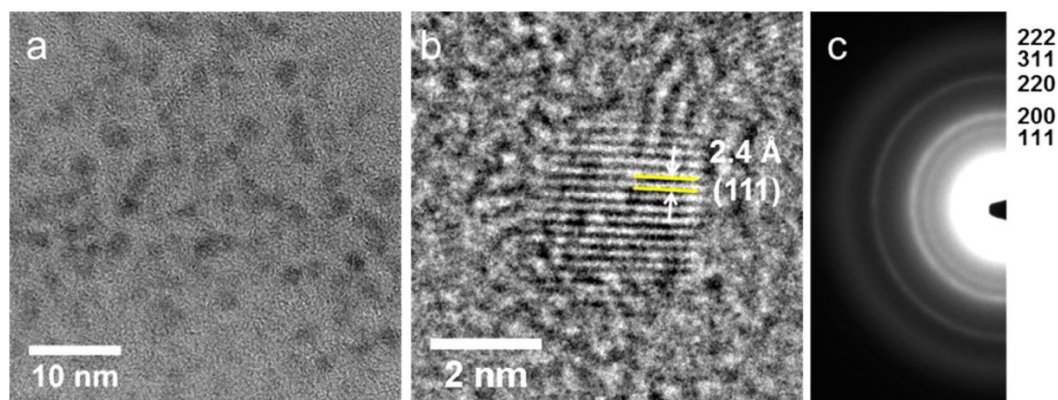


Figure 3 TEM images of Fe_{0.1}Ni_{0.9}O nanoparticles: (a) Overview of dispersed nanoparticles (b) HR-TEM image of a single Fe_{0.1}Ni_{0.9}O particle (c) Electron diffraction pattern with corresponding d-values of the rock salt NiO phase.^[18]

Reproduced with permission from Ref. [18]. Copyright 2015, American Chemical Society.

In addition, the solvothermal synthesis allowed for the formation of NiFeO_x with an unusually high amount of 20 at% Fe, which is above the solubility limit of Fe in the bulk NiO phase.

Mixed nickel cobalt oxide nanoparticles of 2 - 4 nm can be further applied as bifunctional OER and HER catalyst. Depending on the Ni/Co ratio of the $\text{Ni}_{1-x}\text{Co}_x\text{O}$ compositional series an enhanced activity towards the HER (for higher cobalt content) or OER (for higher Ni content) could be observed. With the applied solvothermal synthesis the whole compositional range is accessible in form of small nanoparticles, which is not possible for a respective bulk phase synthesis of the mixed oxide.^[17]

Employing pulsed laser deposition, Xiao *et al.* were able to synthesize an oxygen rich ≈ 8 nm thick Ta_2O_5 layer on carbon fibers with exposed (200) surfaces. The thermodynamically stable (200) surface was thereby identified by DFT calculations as highly OER active with a calculated onset overpotential of 250 mV. Experimentally, an onset overpotential of 0.29 V and an overpotential of 0.385 V at 10 mA cm^{-2} could be determined, which outperforms reported values of IrO_2 as OER catalyst in alkaline media.^[22]

Aiming at the fabrication of more complex metal oxide morphologies and investigating the role of morphology on the catalytic performance, Zhang *et al.* synthesized rod-like (1D), a mixture of rod-like (1D) and sheet-like (2D) or sheet-like (2D) Co_3O_4 as OER catalyst by a microwave-hydrothermal method with a subsequent calcination. Co_3O_4 nanosheets were demonstrated to have the highest performance. It was found that besides the layered sheet structure, this material exhibits an additional mesoporous morphology introduced by the calcination process, thus leading to an extended surface area of $\approx 25 \text{ m}^2 \text{ g}^{-1}$ formed by aggregated nanoparticles of 50 – 100 nm. The catalyst exhibits an overpotential of 399 mV in alkaline media to reach a current density of 0.5 mA cm^{-2} .^[23]

To combine the unique catalytic properties of nanosized transition metal oxides with the high conductivity and porous structure of carbon-based supports, the fabrication of composite materials is a valid approach. It allows for the fabrication of electrodes composed of transition metal oxide nanocatalysts with rather limited conductivity such as manganese oxides. It further

enhances the performance as it allows for a homogeneous dispersion of nanosized catalysts on the conductive carbon support to maximize the utilization.

To obtain a highly active and stable carbon nanotube (CNT)/Au nanoparticle/ Co_3O_4 nanoparticle composite catalyst, Fang *et al.* employed an ultrasonication-assisted loading reaction. The obtained CNT/Au/ Co_3O_4 composite showed an onset potential of 1.56 V vs. RHE and an overpotential of only 350 mV to reach a current density of 10 mA cm^{-2} explained by an accelerated formation of catalytically active Co(IV) sites by the presence of Au nanoparticles.^[24]

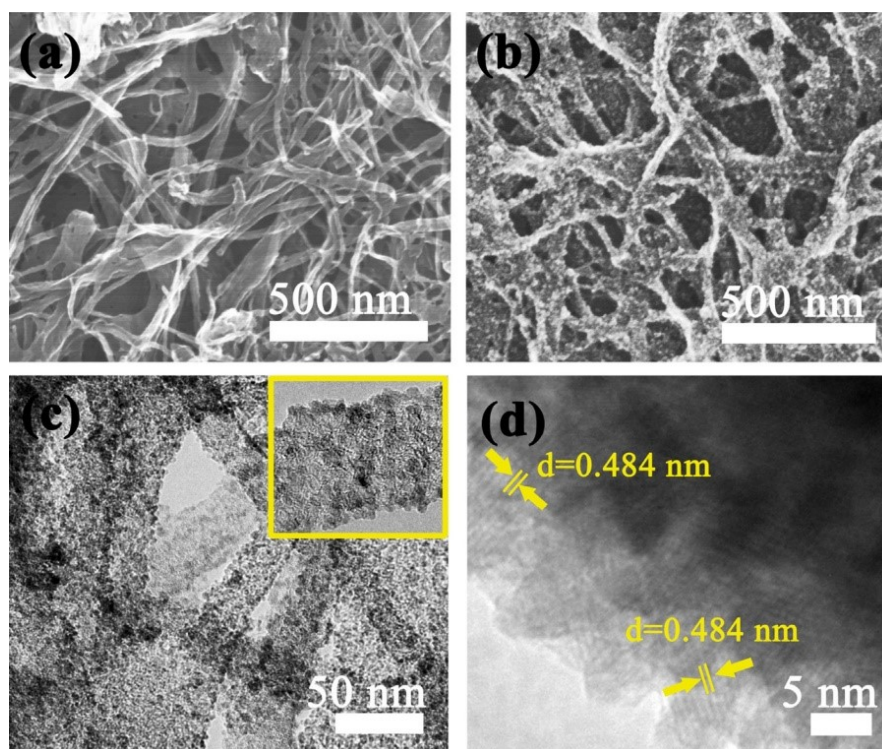


Figure 4 SEM image of bacterial cellulose-derived carbon nanofiber (CNF) (a) and $\text{CoFe}_2\text{O}_4/\text{CNF}$ composite (b). TEM image (c) and HR-TEM image (d) of $\text{CoFe}_2\text{O}_4/\text{CNF}$ composite.^[25]

Reproduced with permission from Ref. [25]. Copyright 2016, Hydrogen Energy Publications, LLC. Published by Elsevier Ltd.

A further example of a composite electrode using a cobalt based OER catalyst was introduced by Liu *et al.* who employed a bacterial-cellulose-derived carbon nanofiber (CNF) 3D network that was loaded with spinel CoFe_2O_4 nanoparticles using a hydrothermal treatment and subsequent pyrolysis. The $\text{CoFe}_2\text{O}_4/\text{CNF}$ catalyst with nanoparticle sizes of $\approx 6 \text{ nm}$ and open

porous morphology advantageous for mass transport of gases is shown in Figure 4. The $\text{CoFe}_2\text{O}_4/\text{CNF}$ composite was evaluated as a highly active bifunctional catalyst with a 72 mV more negative onset potential compared to a commercial Pt/C (20 wt%) HER catalyst and a 50 mV more positive potential compared to a benchmark RuO_2/C (20 wt%) OER catalyst.^[25] Finally, the preparation of transition metal oxide/transition metal/carbon composites was shown by Zhang *et al.* with a Pd-nanoparticle doped MnO_2 nanorod/carbon composite catalyst to lead to synergistic effects that enhance the OER activity beyond the contribution of the individual components. The synergistic effect between Pd and MnO_2 is thereby attributed to the high electronegativity of palladium that acts as an electron drain facilitating the formation of MnOOH-O reaction intermediates in alkaline media through an inductive effect and thereby accelerating the OER kinetics.^[26]

1.2.2 Photoelectrochemical water splitting

The incomplete filling of the electronic d shell of transition metal oxides not only confers unique surface properties used in heterogeneous catalysis but also causes interesting optical and electronic properties applicable in photocatalysis and/or photoabsorption. Among the transition metals a wide range of optical band gaps is observed, which spans from narrow band gap semiconductor like CuO ($E_g = 1.35$ eV) absorbing down to the near infrared to wide band gap semiconductors like SnO_2 ($E_g = 3.8$ eV) with an absorption in the ultra violet region of the electromagnetic spectrum.^[27]

Photoelectrochemical water splitting requires a suitable bulk phase photoabsorption profile to enable fast exciton dissociation and an enhanced light harvesting efficiency, and a proper band alignment for HER or OER, respectively, to provide a thermodynamic driving force for the reaction.^[27] Besides, suitable electrocatalytic properties of the photoabsorber surface are needed to enable the fast reaction of photogenerated electrons and holes with water molecules without charge recombination. Photoelectrochemical as well as electrochemical water splitting

require fast charge transport, high density of catalytic sites, and, concerning charge transport, a long carrier lifetime and high recombination resistance.^[27] These properties can be enhanced via a careful optimization of photoabsorber nanomorphologies as depicted in Figure 5.

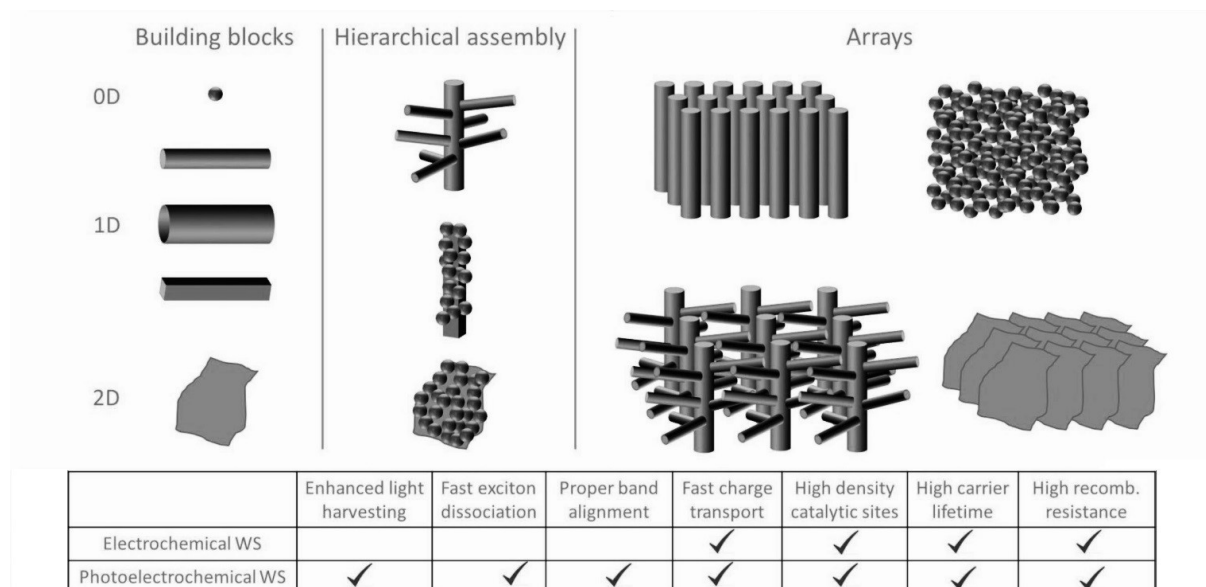


Figure 5 Different kinds of 0D, 1D, 2D MO_x building blocks applied for the fabrication of hierarchical structures and arrays. The collective properties of arrays regarding efficient electrochemical and photoelectrochemical water splitting application are summarized.^[27]

Reproduced with permission from Ref. [27]. Copyright 2017, WILEY-VCH Verlag GmbH & Co. KGaA, Weinheim.

Figure 6 thereby depicts a $\alpha\text{-Fe}_2\text{O}_3$ (hematite) photoanode constructed of an array of nanorods oriented perpendicular to the substrate and optimized in thickness and spacing for an efficient light absorption and charge percolation. Nanowires of 50 – 100 nm thickness and a length of 1 – 5 μm constitute an optimum regarding the limited hole diffusion length to the surface (across the wires) and a sufficient photon absorption across the film thickness as well as a direct electron conduction pathway to the conductive substrate. The spacing between the nanowires can finally further enhance the light absorption by internal reflections and multiple scattering of incoming radiation.^[28]

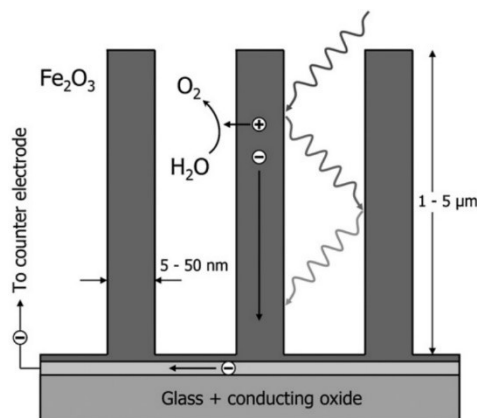


Figure 6 **Optimized morphology for an α -Fe₂O₃ photo-anode for water splitting. The small diameter of the nanowires ensures short hole diffusion path lengths.**^[28]

Reproduced with permission from Ref. [28]. Copyright 2008, The Royal Society of Chemistry.

Another suitable nanomorphology for anodes employed in photoelectrochemical water splitting are inverse opal-like structures that combine a high surface area with thin structural elements resulting in low hole diffusion distances and an increased light absorption due to the possibility of using micrometer thick electrodes.

Among others, α -Fe₂O₃^[29], ZnFe₂O₄^[30] and BiVO₄/WO₃^[31] were synthesized in form of inverse opal structured photoanodes for water splitting. As an example, Figure 7 depicts an inverse opal Sb-doped SnO₂ (ATO) nanostructure with homogeneous ZnFe₂O₄ coating applied by atomic layer deposition by Hufnagel *et al.*^[30]

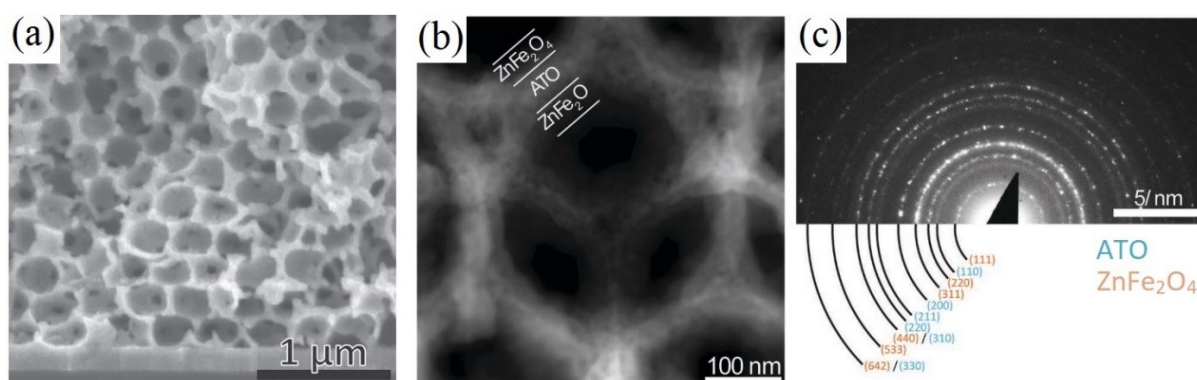


Figure 7 **SEM image (a), TEM image (b) and respective electron diffraction pattern (c) of inverse opal nanostructured Sb-doped SnO₂ coated with a thin layer ZnFe₂O₄ as photoanode for photoelectrochemical water oxidation.**^[30]

Reproduced (modified) with permission from Ref. [30]. Copyright 2016, WILEY-VCH Verlag GmbH & Co. KGaA, Weinheim.

The authors have demonstrated that the inverse opal nanomorphology in conjunction with a conductive ATO photoabsorber and -catalyst support could increase the photocurrent by a factor of 5 as compared to a flat ZnFe_2O_4 film.^[30]

A further advantage of the inverse opal photoabsorber morphology mentioned above is the possibility of loading it with additional highly active OER co-catalysts as demonstrated by Shi *et al.* for (Co-Pi)/ α - Fe_2O_3 electrodes. With this nanoscale structure they could lower the photocurrent onset potential by ≈ 150 mV and improve the photocurrent of the anode especially at low potentials by reducing electron hole recombination.^[29]

1.2.3 Fuel cell and oxygen reduction reaction catalysts

Besides being employed as catalysts for the OER in water electrolysis, transition metal oxides were evaluated regarding their applications in proton-exchange membrane fuel cells (PEFC) as co-catalytic nanostructures and functional support structures.

Nanosized transition metal oxides may not replace the scarce noble metal platinum in PEFCs but they can be successfully employed as co-catalyst to increase the overall catalytic ORR performance at the cathode by synergistic effects based on a bifunctional reaction mechanism. This can be explained by a possible adsorption of reaction intermediates at the hydroxyl group terminated surfaces in spatial proximity to the catalyst active sites.^[32]

TMOs were also evaluated as stable catalyst support materials which allow a high dispersion of scarce noble metal particles, reduce their agglomeration and indirectly influence the catalytic performance by electronic metal-support interactions which further increase the catalytic activity.^[32]

Examples of PEFC ORR co-catalyst and supports include (doped) TiO_x ,^[33] WO_x ,^[34-35] MoO_x ,^[36] and CeO_2 ^[37]. For the case of a Pt/C- MoO_2 composite with ≈ 5 nm MoO_2 particles synthesized by Yan *et al.*, the catalytic performance normalized to the noble metal could be

improved from 98.4 mA mg_{Pt}⁻¹ to 187.4 mA mg_{Pt}⁻¹ at 0.9 V vs. RHE by the addition of the MoO₂ particles.^[36]

Besides the application in PEFCs with a required acid stability of the employed catalysts in contact with the perfluorinated membrane, various nanosized and -structured transition metal ORR catalysts were reported to date.^[38] As an example, nanosized Co₃O₄/N-doped graphene^[39] or Co₃O₄/CNT composites^[40] exhibit high ORR activities, which even outperform state-of-the-art Pt in alkaline solution.

Nanosized copper oxides (CuO_x) are a further non-precious metal alternative as ORR catalyst in alkaline media, which also require a carbon composite formation due to their limited conductivity and catalytic activity.^[38]

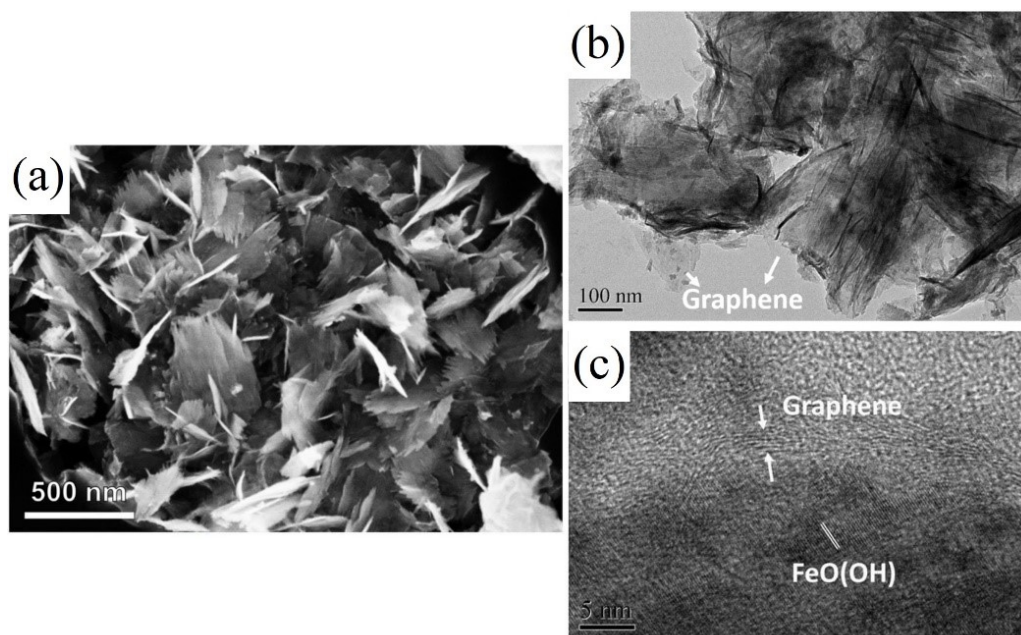


Figure 8 SEM image (a), TEM image (b) and HR-TEM image (c) of nano-Fe₃O₄ / graphene composite ORR catalyst.^[41]

Reproduced (modified) with permission from Ref. [41]. Copyright 2015, 2015, American Chemical Society.

Finally, nanostructured and -sized iron oxides have been reported for their use as non-precious metal ORR catalysts with rather limited electrocatalytic activities and a high dependency on the synthesis method and resulting nanostructure. Among others, nano-Fe₃O₄/graphene

composite synthesized by Zhao *et al.* (Figure 8) exhibits an increased ORR and OER performance that was attributed to the synergistic coupling effects between iron oxide and graphene.^[38]

1.3 Nanomorphology and particle size control

1.3.1 Synthesis of metal oxide nanoparticles

Nanoparticles can be generally synthesized using the “top-down” approach that uses a mechanical disintegration of bulk material by various physical methods, or the “bottom-up” approach that employs solution phase colloidal chemistry with respective precursors, solvents and possibly additional structure directing agents. Although the “top-down” approach is easily scalable, it offers very low control over the particle shape, size and particle size distribution. The “bottom-up” synthesis approach with soluble molecular precursors gained considerable attention in the last decades as it allows the controllable formation of nanoparticles and higher order structures not accessible from the bulk.^[42]

In general, crystalline metal oxide nanoparticles can be obtained by various synthesis routes with a main focus on colloidal and sol-gel chemistry. Among them, the non-aqueous liquid phase synthesis can be divided into surfactant-directed and solvent controlled routes according to the mechanism of particle growth. The surfactant-directed approaches generally provide excellent control over the crystal size and shape, result in a narrow particle size distribution and exhibit a low agglomeration tendency and good redispersibility. However, the good dispersibility related to organic capping agents results in a large amount of organic impurities with often negative effects on electronic or surface related applications of the nanoparticles.^[43]

A typical example of this synthesis approach is the hot injection method, where the reagents are injected in a hot surfactant solution and converted to the oxides at temperatures around 250-350 °C.^[44]

On the other hand, solvent-controlled approaches that are employed in the course of this work and schematically depicted in Figure 9 often result in a low amount of organic impurities with a related good accessibility of the nanoparticle surface, which is favorable for catalytic applications.^[43]



Figure 9 Schematic synthesis scheme of a solvent directed non-hydrolytic metal oxide nanoparticle formation.^[45]

Reproduced (modified) with permission from Ref. [45]. Copyright, 2015 Wiley-VCH Verlag GmbH & Co. KGaA.

The solvent controlled routes offer simple and robust synthesis protocols for many oxides. The disadvantage of this mechanism is however a lower control of the crystallite size and shape, a slightly broader size distribution and the possible formation of agglomerates and a restricted re-dispersibility.^[43]

A prominent example of the solvent controlled nanoparticle synthesis is the non-aqueous benzyl alcohol route introduced by Niederberger *et al.*. The synthesis usually employs metal organic precursors but is applicable also for metal salts and allows for the formation of highly crystalline nanoparticles as well as organic-inorganic hybrid materials.^[46-47] According to spectroscopic studies of the formation of yttrium oxides from an yttrium tris(iso-propoxide) precursor, two parallel reaction mechanism are proposed as shown in Figure 10.

Figure 10a describes a secondary hydride-transfer reaction which leads to the disproportionation of benzyl alcohol to toluene and benzyl aldehyde, whereas Figure 10b depicts the parallel formation of an yttria benzoate nanocomposite.^[48]

The *tert*-butyl alcohol route introduced by Fattakhova-Rohlfing *et al.* is a further prominent solvent-directed nanoparticle synthesis approach successfully applied to a wide range of transition metals oxides as well as transition metal nanoparticles.^[45] Similar to the benzyl alcohol route, *tert*-butyl alcohol acts as the solvent and as an oxygen donor, although the reaction mechanism is not fully understood yet as it has proven difficult to gain experimental

information about the organic–inorganic interphase involving a complex role of the organic species.^[43]

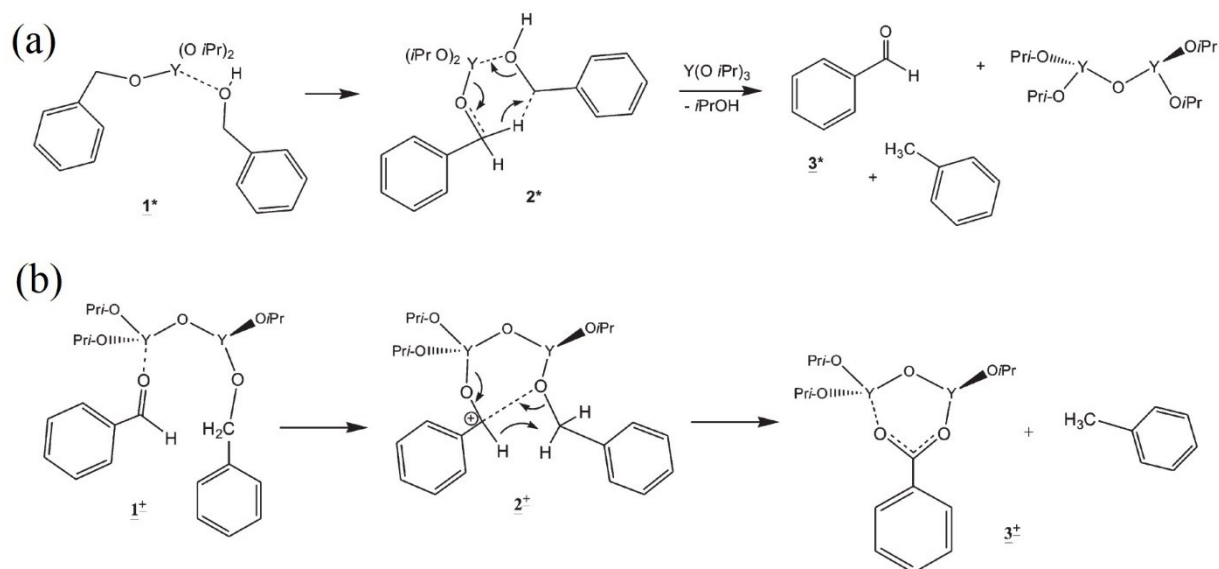


Figure 10 (a) Secondary hydride-transfer reaction with disproportionation of benzyl alcohol. (b) Proposed mechanism for yttria-benzoate formation.^[48]

Reproduced with permission from Ref. [48]. Copyright, 2005 WILEY-VCH Verlag GmbH & Co. KGaA, Weinheim.

Examples of transition metal oxides successfully prepared by this synthesis route are ultra-small and crystalline anatase TiO_2 particles,^[49] Nb-doped conductive TiO_2 nanoparticles,^[50] and nickel and cobalt-oxide based nanocrystals for (photo) electrochemical water splitting^[17-18, 21, 51]. In analogy to the benzyl alcohol route, also the formation of inorganic/organic composite materials was shown by the preparation of Sb-doped SnO_2 nanoparticles on reduced graphene oxide as high capacity and rate capable lithium ion battery anode by Zoller *et al.*^[52] Other solvent assisted synthesis routes for nanoparticles include the diisopropyl ether route that employs chloride precursors and is also suitable for the fabrication of mesoporous structures or xerogels.^[45] Other oxygen containing solvents (e.g. ketones and aldehydes) different from alcohols and ethers were investigated by applying the acetophenone route. The carboxylic acid route uses the non-hydrolytic M-O-M bond formation by elimination of the respective ester

between metal alkoxides and carboxylic acid for the formation of nanoparticles. Finally, the benzylamine route employs acetylacetonate metal precursors reacting with benzylamine and leading to the formation of corresponding metal oxides with the supply of oxygen from the decomposition of acetylacetonate.^[45]

In contrast to the precisely controllable non-hydrolytic mechanisms that often yield highly crystalline nanoparticles, aqueous surfactant-free sol-gel chemistry that was also employed in the course of this thesis is quite complex and often results in the formation of amorphous particles.^[44]

Due to the multiple function of water as the solvent, ligand and reactant a variety of parameters such as the hydrolysis and condensation rate of the metal oxide precursor, pH value, temperature, way of mixing, rate of oxidation and presence and concentration of ions in solution influence the formation of nanoparticles and need to be controlled.^[44]

However, the aqueous synthesis route offers the great advantage of the absence of any organic ligands negatively affecting the nanoparticle surface in terms of their catalytic properties. The formation of an amorphous phase is furthermore not necessarily a disadvantage for the potential application of nanoparticles as electrocatalytic water oxidation catalysts, as reported for highly active amorphous CoO_x ,^[53] CoWO_4 ^[54] or IrO_x ^[55] nanoparticles.^[43]

In general, an aqueous sol-gel process is governed by the conversion of a precursor solution into an inorganic solid via inorganic polymerization reactions caused by hydrolysis in water. Typically, metal alkoxide precursors that easily hydrolyze in water are employed to obtain a sol as depicted in Figure 11, although also simple and less reactive transition metal salts can be employed that require in some cases the change of the pH value.^[44] Generally, the hydrolysis is succeeded by an ageing step of the sol that leads to gelation or particle growth/precipitation. The following processing steps are decisive for the final structure of transition metal oxides as

shown in Figure 11. A final drying step or thermal treatment is required to obtain oxides from the wet hydroxide/oxide containing gels and precipitates.^[44]

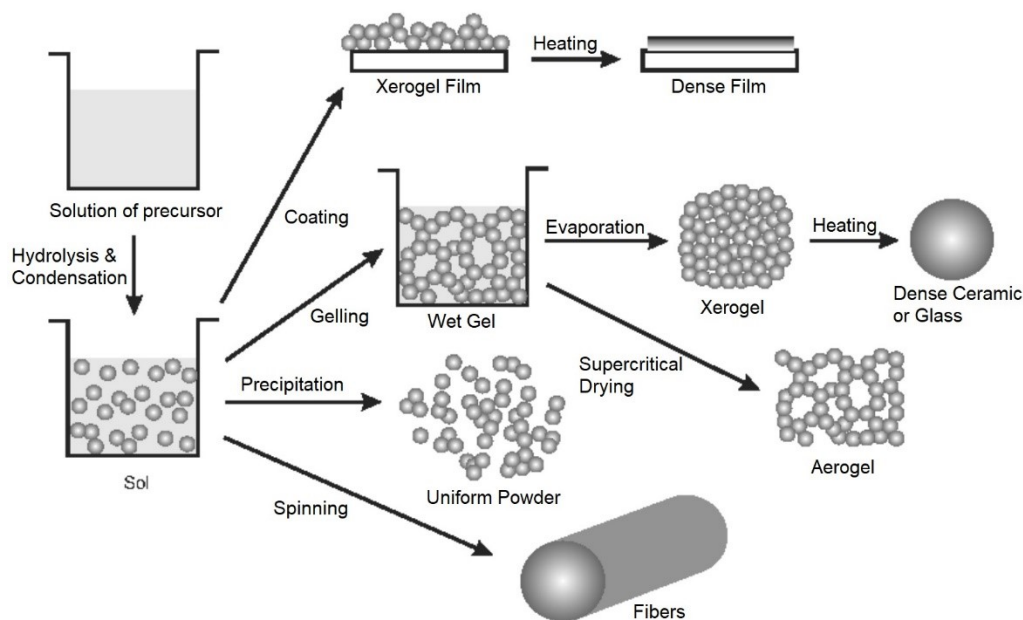
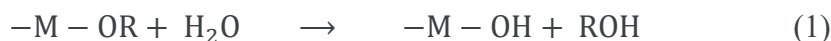


Figure 11 Aqueous sol-gel process and the fabrication of transition metal oxide nanostructures by further processing steps.^[44]

Reproduced with permission from Ref. [44]. Copyright, 2009, Springer-Verlag London Limited.

Concerning the reaction mechanism, the alkoxides need to be distinguished from the salts as the former hydrolyze via a well-studied nucleophilic aliphatic substitution reaction by the oxygen of the water as following:^[44]



The further condensation of formed hydroxides as well as the reaction with the alkoxide precursor result in the formation of an -M-O-M- bond:^[44]



In contrast to the alkoxides, the sol-gel transformation of the transition metal salt precursors proceeds via the formation of condensed species from the aqueous solution. The hydrolysis

reaction is thereby dependent on the change of the pH, the temperature or the oxidation state of the transition metal as well as the presence and the concentration of counter ions, which renders this process rather complex and difficult to predict, especially concerning the formation of different nanomorphologies.^[44]

Besides the aforementioned synthesis methods with liquid solvents, the molten salt synthesis (MSS) route can be used to obtain small transition metal oxide nanoparticles with high uniformity, good control over the crystallite size and morphology as well as a reduced level of agglomeration. Typically, individual salts (NaNO₃, NaCl, KCl, Li₂SO₄, Na₂SO₄ etc.) or (eutectic) mixtures such as 0.5 mol% NaCl - 0.5 mol% KCl are employed to adjust the melting point and define the reaction conditions.^[56-57]

Interestingly, the synthesis conditions in the melt are reported to increase reaction rates when decreasing the synthesis temperature. This fact allows for the formation of uniform transition metal oxide nanoparticles with differing crystallinity not accessible by other synthesis methods (e.g. thermal oxidation/decomposition of precursors in air), which can exhibit unique catalytic properties.^[58-60]

In contrast to the flux method where only minor amounts of salts are introduced to a precursor mixture, in the MSS method an excess of individual salts or mixtures thereof is employed which act as soluble reaction media at elevated temperatures. By the choice of the salt and/or use of eutectic compositions, the melting and thus reaction temperature can be controlled, which directly influences the nanoparticle growth. In principle, the properties of the resulting nanosized transition metal oxides are governed by the choice of the precursor (typically chlorides or sulfates), pH, temperature and duration of the applied heating profile and the melting salts. An advantage of this method is its simplicity, reliability and scalability: If all parameters are well-controlled, highly uniform nanoparticles can be obtained with simple experimental equipment in large quantity.^[56-57]

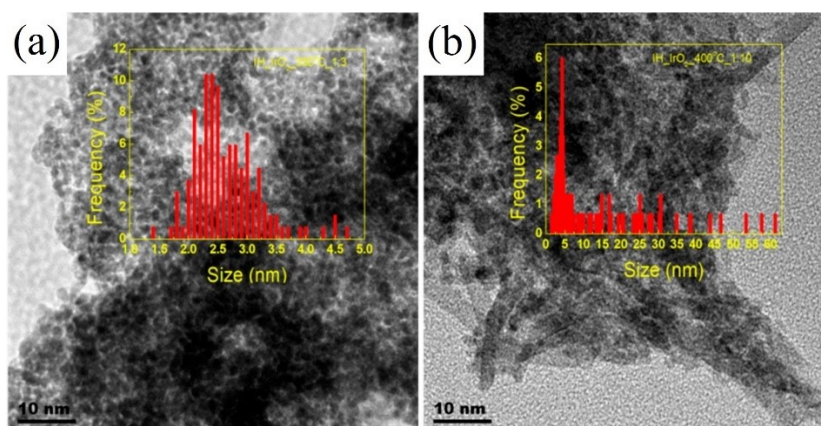


Figure 12 Transmission electron microscope images of small spherical IrO_2 obtained from molten salt (NaNO_3) synthesis at 350 °C (a) and spherical and rod-like IrO_2 crystals obtained at 400 °C (b).^[58]

Reproduced with permission from Ref. [58]. Copyright, 2019, the authors.

Besides the most important routes introduced above, nanosized transition metal oxides can also be obtained by a variety of other less common approaches such as sonochemical synthesis,^[61] thermal decomposition of precursors^[62] or combinations and subtypes of the introduced routes (e.g., two-phase aqueous/organic liquid^[43] or reduction of molecular precursors with subsequent oxidation to form transition oxide nanoparticles^[42]).

1.3.2 Fabrication of 1D - 3D metal oxide nanostructures

Beyond the synthesis of 0D nanoparticles including rod-like particles, there exist numerous methods for the controllable formation of nanowires (1D),^[63] nanosheets (2D)^[64-65] and complex porous and/or hierarchically 3D metal oxide nanostructures.^[43, 66-67] The nanomorphology can decisively influence the performance of materials in electrocatalysis or electrochemical energy storage as compared to a random assembly of nanoparticles.

1D Nanowires of ZnO , CdO , In_2O_3 and TiO_2 can be obtained for example by the vapor-liquid-solid (VLS) mechanism with metal nanoparticles used as nucleation seeds. A variety of transition metal oxides wire structures can further be prepared by electrospinning.^[66, 68-69] The elongated morphology of electrospun nanowires provides the charge percolation pathways

along the wire direction, which, together with an increased surface area and possible confinement effects, can lead to unique electronic properties due to the small wire diameter.

Macías *et al.* reported the fabrication of mesoporous TiO₂ and Ta- and Nb-based oxide nanofibers by electrospinning of a non-ionic surfactant (Pluronic® P-123, F-127 or Brij76) containing gel that was prepared by a sol-gel process with the respective metal oxide precursor.

Figure 13 depicts mesoporous Ta₂O₅ nanofibers that exhibit a surface area of 175 m² g⁻¹ with a pore size of about 2 nm derived from the surfactant induced soft-templating.^[69]

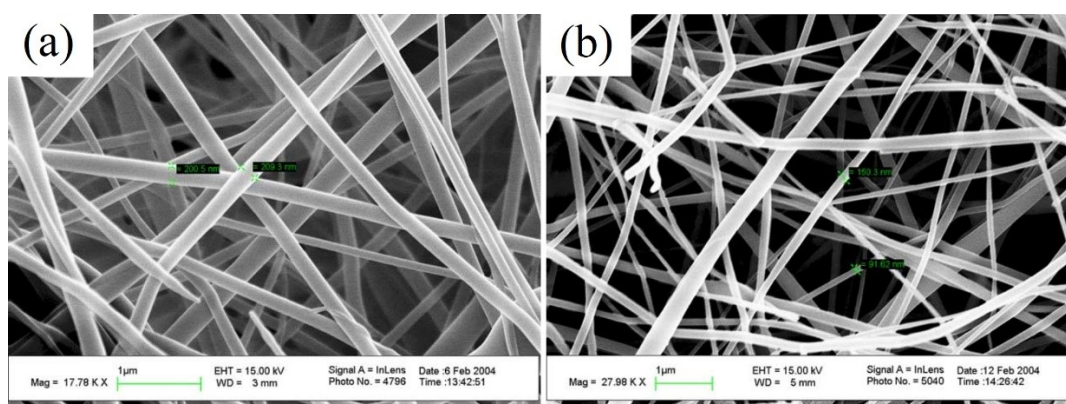


Figure 13 Scanning electron microscope images of mesoporous Ta₂O₅ fibers obtained by electrospinning (a) before and (b) after calcination in air at 350 °C.^[69]

Reproduced with permission from Ref. [69]. Copyright, 2005 Elsevier Inc. All rights reserved.

An example of an ordered nanowire architecture for catalytic applications is given by Cummins *et al.* who synthesized a core-shell MoO₃/MoS₂ nanowire array by chemical vapor deposition, sulfurization and hydrazine treatment for efficient hydrogen evolution reaction.^[70]

2D metal oxide sheet morphologies have attracted significant interest due to their large surface-to-volume ratios and for thin layer thickness and electron confinement in one dimension.^[71]

The large surface area can facilitate heterogeneous catalysis whereas confinement effects of metal oxide nanosheets can lead to altered magnetic properties such as ferro/ferrimagnetic to superparamagnetic transitions or an unexpected insulator-metal behavior.^[66, 72]

There exist a variety of different synthesis techniques based either on exfoliation (the top-down approach) or assembly from molecular precursors (bottom up approach). Exfoliation can be employed for layered transition metal oxides which are composed of slabs of typically corner or edge sharing MO_6 octahedra that form ionic bonds with the adjacent alkali ions between them. By cation-exchange with bulky organocations and expansion by introduction of water in the interlayer region the slabs can finally be separated, typically by shaking or sonication.^[72]

2D nanostructures of non-layered transition metal oxides that are not accessible via exfoliation can be formed as single layers by surface oxidation as shown for Cu_2O or by TiO_2 .^[73-74] A further possibility resulting in individual TMO nanosheets is physical vapor deposition on single crystal metal surfaces or the recently introduced liquid metal-based reaction route with gallium-based alloys at room temperature and above.^[72] Further specialized techniques not relevant for large-scale synthesis of 2D TMOs include pulsed laser deposition (PLD), molecular beam epitaxy (MBE) and metal-organic chemical vapor deposition (MOCVD).^[72]

An alternative approach for the formation of larger quantities of potentially solution processible 2D nanostructures are self-assembly mechanisms described for a variety of layered and non-layered TMOs. Hydrothermal or solvothermal reactions with the respective metal oxide precursors can result in the formation of 2D nanostructures by precisely controlling the reaction conditions such as the solvent, precursor, temperature, concentration and pH-value as shown for the synthesis of CuO or Eu_2O_3 2D structures.^[72] Yang *et al.* have been able to demonstrate that nanosheets of the cobalt and nickel-cobalt rock-salt structure form via self-assembly of an intermediate nanoparticle phase using environmental TEM investigations.^[71]

A more controllable synthesis of 2D structures is given by the usage of surfactants such as cetyltrimethylammonium bromide (CTAB). According to Sun *et al.*, the latter leads to a self-assembly of metal-oxide precursor oligomers into lamellar structures before condensation,

polymerization and crystallization to finally form the 2D sheet structure, thus decreasing the dependence on a precise control of reaction conditions.^[72, 75]

3D metal oxide nanostructures with unique porosity can be obtained by a variety of physical and chemical synthesis routes. The available synthesis routes can in principle be divided, similar to the formation of 2D materials, into a non-templated (spontaneous) formation that is strongly dependent on the exact synthesis conditions (choice of precursors, concentration, temperature, pH-value, solvent, etc.) and templated synthesis approaches of 3D nanomorphologies.

For the synthesis of 3D-nanostructured titania the following synthesis strategies were successfully employed: casting of preformed titania species, sol-gel processes, low-temperature processing, electrostatic, -phoretic and -chemical deposition techniques as well as soft- and hard-templating approaches such as evaporation induced self-assembly (EISA) and colloidal crystal templating.^[67]

A certain porosity required for an application (e.g., catalysis or for electrochemical energy storage) can be adjusted by the choice of suitable metal oxide building blocks and their assembly. A more precise control over the pore structure is however achieved using a templating approach, for example with polymeric soft-templates such as amphiphilic poly(alkylene oxide) block copolymers (e.g. Pluronic® P123, F127).^[76] Soft templating is based on a spontaneous self-assembly of amphiphilic polymers into supramolecular micellar structures acting as the porosity templates. The shape and size of the individual micelles as well as the morphology of the micelle assemblies in more complex secondary structures depend on the type and concentration of the polymer, the type of solvent, the pH value and the ionic strength of the solution, the presence of other species (thus the self-assembly process is strongly influenced by the presence of metal oxide precursors), temperature and humidity. Upon adjusting the synthesis conditions, the metal oxide precursor – polymer hybrids with a defined

morphology can be obtained in a very reproducible way, resulting in 3D-metal oxide frameworks after thermal treatment and polymer removal.^[76-77]

One of the important 3D-nanostructures is the so called “inverse-opal” morphology, which was extensively employed in this thesis for the fabrication of support structures for electrocatalysts. Using soft- or hard-templating and respective sol-gel routes, pure or mixed phase oxides are accessible that exhibit a very high porosity derived from an interconnected pore system with narrow pore size distribution defined by the templating agent. The interconnected metal oxide walls form a continuous framework that provides charge transport pathways through the porous layer as depicted in Figure 14.^[77-78]

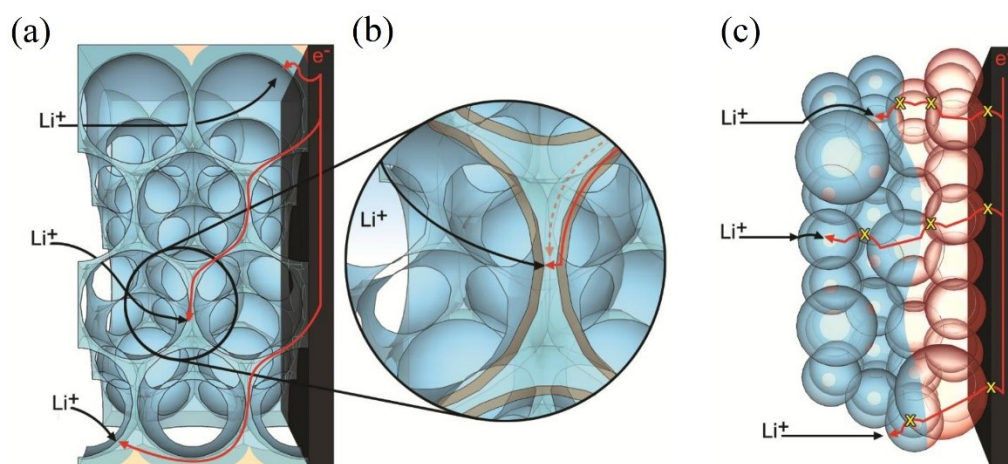


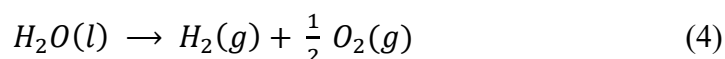
Figure 14 Lithiation and charge percolation pathways in (a, b) 3D ordered transition metal oxide (e.g. TiO_2) and (c) (nano)particle-based electrodes for electrochemical energy storage. Active material indicated in blue and potentially inaccessible material highlighted in red with interfacial boundaries marked with 'x'.^[78]

Reproduced (modified) with permission from Ref. [78]. Copyright, 2016 Elsevier Ltd. All rights reserved.

Typical applications that benefit from this nanomorphology are electrochemical energy storage materials (battery electrodes and supercapacitors)^[77-78] and heterogeneous catalysts (electrochemical and photoelectrochemical water splitting)^[30, 79-80] as it offers an increased electrochemically active surface area, increased conductivity through a continuous charge percolation pathway with increased mean cross section compared to stacked spherical particles (Figure 14b,c) as well as enhanced diffusion and/or mass transport across the macroporous electrode.

1.4 Nanosized transition metal oxide catalysts for water electrolysis

The fundamental process of water electrolysis is defined by a decomposition of typically liquid H₂O into gaseous hydrogen and oxygen at the interface of two opposing electrodes immersed in an electrolyte and driven by an external supply of electrical energy.



It was Michael Faraday in the 18th century who investigated the relation between the measured current i and the amount n (respectively the volume) of hydrogen and oxygen evolving at the cathode and anode respectively to establish his famous relation.^[81-82]

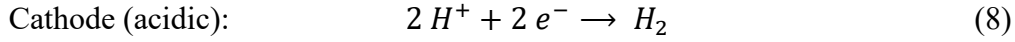
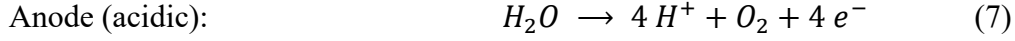
$$i = z n F \quad (5)$$

with z being the number of electrons involved in the redox reaction and F being the Faraday constant of 96485 C mol⁻¹.^[81] As the fundamental redox reactions involved in the water splitting process are invariable, the required cell voltage governed by the thermodynamics of educts and products as well as contributing additional losses (ohmic, kinetic, diffusion, etc.) is of research interest. The theoretical minimum cell voltage required for electrolysis in an open cell can be obtained from the Gibbs free energy for H₂O formation from the elements under standard conditions ($(p, T) = \text{const.}$):^[82]

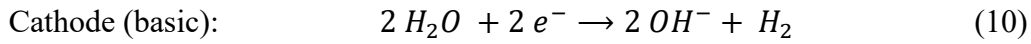
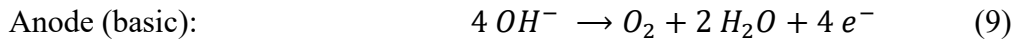
$$E_{cell}^0 = \frac{-\Delta G^0}{zF} \quad (6)$$

At standard reaction conditions ($p^0 = 1 \text{ bar}$, $T^0 = 298 \text{ K}$) the change in Gibbs free energy (ΔG^0) for the reaction is 237.22 kJ mol⁻¹, which corresponds to a required cell voltage of $E_{rev}^0 = 1.23 \text{ V}$. However, considering the thermoneutral voltage derived from the change in standard enthalpy (ΔH^0) without additional heat flux from the surrounding, a voltage of $E_{thermoneutral}^0 = 1.48 \text{ V}$ is required. Reaction with cell potentials of $E_{rev}^0 < V < E_{thermoneutral}^0$ are thereby

endothermic, and voltages exceeding $E^0_{thermoneutral}$ lead to an exothermic reaction.^[81-82] An important factor influencing the reaction mechanism and the standard reaction potentials of the opposing electrodes is the pH-value. Under acidic conditions the following half-cell equations can be formulated, as mainly protons are involved in the redox reactions:^[81]



In alkaline media hydroxide anions are the main redox active species:^[81]



Following from these equations, the Nernst or equilibrium potential of both half-reactions is pH-dependent and shifted by $-0.06 \times \text{pH}$ value, which again results in a pH-value independent $\Delta E = 1.23 \text{ V}$ for the overall water splitting reaction as shown in Figure 15.

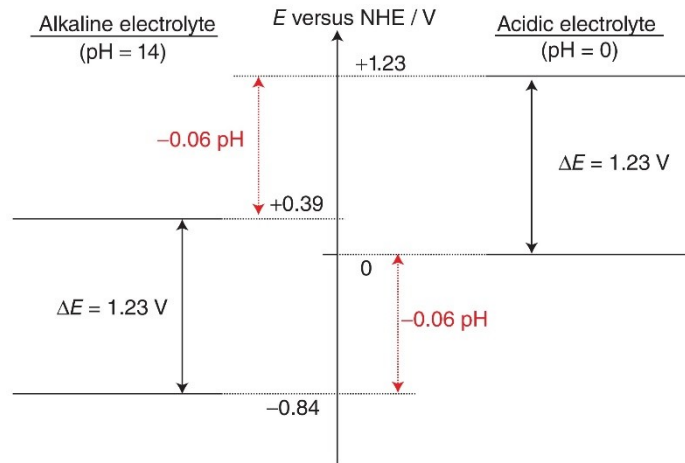


Figure 15 Electrode potentials versus pH for the water splitting reaction.^[82]

Reproduced with permission from Ref. [82]. Copyright, 2015 Wiley-VCH Verlag GmbH & Co. KGaA.

This can be explained, as the potential of the anodic and cathodic half-cell can be formulated as follows:^[82]

$$E_{anode} = E^0_{H_2O/O_2} + \frac{RT}{zF} \ln \frac{(a_{H^+}^2)(f_{O_2}^{\frac{1}{2}})}{a_{H_2O}} \approx 1.23 \text{ V} - 0.06 \text{ pH} \quad (11)$$

$$E_{cathode} = E_{H_2/H^+}^0 + \frac{RT}{zF} \ln \left(\frac{a_{H^+}^2}{f_{H_2}} \right) \approx -0.06 \text{ pH} \quad (12)$$

In a practical electrolyzer the cell voltage (V_{cell}) exceeds the theoretical value of 1.23 V due to overpotentials ($\eta_{cathode}$, η_{anode}) required to overcome kinetic limitations of the cathodic and especially anodic half-reaction as well as the cell resistance (R_{cell}) that becomes relevant at elevated current densities:^[83]

$$V_{cell} = E^0 + (\eta_{cathode} + \eta_{anode} + iR_{cell}) \quad (13)$$

More precisely, the overpotential of each half-cell is composed of an activation overpotential which is dependent on the catalyst material, utilization and loading and a mass transport overpotential governed by diffusion processes.^[84]

There is considerable research interest in the development of novel, highly active catalysts for the oxygen evolution reaction at the anode to increase the overall efficiency of electrolysis. The OER thereby requires a relatively high overpotential due to a rather complex four electron and proton-coupled pH-dependent reaction mechanism. There are several (also material specific) proposed OER reaction pathways, which involve at least two different adsorption intermediates (-OH and -O) with a suggested possible third -OOH intermediate.^[82, 85-87]

Nanosized and -structured transition metal electrodes with defined porosity and nanomorphology can serve as highly active and stable OER catalysts in both acidic and basic environments as well as in the neutral pH-regime.^[88-90]

Platinum group metals (PGM) including Pt, Ru, Rh, Ir and Pd with special focus on Pt have shown excellent catalytic activity towards the hydrogen evolution reaction in both acidic and alkaline environment.^[91-92] To maximize the PGM metal utilization, the increase in the number of catalytic active sites by fabrication of nanostructures, deposition of thin layers (down to monolayers) of Pt on low cost material as well as alloying were investigated.^[91-92]

For the oxygen evolution reaction in acidic media only the scarce PGM iridium and its oxide are proven to be stable enough electrocatalysts under the harsh oxidizing and acidic conditions at the anode to allow for long-term electrolysis in an industrial application in the form of PEM electrolyzers.^[84, 93] Due to the kinetically demanding oxygen evolution reaction, even higher catalyst loadings than the ones for the coupled cathodic reaction are required when the catalyst layer morphology is not optimized.^[94] To decrease the noble metal loading without compromising the electrocatalytic activity, different ways of electrode morphology optimization have been investigated, among which nanostructured iridium oxide, alloys and supported catalysts show the most promising performance as will be discussed in more detail in this thesis (Chapters 1.5.2, 7 and 8).

Electrolysis under alkaline conditions offers the advantage of a possible use of earth abundant, non-noble transition metal oxides with a special focus on the highly OER active Fe-doped $\text{Ni}(\text{OH})_2$ as well as cobalt-based electrocatalysts.^[95-96]

Although there is no strict requirement for an increase of the mass-based activity of earth-abundant transition metal oxide catalysts, research on nanosizing and nanostructuring led to a significantly increased electrocatalytic activity by lowering the overpotential due to an increased number of accessible active sites, optimized mass transport in the electrode layer through a defined porosity or doping elements in unusual high concentrations in nanosized metastable phases.^[18, 97-98] Fabrication and detailed discussion of respective nanosized earth-abundant transition metal oxide OER catalysts are presented in the Section 1.4.1 and Chapters 5 and 6.

1.4.1 Oxygen evolution reaction catalysis with earth abundant transition metals

Alkaline electrolysis is a mature technology that has been industrially employed over the last decades. Nickel-based/stainless steel mesh electrodes are typically used for both hydrogen and

oxygen evolution reactions. The electrodes are typically operated in a concentrated solution of KOH or NaOH at elevated temperatures with current densities of up to 500 mA cm^{-2} .^[96] Although acidic electrolysis allows for higher current densities and avoids the handling of corrosive electrolyte, the main advantage of alkaline electrolysis is the possibility to employ relatively cheap and earth abundant transition metal oxide catalysts that can be stably operated for thousands of hours.^[95-96, 99]

Besides highly active cobalt and nickel-based phosphides,^[100-102] sulfides^[103-104] and selenides,^[105-106] mainly the nickel and cobalt oxides^[18, 107-108] and more specifically their catalytically active form of oxyhydroxides^[109-111] as well as layered double hydroxides^[112-113] are reported as efficient and long-term durable OER catalysts under alkaline conditions.^[99]

A general trend in the OER activity of transition metals and oxides can be explained by the Sabatier principle and calculated by the M-O bond strength (difference in Gibbs free energy of adsorption intermediates with active site M) of the -OH, -O, -OOH and -OO reaction intermediates.^[95-96]

The overall OER reaction in alkaline media can be formulated according to Equation 9 (Section 1.4), but due to several possible reaction pathways and reaction intermediates a descriptor adequately describing the limiting OER kinetic remains challenging.^[114] Figure 16 depicts a generalized scheme for the OER mechanism under alkaline conditions. In a first reaction step, OH^- is bound at the reactive site M via a one-electron oxidation reaction to form a M-OH intermediate. In a second consecutive OH^- -mediated coupled proton and electron removal step, H_2O is released and a M-O bond on the catalyst surface is formed. The M-O species can furthermore undergo two different reaction pathways, finally leading to the release of oxygen. The first pathway (dashed line) describes an O-O double bond formation of neighboring M-O reaction intermediates and thereby a coupled O_2 release.

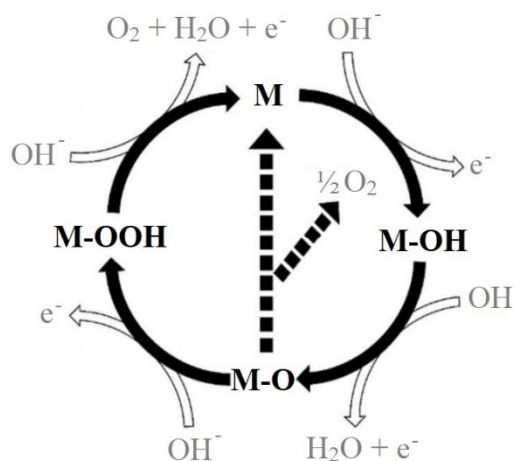


Figure 16 Generalized OER mechanism in alkaline media. M representing catalytically active sites. ^[115]

Reproduced with permission from Ref. [115]. Copyright 2018, American Chemical Society.

In an alternative pathway, an M-OOH peroxide intermediate is formed by a nucleophilic attack of OH⁻ coupled with a further one-electron oxidation reaction on the catalyst surface. The last step in this catalytic cycle includes a further OH⁻ coupled one-electron oxidation with a release of H₂O and O₂ to result in the regeneration of an unoccupied active site M.^[115-116]

Due to the complex reaction mechanism and its dependency on the composition and local structure of the catalyst, it is challenging to determine an absolute trend of the intrinsic activity of transition metal oxide surfaces towards OER catalysis. Depending on the exact theoretical parameters of the study, the OER activities can be ordered as NiO >> CoO ≈ FeO >> MnO or Co₃O₄ > NiO > Mn_xO_y.^[117-118] Experimentally a trend of MnO₂ > NiO > Co₃O₄ >> Fe₃O₄ was proposed by Trasatti *et al.*, whereas an order in OER activity of NiO_xH_y > CoO_xH_y > FeO_xH_y > MnO_xH_y was reported by Subbaraman *et al.* for near-monolayer (oxy)hydroxide films.^[119-120]

The partly opposing trends visualize the difficulty in determining and comparing the intrinsic activity of different transition metal oxides, which is greatly influenced by the local structure and composition of the catalyst.^[96] The local structure and composition thereby directly influence the formation and abundance of catalytically active sites and is a consequence of the synthesis method (bulk vs. nanostructured oxides) and operating conditions (e.g. pH-value and

potential induced formation and transformation of catalytically active phases). A further critical factor investigated in numerous studies in recent years is the presence of electrolyte impurities or doping elements (especially Fe) on the catalytic activity of nickel- and cobalt-based OER catalysts.^[96] Moreover, methods such as defect engineering, coating, and exfoliation as well as hybridization were successfully employed to improve the catalytic activity of transition metal oxides.^[121] Together with secondary (but important) factors such as electrical conductivity, mass transport and chemical stability, the micro- and nanoscale morphology all influence the apparent OER activity that can be described by an apparent potential E_{apparent} (e.g., for a given current density of 10 mA cm^{-2}).^[121]

$$\eta_{\text{total}} = E_{\text{apparent}} - E^0 = \eta_{\Delta G} + \eta_{\text{connection}} + \eta_{\text{surface}} \quad (14)$$

The total overpotential η_{total} is thereby a sum of the thermodynamic overpotential $\eta_{\Delta G}$, the connection overpotential $\eta_{\text{connection}}$ and the surface overpotential η_{surface} . The thermodynamic properties ($\eta_{\Delta G}$) result from the intrinsic electronic structure of the catalyst. The latter can be modified by features such as confinement effects exhibited by ultra-thin structures, doping, the chemical and phase composition as well as defect engineering. The connection overpotential $\eta_{\text{connection}}$ is associated with the potential drop between the catalytically active sites and the external circuit and is thus dependent on the conductivity of the electrodes, which can be manipulated by carbon or metal composite formation, doping and hierarchical nano- and microstructures with optimized charge percolation pathways. Finally, the value of η_{surface} is associated with the number of available catalytically active sites and is thereby related to the catalyst surface area, which can be tuned by synthesis of nanoparticles and nanostructures with significantly increased surface to volume ratios.^[121]

An example of an advanced transition metal oxide catalyst for alkaline OER is given by Fan *et al.* who synthesized hierarchically vanadium-doped FeOOH spheres of $\approx 3 \mu\text{m}$ filled with a

vanadate core that is transformed to hollow vanadium-iron spheres by operation in the KOH electrolyte as shown in Figure 17.^[122]

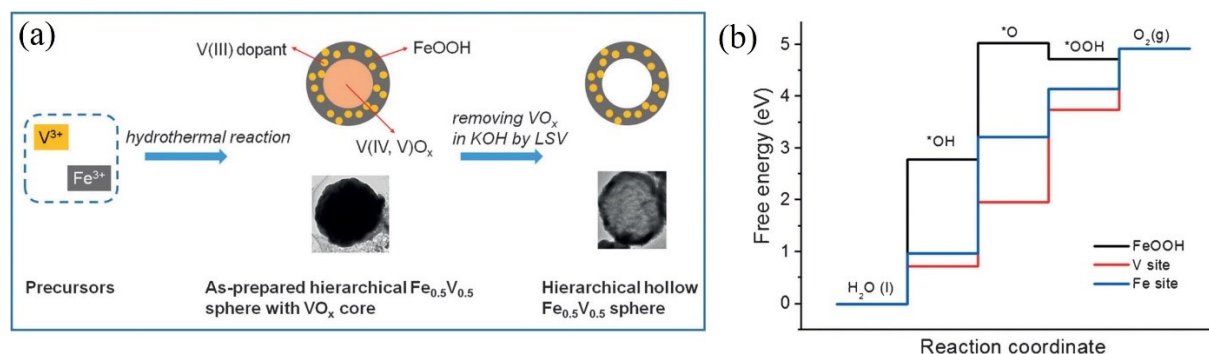


Figure 17 (a) Proposed synthesis scheme of spherical V(III)-doped $FeOOH@VO_x$ core and hollow $Fe_{0.5}V_{0.5}$ sphere OER catalyst. (b) Gibbs free energy scheme of oxygen evolution reaction with ($-OH$, $-O$ and $-OOH$) intermediates catalyzed by undoped $FeOOH$ surface (black curve) and V-(III) doped $FeOOH$ with influence on V (red) and Fe (blue) active sites.^[122]

Reproduced with permission from Ref. [122]. Copyright 2017, Wiley-VCH Verlag GmbH & Co. KGaA, Weinheim.

The material thereby exhibits a comparably high OER activity with a required overpotential of 292 mV to reach a current density of 1 mA cm^{-2} , which approaches the range of nickel or cobalt based electrocatalysts. The significant increase in activity is mainly associated with the altered conductivity, which usually limits the performance of undoped iron oxide/oxyhydroxide based OER catalyst, lowering $\eta_{\text{connection}}$. According to DFT calculations the electronic structure is furthermore modified by vanadium doping to result in lower or more equidistant steps in Gibbs free energy of adsorption intermediates affecting iron as well as vanadium active sites as shown in Figure 17 b, thereby increasing the intrinsic activity of the material ($\eta_{\Delta G}$). Finally, the amount of catalytically available active sites is significantly enhanced by the formation of hierarchical spherical microstructure composed of rod-like building blocks, which in turn are built of small (below 10 nm) individual particles (Figure 17 a). The micro/nanostructure thereby lowers the surface related overpotential η_{surface} and leads to a low experimentally confirmed overpotential η_{total} .^[122]

1.4.2 Oxygen evolution reaction catalysis with Ir-based catalysts

Although alkaline electrolysis discussed in the previous section exhibits a huge potential due to available low cost OER catalysts, electrolysis under acidic conditions as a complementary approach is of equal importance for the future large-scale energy storage by means of hydrogen production.

A first advantage of acidic electrolysis in the form of proton exchange or polymer electrolyte membrane (PEM) electrolysis is the use of a highly proton conducting thin perfluorosulfonic acid (PFSA) membrane (e.g. Nafion® membrane) employed as solid electrolyte, separator and gas permeation barrier.^[89] Membrane technology is also being investigated for the alkaline electrolysis, however still at a non-commercialized early stage of development.^[123] A PEM electrolyzer cell with $\approx 50\text{-}200\ \mu\text{m}$ thin membranes exhibits a significantly lower ohmic resistance as compared to a similar sized alkaline counterpart with alkaline exchange membrane (AEM) with a comparable charge carrier concentration due a considerably higher ionic conductivity of H^+ vs. OH^- . The low ohmic resistance in PEM electrolysis thereby allows high current densities of several A cm^{-2} (typically $1\text{-}3\ \text{A cm}^{-2}$)^[94] as compared to several hundred mA cm^{-2} achievable for alkaline electrolyzers.^[89] In addition, the PFSA membranes employed in acidic PEM electrolysis have a high durability with a possible usage over tens of thousands of hours. To compare, the life time of the currently investigated alkaline exchange membranes is still limited to several hundreds of hours, mainly due to the use of less stable functional groups (e.g. aliphatic heterocyclic quaternary ammonium head groups) required for ion conductivity.^[123]

A major drawback of acidic PEM electrolysis are, however, the strong requirements for the OER catalyst at the anode. Although the PEM electrolyzers use only purified and de-ionized water, the employed catalysts need to be stable under highly acidic conditions as they are in a direct contact with the PTFE-type Nafion® membrane acting as a superacid.^[124] In addition,

the catalyst needs to be long-term oxidation stable due to the applied positive potential at the anode.

Among the possible elements of choice for electrocatalysis, Ir, Pt, Pd, Rh, Ti, Ta, Nb, W and Si theoretically show a thermodynamically stable oxide phase at the potentials that occur during the OER. However, due to the low electrocatalytic activity and limited conductivity of all of the mentioned metal oxides except for Ir and its oxides, the latter remain the only employed catalysts in industrial type PEM electrolyzers.^[81] Also not included in the list above are highly active but less stable ruthenium oxides due to the known stability issues under OER conditions, although these compounds are thoroughly investigated in the literature and have also been proposed as alloying material for iridium-based catalysts.^[125-126]

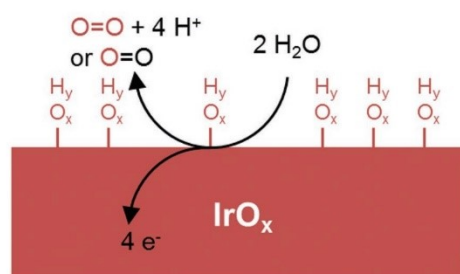
OER reaction mechanism in acidic media

Although iridium and its oxides are used as OER catalysts already for decades, the exact reaction mechanism for the complex four-electron oxidation reaction has long not been validated experimentally. Based on available experimental data and DFT calculations, several reaction mechanisms have been proposed so far that are shown in the upper part of Figure 18. In analogy to the OER mechanism in alkaline media, a first step involves the formation of a M-OH intermediate. Depending on the proposed mechanism, M-O and M intermediates are either formed by elimination of H₂O or an M-O intermediate is formed by a deprotonation and electron transfer reaction. The final O-O bond formation followed by an oxygen release, which is usually a rate determining step, can either proceed from two neighboring M-O intermediates or alternatively via involvement of an M-OOH peroxide intermediate.^[89]

To elucidate the reaction mechanism and to shed light on the stability of Ir-oxides under OER conditions, differential electrochemical mass spectroscopy (DEMS) measurements with isotope-labeled electrolytes were performed. It could be shown that, in addition to oxygen from

the electrolyte, also IrO_x lattice oxygen initially participates in the OER as depicted in the scheme in the lower part of Figure 18.^[89]

I) Oxide Path	II) Electrochemical Oxide Path
1) $\text{H}_2\text{O} + \text{M} \rightarrow \text{M-OH} + \text{H}^+ + \text{e}^-$	1) $\text{H}_2\text{O} + \text{M} \rightarrow \text{M-OH} + \text{H}^+ + \text{e}^-$
2) $2 \text{M-OH} \rightarrow \text{M-O} + \text{M} + \text{H}_2\text{O}$	2) $\text{M-OH} \rightarrow \text{M-O} + \text{H}^+ + \text{e}^-$
3) $2 \text{M-O} \rightarrow 2 \text{M} + \text{O}_2$	3) $2 \text{M-O} \rightarrow 2 \text{M} + \text{O}_2$
III) Electrochemical Metal Peroxide Path	IV) DFT-predicted Peroxide Path
1) $\text{H}_2\text{O} + \text{M} \rightarrow \text{M-OH} + \text{H}^+ + \text{e}^-$	1) $\text{H}_2\text{O} + \text{M} \rightarrow \text{M-OH} + \text{H}^+ + \text{e}^-$
2) $2 \text{M-OH} \rightarrow \text{M-O} + \text{M} + \text{H}_2\text{O}$	2) $\text{M-OH} \rightarrow \text{M-O} + \text{H}^+ + \text{e}^-$
3) $\text{M-O} + \text{H}_2\text{O} \rightarrow \text{M-OOH} + \text{H}^+ + \text{e}^-$	3) $\text{M-O} + \text{H}_2\text{O} \rightarrow \text{M-OOH} + \text{H}^+ + \text{e}^-$
4) $2 \text{M-OOH} \rightarrow \text{M-O} + \text{H}_2\text{O} + \text{O}_2 + \text{M}$	4) $\text{M-OOH} \rightarrow \text{M} + \text{O}_2 + \text{H}^+ + \text{e}^-$



- evolved O_2 arises to some extent from lattice OH_y , not clear if $\text{O}=\text{O}$ or $\text{O}=\text{O}$
- OOH transiently observed during OER
- Ir(III)/(V) reported beside major Ir(IV) contribution during OER

Figure 18 (Upper part) Proposed reaction mechanisms for the oxygen evolution reaction in acidic media. (Lower part) Graphical representation of the experimental in-situ insights into the OER mechanism on Ir-based heterogeneous catalysts. ($0 \leq y \leq 1$, $1 \leq x \leq 2$).^[89]

Reproduced (modified) with permission from Ref. [89]. Copyright 2016, WILEY-VCH Verlag GmbH & Co. KGaA, Weinheim.

Stability and dissolution of Ir-oxides under OER conditions

The participation of lattice oxygen correlates with the electrocatalytic activity and stability of iridium oxides under OER conditions.^[127] Hydrrous iridium oxide, which can be characterized as a defect-rich Ir-oxide by its missing long-range order and complex local structure, exhibits a remarkably high OER activity but only a limited stability.^[128] The high activity of hydrrous iridium oxide films is thereby associated with a bulk-like catalytic activity with a high number of active sites, as compared to an estimated amount of active sites equivalent to only 1-2 at% iridium for crystalline rutile IrO_2 .^[129]

A valid approach to increase the stability of hydrous iridium oxides is therefore a thermal annealing as depicted in Figure 19. Thermal annealing first dehydrates the hydrous IrO_x phase at a temperature of up to ≈ 300 °C. This step is associated with a loss in intrinsic conductivity and electrocatalytic activity but results in an apparently higher stability. The decline in activity is thereby explained by a decreased amount of active sites due to sintering; a limited ion insertion as well as mass transport limitations for reactants and products in the dehydrated IrO_x phase. In the temperature range of 300 - 400 °C a phase transition of the amorphous IrO_x to the crystalline rutile IrO_2 phase can be observed, which leads to the formation of a mixed phase with increased OER activity and conductivity but significantly lower stability.^[129] Heating to 400 - 450 °C is reported as a temperature optimum, which leads to a maximized intrinsic activity with considerable lower Ir dissolution and a high conductivity.^[129-131]

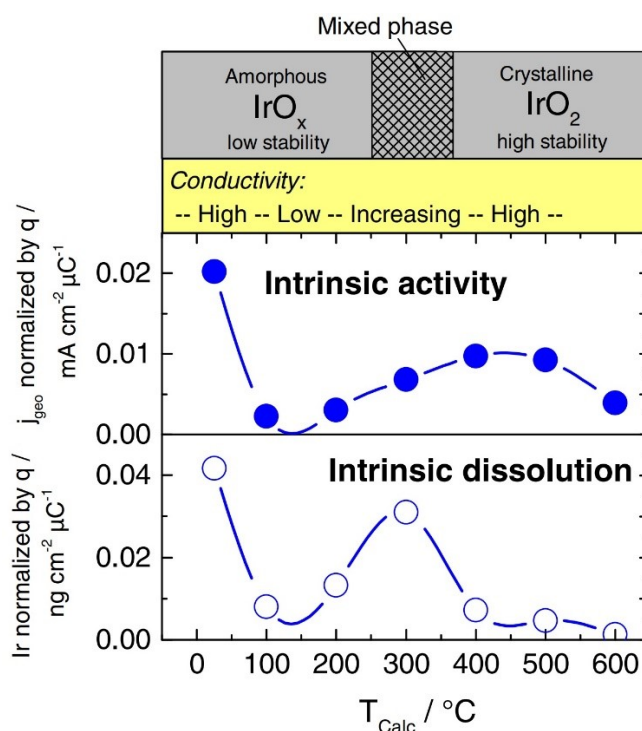


Figure 19 Intrinsic activity and dissolution of thermally treated hydrous iridium oxide films. Values determined by current density at 1.5 V_{RHE} and Ir dissolution rates ($\text{ng}_{\text{Ir}} \text{cm}^{-2} \text{electrode}$) normalized by the charge taken from respective cyclic voltammograms. Iridium oxide phases (grey) and relative conductivities (yellow) indicated in the upper part for the respective temperature regimes.

Reproduced with permission from Ref. [129]. Copyright 2016, the authors. Published by The Electrochemical Society.

Even higher temperatures lead to a further growth of the initially formed nanosized IrO_2 crystalline domains with an accompanied decrease in electrochemically active surface area, as well as to the formation of thermodynamically favored but less OER active 110 crystal facets.^[129, 132]

Although iridium oxides and especially highly crystalline rutile IrO_2 are the most stable catalysts for acidic water electrolysis known to date, dissolution under OER conditions can still be observed that may become significant for long-term operation in a PEM electrolyzer. Figure 20 depicts a scheme describing possible Ir dissolution pathways coinciding with OER reaction intermediates. It starts from metallic iridium that is oxidized to IrO_2 upon application of an anodic potential, thereby a dissolution due to the formation of Ir^{3+} is observable.^[133]

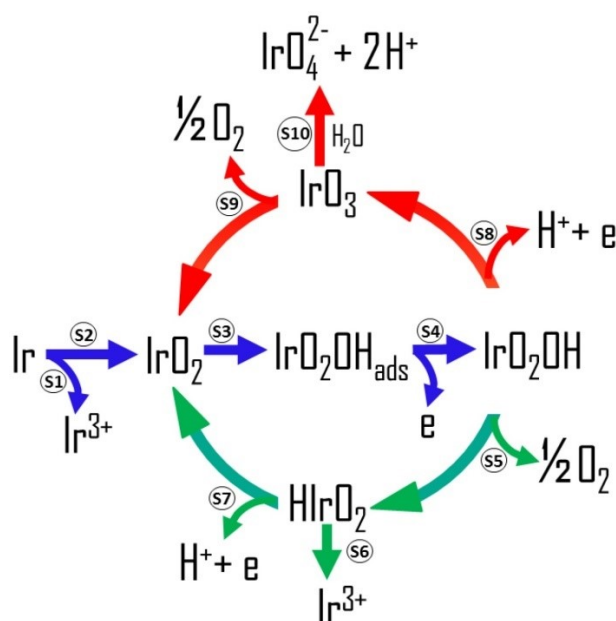


Figure 20 Simplified scheme for possible pathways of Ir dissolution during the OER. Green arrows indicate the mechanism that is more preferable for electrocatalytically active Ir based materials where OER happens at lower potentials. Red arrows present the dissolution route dominating at higher anodic potentials. Blue arrows show intermediate steps that take place regardless of the electrode material and potential.^[133]

Reproduced with permission from Ref. [133]. Copyright 2018, the authors. Published by Wiley-VCH Verlag GmbH & Co. KGaA.

In a first step an OH radical is formed on the IrO_2 electrode surface via an addition of H_2O with concurrent proton removal and a further release of one electron to form an experimentally

validated Ir(V) species. Depending on the synthesis conditions (thermal oxide vs. electrochemically formed Ir-oxides) and the applied OER potential, either a decomposition to HIr(III)O_2 with a release of O_2 or the formation of a Ir(VI)O_3 intermediate is proposed. The Ir(III)-dissolution pathway is thereby associated with electrochemically formed Ir-oxides and relatively low potentials, whereas the Ir(VI)-dissolution pathway is reported to require potentials above 1.6 V vs. RHE and is associated with the more stable thermal IrO_2 . IrO_3 , which is a part of the catalytic OER cycle, can furthermore form soluble Ir(VI)O_4^{2-} causing a net iridium dissolution in the electrolyte. As the observed Ir dissolution rates are low compared to the in situ spectroscopically detectable IrO_3 amount at thermal IrO_2 surfaces during OER, significantly faster kinetics regarding decomposition than hydrolysis can be concluded.^[133]

Increasing Ir mass-based activity for OER catalysis

Besides fabrication of long-term stable iridium oxide phases for catalysis, major research interest is devoted to the lowering of the Ir-content by increasing the mass-based catalytic activity. Decreasing the iridium amount is thereby essential to allow for a future large-scale application of PEM-electrolysis that is otherwise limited by the low natural abundance of the scarce noble metal in addition to its high price.^[89, 134]

In the literature five different and partly complementary approaches were suggested to date:

1. Increasing the activity by intermixing iridium oxide with highly active but less corrosion stable ruthenium oxide. Synthesis of RuIrO_x nanoparticles further enhances the electrocatalytic activity by an increased accessible surface area.^[135-137]
2. Increasing the OER activity by the stabilization^[138] of a highly active but less stable^[128] hydrous IrO_x phase.
3. Maintaining or increasing the high catalytic activity of IrO_2 by either alloying or substitutional doping with various noble and non-precious metals and oxides. Examples include ternary and quaternary (RuO_2) mixed oxides with cobalt,^[139-140] molybdenum,^[141]

bismuth,^[142] niobium,^[143] ternary and quaternary (RuO₂) tin oxides,^[144-146] quaternary oxides including titanium^[147] and catalytically highly active nickel/iridium^[148-149] compounds as well as IrO_x/Au nanoflower composites^[150] with enhanced OER activity. Literature on doping has been focused on ternary^[151-152] and quaternary (including Nb and Sn)^[153-154] fluorine containing oxides.

4. Increasing the iridium mass-based OER activity by increasing the electrochemical active surface area of the heterogeneous catalyst by means of thin film electrodes, nanostructuring or nanoparticle synthesis. Examples are thin sputtered IrO₂ films,^[155] high surface area IrO₂ from electrochemically leached ternary RuIr compounds^[156] or pure Ir and RuIr ternary oxide nanoparticles^[135, 137] with high surface area accessible by various synthesis techniques.

Using amphiphilic block co-polymers such as PEO-PB-PEO^[157-158] or Pluronic® F127,^[144] mesoporous iridium oxide and ternary iridium oxide electrodes with significantly increased surface area could be produced.

Furthermore, high aspect ratio structures of binary and ternary iridium oxides with wire,^[159] rod^[145] or dendrite^[160-161] morphologies with increased electrocatalytic surface area were synthesized.

A further thoroughly investigated concept are core-shell structures including either a nitride (Fe₄N, Co₄N or Ni₄N) core,^[162] a conductive Sb-doped SnO₂ core,^[163] a conductive and catalytically active RuO₂ core^[164] or binary or ternary iridium oxide particles with differing surface composition controlled by synthesis parameters^[146] or by a post-synthetic leaching process^[149].

Other less investigated structures include a nanosheet-like morphology created by exfoliation,^[165] nanoflower morphology,^[150] nanocage morphology^[166] or complex structures like SBA15-templated material^[167].

5. An approach thoroughly investigated in recent years includes the dispersion of the Ir(oxide) active phase on a (ideally conductive) catalyst support to increase the accessible electrocatalytic surface area and thereby lower the iridium content of the electrode.

First examples include highly conductive, high surface area carbon supports such as activated carbon,^[168] carbon paper,^[169] graphitic foam,^[170] Vulcan®^[171] or reduced graphene oxide (rGO)^[172] that are however not oxidation stable in the long term.

One of the first catalysts based on oxidation-stable oxidic support materials is a titania-supported IrO₂, which is used for years as dimensionally stable electrodes (DSA®)^[173] in chlorine-alkali electrolysis and was also investigated for a possible use in acidic OER. In recent years, attempts to optimize the morphology of the TiO₂ support were made with an aim to further increase the accessible surface area and therefore the noble metal mass-based activity of the catalyst by means of nanostructuring^[174-175].

Besides titania, other corrosion stable non-conductive SnO₂,^[176] mixed TaSnO_x^[177] and NbO₂^[178] were investigated as OER catalyst support materials.

To further increase the electrocatalytic activity and to enable low iridium loading, efforts were undertaken to increase the conductivity of the wide bandgap semiconductor TiO₂. The electrical conductivity can be increased by introducing donor energy levels via a partial reduction of Ti⁴⁺ to Ti³⁺ existing in sub stoichiometric, oxygen deficient TiO_x. This is synthetically accessible via the hydrogenation of TiO₂^[179] or via the direct synthesis of sub stoichiometric conductive Magnéli phases.^[180] Alternatively, hetero-atom doping with niobium can significantly increase the conductivity,^[181] which is reported to result from the formation of an impurity band overlapping with the TiO₂ anatase conduction band^[182].

Besides the decreased loading of active phase, another positive effect of the TiO₂ support is the increased OER activity of the catalyst due to a beneficial catalyst-support interaction.^[183-184] A further alternative approach towards a stable and conductive titania-based iridium catalyst

support material was recently introduced by Bele *et al.* who fabricated high surface area, nanostructured nitrogen-rich TiON_x with an exceptionally high macroscopic conductivity of 3 - 8 S cm^{-1} .^[185]

The results of research in recent years have demonstrated that the properties (Ir loading and electrocatalytic activity) of titania-supported iridium oxide OER catalysts can be improved by nanostructuring of the titania support. However, the conductivity remains an important issue as the sub-stoichiometric TiO_x or TiON_x are expected to be (re)-oxidized under ongoing OER conditions.^[185] The stability of Nb-doped TiO_2 also needs to be further investigated under long term OER conditions, as the conductivity may be negatively influenced by a potential cation leaching process.

Besides Ti-based materials, other conductive oxidic and carbidic materials were investigated as catalyst supports by different groups. Some transition metal carbides showed high conductivities of up to 170 S cm^{-1} for NbC, but their low surface areas (below 1 $\text{m}^2 \text{g}^{-1}$ for NbC) limit their performance significantly as compared to conducting oxides such as Nb: TiO_2 or Sb: SnO_2 .^[178] Furthermore, metal carbides remain a challenging class of material for nanostructuring as top-down approaches such as ball milling were shown to significantly reduce the conductivity possibly due to oxidation and thus passivation of the surface.^[178]

Bottom-up synthesis approaches using carbothermal methods with specifically designed carbon sources (structural template and reactant) also remain challenging due to inhomogeneous carburization at the required high reaction temperatures and resulting aggregation.^[186] Carbides investigated so far include NbC, TiC, WC^[178] and TaC^[178, 187] with highest OER performance shown for TaC supported IrO_2 of $\approx 400 \text{ A g}_{\text{Ir}}^{-1}$, which is significantly lower than $\approx 850 \text{ A g}_{\text{Ir}}^{-1}$ at $\approx 1.67 \text{ V vs. RHE}$ for Sb: SnO_2 support shown in a comparative study.^[178]

Another promising group of OER supports are conducting oxides such as $\text{In}_{2-x}\text{Sn}_x\text{O}_3$ (ITO) and $\text{Sb}:\text{SnO}_2$ (ATO). Although the conductivity of these compounds is up to 6 orders of magnitude lower compared to carbides^[178] (mS cm^{-1} ^[188] and S cm^{-1} ^[189] range for ATO and ITO, respectively), there exist various synthetic routes to obtain nanostructured and conductive electrodes^[190-192] which exhibit surface areas 1 - 2 orders of magnitude higher than those of the reported carbides. With this approach, highly active OER catalysts could be synthesized including IrO_2 nanoparticles supported on ITO^[188] or on ATO^[193] nanopowder, which was also explored as a support for ternary RuIr oxide particles.^[194] Besides commercially available nanoparticle aggregates, also high surface area mesoporous ATO electrodes prepared by soft-templating methods were loaded with highly active IrNiO_x ^[163] or Ir nanodendrites^[160]. Still, although Sb-doped SnO_2 (ATO) or indium tin oxide (ITO) catalyst supports show very promising performance, their long-term stability and conductivity remain questionable as was pointed out by Geiger *et al.*^[195] The same group has however revealed that fluorine doped tin oxide (FTO) showed the highest stability under their OER conditions up to 2.7 V vs. RHE, therefore FTO could be investigated in the future as a possible conductive oxidation-stable catalyst support.^[195]

OER catalyst design principles for PEM electrolyzers - Increasing the Ir volume dispersion

The construction principle of membrane based electrolyzers is inspired by fuel cells with bipolar plates including flow fields, porous transport layers (PTL) and a catalyst coated membrane in the center as shown in Figure 21a. For electrolyzers as well as for fuel cells a Pt/C catalyst in contact with a carbon-based gas diffusion layer (GDL) or PTL can be employed for HER or HRR on the cathode side, respectively.^[196]

A significant difference in the fuel cell and the PEM electrolyzer setups is that in the latter the carbon-based catalyst supports or PTLs cannot be used for the oxygen evolution reaction on

the anode side, as they are not long-term oxidation stable under the applied potentials of >1.5 V vs. RHE. PEM electrolyzers typically employ Ti-sinters with mean pore sizes of 10 - 20 μm acting as current collectors and allowing efficient gas and water permeation.^[134, 196-197]

State-of-the-art electrolyzers employ relatively high anode catalyst loadings of ≈ 2 $\text{mg}_{\text{Ir}} \text{cm}^{-2}$ of an unsupported or TiO_2 supported Ir-oxide based catalyst with high Ir content of ≈ 75 wt% Ir.^[134, 198-199] The high loading of several mg cm^{-2} of the precious Ir-oxide catalyst is not only based on the limited kinetics of the OER, but is mainly required to obtain a stable micrometer thick conductive electrode as depicted in Figure 21b.

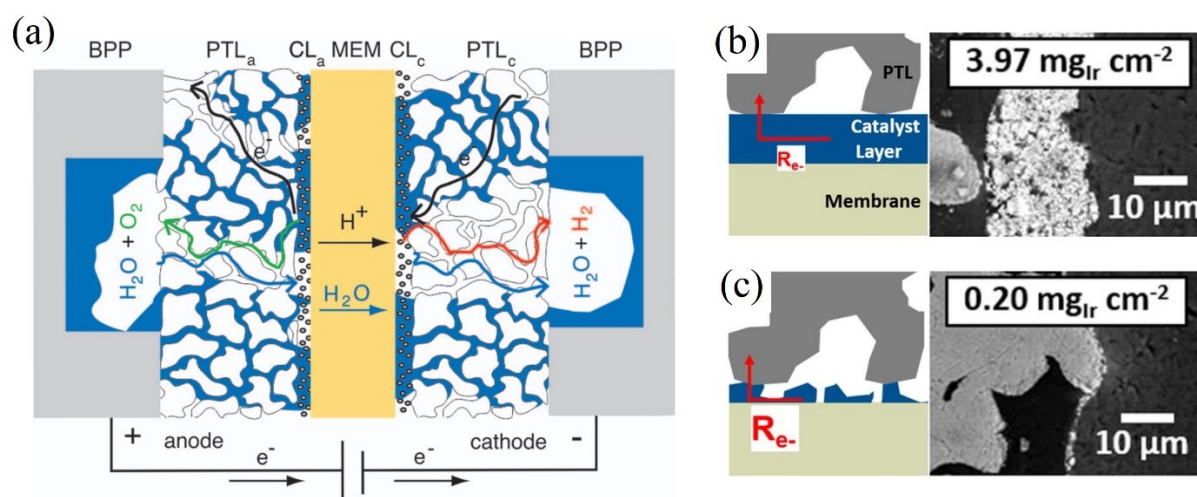


Figure 21 (a) Schematic cross-section of PEM electrolysis cell, consisting of a membrane (MEM) coated with cathodic and anodic catalyst layer (CL_c , CL_a) sandwiched between two porous transport layers (PTL_c , PTL_a) and bipolar plates (BPPs).^[196] Schematic and corresponding SEM cross-section of PTL-catalyst layer-membrane region of an electrolysis cell with (b) high and (c) low Ir catalyst loading. Red arrow, labeled R_{e-} indicating the charge percolation pathway within the catalyst layer to the PTL current collector.^[198]

(a) Reproduced with permission from Ref. [196]. Copyright 2017, the authors. Published by The Electrochemical Society.

(b) and (c) reproduced (modified) with permission from Ref. [198]. Copyright 2018, the authors. Published by The Electrochemical Society.

Low loadings (< 0.5 $\text{mg}_{\text{Ir}} \text{cm}^{-2}$) of unsupported or $\text{TiO}_2/\text{IrO}_2$ mixed oxide catalyst without an optimized morphology result in thin (below 2 μm) discontinuous electrode layers with decreased in-plane conductivity caused by electronically isolated regions of catalyst on the non-conductive Nafion® membrane. The lowered Ir loading further results in a decreased catalyst utilization due to the presence of electrically isolated active material not in the direct

contact with the PTL current collector, as the latter has a relatively large pore size required for efficient mass transport at high current densities.^[198]

Overall voltage losses related to the electrical conductivity and mass transport in the electrode layer are minimized for anode electrode thicknesses of $\approx 4 - 8 \mu\text{m}$, which translates to an Ir loading of $\approx 1 - 2 \text{ mg}_{\text{Ir}} \text{ cm}^{-2}$ for a conventional industrially available $\text{TiO}_2/\text{IrO}_2$ mixed oxide OER catalyst.^[198]

Due to the aforementioned requirements, a lowering of the iridium loading in PEM electrolyzer anodes is only possible by an increase of the iridium volume dispersion. The latter can be realized either by the use of highly porous Ir-oxide structures or of non-precious, ideally conductive and stable support materials.

Unfortunately, a simple reduction of the Ir-content in $\text{TiO}_2/\text{IrO}_2$ mixed oxide catalysts is not possible, as the material is practically insulating when Ir content drops below 25 wt% Ir. At low iridium contents, electrically insulating TiO_2 domains prevent electron transfer across the electrode layer. Theoretically, 25 wt% of highly conductive IrO_2 domains should ensure sufficient overall conductivity as they are statistically in contact throughout the material to allow charge percolation. However, much higher iridium contents (typically >40 wt%) are required in practice as a minimum required conductivity of $10^{-3} \text{ S cm}^{-1}$ is reported as a threshold for unrestricted OER.^[134, 200] Due to the voltage loss at industrially relevant current densities of several A cm^{-2} , even higher Ir contents (typically 75 wt%) are employed in $\text{TiO}_2/\text{IrO}_2$ catalysts to obtain a macroscopic conductivity of several tens of S cm^{-2} .^[198-200]

To circumvent these problems, nanostructured IrO_2 catalyst with high void volume and an interconnected Ir-oxide phase were introduced, which allow for the fabrication of highly conductive electrode layers of sufficient thickness of $4 - 8 \mu\text{m}$ with a reduced Ir-loading per membrane area at the same time.^[134]

A suitable morphology is represented by an inverse opal type oxide nanomorphology described in Section 1.4.2, which is derived from an ordered 3D array of interconnected spherical voids resulting from a self-assembly of polymer bead templates (e.g. poly(methyl methacrylate) or polystyrene) with subsequent removal by thermal oxidation or organic solvents. Depending on the polymer bead size, void diameters of ≈ 50 nm to several hundred nanometers with wall thicknesses of only tens of nanometers and below can be obtained, resulting in a high void volume of the structure of $>90\%$ and high-surface to volume ratio reaching several tens of meters per gram.^[201-202]

In a recent work Park *et al.* described the fabrication of IrO₂ inverse-opal electrodes for the application as PEM electrolyzer anodes. These structures were synthesized using pulse electrodeposition of an iridium solution and a preformed polystyrene-based colloidal crystal template thin film on a conductive substrate. By variation of the electrodeposition parameters, porous structures with ultra-low IrO₂ loadings of $0.001 - 0.03 \text{ mg cm}^{-2}$ could be realized in the membrane electrode assemblies. The electrodes showed excellent performance with current density as high as 870 mA cm^{-2} at a cell voltage of 1.6 V, which is ≈ 2.5 times that of a conventional MEA with significantly higher Ir loading. The improved performance was attributed to an enhanced electron transfer throughout the electrode layer and the increased surface area of the inverse-opal structure that allows for an increased utilization of the IrO₂ phase.^[79]

A further successful application of the inverse opal nanomorphology is given by Faustini *et al.* who prepared MEAs from microparticles ($\approx 1 - 2 \text{ }\mu\text{m}$) of inverse opal-structured IrO₂ and IrRuO_x.^[203] An advantage of the employed ultrasonic spray pyrolysis synthesis approach with resulting individual particles is a facile processability for MEA fabrication and the possibility of tuning the final IrO_x or IrO₂ phase and nanostructure by a thermal oxidation procedure. By increasing the oxidation temperature to over $450 \text{ }^\circ\text{C}$, a transition from pure inverse-opal like

morphology with small spherical nanosized building blocks to the formation of a hierarchical structure with rod-like building blocks due the growth of crystalline domains could be observed.^[203] Figure 22a-c depicts similarly prepared macroporous inverse opal IrO_x microparticles (preparation in analogy to experimental section in Chapter 8) with high resolution TEM and STEM images (Figure 22b,c) to visualize the highly porous and accessible structure built from individual domains of below 10 nm.

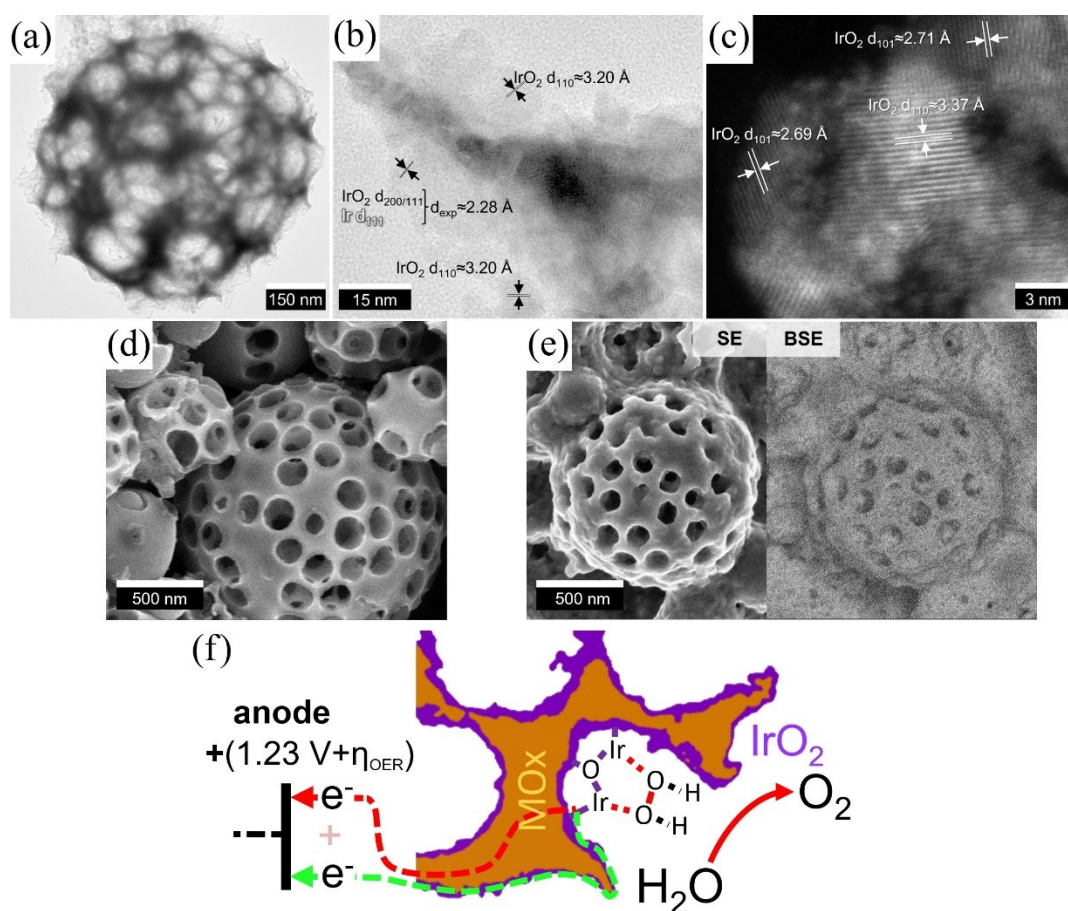


Figure 22 (a) TEM micrograph of unsupported macroporous IrO_2 microparticle with high-resolution TEM (b) and STEM (c) images of individual IrO_2 nanocrystal building blocks. SEM image of macroporous TiO_2 microparticle before (d) and after (e) coating with IrOH_x layer. Secondary electron (SE) and back-scattered electron (BSE) sensor-based images for visualization of smooth IrOH_x coating. (f) Proposed morphology of supported IrO_2 nanoparticle catalyst with high Ir dispersion and conductive MO_x support for highly efficient OER catalysts for PEM electrolysis.

Electron microscopy data recorded by Beetz M. (a-c) and Böhm D. (d,e). Artwork (f) created by the author.

A further development in the synthesis of low-Ir content OER catalysts could make use of the inverse opal-type nanomorphology to create an oxidic support for a nanosized Ir-oxide based catalyst. Figure 22d shows macroporous TiO_2 microparticles that can be homogeneously coated

by an Ir-oxide phase as shown in Figure 22e (morphology (SE) vs. morphology/material contrast (BSE) SEM image) to even further increase the iridium dispersion and maximize its utilization. By employing a conductive oxide support as schematically depicted in Figure 22f, the required Ir-oxide layer could be minimized due to an additional charge percolation pathway through the support, and even a discontinuous layer of active material would still result in full utilization of the precious catalyst material.

Although the share of the catalyst material of electrolyzers in the kW range only accounts for $\approx 5\%$ of the total cost, this value increases for electrolyzers at the MW scale as the contribution by the balance of plant cost are reduced due to scaling relations in the production. However, for potential installation strategies involving the GW scale not the price alone but the natural abundance and availability of iridium will be a limiting factor with current industrially employed OER catalyst and loadings. To allow for large-scale applications of this technology, a reduction of the iridium loading down to $\approx 0.05 \text{ mg}_{\text{Ir}} \text{ cm}^{-2}$ is required according to an estimation by Bernt *et al.*. This value is regarded to be achievable using the advanced nanostructured and supported catalyst concepts discussed above.^[134, 196, 198]

1.5 Electrochemical energy storage by transition metal oxides in secondary alkali metal ion batteries

Short history and construction of conventional lithium ion batteries (LIBs)

With an increasing interest in portable electronic devices and after reaching technological limits in the energy density of Ni-Cd batteries in the 1980s, Sony Corporation started research activities on lithium-based anodes. At that time, primary lithium cells with metallic anodes and non-aqueous electrolyte were already widely employed for special applications as they offered a high cell voltage, high energy density, a low self-discharge and allowed for operation over a wide temperature range.^[204]

The use of metallic lithium as high energy density anodes for secondary lithium ion batteries is still very appealing.^[205] However, lithium dendrite formation that occurs inevitably during the charging process leads to poor safety characteristics due to short-circuits and a resulting poor cyclability.^[204]

Although recent studies on metallic lithium anodes have shown that the dendrite formation can be generally limited by adding nanometer thin inorganic coatings (e.g. Al₂O₃ by atomic layer deposition), it still does not allow the fabrication of highly stable and cyclable anodes in a conventional LIB design with liquid electrolytes.^[206]

The breakthrough in the commercialization of lithium ion secondary batteries was achieved when graphite intercalation compounds (GIC) were discovered as anode materials, which were known at that time to reversibly accommodate different atoms and atomic groups between the layers. It could be further shown that GICs could be used for electrochemical lithium intercalation when used with lithium containing salts such as LiPF₆, LiBF₄, LiAsF₆ or LiClO₄ in aprotic organic solvents.^[204]

Inspired by the development of AgNO₂ anodes for primary silver oxide cells and literature reports of layered LiNiO₂ and LiCoO₂, Sony managed to construct their first-generation LIB

full cell with a LiCoO_2 cathode, microporous polyethylene film separator and a soft carbon-based anode according to Figure 23 that was commercialized in 1991.^[204]

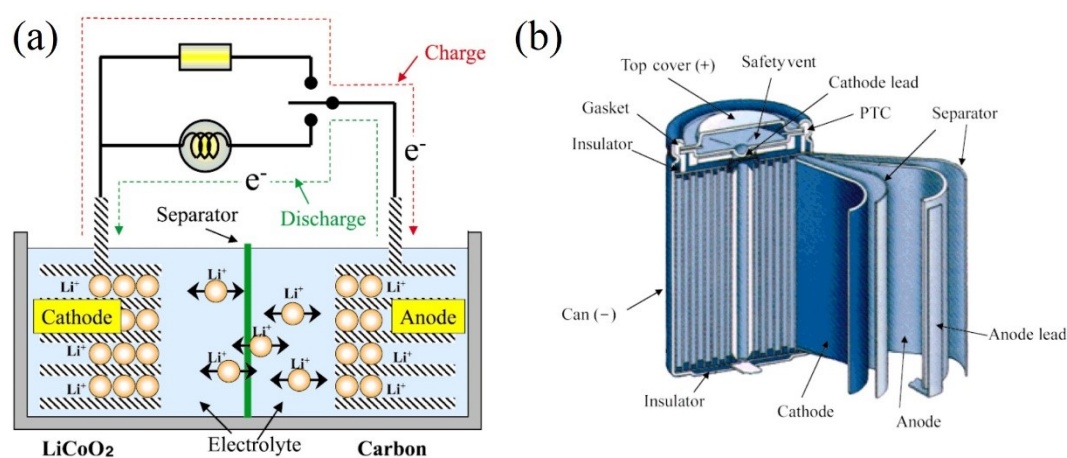


Figure 23 (a) Schematic construction and working principal of a secondary lithium ion battery. (b) Schematic construction of a cylindrical secondary lithium ion battery.^[204]

(a) Reproduced with permission from Ref. [204]. Copyright 2001, John Wiley & Sons, Inc. and The Japan Chemical Journal Forum.

In a typical LIB cell, a slurry of the microscale cathode active material (e.g. LiCoO_2 powder) with a polymeric binder such poly(vinylidene fluoride) (PVDF), organic solvent (e.g. N-methyl-2-pyrrolidone (NMP)) and a specific amount of carbonaceous conduction additive (e.g. Super C65 carbon black) are mixed in a defined ratio to be coated on an aluminum foil. The anode active material (e.g. soft/hard or graphitic carbon) is prepared in a similar fashion and coated on a copper foil.^[207]

Although the energy density of the first generation of LIBs with soft carbon anodes with 200 Wh l^{-1} and 80 Wh kg^{-1} was not much higher than that of the existing Ni-Cd cell technology, it could be improved by the use of hard carbon based anodes to a capacity value of 295 Wh l^{-1} and 120 Wh kg^{-1} due to an increased cell voltage of up to 4.2 V .^[204] The third generation LIB cells from Sony employed graphitic carbon and advanced electrolyte formulations and thereby allowed an increase of the energy density to 400 Wh l^{-1} and 155 Wh kg^{-1} .^[204] Further improvements of cell design and fabrication together with an optimization of the active material

led to a reported energy density of 697 Wh l^{-1} and a specific energy of 256 Wh kg^{-1} in 2017.^[204, 208]

Nanostructured transition metal oxide anodes

Due to the increased demand for high-energy density portable power sources - also beyond consumer electronics (e.g. battery electric vehicles, portable electrical power tools or medical equipment and more), research on novel battery active materials was continued. Metallic lithium anodes exhibit practically the upper capacity limit with a theoretical gravimetric and volumetric capacity of 3860 mAh g^{-1} and 2047 mAh cm^{-3} respectively, which translates to a theoretical full-cell capacity of 1177 Wh l^{-1} with a $100 \mu\text{m}$ nickel cobalt aluminum oxide (NCA) cathode and poly propylene (PP) separator as depicted in Figure 24. A further advantage of a metallic lithium electrode is its low electrode potential of -3.05 V vs. SHE , which theoretically enables a large voltage window of the full cell.^[208]

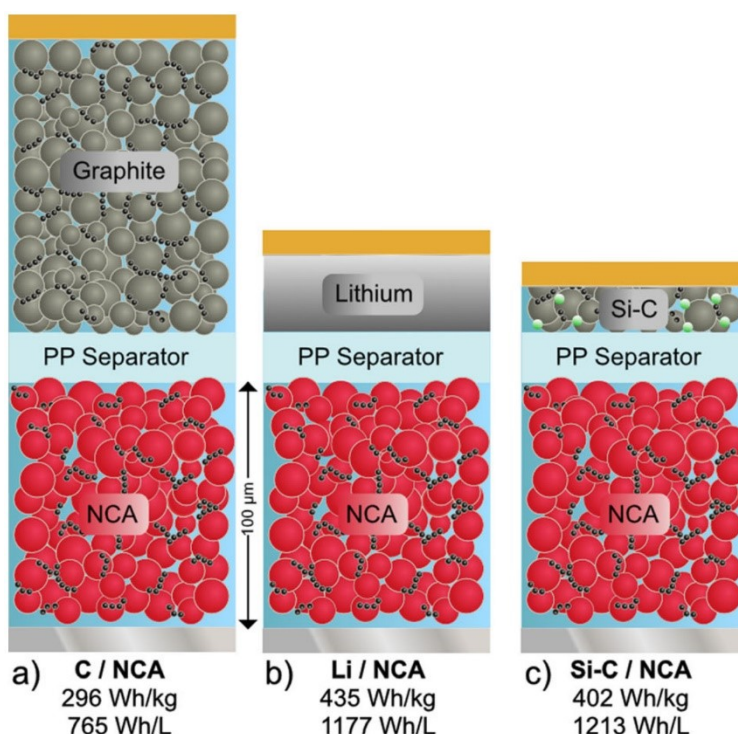


Figure 24 Schematic representation of various LIB electrode stacks with calculated specific energies and energy densities (a) Graphite / nickel cobalt aluminum oxide (NCA), (b) metallic lithium / NCA, (c) Carbon-coated Si (SiC) / NCA. The shown scale arrows refer to the thickness of the composite cathode of $100 \mu\text{m}$.^[208]

Reproduced (modified) with permission from Ref. [208]. Copyright 2017, Springer Nature.

However, due to the thermodynamic instability of the organic electrolyte in contact with high-surface area lithium and a moss-like or dendritic growth of lithium metal during charging, alternative novel and safe anode materials were explored.

Besides the introduced carbonaceous anode materials, insertion-type transition metal oxides such as lithium titanate ($\text{Li}_4\text{Ti}_5\text{O}_{12}$) or TiO_2 -based oxides exhibit negligible volume changes upon lithium extraction and insertion, which enables high rate applications.^[49, 209] A drawback of these oxide-based insertion-type anodes is however an increased density, which lowers the overall gravimetric capacity. In addition, the relatively high Li-ion insertion potential of over 1 V versus metallic lithium further limits the power density by a reduced cell voltage. However, due to their low volume changes, insertion-type anode materials are ideal candidates for the construction of all-solid-state batteries as depicted in Figure 25 that use solid ion conducting electrolytes (e.g. $\text{Li}_{1.3}\text{Al}_{0.3}\text{Ti}_{1.7}(\text{PO}_4)_3$ (LATP)).^[208] It is believed that solid state electrolytes can increase the operational safety, as the thermally/chemically unstable liquid organic solvents and moisture sensitive and toxic conducting salts such as LiPF_6 can be avoided.^[210-211]

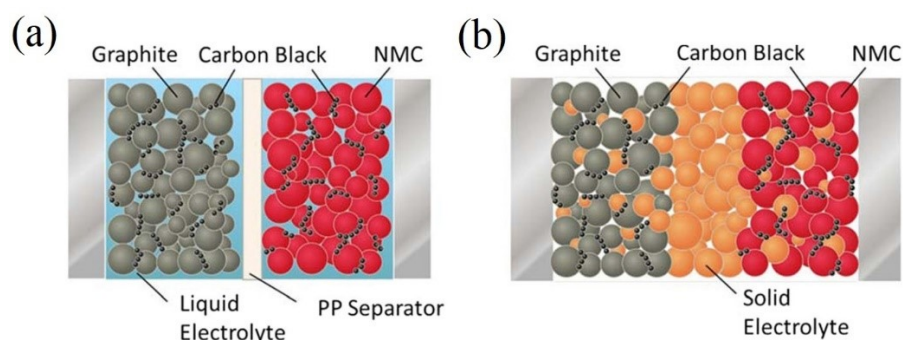


Figure 25 Schematic illustrations of a conventional lithium ion cell with graphite anode and lithium nickel manganese cobalt oxide (NMC) cathode containing a liquid electrolyte and a polypropylene (PP) separator (a) and an all-solid-state battery (ASSB) cell with an electrolyte and separating layer consisting of an ionically conductive material (b).^[208]

Reproduced with permission from Ref. [208]. Copyright 2017, Springer Nature.

For a significant increase in gravimetric and volumetric energy density, the alloying-type anodes of transition metals and metalloids such as Si, Sn, Ge or Zn can be used. Alloys with lithium or sodium such as $\text{Li}_{15}\text{Si}_4$ or $\text{Li}_{4.4}\text{Sn}$ have unprecedented high gravimetric capacities of

3579 mAh g⁻¹[212] (Si) and 790 mAh g⁻¹[213] (Sn), which are however accompanied by huge volume changes of ≈ 280 [214] and up to 300 % [213] for Si and Sn, respectively. This fact drastically limits the cyclability due to a mechanical disintegration - often termed 'pulverization' - of the electrodes. In addition, the continuous increase of the electrode/electrolyte interface due this pulverization process leads to an ongoing decomposition of the electrolyte, as no stable solid electrolyte interface can be formed.[215]

To overcome these problems, (transition) metal oxide nanostructures instead of the respective (transition) metals were explored as active material in alkali ion battery anodes. On the one hand, the resulting conversion reactions further increase the maximum theoretical gravimetric capacity to 4200 mAh g⁻¹[216] and 1491 mAh g⁻¹[217] for SiO₂ and SnO₂, respectively. On the other hand, the use of oxides instead of metals also leads to the formation of an amorphous alkali ion super oxide (MO₂) matrix around the ideally nanosized (transition) metal. The formed metallic nanostructure thereby allows for an efficient charge transfer and the amorphous LiO₂ or SnO₂ phase effectively buffers the huge volume changes upon alloying.[215]

In summary, (transition) metal oxide nanostructure-based conversion and alloying type anodes may be regarded as a safe alternative to metallic alkali metal electrodes with otherwise comparable calculated full-cell capacities, as indicated in Figure 24b,c.

The introduction of transition metal oxides for energy storage in secondary alkali ion batteries is continued in Chapter 3 of this thesis, which will give a brief literature overview of advanced ceramic anodes for secondary lithium and sodium ion batteries including those for all-solid-state batteries. Chapter 4 gives a further, more detailed literature overview of recent developments in the field of nanostructured tin-oxide based anodes for lithium, sodium and potassium ion batteries.

1.6 References

- [1] A. D. McNaught, A. Wilkinson, IUPAC Compendium of Chemical Terminology 2nd ed., Blackwell Scientific Publications, Oxford **1997**.
- [2] C. N. R. Rao, *Annu. Rev. Phys. Chem.* **1989**, 40, 291.
- [3] G. Cao, L. E. DeLong, in *Frontiers of 4d- and 5d-Transition Metal Oxides* (Eds. G. Cao, L. E. DeLong), World Scientific Publishing **2013**, p. 1.
- [4] J. A. Rodríguez, M. Fernández-García, in *Synthesis, Properties, and Applications of Oxide Nanomaterials* (Eds: J. A. Rodríguez, M. Fernández-García), John Wiley & Sons **2006**, p. 1.
- [5] J. F. Weaver, *Chem. Rev.* **2013**, 113, 4164.
- [6] H. Over, Y. D. Kim, A. P. Seitsonen, S. Wendt, E. Lundgren, M. Schmid, P. Varga, A. Morgante, G. Ertl, *Science* **2000**, 287, 1474.
- [7] W. H. Qi, M. P. Wang, *Mater. Chem. Phys.* **2004**, 88, 280.
- [8] K. Suttiponparnit, J. Jiang, M. Sahu, S. Suvachittanont, T. Charinpanitkul, P. Biswas, *Nanoscale Res. Lett.* **2010**, 6, 27.
- [9] J. Pal, T. Pal, *Nanoscale* **2015**, 7, 14159.
- [10] D. Friebel, M. W. Louie, M. Bajdich, K. E. Sanwald, Y. Cai, A. M. Wise, M.-J. Cheng, D. Sokaras, T.-C. Weng, R. Alonso-Mori, R. C. Davis, J. R. Bargar, J. K. Nørskov, A. Nilsson, A. T. Bell, *J. Am. Chem. Soc.* **2015**, 137, 1305.
- [11] C. Yu, X. Han, Z. Liu, C. Zhao, H. Huang, J. Yang, Y. Niu, J. Qiu, *Carbon* **2018**, 126, 437.
- [12] K. A. Stoerzinger, L. Qiao, M. D. Biegalski, Y. Shao-Horn, *J. Phys. Chem. Lett.* **2014**, 5, 1636.
- [13] K. Fominykh, D. Böhm, S. Zhang, A. Folger, M. Döblinger, T. Bein, C. Scheu, D. Fattakhova-Rohlfing, *Chem. Mater.* **2017**, 29, 7223.
- [14] H. Peng, J. Li, *J. Phys. Chem. C* **2008**, 112, 20241.
- [15] L. Vayssieres, C. Sathe, S. M. Butorin, D. K. Shuh, J. Nordgren, J. Guo, *Adv. Mater.* **2005**, 17, 2320.
- [16] X. Xue, W. Ji, Z. Mao, H. Mao, Y. Wang, X. Wang, W. Ruan, B. Zhao, J. R. Lombardi, *J. Phys. Chem. C* **2012**, 116, 8792.
- [17] K. Fominykh, G. C. Tok, P. Zeller, H. Hajiyani, T. Miller, M. Döblinger, R. Pentcheva, T. Bein, D. Fattakhova-Rohlfing, *Adv. Funct. Mater.* **2017**, 27, 1605121.

- [18] K. Fominykh, P. Chernev, I. Zaharieva, J. Sicklinger, G. Stefanic, M. Döblinger, A. Müller, A. Pokharel, S. Böcklein, C. Scheu, T. Bein, D. Fattakhova-Rohlfing, *ACS Nano* **2015**, 9, 5180.
- [19] S. Yoo, B. Kang, *Nanotechnology* **2013**, 24, 424012.
- [20] M. Yu, F. Waag, C. K. Chan, C. Weidenthaler, S. Barcikowski, H. Tüysüz, *ChemSusChem* **2020**, 13, 520.
- [21] K. Fominykh, J. M. Feckl, J. Sicklinger, M. Döblinger, S. Böcklein, J. Ziegler, L. Peter, J. Rathousky, E.-W. Scheidt, T. Bein, D. Fattakhova-Rohlfing, *Adv. Funct. Mater.* **2014**, 24, 3123.
- [22] W. Xiao, X. Huang, W. Song, Y. Yang, T. S. Heng, J. M. Xue, Y. P. Feng, J. Ding, *Nano Energy* **2016**, 25, 60.
- [23] L. Zhang, H. Li, K. Li, L. Li, J. Wei, L. Feng, Q. Fu, *J. Alloy Compds.* **2016**, 680, 146.
- [24] Y. Fang, X. Li, Y. Hu, F. Li, X. Lin, M. Tian, X. An, Y. Fu, J. Jin, J. Ma, *J. Power Sources* **2015**, 300, 285.
- [25] S. Liu, W. Yan, X. Cao, Z. Zhou, R. Yang, *Int. J. Hydrogen Energ.* **2016**, 41, 5351.
- [26] J.-H. Zhang, J.-Y. Feng, T. Zhu, Z.-L. Liu, Q.-Y. Li, S.-Z. Chen, C.-W. Xu, *Electrochim. Acta* **2016**, 196, 661.
- [27] I. Concina, Z. H. Ibupoto, A. Vomiero, *Adv. Energy Mater.* **2017**, 7, 1700706.
- [28] R. van de Krol, Y. Liang, J. Schoonman, *J. Mater. Chem.* **2008**, 18, 2311.
- [29] X. Shi, K. Zhang, J. H. Park, *Int. J. Hydrogen Energ.* **2013**, 38, 12725.
- [30] A. G. Hufnagel, K. Peters, A. Müller, C. Scheu, D. Fattakhova-Rohlfing, T. Bein, *Adv. Funct. Mater.* **2016**, 26, 4435.
- [31] M. Ma, J. K. Kim, K. Zhang, X. Shi, S. J. Kim, J. H. Moon, J. H. Park, *Chem. Mater.* **2014**, 26, 5592.
- [32] Z. Zhang, J. Liu, J. Gu, L. Su, L. Cheng, *Energ. & Environ. Sci.* **2014**, 7, 2535.
- [33] K.-W. Park, K.-S. Seol, *Electrochem. Commun.* **2007**, 9, 2256.
- [34] M. Nagarajan, G. Paruthimal Kalaignan, G. A. Pathanjali, *Ionics* **2013**, 19, 127.
- [35] Z. Yan, W. Wei, J. Xie, S. Meng, X. Lü, J. Zhu, *J. Power Sources* **2013**, 222, 218.
- [36] Z. Yan, J. Xie, J. Jing, M. Zhang, W. Wei, S. Yin, *Int. J. Hydrogen Energ.* **2012**, 37, 15948.
- [37] H. Xu, X. Hou, *Int. J. Hydrogen Energ.* **2007**, 32, 4397.
- [38] C. Goswami, K. K. Hazarika, P. Bharali, *Mater. Sci. Energ. Techn.* **2018**, 1, 117.

- [39] Y. Liang, Y. Li, H. Wang, J. Zhou, J. Wang, T. Regier, H. Dai, *Nat. Mater.* **2011**, 10, 780.
- [40] M. S. Ahmed, B. Choi, Y.-B. Kim, *Sci. Rep.* **2018**, 8, 2543.
- [41] B. Zhao, Y. Zheng, F. Ye, X. Deng, X. Xu, M. Liu, Z. Shao, *ACS Appl. Mater. Inter.* **2015**, 7, 14446.
- [42] J. Park, J. Joo, S. G. Kwon, Y. Jang, T. Hyeon, *Angew. Chem. Int. Edit.* **2007**, 46, 4630.
- [43] N. Pinna, M. Niederberger, *Angew. Chem. Int. Edit.* **2008**, 47, 5292.
- [44] M. Niederberger, N. Pinna, in *Metal Oxide Nanoparticles in Organic Solvents: Synthesis, Formation, Assembly and Application* (Eds: M. Niederberger, N. Pinna), Springer London, London **2009**, p. 7.
- [45] R. Deshmukh, M. Niederberger, in *The Sol-Gel Handbook*, (Eds: D. Levy, M. Zayat), Wiley-VCH Verlag, Weinheim **2015**, p. 29.
- [46] N. Pinna, *J. Mater. Chem.* **2007**, 17, 2769.
- [47] V. Müller, M. Rasp, G. Štefanić, J. Ba, S. Günther, J. Rathousky, M. Niederberger, D. Fattakhova-Rohlfing, *Chem. Mater.* **2009**, 21, 5229.
- [48] N. Pinna, G. Garnweitner, P. Beato, M. Niederberger, M. Antonietti, *Small* **2005**, 1, 112.
- [49] J. M. Szeifert, J. M. Feckl, D. Fattakhova-Rohlfing, Y. Liu, V. Kalousek, J. Rathousky, T. Bein, *J. Am. Chem. Soc.* **2010**, 132, 12605.
- [50] Y. Liu, J. M. Szeifert, J. M. Feckl, B. Mandlmeier, J. Rathousky, O. Hayden, D. Fattakhova-Rohlfing, T. Bein, *ACS Nano* **2010**, 4, 5373.
- [51] J. M. Feckl, H. K. Dunn, P. M. Zehetmaier, A. Müller, S. R. Pendlebury, P. Zeller, K. Fominykh, I. Kondofersky, M. Döblinger, J. R. Durrant, C. Scheu, L. Peter, D. Fattakhova-Rohlfing, T. Bein, *Adv. Mater. Interfaces* **2015**, 2, 1500358.
- [52] F. Zoller, K. Peters, P. M. Zehetmaier, P. Zeller, M. Döblinger, T. Bein, Z. k. Sofer, D. Fattakhova-Rohlfing, *Adv. Funct. Mater.* **2018**, 28, 1706529.
- [53] Z. Chen, Z. Duan, Z. Wang, X. Liu, L. Gu, F. Zhang, M. Dupuis, C. Li, *ChemCatChem* **2017**, 9, 3641.
- [54] H. Jia, J. Stark, L. Q. Zhou, C. Ling, T. Sekito, Z. Markin, *RSC Adv.* **2012**, 2, 10874.
- [55] H. Yu, N. Danilovic, Y. Wang, W. Willis, A. Poozhikunnath, L. Bonville, C. Capuano, K. Ayers, R. Maric, *Appl. Catal. B Environ.* **2018**, 239, 133.

- [56] T. Kimura, in *Advances in Ceramics-Synthesis and Characterization, Processing and Specific Applications*, (Ed: C. Sikalidis), IntechOpen Limited, London **2011**, p. 75.
- [57] J. P. Zuniga, M. Abdou, S. K. Gupta, Y. Mao, *J. Vis. Exp.* **2018**, (140), e58482
- [58] C. Felix, B. J. Bladergroen, V. Linkov, B. G. Pollet, S. Pasupathi, *Catalysts* **2019**, 9, 318.
- [59] H. Lv, G. Zhang, C. Hao, C. Mi, W. Zhou, D. Yang, B. Li, C. Zhang, *RSC Adv.* **2017**, 7, 40427.
- [60] E. Oakton, D. Lebedev, M. Povia, D. F. Abbott, E. Fabbri, A. Fedorov, M. Nachtegaal, C. Copéret, T. J. Schmidt, *ACS Catal.* **2017**, 7, 2346.
- [61] R. V. Kumar, Y. Diamant, A. Gedanken, *Chem. Mater.* **2000**, 12, 2301.
- [62] S. Musić, S. Popović, M. Maljković, Z. Skoko, K. Furić, A. Gajović, *Mater. Lett.* **2003**, 57, 4509.
- [63] H. Yan, Y. Sun, L. He, J.-C. Nie, *Mater. Res. Bull.* **2011**, 46, 2120.
- [64] J. Zhang, X. Lin, D. Xue, B. Xu, D. Long, F. Xue, X. Duan, W. Ye, M. Wang, Q. Li, *Nanoscale* **2019**, 11, 3200.
- [65] R. Ma, T. Sasaki, *Accounts Chem. Res.* **2015**, 48, 136.
- [66] T. Guo, M.-S. Yao, Y.-H. Lin, C.-W. Nan, *CrystEngComm* **2015**, 17, 3551.
- [67] D. Fattakhova-Rohlfing, A. Zaleska, T. Bein, *Chem. Rev.* **2014**, 114, 9487.
- [68] G. Binitha, M. S. Soumya, A. A. Madhavan, P. Praveen, A. Balakrishnan, K. R. V. Subramanian, M. V. Reddy, S. V. Nair, A. S. Nair, N. Sivakumar, *J. Mater. Chem. A* **2013**, 1, 11698.
- [69] M. Macías, A. Chacko, J. P. Ferraris, K. J. Balkus, *Mat. Res. S. C.* **2005**, 86, 1.
- [70] D. R. Cummins, U. Martinez, A. Sherehiy, R. Kappera, A. Martinez-Garcia, R. K. Schulze, J. Jasinski, J. Zhang, R. K. Gupta, J. Lou, M. Chhowalla, G. Sumanasekera, A. D. Mohite, M. K. Sunkara, G. Gupta, *Nat. Commun.* **2016**, 7, 11857.
- [71] J. Yang, Z. Zeng, J. Kang, S. Betzler, C. Czarnik, X. Zhang, C. Ophus, C. Yu, K. Bustillo, M. Pan, J. Qiu, L.-W. Wang, H. Zheng, *Nat. Mater.* **2019**, 18, 970.
- [72] T. Yang, T. T. Song, M. Callsen, J. Zhou, J. W. Chai, Y. P. Feng, S. J. Wang, M. Yang, *Adv. Mater. Interfaces* **2019**, 6, 1801160.
- [73] G. Zhou, L. Luo, L. Li, J. Ciston, E. A. Stach, J. C. Yang, *Phys. Rev. Lett.* **2012**, 109, 235502.
- [74] J. Tao, T. Luttrell, M. Batzill, *Nat. Chem.* **2011**, 3, 296.

- [75] Z. Sun, T. Liao, Y. Dou, S. M. Hwang, M.-S. Park, L. Jiang, J. H. Kim, S. X. Dou, *Nat. Commun.* **2014**, 5, 3813.
- [76] P. Yang, D. Zhao, D. I. Margolese, B. F. Chmelka, G. D. Stucky, *Chem. Mater.* **1999**, 11, 2813.
- [77] Z. Liu, X. Yuan, S. Zhang, J. Wang, Q. Huang, N. Yu, Y. Zhu, L. Fu, F. Wang, Y. Chen, Y. Wu, *NPG Asia Mater.* **2019**, 11, 12.
- [78] G. Lui, G. Li, X. Wang, G. Jiang, E. Lin, M. Fowler, A. Yu, Z. Chen, *Nano Energy* **2016**, 24, 72.
- [79] J. E. Park, S. Kim, O.-H. Kim, C.-Y. Ahn, M.-J. Kim, S. Y. Kang, T. I. Jeon, J.-G. Shim, D. W. Lee, J. H. Lee, Y.-H. Cho, Y.-E. Sung, *Nano Energy* **2019**, 58, 158.
- [80] Y. Liu, K. Peters, B. Mandlmeier, A. Müller, K. Fominykh, J. Rathousky, C. Scheu, D. Fattakhova-Rohlfing, *Electrochim. Acta* **2014**, 140, 108.
- [81] M. Schalenbach, A. Zeradjanin, O. Kasian, S. Cherevko, K. Mayrhofer, *Int. J. Electrochem. Sc.* **2018**, 13, 1173.
- [82] P. Millet, in *Hydrogen Production* (Ed: A. Godula-Jopek), Wiley-VCH Verlag GmbH & Co. KGaA, **2015**, p. 33.
- [83] A. P. Fickett, F. R. Kalhammer, in *Hydrogen: Its technology and implications. Volume 1- Hydrogen production technology.*, Vol. 1 (Eds: K. E. Cox, K. D. Williamson), CRC Press **1977**, p. 153.
- [84] M. Carmo, D. L. Fritz, J. Mergel, D. Stolten, *Int. J. Hydrogen Energ.* **2013**, 38, 4901.
- [85] M. E. G. Lyons, S. Floquet, *Phys. Chem. Chem. Phys.* **2011**, 13, 5314.
- [86] Z. Ma, Y. Zhang, S. Liu, W. Xu, L. Wu, Y.-C. Hsieh, P. Liu, Y. Zhu, K. Sasaki, J. N. Renner, K. E. Ayers, R. R. Adzic, J. X. Wang, *J. Electroanal. Chem.* **2018**, 819, 296.
- [87] Y. Ping, R. J. Nielsen, W. A. Goddard, *J. Am. Chem. Soc.* **2017**, 139, 149.
- [88] H. Seo, K. H. Cho, H. Ha, S. Park, J. S. Hong, K. Jin, K. T. Nam, *J. Korean Ceram. Soc.* **2017**, 54, 1.
- [89] T. Reier, H. N. Nong, D. Teschner, R. Schlögl, P. Strasser, *Adv. Energy Mater.* **2017**, 7, 1601275.
- [90] N.-T. Suen, S.-F. Hung, Q. Quan, N. Zhang, Y.-J. Xu, H. M. Chen, *Chem. Soc. Rev.* **2017**, 46, 337.
- [91] X. Li, X. Hao, A. Abudula, G. Guan, *J. Mater. Chem. A* **2016**, 4, 11973.
- [92] M. Zeng, Y. Li, *J. Mater. Chem. A* **2015**, 3, 14942.

- [93] C. Wang, F. Lan, Z. He, X. Xie, Y. Zhao, H. Hou, L. Guo, V. Murugadoss, H. Liu, Q. Shao, Q. Gao, T. Ding, R. Wei, Z. Guo, *ChemSusChem* **2019**, 12, 1576.
- [94] M. Bernt, H. A. Gasteiger, *J. Electrochem. Soc.* **2016**, 163, F3179.
- [95] M. S. Burke, S. Zou, L. J. Enman, J. E. Kellon, C. A. Gabor, E. Pledger, S. W. Boettcher, *J. Phys. Chem. Lett.* **2015**, 6, 3737.
- [96] M. S. Burke, L. J. Enman, A. S. Batchellor, S. Zou, S. W. Boettcher, *Chem. Mater.* **2015**, 27, 7549.
- [97] G. Liu, K. Wang, X. Gao, D. He, J. Li, *Electrochim. Acta* **2016**, 211, 871.
- [98] X. Long, Z. Ma, H. Yu, X. Gao, X. Pan, X. Chen, S. Yang, Z. Yi, *J. Mater. Chem. A* **2016**, 4, 14939.
- [99] M.-I. Jamesh, X. Sun, *J. Power Sources* **2018**, 400, 31.
- [100] J. Zheng, W. Zhou, T. Liu, S. Liu, C. Wang, L. Guo, *Nanoscale* **2017**, 9, 4409.
- [101] Y. Li, H. Zhang, M. Jiang, Q. Zhang, P. He, X. Sun, *Adv. Funct. Mater.* **2017**, 27, 1702513.
- [102] C. Tang, R. Zhang, W. Lu, L. He, X. Jiang, A. M. Asiri, X. Sun, *Adv. Mater.* **2017**, 29, 1602441.
- [103] B. Dong, X. Zhao, G.-Q. Han, X. Li, X. Shang, Y.-R. Liu, W.-H. Hu, Y.-M. Chai, H. Zhao, C.-G. Liu, *J. Mater. Chem. A* **2016**, 4, 13499.
- [104] Y. Liu, Q. Li, R. Si, G.-D. Li, W. Li, D.-P. Liu, D. Wang, L. Sun, Y. Zhang, X. Zou, *Adv. Mater.* **2017**, 29, 1606200.
- [105] I. H. Kwak, H. S. Im, D. M. Jang, Y. W. Kim, K. Park, Y. R. Lim, E. H. Cha, J. Park, *ACS Appl. Mater. Inter.* **2016**, 8, 5327.
- [106] X. Wang, Y. Zheng, J. Yuan, J. Shen, J. Hu, A.-j. Wang, L. Wu, L. Niu, *Electrochim. Acta* **2017**, 225, 503.
- [107] R. Li, D. Zhou, J. Luo, W. Xu, J. Li, S. Li, P. Cheng, D. Yuan, *J. Power Sources* **2017**, 341, 250.
- [108] H. Jin, J. Wang, D. Su, Z. Wei, Z. Pang, Y. Wang, *J. Am. Chem. Soc.* **2015**, 137, 2688.
- [109] Y. Rao, Y. Wang, H. Ning, P. Li, M. Wu, *ACS Appl. Mater. Inter.* **2016**, 8, 33601.
- [110] J. Chi, H. Yu, B. Qin, L. Fu, J. Jia, B. Yi, Z. Shao, *ACS Appl. Mater. Inter.* **2017**, 9, 464.
- [111] H. Yang, Y. Long, Y. Zhu, Z. Zhao, P. Ma, J. Jin, J. Ma, *Green Chem.* **2017**, 19, 5809.

- [112] X. Li, X. Hao, Z. Wang, A. Abudula, G. Guan, *J. Power Sources* **2017**, 347, 193.
- [113] X. Long, S. Xiao, Z. Wang, X. Zheng, S. Yang, *Chem. Commun.* **2015**, 51, 1120.
- [114] S. Marini, P. Salvi, P. Nelli, R. Pesenti, M. Villa, M. Berrettoni, G. Zangari, Y. Kiros, *Electrochim. Acta* **2012**, 82, 384.
- [115] F. Song, L. Bai, A. Moysiadou, S. Lee, C. Hu, L. Liardet, X. Hu, *J. Am. Chem. Soc.* **2018**, 140, 7748.
- [116] C. Hu, L. Zhang, J. Gong, *Energ. Environ. Sci.* **2019**, 12, 2620.
- [117] F. Calle-Vallejo, O. A. Díaz-Morales, M. J. Kolb, M. T. M. Koper, *ACS Catal.* **2015**, 5, 869.
- [118] I. C. Man, H.-Y. Su, F. Calle-Vallejo, H. A. Hansen, J. I. Martínez, N. G. Inoglu, J. Kitchin, T. F. Jaramillo, J. K. Nørskov, J. Rossmeisl, *ChemCatChem* **2011**, 3, 1159.
- [119] S. Trasatti, *J. Electroanal. Chem.* **1980**, 111, 125.
- [120] R. Subbaraman, D. Tripkovic, K.-C. Chang, D. Strmcnik, A. P. Paulikas, P. Hirunsit, M. Chan, J. Greeley, V. Stamenkovic, N. M. Markovic, *Nat. Mater.* **2012**, 11, 550.
- [121] F. Lu, M. Zhou, Y. Zhou, X. Zeng, *Small* **2017**, 13, 1701931.
- [122] K. Fan, Y. Ji, H. Zou, J. Zhang, B. Zhu, H. Chen, Q. Daniel, Y. Luo, J. Yu, L. Sun, *Angew. Chem. Int. Edit.* **2017**, 56, 3289.
- [123] V. Vijayakumar, S. Y. Nam, *J. Ind. Eng. Chem.* **2019**, 70, 70.
- [124] S. J. Sondheimer, N. J. Bunce, M. E. Lemke, C. A. Fyfe, *Macromolecules* **1986**, 19, 339.
- [125] S. Cherevko, S. Geiger, O. Kasian, N. Kulyk, J.-P. Grote, A. Savan, B. R. Shrestha, S. Merzlikin, B. Breitbach, A. Ludwig, K. J. J. Mayrhofer, *Catal. Today* **2016**, 262, 170.
- [126] O. Kasian, S. Geiger, P. Stock, G. Polymeros, B. Breitbach, A. Savan, A. Ludwig, S. Cherevko, K. J. J. Mayrhofer, *J. Electrochem. Soc.* **2016**, 163, F3099.
- [127] O. Kasian, S. Geiger, T. Li, J.-P. Grote, K. Schweinar, S. Zhang, C. Scheu, D. Raabe, S. Cherevko, B. Gault, K. J. J. Mayrhofer, *Energ. Environ. Sci.* **2019**, 12, 3548.
- [128] S. Cherevko, S. Geiger, O. Kasian, A. Mingers, K. J. J. Mayrhofer, *J. Electroanal. Chem.* **2016**, 774, 102.
- [129] S. Geiger, O. Kasian, B. R. Shrestha, A. M. Mingers, K. J. J. Mayrhofer, S. Cherevko, *J. Electrochem. Soc.* **2016**, 163, F3132.
- [130] M. Vuković, *J. Appl. Electrochem.* **1987**, 17, 737.
- [131] M. Vuković, *J. Appl. Electrochem.* **1990**, 20, 969.

- [132] D. F. Abbott, D. Lebedev, K. Waltar, M. Povia, M. Nachtegaal, E. Fabbri, C. Copéret, T. J. Schmidt, *Chem. Mater.* **2016**, 28, 6591.
- [133] O. Kasian, J.-P. Grote, S. Geiger, S. Cherevko, K. J. J. Mayrhofer, *Angew. Chem. Int. Edit.* **2018**, 57, 2488.
- [134] M. Bernt, A. Hartig-Weiß, M. F. Tovini, H. A. El-Sayed, C. Schramm, J. Schröter, C. Gebauer, H. A. Gasteiger, *Chem.-Ing.-Tech.* **2019**, 92, 31.
- [135] J. Cheng, H. Zhang, G. Chen, Y. Zhang, *Electrochim. Acta* **2009**, 54, 6250.
- [136] L.-E. Owe, M. Tsytkin, K. S. Wallwork, R. G. Haverkamp, S. Sunde, *Electrochim. Acta* **2012**, 70, 158.
- [137] S. Siracusano, N. Van Dijk, E. Payne-Johnson, V. Baglio, A. S. Aricò, *Appl. Catal. B-Environ.* **2015**, 164, 488.
- [138] P.-Y. Liu, C.-C. Hsu, M.-C. Chuang, *J. Mater. Chem. A* **2017**, 5, 2959.
- [139] J. L. Corona-Guinto, L. Cardeño-García, D. C. Martínez-Casillas, J. M. Sandoval-Pineda, P. Tamayo-Meza, R. Silva-Casarin, R. G. González-Huerta, *Int. J. Hydrogen Energ.* **2013**, 38, 12667.
- [140] R. G. González-Huerta, G. Ramos-Sánchez, P. B. Balbuena, *J. Power Sources* **2014**, 268, 69.
- [141] M. Tariq, W. Q. Zaman, W. Sun, Z. Zhou, Y. Wu, L.-m. Cao, J. Yang, *ACS Sustain. Chem. Eng.* **2018**, 6, 4854.
- [142] K. Sardar, S. C. Ball, J. D. B. Sharman, D. Thompsett, J. M. Fisher, R. A. P. Smith, P. K. Biswas, M. R. Lees, R. J. Kashtiban, J. Sloan, R. I. Walton, *Chem. Mater.* **2012**, 24, 4192.
- [143] A. Zlotorowicz, F. Seland, S. Sunde, *ECS Transactions* **2013**, 50, 71.
- [144] G. Li, H. Yu, X. Wang, D. Yang, Y. Li, Z. Shao, B. Yi, *J. Power Sources* **2014**, 249, 175.
- [145] G. Li, H. Yu, D. Yang, J. Chi, X. Wang, S. Sun, Z. Shao, B. Yi, *J. Power Sources* **2016**, 325, 15.
- [146] A. Marshall, B. Børresen, G. Hagen, S. Sunde, M. Tsytkin, R. Tunold, *Russ. J. Electrochem.* **2006**, 42, 1134.
- [147] K. B. Kokoh, E. Mayousse, T. W. Napporn, K. Servat, N. Guillet, E. Soye, A. Grosjean, A. Rakotondrainibé, J. Paul-Joseph, *Int. J. Hydrogen Energ.* **2014**, 39, 1924.
- [148] S. Xu, Y. Liu, J. Tong, W. Hu, Q. Xia, *Russ. J. Electrochem.* **2016**, 52, 1021.

- [149] H. N. Nong, L. Gan, E. Willinger, D. Teschner, P. Strasser, *Chem. Sci.* **2014**, 5, 2955.
- [150] C. Zhao, E. Yifeng, F. Louzhen, *Microchim. Acta* **2012**, 178, 107.
- [151] K. Kadakia, M. K. Datta, P. H. Jampani, S. K. Park, P. N. Kumta, *J. Power Sources* **2013**, 222, 313.
- [152] K. S. Kadakia, P. H. Jampani, O. I. Velikokhatnyi, M. K. Datta, S. K. Park, D. H. Hong, S. J. Chung, P. N. Kumta, *J. Power Sources* **2014**, 269, 855.
- [153] K. Kadakia, M. K. Datta, O. I. Velikokhatnyi, P. H. Jampani, P. N. Kumta, *Int. J. Hydrogen Energ.* **2014**, 39, 664.
- [154] K. S. Kadakia, P. H. Jampani, O. I. Velikokhatnyi, M. K. Datta, P. Patel, S. J. Chung, S. K. Park, J. A. Poston, A. Manivannan, P. N. Kumta, *Mater. Sci. Eng. B* **2016**, 212, 101.
- [155] E. Slavcheva, I. Radev, S. Bliznakov, G. Topalov, P. Andreev, E. Budevski, *Electrochim. Acta* **2007**, 52, 3889.
- [156] L. Wang, V. A. Saveleva, S. Zafeiratos, E. R. Savinova, P. Lettenmeier, P. Gazdzicki, A. S. Gago, K. A. Friedrich, *Nano Energy* **2017**, 34, 385.
- [157] M. Bernicke, E. Ortel, T. Reier, A. Bergmann, J. Ferreira de Araujo, P. Strasser, R. Kraehnert, *ChemSusChem* **2015**, 8, 1908.
- [158] E. Ortel, T. Reier, P. Strasser, R. Kraehnert, *Chem. Mater.* **2011**, 23, 3201.
- [159] S. M. Alia, S. Shulda, C. Ngo, S. Pylypenko, B. S. Pivovar, *ACS Catal.* **2018**, 8, 2111.
- [160] H.-S. Oh, H. N. Nong, T. Reier, M. Gliech, P. Strasser, *Chem. Sci.* **2015**, 6, 3321.
- [161] S. Kim, M. Cho, Y. Lee, *J. Electrochem. Soc.* **2017**, 164, B3029.
- [162] B. M. Tackett, W. Sheng, S. Kattel, S. Yao, B. Yan, K. A. Kuttiyiel, Q. Wu, J. G. Chen, *ACS Catal.* **2018**, 8, 2615.
- [163] H. N. Nong, H. S. Oh, T. Reier, E. Willinger, M. G. Willinger, V. Petkov, D. Teschner, P. Strasser, *Angew. Chem. Int. Edit.* **2015**, 127, 3018.
- [164] T. Audichon, T. W. Napporn, C. Canaff, C. Morais, C. Comminges, K. B. Kokoh, *J. Phys. Chem. C* **2016**, 120, 2562.
- [165] D. Takimoto, K. Fukuda, S. Miyasaka, T. Ishida, Y. Ayato, D. Mochizuki, W. Shimizu, W. Sugimoto, *Electrocatalysis* **2017**, 8, 144.
- [166] C. Wang, Y. Sui, G. Xiao, X. Yang, Y. Wei, G. Zou, B. Zou, *J. Mater. Chem. A* **2015**, 3, 19669.
- [167] F.-D. Kong, J. Liu, A.-X. Ling, Z.-Q. Xu, H.-Y. Wang, Q.-S. Kong, *J. Power Sources* **2015**, 299, 170.

- [168] D.-H. Kim, S.-H. Park, J. Choi, M. H. Yi, H.-S. Kim, *Mater. Sci. Eng. B* **2015**, 201, 29.
- [169] B.-S. Lee, S. H. Ahn, H.-Y. Park, I. Choi, S. J. Yoo, H.-J. Kim, D. Henkensmeier, J. Y. Kim, S. Park, S. W. Nam, K.-Y. Lee, J. H. Jang, *Appl. Catal. B-Environ.* **2015**, 179, 285.
- [170] J. Zhang, G. Wang, Z. Liao, P. Zhang, F. Wang, X. Zhuang, E. Zschech, X. Feng, *Nano Energy* **2017**, 40, 27.
- [171] T. Audichon, B. Guenot, S. Baranton, M. Cretin, C. Lamy, C. Coutanceau, *Appl. Catal. B-Environ.* **2017**, 200, 493.
- [172] F.-D. Kong, S. Zhang, G.-P. Yin, J. Liu, Z.-Q. Xu, *Int. J. Hydrogen Energ.* **2013**, 38, 9217.
- [173] S. Trasatti, *Electrochim. Acta* **2000**, 45, 2377.
- [174] H. Yoo, K. Oh, Y. R. Lee, K. H. Row, G. Lee, J. Choi, *Int. J. Hydrogen Energ.* **2017**, 42, 6657.
- [175] C. Hao, H. Lv, Q. Zhao, B. Li, C. Zhang, C. Mi, Y. Song, J. Ma, *Int. J. Hydrogen Energ.* **2017**, 42, 9384.
- [176] J. Xu, G. Liu, J. Li, X. Wang, *Electrochim. Acta* **2012**, 59, 105.
- [177] H. Ohno, S. Nohara, K. Kakinuma, M. Uchida, A. Miyake, S. Deki, H. Uchida, *J. Electrochem. Soc.* **2017**, 164, F944.
- [178] F. Karimi, B. A. Peppley, *Electrochim. Acta* **2017**, 246, 654.
- [179] Z.-X. Lu, Y. Shi, C.-F. Yan, C.-Q. Guo, Z.-D. Wang, *Int. J. Hydrogen Energ.* **2017**, 42, 3572.
- [180] S. Siracusano, V. Baglio, C. D'Urso, V. Antonucci, A. S. Aricò, *Electrochim. Acta* **2009**, 54, 6292.
- [181] W. Hu, S. Chen, Q. Xia, *Int. J. Hydrogen Energ.* **2014**, 39, 6967.
- [182] A. V. Emeline, Y. Furubayashi, X. Zhang, M. Jin, T. Murakami, A. Fujishima, *J. Phys. Chem. B* **2005**, 109, 24441.
- [183] T. Reier, I. Weidinger, P. Hildebrandt, R. Kraehnert, P. Strasser, *ECS Transactions* **2013**, 58, 39.
- [184] T. Reier, D. Teschner, T. Lunkenbein, A. Bergmann, S. Selve, R. Kraehnert, R. Schlögl, P. Strasser, *J. Electrochem. Soc.* **2014**, 161, F876.

- [185] M. Bele, K. Stojanovski, P. Jovanovič, L. Moriau, G. Koderman Podboršek, J. Moškon, P. Umek, M. Sluban, G. Dražič, N. Hodnik, M. Gaberšček, *ChemCatChem* **2019**, 11, 5038.
- [186] K. N. Dinh, Q. Liang, C.-F. Du, J. Zhao, A. I. Y. Tok, H. Mao, Q. Yan, *Nano Today* **2019**, 25, 99
- [187] J. Polonský, P. Mazúr, M. Paidar, E. Christensen, K. Bouzek, *Int. J. Hydrogen Energ.* **2014**, 39, 3072.
- [188] V. K. Puthiyapura, S. Pasupathi, H. Su, X. Liu, B. Pollet, K. Scott, *Int. J. Hydrogen Energ.* **2014**, 39, 1905.
- [189] V. Skoromets, H. Němec, J. Kopeček, P. Kužel, K. Peters, D. Fattakhova-Rohlfing, A. Vetushka, M. Müller, K. Ganzerová, A. Fejfar, *J. Alloy Compd.* **2015**, 119, 19485.
- [190] K. Peters, H. N. Lokupitiya, D. Sarauli, M. Labs, M. Pribil, J. Rathouský, A. Kuhn, D. Leister, M. Stefik, D. Fattakhova-Rohlfing, *Adv. Funct. Mater.* **2016**, 26, 6682.
- [191] D. Wang, Y. Zhang, J. Wang, C. Peng, Q. Huang, S. Su, L. Wang, W. Huang, C. Fan, *ACS Appl. Mater. Inter.* **2014**, 6, 36.
- [192] J. Mazloom, F. E. Ghodsi, M. Gholami, *J. Alloy Compd.* **2013**, 579, 384.
- [193] V. K. Puthiyapura, M. Mamlouk, S. Pasupathi, B. G. Pollet, K. Scott, *J. Power Sources* **2014**, 269, 451.
- [194] A. T. Marshall, R. G. Haverkamp, *Electrochim. Acta* **2010**, 55, 1978.
- [195] S. Geiger, O. Kasian, A. M. Mingers, K. J. J. Mayrhofer, S. Cherevko, *Sci. Rep.* **2017**, 7, 4595.
- [196] U. Babic, M. Suermann, F. N. Büchi, L. Gubler, T. J. Schmidt, *J. Electrochem. Sci.* **2017**, 164, F387.
- [197] L. Zielke, A. Fallisch, N. Paust, R. Zengerle, S. Thiele, *RSC Adv.* **2014**, 4, 58888.
- [198] M. Bernt, A. Siebel, H. A. Gasteiger, *J. Electrochem. Soc.* **2018**, 165, F305.
- [199] M. Lopez, A. Schleunung, P. Biberbach (Umicore AG) *U.S. 7,976,989B2*, **2004**.
- [200] D. Bernsmeier, M. Bernicke, R. Schmack, R. Sachse, B. Paul, A. Bergmann, P. Strasser, E. Ortel, R. Kraehnert, *ChemSusChem* **2018**, 11, 2367.
- [201] A. Stein, F. Li, N. R. Denny, *Chem. Mater.* **2008**, 20, 649.
- [202] S. Y. Lee, L. Gradon, S. Janeczko, F. Iskandar, K. Okuyama, *ACS Nano* **2010**, 4, 4717.

-
- [203] M. Faustini, M. Giraud, D. Jones, J. Rozière, M. Dupont, T. R. Porter, S. Nowak, M. Bahri, O. Ersen, C. Sanchez, C. Boissière, C. Tard, J. Peron, *Adv. Energy Mater.* **2019**, 9, 1802136.
- [204] Y. Nishi, *Chem. Rec.* **2001**, 1, 406.
- [205] D. Lin, Y. Liu, Y. Cui, *Nat. Nanotechnol.* **2017**, 12, 194.
- [206] A. C. Kozen, C.-F. Lin, A. J. Pearse, M. A. Schroeder, X. Han, L. Hu, S.-B. Lee, G. W. Rubloff, M. Noked, *ACS Nano* **2015**, 9, 5884.
- [207] A. Kraytsberg, Y. Ein-Eli, *Adv. Energy Mater.* **2016**, 6, 1600655.
- [208] T. Placke, R. Kloepsch, S. Dühren, M. Winter, *J. Solid State Electr.* **2017**, 21, 1939.
- [209] V. Aravindan, Y.-S. Lee, S. Madhavi, *Adv. Energy Mater.* **2015**, 5, 1402225.
- [210] A. Aboulaich, R. Bouchet, G. Delaizir, V. Seznec, L. Tortet, M. Morcrette, P. Rozier, J.-M. Tarascon, V. Viallet, M. Dollé, *Adv. Energy Mater.* **2011**, 1, 179.
- [211] S. Yu, A. Mertens, H. Tempel, R. Schierholz, H. Kungl, R.-A. Eichel, *ACS Appl. Mater. Inter.* **2018**, 10, 22264.
- [212] M. N. Obrovac, L. Christensen, *Electrochem. Solid-St.* **2004**, 7, A93.
- [213] M. Winter, J. O. Besenhard, *Electrochim. Acta* **1999**, 45, 31.
- [214] M. N. Obrovac, L. J. Krause, *J. Electrochem. Soc.* **2007**, 154, A103.
- [215] S. Fang, D. Bresser, S. Passerini, *Adv. Energy Mater.* **2020**, 10, 1902485.
- [216] N. Yan, F. Wang, H. Zhong, Y. Li, Y. Wang, L. Hu, Q. Chen, *Sci. Rep.* **2013**, 3, 1568.
- [217] G. Ferraresi, C. Villeveille, I. Czekaj, M. Horisberger, P. Novák, M. El Kazzi, *ACS Appl. Mater. Inter.* **2018**, 10, 8712.

2. Characterization

For the development of novel nanosized oxide-based materials discussed in this thesis a variety of physico-chemical characterization techniques was employed, which allowed a comprehensive structural and functional description of the respective systems.

The atomic arrangement of inorganic materials encoded in their crystal structure is of fundamental importance for their physico-chemical properties. X-ray diffraction (XRD) is thereby a common method for an initial characterization of synthesis products providing primarily information about the crystallinity in general, the specific phase and the crystalline domain size as well as the presence of a preferential growth along the crystallographic axes.

The information about the crystalline phase and domain size can be complemented with results from vibrational spectroscopy such as Raman spectroscopy, which does not require a long-range crystalline order to be observed in contrast to X-ray diffraction. Therefore, Raman spectroscopy is a useful tool to investigate the phase or surface termination of small oxide nanoparticles and further allows the detection of non-crystalline carbonaceous materials as present in oxide/carbon composite materials used in battery materials, for example.

The properties of phase transitions and related temperatures, as well as (residual) carbon content was furthermore determined by thermogravimetric analysis and differential scanning calorimetry.

To determine the size of synthesized particles, dispersions can be measured by dynamic light scattering (DLS) to assess the hydrodynamic radius and compare it to the crystalline domain size calculated by XRD line broadening. Furthermore, zeta potential measurements as a DLS-based technique can be performed as well, to determine the surface charge of particles which in turn allows one to draw conclusions about the agglomeration behaviour in different solvents.

To determine the overall atomic composition of synthesized materials or dissolved atoms in solution, inductively coupled plasma optical emission spectroscopy (ICP-OES) was used.

The pore structure, surface area and pore size distribution of nanostructured metal oxides was further analyzed quantitatively by nitrogen sorption measurements.

Electron microscopy combined with energy dispersive X-ray spectroscopy (EDX) is a most powerful technique, employed to analyse the local sample composition (by EDX), nanomorphology by scanning or transmission electron microscopy and the local crystal structure by electron diffraction.

For a quantitative description of catalyst activities, quartz crystal microbalance (QCM) sensors were employed for accurately determining the mass as well as the direct use as working electrodes in electrochemical measurements.

The bulk conductivity of samples, as a further important property influencing the OER activity, was determined by 4-point Van der Pauw and for selected samples by 2-point direct current (DC) measurements.

The functionality of synthesized catalysts was investigated concerning their redox activity by cyclic voltammetry. OER performance parameters were furthermore obtained by linear sweep voltammetry and for selected specimens by rotating disc electrode measurements. The stability of samples under OER conditions was finally investigated by chronopotentiometry measurements.

2.1 X-ray diffraction (XRD)

X-ray diffraction (XRD) is a powerful non-destructive analytical tool to derive structural and phase compositional information of a given specimen with higher order structure of its constituents. XRD measurements are commonly performed on organic and inorganic materials with crystalline structure, but also measurements on single crystal biomolecules are performed for structure-solving purposes.

X-rays, discovered in 1895 by Wilhelm Conrad Röntgen, were first employed by Max von Laue to investigate the scattering properties of this electromagnetic radiation with a wavelength in the range of chemical bonds of around 1 Å. The first diffraction pattern of Cu-sulfate published by them in 1912 supported the hypothesis of the wave-like nature of X-rays and further the hypothesis of Paul Peter Ewald regarding the space-lattice-like construction of crystalline materials. Inspired by these results, William Henry and William Lawrence Bragg developed a first diffractometer in 1913 and solved the crystal structure of NaCl.^[1-4]

$$\lambda = 2 d_{hkl} \sin \theta \quad (1)$$

Bragg's Law (equation 1) describes the condition for constructive interference of X-rays by scattering on the lattice planes of a crystalline structure and therefore the possible appearance of diffraction peaks.

According to Figure 1a, all X-rays coming from a collimated beam are elastically scattered by independent scattering centers (lattice planes) of the crystal and appear as constructive interference under the specific Bragg angle 2θ . This is true if the difference of the path length of the radiation is a multiple of λ . Bragg's Law relates the wavelength λ of the X-ray radiation, which is defined by the source material (≈ 1.54 Å for CuK_α)^[5] and the interplanar lattice spacing d_{hkl} to the diffraction angle 2θ .^[4]

An equivalent condition for constructive interference to the Bragg law is given by the Laue model (Figure 1b) for the reciprocal space. The latter introduces scattering vectors k and k' that sum up to the wavevector transfer Q . The condition of constructive interference is fulfilled if the wavevector transfer Q equals the reciprocal lattice vector G_{hkl} (Figure 1b). A direct connection of the reciprocal and real lattice is thereby given by the reciprocal lattice vector G_{hkl} , which is perpendicular to a set of (h,k,l) lattice planes (Figure 1c) and has a magnitude equal to $2\pi / d_{hkl}$.

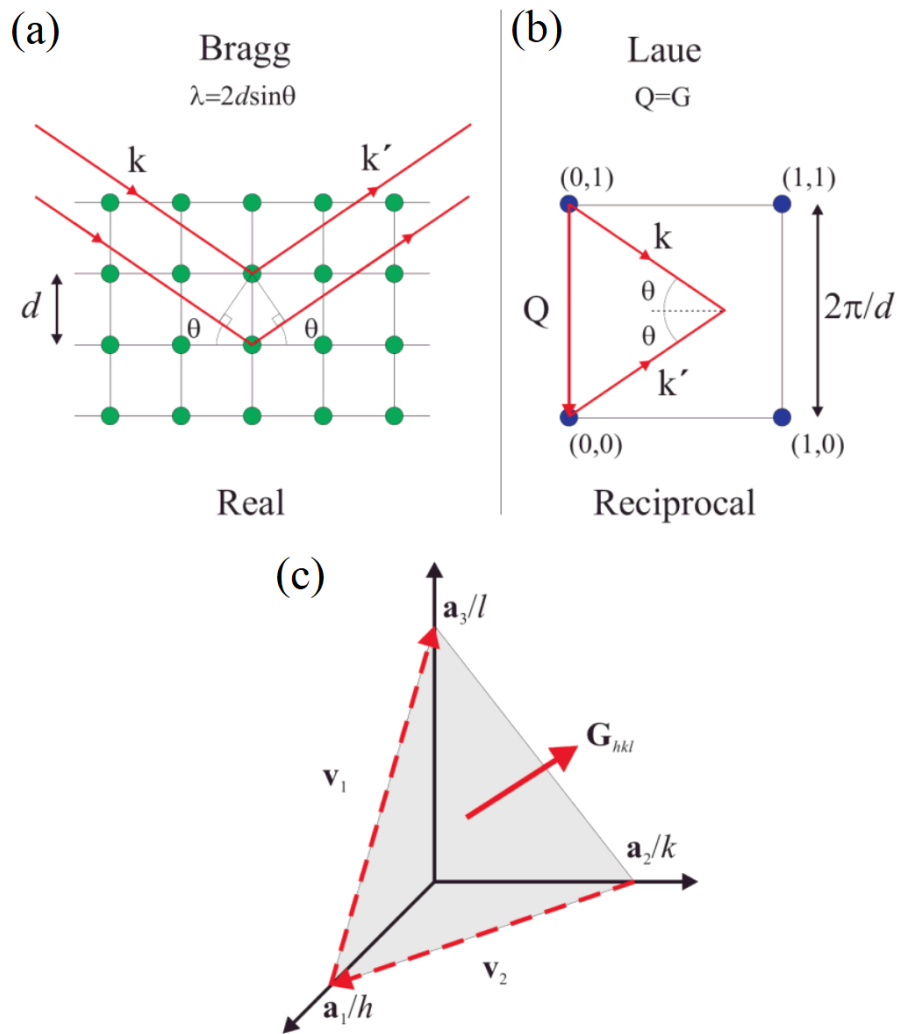


Figure 1 Schematic representation of Bragg (a) and Laue (b) conditions on constructive interference from elastic scattering of X-rays by a crystal lattice in real and reciprocal space. (c) Relation of scattering lattice vector G_{hkl} (reciprocal space) and (h,k,l) lattice planes in real space.^[1]

Reproduced (adapted) with permission from Ref. [1]. Copyright 2011, John Wiley and Sons.

The Miller indices of the lattice planes describe the orientation in the unit cell (Figure 1c) and are therefore used to label reflections representing reciprocal lattice vectors of the crystal in the diffractograms.^[4] Fulfilling Bragg's Law or the Laue relation is however only one prerequisite for the presence of reflections in a diffractogram, while the intensity (equation 1) is determined by the structure factor F_{hkl} that is composed of all scattering atoms in the crystal.

$$I_{hkl} \propto |F_{hkl}|^2 \quad (1)$$

The structure factor F_{hkl} is thereby the sum (N_j) of the scattering factors f_j of the individual scattering centers (atomic planes) of the whole crystal and related to them by equation 2:

$$F_{hkl} = \sum_{j=1}^m N_j f_j e^{[2\pi i(hx_j + ky_j + lz_j)]} \quad (2)$$

F_{hkl} further depends on the position of scattering factors in the unit cell $x_j y_j z_j$ and on the quantity of the scattering factor f_j , which describes the X-ray scattering ability with respect to the incident angle and whose magnitude is a function of the electron density, strongly related to the atomic number or charge distribution within a molecule.^[1]

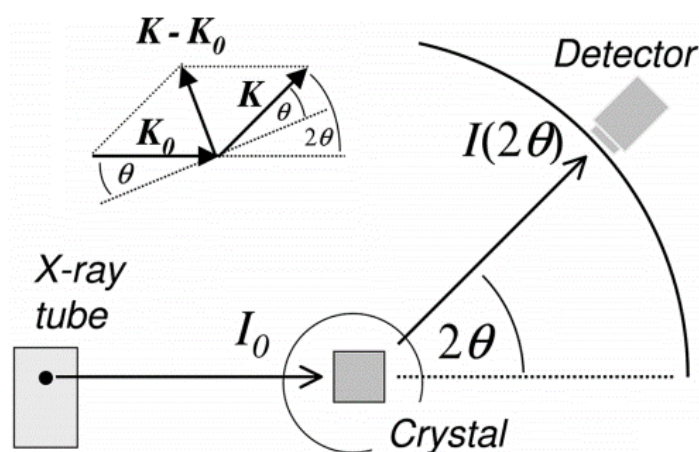


Figure 2 Schematic construction of an X-ray diffractometer in transmission mode geometry.^[6]

Reproduced (adapted) with permission from Ref. [6]. Copyright 2006, Wiley-VCH Verlag GmbH & Co. KGaA, Weinheim.

Figure 2 depicts the schematic construction of an X-ray diffractometer with transmission mode geometry, opposed to the second available Bragg-Brentano parafocusing geometry, where the incident X-ray radiation is reflected by a crystalline film or powder sample. In the geometry shown above the X-rays generated by a source are collimated by slit-like apertures and are possibly filtered by a single crystal (e.g. Ge 111) used as monochromator if present before hitting the target crystal. Incident X-rays fulfilling the conditions for constructive interference and exhibiting a measurable intensity determined by the structure factor F_{hkl} are scattered in the angle of 2θ . The detector located on a semicircle scans a given range of 2θ to record all

possible reflections. Polycrystalline samples (powders) are thereby rotated while measuring to average out orientation-induced intensity variations of the individual crystalline domains and to record all possible reflections of the respective material.

X-ray diffractograms can provide a variety of information about a sample that is encoded in the position, intensity and shape of the reflections. Comparison with crystallographic database entries and Rietveld refinement can reveal the phase composition, unit cell lattice parameters and Bravais lattice symmetry as well as residual strain (macrostrain), crystal structure, epitaxy/texture/orientation and crystallite size and microstrain.^[1, 7-8]

A common method very useful for nanosized inorganic materials to determine the crystallite domain size is to analyze the broadening of diffraction peaks. With the following Debye-Scherrer formula introduced in 1918, the crystallite size B is related to the full width at half maximum of a reflection (L) at a certain scattering angle θ with the shape-dependent proportionality factor K and the wavelength of the incident X-ray radiation λ .^[7]

$$B(2\theta) = \frac{K \lambda}{L \cos \theta} \quad (3)$$

The shape-dependent proportionality factor K is usually around 0.9 for spherical particles and the FWHM is corrected for the intrinsic instrumental broadening. The crystallite size should be determined for several reflections over a broad range of 2θ as microstrain or a strong contribution of one of the Miller indices (by elongated nanocrystals) may distort the result if microstrain is present or anisotropic particles are investigated.^[1, 7]

In the context of this thesis, wide-angle X-ray diffraction analysis was carried out in transmission mode using a STOE STADI P diffractometer with Cu- $K_{\alpha 1}$ radiation ($\lambda = 1.54060 \text{ \AA}$) and a Ge(111) single crystal monochromator equipped with a DECTRIS solid state strip detector Mythen 1K. For a typical measurement few milligrams of powdered material were enclosed between thin amorphous acetate foils in a STOE sample holder. Powder XRD patterns of the samples were collected under sample rotation with an Ω - 2θ scan in the 2θ

range from 5° to 90° with a step size of 1° and fixed integration times of 25 – 35 s per step and a resolution of 0.05° . Experimentally obtained diffraction patterns were indexed according to ICDD database entries from the Powder Diffraction File-2 (PDF-2) 2015-2019. The size of the crystalline domains was calculated from the XRD patterns for the Ir 111 (ICDD#00-006-0598), IrO_2 112 (ICDD#00-015-0870), and SnO_2 110 (ICDD#00-041-1445), β - $\text{Ni}(\text{OH})_2$ 101 (ICDD#00-014-0117), NiO 111 (ICDD#01-071-1179), β - FeOOH 112 and 301 (ICDD#01-074-2567) reflections, respectively, using the Scherrer equation (equation 3, 4).

$$B(2\theta) [nm] = \frac{0.9 \times 1.5418 \text{ \AA}}{L \times \cos\left(\frac{2\theta}{360} \pi\right)} \times 10^{-1} \quad (4)$$

with: proportionality factor $K = 0.9$

$$L = \frac{L_{hkl} - L_{instrument}}{180} \pi$$

$$L_{hkl} = FWHM(hkl)_{2\theta}$$

$$L_{instrument} = 0.107 \text{ (instrumental broadening factor)}$$

2.2 Raman spectroscopy

Raman spectroscopy is a non-destructive inelastic light scattering characterization technique that can be applied on solid, liquid and gaseous specimens. With its use the structure of molecules and inorganic compounds can be investigated through interaction of the incident electromagnetic radiation and induced population of vibrational and rotational modes.^[9]

For inorganic compounds, Raman spectroscopy can provide not only the information about the crystal structure, but it can be employed to elucidate the structure of materials without crystallinity or long-range order, or with limited dimensions as typical for nanoparticles smaller than ≈ 1.5 nm that are too small for X-ray diffraction analysis due to line broadening. The spectroscopic technique can furthermore provide information about the stress or strain present

in the phase, the grain size or defect concentrations or the presence of doping atoms which lead to a slightly altered local structure that affects the energy of vibrational modes.^[10]

It was C. V. Raman and K. S. Krishnan in 1928 who first reported the inelastic scattering of monochromatic light described as a new type of secondary radiation by organic molecules.^[11]

At that time Raman spectroscopy was not a very sensitive tool, as the scattering cross sections for inelastic (Raman) scattering of photons is very low with $1.05 \times 10^{-29} \text{ cm}^2 / \text{molecule, sr, cm}^{-1}$ for benzene as an example.^[12] It was not until the introduction of LASER technology that monochromatic light sources of sufficient intensity were available that allowed the application of Raman spectroscopy also on samples with low concentration and poor scattering properties.

In general, the illumination of a specimen with monochromatic light leads to elastic Rayleigh scattering (equation 5) of photons by the molecule or crystal structure, so that no net change in photon energy occurs.

$$\hbar\omega_{incident} = \hbar\omega_{scattered} \quad (1)$$

The energy difference exhibited by inelastic Raman scattering originates from vibrational, rotational or other low frequency modes (referred to as Ω in equation 6) of molecules or inorganic compounds.

$$\hbar\omega_{incident} = \hbar\omega_{scattered} \pm \hbar\Omega \quad (6)$$

Figure 3 depicts the energy levels of a molecule upon laser irradiation with ν_{0-2} associated with the vibrational ground and excited states as an example and higher, only transiently occupied virtual energy levels (dashed lines). The photon energy of the incident light can generally lead to multiple excitations such as molecular vibrations, optical and acoustical phonons, magnons, collective excitations (plasmons) of electrons and phonons and resonant excitations such as spin-flip excitations.

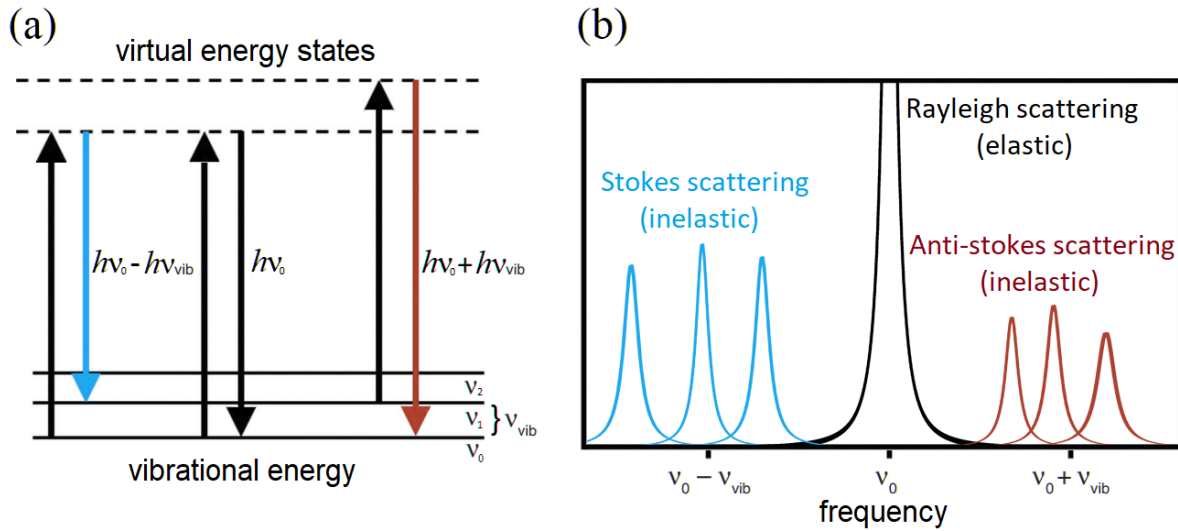


Figure 3 Schematic energy level diagram of vibrational Raman process (a) and resulting Stokes (blue peaks) and anti-Stokes (red peaks) shift of the incident frequency (b).

Elastic (Rayleigh) scattered photons are absorbed by the molecule or crystal lattice and lead to a transition from the ground state to an excited virtual state. Subsequent relaxation to the ground state then leads to the emission of a photon of the same wavelength. In inelastic Raman scattering the energy of the emitted photons can be reduced ($h\nu_0 - h\nu_{\text{vibration/rotation}}$: Stokes-shift) or increased ($h\nu_0 + h\nu_{\text{vibration/rotation}}$: Anti-Stokes shift) by either excitation from the vibrational/rotational ground state and subsequent relaxation to an excited vibrational/rotational state (Figure 3a blue transition) or vice versa (Figure 3a red transition). The intensity of Stokes Raman scattering is thereby higher than for anti-Stokes scattering, because the latter requires occupied excited states that are limited at room temperature and available according to the Boltzmann distribution.^[9]

One requirement for inelastic Raman scattering is a non-zero derivative of the electronic polarizability at the equilibrium geometry along the normal coordinate (q), which constitutes a “selection rule” for the presence or absence of Raman active modes:^[9]

$$\left(\frac{\partial\alpha}{\partial q}\right)_{q_0} \neq 0 \quad (7)$$

The intensity of stokes scattering is thereby proportional to the total power emitted by the induced dipole moment and can be written as:^[9]

$$I_{\text{Stokes}} \propto \left(\frac{\partial \alpha}{\partial q} \right)_{q_0}^2 \times (\omega_0 - \omega_q)^4 \times E_0^2 \quad (8)$$

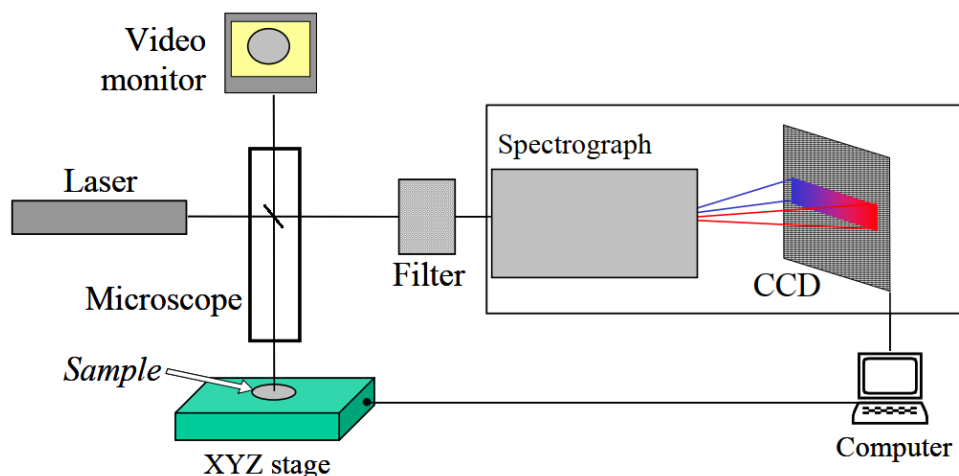


Figure 4 Schematic representation of a micro-Raman spectrometer.^[10]

Reproduced (modified) with permission from Ref. [10]. Copyright 2007, Elsevier Ltd.

Raman spectroscopy was carried out using a LabRAM HR UV–Vis (HORIBA JOBIN YVON) Raman Microscope (OLYMPUS BX41) with a SYMPHONY CCD detection system and a He–Ne laser ($\lambda = 633 \text{ nm}$) with 10 mW and an illumination spot size of $\approx 100 \mu\text{m}$ with a setup as schematically depicted in Figure 4. Spectra were recorded using a lens with a 10-fold magnification in the range from 100 to 1000 cm^{-1} with filters of OD 0.3–0.6. Spectrum accumulation mode was used with integration times of 30 s per spectrum and 600 cycles. The data acquisition was carried out with LabSpec software.

For the case of (heat) sensitive materials (e.g. $\beta\text{-FeOOH}$, $\alpha/\beta\text{-Ni(OH)}_2$, IrOOH_x) the intensity of the laser was reduced by OD filters up to 4 with prolonged integration time to avoid heat induced phase transformations.

2.3 Thermogravimetric analysis (TGA) and differential scanning calorimetry (DSC)

Thermogravimetric analysis is a technique established in the late 1950s with the introduction of automatic and recording balances in combination with programmable furnaces. With this instrumentation, a specific amount of sample is linearly heated to temperatures up to 1000 °C and more under controlled atmosphere of a purging gas to precisely monitor weight changes. The choice of the gas can provide an inert, oxidizing or reducing atmosphere by using a stream of nitrogen, argon, oxygen, synthetic air or forming gas, respectively.^[13-14]

The measured data can provide information about the temperature regime of physical and chemical phenomena occurring in the course of heating under a specific atmosphere. Physical phenomena thereby include crystalline and second-order transitions, fusion, vaporisation, sublimation, absorption, adsorption and desorption. Chemical phenomena include chemisorption, desolvation (dehydration), decomposition, oxidative degradation, solid-state reaction as well as solid-gas reactions.^[14]

Differential thermogravimetric analysis is a convenient representation of the measured data as $\left(\frac{\partial w}{\partial t}\right)$ which displays regions of mass loss as peaks to determine and compare transition or decomposition temperatures.

Differential scanning calorimetry (DSC) is a second and additional thermal analysis technique integrated in thermogravimetric analysis devices, which determines the difference in heat flow into the sample substance and a reference. DSC can thereby provide information about melting and crystallization temperatures, the heat capacity, the heat of fusion and other thermal parameters.^[15]

The basis of DSC is the equation 9, which represents the first law of thermodynamics that describes the change in internal energy equaling the sum of the exchanged heat and work:

$$\Delta U = Q + W \tag{9}$$

If a process occurs at constant volume, which is a valid approximation for solids and liquids below their melting or evaporation point, the work W is zero and the internal energy of the system equals the heat added or extracted to or from the system:

$$dU = \delta Q \quad (10)$$

The change in enthalpy of the system with including volume changes could be formulated as follows:

$$dH = dU + p dV \quad (11)$$

By the assumption of a constant volume, the DSC can measure enthalpy changes from temperature differences between the sample and a reference.

$$\Delta H = Q \quad (12)$$

Endothermic processes with positive heat flow in direction of the sample include melting or evaporation that show an increased enthalpy of the system, while exothermic processes like condensation or crystallization exhibit a decreased enthalpy versus an inert reference.^[15]

Dynamic thermogravimetric analysis (TGA) and differential scanning calorimetry (DSC) of a few milligrams of the respective samples was performed on a NETZSCH STA 440 C TG/DSC device with a heating rate of 10 K min⁻¹ in a stream of synthetic air of about 25 mL min⁻¹. Measurement data were analyzed by NETZSCH Proteus (R) Software for thermal analysis.

2.4 Dynamic light scattering (DLS)

To gain information about the apparent size or hydrodynamic radius and agglomeration behavior of nanoparticles in different solvents, the photon correlation spectroscopy (PCS) technique of dynamic light scattering (DLS) can be used. Prerequisite for this technique is a dispersibility of the particles, as a laser beam is scattered by particles in solution crossing the beam path as depicted in Figure 5a known as the Tyndall effect. The thermal activation of the

dispersed particles in solution known as Brownian motion thereby leads to a random movement of the colloidal particles.

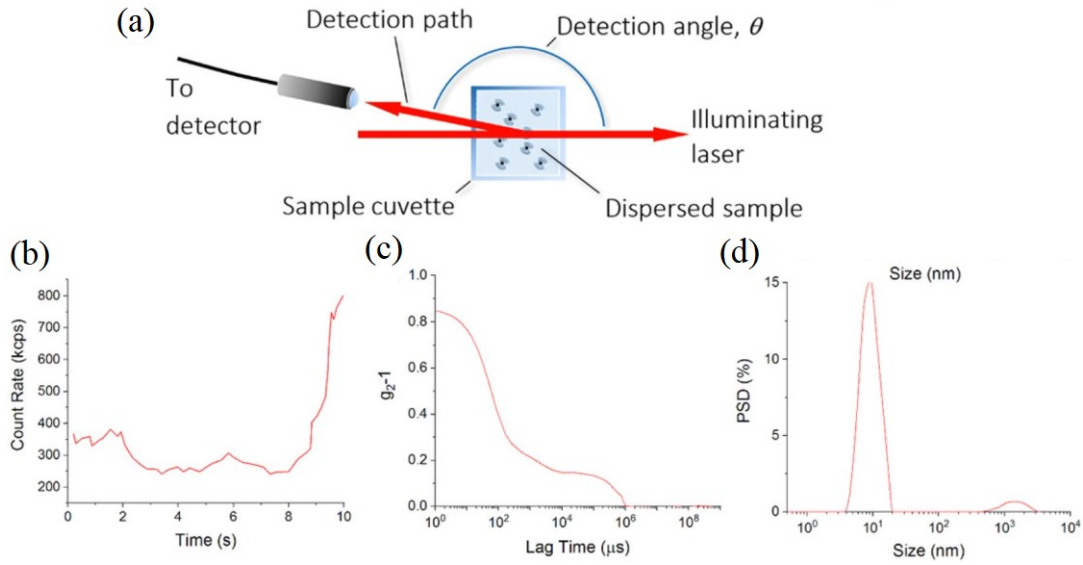


Figure 5 Schematic representation of a dynamic light scattering setup (a). Light scattering intensity (b) with derived correlation function (g_2-1) (c) and intensity weighted particle size distribution (d).^[16]

Reproduced (adapted) with permission from Ref. [16]. Copyright 2019, Springer Nature.

Upon laser irradiation each particle acts as a secondary scattering center that randomly moves in solution. The changing distance of the multiple scattering centers to the detector thereby leads to a fluctuation of (constructive or destructive) interference with time. The fluctuation of the signal intensity is dependent on the stochastic process of the nanoparticle diffusion in the solvent, which can be described by the Stokes-Einstein equation for spherical particles in dilute dispersions:^[16-19]

$$D = \frac{k_B T}{6\pi\eta R_h} \quad (13)$$

Known parameters in the DLS experiment should be the adjusted temperature T and the viscosity η of the solvent. To determine the apparent hydrodynamic radius R_h the diffusion coefficient is obtained by processing the intensity signal by an autocorrelation function:^[17]

$$g^2(\tau) = \frac{\langle I(t)I(t+\tau) \rangle}{\langle I(t) \rangle^2} \quad (14)$$

With $I(t)$ being the detected intensity at time t and $I(t+\tau)$ the intensity after a delay time τ .

This autocorrelation function $g^2(\tau)$ is related to the 1st order correlation function of the electric field according to following equation 15:^[17]

$$g^1(\tau) = \sqrt{[g^2(\tau) - 1]} \quad (15)$$

$g^1(\tau)$ is thereby related to the diffusion coefficient as following:^[17]

$$g^1(\tau) = A e^{-Dq^2\tau} + B \quad (16)$$

A equals the amplitude of the correlation function, B the baseline and q is the magnitude of the scattering vector related to the scattering angle theta, and the refractive index of the solvent by:^[17]

$$q = \left(\frac{4\pi n}{\lambda}\right) \sin\left(\frac{\theta}{2}\right) \quad (17)$$

Dynamic light scattering measurements were performed on a MALVERN Zetasizer-Nano instrument equipped with a 4 mW He-Ne laser (633 nm) and an avalanche photodiode detector. For a typical measurement ≈ 1 -2 mg of nanoparticles or powder were dispersed in 1-3 mL H₂O or EtOH. Turbid dispersions with larger aggregates eventually required ultrasonication or filtration (0.2 μ m).

2.5 Inductively coupled plasma optical emission spectroscopy

Atomic emission spectroscopy (AES) in form of flame atomic emission spectroscopy (F-AES) is a classical analytical technique to quantify the presence of metallic elements according to the emission of specific wavelengths separated by a dispersive element.

In general, atomic spectroscopy observes well-defined electronic transitions between excited state and ground state valence shell electrons of free atoms (atomized sample). These energetically well-defined transitions of valence shell electrons of free atoms (atomized sample) originating from element specific orbital energies are observable as sharp spectral lines. Although only electronic transitions involving a change in the parity of the orbital are allowed in centrosymmetric systems (e.g. s-p, s-d, s-f, p-d, p-f, d-f) according to the Laporte

rule, hydrogen already shows 374 spectral lines with transition probabilities greater than zero.^[20] Transition metals with an increased number of occupied orbitals and multiple ionization probabilities thereby lead to a spectral richness (e.g. 1573 spectral lines with transition probability for iridium)^[20] that requires an advanced excitation source and dispersive element or monochromator.^[21-23]

An inductively coupled plasma (ICP) employed as excitation source in modern optical emission spectroscopy (OES) devices typically reaches ~ 10000 K to quickly vaporize introduced aerosol samples. The plasma (typically argon) further leads to an ionization and an excitation of valence shell electrons of sample atoms. Upon relaxation to orbitals of lower energy (or the ground state), the energy difference between the respective atomic orbitals is emitted as a photon with corresponding wavelength resulting in the formation of atom specific spectral lines.^[21-22]

Generated photons are collected by a lens or concave mirror and focused on the aperture of a wavelength selector or monochromator before they are registered by a photodetector. The signal is processed by a computer.^[21]

Advantages of the ICP technique over conventional sources such as an acetylene flame are the high temperature (up to 10000 K), leading to a rapid atomization, high electron densities of the plasma and a high degree of ionization allowing multi-element detection, a high stability and low background and a wide linear dynamic range (10^4 - 10^6) leading to excellent limits of detection (0.1 - 100 ng mL⁻¹).^[21, 23]

The development of gratings in the dispersive system and photoelectric detection enabled high resolution spectral imaging, which allows for a parallel detection and quantification of up to about 70 elements within a sample by the exact assignment and quantification of spectral lines.^[22]

For determining the concentration of dissolved Ir and Ti in the diluted sulfuric acid electrolyte after continuous OER over 24 h as corrosion products, ICP-OES measurements were performed. IrOOH_x/TiO₂ and IrO_x/TiO₂ samples on fluorine-doped tin oxide (FTO) glass substrates were first immersed for ≈5 min in ≈3 mL electrolyte before the samples were immersed in 20 mL of fresh electrolyte used for continuous OER over 24 h. 2 mL sample volumes were taken for each catalyst sample and element to be analyzed, with fresh electrolyte (0.5 M H₂SO₄) as reference. Inductively coupled plasma optical emission spectroscopy was performed on a VARIAN VISTA RL CCD simultaneous ICP-OES.

2.6 Nitrogen sorption

The heterogeneous OER catalyst for the water splitting reaction under acidic conditions presented in this thesis exhibits a specifically designed porous structure to maximize the surface area of the iridium precious metal and provide an optimized environment for efficient mass transport. A further prerequisite for Ir-based OER catalysts employed in PEM electrolyzer anodes is a significant reduction of the apparent precious metal density, which can be controlled by the fabrication of highly porous nanostructures with high void volume. However, full utilization of the precious metal catalyst is only possible if an interconnected and thus accessible pore structure is present.

To determine the available surface area that is correlated to the electrochemically active surface area and the pore structure, nitrogen sorption measurements were performed. Physisorption of nitrogen is an interfacial non-specific process governed by long-range London dispersion forces and short-range intermolecular repulsion, which are also responsible for the condensation of vapors and the deviation from the ideal gas behavior.^[24]

In a typical measurement the amount of gas adsorbed is dependent on the equilibrium pressure p , the temperature T and the nature of the gas-solid system to be written as:

$$n_{N_2} = f(p, T, \text{system}_{\text{solid-gas}}) \quad (18)$$

A typical nitrogen sorption measurement is performed at the boiling point of liquid N₂ with a constant temperature of the adsorbent, which allows to formulate the equation of the adsorption isotherm as follows:

$$n_{N_2} = f\left(\frac{p}{p_0}\right)_T \quad (19)$$

The adsorption isotherm is the graphical representation or relation between the amount of adsorbed gas (n_{N_2}) and the relative pressure (p/p_0) with p_0 being the equilibrium pressure at $T_{N_2\text{-boiling}} = 77 \text{ K}$.

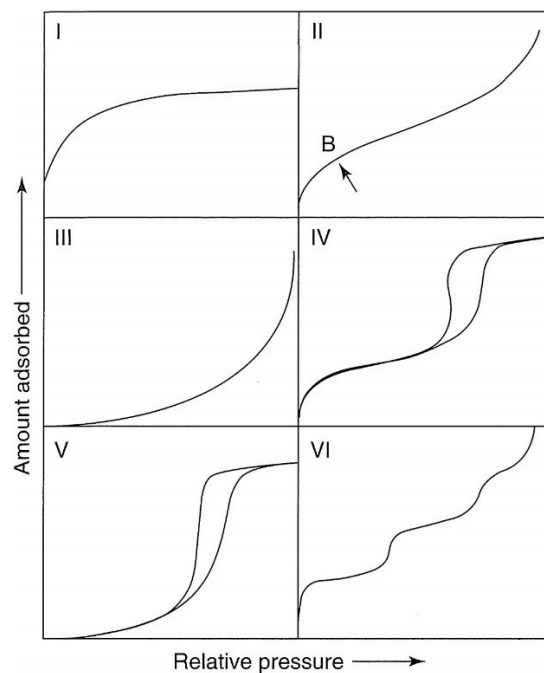


Figure 6 Type of physisorption isotherms proposed by IUPAC.^[24-25]

Reproduced with permission from Ref. [24]. Copyright 1997, VCH Verlagsgesellschaft mbH.

The shape of the graphical representation of the sorption isotherm can be classified according to the IUPAC in six main types [I-VI] with additional sub-types, which allow one to draw conclusions on the porosity and pore size of the adsorbent.^[24, 26]

The type I isotherm is associated with adsorbents with narrow slit-like, cylindrical or randomly shaped nanopores (micropores), whereas type II represents the sorption isotherm of non-porous or macroporous material. Type III, which does not display a turning point indicating the formation of an adsorption monolayer, is associated with relatively weak and non-uniform adsorbent-adsorbate interactions. Type V is thereby based on the shape of type III isotherm with an additional hysteresis originating from the presence of mesopores. Mesoporous materials with pores ranging between 2 and 50 nm show an isotherm (type IV) with an initial steep increase of adsorbate originating from monolayer formation and eventual mesopore filling, and a hysteresis loop (depending on pore diameter) caused by the pore blocking and cavitation phenomena upon desorption of mesopores and by capillary condensation well below the saturated bulk vapor pressure during adsorption. Finally, isotherms related to type VI are associated with uniform adsorbents that display a layer-by-layer adsorption characteristic.^[24-25]

The adsorbents analyzed in the course of this work are mainly macroporous oxides with additional textural porosity and micro/small mesopores arising from aggregated nanoparticle building blocks. This results in isotherms resembling features of type II (larger macropores) and type IV (micro and mesopores).^[24]

From the physisorption data the accessible surface area can be determined by the Brunauer-Emmett-Teller (BET) method with a restriction on the partial pressure range of $p/p^0 \approx 0.05 - 0.30$, which is caused by an over-simplification of the model. The BET equation is formulated accordingly:^[27]

$$\frac{\left(\frac{p}{p^0}\right)}{\left[n\left(\frac{1-p}{p^0}\right)\right]} = \left(\frac{1}{n_m C}\right) + \left[\frac{(C-1)}{n_m C}\right] \left(\frac{p}{p^0}\right) \quad (20)$$

with n_m being the BET monolayer capacity and C being an empirical constant related to the adsorbent-adsorbate interactions.^[27]

$$C = e^{\left[\frac{(E_1 - E_L)}{RT}\right]} \quad (21)$$

In this region the BET-plot defined as $\frac{p}{n(p^0-p)}$ vs. $\frac{p}{p^0}$ is linear and the BET monolayer capacity n_m and the parameter C can be determined by the slope and the intercept of the curve. Together with the molecular area σ_{N_2} of nitrogen of 0.162 nm^2 and Avogadro number L the BET area is calculated as follows:^[24, 27]

$$a_{BET} = n_m L \sigma \quad (22)$$

For the analysis of the porosity of Sb:SnO₂ and TiO₂/IrO_x catalysts, the samples were degassed for 12 h at 120 °C under vacuum. Nitrogen sorption measurements were performed on a QUANTACHROME Autosorb-1 instrument at the boiling point of liquid nitrogen (77 K). Data were processed by QUANTACHROME(R) ASiQwin (TM) sorption analysis software. The specific surface area was determined with the Brunauer–Emmett–Teller (BET) method at $p/p_0 = 0.05-0.2$. The pore size distribution was calculated using a nonlocal DFT equilibrium model for silica with cylindrical pores.

2.7 Electron microscopy

A very powerful and essential analytical technique for the development of novel nanostructured composite catalysts is electron microscopy. Within this thesis the electron microscopy was used to visualize oxidic support structures at the micrometer size range as well as catalyst nanoparticles with atomic precision. In addition to morphology and structural analysis, analytical electron microscopy can provide information about the phase (electron diffraction by elastically scattered electrons), chemical identity (characteristic X-rays, backscattered electrons, Auger electrons) and electronic structure (energy loss of direct beam by inelastic scattering) resulting from the complex interactions of accelerated electrons with matter as depicted in Figure 7.^[24, 28]

Two type of microscopes exist that make use of signals below and above the specimen plane, namely the transmission and the scanning electron microscope. In (HR)-TEM, primarily a phase change of the direct beam and elastically scattered electrons are detected for image synthesis, with a registration of secondary and backscattered electrons in scanning electron microscopy.

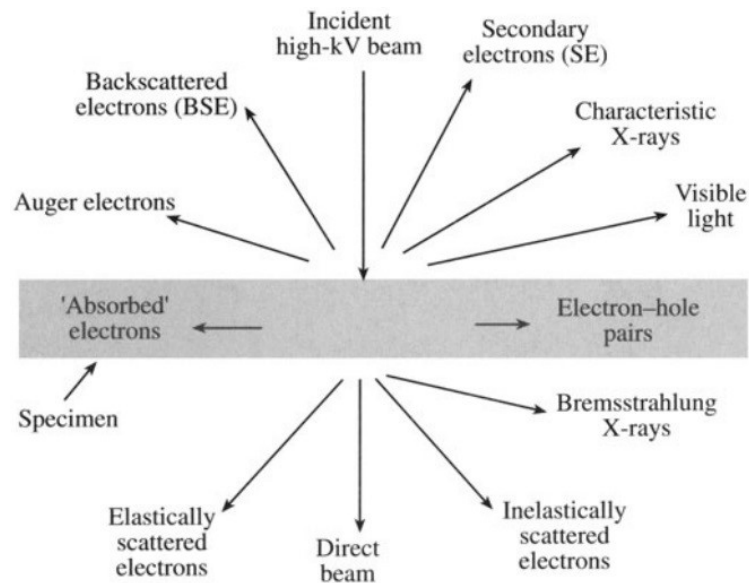


Figure 7 Schematic representation of high-energy electron-matter interaction.^[29]

Reproduced with permission from Ref. [29]. Copyright 1996, Springer Science Business Media, New York.

In contrast to photons employed as radiation carriers in light microscopy, electrons strongly interact with matter due to their negative charge, which requires high vacuum for the operation of an electron microscope. In addition, electrons possess a considerable mass of $m_0 \left[1 - \left(\frac{v^2}{c^2}\right)\right]^{-\frac{1}{2}}$ compared to photons $\left(\frac{h\nu}{c^2}\right)$ with a rest mass of m_0 . Based on the two aforementioned properties, a momentum of the electron of mv results with a potential energy of $E = \frac{mv^2}{2}$ that is directly related to the acceleration voltage U by $p = m_0v = \sqrt{2m_0eU}$ with e being the elemental charge of the electron.^[29-30]

According to the De-Broglie relation (eqn. 23) the wavelength of a particle is related to its momentum by the Planck's constant:^[29]

$$\lambda = \frac{h}{p} = \frac{h}{m_0 v} \quad (23)$$

The resolution of a conventional optical microscope is furthermore ultimately limited by Abbe's equation (24) and therefore by the wavelength. As electrons share the wave-particle duality with photons by exhibiting respective diffraction properties, the formula for the resolution limit also applies in electron microscopy:^[29]

$$d = \frac{0.61 \lambda}{NA} \quad \text{with} \quad NA = n \sin \alpha \quad (24)$$

As the acceleration of electrons in an applied potential field determines the wavelength by the following formula:^[31]

$$\lambda = \frac{h}{\sqrt{2m_0 eU}} \approx \frac{1.23}{\sqrt{U}} \text{ nm} \quad (25)$$

The theoretical (non-relativistic) resolution limit of an electron microscope is obtained when the accelerating voltage dependent wavelength λ (eqn. 25) is used as input in Abbe's formula together with the approximation of a small half opening angle (e.g. 10^{-2} rads) of the objective lens in a transmission electron microscope ($n \approx 1$ and $n \sin \alpha \approx \alpha$) according to equation (26).

$$d = \frac{0.753}{\alpha \sqrt{U}} \text{ nm} \quad (26)$$

The theoretical (non-relativistic) resolution limit d of a TEM operated at 300 kV with a half opening angle of $\approx 10^{-2}$ rads can be calculated to be ≈ 0.14 nm.

2.7.1 Transmission electron microscopy

In transmission electron microscopy (TEM) the acceleration voltage of several hundred kV results in wavelengths in the picometer range (e.g. 1.64 pm at 400 keV) which would suggest the spatial resolution in a similar range.^[24] In practice, however, a spatial resolution down to 0.12 nm can be obtained, which still enables the observation of single atom columns in thin

samples suitable for high resolution imaging. The main limitations are astigmatism, spherical and chromatic aberrations in the imperfect objective lenses as well as an incoherent illumination and mechanical instabilities.^[24]

In principle, a transmission electron microscope and a wide field light microscope share a common construction design (see Figure 8) that consists of an illumination system, condenser lens system, specimen, objective lens, projective lens and finally the image plane with a detector.^[24, 30]

However, due to the nature of electrons, the components of the TEM differ from the conventional light microscope as the illumination system is no lamp but an electron gun (filament/thermoionic/Schottky or cold field emission) and electromagnetic lenses are used to focus the electron beam which can be operated dynamically.^[28, 30]

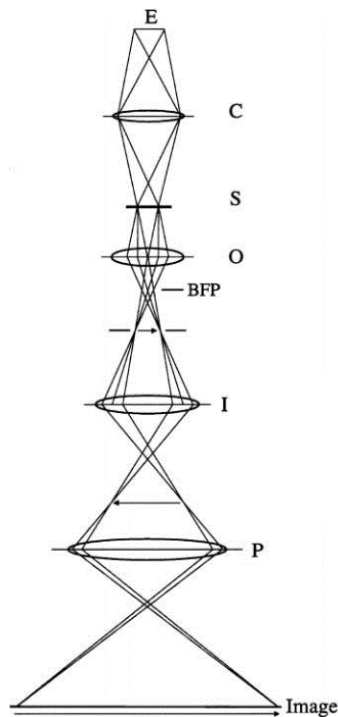


Figure 8 Ray diagram in the electron microscope under imaging conditions. E: electron source, C: condenser lens, S: specimen, O: objective lens, bfp: back focal plane of O, I: intermediate lens, P: projector lens.^[32]

Reproduced with permission from Ref. [32]. Copyright 2004, Elsevier Inc.

The similarities between the two types of microscope imply that electrons and photons also share a similar optical behavior. Diffraction, chromatic aberration, spherical aberration and astigmatism are known for both types of instruments and need to be corrected for high resolution imaging.^[28]

An advantage of the TEM with its adjustable electromagnetic lenses is the capability of switching between imaging mode (information in real space) and diffraction mode (information in reciprocal space) by adjusting the lens current and thus the focus plane as indicated in Figure 9.

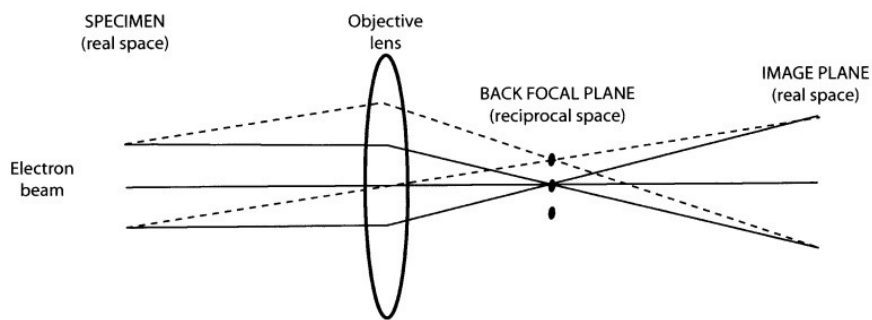


Figure 9 Optical ray diagram of a TEM with objective lens.^[33]

Reproduced with permission from Ref. [33]. Copyright 2001, the authors.

The diffraction patterns formed in the back focal plane thereby represent a Fourier transform of the crystal observed and inverse Fourier transform of the image formed in the objective lens.^[32] By inserting a selected area aperture in the back focal plane and by using a convergent beam illumination, diffraction patterns of nanosized structures can be obtained.

Another very useful technique for the analysis of nanocomposites such as supported catalysts developed in this work is Z-contrast imaging. The latter is achieved by selecting only the high angle annular darkfield (HAADF) signal defined at >50 mrad off-axis of the direct beam after the specimen plane for image synthesis. The signal at high angles thereby corresponds to the totally incoherent scattering with an intensity variation proportional to the atomic number Z (or Z^2).^[34]

In addition to the high-resolution capability and diffraction imaging mode of the transmission electron microscope, various signals from below or above the specimen plane can be detected that originate from interactions of electrons with matter (Figure 7). Besides the elastically scattered electrons which are used for high resolution imaging, inelastically scattered electrons can be used in electron energy loss spectroscopy (EELS) to gain information about the composition, chemical bonding, coordination, band structure as well as plasmons and phonons on the local scale of the specimen. Signals collected above the sample include characteristic X-ray radiation, which can be used in an energy dispersive X-ray (EDX) measurement to obtain qualitative and quantitative information about the composition of the specimen and also map the spatial distribution of elements on the nanoscale.^[28]

HR-TEM and HAADF-STEM images as well as electron diffraction patterns shown in this thesis were recorded using an FEI Titan Themis 80-300 transmission electron microscope with aberration correction of the probe-forming lenses operated at 120 kV or 300 kV, respectively. EDX was performed using a SuperX windowless, four quadrant Silicon drift detector with a solid angle of 0.7 sr. TEM specimens in this work were prepared by dispersing IrO_x colloids, catalyst nanoparticles, or Ir loaded ATO microparticles, respectively in a 1:1 (v:v) ratio of water to ethanol and depositing them on a carbon-film coated copper grid, followed by drying in air. HAADF-STEM tilt series of 29 images for TEM tomography were recorded in 5° steps from -70° to +70°. For a reconstruction of the 3D intensity volume and a presentation of different phases of Ir and ATO, respectively, a masked simultaneous iterative reconstruction technique (SIRT) with further refinement by a discrete algebraic reconstruction technique (DART) were employed (see the Supporting Information for further details).

2.7.2 Scanning electron microscopy

Besides transmission electron microscopy, a second major technique to investigate a sample on the nanoscale is scanning electron microscopy (SEM). The construction principle of an SEM

shares the geometric arrangement and basic working principle with a confocal scanning laser microscope. Both types of microscopes use a convergent beam that is focused on the specimen. The image in SEM is formed by rastering across the surface and detecting back-scattered (BSE) and secondary electrons (SE) or characteristic X-ray radiation (EDX mapping).

Auger electrons and X-ray radiation are can be further used for material characterization of surface-near structures.

The resolution limit of an SEM is as well as for TEM is significantly below the Abbe limit of conventional light microscopes due to the short wavelengths of electrons accelerated up to 20-30 kV. However, in SEM imaging the signals above the specimen plane are used, which avoids the restrictions of thin, electron transparent samples investigated with TEM. Together with the fundamental properties of electron-matter interactions already discussed in the TEM section, the resolution is not solely influenced by the acceleration voltage but is restricted by the size of the interaction volume from which the detected signal (secondary and back scattered electrons or characteristic X-rays) originated.^[35]

For high topographical contrast, secondary electrons (SE) are used for imaging. SE are generated on the specimen surface within escape depth (dark blue volume indicated in Figure 10a), which is independent of acceleration voltage. The resolution of SE imaging is limited by the electron beam minimum spot size and the type of surface atoms as the escape depth decreases with increasing atomic number Z (density).^[35]

A second type of signal obtained by electron-matter interactions in the SEM are back scattered electrons (BSE) from the interaction volume (volume occupied by red trajectories indicated in Figure 10b).

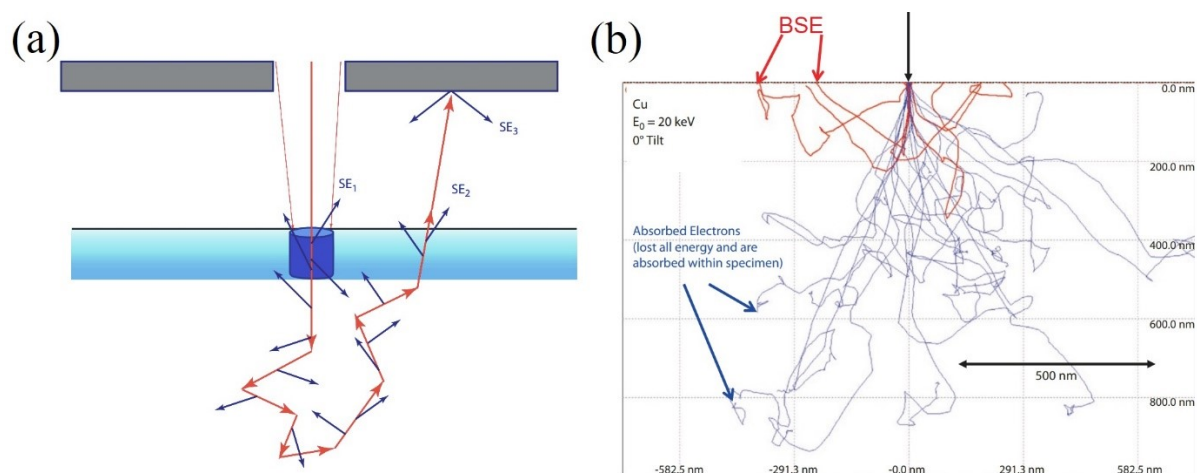


Figure 10 Schematic diagram (a) showing the origins of different classes of secondary electrons (SE) and the near surface interaction volume of SE₁.^[36] Monte Carlo simulation of a flat, bulk target of copper at 0° tilt. Red trajectories lead to backscattering events.^[37]

Reproduced with permission from Ref. [36] (a) and Ref [37] (b). Copyright 2018, Springer Science Business Media LLC.

In contrast to TEM, an increased accelerating voltage of the primary electrons does not improve the resolution. The reason for that is that the resolution limiting factor is not the wavelength of the electrons but the interaction volume, which increases with the increasing accelerating voltage. BSE imaging provides higher material contrast, as the scattering cross-section is related to the atomic number Z that enables the investigation of structures beneath the specimen surface.^[35] BSE imaging can be a useful mode to discriminate noble metal catalyst nanoparticles on oxidic support structures as investigated in the scope of this work.

SEM images in this work were obtained with a FEI Helios Nanolab G3 UC scanning electron microscope equipped with a field emission gun operated at 3–5 kV. SEM specimens were prepared by dispersing dried catalyst nanoparticles, microparticles, and composites in a (1:1 v/v) water to ethanol ratio on FTO or Si substrates that were glued onto a stainless-steel sample holder with silver lacquer. EDX measurements were performed at an operating voltage of 20 kV with a X-Max^N Silicon Drift Detector with 80 mm² detector area (OXFORD INSTRUMENTS) and quantified with the AZTec acquisition software (OXFORD INSTRUMENTS).

2.8 Quartz crystal microbalance (QCM)

To precisely determine the mass-based current and therefore the electrocatalytic activity of a catalyst, an accurate measurement of the deposited mass on the electrode is required. The quartz crystal microbalance (QCM) can be employed to accurately measure the mass of thin films of catalyst particles in the μg -range and below.

The QCM is based on the piezoelectric properties of a thin slice of quartz crystal with partially overlapping thin evaporated top and bottom metal (mostly Au, Pt) electrodes as depicted in Figure 11. The quartz exhibits a piezoelectric effect causing a deformation by shear forces upon applying a sinusoidal electrical field by the opposing metal electrodes. The oscillation thereby shows a mechanical resonant mode at a frequency f_0 , which depends on the dimensions (diameter and thickness) of the crystal.^[38]

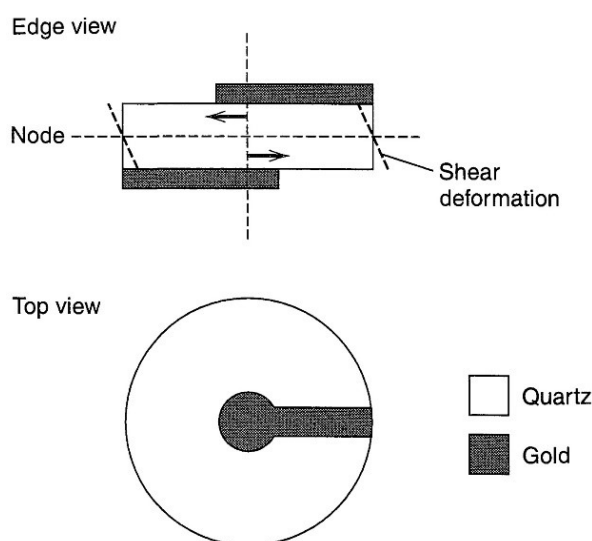


Figure 11 Schematic edge and top views of a QCM crystal with deposited Au electrodes.^[38]

Reproduced with permission from Ref. [38]. Copyright 2000, John Wiley and Sons.

Quartz crystals that exhibit the desired shear forces with acoustic waves perpendicular to the crystal faces need to be cut along a specific orientation. Generally, 'AT-cut' quartz crystals are used besides possible 'BT-cuts' as they show a small inherent temperature coefficient of only $\approx 5 \text{ Hz K}^{-1}$.^[38]

A resonant oscillation is obtained by driving the crystal in an oscillator circuit near the fundamental frequency f_0 (e.g. ≈ 5 MHz for a 1-inch diameter crystal with ≈ 330 μm thickness). As the oscillation frequency of the crystal at the resonant frequency is dependent on the crystal dimension and shear modulus of quartz which are both fixed, the main influence remaining is the physical properties of the adjacent media in form of a viscous liquid or an acoustically coupled rigid thin film on the overlapping area of the metal electrodes.^[38-39]

The Sauerbrey equation describes the relation between change in resonant frequency and mass loading attached to the crystal electrodes:^[40]

$$\Delta f = \frac{-2f_0^2 mn}{\sqrt{\rho\mu}} = -C_f m \quad (27)$$

Where

$\Delta f = f - f_0$ = frequency change in Hz (f_0 being nominal oscillation frequency of resonant mode)

m = change in mass per unit area in g cm^{-2}

n = harmonic number of oscillation ($n=1$ for 5 MHz for 1-inch crystal)

ρ = density of the quartz crystal (2.648 g cm^{-3})

μ = shear modulus of quartz ($2.947 \times 10^{11} \text{ g cm}^{-1} \text{ s}^{-2}$)

The constants are taken together to obtain the sensitivity factor C_f , which is $56.6 \text{ Hz cm}^2 \mu\text{g}^{-1}$ for a 5 MHz crystal in air.^[38]

As the Sauerbrey equation is only strictly applicable to uniform, acoustically rigid, thin films with a maximum mass loading not exceeding a corresponding frequency difference of $\Delta f \leq 2\%$ f_0 ,^[39] catalyst thin films of $\approx 5 \mu\text{g}$ and less were deposited in the course of this work.

Unsupported IrO_x , IrO_2 nanoparticles and ATO supported IrO_2 nanoparticles as well as undoped or V-doped $\text{Ni}(\text{OH})_2$ were dispersed in 1:1 (v/v) H_2O to isopropanol and drop-cast onto Au-coated QCM sensors (14 mm, 5 and 10 MHz AT-cut Cr/Au crystals from KVG QUARTZ CRYSTAL TECHNOLOGY GMBH and QUARTZ PRO AB). Electrodes were masked with tape to leave a circular area 0.126 cm^2 centered on the 0.169 cm^2 Au electrodes.

Prior to each measurement, the samples were dried at 60 °C in air over night. The frequency of uncoated and coated QCM sensor crystals was determined with a QCM200 5 MHz measurement system (STANFORD RESEARCH SYSTEMS INC.) and an openQCM 5/10 MHz measurement system (NOVAETECH SRL). Deposited mass loadings on QCM chips were calculated according to the Sauerbrey equation^[40] from determined frequency differences Δf , an overlapping electrode area A of 0.196 cm² and a sensitivity factor C_f of 56.6 and 4.4 Hz μg^{-1} cm² for 5 and 10 MHz AT-cut crystals, respectively.

2.9 4-Point probe (Van-der-Pauw) and 2-point direct current (DC) conductivity measurements

The electrical conductivity of a catalyst layer strongly influences the electrochemical performance at elevated current densities. To probe the conductivity of (oxide supported) noble metal catalysts, either two-point direct current or 4-point probe Van-der-Pauw measurements were conducted.

The conductivity value σ is equal to the inverse of the resistivity ρ and related to it by the relation:^[41]

$$\sigma = \frac{1}{\rho} \quad (28)$$

with the units: ρ [Ω m] and σ [S m^{-1}] (conductivity).

The resistivity is thereby defined in the continuum form of ohm`s law as:^[41]

$$E = \rho \times J \quad (29)$$

with the electric field E [V m^{-1}], the current density J [A m^{-2}] and the resistivity ρ [Ω m].

Figure 12 depicts a schematic representation of a two-point probe conductivity/resistivity measurement.

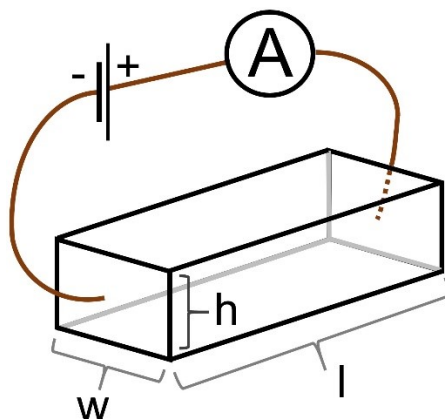


Figure 12 Schematic representation of the 2-point technique for measuring resistivity/conductivity of a bar of material. The amperemeter measures the current flowing at a respective applied potential across the bar.

The electric field across the two ends of the material is given by:^[41]

$$E = \frac{V}{l} \quad (30)$$

And the current density equals

$$J = \frac{I}{A} = \frac{I}{w \times h} \quad (31)$$

To determine the resistivity the current at a respective voltage needs to be measured and the dimensions of the sample need to be known:^[41]

$$\rho = \frac{V \times A}{I \times l} \quad \text{in } [\Omega\text{m}] \quad (32)$$

The conductivity as the inverse resistivity can be therefore written as:^[41]

$$\sigma = \frac{I \times l}{V \times A} \quad \text{in } [\text{S m}^{-1}] \quad (33)$$

The conductivity, as a fundamental materials property, strongly depends on the electronic structure and properties of inorganic and organic materials and ranges from $\sigma = 10^{-18} - 10^{-22} \text{ S cm}^{-1}$ for solid insulators like aromatic hydrocarbons to $\sigma = 6 \times 10^5 \text{ S cm}^{-1}$ for metallic conductors (e.g. copper).^[42]

Although the two-point measurement is a simple and theoretically valid approach to determine the conductivity of samples, it is regarded to be not fully reliable as various factors can

influence the result. Among possible factors, the contact resistance between the measurement device and sample needs to be considered, especially for semiconducting samples as well as a potential dependence of the current flowing by probing semiconducting materials.^[41]

However, the main advantage of two-point measurement is the capability of measuring small amounts of material down to the milligram scale in a simple measurement setup.^[42]

To accurately determine the conductivity, the four-point probe technique can be used that overcomes many of the problems of the two-point technique such as contact resistances. For the simple case of a bar-like sample, the four-point measurement can be realized by driving a current I through the sample and measuring the voltage drop in an inner section of known length.^[41]

A more flexible approach towards the four-point probe technique for samples with arbitrary shape is the van der Pauw technique. It requires a flat and uniform sample thickness composed of a homogeneous and isotropic sample free of isolated holes, and four contacts at the outer edges achieved by small contacting tips (with an area of at least one order of magnitude smaller than that of a sample) as depicted in Figure 13.^[41, 43-44]

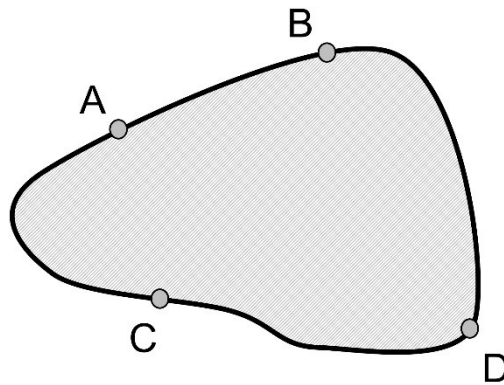


Figure 13 Schematic representation of the 4-point van der Pauw technique for measuring resistivity/conductivity of a disc sample of arbitrary shape.

The van der Pauw theorem states that the resistivity of a material which is regarded as isotropic, can be formulated according to equation 34:^[43-44]

$$e \frac{\pi \times d \times R_{AB,CD}}{\rho} + e \frac{\pi \times d \times R_{BC,DA}}{\rho} = 1 \quad (34)$$

$R_{AB,CD}$ is thereby defined as the resistance calculated from the voltage difference measured between C and D per unit current through A and B. The resistance $R_{BC,AD}$ is defined analogously.^[43] The only remaining variable is the thickness of the sample (typically pressed pellets), which is determined by a caliper.

In this work, conductivity measurements of macroporous ATO microparticles and $\text{IrOOH}_x/\text{TiO}_2$ and $\text{IrO}_x/\text{TiO}_2$ catalysts were carried out on an HMS 3000 apparatus (ECOPIA) in the van der Pauw geometry (≈ 5 mm separation of electrodes). Powder samples were measured in form of pellets that were compressed for ≈ 10 min at 150 kg cm^{-2} with a typical thickness of $\approx 200 - 400 \text{ }\mu\text{m}$. Conductivity measurements of ATO/ IrO_2 and commercial TiO_2 supported reference catalysts were conducted - due to restrictions on sample volume - on an in house constructed dc-conductivity measurements cell on loosely compressed powders by recording $I-V$ curves between -5 to $+5$ V by an AUTOLAB 302N.

2.10 Electrochemical characterization

Catalyst thin films prepared in the context of this thesis were characterized by potentiostatic and galvanostatic methods to elucidate electrode kinetics and the stability of oxygen evolution reaction catalysts under continuous operation.

A basic electrochemical cell is composed of two separate metallic electrodes or electronic conductors that are immersed in an electrolyte or ionic conductor. The electrodes are connected over an outer circuit to a voltage source (or a voltmeter and an amperemeter) to apply an electric field in the cell and drive chemical reactions or measure the voltage or current generated by spontaneous electrode reactions. The force that acts on ions in the electrolyte is related to the electric field E over the elemental charge e_0 and the charge identity $z = \pm 1$ for anions and cations, respectively, according to following equation:^[38, 45]

$$F = z \times e_0 \times E \quad (35)$$

The fundamental process for the charge flow over an external circuit in an electrochemical cell is the spatial separation of redox reactions at the opposing electrodes. Oxidation of redox active species in the electrolyte takes place at the anode which is the positively polarized electrode. The reduction takes place at the cathode which is the negatively polarized electrode. Charges from the reduced active center to the oxidized species flow through the external circuit that connects the electrodes and may thereby perform electrical work. Depending on the combination of electrode materials and electrolyte a potential difference of the electrochemical cell can be measured. The absolute values as well as potential differences are expressed in volt (V) and are normally measured with a high impedance voltmeter.^[38, 45]

The aforementioned process describes an electrochemical cell with a negative potential difference derived from spontaneous (exergonic) oxidation and reduction reactions at the electrodes indicating a negative Gibbs free energy. In contrary to the exergonic reactions in the electrochemical cells, a voltage exceeding the open circuit potential of the cell has to be applied to drive a chemical reaction in an electrolytic cell.^[38]

The difference in Gibbs free energy for an electrochemical cell is defined as the sum over the change of the chemical potentials which can be formulated as following:^[45]

$$\Delta_{rxn}G = \sum_i \nu_i \mu_i \quad (36)$$

with ν_i being the stoichiometric number of reactants and μ_i the chemical potentials.

The Gibbs free energy is furthermore related to the electromotive force EMF (reversible potential difference of the cell) and amount of charges that flow ($n \times F$) in the cell by:^[38]

$$\Delta G = -nFE_{rxn} \quad (37)$$

The Gibbs free energy and the EMF are further related to the equilibrium constant by:^[38]

$$RT \ln K_{rxn} = -\Delta G^0 = nFE_{rxn}^0 \quad (38)$$

This allows, for example, the prediction of cell voltages of concentration elements or the construction of electrochemical sensors. As the equilibrium constant is related to the activity, the formula can be rewritten to express the equilibrium potential known as the Nernst equation:^[38, 46]

$$E_{eq} = E_{rxn}^0 + \frac{RT}{nF} \ln \frac{\prod a_{O_i}^{v_{O_i}}}{\prod a_{R_i}^{v_{R_i}}} \quad (39)$$

From this representation and the spatially separated oxidation and reduction processes in an electrochemical cell it can be concluded that the cell potential is the difference of potentials of two coupled half-cell reaction:^[38]

$$E_{cell}^0 = E_R^0 - E_O^0 \quad (40)$$

The electrode at which the reaction of interest takes place is called working electrode. For the characterization of an electrocatalytic electrode in an electrolytic cell, the counter electrode is typically an inert noble metal electrode (e.g. Pt, Au) that facilitates redox reactions at the surface but does not undergo chemical changes itself in the applied potential range. To be able to apply a defined potential on the working electrode, a reference electrode with constant potential is employed in a standard 3-electrode measurement setup.^[38, 45-46]

One of the most important reference electrodes is the normal hydrogen electrode (NHE), which is constructed of a platinum electrode immersed in a 1 M acidic solution (e.g. HCl) with hydrogen of 1 atm bubbled through. The potential of the standard hydrogen electrode (SHE) which equals that of the normal hydrogen electrode but with an ideal solution (unit activity and no interaction between ions), has thereby a defined standard reaction potential of $E_\theta = 0$ V.^[47] A more practical implementation of the NHE is the reversible hydrogen electrode which is directly in contact with the electrolyte and whose potential is dependent on the pH value as follows:^[38]

$$E = E_{H_2/H^+}^0 + \frac{RT}{zF} \ln(a_{H^+}) = E^0 - \frac{2.303 RT}{zF} pH = 0.000 - 0.059 \times pH \quad (41)$$

Besides the reversible hydrogen electrode, other reference electrodes such as Ag/AgCl/KCl, Hg/HgSO₄/K₂SO₄, Hg/HgO/KOH or other electrodes with stable electrode potentials are used depending on the measurement conditions (e.g. acidic or basic electrolyte, avoid chloride contaminations etc.).

For the description of electrode kinetics at first the equilibrium concentration ratio ($\frac{c_B}{c_A}$) and

corresponding ratio of reaction rates ($\frac{k_f}{k_r}$) can be formulated to be constant:

$$\frac{k_f}{k_r} = K = \frac{c_B}{c_A} \quad (42)$$

Where

c_A, c_B = equilibrium concentrations of educt (c_A) and product (c_B)

k_f, k_r = rate constant of forward and reverse electrode reaction

It is further known that most rate constants vary with the temperature according to the Arrhenius law, which introduces E_A as the activation energy for the reaction:^[38, 48]

$$k = Ae^{-\frac{E_A}{RT}} \quad (43)$$

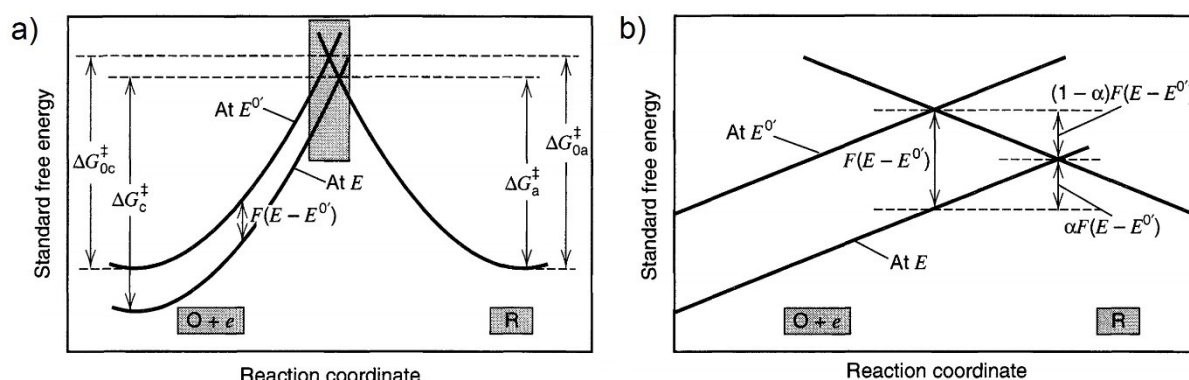


Figure 14 Effects of a potential change ($E - E^0$) on the standard free energies of activation for oxidation and reduction ($\Delta G_a^{\ddagger}, \Delta G_c^{\ddagger}$) (a). Magnification of the boxed area of intersection (b) that depicts a shift of the potential energy of the oxidized species by $F(E - E^0)$ and an accompanied shift of the point of intersection towards the reduced species (R) on the reaction coordinate. The angle of intersection and the difference in standard free energy versus the equilibrium point of intersection is defined by the parabola shaped potential energy curves of oxidized and reduced species and is quantified by the transfer coefficient α .^[38]

Reproduced with permission from Ref. [38]. Copyright 2000, John Wiley and Sons.

The Arrhenius concept and activation energies lead to a model with educts and products with parabolically shaped standard free energies as function of the reaction coordinate that are separated on the reaction coordinate but intercept at some point as shown in Figure 14.

This point can be understood as the activated complex between oxidized and reduced species or the transition point according to transition state theory. For the case of an applied potential $E^{0'}$ the standard free energy of the educt is shifted by $F(E-E^{0'})$, which lowers the required activation energy to reach the transition point and hence influences the rate constant of the respective forward reaction according to the following formula:^[38, 48]

$$k_f = k^0 e^{-\frac{\alpha F}{RT}(E-E^{0'})} \quad (44)$$

with α being the transfer coefficient for the forward reaction which describes the symmetry of the activation barrier as shown in Figure 14. The transfer coefficient ranges from zero to unity and depends on the shape of the intersection region. For an electrode reaction with equal potential energy curves of oxidized and reduced species it equals 0.5 and is decreased for an asymmetric activation barrier in favor of the forward reaction (reduction reaction as formulated in Figure 14) and increased in the opposite case. The transfer coefficient of the backwards reaction is defined as $1-\alpha$. The current relates to the applied overpotential $\eta = (E - E^{0'})$ via the following equation (an alternative writing of the Tafel equation):^[38, 48]

$$i = a e^{\frac{\eta}{b}} \quad (45)$$

Furthermore, the net conversion rate of educt to product defined as the product of reaction rate k and surface concentration $C_{O/R}(0,t)$ is also linked to the current by the following equation:^[38, 48]

$$v_f = k_f C_O(0,t) = \frac{i_c}{nFA} \quad (46)$$

Combining the relations on the net conversion rate, the current and overpotential, the complete current-potential characteristic expressed by the Butler-Volmer equation can be formulated:^{[38,}

48]

$$i = F A k^0 \left[C_O(0, t) e^{-\frac{\alpha F \eta}{RT}} - C_R(0, t) e^{-\frac{(1-\alpha) F \eta}{RT}} \right] \quad (47)$$

Where

i = electrode current

F = Faraday constant

A = electrode area

k^0 = standard rate constant

α = transfer coefficient

$C_O(0, t) / C_R(0, t)$ = surface concentration of oxidized and reduced species at time t

η = activation overpotential ($E - E_0'$)

R = universal gas constant

T = temperature

2.10.1 Redox activity probed by cyclic voltammetry

In a cyclic voltammetry experiment the current response upon a continuous potential sweep with controlled scan speed between an upper (E_2) and lower limit (E_1) is recorded and analyzed for characteristic peaks representing oxidation or reduction events of the analyte on the working electrode:



The observed voltammogram and its peak heights will depend on the standard rate constant k^0 , the diffusion coefficients of A and B for solution species and the voltage sweep rate ν (in $V s^{-1}$) and the potential window (E_1, E_2).

The peak height defined by the maximum current flowing for a reversible charge transfer at 25 °C under given parameters can be calculated for soluble analytes according to the Randles-Sevcik equation:^[38]

$$i_p = 0.4463 n F A C_0 \sqrt{\frac{n F \nu D}{RT}} \quad (49)$$

The current thereby depends on the number of electrons n transferred by the redox process, the electrode area A , the concentration of the redox species in solution C , the scan rate ν and the diffusion coefficient D .

Figure 15b depicts the resulting I - V curve of a diffusion limited reduction. The reduction current starts below the standard potential $E^{0'}$ and increases further due to depletion of oxidized species at the electrode-electrolyte interface. This leads to an increased diffusion to the electrode surface of oxidized species and further increases the current. For higher overpotentials the current reaches a maximum (i_p at E_p) and levels out when the diffusion limit is reached.

For the irreversible multi electron process of the oxygen evolution reaction the current increase is dependent on the overpotential but no diffusion limit is reached (within reasonable potential windows) as the redox active species (H_2O) is at the same time solvent of the electrolyte.

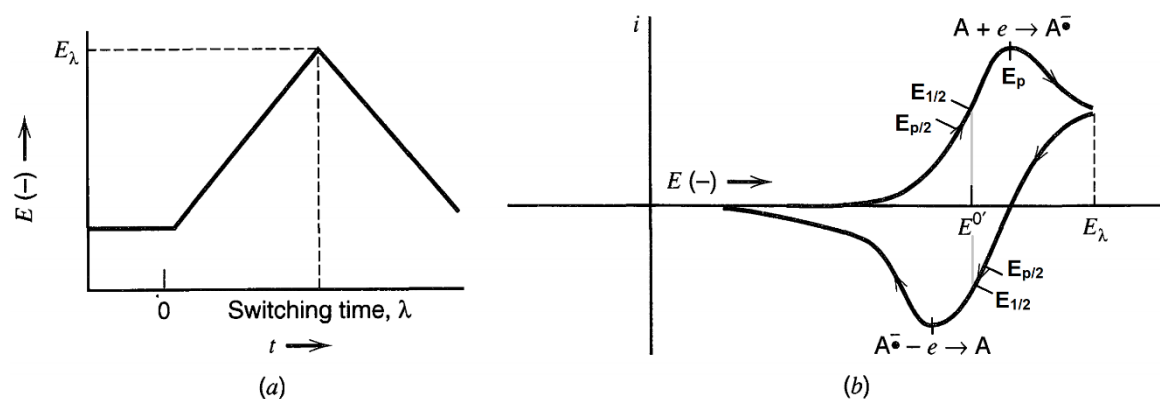


Figure 15 Cyclic potential sweep (a) and resulting cyclic voltammogram (b).^[38]

Reproduced (modified) with permission from Ref. [38]. Copyright 2000, John Wiley and Sons.

Besides the peak current i_p the position of the oxidation and reduction peaks and their separation ΔE_{pp} can be seen as an indicator for a reversible or irreversible redox reaction. A fully reversible cyclic voltammogram thereby shows a $\Delta E_{pp} \approx 57$ mV at 298 K with increased peak-to-peak separation for non-reversible reactions and less for a totally irreversible system. Analysis of the wave-shape can give further evidence of reversible or irreversible reactions. A

reversible system shows a separation of peak potential E_p to half-peak potential $E_{p/2}$ as follows:^[49]

$$\left| E_p - E_{\frac{p}{2}} \right| = 2.218 \frac{RT}{zF} = \frac{56.5}{z} \text{ mV at } 25^\circ\text{C} \quad (50)$$

Where the half-peak potential $E_{p/2}$ is defined at the potential of the half peak current ($\frac{i_p}{2}$).

And for a totally irreversible redox system:^[49]

$$\left| E_p - E_{\frac{p}{2}} \right| = 1.857 \frac{RT}{\alpha z F} = \frac{47.7}{\alpha z} \text{ mV at } 25^\circ\text{C} \quad (51)$$

For the characterization of oxygen evolution reaction electrocatalysts by cyclic voltammetry in this work, the lower vertex potential was selected slightly above the hydrogen evolution reaction (0.05 V vs. RHE) and an upper potential limit of 1.45 V vs. RHE was chosen, which is close to the oxygen evolution reaction onset ($E^0_{\text{OER}}=1.23\text{V vs. RHE} + \eta$). This allows for the observation of potential redox reactions of the electrocatalyst.

Cyclic voltammograms of Ir-based (oxide supported) catalysts discussed in the framework of this thesis were recorded in a rotating disc electrode (RDE) setup without rotation which allowed the precise control of the measurement conditions (catalyst loading, temperature, electrode area, O₂ saturation) before and after linear sweep voltammetry scan cycles (performed with electrode rotation).

RDE measurements were conducted with an MSR electrode rotator with mirror finished polished 5 mm diameter glassy carbon disc insets (PINE RESEARCH INSTRUMENTATION) connected to an Autolab PGSTAT302N potentiostat/galvanostat equipped with a FRA32 M impedance analyzer (METROHM AUTOLAB B.V.) and an in-house constructed glass/silicone cell with Luggin-capillary for the reference electrode (HYDROFLEX reversible hydrogen electrode by GASKATEL GESELLSCHAFT FÜR GASSYSTEME DURCH KATALYSE UND ELEKTROCHEMIE MBH) compartment or an commercial double walled glass cell (PINE RESEARCH INSTRUMENTATION) connected

to a KISS 104A thermostat (PETER HUBER KÄLTEMASCHINENBAU AG). An electrolyte temperature of 60 °C was maintained by an oil bath with external stirrer or thermostat and monitored with an immersed silicone coated K-element temperature sensor. The Nernst potential for water oxidation was kept constant by continuous O₂ (AIR LIQUIDE, AlphaGaz2 N5 purity) purging of the electrolyte (0.5 M H₂SO₄, SIGMA-ALDRICH, Titripur volumetric standard). Catalyst loadings of 50 μg_{Ir} cm⁻² (10 μg_{Ir} per disc) were drop-casted on cleaned glassy carbon discs and dried at 60 °C before applying 10 μL of a 1:100 dilution of a Nafion perfluorinated resin solution (SIGMA-ALDRICH, 5 wt% in lower aliphatic alcohols and water (15 – 20% water)) in a H₂O/*i*PrOH mixture (1:1 v/v).

Cyclic voltammograms were recorded over a potential range of 0.05 – 1.52 V vs. RHE without RDE rotation to identify redox active features and to compare the electrocatalytically active surface area of catalyst samples (see section 2.10.4 for further details). RDE rotation was disabled during the cyclic voltammetry measurements to obtain accurate data also in the non-Faradaic regions with low observable currents. Three cyclic voltammograms at a scan rate of 50 mV s⁻¹ were therefore recorded prior to each RDE measurement after 50 and after 75 linear sweep voltammetry cycles between 1.0 and ≈1.45 – 1.5 V vs. RHE (upper vertex potential defined at $j = 1 \text{ mA cm}^{-2}$).

2.10.2 Characterization of oxygen evolution reaction kinetics by linear sweep voltammetry

In a typical linear sweep voltammetry experiment with a three-electrode-setup, the working electrode is polarized starting from the open circuit voltage in small potential steps (μV – mV range per second) and with a certain scan rate (normally 0.05 – 50 mV s⁻¹) towards negative (cathodic) or positive (anodic) potentials. Similar to a cyclic voltammogram, the applied potential is linearly increased to an upper vertex potential (anodic scan) and reversed to a lower vertex potential (cathodic scan) in consecutive cycles.

For the characterization of oxygen evolution reaction catalysts discussed in the context of this thesis, a potential range of well below the OER onset at 1.0 V vs. RHE up to 1.8 V vs. RHE was chosen with a cycling range of 10 – 75 cycles.

To determine the electrocatalytic performance of catalysts towards the oxygen evolution reaction, the catalyst samples were measured at room temperature on conductive fluorine doped tin oxide glass substrates or, for accurate mass determination, on Au-coated quartz crystal microbalance sensors. Electrochemical measurements at room temperature were carried out with a three-electrode setup in a quartz cell filled with ≈ 20 mL 0.5 M H_2SO_4 (SIGMA-ALDRICH, Titripur volumetric standard) for Ir-based catalysts as electrolyte or with 0.5 M KOH (SIGMA-ALDRICH, volumetric solution) for $\text{Ni}(\text{OH})_2$ -based catalysts. A PGSTAT302N potentiostat/galvanostat (METROHM AUTOLAB B.V.) equipped with a FRA32 M impedance analyzer connected to a Hydroflex reversible hydrogen electrode (GASKATEL GESELLSCHAFT FÜR GASSYSTEME DURCH KATALYSE UND ELEKTROCHEMIE MBH) was used as potentiostat and reference electrode together with a Pt-wire counter electrode.

Prior to each measurement the electrolyte resistance was determined by impedance spectroscopy and further measurements were iR -drop corrected during the measurement by NOVA 1.11 control software and the potentiostat (METROHM AUTOLAB B.V.). For further details see section “2.10.5 Impedance spectroscopy”.

The electrochemical activity of catalysts on FTO and QCM substrates was measured by linear sweep voltammetry (LSV) in a potential window of 1.0–1.8 V vs. RHE and 1.0–1.65 V vs. RHE, respectively. 10 or 20 scan cycles with a scan rate of 10 mV s^{-1} were recorded each.

The mass-based catalyst activity was either directly calculated with measured QCM-determined mass loadings (for $\text{Ni}(\text{OH})_2$) or for supported catalysts calculated from the coating volume (3–15 μL) of a dispersion of known concentration (2 mg mL^{-1}) in combination with

the atomic fraction of catalyst in a catalyst/oxide support composite determined by SEM/EDX (mean value of at least three independent measurements).

Reported current densities were determined from the mean value of capacity current-corrected (mean current in the potential region 1.0 – 1.23 V vs RHE) anodic and cathodic scans of the respective LSV cycle.

For determining the onset potentials and catalyst activities at low overpotential, the linear sweep voltammetry measurements were recorded with an RDE setup under controlled measurement parameters (for further details see section “2.10.4 Rotating disc electrode cyclic voltammetry”).

2.10.3 Characterization of oxygen evolution reaction kinetics by chronopotentiometry

In the constant current chronopotentiometry, a certain current is applied between the working and counter electrode and held for a certain time t while recording the potential E . For a system with soluble redox species the constant current leads to a constant flux of oxidized species to be reduced at the cathode. If the current exceeds the flux the concentration of the oxidized species will drop to zero at the electrode interface and the potential will increase to enable an alternative second reduction process.^[38]

For water oxidation at the anode being an irreversible and non-diffusion limited process, the obtained potential can be related to the electrocatalytic activity of the working electrode under continuous OER. In addition, measurements over longer periods of time (several hours) can provide information about the stability of the respective OER catalyst, as dissolution or inactivation would cause a shift in the overpotential and increase the measured potential over time. In general, for a totally irreversible reduction/oxidation wave the whole $E-t$ curve shifts towards more negative/positive potentials with increasing current. A tenfold increase in the current causes a shift of $\frac{2.3 RT}{\alpha F}$ ($\frac{59 mV}{\alpha}$ at 298 K).^[38]

All constant current chronopotentiometry measurements in this work were carried out in a three-electrode setup with a quartz cell filled with ≈ 20 mL 0.5 M H_2SO_4 (SIGMA-ALDRICH, Titripur volumetric standard) as electrolyte at room temperature using an PGSTAT302N potentiostat/galvanostat (METROHM AUTOLAB B.V.) connected to a $\text{Hg}/\text{HgSO}_4/\text{K}_2\text{SO}_4$ (sat.) (REF601, RADIOMETER ANALYTICALHACH COMPANY) reference electrode. Potentials versus the reversible hydrogen electrode E_{RHE} were calculated by measuring the open circuit potential of the $\text{Hg}/\text{HgSO}_4/\text{K}_2\text{SO}_4$ (sat.) reference electrode against a Hydroflex RHE (GASKATEL Gesellschaft für Gassysteme durch Katalyse und Elektrochemie mbH) before and after each chronopotentiometry measurement and by shifting the measured potential accordingly. Stability measurements of electrodes (active material corresponding to $15 \mu\text{g}_{\text{Ir}}$ ($76 \mu\text{g}_{\text{Ir}} \text{cm}^{-2}$) deposited on FTO glass substrates) were performed with an $\text{Hg}/\text{HgSO}_4/\text{K}_2\text{SO}_4$ (sat.) reference electrode at room temperature under constant stirring of the electrolyte. Potentials versus the reversible hydrogen electrode E_{RHE} were calculated by measuring the open circuit potential of the $\text{Hg}/\text{HgSO}_4/\text{K}_2\text{SO}_4$ (sat.) reference electrode against a Hydroflex RHE (GASKATEL Gesellschaft für Gassysteme durch Katalyse und Elektrochemie mbH) before and after each chronopotentiometry measurement and by shifting the measured potential accordingly.

2.10.4 Cyclic voltammetry on rotating disc electrode

Rotating disc electrode (RDE) measurements are a class of hydrodynamic electrodes that do not only rely on Fick's law on diffusion of the redox species in the electrolyte but introduce a forced convection. For an electrochemical cell with stationary electrodes and soluble freely diffusive redox species, the increasing polarization of the electrodes accelerates the rate of the electrochemical reaction and thus the current until the peak current is reached. In the absence of convection, however, the current decreases even in spite of the increasing electrode polarization due to a reduced flow of reacting species to the electrode interface because of slow

diffusion (as in classical cyclic voltammograms on stationary electrodes). A hydrodynamic voltammogram shows a similar increase of the current reaching a maximum but without levelling off due to the continuous flux of educts established by the forced convection. A hydrodynamic voltammogram is thereby characterized by the mass transport limited current i_{lim} and the half-wave potential $E_{1/2}$, which is located at $\frac{i_{lim}}{2}$.^[50]

The total mass-transfer-limited current i_{lim} at the RDE can thereby be described by the Levich

equation:
$$i_{lim,c} = 0.62 nFA D_0^{\frac{2}{3}} \sqrt{\omega \nu}^{-\frac{1}{6}} C_0^* \quad (52)$$

which is dependent on the electrode area A (cm²), the diffusion coefficient D_0 (cm² s⁻¹), the angular rotation rate ω (rad s⁻¹), the kinematic viscosity ν (cm² s⁻¹) and the analyte concentration C_0^* .^[38, 50]

When RDE measurements are applied for OER catalyst characterization it is not the stationary flux of educt (water) that is of interest, but gaseous oxygen. By rotation and convection, the O₂ bubbles formed on the electrode surface are constantly removed, which avoids inactivation of the catalyst surface due to educt depletion.

RDE measurements with linear sweep voltammetry of Ir-based (oxide supported) catalysts discussed in this thesis were conducted with an MSR electrode rotator with mirror finished polished 5 mm diameter glassy carbon disc insets (PINE RESEARCH INSTRUMENTATION) connected to an Autolab PGSTAT302N potentiostat/galvanostat (METROHM AUTOLAB B.V.) and an in-house constructed glass/silicone cell with Luggin-capillary for the reference electrode (HYDROFLEX reversible hydrogen electrode by GASKATEL GESELLSCHAFT FÜR GASSYSTEME DURCH KATALYSE UND ELEKTROCHEMIE MBH) compartment. Alternatively, a commercial double walled glass cell (PINE RESEARCH INSTRUMENTATION) connected to a KISS 104A thermostat (PETER HUBER KÄLTEMASCHINENBAU AG) was used. An electrolyte temperature of

60 °C was maintained by an oil bath with external stirrer or thermostat and monitored with an immersed silicone coated K-element temperature sensor. The Nernst potential for water oxidation was kept constant by continuous O₂ (AIR LIQUIDE, AlphaGaz 2 N5 purity) purging of the electrolyte (0.5 M H₂SO₄, SIGMAALDRICH, Titripur volumetric standard). Catalyst loadings of 50 μg_{Ir} cm⁻² (10 μg_{Ir} per disc) were drop-cast on cleaned glassy carbon discs and dried at 60 °C before applying 10 μL of a 1:100 dilution of a Nafion perfluorinated resin solution (SIGMA-ALDRICH, 5 wt% in lower aliphatic alcohols and water (15–20% water)) in a H₂O/*i*PrOH mixture (1:1 v/v).

75 linear sweep voltammetry cycles between 1.0 and ≈1.45 – 1.5 V vs. RHE with a variable upper vertex potential defined at $j = 1 \text{ mA cm}^{-2}$ were recorded at a scan rate of 5 mV s⁻¹. The cyclic voltammograms were recorded for the first cycles and after 50 and 75 LSV cycles (for further details see section “2.10.1 Redox activity probed by cyclic voltammetry”). The overpotentials for each LSV cycle were determined as a mean value of the anodic and cathodic scan. Reported overpotential values were taken from the 75th scan cycle each.

2.10.5 Impedance spectroscopy

Electrochemical impedance spectroscopy (EIS) was employed in the context of this work to determine the electrolyte resistance in linear sweep voltammetry experiments. This allows for a correction of the iR -drop in the respective measurements to obtain comparable current densities of OER catalysts. Besides this rather straightforward application, EIS is a powerful tool for the investigation of electrochemical reaction mechanisms, for measuring dielectric and transport properties of materials, for analyzing properties of porous electrodes and to examine passivation of surfaces.^[38]

Impedance is a generalized complex form of the classical electrical resistance described by Ohm's law ($R = \frac{E}{I}$). Impedance is the complex and time dependent form of the classical

resistance relation that takes the phase differences between input voltage and output current into account and is defined according to following equations:

Perturbation:
$$E_t = E_0 \sin(\omega t) \quad (53)$$

Response:
$$I_t = I_0 \sin(\omega t + \phi) \quad (54)$$

Impedance:
$$Z(\omega) = \frac{E_t}{I_t} = \frac{E_0 \sin(\omega t)}{I_0 \sin(\omega t + \phi)} = Z_0 \frac{\sin(\omega t)}{\sin(\omega t + \phi)} \quad (55)$$

E_t and I_t are the potential and current at time t with ϕ being the phase shift of the responding current versus the potential. The impedance of an electrochemical system and thus the phase shift is thereby dependent on the perturbation frequency ω that typically ranges from several hundred kHz to few Hz.

In an EIS experiment an electrochemical cell is held at a given potential such that the system remains in a steady state. The actual frequency response experiment superimposes an alternating sinusoidal potential (usually 5 – 10 mV RMS) on the constant potential to get a linear electrical perturbation/response of the system. This perturbation is repeated for a wide range of frequencies to probe for different electrochemical mechanisms and to record a full spectrum.^[38]

The impedance, as a complex entity, consists of an amplitude and phase with different common representations. There are Lissajous figures that plot $E(t)$ vs. $I(t)$, Nyquist plots with $\text{Re}(Z)$ vs. $-\text{Im}(Z)$ (Figure 16a) and Bode frequency plots with ω vs. $\log(Z)$ or Φ (Figure 16b).^[38, 46]

In the complex representation of the impedance (Nyquist plot) the x -axis (Z') or real part represents the resistive part of the impedance and the y -axis as the imaginary axis ($-Z''$) the reactive part, which can be attributed to, e.g., capacitive behavior.

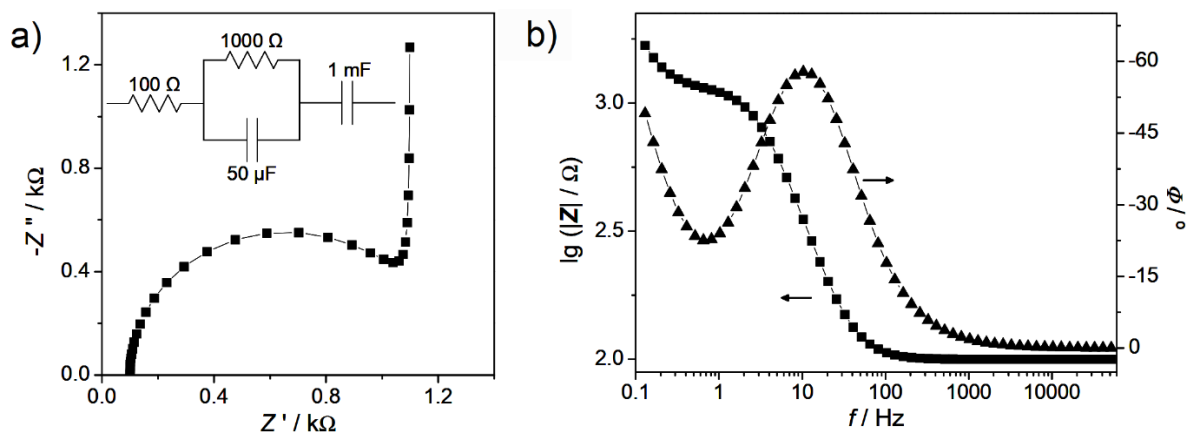


Figure 16 Electrochemical impedance spectrum (a) in a complex plane (Nyquist plot) representation and (b) Bode diagram with impedance magnitude (squares) and phase angle (triangles) representation for the equivalent circuit shown as inset in (a).^[46]

Reproduced with permission from Ref. [46]. Copyright 2004, Springer-Verlag Berlin Heidelberg.

For the interpretation of an impedance spectrum the data are often fitted to equivalent electrical circuit models. These models are derived from the interconnection of individual building blocks (e.g. resistors, capacitors, inductors, etc.) with a known mathematical description of their impedance to adequately describe the actual electrochemical system.

In the framework of this thesis the impedance was measured to determine the electrolyte resistance under non-faradaic conditions (0.5 V vs. RHE). For this purpose, the series resistance R_s (also denoted as high-frequency resistance R_{hf}) is of interest, which can be extracted from fitting the impedance data (semi circles consisting of series and charge transfer resistance) by an $R_s(R_{ct} \text{ CPE})$ “electrochemical-circle” equivalent circuit by NOVA 1.11 data acquisition software (METROHM AUTOLAB B.V.), with CPE being a constant phase element.

The electrolyte resistance was determined before and after each RDE measurement in the high frequency region of recorded impedance spectra at 0.5 V vs. RHE. Due to low current densities reached in the measurement protocol and repeatedly low electrolyte resistance values around 5Ω , an iR drop correction of the recorded data was not performed.

The electrolyte resistance was further determined before and after each LSV measurement of catalyst samples on FTO and QCM chips that reached current densities up to $\approx 100 \text{ mA cm}^{-2}$ at potentials up to 1.8 V vs. RHE, therefore an iR drop compensation was required. The impedance spectra were recorded at 0.5 V vs. RHE over a frequency range of 1.6 – 100 kHz with a sinusoidal perturbation of 10 mV (RMS). The electrolyte resistance was taken as 95 % of the series resistance R_s obtained from an $R_s(R_{ct} \text{ CPE})$ electrochemical circle fit.

2.11 References

- [1] J. Als-Nielsen, D. McMorrow, in *Elements of modern X-ray physics*, John Wiley & Sons, Ltd. **2011**, p. 29.
- [2] A. Schuster, *Brit. Med. J.* **1896**, 1, 172.
- [3] P. P. Ewald, in *Fifty Years of X-Ray Diffraction: : Dedicated To The International Union Of Crystallography On The Occasion Of The Commemoration Meeting In Munich July 1962* (Ed: P. P. Ewald), Springer **1962**, Ch. II. The Beginning, p. 6.
- [4] W. H. Bragg, W. L. Bragg, *Proc. R. Soc. Lond. A.* **1913**, 88, 428.
- [5] J. A. Bearden, *Rev. Mod. Phys.* **1967**, 39, 78.
- [6] M. Birkholz, in *Thin Film Analysis by X-Ray Scattering*, Wiley-VCH Verlag GmbH & Co. KGaA **2006**, p. 1.
- [7] P. Scherrer, in *Kolloidchemie Ein Lehrbuch*, Springer Berlin Heidelberg **1912**, p. 387.
- [8] H. Rietveld, *J. Appl. Crystallogr.* **1969**, 2, 65.
- [9] B. Dietzek, D. Cialla, M. Schmitt, J. Popp, in *Confocal Raman Microscopy* (Eds: T. Dieing, O. Hollricher, J. Toporski), Springer Berlin Heidelberg **2011**, p. 21.
- [10] G. Gouadec, P. Colomban, *Prog. Cryst. Growth Ch.* **2007**, 53, 1.
- [11] C. V. Raman, K. S. Krishnan, *Indian J. Phys.* **1928**, 399.
- [12] J. G. Skinner, W. G. Nilsen, *J. Opt. Soc. Am.* **1968**, 58, 113.
- [13] R. B. Prime, H. E. Bair, S. Vyazovkin, P. K. Gallagher, A. Riga, in *Thermal Analysis of Polymers* (Eds: J. D. Menczel, R. B. Prime), John Wiley & Sons, Inc. **2008**, Ch. III. Thermogravimetric Analysis (TGA), p. 241.
- [14] A. W. Coats, J. P. Redfern, *Analyst* **1963**, 88, 906.
- [15] R. B. Prime, H. E. Bair, S. Vyazovkin, P. K. Gallagher, A. Riga, in *Thermal Analysis of Polymers* (Eds: J. D. Menczel, R. B. Prime) **2008**, Ch. II. Differential Scanning Calorimetry (DSC), p. 7.
- [16] A. V. Malm, J. C. W. Corbett, *Sci. Rep.* **2019**, 9, 13519.
- [17] P. A. Hassan, S. Rana, G. Verma, *Langmuir* **2015**, 31, 3.
- [18] F. Ross Hallett, *Food Res. Int.* **1994**, 27, 195.
- [19] J. Stetefeld, S. A. McKenna, T. R. Patel, *Biophys. Rev.* **2016**, 8, 409.
- [20] A. Kramida, R. Yu., J. Reader and NIST-ASD-Team, (DOI: 10.18434/T4W30F), National Institute of Standards and Technology, Gaithersburg, MD, **2019**.

- [21] X. Hou, R. S. Amais, B. T. Jones, G. L. Donati, in *Encyclopedia of Analytical Chemistry*, (DOI: 10.1002/9780470027318.a5110.pub3) (Ed: R. A. Meyers) **2016**, p. 1.
- [22] G. L. Donati, R. S. Amais, C. B. Williams, *J. Anal. Atom. Spectrom.* **2017**, 32, 1283.
- [23] S. Ghosh, V. L. Prasanna, B. Sowjanya, P. Srivani, M. Alagaraja, D. Banji, *Asian J. Pharm. Ana.* **2013**, 3, 24.
- [24] K. S. W. Singh, J. Rouquerol, G. Bergeret, P. Gallezot, M. Vaarkamp, D. C. Koningsberger, A. K. Datye, J. W. Niemandsverdriet, T. Butz, G. Engelhardt, G. Mestl, H. Knözinger, H. Jobic, in *Handbook of Heterogeneous Catalysis*, Vol. 2 (Eds: G. Ertl, H. Knözinger, J. Weitkamp), Wiley-VCH **2008**.
- [25] K. S. W. Sing, *Pure Appl. Chem.* **1985**, 57, 603.
- [26] J. Rouquerol, D. Avnir, C. Fairbridge, D. Everett, J. Haynes, N. Pernicone, J. Ramsay, K. Sing, K. Unger, *Pure Appl. Chem.* **1994**, 66, 1739.
- [27] S. Brunauer, P. H. Emmett, E. Teller, *J. Am. Chem. Soc.* **1938**, 60, 309.
- [28] W. Sigle, *Ann. Rev. Mater. Res.* **2005**, 35, 239.
- [29] D. B. Williams, C. B. Carter, in *Transmission Electron Microscopy: A Textbook for Materials Science*, Springer US, Boston, MA **1996**, p. 3.
- [30] L. Marton, *J. Opt. Soc. Am.* **1950**, 40, 269.
- [31] S. Gaponenko, H. Demir, in *Applied Nanophotonics* (Eds: H. V. Demir, S. V. Gaponenko), Cambridge University Press, Cambridge **2018**, p. 9.
- [32] J. M. Thomas, P. L. Gai, *Adv. Catal.* **2004**, 48, 171.
- [33] L. A. Bendersky, F. W. Gayle, *J. Res. Natl. Inst. Stand. Technol.* **2001**, 106, 997.
- [34] M. J. Yacamán, J. A. Ascencio, S. Tehuacanero, M. Marín, *Top. Catal.* **2002**, 18, 167.
- [35] J. I. Goldstein, D. E. Newbury, J. R. Michael, N. W. M. Ritchie, J. H. J. Scott, D. C. Joy, in *Scanning Electron Microscopy and X-Ray Microanalysis*, Springer New York **2018**, Ch I. Electron Beam—Specimen Interactions: Interaction Volume. p. 1.
- [36] J. I. Goldstein, D. E. Newbury, J. R. Michael, N. W. M. Ritchie, J. H. J. Scott, D. C. Joy, in *Scanning Electron Microscopy and X-Ray Microanalysis*, Springer New York **2018**, Ch. III. Secondary Electrons. p. 29.
- [37] J. I. Goldstein, D. E. Newbury, J. R. Michael, N. W. M. Ritchie, J. H. J. Scott, D. C. Joy, in *Scanning Electron Microscopy and X-Ray Microanalysis*, Springer New York, **2018**, Ch. II. Backscattered Electrons. p. 15.

-
- [38] A. J. Bard, L. R. Faulkner, *Electrochemical Methods: Fundamentals and Applications, 2nd Edition*, Wiley Textbooks, **2000**.
- [39] C. K. O'Sullivan, G. G. Guilbault, *Biosens. Bioelectron.* **1999**, 14, 663.
- [40] G. Sauerbrey, *Z. Phys.* **1959**, 155, 206.
- [41] M. B. Heaney, in *Electrical Measurement, Signal Processing, and Displays* (Ed: J. G. Webster), CRC Press **2003**.
- [42] F. Wudl, M. R. Bryce, *J. Chem. Educ.* **1990**, 67, 717.
- [43] W. L. V. Price, *J. Phys. D Appl. Phys.* **1972**, 5, 1127.
- [44] J. L. van-der-Pauw, *Philips Res. Rep.* **1958**, 13, 1.
- [45] C. H. Hamann, A. Hamnett, W. Vielstich, in *Electrochemistry* (Eds: C. H. Hamann, A. Hamnett, W. Vielstich), Wiley-VCH Verlag GmbH & Co. KGaA, Weinheim **2007**.
- [46] C. Brett, in *Piezoelectric Transducers and Applications*, (Ed: A. A. Vives), Springer Berlin Heidelberg **2008**, p. 223.
- [47] S. Trasatti, *Pure Appl. Chem.*, **1986**, 58, 955.
- [48] R. G. Compton, C. E. Banks, in *Understanding Voltammetry 2010*, Ch II. Electrode Kinetic, p. 35.
- [49] R. G. Compton, C. E. Banks, in *Understanding Voltammetry 2010*, Ch IV. Cyclic Voltammetry at Macroelectrodes, p. 107.
- [50] R. G. Compton, C. E. Banks, in *Understanding Voltammetry 2010*, ChVIII. Hydrodynamic Electrodes, p. 291.

3. Ceramic anodes for Li and Na-ion batteries

This chapter is based on the following book chapter:

Arinicheva Y., Wolff M., Lobe S., Dellen C., Fattakhova-Rohlfing, D., Guillon, O., Böhm, D., Zoller, F., Schmuck, R., Li, J., Winter, M., Adamczyk, E., Pralong, V., 10 - Ceramics for electrochemical storage. In *Advanced Ceramics for Energy Conversion and Storage*, Guillon, O., Ed. Elsevier: 2020, pp 549-709.

Specific: Chapter 10 - Subsection 2 – Ceramic anodes for Li and Na-ion batteries, pp 563-593 – Böhm, D.*, Zoller, F.*, Pralong V. and Fattakhova-Rohlfing, D. (*these authors contributed equally to the work)

3.1 Introduction

Anodes (negative electrodes) of rechargeable batteries should ideally possess a possible low insertion/extraction potential and a high reversible gravimetric and volumetric capacity to provide maximum energy density. Metallic lithium is the best possible anode for LIBs as it is the most electropositive element (3.04 V vs. SHE) with the highest theoretical gravimetric capacity ($\sim 3862 \text{ mA g}^{-1}$) due to its light weight (6.94 g mol^{-1}) and low density (0.534 g cm^{-3}). However, the high reactivity of metallic lithium and the tendency to mossy growth and dendrite formation upon cycling in conventional aprotic solvent are still serious challenges preventing its application as an anode in secondary lithium batteries. A similar situation applies for the use of metallic sodium in secondary SIBs, as sodium is chemically even more reactive than lithium and has a relatively low melting point ($97.7 \text{ }^\circ\text{C}$).^[1-2] As a practical solution of this problem, graphitic carbons were introduced as anode materials, and currently, they dominate the market of the commercially available rechargeable lithium cells. Graphitic carbon is an insertion-type anode material acting as a stable host structure for lithium

intercalation able to withstand several hundreds of charge/discharge cycles without structure degradation. Due to a slightly more positive lithium insertion potential (~ 0.1 V vs. Li/Li^+), graphitic carbons do not suffer from lithium plating and lithium dendrite issues, rendering them safe anode material at moderate charging rates. Shortcomings of graphitic anodes, however, are a much lower insertion capacity as compared to lithium metal (372 mAh g^{-1}) and a limited rate capability (power density). In spite of the progress achieved in the performance of state-of-the-art rechargeable lithium cell, there is a strong need for anode materials with high-energy and power density, low-cycle life, and safe operation.

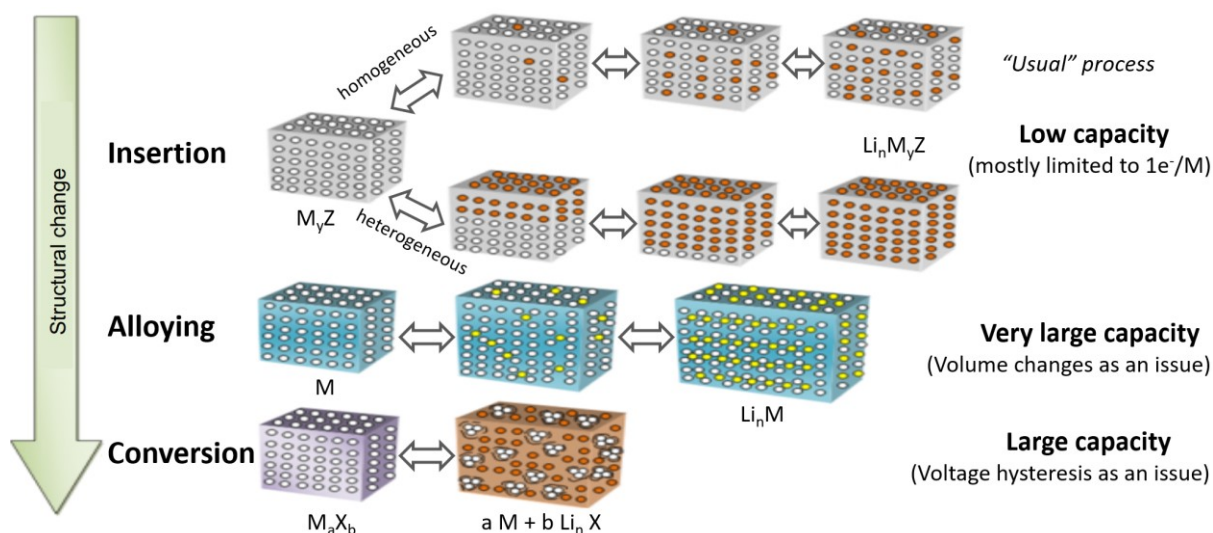


Figure 1 Structural changes during charge-discharge of insertion, alloying, and conversion anodes materials.^[3]

Reproduced (modified) with Permission from Ref. [3]. Copyright 2016 Bensalah N., *et al.*

Ceramic materials are in the focus of intensive research activity as possible anode materials due to a huge variety of their compositions and hence, possible solid-state chemistries available for ion/electron storage. Ceramic materials can be produced by scalable methods with an unlimited variety of different morphologies and microstructures, making them attractive for commercialization and large-scale production. From the point of view of electrochemical energy storage mechanism, ceramic anodes can be broadly divided in three classes: insertion-type, conversion-type, and conversion and alloying-type materials (Figure 1). Insertion-type

materials can incorporate additional ions in their structure without significant structural changes. The benefits of such materials are low volume changes and low structure reorganization energies ensuring reversible insertion/extraction and long cycle life. The penalty for the structure stability is, however, the unavoidably lower insertion capacity, which is determined by the available ion vacancies in the host structure.

So far, a variety of transition metal-based insertion-type anodes for alkali metal ions were introduced but among them ceramic compositions including titania-based materials are projected to be able to replace graphitic anodes as they provide the required cell safety, cost effectiveness, compatibility with cathodes, and improved electrochemical activity for high-rate applications.^[2] The electrochemical potential of these non-carbonaceous anodes is, however, comparably high (>1 V vs. Li/Li^+), lowering the applicable potential window of the cell. In addition, the practical reversible capacity is less than that of graphite and most ceramic materials possess a rather limited electronic conductivity.

Conversion-type anode materials (CTAMs) undergo a complete transformation from oxidized (transition metal ions) to fully reduced (metal state) during charge and discharge cycles. In some cases, the metal phase can be reduced further with formation of lithium (or sodium) alloys (conversion and alloying mechanism). Because of the multiple electron reactions, conversion and combined conversion/alloying-type anodes can provide much higher storage capacities as compared to the insertion-type anodes. However, a significant drawback of such anodes is a huge structure reorganization accompanied by significant (up to several 100%) volume changes, which typically results in a very fast degradation during charge/discharge and rapid capacity loss.

It should be noted that practically all the ceramic materials feature in their bulk (macroscopic) state low electronic and ionic conductivities, and often also lower reversibility and higher degradation as compared to graphite anodes. These shortcomings can be, however, successfully

mitigated via nanoscaling of ceramic materials. Particularly, a very small size of crystalline domains of only a few nanometers drastically improves the performance of ceramic anodes due to the change in electrochemical storage mechanism as it will be shown below. Furthermore, coating of ceramic powders with carbonaceous materials, optimization of nanostructures, and combination of nanostructures with conducting carbonaceous compounds to form nanocomposites are extremely efficient strategies to enhance storage capacity, improve the rate performance, sustain the volume variation, and thus improve the cycling stability of ceramic anode materials. A dominating majority of ceramic anode materials are prepared as nanostructured materials or nanocomposites, with the number of available compositions and morphologies increasing daily. As it is practically impossible to hold step with this dynamically developing field, this chapter intends at introducing only the most established and promising classes of ceramic anode materials for rechargeable lithium batteries, with a special focus on their structure and the basic electrochemical properties. Moreover, for the interested reader there are several reviews dedicated to the anode materials for SIBs^[4-9] that are at an earlier stage of development compared to LIBs. In the following, we summarize the main advances regarding the three main types of ceramic anodes for SIBs and LIBs.

3.2 Insertion-type ceramic anodes

3.2.1 Titanate-related battery anodes — Structure and key properties

Titanium dioxide (TiO₂) anodes

TiO₂-based materials are among the most studied and attractive ceramic anodes for the Li-ion^[10] and increasingly also for Na-ion batteries^[11-16]. TiO₂ exists in eight polymorphs, namely rutile, anatase, brookite, TiO₂-B, TiO₂-R, TiO₂-H, TiO₂-II, and TiO₂-III.^[17] Among these phases, anatase, rutile and bronze are the most investigated as battery anodes due to the abundance of TiO₂, availability, and suitable electrochemical performance.^[18] For all TiO₂ phases, irrespective of their crystalline structure, storage of 1 mol Li⁺ per mole is theoretically possible due to the reversible transformation of Ti⁴⁺ to Ti³⁺ state, resulting in a theoretical insertion capacity of 335 mAh g⁻¹. In practice, however, typically only 0.5 mol Li can be reversibly inserted/extracted per mole TiO₂ resulting in a moderate insertion capacity of 170–180 mAh g⁻¹.^[10] Insertion of Li in all titania polymorphs takes place at potentials of around 1.5–1.8 V vs. Li/Li⁺. The relatively high insertion potential renders titania a safe anode material due to a greatly minimized risk of lithium dendrite growth, but on the other hand it limits the voltage (and thereby the energy density) of the respective full cells.

TiO₂ anatase

Anatase is one of the most investigated titania phases for lithium storage.^[19] Bulk anatase is a metastable phase^[20], however, it is the thermodynamically most stable phase on the nanoscale. Anatase crystallizes in a tetragonal symmetry with the body-centered *I4₁/amd* space group in which distorted edge-sharing [TiO₆] octahedra are stacked in one-dimensional (1D) zigzag chains (Figure 2a).^[21-23] Upon insertion, Li ions can diffuse along the empty [TiO₆] zigzag channels connecting octahedral interstitial sites. The diffusion coefficient for Li ions in the anatase phase is relatively low, being in the range of $2 - 6 \times 10^{-13} \text{ cm}^2 \text{ s}^{-1}$, as reported for single

crystals by Kavan *et al.*^[24] to $4.7 \times 10^{-12} \text{ cm}^2 \text{ s}^{-1}$ determined by ^7Li MAS nuclear magnetic resonance (NMR).^[25] Li insertion into the anatase phase induces the phase transformation from the tetragonal to the orthorhombic $\text{Li}_{0.5}\text{TiO}_2$ phase (space group $Pnm2_1$) because of a loss of symmetry in the y -direction, resulting in an increase of the unit cell volume by 3.7%.^[2] In addition to nanostructuring, carbon coating of the titania surface and fabrication of carbon-titania nanocomposites are other efficient and intensively explored ways to overcome the poor lithium-ion diffusion and low electrical conductivity in titania materials. In typical synthesis methods, incorporation of carbon into TiO_2 is conducted by hydrothermal heating of metal salts in presence of carbon sources such as glucose.^[26-27]

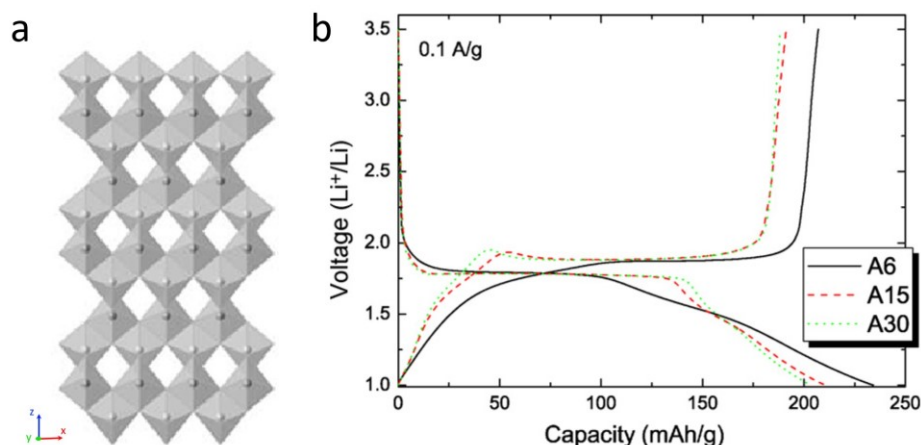


Figure 2 (a) The structure of anatase^[28] and (b) potential-capacity profiles of anatase anodes with different particle sizes: 6 nm (A6), 15 nm (A15), and 30 nm (A30).^[29]

(a) Reproduced (modified) with permission from Ref. [28]. Copyright 2013 Chinese Materials Research Society. Production and hosting by Elsevier B.V.

(b) Reproduced with permission from Ref. [29]. Copyright 2007 Elsevier.

Li insertion/extraction in the anatase phase takes place at a potential around 1.75 V vs. Li/Li^+ . The major part of Li ions is stored in a two-phase reaction manifested by a plateau at 1.75 V vs. Li/Li^+ , with a total insertion of 0.5 mol Li and a gravimetric capacity of 175 mAh g^{-1} (Figure 2b). Further Li-ion storage into the TiO_2 framework is restrained because of the strong repulsive forces among the Li ions.^[10] At the initial steps of the Li-insertion process, a solid solution is formed, observed as a monotonous curve at potentials below 1.75 V vs. Li/Li^+ , while

for a fully lithiated material some amount of Li can be stored interfacially at a potential above 1.75 V vs. Li/Li⁺.^[30] The mechanism of lithium insertion, the amount of Li ions stored via different mechanisms, and also the rate of the Li-insertion process greatly depends on the size of crystalline domains and the microstructure of the anatase phase (Figure 2b).^[31] Generally, the slower two-phase reaction mechanism dominates the storage in bulk macroscopic materials, while the faster processes of solid solution and interfacial lithium storage play an increasing role in the nanostructured materials.^[32] The strong impact of microstructure on the lithium insertion process provides broad possibilities to optimize the performance of anatase anodes by controlling their morphology, which boosted research on nanostructured titania materials.^[33] Systematic investigation of the impact of particle size on the electrochemical performance of anatase was performed by Wagemaker *et al.*^[34] The authors have demonstrated that, in contrast to the bulk phase, nanoparticles below 7 nm in size can deliver up to 1 mol of Li ions per formula unit (f.u.) due to a greatly increased solubility on the nanoscale. The very small particles size, however, often negatively affects the cycling stability. Therefore, an optimum range exists for different materials to achieve the highest possible capacity, fast insertion rate, and cycling stability. For anatase, the optimum particle size is considered to be between 8 and 25 nm, thereby the anodes demonstrate a rather high cycling stability.^[35] Thus, full-Li cells with respective anodes were reported to retain 90% of their initial capacity after 700 cycles.^[36] The electrochemical properties of anatase TiO₂ vs. Na/Na⁺ offer an appealing working voltage of 0.8 V, and researchers have already demonstrated high-rate capability, suggesting potential use in commercial SIBs.^[37-39]

TiO₂ rutile

In contrast to anatase, the most thermodynamically stable polymorph, rutile, attracts much less attention as an anode material. The Li-insertion potential of 1.85 V vs. Li/Li⁺ is the most positive among all titania polymorphs, which makes it less suitable for the application as an

anode.^[40] Furthermore, bulk rutile features a lower Li-insertion capacity given by its crystalline structure. Rutile crystallizes in a tetragonal symmetry with the space group $P4_2/mnm$, with $[\text{TiO}_6]$ octahedra sharing edges along the c -direction and corners located along the ab -planes (Figure 3a).^[41]

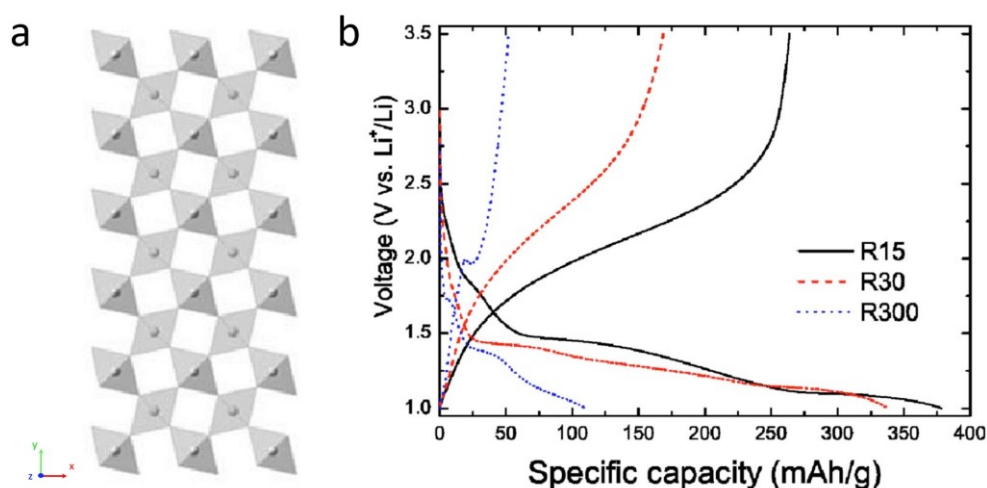


Figure 3 (a) Structure of rutile^[28] and (b) potential-capacity profiles of rutile electrodes with particle sizes of 15 nm (R15), 30 nm (R30), and 300 nm (R300) (the initial cycles at 0.05 A g⁻¹).^[29]

(a) Reproduced (modified) with permission from Ref. [28]. Copyright 2013 Chinese Materials Research Society. Production and hosting by Elsevier B.V.

(b) Reproduced with permission from Ref. [29]. Copyright 2007 Elsevier.

This property explains the different availability of tetrahedral and octahedral sites and a strong anisotropy for Li diffusion. The Li-ion diffusion into rutile is thermodynamically favorable only along the c -axis channels between the tetrahedral sites, with a diffusion coefficient of 10^{-6} cm² s⁻¹. In contrast to that, the octahedral interstitial sites are practically unavailable for Li insertion^[42], with diffusion along the ab -planes being prohibitively slow^[25, 42]. In addition, the strong repulsive Li-Li interactions in the c -channels, together with trapped Li-ion pairs in the ab -planes, block the c -channels and restrict insertion to well below its theoretical limit.^[22] As a result, in the bulk crystalline form, it is able to accommodate up to 0.1 mol Li only.^[2] The storage capacity of rutile, however, strongly benefits from nanostructuring.^[33, 43-44] Thus, it was reported that nanosized rutile shows a stable capacity of 346 mAh g⁻¹ and a superior rate

capability (Figure 3b).^[45] The absence of phase boundaries in nanoparticles is believed to be the main reason for the enhanced Li-ion solubility.

TiO₂-B (bronze)

Among other polymorphs, TiO₂-B (bronze) has attracted particular attention as a promising anode for lithium batteries due to a combination of favorable properties.^[46] TiO₂-B features the lowest insertion potential of 1.55 V vs. Li/Li⁺ (Figure 4c) among all TiO₂ materials, which is beneficial for its use as an anode.^[46] TiO₂-B crystallizes in a monoclinic structure with *C2/m* symmetry. It is composed of corrugated sheets of edge and corner-sharing [TiO₆] octahedra^[47], which are joined together to form a three-dimensional (3D) framework containing 1D channels (Figure 4a).^[48] In the unique open structure of TiO₂-B, practically all octahedral sites are accessible, resulting in an insertion capacity close to the theoretical value of 335 mAh g⁻¹ (Figure 4b).^[46] Moreover, the structure is capable of buffering structure changes during lithium-ion insertion without lattice deformation, promoting a high reversibility of the insertion/extraction process and a long cycle life.^[48] Different to other TiO₂ polymorphs whose lithium insertion rate is diffusion limited, lithium insertion into the bronze phase has a pseudocapacitive behavior resulting in a high-power capability.^[49] Although practically infinite unidirectional channels provide fast pathways for Li diffusion, long transport distances are responsible for poor rate capability of bulk TiO₂-B material.^[48]

Nanostructuring was demonstrated to be a very efficient means to overcome this limitation and to improve the charging rate of TiO₂-B.^[50] The numerous reported nano-morphologies include, among others, nanoparticles^[51], nanosheets^[52], nanowires^[53], nanorods^[54], and microspheres^[55] which show a greatly improved rate performance (Figure 4c).

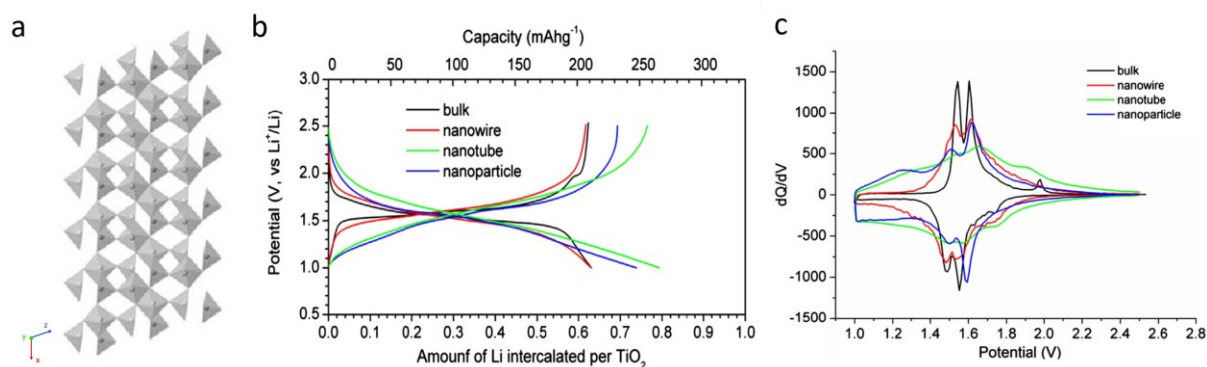


Figure 4 (a) The structure of TiO₂-B, (b) variation of voltage with state-of-charge for discharge then charge of bulk TiO₂-B, TiO₂-B nanowires, nanotubes, and nanoparticles on the second cycle, and (c) corresponding differential capacity plots at 50 mA g⁻¹.^[28]

Reproduced (modified) with permission from Ref. [28]. Copyright 2013 Chinese Materials Research Society. Production and hosting by Elsevier B.V.

A serious drawback of nanosized TiO₂-B is, however, an ICL in the first charging cycle, which was explained by irreversible reactions on the surface.^[47] Coating with carbonaceous species, like for other titania polymorphs, is a promising way to minimize these contributions. Another efficient strategy to boost the rate performance of TiO₂-B-based anodes and to increase their cycling stability is hybridization with different conductive carbon materials such as reduced graphene oxide (rGO) for the fabrication of nanocomposites.^[56-57]

Lithium titanate Li₄Ti₅O₁₂/LiTi₂O₄ (LTO)

Among all Ti-based ceramic anodes, Li₄Ti₅O₁₂ (LTO) is the most prominent member of the Li solid-solution family Li_{3+x}Ti_{6-x}O₁₂ (0 ≤ x ≤ 1)^[58] that has been developed to a marketable product for electrochemical energy storage (including batteries for EVs)^[59] since its discovery as a Li-insertion host by Murphy *et al.*^[60] and first electrochemical measurements in 1989 by Colbow *et al.*^[61-63] The unique and advantageous properties of LTO as a LIB anode material are mainly caused by its spinel (AB₂X₄) crystal structure (Fd $\bar{3}$ m) that can accommodate three Li⁺ ions per f.u. with a negligible change of ~0.07%^[64] of the lattice parameters also known as “zero-strain” Li⁺ insertion.^[62-63] The spinel structure of Li₄Ti₅O₁₂ [alternative writing: Li(Li_{1/3}Ti_{2/3})O₄] is built from a cubic-close-packing (ccp) of oxygen atoms (32e sites) with

tetrahedrally (8a, 8b, and 48c) as well as octahedrally (16c and 16d) interstitial sites partially occupied by Li and Ti atoms which can be expressed in space notation as $[\text{Li}_3]_{8a}[\text{Ti}_5\text{Li}]_{16d}[\text{O}_{12}]_{32e}$ (Figure 5).^[62-63]

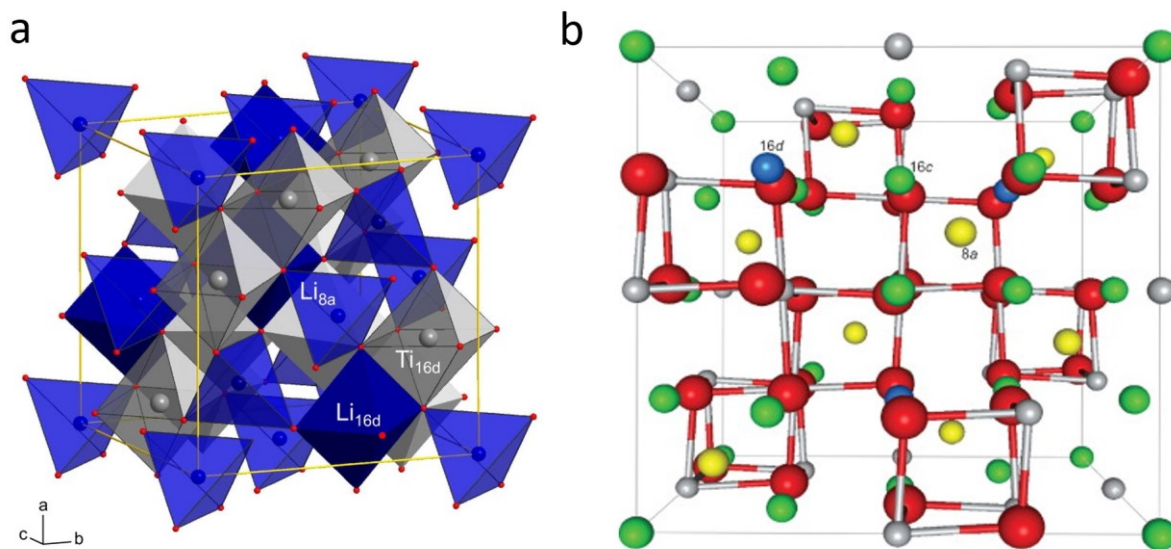
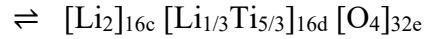
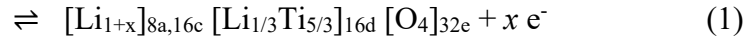


Figure 5 (a) Schematic representation of spinel-type $\text{Li}_4\text{Ti}_5\text{O}_{12}$ crystal structure with octahedral and tetrahedral coordination of Ti (16d site) and Li (8a and 16d sites) by O atoms^[65] and (b) ball and stick representation of the unit cell with Li occupation sites (16d, 16c, and 8a for fully lithiated structure). O atoms represented with big red spheres and Ti atoms represented by small light gray spheres. Yellow, green and blue spheres represent Li occupancies.^[66]

(a) Reproduced with permission from Ref. [65]. Copyright 2015 American Chemical Society.
 (b) Reproduced with permission from Ref. [66]. Copyright 2011 Elsevier.

Upon cell charging the LTO anode can reversibly accommodate up to three Li^+ ions per formula unit in differing tetrahedral (8a) and/or octahedral (16c) interstitial sites within the packed oxygen array. Following Eq. (1) and Figure 6a describe the insertion of Li^+ ions (beyond the present Li^+ ions of the $\text{Li}_4\text{Ti}_5\text{O}_{12}$) into empty octahedral sites (16c) that cause a further population of octahedral (16c) sites (and removal from tetrahedral 8a sites) by Li^+ ions initially present in the spinel structure by electrostatic repulsion. Fully lithiated $\text{Li}_7\text{Ti}_5\text{O}_{12}$, also noted as $[\text{Li}_6]_{16c}[\text{Ti}_5\text{Li}]_{16d}[\text{O}_{12}]_{32e}$, thereby constitutes a rock-salt structure with coinciding lattice symmetry ($\text{Fd}\bar{3}\text{m}$).^[62-63]





Galvanostatic charge/discharge curves reflecting the electrochemical potential of the LTO phase according to its lithiation state are governed by three regimes (Figure 6b). During charging, initial Li^+ ions (α) are inserted into an isostructural $\text{Li}_{4+\alpha}\text{Ti}_5\text{O}_{12}$ phase resulting in a continuous drop of the electrochemical potential stabilizing with the formation of a parallel existing rock-salt $\text{Li}_{7-\gamma}\text{Ti}_5\text{O}_{12}$ structure. Ongoing Li^+ insertion into the $\text{Li}_{4+\alpha}\text{Ti}_5\text{O}_{12}$ - $\text{Li}_{7-\gamma}\text{Ti}_5\text{O}_{12}$ two-phase system results in a flat operating potential of ~ 1.55 V vs. Li/Li^+ until the remaining spinel phase is fully converted to the rock-salt phase, which again results in a single-phase system with a final insertion potential of 1.0 V vs. Li/Li^+ .^[62-63]

The electrochemical potential of ~ 1.55 V vs. Li/Li^+ of LTO^[67] limits the overall cell voltage compared to carbonaceous anodes but significantly increases the LIB safety and stability. The relative high potential prevents the SEI formation, the reduction of an organic electrolyte and dendritic lithium growth. Beyond that, LTO is nontoxic, possesses a high thermodynamic stability (compared to carbonaceous anodes) and has a well-characterized stable crystal structure upon lithium insertion making it a “zero-strain” material.^[62, 64] In addition, LTO anodes have a negligible amount of ICL, are not prone to solvent co-intercalation or electrolyte decomposition and are in principle capable of delivering high-power density.^[2, 62-63]

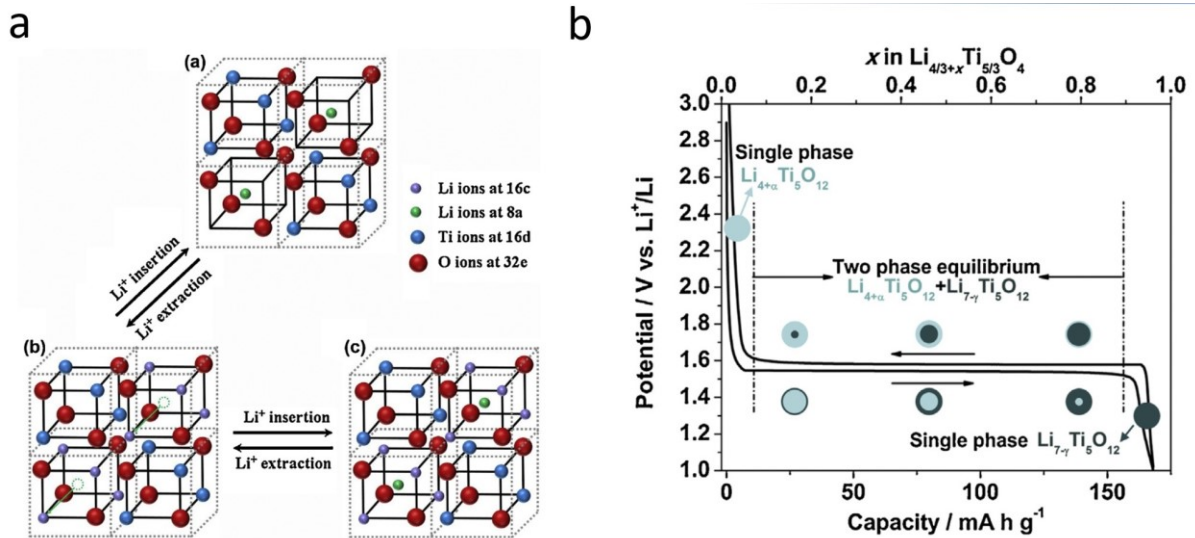


Figure 6 (a) Schematic illustration of Li^+ intercalation and deintercalation into spinel-type $\text{Li}_4\text{Ti}_5\text{O}_{12}$ structure^[68] and (b) galvanostatic charge/discharge curve with indicated one and two-phase potential regions.^[62]

(a) Reproduced with permission from Ref. [68]. Copyright 2011 Elsevier.

(b) Reproduced with permission from Ref. [62]. Copyright 2015 Elsevier.

Bulk phase spinel $\text{Li}_4\text{Ti}_5\text{O}_{12}$ shows a rather poor electrochemical performance due to its low electronic ($<10^{-13} \text{ S cm}^{-1}$)^[69] and ionic conductivity ($\sim 1.6 \times 10^{-11} \text{ cm}^2 \text{ s}^{-1}$)^[70], which requires nanostructuring and the fabrication of carbon composite anodes to shorten the Li^+ ion diffusion length and enhance the conductivity within the electrode.^[2, 62-63] Due to a simple and inexpensive synthesis of nanostructured LTO, primarily by sol-gel-based synthesis routes, research advanced rapidly in the recent years so that composite anodes with a high reversibility (Coulombic efficiency $>95\%$) even at high current rates of up to $>1000\text{C}$ could be obtained.^[2] Nano- and microstructures accessible primarily by sol-gel-based synthesis range from zero-dimensional (0D) (nanoparticles) over 1D in the form of nanofibers, -wires, -tubes, or -rods to two-dimensional (2D) nanoplate or -sheet structures. By use of advanced templating techniques and/or suitable synthesis conditions, a variety of porous, hierarchical, or array 3D structures could be fabricated.^[62-63, 71] As an example, a mesoporous thin film built from nanocrystalline spinel LTO particles could reach the theoretical 175 mA g^{-1} up to a rate of 25C (144 s charge/discharge duration) and maintain up to $\sim 115 \text{ mA g}^{-1}$ at a rate of 800C (4.5 s

charge/discharge duration) with a capacity retention of 89% after 1000 cycles at a rate of 100C (Figure 7).^[72]

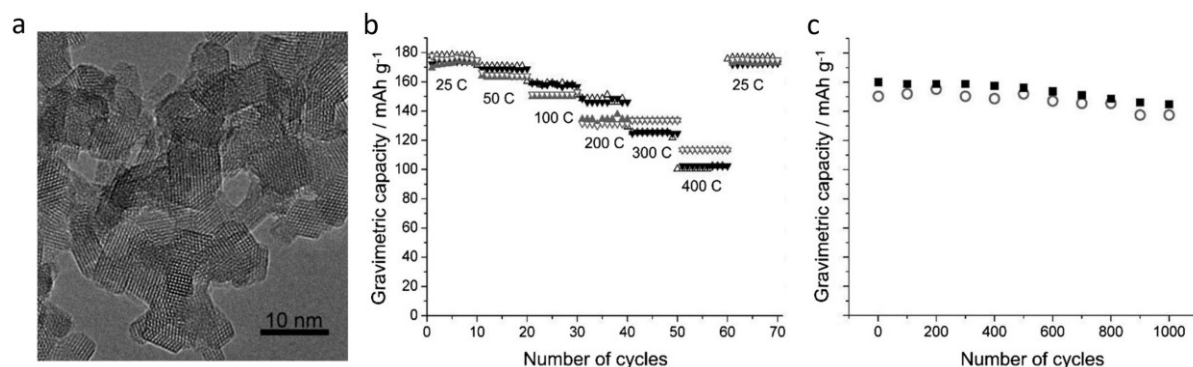


Figure 7 (a) Transmission electron micrograph of spinel $\text{Li}_4\text{Ti}_5\text{O}_{12}$ nanocrystals forming mesoporous thin film electrode. (b) Gravimetric capacity of mesoporous thin film LTO nanocrystal electrodes at different C-rates and (c) capacity retention at a rate of 100C.^[72]

Reproduced (modified) with permission from Ref. [72]. Copyright 2012 John Wiley and Sons.

For the preparation of anodes and full cells with thicker electrodes enabling high rate and high gravimetric and volumetric capacities, composites with carbonaceous materials [e.g., (reduced) graphene oxide (GO, rGO), carbon nanotubes] and carbon coatings are prepared.^[62-63] Zhu *et al.* prepared spherical LTO microparticles with a porous morphology resulting from close packing of nanoparticle building blocks.^[73] The conductivity of the material was significantly increased to $\sim 10 \text{ S cm}^{-1}$ by applying a $\sim 6 \text{ nm}$ homogeneous carbon coating. Due to a relatively high electrode/electrolyte interface of the porous structure increasing and facilitating the Li^+ ion flux, a reversible capacity of 126.4 mAh g^{-1} could be demonstrated at a rate of 20C (corresponding to 3 min charge or discharge time). In addition, the high stability of the composite anode was shown by a capacity retention of 95% after 1000 cycles at a rate of 1C (1 h charge/discharge time).^[74]

The electrochemical performance of $\text{Li}_4\text{Ti}_5\text{O}_{12}/\text{C}$ electrodes is dependent on various parameters such as the carbon coating thickness and uniformity, the choice of precursor, the preparation technique as well as the synthesis conditions. Thin, $<10 \text{ nm}$ carbon coatings can be applied by using sugar (glucose), polyvinylpyrrolidone (PVP), polyacrylonitrile (PAN), citric acid (CA),

polyacrylate (PAA), maleic acid (MA), or LTO acetate precursors with an adjacent thermal decomposition and graphitization under nitrogen atmosphere.^[62-63] Beyond carbon composites, also metal (Ag, Au, or Cu) composites were prepared to increase the overall conductivity within the electrode and to enable a high capacity retention of ~75% [131 mAh g⁻¹ for LTO/Ag composite^[75]] at a rate of 30C (2 min charge/discharge time).^[62-63] The electrochemical performance of active LTO phases is greatly affected by the way of their fabrication. Possible preparation techniques include solid-state reactions at high temperatures of 600–1000 °C, microwave-assisted synthesis, molten-salt synthesis, hydrothermal, and combustion synthesis.^[2, 63] Among them, combustion and sol-gel-based LTO anodes show a superior performance as compared to the anodes containing solid-state derived active material. Furthermore, electrodes with hydro- or solvothermally derived LTO product also show an excellent cyclability and high-rate capability.^[63] Full-cell assemblies with high-voltage cathodes like LiCoO₂ (LCO) or LiMn₂O₄ provide cell voltages of 2.5–3.0 V, whereby LTO shows a better compatibility with LiCoO₂ than with Mn-based layered oxide cathodes.^[2, 62] For a LTO/LCO full-cell configuration, an ultralong cyclability of 117,000 cycles could be demonstrated.^[2, 76] A cell composed of a LiMn₂O₄ cathode with a nanostructured LTO anode has exhibited an extended stability for 30,000 cycles at a rate of 10C (6 min charge and discharge time) with a capacity retention of 95%.^[77] A full cell with LiFePO₄ cathode in a 18,650 cell configuration retained its full capacity for 20,000 cycles at a charging rate of 10C (6 min charge/discharge time) and still retained 95% after 30,000 cycles at a charging rate of 15C with discharge rates of 5C, respectively.^[78] In total, the high structural stability upon Li⁺ insertion, cyclability, and rate capability render Li₄Ti₅O₁₂-based anodes suitable for the application in battery electric vehicles (BEVs) or stationary power supply with high-power and safety demands.

LTO has been also investigated as an anode material for SIBs. A capacity of 155 mAh g⁻¹ at 0.91 V was reported and presented the best cyclability among all reported oxide-based anode materials.^[79]

Two sodium ions were inserted per formula unit of the zigzag layered Na₂Ti₃O₇ phase through a biphasic process at a very low potential of 0.3 V vs. Na/Na⁺—the lowest voltage ever reported for a transition metal oxide in Na-ion batteries.^[80] The fully reduced phase Na₄Ti₃O₇ formed in this process was reported to crystallize in an ordered rock-salt-type structure.^[81]

TiNb₂O₇ (TNO)

Besides the already commercialized LTO, TiNb₂O₇ (TNO) is in the focus of research for an application as novel high rate, high-capacity LIB anode material based on its discovery as a Li⁺ ion insertion host by Cava *et al.* and the work of Goodenough and Kim proposing its application as an anode material.^[82-83] TiNb₂O₇ crystallizes in a layered monoclinic structure (C2/m space group), where all Ti⁴⁺ and Nb⁵⁺ metal ions are octahedrally coordinated by oxygen. Edge and corner shared octahedral [MO₆] units form a crystallographic shear structure that can reversibly accommodate Li⁺ ions in its interstitial sites (Figure 8a (a–d)) oriented along the crystallographic [010] direction.^[84] Due to the similar ionic radii of Ti⁴⁺ and Nb⁵⁺ ions, an anti-site disorder can be found for this structure.^[2, 85] In contrast to LTO, the unit cell volume of TiNb₂O₇ is enlarged by ~7.22% upon Li⁺ insertion, which can be a reason for experimentally observed capacity fading.^[2, 85] The maximum theoretical capacity of the material depends on the number of transferred electrons and thus on the applied potential window for cycling. For a five electron transfer involving the Ti³⁺/Ti⁴⁺ and Nb³⁺/Nb⁵⁺ redox couples, a theoretical capacity of 387.6 mAh g⁻¹ is obtained. Cycling in a smaller potential window involving only the Nb³⁺/Nb⁵⁺ redox couple and thus a four-electron transfer process TiNb₂O₇ shows a maximum capacity of 310 mAh g⁻¹.^[84] The experimentally observed maximum reversible

capacity is about 280 mAh g^{-1} (Figure 8c) when operated in a potential window from 1.0 to 2.5 V.^[86] This corresponds to an insertion of 3.6 Li^+ ions per f.u. of TiNb_2O_7 and is associated with a full reduction of Nb^{5+} and Ti^{4+} to Nb^{4+} and Ti^{3+} , respectively, and a partial contribution by the Nb^{4+} to Nb^{3+} redox couple.^[84, 86] The clearly visible feature between 1.5 and 1.75 V vs. Li/Li^+ in the cyclic voltammogram of NTO^[87] (Figure 8b) originates thereby from the $\text{Nb}^{4+}/\text{Nb}^{5+}$ and $\text{Ti}^{3+}/\text{Ti}^{4+}$ redox couples, resulting in an average insertion voltage of about 1.64 V vs. Li/Li^+ at a rate of 0.1C (10 h charge/discharge time).^[84] The broader $\text{Nb}^{3+}/\text{Nb}^{4+}$ redox couple around 1.25 V vs. Li/Li^+ thereby only partially contributes to the total capacity when cycled down to 1.0 V vs. Li/Li^+ .^[84]

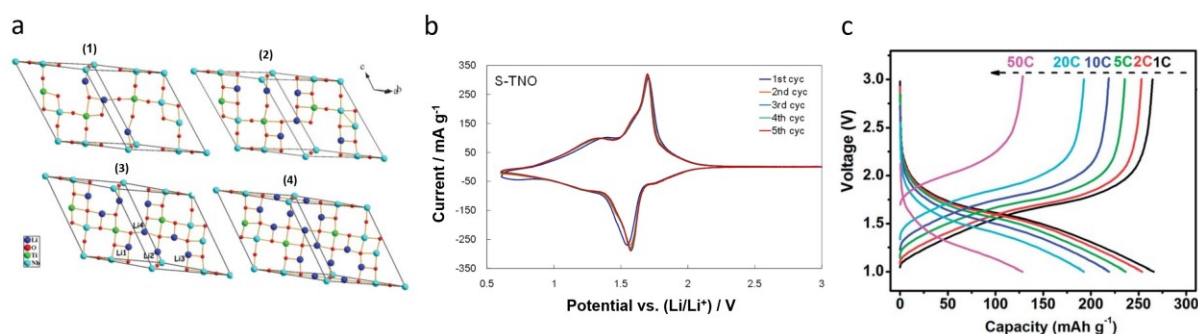


Figure 8 (a) Schematic representation of calculated primitive cell of (1) $\text{LiTiNb}_2\text{O}_7$, (2) $\text{Li}_2\text{TiNb}_2\text{O}_7$, (3) $\text{Li}_3\text{TiNb}_2\text{O}_7$, and (4) $\text{Li}_4\text{TiNb}_2\text{O}_7$ with Li-ion insertion sites^[84]. (b) Cyclic voltammetry of solid-state synthesized TiNb_2O_7 particle.^[87] (c) Galvanostatic charge/discharge curves of mesoporous TiNb_2O_7 templated the block copolymer at different current rates.^[85]

(a) Reproduced (modified) with permission from Ref. [84]. Copyright 2011 Royal Society of Chemistry (Great Britain).

(b) Reproduced with permission from Ref. [87]. Copyright 2018 Elsevier.

(c) Reproduced with permission from Ref. [85]. Copyright 2018 Elsevier.

Band structure calculations of TiNb_2O_7 suggest that the material is an indirect semiconductor with a bandgap of 2.17 eV^[84], whose conductivity significantly increases upon Li^+ insertion due to a transformation to a metal-like band structure.^[84, 86] To alter the band structure and to increase the conductivity of delithiated TNO, Nb(IV) doping into the Ti sites can be used as was demonstrated for a $\text{Ti}_{0.9}\text{Nb}_{0.1}\text{Nb}_2\text{O}_7$ stoichiometry.^[88] Besides doping, carbon coating or nanostructuring of the TiNb_2O_7 active phase is necessary to enable fast electron and Li^+ ion

migration at high charge/discharge rates similar to other low-conducting ceramic anode materials previously discussed in this chapter.^[2] In addition to the increasing power density, nanostructuring also mitigates capacity fading of TNO upon extended cycling attributed to its unit cell volume expansion^[2], which is the prime issue of using TNO as LIB anode material.

In the recent years, different synthesis approaches for the fabrication of TiNb_2O_7 as high-rate LIB anode material were used, including solid-state reactions of TiO_2 and Nb_2O_5 ^[84], sol-gel routes with polymer templates to generate mesoporous structures^[85, 89] (Figure 9), and electrospinning of TNO nanofibers^[86, 90].



Figure 9 Schematic diagram of the synthesis and formation of block-copolymer-templated mesoporous TiNb_2O_7 .^[85]

Reproduced with permission from Ref. [85]. Copyright 2014 The Royal Society of Chemistry.

Nanostructured mesoporous sol-gel-based TiNb_2O_7 (Figure 9) anode material shows a high reversible capacity of 281 mAh g^{-1} at a low rate of 0.1C greatly surpassing that of LTO. At a rate of 20C (3 min charge/discharge duration) still over 180 mAh g^{-1} could be realized. The cyclability of nanostructure TiNb_2O_7 is promising with a capacity retention of 84% after 1000 cycles at 5C (12 min charge/discharge duration) and Coulombic efficiencies close to 100%.^[85] Research on nanofiber-based $\text{TiNb}_2\text{O}_7/\text{LiNi}_{0.5}\text{Mn}_{1.5}\text{O}_4$ full cells showed an operating voltage of $\sim 3 \text{ V}$ with a reversible capacity of $\sim 100 \text{ mAh g}^{-1}$ at high C-rates and a capacity retention of $\sim 90\%$ over 700 cycles.^[90] Due to the superior reversible gravimetric capacity together with its

high-rate capability, TiNb_2O_7 is a potential LIB anode material for future commercialization (BEVs and stationary energy storage batteries) and replacement of LTO, if capacity fading upon extended cycling can be affectively addressed and minimized.^[2, 84]

3.2.2 Other transition metal oxides: $\text{Li}_3\text{Nd}_3\text{W}_2\text{O}_{12}$ —A garnet-type ceramic anode

Garnet framework materials composed of $\text{Li}_3\text{A}_3\text{B}_2\text{O}_{12}$ structures gained lots of interest since Weppners' group reported $\text{Li}_5\text{La}_3\text{M}_2\text{O}_{12}$ ($\text{M} = \text{Nb}, \text{Ta}$) garnet materials as potential solid-state lithium-ion conductors exhibiting ionic conductivities of $> 10^{-4} \text{ S cm}^{-1}$ at ambient conditions.^[2, 91-92] $\text{Li}_3\text{Nd}_3\text{W}_2\text{O}_{12}$ is a member of the garnet framework structure family and was investigated by Goodenough and his coworkers as a possible insertion-type anode material.

The crystal structure of $\text{Li}_3\text{Nd}_3\text{W}_2\text{O}_{12}$ can be described as a $\text{Li}_3\text{A}_3\text{B}_2\text{O}_{12}$, where Li occupies square antiprismatic, octahedral, and tetrahedral sites in a 3:2:3 ratio (Figure 10).^[92-93] The tetrahedral Li-sites are bridged by empty octahedral sharing opposite faces with two tetrahedral sites. Every face of a Li-site is bridged to neighboring Li-sites by the means of octahedral sites creating a 3D interstitial space, which can theoretically host up to 9 mol of lithium.

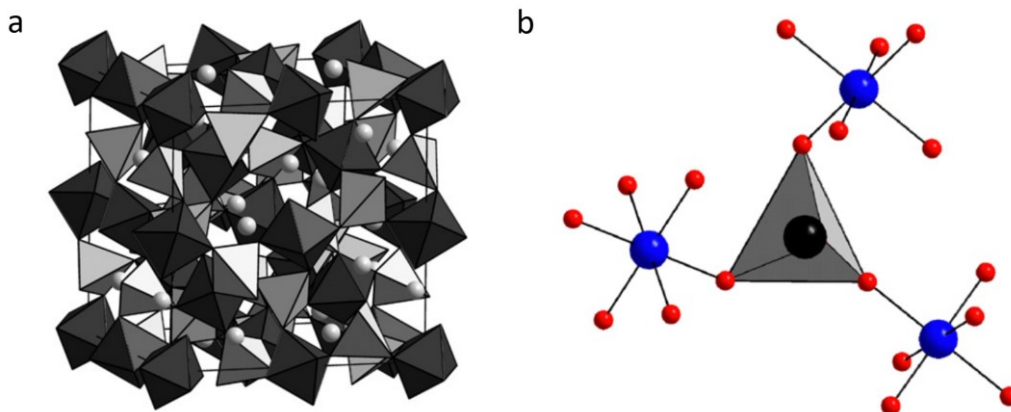


Figure 10 (a) Schematic representation of $\text{Li}_3\text{A}_3\text{B}_2\text{O}_{12}$ garnet framework and (b) octahedral and tetrahedral Li^+ ion occupancies.^[93]

Reproduced with permission from Ref [93]. Copyright 2007 Elsevier.

However, there is a practical limit of 7 mol of Li per formula unit. The $W^{4+}/5+$ and $W^{5+}/6+$ redox couples (Figure 11a) in $Li_3Nd_3W_2O_{12}$ can be used to host reversibly Li ions resulting in a theoretical capacity of 106 mAh g^{-1} . This material benefits from a low operating voltage of 0.3 V vs. Li/Li^+ with high-power capability (Figure 11). Nevertheless, an irreversible huge capacity loss in the first cycle and the high sensitivity toward H_2O and CO_2 with the formation of insulating carbonates are the main drawbacks of this material.^[92, 94] In order to address the last point, Satish *et al.* were able to protect the lithium garnet network and keep it electrochemically active by a uniform carbon coating.^[92] Moreover, Luo *et al.* showed that $Li_3Nd_3W_2O_{12}$ synthesized via a sol-gel route consists of smaller primary particles and shows a superior rate performance and cycling stability as compared to $Li_3Nd_3W_2O_{12}$ prepared by a conventional solid-state method.^[91]

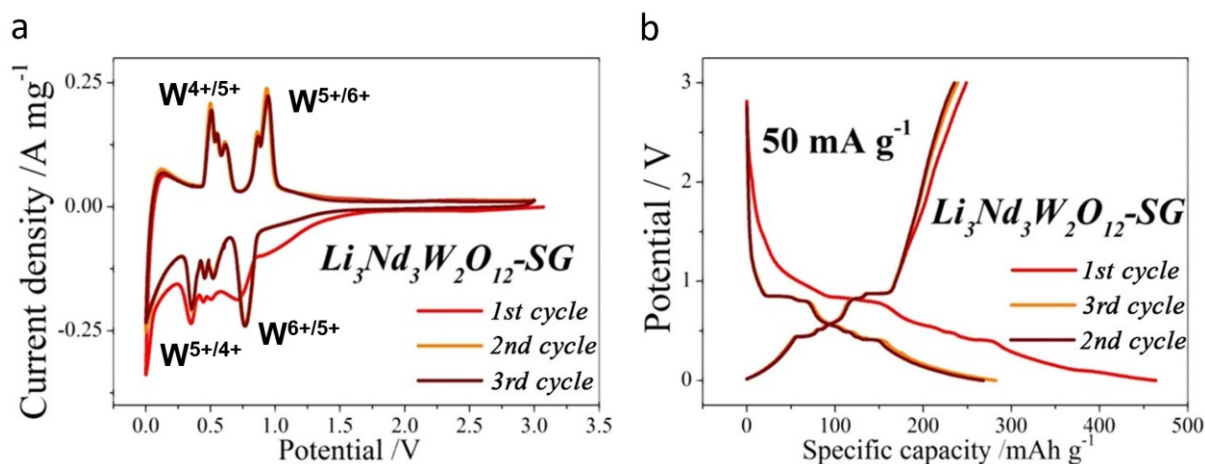


Figure 11 (a) CV curve of $Li_3Nd_3W_2O_{12}$ with indicated wolfram redox couples and (b) galvanostatic charge/discharge curve for first two cycles.^[91]

Reproduced (modified) with permission from Ref. [91]. Copyright 2018 American Chemical Society.

Satish *et al.* and Luo *et al.* also reported the electrochemical performance on a full-cell level with $Li_3Nd_3W_2O_{12}$ as anode and $LiMn_2O_4$ and $LiFePO_4$ as a cathode, respectively.^[91-92] Satish *et al.* reported that the $Li_3Nd_3W_2O_{12}/LiMn_2O_4$ full cells deliver an initial discharge capacity of around 115 mAh g^{-1} at 1C (100 mA g^{-1}) and 82 mAh g^{-1} after 100 cycles (capacity retention of 71%) within a working window of 2.95–3.9 V.^[92] The $Li_3Nd_3W_2O_{12}/LiFePO_4$ full cell reported

by Luo *et al.* exhibits an initial discharge capacity of around 110 mAh g^{-1} within a working window of 2–3.4 V, which only slightly decreases during the following 20 cycles to reach 100 mAh g^{-1} .^[92]

3.2.3 Silicon (SiON, SiCN, SiOC and related)-based ceramic anodes

Polymer-derived silicon oxycarbide (SiOC) and silicon carbonitride (SiCN) have emerged as potential anode materials in the middle of the 1990s. SiOC and SiCN ceramics are typically prepared by pyrolysis of organic polymers containing Si, H, C and N, or/and O in an inert atmosphere at 1000–1600 °C, or alternatively via a sol-gel approach.^[95-96] The microstructure of SiOC consists of an amorphous polymer-like Si-O-C network interpenetrated by a disordered free carbon phase. Silicon atoms in the Si-O-C network are tetrahedrally bonded to oxygen and carbon coincidentally forming $\text{SiO}_{4-x}\text{C}_x$ ($x = 1-4$) building units, which include also SiO_2 and carbonrich regions.^[96-99] The amorphous free carbon phase is composed of isolated carbon nanodomains (lower free carbon content) or a carbon percolation network (higher amount of free carbon) (Figure 12).^[96] The major lithium storage sites aren't fully ensured, yet, whether they are the Si-O-C units or the free carbon phase.^[100] Nevertheless, it is expected that a reversible capacity of up to 1350 mAh g^{-1} for SiOC ceramics should be possible.^[98]

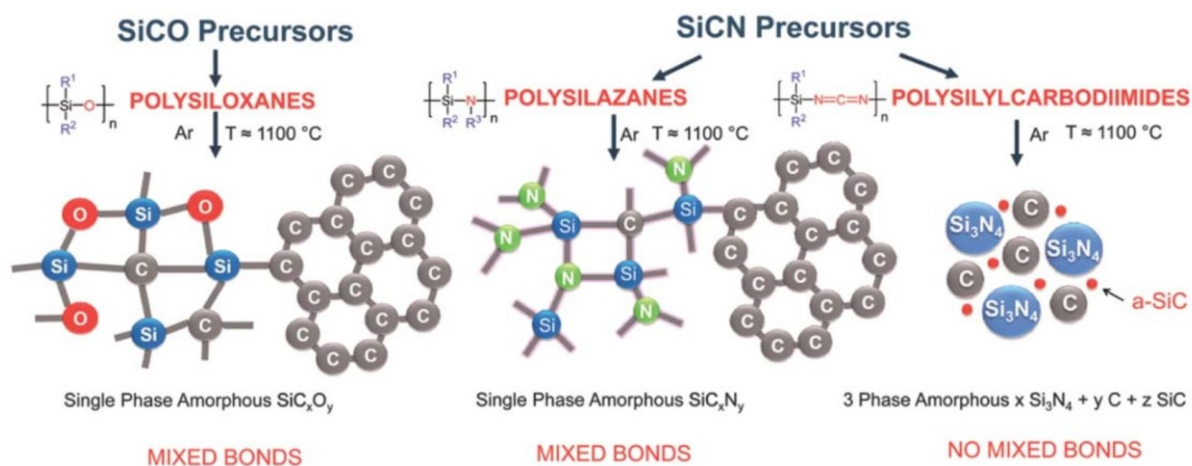


Figure 12 Schematic synthesis routes of polymer-derived SiOC and SiCN ceramics and sketches of the resulting microstructures.^[99]

Reproduced with permission from Ref. [99]. Copyright 2013 Royal Society of Chemistry (Great Britain).

SiCN can be obtained with a broad variety of different microstructures tunable by the choice of polymers, typically polysilylcarbodiimides or polysilazanes. Polysilylcarbodiimides lead to tetrahedrally coordinated silicon $\text{SiN}_{4-x}\text{C}_x$ ($x = 1-4$) building units and an amorphous carbon phase analogous to SiOC. Polysilazanes initiate nanocomposites of Si_3N_4 , SiC, and a free carbon phase (Figure 12).^[99, 101]

Nevertheless, the intrinsically poor electrical/ionic conductivity of SiOC and SiCN ceramics results in a rather poor electrochemical performance (Figure 13).^[95, 97-98] SiOC and SiCN ceramics with high free carbon content exhibit a better electrical conductivity and usually a better electrochemical performance.^[95, 98, 102] Introducing conductive carbonaceous compounds such as carbon nanotubes, graphite, or graphene is another strategy to further improve the conductivity as was demonstrated by Sang *et al.* by comparing SiOC and a 3D-graphene-SiOC composite.^[98] Using SiCN or SiOC ceramics together with Si or Sn nanoparticles is a promising approach to increase the capacity, as was demonstrated by Rohrer *et al.* and Kaspar *et al.*.^[96, 103]

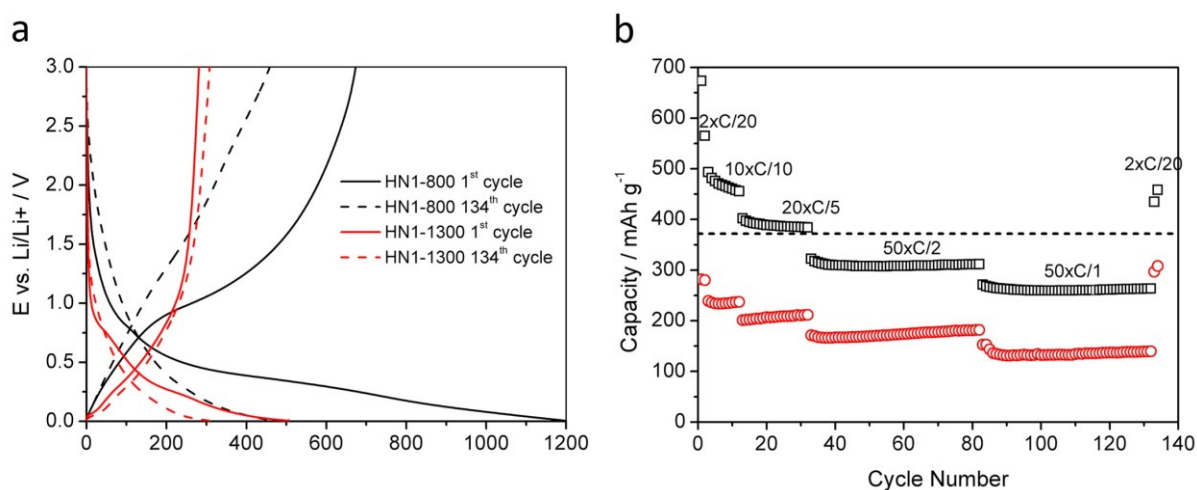


Figure 13 (a) Galvanostatic charge/discharge curves and (b) cycling performance of SiCN synthesized from polysilylcarbodiimide at 800 °C [HN1-800(black)] and at 1300 °C [HN1-1300(red)], respectively.^[102]

Reproduced with permission from Ref. [102]. Copyright 2015 Elsevier.

3.2.4 Na-Super-Ionic-CONductor (NASICON)-type battery anodes

The abbreviation NASICON standing for Na-Super-Ionic-CONductor describes a class of ceramic compounds with a stable 3D framework built from two types of transition metal-oxygen (MO_6 and $\text{M}'\text{O}_6$) octahedra that share all corners with sulfate, phosphate, silicate, or arsenate tetrahedra. The resulting interstitial space in the prototype structure of the $\text{A}_x\text{MM}'(\text{XO}_4)_3$ composition can accommodate up to five alkali metal ions depending on the oxidation state of the transition metals M, M' (Fe, V, Ti, Zr, Sc, Mn, Nb, In) and the polyanion forming center atom X (S, P, Si, As).^[104] Due to the interconnected voids in all directions of the structure, an outstanding sodium (also a high lithium and a reasonable K^+ , Mg^{2+} , Ca^{2+}) conductivity is reached which led to an investigation of NASICON structures as solid electrolytes from the discovery in 1976 onwards.^[104]

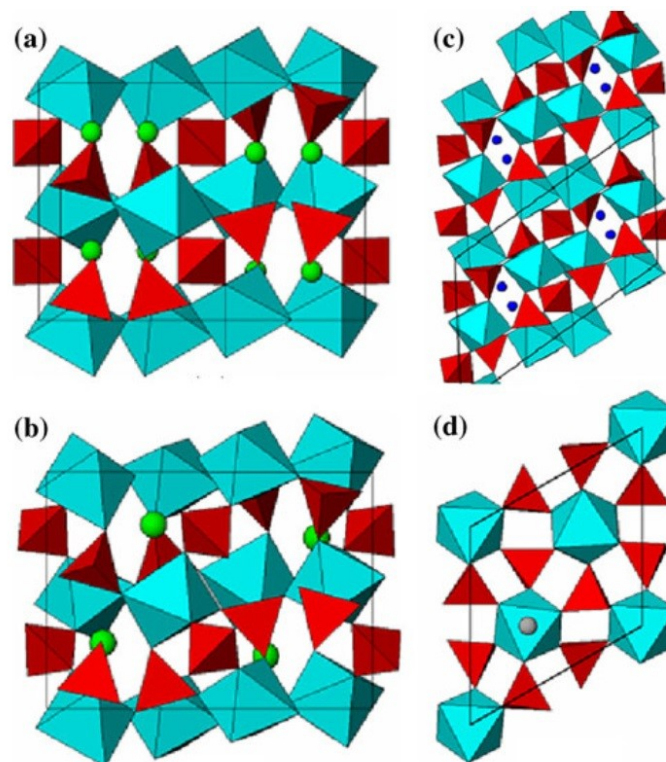


Figure 14 Schematic representation of NASICON polymorphs: (a) orthorhombic (Pbn), (b) monoclinic ($P2_1/c$), (c) triclinic (C_1), and (d) corundum like.^[105]

Reproduced with permission from Ref. [105]. Copyright 2011 Springer Nature.

Besides the use as solid ion conductors, the capability of sodium and lithium-ion insertion for energy storage applications was also systematically investigated for this class of materials. The electrochemical potential for (de)sodation or (de)lithiation of a NASICON compound is in the first place affected by the comprised transition metals (M, M') and their oxidation state but is in addition altered by the electron-withdrawing properties of the polyanions (XO_4), termed as induction effect in that context. Furthermore, there exist four structural polymorphs (Figure 14) for a given composition, namely an orthorhombic (*Pbna*), monoclinic ($P2_1/c$), triclinic (C_1), and a corundum-like structure that mainly differ in the alignment of M-M' dimers ($[MO_6]_2[XO_4]_3$) along the crystallographic *c*-axis and which affects the electrochemical potential of inserted ions.^[104]

The electrochemical potentials for (de)lithiation of selected NASICON structures with differing transition metal redox couple can in principle be ordered as following: V^{4+}/V^{5+} (4.6 V vs. Li/Li⁺) > V^{3+}/V^{4+} (3.8 V vs. Li/Li⁺) > Fe^{2+}/Fe^{3+} (2.8 V vs. Li/Li⁺) > Ti^{3+}/Ti^{4+} (2.5 V vs. Li/Li⁺) > Nb^{4+}/Nb^{5+} (2.2 V vs. Li/Li⁺) > Nb^{3+}/Nb^{4+} (1.8 V vs. Li/Li⁺) > V^{2+}/V^{3+} (1.7 V vs. Li/Li⁺) > Ti^{2+}/Ti^{3+} (0.4 V vs. Na/Na⁺).^[104, 106] The relatively high operating potentials of most NASICON compounds mainly led to the development and application as cathode materials in solid-state batteries.^[107] NASICON structures applicable as anodes are mainly limited to zirconium, vanadium, and titanium-containing compounds with electrochemical potentials ranging from 0.4 V vs. Na/Na⁺ (roughly equals 0.7 V vs. Li/Li⁺) for $Na_3Ti_2(PO_4)_3$ (NTP) Ti^{2+}/Ti^{3+} (0.7 V vs. Li/Li⁺) up to 2.1 V vs. Na/Na⁺ for $NaTi_2(PO_4)_3$ (NTP) based on the Ti^{3+}/Ti^{4+} conversion.^[106] In a full-cell solid-state battery configuration with suitable solid electrolytes (e.g., NASICON or garnet type) and high-voltage cathodes (e.g., NASICON, layered transition metal oxides or spinel structures) cell voltages of 1.7 V and more are obtained.^[106, 108] Although the reversible capacity of NASICON-type anodes is below that of graphite, the ICL due to the initial formation of a metal ion intercalated anode structure is omitted. A further advantage of

the NASICON-type anodes conditioned by its relatively high electrode potential is an avoided SEI formation.^[1]

Zr-based NASICON anodes (NZN)

$\text{NaZr}_2(\text{PO}_4)_3$ (NZN) was among the first compounds structurally characterized in 1968 and later known to be a representative composition of the NASICON structure family.^[109] The structure is built up from edge-sharing $[\text{PO}_4]$ tetrahedra with $[\text{ZrO}_6]$ octahedra that form interstitial voids in shape of tunnels for an efficient sodium-ion migration and storage (Figure 15).^[1]

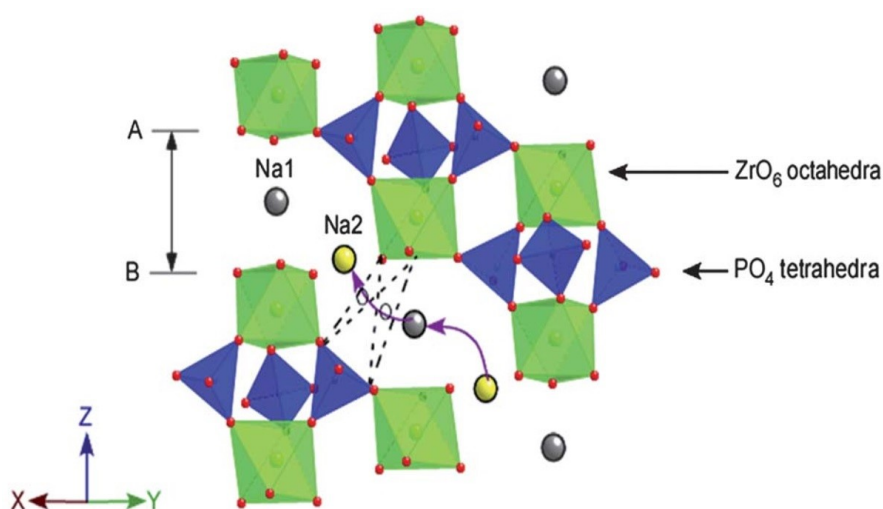


Figure 15 Schematic representation of $\text{NaZr}_2(\text{PO}_4)_3$ (NZN) structure with Na^+ ion migration pathways.^[111]

Reproduced with permission from Ref. [111]. Copyright 2013 Royal Society of Chemistry (Great Britain).

In the range of $x = 1-2.5$ Na^+ per formula unit, $\text{Na}_x\text{Zr}_2(\text{PO}_4)_3$ no change in the crystal structure is observed, but to reach the full theoretical capacity with three Na^+ ions a change in the structure can be observed with an accompanied volume change of 10% from $\text{NaZr}_2(\text{PO}_4)_3$ to $\text{Na}_3\text{Zr}_2(\text{PO}_4)_3$. In a half-cell configuration, an initial capacity of 150 mAh g^{-1} could be obtained which is close to the theoretical value of 153 mAh g^{-1} for solid-state synthesized material. The reversibility and stability of the NZN structure shown by galvanostatic measurements and also by high Coulombic efficiencies over 100 cycles render this composition promising for the application as SIB anodes.^[1, 110]

Ti-based NASICON anodes (NTP/LTP)

Titanium-based NASICON $A_3Ti_2(PO_4)_3$ ($A = Na, Li$) shares the common 3D framework structure of [metal- O_6] octahedra and $[PO_4]$ tetrahedra connected by shared oxygen corner atoms. Sodium-containing $Na_3Ti_2(PO_4)_3$ NTP has been shown to be ordered as a triclinic variant of the NASICON prototype structure shown in Figure 16.^[106]

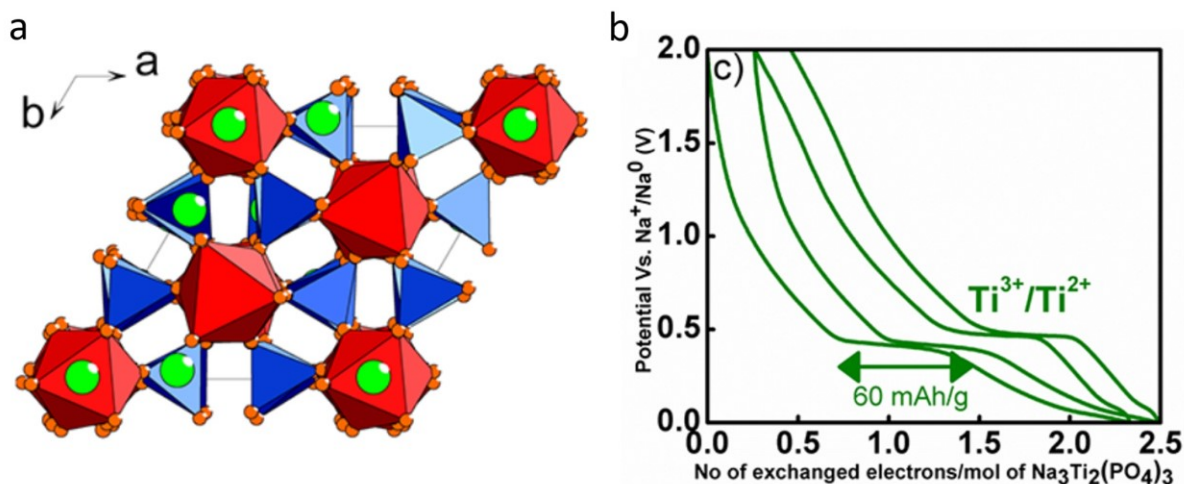


Figure 16 Schematic representation of triclinic $Na_3Ti_2(PO_4)_3$ (NTP) structure (a) and galvanostatic cycling curve (b) at potential region of Ti^{3+}/Ti^{2+} plateau.^[106]

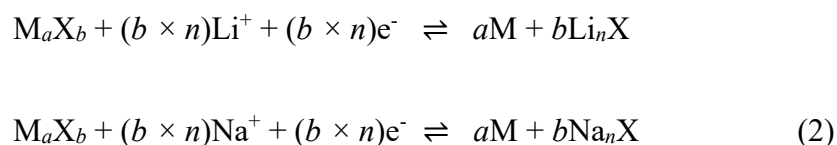
Reproduced with permission from Ref. [106]. Copyright 2013 American Chemical Society.

Remarkable for the Ti-containing NASICON structure (LTP) that can be used as an anode is its high room-temperature ionic conductivity of $\sim 10^{-6} \text{ S cm}^{-1}$ ^[112], which renders the material a suitable solid electrolyte for SIBs and LIBs. However, comparable to other ceramic NASICON materials, pure NTP and LTP suffer from a low electronic conductivity which requires carbon coating, particle size reduction and transition metal doping to achieve higher rate performances.^[1, 104] NTP as well as $Li_3Ti_2(PO_4)_3$, LTP are widely investigated electro-active materials for SIB and LIB applications in terms of their use as anode, cathode, and electrolyte material. However, the insertion potential related to the Ti^{3+}/Ti^{4+} redox couple with $\sim 2.5 \text{ V}$ vs. Li/Li^+ or 2.2 V vs. Na/Na^+ in LTP or NTP, respectively, are considered to be too high to be used as anodes and too low to be employed as cathodes in nonaqueous LIBs or SIBs.^[104] To apply Ti-based NASICON as anode in nonaqueous environment, insertion at $\sim 0.4 \text{ V}$ vs. Na/Na^+

assigned to the $\text{Ti}^{2+}/\text{Ti}^{3+}$ redox couple (Figure 16b) is used, which provides a reversible capacity of $\sim 60 \text{ mAh g}^{-1}$. The reduction of $\text{Na}_3\text{Ti}_2(\text{PO}_4)_3$ to $\text{Na}_4\text{Ti}_2(\text{PO}_4)_3$ thereby causes a structural rearrangement from triclinic to rhombohedral unit cell symmetry.^[106] Beyond solid-state or nonaqueous battery application, Ti-based NTP^[113] and LTP^[114] NASICON structures are investigated as anodes for aqueous batteries in combination with high-voltage layered oxide cathodes (LiMn_2O_4 , LiCoO_2 , etc.). For this application, the anode is operated at a potential of $\sim 2.6 \text{ V}$ vs. Li/Li^+ corresponding to the $\text{Ti}^{3+}/\text{Ti}^{4+}$ redox couple located within the stability window of H_2O .^[1, 104] High-rate NTP/LTP anode material may be synthesized by various approaches; an example is a hydrothermal synthesis of small nanocrystals that are embedded in a carbon matrix to form the anode. In combination with a layered oxide cathode and liquid electrolyte a capacity of $\sim 40 \text{ mAh g}^{-1}$ with respect to the combined mass of cathode and anode is reached at high charge-discharge rates. Furthermore, for aqueous full cells with LTP-C composites, a high cycling stability and capacity retention of up to 90% after 1000 cycles at high rates of 6C (equals 10 min for full charge/discharge cycle) could be obtained.^[104, 115]

3.3 Conversion-type ceramic anode materials

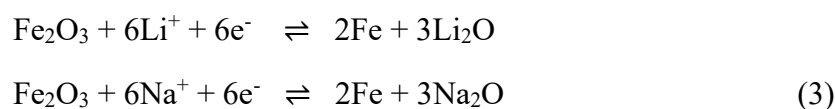
A lot of attention has been given to CTAMs for LIBs and SIBs, including mainly transition metal compounds (M_aX_b , $M = \text{Mn, Fe, Co, Ni, Cu}$ and $X = \text{O, S, Se, F, N, P, etc.}$). The M_aX_b materials undergo reversible electrochemical redox reactions with Li^+/Na^+ leading to the formation of transition metal particles M and a binary lithium/sodium compound $\text{Li}_n\text{X}/\text{Na}_n\text{X}$. After delithiation, the initial state is (theoretically) formed again (Eq. 2):



The reaction potential determined by the ionicity of the M-X bond is normally in the range of 0.5–1.0 V vs. Li/Li^+ , with increasing ionicity the potential shifts to higher values. The low and safe lithiation potential together with a high theoretical specific capacity are the main advantages of the CTAMs.^[116-118] Nevertheless, the conversion-type compounds suffer from poor reaction kinetics, low electronic and ionic conductivity, huge volume expansion (>200%), large potential hysteresis, and continuous electrolyte decomposition.^[116-118] CTAMs used in SIBs reveal additionally a low initial Coulombic efficiency and a poor cycling stability.^[118]

Nanoengineering is a very promising strategy to address these drawbacks. Downsizing is of great interest because the reaction of the formed nanosized transition metal M with the binary lithium/sodium compound is more favorable due to an increased electrode-electrolyte interphase and a decreased diffusion length enabling faster reaction kinetics. In addition, it has been demonstrated by numerous research groups that nanostructured materials can at least partially accommodate volume changes during cycling. The conductivity of the CTAMs can be further improved by introducing carbonaceous support materials, which inhibits the electrolyte from decomposition.^[116, 118] Even more efficient is using the CTAMs together with an alloying-type material as composites, which enable to efficiently reduce the voltage

hysteresis.^[116] Iron oxides are well-studied CTAMs in both LIBs and SIBs. Besides the high specific capacities, additional advantages of this class of materials are their low cost, high abundance, environmental friendliness, and the high corrosion resistance. Especially, the hematite α -Fe₂O₃ and the magnetite Fe₃O₄ phase are thoroughly investigated. The hematite phase α -Fe₂O₃ has a theoretical specific capacity of 1008 mAh g⁻¹, involving a six-electron redox reaction (Eq. 3):^[2, 118-119]



Nevertheless, the low electrical conductivity and the large volume changes during electrochemical cycling are serious drawbacks of hematite. Nanoengineering, as mentioned before, and the addition of carbon support materials are successful strategies to alleviate this problem, as, for example, proved by Zhao *et al.*, Zhang *et al.*, Aravindan *et al.*, and Kong *et al.*.^[2, 26, 118-119]

Zhao *et al.* reported a yolk-shell Fe₂O₃/C composite anchored on multiwalled carbon nanotubes (MWNT).^[119] They could demonstrate that this composite exhibits a promising cycling stability together with high specific capacities for both lithium and sodium storage (Figure 17). That excellent performance was attributed to the good electrical conductivity provided by the MWNT and the carbon coating and the void space which has a buffering effect on the volume changes of Fe₂O₃.^[119]

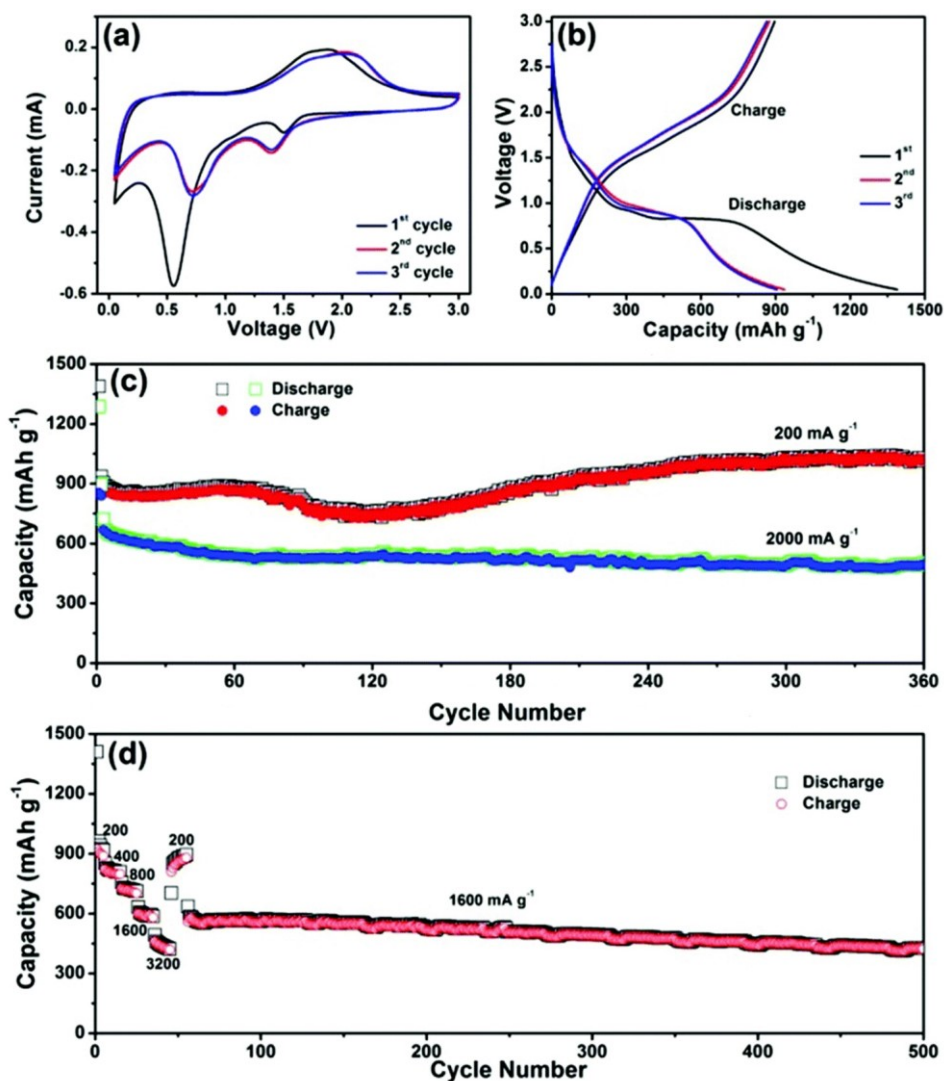
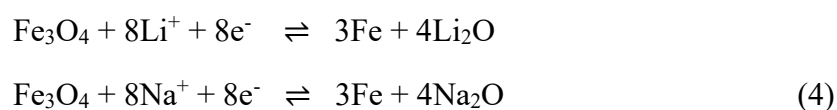


Figure 17 Hematite phase $\alpha\text{-Fe}_2\text{O}_3/\text{MWNT}/\text{C}$ anode in LIBs: (a) CV curves at a scan rate of 0.5 mV s^{-1} , (b) discharge/charge curves at 0.2 A g^{-1} , (c) cycling performance at 0.2 and 2 A g^{-1} and in SIBs (d) cycling performance at $0.2\text{--}1.6 \text{ A g}^{-1}$.^[119]

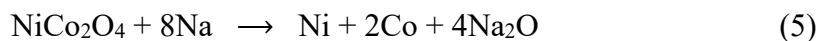
Reproduced with permission from Ref. [119]. Copyright 2015 Royal Society of Chemistry (Great Britain).

Magnetite Fe_3O_4 is also a promising CTAM. It has a better electrical conductivity compared to $\alpha\text{-Fe}_2\text{O}_3$ due to an electron exchange between the Fe^{2+} and Fe^{3+} centers. The theoretical specific capacity is a little bit lowered with 926 mAh g^{-1} , involving an eight-electron process (Eq. 4):^{[2,}

118]



The reduction of Fe_3O_4 to Fe^0 takes place at a potential around 0.7 V vs. Li/Li^+ and the back reactions from Fe^0 to Fe^{2+} to Fe^{3+} occur at around 1.7 and 1.8 V vs. Li/Li^+ . Unfortunately, similar to hematite and the other CTAMs, magnetite also suffers from relatively high volume changes during electrochemical cycling that rapidly lead to the deterioration of the electrode morphology. Among others, Fu *et al.* successfully demonstrated that nanosizing and nanostructuring are beneficial for the electrochemical performance of Fe_3O_4 . Combining Fe_3O_4 nanoparticles with a conductive support like graphene in the form of a composite material is an even more promising approach to stabilize and fully utilize the material.^[120] Spinel oxide NiCo_2O_4 was first reported as a conversion material for SIBs.^[121] A reversible conversion reaction was then reported (Eq. 5):



Following this work, many transition metal oxides have been reported as anode materials for SIBs showing a conversion reaction, such as iron oxides Fe_2O_3 and Fe_3O_4 ^[122], cobalt oxide Co_3O_4 ^[123], nickel oxide NiO ^[124], tin oxides SnO and SnO_2 ^[125], and copper oxide CuO ^[126]. Similar to the conversion-type anodes for the LIBs discussed above, nanosizing and carbon coating were shown to tremendously improve the performance of conversion-type anodes also in SIBs to reach reversible capacities up to 400 mAh g^{-1} . Similar to the above-mentioned CTAMs, Sn, Sb, and Zn-based compounds (M_aX_b , $\text{M} = \text{Sn}, \text{Sb}, \text{Zn}$ and $\text{X} = \text{O}, \text{S}, \text{P}$, etc.) undergo conversion reactions with Li^+ or Na^+ up to respective metal state. In addition to the conversion process, the formed metals can accommodate further amounts of Li^+/Na^+ upon subsequent polarization to form Li_xM or Na_xM alloys. The theoretical specific capacity of such conversion and alloying materials is, therefore, higher than that of “pure” conversion-type materials, which is one of their biggest advantages. The alloying/dealloying reaction suffers from huge volume changes upon lithiation and delithiation leading to internal stress and the so-

called pulverization, which is probably the most challenging problem of conversion-alloying materials (Figure 18).

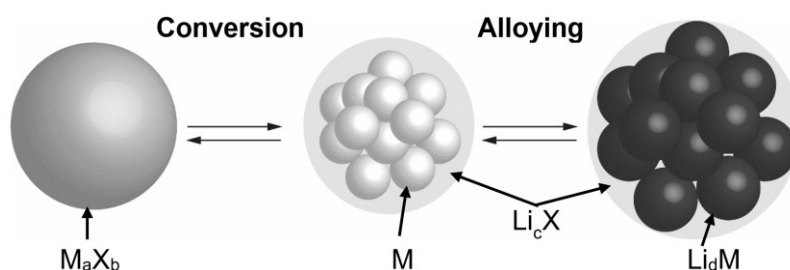
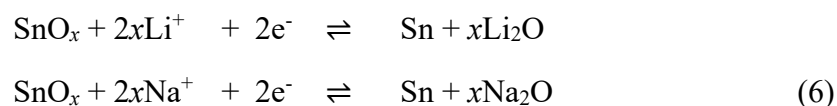


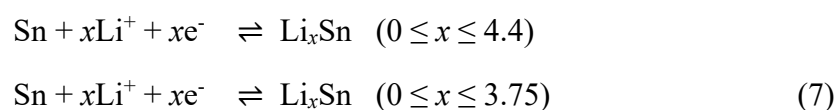
Figure 18 Schematic representation of volume changes accompanying conversion and alloying processes in LIB and SIB anode materials.

Reproduced with permission from F. Zoller (2019).

Those problems are even more severe in the case of SIBs. The volume expansions are more pronounced compared to the Li^+ counterparts due to the larger ionic radius of Na^+ (1.02 Å; Li^+ : 0.59 Å). Resulting volume changes also cause an unstable SEI. Both, pulverization of the electrode and an unstable SEI thereby result in a limited cycling stability and performance.^[2, 118] Tailoring the bulk materials down to the nanosized range is again proven as a promising strategy. In addition, the use of soft carbonaceous support material can be beneficial to buffer volume changes. Among others, tin oxides are considered to be promising conversion-alloying anode materials for SIBs and LIBs due to their environmental friendliness, the low costs, and their high specific capacities. The reaction of SnO_x with Li^+/Na^+ can be divided into two parts. At first, SnO_x undergoes a conversion reaction (Eq. 6):^[2, 118]



Followed by the alloying step (Eq. 7):



According to these equations, a theoretical specific capacity of 1138 and 1494 mAh g⁻¹ for SnO and SnO₂ are obtained upon the reaction with Li⁺, respectively. In the case of Na⁺, values of 1022 (SnO) and 1378 mAh g⁻¹ (SnO₂) are theoretically achievable. Tin oxides suffer from huge volume changes which result in an inferior electrochemical performance as pointed out above. It should be also mentioned that the conversion step is often discussed to be irreversible, especially in the case of bulk material. It is, however, reported that the conversion step becomes reversible or at least partially reversible in the case of nanosized tin oxides. Hence, nanoengineering and also the use of carbonaceous support materials is a promising way to improve the performance. Nanomaterials can provide voids that accommodate the internal structural strain during cycling. Together with the buffering effect of the carbonaceous support materials and the increased overall electrical conductivity, this leads to an improved electrochemical performance. Introducing dopants (such as antimony) into tin oxides is an additional strategy to ameliorate the conductivity and thus the cycling behavior.^[127]

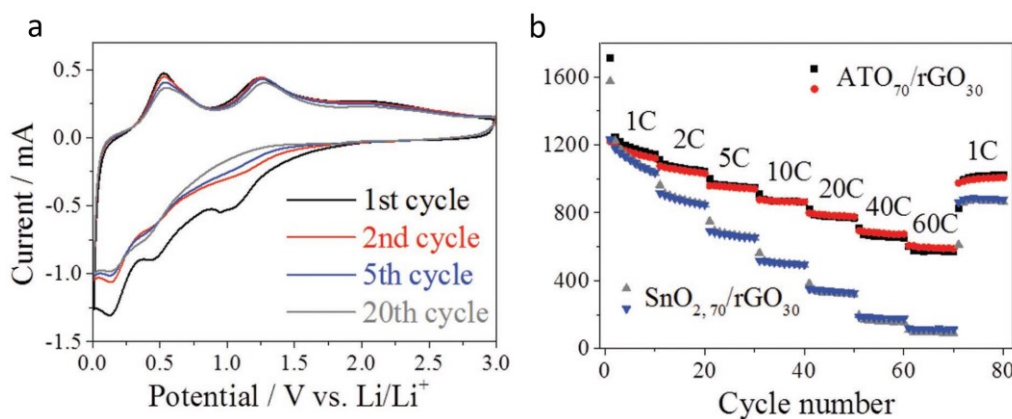


Figure 19 (a) Cyclic voltammetry of Sb:SnO₂ nanoparticles on rGO and (b) cycling performance of conversion and alloying-type (Sb:)SnO₂ nanoparticles on rGO.^[128]

Reproduced with permission from Ref. [128]. Copyright 2018 John Wiley and Sons.

Combining these strategies is also very promising as it was demonstrated recently by the Fattakhova-Rohlfing group using nanosized Sb-doped SnO₂ and reduced graphene as support material exhibiting an excellent electrochemical performance (Figure 19).^[128]

Since the M-S bonds in metal sulfide are weaker than the corresponding M-O bonds in metal oxides, sulfides can be kinetically favorable for conversion reactions with Na⁺ ions. Therefore, many transition metal sulfides such as MS or MS₂ with M = Co, Mo, Fe, Sn, Cu, Mn, Zn, Ni, or Ti, have been studied.^[5, 13] Depending on the transition metal elements, the Na⁺ ion storage mechanism of metal sulfide materials could be classified as the conversion reaction and/or combined insertion and the alloying reaction. The introduction of carbon additives such as graphene or carbon nanotubes into active materials is indispensable to have advantages over conversion materials such as accommodation of large volume expansion/shrinkage resulting in effective stress relief.

The alloying materials have been also studied as anodes for SIBs for the same reasons as the conversion materials, that is to say the possibility to react with a large number of sodium reversibly at relatively low operating voltage (<1 V).^[8] However, the main drawback of these materials (metals, metalloids, or polyatomic nonmetal compounds) is a large volume change during the alloying-dealloying reaction. Because of constraints imposed by the battery packaging, such volume change leads to mechanical stress of the active particles. Due to the relatively large abundance in the Earth crust, silicon has been widely studied but Morito *et al.*,^[129] who report that contrary to the 4.4 lithium-ions uptake, only one sodium per Si could be uptaken with a very low diffusion. Nevertheless, Xu *et al.* demonstrated an excellent reversibility of Si nanoparticles composed of both amorphous and crystalline Si with a capacity of 279 mAh g⁻¹ at 10 mA g⁻¹.^[130] Later, the sodiation/desodiation behavior of microsized and nanosized crystalline Si was investigated and it was shown that the amorphization of Si in the course of the first sodiation leads to the break of the majority of the Si-Si bonds, and crystalline Si is transformed into an amorphous Na-Si alloy. Finally, after the desodiation process, the amorphous structure is maintained. Similarly to silicon, germanium could form bonds with only one sodium and cannot store it in its crystalline structure due to the large ionic size of

sodium. Then, numerous studies have been performed in order to design nanostructured materials as nanowires or thin films achieving almost the theoretical capacity of 350 mAh g^{-1} .^[5] Another element of choice from the group 14 of the periodic table remains tin. Indeed, the metal could in theory form $\text{Na}_{15}\text{Sn}_4$ alloy (847 mAh g^{-1}) through several intermediates. Ellis *et al.* and Ong *et al.* have experimentally demonstrated that Sn undergoes a reversible electrochemical redox reaction to reversibly form Sn-Na intermetallic phases.^[131-132] The microstructural evolution and phase transformation study proves, however, the volume expansion from 56% for the amorphous NaSn_2 to 336% and 420% to Na_9Sn_4 and $\text{Na}_{15}\text{Sn}_4$, respectively.^[133-134] Therefore, the major part of the published work deals with the serious volume changes during alloying-dealloying reactions. In order to buffer the volume changes, carbon coatings using sophisticated core-shell architectures were mostly explored, leading to the delivery of a high specific capacity of 443 mAh g^{-1} and reversible sodium storage properties with negligible capacity fading after 100 cycles.^[135-136] Similarly, the group 15 elements of the periodic table (Sb, P, Bi, and As) offer the possibility of a large specific capacity as anode materials with the same drawback of volume expansion during the charge. Antimony delivers a theoretical capacity of 660 mAh g^{-1} according to the formation of Na_3Sb (full sodiation state).^[137] The same strategy of carbon coating was then investigated to limit the large volume expansion (390%). Nanostructuring of Sb to 10–20 nm significantly improved the kinetics. For example, the preparation of uniform nanofiber structures with Sb nanoparticles embedded homogeneously in the carbon nanofibers leads to a large reversible capacity of 631 mAh g^{-1} at C/15, a greatly improved rate capability of 337 mAh g^{-1} at a rate of 5C and an excellent cycling stability for over 400 cycles.^[138] With a theoretical capacity of 2596 mAh g^{-1} associated with the formation of Na_3P , phosphorous is another element of choice as anode for SIBs. Among three known allotropes of phosphorous, the white one cannot be used due to its instability. The crystalline black phosphorous transforms at $550 \text{ }^\circ\text{C}$ to the amorphous red form. These two

forms of phosphorous were tested as electrode materials, showing a huge volume change (490%) during the electrochemical sodiation/desodiation process. An amorphous red phosphorous/carbon composite anode has been reported showing a reversible capacity of 1890 mAh g⁻¹ and good rate capability delivering 1540 mAh g⁻¹ at a high current density of 2.86 A g⁻¹.^[7] Recently, a variety of amorphous phosphorous with nano-architectures and 2D or 3D carbon matrices exhibiting high conductivities were applied to achieve high capacities and stable cycling.^[139-141] Bismuth reacts with sodium as well to form Na₃Bi with an intermediate NaBi alloy leading to a capacity of 385 mAh g⁻¹.^[142] Binary intermetallic alloys have also been studied which implies the use of an electrochemically inactive transition element (Ni, Cu, Zn, and Mo) together with an active element (Sn, Sb, and Bi). The beneficial role of the inactive element is to buffer volume changes in the course of the alloying-dealloying process. As proposed by Liu *et al.* with highly porous Ni₃Sn₂ microcages composed of tiny nanoparticles, the mechanical strain of Sn during charge/discharge processes is effectively suppressed by the hollow core structure and the presence of a Ni matrix in the hollow microcages.^[143] Moreover, homogeneously encapsulated Ni converted from the sodiation of Ni₃Sn₂ is beneficial for the required electron transport. As a result, a high reversible capacity of 348 mAh g⁻¹ and a stable cycle retention of 91% after 300 cycles at 1C were demonstrated.

3.4 Protective ceramic coating of alkali metal anodes

There is an increasing need for high-energy density storage to boost the performance of BEVs or large energy storage systems. Solid-state LIBs and SIBs employing (mostly) ceramic electrolytes are intrinsically safer than their conventional moisture-sensitive counterparts employing organic solvents. To further increase the safety of LIBs and SIBs and prevent possible thermal runaways, the use of carbonaceous anodes (graphite, etc.) should therefore be avoided. The use of ceramic anodes, as discussed in the previous part of this chapter, provides a possible solution. However, due to the relatively high potential vs. Li/Li^+ (e.g., most NASICON or LTO anodes >1 V vs. Li/Li^+) or Na/Na^+ (e.g., most NASICON or LTO anodes >1 V vs. Na/Na^+), the overall capacity of the cell employing ceramic anodes is rather limited. A breakthrough in the energy density of LIBs and SIBs can be achieved only when light-weight lithium or sodium-containing anodes with a very high specific capacity are used as anodes, and light-weight multi-ion reaction enabling elements such as sulfur and oxygen are used as cathodes. The main reason for the capacity limitation of today's LIBs is the cathode and its single-ion intercalation mechanism (valid for most layered transition metal oxides like LiCoO_2) exhibiting a theoretical capacity at a maximum of only 250 mAh g^{-1} . In contrast, the cathodes based on multi-ion reactions like S and O_2 have a really significantly higher theoretical capacity of 1672 mAh g^{-1} . Metallic lithium itself is an ideal candidate as anode for S and O_2 cathodes due to its highest theoretical capacity of 3860 mAh g^{-1} and the most negative electrochemical potential of 3.04 V vs. SHE. Furthermore, the theoretical energy densities of Li- O_2 (3505 Wh kg^{-1}) and Li-S (2567 Wh kg^{-1}) systems are remarkably higher than that of present LIBs (387 Wh kg^{-1} ; commercialized graphite/ LiCoO_2). Using metallic lithium directly as anode has been long seen as not achievable due to the following reasons: first, and probably the most important issue is the unrestrained formation of dendrites which can lead to short circuits, fire, or explosion in the presence of flammable electrolytes. Moreover, irreversible

reactions of the metallic lithium with the electrolyte, or the cathode materials result in a loss of active material and a fast increase of the cell impedance which means a rapid capacity fading. Another problem is caused by the volume changes within the metal anode upon cycling. This can cause lithium corrosion, pulverization of the anode, and the formation of a large amount of inaccessible (electrochemically inactive) lithium.

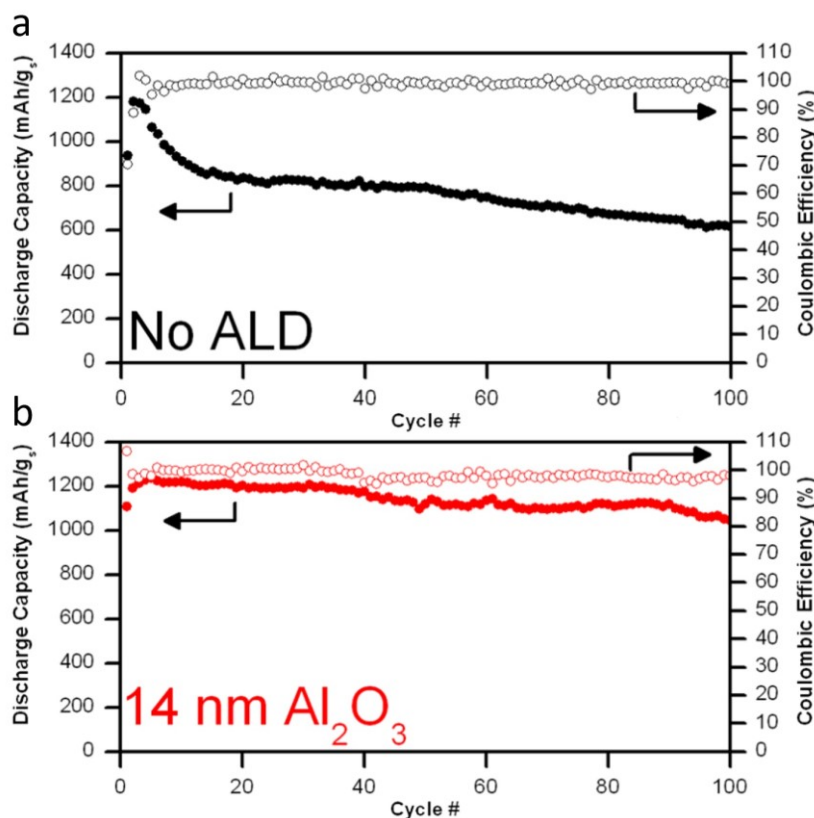


Figure 20 Discharge capacities and Coulombic efficiencies of bare (a) and ALD-protected (b) Li metal anodes of Li-S cells.^[144]

Reproduced with permission from Ref. [144]. Copyright 2015 American Chemical Society.

There are different strategies to address those problems, for example, tailoring the anode structure, using new and/or optimized electrolytes or building a protective layer (or artificial SEI).^[145] Protective coatings have to fulfill certain requirements. They should be stable against lithium and the electrolyte, both mechanically strong and flexible, ionically conductive, and electrically insulating and have a high transference number. Protective layers based on polymers or ceramics are probably the most promising material classes.^[145-146] LiF, Al₂O₃,

Li₃N, SiO₂, Li₃PO₄, or LiPON have been, for example, explored as possible inorganic surface protective layers. Atomic layer deposition (ALD) is a very promising method for preparing those layers because it enables a high uniformity with a very low layer thickness down to the subnanometer range at the same time.^[144-147]

Kozen *et al.* prepared ALD-protected Li-metal anodes with a 14 nm layer of Al₂O₃ and used them in Li-S batteries. They could demonstrate the superior electrochemical performance of the ALD-protected anode compared to the bare Li-foil exhibiting after 100 cycles a specific capacity of around 1080 mAh g⁻¹ compared to 600 mAh g⁻¹, respectively (Figure 20).^[144]

3.5 References

- [1] S. Chen, C. Wu, L. Shen, C. Zhu, Y. Huang, K. Xi, J. Maier, Y. Yu, *Adv. Mater.* **2017**, 29, 1700431.
- [2] V. Aravindan, Y.-S. Lee, S. Madhavi, *Adv. Energy Mater.* **2015**, 5, 1402225.
- [3] N. Bensalah, H. Dawoud, *J. Mater. Sci. Eng.* **2016**, 5, 1000258.
- [4] M. Dahbi, N. Yabuuchi, K. Kubota, K. Tokiwa, S. Komaba, *Phys. Chem. Chem. Phys.* **2014**, 16, 15007.
- [5] J.-Y. Hwang, S.-T. Myung, Y.-K. Sun, *Chem. Soc. Rev.* **2017**, 46, 3529.
- [6] E. Irisarri, A. Ponrouch, M. R. Palacin, *J. Electrochem. Soc.* **2015**, 162, A2476.
- [7] Y. Kim, K.-H. Ha, S. M. Oh, K. T. Lee, *Chem.-Eur. J.* **2014**, 20, 11980.
- [8] M. Lao, Y. Zhang, W. Luo, Q. Yan, W. Sun, S. X. Dou, *Adv. Mater.* **2017**, 29, 1700622.
- [9] N. Yabuuchi, S. Komaba, *Sci. Technol. Adv. Mater.* **2014**, 15, 043501.
- [10] M. Madian, A. Eychmüller, L. Giebeler, *Batteries* **2018**, 4, 7.
- [11] J. Ni, S. Fu, Y. Yuan, L. Ma, Y. Jiang, L. Li, J. Lu, *Adv. Mater.* **2018**, 30, 1704337.
- [12] W. Li, M. Fukunishi, B. J. Morgan, O. J. Borkiewicz, V. Pralong, A. Maignan, H. Groult, S. Komaba, D. Dambournet, *Inorg. Chem. Front.* **2018**, 5, 1100.
- [13] M. Zhou, Y. Xu, J. Xiang, C. Wang, L. Liang, L. Wen, Y. Fang, Y. Mi, Y. Lei, *Adv. Energy Mater.* **2016**, 6.
- [14] J. Chen, Z. Ding, C. Wang, H. Hou, Y. Zhang, C. Wang, G. Zou, X. Ji, *ACS Appl. Mater. Inter.* **2016**, 8, 9142.
- [15] B. Wang, F. Zhao, G. Du, S. Porter, Y. Liu, P. Zhang, Z. Cheng, H. K. Liu, Z. Huang, *ACS Appl. Mater. Inter.* **2016**, 8, 16009.
- [16] Y. Wu, X. Liu, Z. Yang, L. Gu, Y. Yu, *Small* **2016**, 12, 3522.
- [17] D. T. Cromer, K. Herrington, *J. Am. Chem. Soc.* **1955**, 77, 4708.
- [18] J. Z. Chunhai Jiang, *J. Mater. Sci. Technol.* **2013**, 29, 97.
- [19] L. Kavan, *Chem. Rec.* **2012**, 12, 131.
- [20] R. D. Shannon, J. A. Pask, *J. Am. Ceram. Soc.* **1965**, 48, 391.
- [21] F. Dacheille, P. Simons, R. Roy, *Am. Mineral.* **1968**, 53, 1929.
- [22] Z. Yang, D. Choi, S. Kerisit, K. M. Rosso, D. Wang, J. Zhang, G. Graff, J. Liu, *J. Power Sources* **2009**, 192, 588.
- [23] X. Su, Q. Wu, X. Zhan, J. Wu, S. Wei, Z. Guo, *J. Mater. Sci.* **2012**, 47, 2519.

- [24] L. Kavan, M. Grätzel, S. E. Gilbert, C. Klemen, H. J. Scheel, *J. Am. Chem. Soc.* **1996**, 118, 6716.
- [25] M. Wagemaker, R. van de Krol, A. P. M. Kentgens, A. A. van Well, F. M. Mulder, *J. Am. Chem. Soc.* **2001**, 123, 11454.
- [26] D. Kong, C. Cheng, Y. Wang, B. Liu, Z. Huang, H. Y. Yang, *J. Mater. Chem. A* **2016**, 4, 11800.
- [27] V. Aravindan, Y.-S. Lee, S. Madhavi, *Adv. Energy Mater.* **2017**, 7, 1602607.
- [28] Z. Liu, Y. G. Andreev, A. R. Armstrong, S. Brutti, Y. Ren, P. G. Bruce, *Prog. Nat. Sci.-Mater.* **2013**, 23, 235.
- [29] C. Jiang, M. Wei, Z. Qi, T. Kudo, I. Honma, H. Zhou, *J. Power Sources* **2007**, 166, 239.
- [30] J.-Y. Shin, D. Samuelis, J. Maier, *Adv. Funct. Mater.* **2011**, 21, 3464.
- [31] M. Wagemaker, W. J. H. Borghols, E. R. H. van Eck, A. P. M. Kentgens, G. J. Kearley, F. M. Mulder, *Chem.-Eur. J.* **2007**, 13, 2023.
- [32] O. Wilhelm, S. E. Pratsinis, E. de Chambrier, M. Crouzet, I. Exnar, *J. Power Sources* **2004**, 134, 197.
- [33] Y.-S. Hu, L. Kienle, Y.-G. Guo, J. Maier, *Adv. Mater.* **2006**, 18, 1421.
- [34] M. Wagemaker, W. J. H. Borghols, F. M. Mulder, *J. Am. Chem. Soc.* **2007**, 129, 4323.
- [35] J. W. Kang, D. H. Kim, V. Mathew, J. S. Lim, J. H. Gim, J. Kim, *J. Electrochem. Soc.* **2011**, 158, A59.
- [36] V. Aravindan, J. Sundaramurthy, P. S. Kumar, N. Shubha, W. C. Ling, S. Ramakrishna, S. Madhavi, *Nanoscale* **2013**, 5, 10636.
- [37] J.-Y. Hwang, S. T. Myung, J. H. Lee, A. Abouimrane, I. Belharouak, Y.-K. Sun, *Nano Energy* **2015**, 16, 218.
- [38] W. Li, M. Fukunishi, B. J. Morgan, O. J. Borkiewicz, K. W. Chapman, V. Pralong, A. Maignan, O. I. Lebedev, J. Ma, H. Groult, *Chem. Mater.* **2017**, 29, 1836.
- [39] M. N. Tahir, B. Oschmann, D. Buchholz, X. Dou, I. Lieberwirth, M. Panthöfer, W. Tremel, R. Zentel, S. Passerini, *Adv. Energy Mater.* **2016**, 6, 1501489.
- [40] L. Kavan, D. Fattakhova, P. Krtil, *J. Electrochem. Soc.* **1999**, 146, 1375.
- [41] X. Yan, Z. Wang, M. He, Z. Hou, T. Xia, G. Liu, X. Chen, *Energy Technol.-Ger.* **2015**, 3, 801.

- [42] M. V. Koudriachova, N. M. Harrison, S. W. de Leeuw, *Solid State Ionics* **2003**, 157, 35.
- [43] W. J. H. Borghols, M. Wagemaker, U. Lafont, E. M. Kelder, F. M. Mulder, *Chem. Mater.* **2008**, 20, 2949.
- [44] D. McNulty, E. Carroll, C. O'Dwyer, *Adv. Energy Mater.* **2017**, 7, 1602291.
- [45] Z. Hong, J. Hong, C. Xie, Z. Huang, M. Wei, *Electrochim. Acta* **2016**, 202, 203.
- [46] L. Pan, Z.-W. Zhou, Y.-T. Liu, X.-M. Xie, *J. Mater. Chem. A* **2018**, 6, 7070.
- [47] A. Vittadini, M. Casarin, A. Selloni, *J. Phys. Chem. C* **2009**, 113, 18973.
- [48] A. G. Dylla, G. Henkelman, K. J. Stevenson, *Accounts Chem. Res.* **2013**, 46, 1104.
- [49] M. Zukalová, M. Kalbáč, L. Kavan, I. Exnar, M. Graetzel, *Chem. Mater.* **2005**, 17, 1248.
- [50] Y. Zhang, Y. Tang, W. Li, X. Chen, *ChemNanoMat* **2016**, 2, 764.
- [51] Y. Ren, Z. Liu, F. Pourpoint, A. R. Armstrong, C. P. Grey, P. G. Bruce, *Angew. Chem. Int. Edit.* **2012**, 51, 2164.
- [52] Q. Wu, J. Xu, X. Yang, F. Lu, S. He, J. Yang, H. J. Fan, M. Wu, *Adv. Energy Mater.* **2015**, 5, 1401756.
- [53] A. R. Armstrong, G. Armstrong, J. Canales, R. García, P. G. Bruce, *Adv. Mater.* **2005**, 17, 862.
- [54] V. Aravindan, N. Shubha, Y. L. Cheah, R. Prasanth, W. Chuiling, R. R. Prabhakar, S. Madhavi, *J. Mater. Chem. A* **2013**, 1, 308.
- [55] H. Liu, Z. Bi, X.-G. Sun, R. R. Unocic, M. P. Paranthaman, S. Dai, G. M. Brown, *Adv. Mater.* **2011**, 23, 3450.
- [56] V. Etacheri, J. E. Yourey, B. M. Bartlett, *ACS Nano* **2014**, 8, 1491.
- [57] X. Yan, Y. Li, M. Li, Y. Jin, F. Du, G. Chen, Y. Wei, *J. Mater. Chem. A* **2015**, 3, 4180.
- [58] A. Deschanvres, B. Raveau, Z. Sekkal, *Mater. Res. Bull.* **1971**, 6, 699.
- [59] A. Vezzini, *Manufacturers, Materials and Recycling Technologies in Lithium-Ion Batteries* (Ed: G. Pistoia), Elsevier, Amsterdam **2014**, Ch. 23.
- [60] D. W. Murphy, R. J. Cava, S. M. Zahurak, A. Santoro, *Solid State Ionics* **1983**, 9-10, 413.1
- [61] K. M. Colbow, J. R. Dahn, R. R. Haering, *J. Power Sources* **1989**, 26, 397.
- [62] B. Zhao, R. Ran, M. Liu, Z. Shao, *Mater. Sci. Rep.* **2015**, 98, 1.
- [63] T.-F. Yi, S.-Y. Yang, Y. Xie, *J. Mater. Chem. A* **2015**, 3, 5750.

- [64] F. Ronci, P. Reale, B. Scrosati, S. Panero, V. Rossi Albertini, P. Perfetti, M. di Michiel, J. M. Merino, *J. Phys. Chem. B* **2002**, 106, 3082.
- [65] W. Schmidt, P. Bottke, M. Sternad, P. Gollob, V. Hennige, M. Wilkening, *Chem. Mater.* **2015**, 27, 1740.
- [66] M. Vijayakumar, S. Kerisit, K. M. Rosso, S. D. Burton, J. A. Sears, Z. Yang, G. L. Graff, J. Liu, J. Hu, *J. Power Sources* **2011**, 196, 2211.
- [67] T. Ohzuku, A. Ueda, N. Yamamoto, *J. Electrochem Soc.* **1995**, 142, 1431.
- [68] C.-T. Hsieh, I. L. Chen, Y.-R. Jiang, J.-Y. Lin, *Solid State Ionics* **2011**, 201, 60.
- [69] C. H. Chen, J. T. Vaughey, A. N. Jansen, D. W. Dees, A. J. Kahaian, T. Goacher, M. M. Thackeray, *J. Electrochem Soc.* **2001**, 148, A102.
- [70] N. Takami, K. Hoshina, H. Inagaki, *J. Electrochem Soc.* **2011**, 158, A725.
- [71] G.-N. Zhu, Y.-G. Wang, Y.-Y. Xia, *Energ. Environ. Sci.* **2012**, 5, 6652.
- [72] J. M. Feckl, K. Fominykh, M. Döblinger, D. Fattakhova-Rohlfing, T. Bein, *Angew. Chem.* **2012**, 124, 7577.
- [73] G.-N. Zhu, H.-J. Liu, J.-H. Zhuang, C.-X. Wang, Y.-G. Wang, Y.-Y. Xia, *Energ. Environ. Sci.* **2011**, 4, 4016.
- [74] X. Zhu, Y. Zhu, S. Murali, M. D. Stoller, R. S. Ruoff, *ACS Nano* **2011**, 5, 3333.
- [75] Z. Liu, N. Zhang, Z. Wang, K. Sun, *J. Power Sources* **2012**, 205, 479.
- [76] A. N. Jansen, A. J. Kahaian, K. D. Kepler, P. A. Nelson, K. Amine, D. W. Dees, D. R. Vissers, M. M. Thackeray, *J. Power Sources* **1999**, 81-82, 902.
- [77] N. Takami, H. Inagaki, Y. Tatebayashi, H. Saruwatari, K. Honda, S. Egusa, *J. Power Sources* **2013**, 244, 469.
- [78] K. Zaghib, M. Dontigny, A. Guerfi, P. Charest, I. Rodrigues, A. Mauger, C. M. Julien, *J. Power Sources* **2011**, 196, 3949.
- [79] Y. Sun, L. Zhao, H. Pan, X. Lu, L. Gu, Y.-S. Hu, H. Li, M. Armand, Y. Ikuhara, L. Chen, X. Huang, *Nat. Commun.* **2013**, 4, 1870.
- [80] P. Senguttuvan, G. Rousse, V. Seznec, J.-M. Tarascon, M. R. Palacín, *Chem. Mater.* **2011**, 23, 4109.
- [81] G. Rousse, M. E. Arroyo-de Dompablo, P. Senguttuvan, A. Ponrouch, J.-M. Tarascon, M. R. Palacín, *Chem. Mater.* **2013**, 25, 4946.
- [82] R. J. Cava, D. W. Murphy, S. M. Zahurak, *J. Electrochem Soc.* **1983**, 130, 2345.
- [83] J. B. Goodenough, Y. Kim, *J. Power Sources* **2011**, 196, 6688.

- [84] X. Lu, Z. Jian, Z. Fang, L. Gu, Y.-S. Hu, W. Chen, Z. Wang, L. Chen, *Energ. Environ. Sci.* **2011**, 4, 2638.
- [85] B. Guo, X. Yu, X.-G. Sun, M. Chi, Z.-A. Qiao, J. Liu, Y.-S. Hu, X.-Q. Yang, J. B. Goodenough, S. Dai, *Energ. Environ. Sci.* **2014**, 7, 2220.
- [86] K. Tang, X. Mu, P. A. van Aken, Y. Yu, J. Maier, *Adv. Energy Mater.* **2013**, 3, 49.
- [87] K. Ise, S. Morimoto, Y. Harada, N. Takami, *Solid State Ionics* **2018**, 320, 7.
- [88] J.-T. Han, Y.-H. Huang, J. B. Goodenough, *Chem. Mater.* **2011**, 23, 2027.
- [89] C. Jo, Y. Kim, J. Hwang, J. Shim, J. Chun, J. Lee, *Chem. Mater.* **2014**, 26, 3508.
- [90] V. Aravindan, J. Sundaramurthy, P. Suresh Kumar, Y.-S. Lee, S. Ramakrishna, S. Madhavi, *Chem. Commun.* **2015**, 51, 2225.
- [91] M. Luo, H. Yu, X. Cheng, W. Ye, H. Zhu, T. Liu, N. Peng, M. Shui, J. Shu, *ACS Appl. Mater. Inter.* **2018**, 10, 12716.
- [92] R. Satish, V. Aravindan, W. C. Ling, J. B. Goodenough, S. Madhavi, *Adv. Energy Mater.* **2014**, 4, 1301715.
- [93] E. J. Cussen, T. W. S. Yip, *J. Solid State Chem.* **2007**, 180, 1832.
- [94] H. Xie, K.-S. Park, J. Song, J. B. Goodenough, *Electrochem. Commun.* **2012**, 19, 135.
- [95] Y. Feng, S. Dou, Y. Wei, Y. Zhang, X. Song, X. Li, V. S. Battaglia, *ACS Omega* **2017**, 2, 8075.
- [96] J. Rohrer, D. Vrankovic, D. Cupid, R. Riedel, H. J. Seifert, K. Albe, M. Graczyk-Zajac, *Int. J. Mater. Res.* **2017**, 108, 920.
- [97] L. David, R. Bhandavat, U. Barrera, G. Singh, *Nat. Commun.* **2016**, 7, 10998.
- [98] Z. Sang, Z. Zhao, D. Su, P. Miao, F. Zhang, H. Ji, X. Yan, *J. Mater. Chem. A* **2018**, 6, 9064.
- [99] G. Mera, A. Navrotsky, S. Sen, H.-J. Kleebe, R. Riedel, *J. Mater. Chem. A* **2013**, 1, 3826.
- [100] M. Graczyk-Zajac, L. M. Reinold, J. Kaspar, P. V. W. Sasikumar, G.-D. Soraru, R. Riedel, *Nanomaterials* **2015**, 5, 233.
- [101] L. M. Reinold, M. Graczyk-Zajac, Y. Gao, G. Mera, R. Riedel, *J. Power Sources* **2013**, 236, 224.
- [102] L. M. Reinold, Y. Yamada, M. Graczyk-Zajac, H. Munakata, K. Kanamura, R. Riedel, *J. Power Sources* **2015**, 282, 409.
- [103] J. Kaspar, C. Terzioglu, E. Ionescu, M. Graczyk-Zajac, S. Hapis, H.-J. Kleebe, R. Riedel, *Adv. Funct. Mater.* **2014**, 24, 4097.

- [104] Z. Jian, Y.-S. Hu, X. Ji, W. Chen, *Adv. Mater.* **2017**, 29, 1601925.
- [105] N. Anantharamulu, K. Koteswara Rao, G. Rambabu, B. Vijaya Kumar, V. Radha, M. Vithal, *J. Mater. Sci.* **2011**, 46, 2821.
- [106] P. Senguttuvan, G. Rousse, M. E. Arroyo y de Dompablo, H. Vezin, J. M. Tarascon, M. R. Palacín, *J. Am. Chem. Soc.* **2013**, 135, 3897.
- [107] R. Huggins, *Positive Electrodes in Lithium Systems in Advanced batteries: materials science aspects*, Springer Science & Business Media **2008**, Ch 9.
- [108] S. Yu, A. Mertens, H. Tempel, R. Schierholz, H. Kungl, R.-A. Eichel, *ACS Appl. Mater. Inter.* **2018**, 10, 22264.
- [109] H. Y. P. Hong, *Mater. Res. Bull.* **1976**, 11, 173.
- [110] W. Wang, B. Jiang, L. Hu, S. Jiao, *J. Mater. Chem. A* **2014**, 2, 1341.
- [111] K. B. Hueso, M. Armand, T. Rojo, *Energ. Environ. Sci.* **2013**, 6, 734.
- [112] H. Aono, E. Sugimoto, Y. Sadaoka, N. Imanaka, G.-y. Adachi, *J. Electrochem. Soc.* **1990**, 137, 1023.
- [113] G. Pang, C. Yuan, P. Nie, B. Ding, J. Zhu, X. Zhang, *Nanoscale* **2014**, 6, 6328.
- [114] G.-M. Weng, L.-Y. Simon Tam, Y.-C. Lu, *J. Mater. Chem. A* **2017**, 5, 11764.
- [115] X.-y. Wu, M.-y. Sun, Y.-f. Shen, J.-f. Qian, Y.-l. Cao, X.-p. Ai, H.-x. Yang, *ChemSusChem* **2014**, 7, 407.
- [116] Y. Lu, L. Yu, X. W. Lou, *Chem* **2018**, 4, 972.
- [117] Y. Tang, Y. Zhang, W. Li, B. Ma, X. Chen, *Chem. Soc. Rev.* **2015**, 44, 5926.
- [118] H. Zhang, I. Hasa, S. Passerini, *Adv. Energy Mater.* **2018**, 8, 1702582.
- [119] Y. Zhao, Z. Feng, Z. J. Xu, *Nanoscale* **2015**, 7, 9520.
- [120] Y. Fu, Q. Wei, X. Wang, G. Zhang, H. Shu, X. Yang, A. C. Tavares, S. Sun, *RSC Adv.* **2016**, 6, 16624.
- [121] R. Alcántara, M. Jaraba, P. Lavela, J. L. Tirado, *Chem. Mater.* **2002**, 14, 2847.
- [122] S. Komaba, T. Mikumo, N. Yabuuchi, A. Ogata, H. Yoshida, Y. Yamada, *J. Electrochem. Soc.* **2010**, 157, A60.
- [123] M. M. Rahman, A. M. Glushenkov, T. Ramireddy, Y. Chen, *Chem. Commun.* **2014**, 50, 5057.
- [124] Y. Jiang, M. Hu, D. Zhang, T. Yuan, W. Sun, B. Xu, M. Yan, *Nano Energy* **2014**, 5, 60.
- [125] Y. C. Lu, C. Ma, J. Alvarado, T. Kidera, N. Dimov, Y. S. Meng, S. Okada, *J. Power Sources* **2015**, 284, 287.

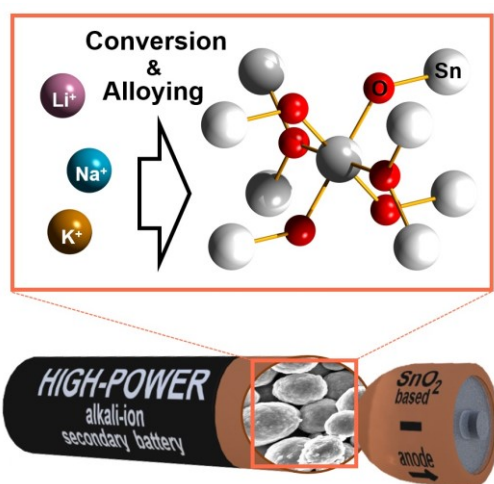
- [126] Y. Lu, N. Zhang, Q. Zhao, J. Liang, J. Chen, *Nanoscale* **2015**, 7, 2770.
- [127] J. S. Chen, X. W. Lou, *Small* **2013**, 9, 1877.
- [128] F. Zoller, K. Peters, P. M. Zehetmaier, P. Zeller, M. Döblinger, T. Bein, Z. k. Sofer, D. Fattakhova-Rohlfing, *Adv. Funct. Mater.* **2018**, 28, 1706529.
- [129] H. Morito, T. Yamada, T. Ikeda, H. Yamane, *J. Alloys Compd.* **2009**, 480, 723.
- [130] Y. Xu, E. Swaans, S. Basak, H. W. Zandbergen, D. M. Borsa, F. M. Mulder, *Adv. Energy Mater.* **2016**, 6, 1501436.
- [131] L. D. Ellis, T. D. Hatchard, M. N. Obrovac, *J. Electrochem. Soc.* **2012**, 159, A1801.
- [132] S. P. Ong, V. L. Chevrier, G. Hautier, A. Jain, C. Moore, S. Kim, X. Ma, G. Ceder, *Energ. Environ. Sci.* **2011**, 4, 3680.
- [133] J. W. Wang, X. H. Liu, S. X. Mao, J. Y. Huang, *Nano Lett.* **2012**, 12, 5897.
- [134] J. Wang, C. Eng, Y.-c. K. Chen-Wiegart, J. Wang, *Nat. Commun.* **2015**, 6, 7496.
- [135] B. Luo, T. Qiu, D. Ye, L. Wang, L. Zhi, *Nano Energy* **2016**, 22, 232.
- [136] X. Xie, K. Kretschmer, J. Zhang, B. Sun, D. Su, G. Wang, *Nano Energy* **2015**, 13, 208.
- [137] A. Darwiche, C. Marino, M. T. Sougrati, B. Fraisse, L. Stievano, L. Monconduit, *J. Am. Chem. Soc.* **2012**, 134, 20805.
- [138] L. Wu, X. Hu, J. Qian, F. Pei, F. Wu, R. Mao, X. Ai, H. Yang, Y. Cao, *Energ. Environ. Sci.* **2014**, 7, 323.
- [139] T. Ramireddy, T. Xing, M. M. Rahman, Y. Chen, Q. Dutercq, D. Gunzelmann, A. M. Glushenkov, *J. Mater. Chem. A* **2015**, 3, 5572.
- [140] J. Song, Z. Yu, M. L. Gordin, X. Li, H. Peng, D. Wang, *ACS Nano* **2015**, 9, 11933.
- [141] C. Zhang, X. Wang, Q. Liang, X. Liu, Q. Weng, J. Liu, Y. Yang, Z. Dai, K. Ding, Y. Bando, J. Tang, D. Golberg, *Nano Letters* **2016**, 16, 2054.
- [142] L. D. Ellis, B. N. Wilkes, T. D. Hatchard, M. N. Obrovac, *J. Electrochem. Soc.* **2014**, 161, A416.
- [143] J. Liu, Y. Wen, P. A. van Aken, J. Maier, Y. Yu, *Nano Letters* **2014**, 14, 6387.
- [144] A. C. Kozen, C.-F. Lin, A. J. Pearse, M. A. Schroeder, X. Han, L. Hu, S.-B. Lee, G. W. Rubloff, M. Noked, *ACS Nano* **2015**, 9, 5884.
- [145] Y. Guo, H. Li, T. Zhai, *Adv. Mater.* **2017**, 29, 1700007.
- [146] D. Lin, Y. Liu, A. Pei, Y. Cui, *Nano Res.* **2017**, 10, 4003.
- [147] L. Li, S. Li, Y. Lu, *Chem. Commun.* **2018**, 54, 6648

4. Tin Oxide Based Nanomaterials and Their Application as Anodes in Lithium-Ion Batteries and Beyond

This chapter is based on the following publication:

Zoller, F.,* Böhm, D.,* Bein, T. and Fattakhova-Rohlfing, D., *ChemSusChem*, **2019**, *12*, 4140 – 4159 (* the authors contributed equally to the work)

A cover image (*ChemSusChem*, 18/2019) and profile associated with this publication can be found in the following Section 4.1.

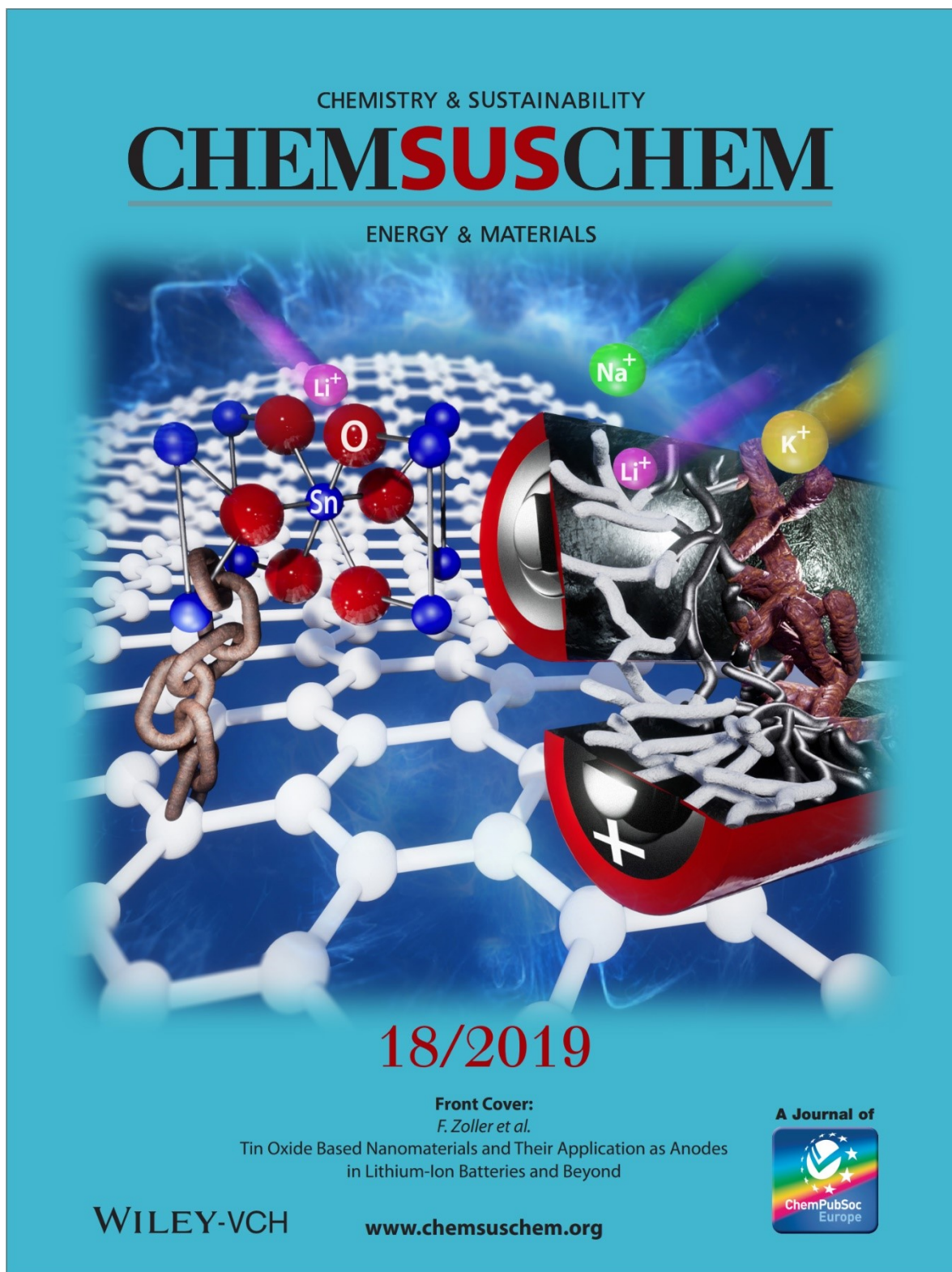


The TOC graphic shows the lithiation, sodation and potassiation of SnO_2 based composite materials. Occurring large volume changes related to the conversion and alloying reaction with alkali metal ions and its detrimental effect on the nano- and microstructure are identified as main obstacle for commercial application as anode material in secondary batteries. Fabrication of diverse 3D nanostructures, composite formation and doping are presented as possible solutions to enhance the cycling life and rate capability.

Reprinted with permission from: Zoller, F., Böhm, D., Bein, T. and Fattakhova-Rohlfing, D., *ChemSusChem*, **2019**, *12*, 4140 – 4159. Copyright (2019) The Authors. Published by Wiley-VCH Verlag GmbH & Co. KGaA.

4.1 Cover image and profile

Artwork created by Maltopol R. (TUT GmbH) and Böhm D. (2019)



Reprinted with permission from: Zoller, F., Böhm, D., Bein, T. and Fattakhova-Rohlfing, D., ChemSusChem, 2019, 12, 4140 – 4159. Copyright (2019). © 2019 Wiley-VCH Verlag GmbH & Co. KGaA, Weinheim

Tin oxide-based Nanomaterials and their Application as Anodes in Lithium-Ion Batteries and Beyond



Florian Zoller



Daniel Böhm



Prof. T. Bein



Prof. D. Fattakhova-Rohlfing*



Institute of Energy and Climate Research (IEK-1) Materials Synthesis and Processing, Forschungszentrum Jülich GmbH, Wilhelm-Johnen-Strasse, 52425 Jülich (Germany), E-Mail: d.fattakhova@fz-juelich.de

and

Faculty of Engineering and Center for Nanointegration Duisburg-Essen (CENIDE), Universität Duisburg-Essen, (UDE), Lotharstraße 1, 47057 Duisburg (Germany)

Invited for this month's cover are the groups of Fattakhova-Rohlfing and Bein at Forschungszentrum Jülich (FZJ), University of Duisburg-Essen (UDE) and Ludwig-Maximilians-Universität München (LMU). The image shows the lithiation, sodation and potassiation of a SnO_2 /graphene composite material represented by a chain-linked SnO_2 unit cell to an underlying graphene sheet. The cross-sectional representation of a battery anode depicts a branched SnO_2 based nanostructure undergoing conversion and alloying reactions with alkali ions affecting its nano- and microstructure as indicated by volume and textural changes.

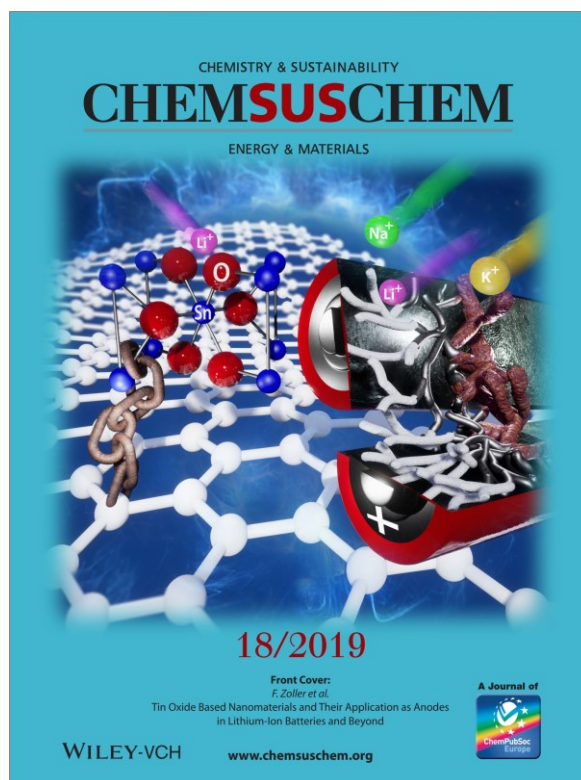
Who contributed to the idea behind the cover and who designed the cover? The central components of the cover art namely the composite formation and nanostructuring approach for fabrication of advanced SnO_2 based anodes in secondary batteries were identified by the authors during the writing process and specified in a sketch. The 3D artwork was realized in continuous feedback by Robert Maltopol.

What prompted you to investigate this topic/problem?

In the recent years, the groups of Prof. Fattakhova-Rohlfing and Prof. Bein conducted research in in the field of SnO_2 based materials for energy application such as batteries and catalysis. Based on that expertise the authors try to give the interested reader an essential overview of this fast-growing topic.

Acknowledgements

We are grateful to the German Research Foundation (DFG; grant nos. FA 839/3-1 and SPP 1613), the NIM Excellence Cluster (DFG), the research network "Solar Technologies Go Hybrid" (State of Bavaria), and the Center for NanoScience (CeNS). The authors furthermore acknowledge Robert Maltopol (TUT GmbH) for the 3D cover design.



4.2 Introduction

Lithium-ion batteries (LIBs) represent the most advanced electrochemical energy-storage technology for powering mobile and consumer applications, with energy and power densities greatly exceeding those of other battery systems. Although enormous progress in the performance of LIBs has been achieved in recent decades, making even large-scale energy storage applications, such as electric vehicles feasible, the constantly growing demand for electrical energy storage devices necessitates the development of novel battery chemistries to further increase the energy density on the cell level.^[1-2]

By using materials with different energy-storage mechanisms, such as alloying or conversion, instead of the state-of-the-art insertion anode material, graphite, is a promising way to significantly increase the charge-storage capacity.

Tin-based conversion and alloying anode materials gained considerable attention in recent years due to their high theoretical capacity. Metallic tin, tin alloys, stannates, or tin chalcogenides such as tin (di)sulfide and tin (di)oxide were intensively investigated as battery anode materials.^[3] Among the listed materials classes, metallic tin features the highest theoretical capacity, but suffers from severe stability issues upon cycling. Although nanostructuring or alloying were shown to be promising concepts to improve long-term stability, the use of metallic tin as an anode remains very challenging.^[3]

Tin dioxide (SnO_2) and layered sulfides (SnS or SnS_2) exhibit comparable theoretical capacities. However, tin oxides show faster lithiation/delithiation kinetics and a greatly enhanced cyclability, whereas the Li insertion and conversion reaction with SnS_2 is only partly reversible.^[3] Therefore, SnO_2 is believed to be a potential candidate as an active anode material for nextgeneration LIBs.

It was more than 20 years ago that tin oxide materials were reported, for the first time, by Idota *et al.* from the Fuji Photo Film Celltec Co. (Japan) company as highly promising anode

materials.^[4] Since that time, tin oxide containing materials have gained tremendous attention due to the high theoretical and volumetric capacity, biological compatibility, environmental friendliness, and rather low cost. Moreover, the low discharge potential of SnO₂ makes it even more attractive as an anode material in LIBs.^[5-6]

The lithium reaction with SnO₂ has been long believed to proceed through two major steps, namely, a conversion reaction followed by a subsequent alloying/dealloying process; this was substantiated by various in situ studies.^[7-11]

However, more recent theoretical calculations^[12-13] and in situ scanning transmission electron microscopy on nanowires^[12] suggested the occurrence of Li⁺ insertion into the SnO₂ lattice preceding the abovementioned steps (Figure 1).

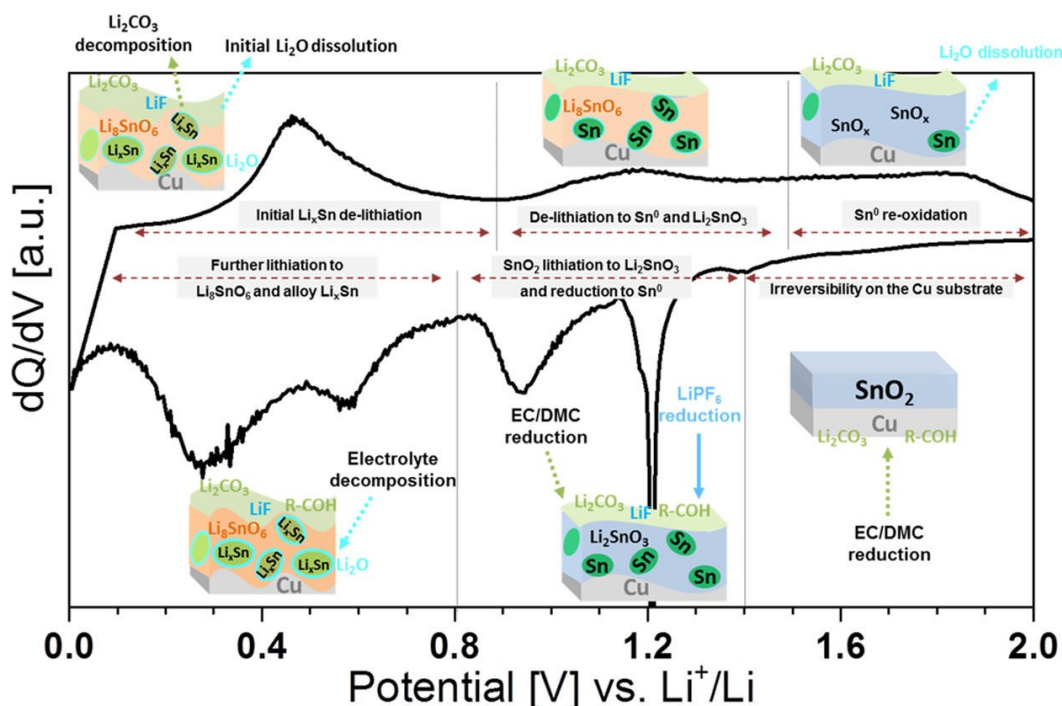


Figure 1 Cyclic voltammogram of a flat SnO₂ model electrode with a schematic representation of the electrode composition, intermediate phases during lithiation, and redox features associated with interfacial reactions with the organic and inorganic part of the electrolyte. EC=ethylene carbonate, DMC=dimethyl carbonate.^[14]

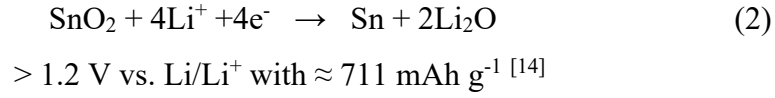
Reproduced with permission from Ref. [14]. Copyright 2018, American Chemical Society.

Based on the latest findings, the total process of the lithium reaction with SnO₂ can be presented as Equations (1)–(3).

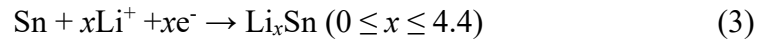
Insertion (intermediate phase):



Conversion:



Alloying/De-alloying:



< 0.5 V vs. Li/Li⁺ $\approx 783 \text{ mAh g}^{-1}$ [14]

The Li_xSnO_2 intercalation compound (according to Eq. 1) is an intermediate phase formed by a long-range Li^+ diffusion into the SnO_2 phase mediated by the nucleation of dislocations.^[12] Ab initio calculations for the first lithiation cycle predicted Li_2SnO_3 and Li_8SnO_6 as compositions of intermediate phases.^[13] Recently, Ferraresi *et al.* found strong experimental evidence for the existence of these phases by combining electrochemistry, post-mortem XPS, and SEM imaging together with DFT calculations.^[14] Scarce literature reports indicate that the composition and spatial distribution of intermediate Li-Sn-O phases and the reversibility of subsequent reactions steps are strongly affected by the composition and morphology of parent SnO_2 electrodes.

The crystallinity and the composition (exact stoichiometry, defects, surface termination, impurities) as important parameters of SnO_2 materials, all influenced by the choice of precursors and the way of fabrication, are viewed as factors affecting their electrochemical performance and stability. Studies on a flat amorphous SnO_2 film taken as a model electrode demonstrate that the reversibility of the reaction steps strongly depends on the reactions during the first lithiation cycle, as proposed by calculations on the Li_xSn phase diagram.^[12-14]

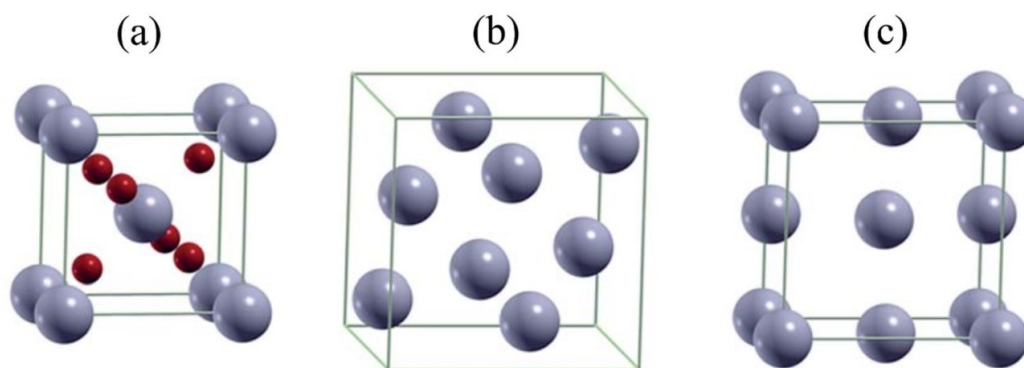


Figure 2 Schematic representation of unit cells of (a) SnO₂ (rutile $P4_2/mnm$), (b) α -Sn (cubic $Fd\bar{3}m$), and (c) β -Sn ($I4_1/amd$). Grey and red spheres represent Sn and O atoms, respectively.^[13]

Reproduced (adapted) with permission from Ref. [13]. Copyright 2015, Royal Society of Chemistry.

The typical cyclic voltammogram (Figure 1) furthermore shows redox features of side-reactions at the interface associated with solid electrolyte interface (SEI) formation and electrolyte reduction contributing to the irreversible capacity loss of SnO₂ based anodes in the first cycles.^[14]

In a subsequent conversion reaction (Eq. 2) the intermediate Li_xSnO₂ compounds are reduced to metallic Sn that crystallizes in a Li₂O matrix.^[12-13] The conversion reaction of SnO₂ to metallic tin is reported to be irreversible for bulk SnO₂, but it can get (partially) reversible for nanosized SnO₂, greatly depending on the particle size and the morphology.^[6-7, 15-18]

Upon further Li-ion uptake the surrounding matrix with metallic Sn particles is lithiated to form Li_xSn alloys (Eq. 3). It has been shown that, starting from the β -Sn phase, a mixture of the cubic α - and the tetragonal β -Sn (Figure 2b and c) is formed, with the α -phase being stabilized for small nanostructures.^[13, 19] The alloying/de-alloying process between Sn and Li⁺ is considered to be reversible.^[17-18]

According to the experimentally determined and ab initio calculated Li_xSn phase diagrams, the following Li-Sn alloys are proposed to form during the lithiation/delithiation cycles with increasing Li content : LiSn – Li₁₃Sn₅ – Li₇Sn₂ up to Li₁₇Sn₄ (Figure 3 a-d).^[13]

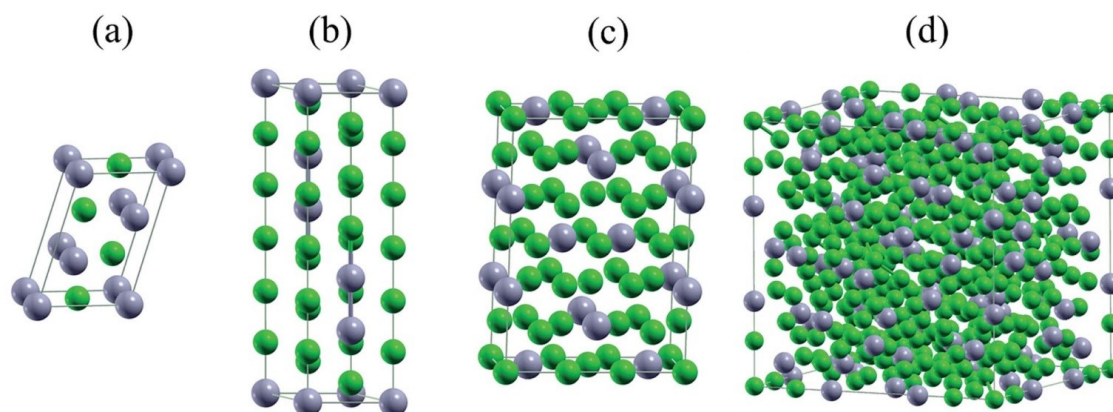


Figure 3 Schematic representation of theoretically predicted intermediate Li_xSn alloys: (a) LiSn , (b) $\text{Li}_{13}\text{Sn}_5$, (c) Li_7Sn_2 , and (d) $\text{Li}_{17}\text{Sn}_4$. Green and grey spheres represent Li and Sn atoms, respectively.^[13]

Reproduced (adapted) with permission from Ref. [13]. Copyright 2015, Royal Society of Chemistry.

The specific capacity of the SnO_2 anodes is greatly dependent on the reversibility of different reaction steps. The theoretical capacity of the complete reaction, including both conversion and alloying is as high as 1494 mAh g^{-1} , but it reduces to 783 mAh g^{-1} if only the alloying/dealloying reaction is reversible. It should be noted, however, that, even if only partial reversibility of the alloying/dealloying step is possible, the specific capacity still significantly exceeds that of graphite (372 mAh g^{-1}).^[20]

Apart from the quasi-irreversibility of the conversion reaction and subsequent severe capacity loss during the first cycles, SnO_2 -based anodes suffer from large volume changes of up to 250% during the alloying and dealloying process.^[8] This causes internal stress that leads to pulverization of the electrode. Moreover, in situ XRD and TEM measurements also reveal that the formed tin particles can agglomerate into tin clusters that are less electrochemically active. Last, but not least, volume changes impede the formation of a stable SEI, which prevents further electrolyte decomposition. These factors are responsible for fast capacity fading and decreased cycling performance upon repeated cycling,^[7, 15, 17-20] and are the main reasons that SnO_2 -based anodes have not yet been commercialized.

The shortcomings of SnO₂-based anodes are mainly addressed by using two main strategies. One is to tailor bulk SnO₂ down to the nanosize and/or to nanostructure the SnO₂ compounds towards nanoparticles,^[19, 21-22] 1D nanorods,^[23] nanowires,^[24-25] nanotubes,^[26] 2D nanosheets,^[27-28] and 3D porous^[29-30] or hollow^[18,31] structures. Nanosized materials are known to accommodate large volume changes and to shorten diffusion paths for electrons and lithium ions. Porous or hollow structured (nanosized) SnO₂ can provide additional free space to reduce the problems of pulverization and large volume changes.^[2] Another effective approach is the fabrication of composites of SnO₂ and carbonaceous materials. The carbonaceous supports increase the overall conductivity of the composites and can also buffer large volume changes of SnO₂ during alloying and dealloying. There are many reports on carbon coating of SnO₂,^[32-37] as well as composites consisting of SnO₂ and carbonaceous materials, including carbon nanotubes (CNTs),^[38-42] fibers,^[43-44] aerogels,^[45] hollow spheres,^[46-47] and graphene^[48-50]. Herein, we introduce recent developments regarding different tin oxide-based anode materials systems, with a focus on the properties of the materials that affect their application in future energy-storage devices. Based on the analysis of key electrochemical properties, the phases identified during electrochemical transformations and the consequences arising for the reversibility of their transformations, the general goal of this Minireview is to indicate solutions to maximize the initial storage capacity and to overcome ICL, which is mainly associated with the conversion reaction. The most promising strategies to improve the performance of SnO₂-based anodes, such as nanostructuring, doping, and composite formation, to obtain high-rate and high-capacity anodes for future LIBs, and potentially also for sodium- (NIBs) and potassium-ion batteries (KIBs), are discussed in separate sections.

4.3 Nanostructured Phase-Pure SnO₂ LIB Anodes

Large volume changes, together with repeated cycling of bulk SnO₂, leads to pulverization of the anode and to decreased electrical contact, which causes a drastic loss in capacity within a few cycles. Other serious drawbacks of pure SnO₂ are its low electronic and ionic conductivity. A very low room-temperature conductivity of SnO₂ of $1.82 \times 10^{-8} \text{ S cm}^{-1}$ [51] drastically limits its storage and rate capability as an anode material. The measured apparent lithium-ion diffusion coefficient is also low; the reported values range from 10^{-16} – $10^{-14} \text{ cm}^2 \text{ s}^{-1}$ for a sputtered metallic Sn film (3 μm thick) to 10^{-15} – $10^{-13} \text{ cm}^2 \text{ s}^{-1}$ for amorphous SnO₂ tin oxide films ($\approx 1.5 \mu\text{m}$). [52]

Similar to other electrode materials with comparable properties (Si can be mentioned as an important example), nanostructuring is considered to be a promising strategy to mitigate the intrinsic drawbacks of the materials. Nanocrystalline SnO₂, with various nanomorphologies, can accommodate volume expansion through built-in porosity and reduce the agglomeration of Sn clusters by a homogeneous dispersion within a Li₂O matrix. It can furthermore decrease the required Li⁺ diffusion pathway by a significantly increased electrode– electrolyte interface, and thereby enable a higher flux of ions, resulting in high rate-capable anodes. [1, 53]

In addition, nanostructured SnO₂ may display altered properties, depending on the synthetic conditions, such as a significantly increased electrical conductivity of $0.1 - 0.9 \text{ S cm}^{-1}$ measured on single nanorods [54] or the preservation of nanocrystallinity indicated by the presence of an α -Sn phase upon repeated cycling. [13, 19] The presence of a nanocrystalline α -Sn phase is thereby correlated to the reversibility of the alloying reaction; however, it is not clear whether it is actually the phase that influences reversibility. The α -phase, which is more stable on a nanoscale, might indicate the intactness of the initial nanomorphology and, particularly the fine distribution of Sn within the Li₂O matrix, which is important for reversibility. A comprehensive review, with a focus on synthetic routes and electrochemical performance of

phase-pure SnO₂-based anodes, was published by Chen and Lou in 2013.^[1] Hence, we aim to provide an update on recent developments of SnO₂-based nanostructures applicable as anodes in LIBs and to link the properties of materials and initial SnO₂ morphologies defined by the synthetic parameters with electrochemical performance and stability of the resulting electrodes.

4.3.1 Nanoparticles

Diffraction studies on SnO₂ anodes revealed an ICL due to the formation of the amorphous Li₂O matrix and afterwards the loss in reversible capacity upon cycling. The reversibility of the reaction upon cycling was correlated to the initial SnO₂ crystallite size.^[55] Generally, it can be said that only if the active Sn material resulting from the conversion of nanosized SnO₂ crystals is well dispersed in the amorphous Li₂O matrix is a reversible alloying reaction without drastic capacity fading possible (Figure 4a). Larger Sn particles that are not homogeneously dispersed in the amorphous Li₂O matrix aggregate to form even larger clusters upon cycling, which leads to mechanical and electronic disintegration of the electrode (Figure 4b).^[6, 55]

In 2004, Ahn *et al.* reported SnO₂ particles about 11 nm in size, which were prepared through a colloidal method, to be an optimum size for lithium storage and reversibility with respect to the alloying reaction.^[15] In contrast, even smaller SnO₂ nanoparticles (e.g., 2 nm) have shown a high ICL.

As a possible reason, increased SEI formation on very small nanoparticles, due to their larger electrochemical surface area, as well as a decreased formation of the surrounding Li₂O phase, were proposed; this may lead to increased aggregation, and thus, capacity fading.^[15]

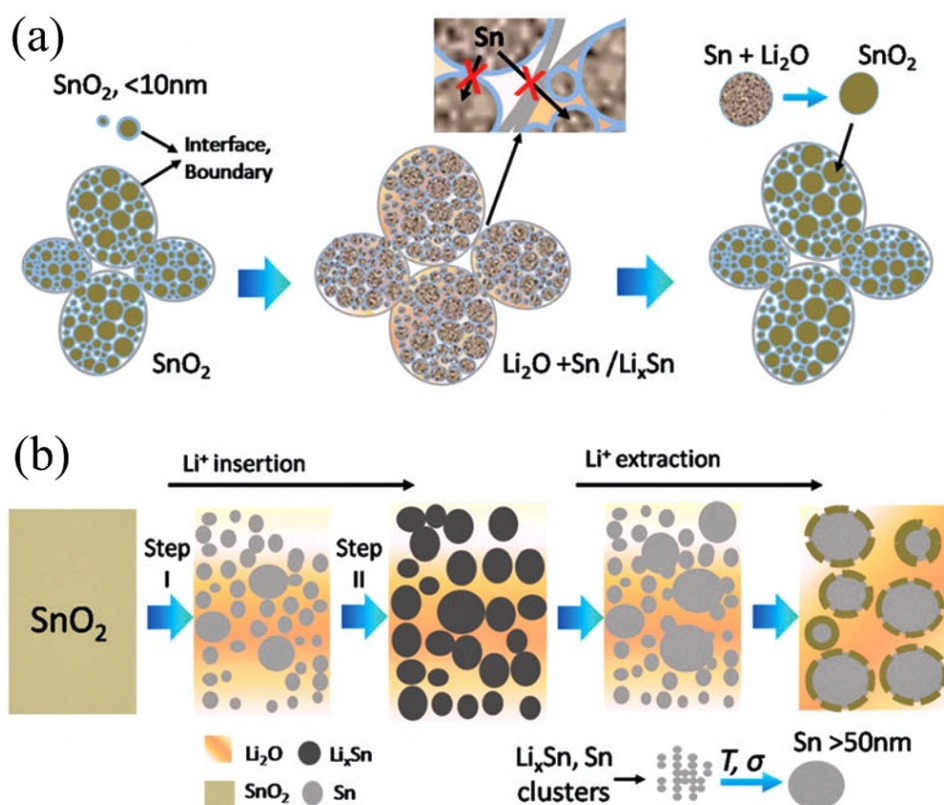


Figure 4 Schematic representation of SnO₂ anode microstructures formed in the course of de-/lithiation cycles and resulting structural changes. a) Structural evolution of a hierarchically nanostructured SnO₂ electrode, with a large number of interfaces and grain boundaries that inhibit Sn/Li_xSn coarsening and allow for a reversible conversion reaction. b) Structural evolution of the initial conversion and first lithiation cycle of bulk (>50 nm) SnO₂ electrode that permits a quantitative reversible conversion reaction.^[6]

Reproduced (adapted) with permission from Ref. [6]. Copyright 2016, Royal Society of Chemistry.

Conclusions about the optimum particle sizes are, however, not corroborated by other reports and seem to be strongly influenced by the synthetic route. Thus, Kim *et al.* reported that hydrothermally synthesized particles of about 3 nm in size showed an optimum initial (~740 mAh g⁻¹ at 60 mA g⁻¹ for the first cycle discharge current) and reversible capacity and cycling stability (negligible fading over 60 cycles at 300 mA g⁻¹ discharge current).^[19]

It can be suggested that the optimum size of SnO₂ nanocrystals, with respect to reversible capacity and capacity retention, is strongly dependent on the exact nature and amount of amorphous Li₂O matrix surrounding Sn formed during the initial conversion reaction, which is, in turn, affected by the SnO₂ nanoparticle synthetic route and initial cycle lithiation

parameters (see also the discussion about the reaction mechanism in the Introduction). A recent study by Hu *et al.* suggested that the capacity decay of SnO₂-based electrodes with larger nanoparticles was not directly induced by mechanical disintegration of the electrode due to large volume changes, but associated with a gradual degradation of the reversible conversion reaction at potentials below 1.0 V versus Li/Li⁺.^[20]

Thermal and stress-driven Sn coarsening that could be correlated to the average crystallite size has been identified as a main factor responsible for the reversibility of the conversion reaction, and thus, the reversible capacity of SnO₂-based electrodes. Furthermore, a quantitative relation between Sn-grain coarsening and the initial SnO₂ crystallite size was found, with a critical size of 11 nm for a fully reversible conversion reaction. Smaller crystallites with high-density Sn/Li₂O interfaces are reported to possess fast enough interdiffusion kinetics that enable a fully reversible conversion reaction. Through their synthetic approach based on magnetron-sputtered pure SnO₂ thin films, Hu *et al.* obtained an initial capacity of 1066 mAh g⁻¹, with a reversible capacity of about 915 mAh g⁻¹ at a rate of 0.2 A g⁻¹ after 20 cycles, which remained stable for over 100 cycles followed by a slow decay.^[20]

A further recent example of SnO₂ nanoparticles includes the fast and scalable microwave-assisted hydrothermal synthesis of fine particles of about 14 nm in size. An initial discharge capacity of about 1197 mAh g⁻¹, with a reversible capacity of 520 mAh g⁻¹ (2nd cycle), and a capacity retention of about 53% (273 mAh g⁻¹) after 50 cycles at 100 mA g⁻¹ were reported for this material by Yin *et al.*.^[21]

Jiang *et al.* demonstrated a large-scale hydrothermal synthesis of SnO₂ nanoparticles about 6 nm in size.^[22] Fabricated anodes that were cycled between 0.01 and 3.0 V versus Li/Li⁺ showed an initial discharge capacity of 2223 mAh g⁻¹ at a rate of 0.1 A g⁻¹ with a fast capacity fading to about 800 mAh g⁻¹ within the first 20 cycles and a slow decay to 760 mAh g⁻¹ after 40 cycles.^[22] The reported capacity outperforms the values published for other morphologies,

such as nanosheets, -tubes, -rods, or -spheres, and is in the range of tin oxide based carbon and transition-metal oxide composites. To enhance the rate capability and lithium-storage capacity of SnO₂-based anodes, Hameed *et al.* used a hydrothermal synthetic method with the micelle-forming surfactant Tween-80 to obtain mesoporous powders of connected SnO₂ nanoparticles (Figure 5) or -rods.^[56]

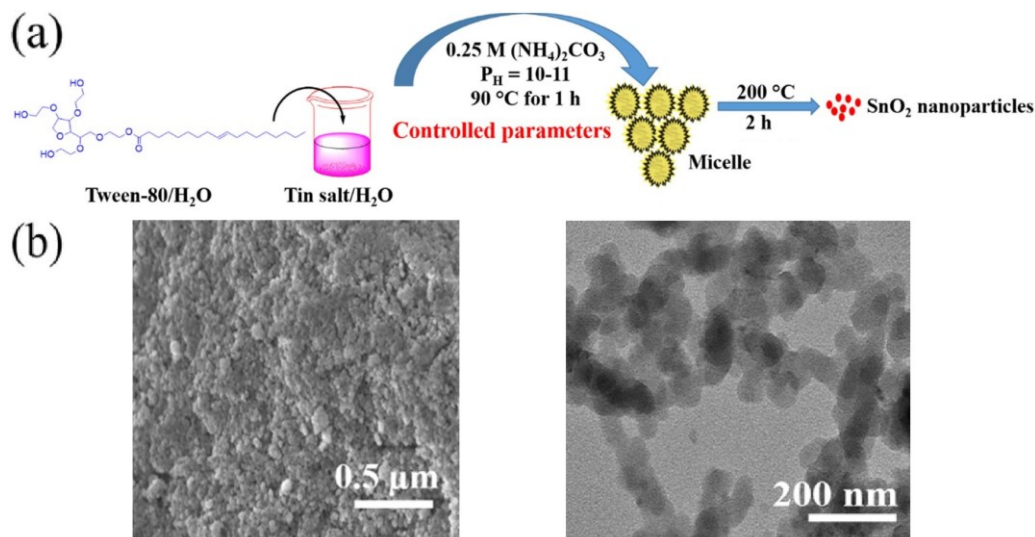


Figure 5 Schematic representation of the synthesis of porous SnO₂ electrode materials built from nanoparticles. (a) Tween-80 surfactant-mediated synthesis of SnO₂ nanoparticles. (b) SEM and TEM images of porous SnO₂ consisting of interconnected nanoparticles.^[56]

Reproduced (adapted) with permission from Ref. [56]. Copyright 2017, Elsevier.

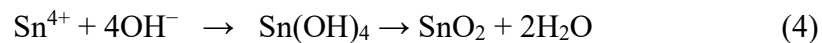
The resulting electrodes showed an initial discharge capacity of 1877.8 mAh g⁻¹, with fast capacity fading within the first 20 cycles to stabilize with prolonged cycling at 641.1 mAh g⁻¹ at a high discharge rate of 200 mA g⁻¹ (doubled in comparison to the majority of examples reported in the literature). The rate capability of the porous nanoparticle electrodes is thereby outstanding, with values of 629, 490, and 340 mAh g⁻¹ at current densities of 300, 500, and 1000 mA g⁻¹, respectively; this is attributed to their open and accessible morphology.^[56] Apart from 0D structures, in the form of nanoparticles, considerable effort was made, in recent years, to fabricate anodes with diverse 1D to 3D morphologies. The goal is to form an optimized electrode–electrolyte interface that enables fast lithium diffusion kinetics from the electrolyte,

but also a maximized utilization of active material by offering short diffusion pathways in nanostructures. The second aim is to fabricate “breathable” structures that can accommodate volume changes induced by the alloying/dealloying reaction during cycling, and therefore, prevent mechanical and electrical disintegration of the active material.

4.3.2 Nanorods

The synthesis of high aspect ratio SnO₂ structures was initially demonstrated by Liu *et al.* in 2001 for an inverse microemulsion system (I μ E).^[57] The reaction conditions, including the choice of precursors and a high calcination temperature (≈ 800 °C), are thereby similar to those used in the molten salt synthetic method widely applied for the formation of nanostructured ceramic powders. Since then, several groups have adapted the concept of I μ E-based synthesis; first with a high or moderate temperature and/or salt-assisted calcination and later also by using a solvo-/ hydrothermal approach at temperatures as low as 150 °C.^[1, 23, 58]

In 2010, Xi and Yi synthesized nanorods with diameters down to 1–1.5 nm that exhibited a strong quantum confinement effect, increasing E_g by about 0.9 eV relative to that of bulk SnO₂.^[59] A main focus of the work, however, was to investigate the nanorod growth mechanism through time-dependent diffraction and high-resolution (HR) TEM measurements. According to Equation (4), the formation of sphere-like SnO₂ nanoparticles is driven by a mild hydrolysis reaction (aqueous urea solution at 90 °C):



Larger cubelike SnO₂ nanoparticles with defined crystal facets evolve from a classical crystallization process known as Ostwald ripening. The 1D nanorod morphology is then obtained without templating agents or long-chain organic solvents through an energetically driven assembly of particles on their (001) facets to reduce the surface energy, ultimately leading to a growth along the [001] orientation. These 1D aggregates of SnO₂ nanoparticles recrystallize to finally form singlecrystalline SnO₂ nanorods.^[59] Examples of the nanorod

morphology employed in SnO₂-based anodes in recent years include the synthesis of SBA-15-templated active material by Jiao *et al.* in 2014.^[60] In this work, a solution of SnCl₂ is used for the infiltration of a mesoporous silica (SBA-15) hard template, which is removed after drying and calcination of the SnO₂ nanorods inside its aligned pores (Figure 6).

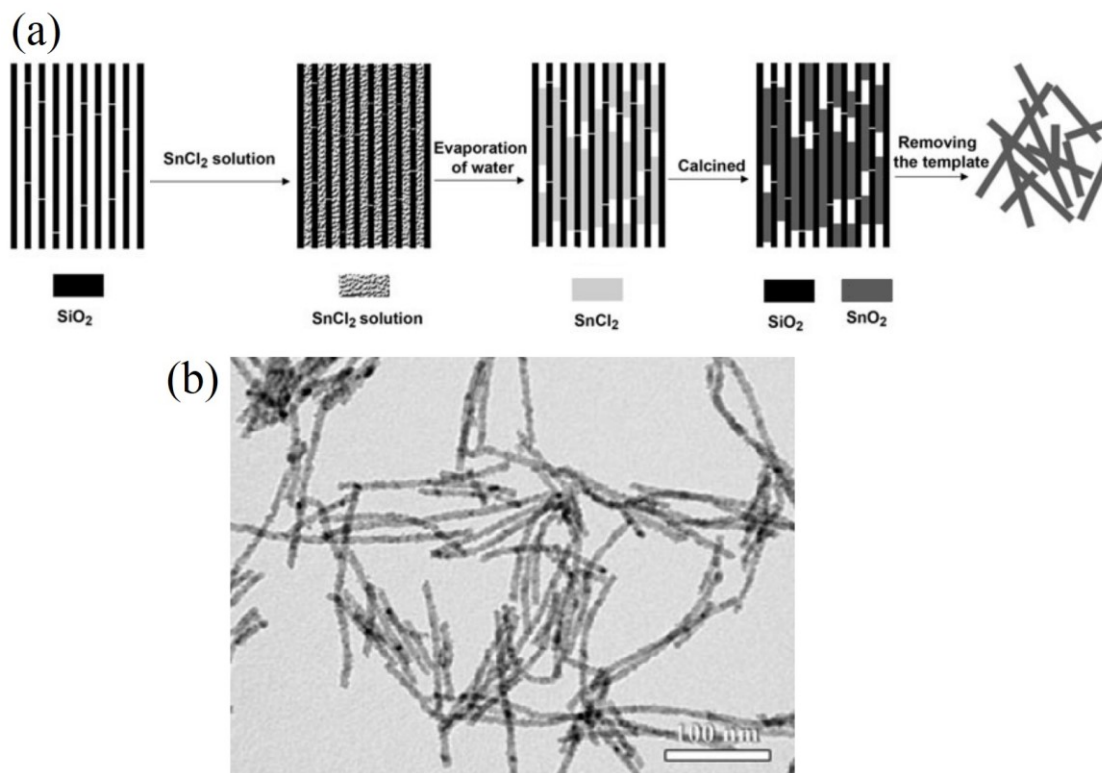


Figure 6 (a) Schematic representation of the proposed mechanism for the formation of rodlike SnO₂ by using a mesoporous SBA-15 silica template, (b) along with a transmission electron micrograph of the product.^[60]

Reproduced (adapted) with permission from Ref. [60]. Copyright 2014, Materials Research Society.

The resulting anode material showed an initial discharge capacity of 1119 mAh g⁻¹ and a reversible capacity of about 700 mAh g⁻¹ (2nd cycle) that declined to about 300 mAh g⁻¹ within 50 cycles at a rate of 100 mAh g⁻¹, which corresponded to a capacity retention of about 43%.^[60]

In 2015, Han *et al.* synthesized larger, highly aligned SnO₂ nanorods in the size range of about 50 × 100–150 nm on a self-produced Na₂Sn(OH)₆ substrate through a one-step, template-free hydrothermal synthetic method.^[61] Single-crystalline rods grew along the [001] orientation on the substrate and exposed (110) facets. An initial discharge capacity of 1930 mAh g⁻¹ was

determined for this material, with a high reversible capacity of around 1000 mAh g⁻¹ that was retained at about 60% at a rate of 100 mA g⁻¹ after 20 cycles (≈600 mAh g⁻¹).

In 2017, Sennu *et al.* used a modified precipitation route, with a related mild hydrothermal treatment and calcination, to obtain bundles of SnO₂ nanorods with dimensions of 2 – 3.5 and 0.2 – 0.3 μm in length and diameter, respectively.^[62] The material morphology resembling marine algae is polycrystalline in nature and built up from individual SnO₂ particles of around 10 – 20 μm (Figure 7).

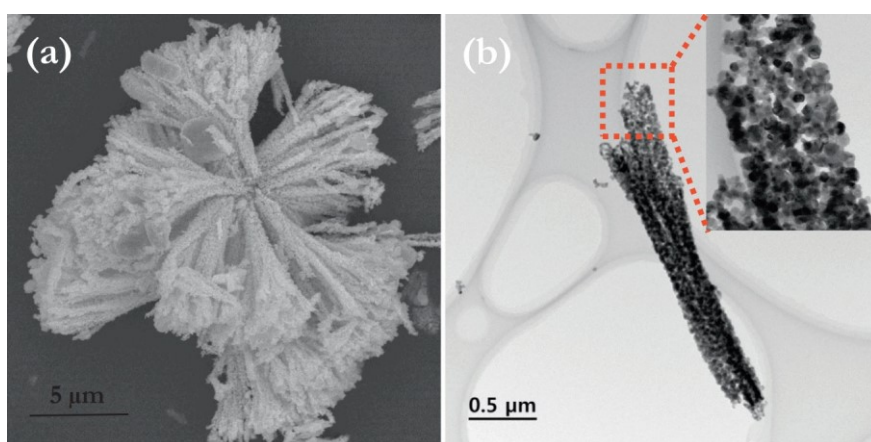


Figure 7 (a) SEM and (b) TEM images of hydrothermally prepared SnO₂ nanorod bundle(s).^[62]

Reproduced (adapted) with permission from Ref. [62]. Copyright 2017, Elsevier B.V.

In corresponding half-cell measurements, a high initial discharge capacity of 2697 mAh g⁻¹ was measured. A reversible capacity of about 695 mAh g⁻¹ fades within 50 cycles to reach about 650 mAh g⁻¹, which represents a remarkably high capacity retention of about 94% (scan rate of 100 mA g⁻¹ and 24 wt% conductive additive).

4.3.3 Nanowires and -tubes

SnO₂ conversion and alloying anodes with 1D nanowire morphology were fabricated by various synthesis approaches in recent years. Wu *et al.* synthesized nanowires of about 200 nm in diameter and several micrometers in length through a carbon-assisted thermal evaporation technique under ambient conditions in a single zone tube furnace.^[63] A promising initial

reversible capacity of about 1350 mAh g⁻¹, with a capacity retention of about 46% (≈620 mAh g⁻¹) after 50 cycles, was achieved at 100 mA g⁻¹. Lee and Kim synthesized SnO₂ nanowire arrays by means of chemical vapor deposition (CVD) with distinct patterns by using a photolithographic process.^[25] The best performing samples of this type showed an initial discharge capacity of about 1600 mAh g⁻¹ and a reversible capacity of about 700 mAh g⁻¹ that faded to about 500 mAh g⁻¹ within 50 cycles (≈71% capacity retention), and down to 400 mAh g⁻¹ within 100 cycles.

In 2017, Lee *et al.* were able to synthesize hierarchically branched SnO₂ nanowires through a two-step CVD method,^[24] which showed a slightly increased performance compared with that of the work of Lee and Kim.^[25] The material also showed initial discharge and reversible capacities of about 1600 and 800 mAh g⁻¹, respectively, with 69% capacity retention (≈550 mAh g⁻¹) after 50 cycles, and about 400 mAh g⁻¹ after 100 cycles at a rate of 0.1C (1C ≅ 400 mA g⁻¹).^[24]

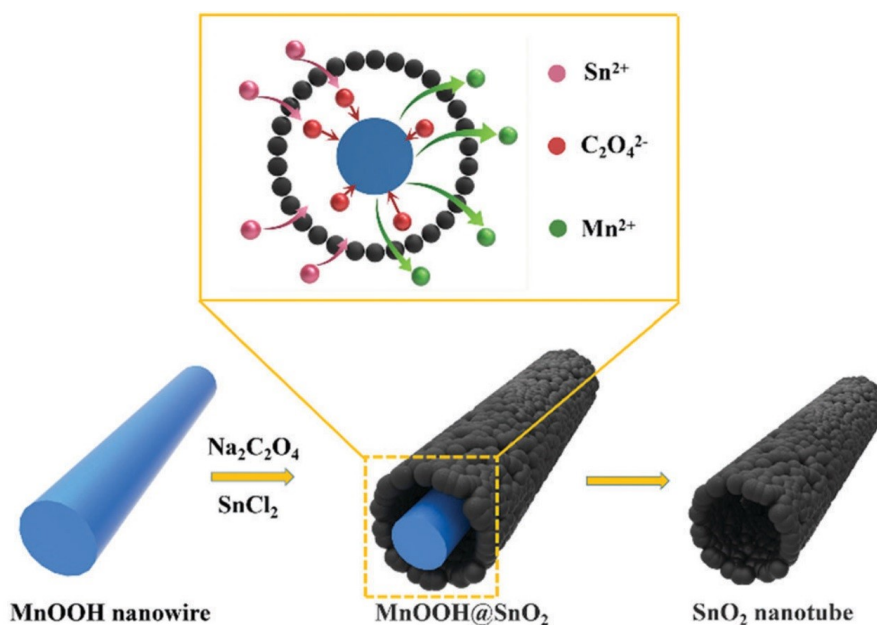


Figure 8 Schematic illustration of the formation of SnO₂ nanotubes through an oxalate-assisted redox etching and precipitating' route.^[64]

Reproduced with permission from Ref. [64]. Copyright 2017, The Royal Society of Chemistry.

Related nanotube SnO₂ morphologies were recently investigated by Han *et al.* in an oxalate-assisted “redox etching and precipitating” route involving MnOOH nanowires and Sn²⁺ ions. SnO₂ nanotubes with a diameter of 200 – 250 nm and several micrometers in length were synthesized (Figure 8).^[64]

Electrode measurements showed an initial discharge capacity of about 2000 mAh g⁻¹ with a high reversible capacity of 1400 mAh g⁻¹ that faded to 700 mAh g⁻¹ within 50 cycles (50% capacity retention). Extended cycling showed a rather high stability of the electrode material, with a discharge capacity of 500 mAh g⁻¹ after 100 cycles at an elevated rate of 500 mA g⁻¹.^[64]

4.3.4 Nanosheets

The 2D SnO₂ nanosheet morphology and its application as a LIB anode material was thoroughly discussed in a review by Chen and Lou in 2012.^[65] The electrochemical performance of nanosheet-based anodes was found to be greatly influenced by the morphology, crystallinity, and phase purity of SnO₂, with a strong effect of the precursors used on the resulting product. Thus, anisotropic growth of SnO₂ with the formation of nanosheets was successfully achieved through hydrothermal synthesis with SnCl₂ as the precursor.^[65] However, the presence of fluoride ions, either by using SnF₂ as the tin oxide precursor or by using an additional fluoride source, such as NH₄F, with the actual tin oxide precursor (e.g., SnCl₂) was shown to lead to the formation of an SnO/SnO₂ mixture (for SnF₂ as the precursor) or phase-pure SnO₂ nanosheets (for NH₄F as an additive), respectively, under hydrothermal conditions.^[66-67]

A recent example for the fabrication of SnO₂ nanosheets is given by the work of Narsimulu *et al.*, who described the surfactant-and template-free hydrothermal and microwave-assisted synthesis of agglomerated SnO₂ nanosheets (Figure 9).^[27] The respective electrodes showed a moderate initial discharge capacity of 1350 mAh g⁻¹, with a reversible capacity of 873 mAh g⁻¹ that faded to 258 mAh g⁻¹ within 50 cycles at a rate of 100 mA g⁻¹.^[27]

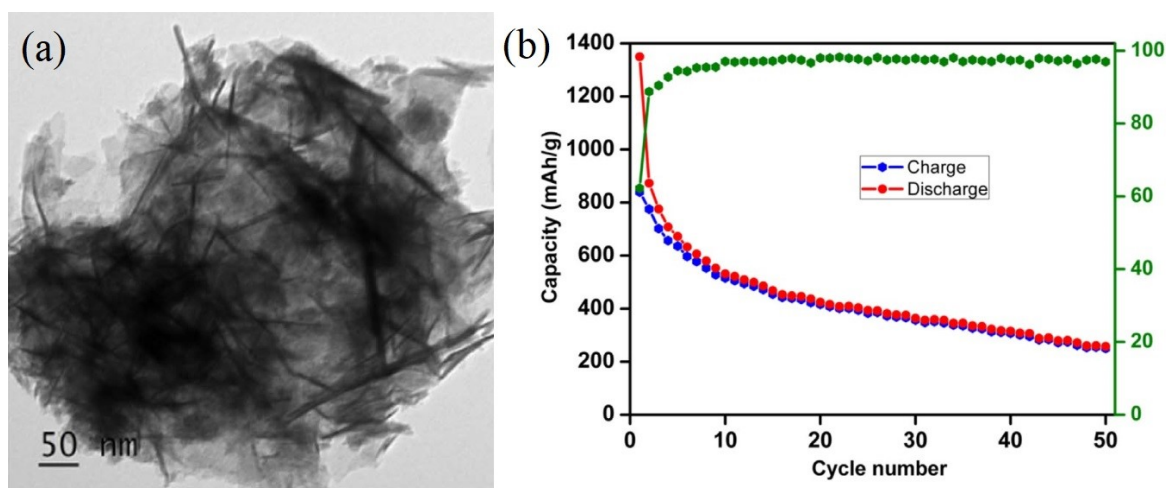


Figure 9 (a) TEM image of agglomerated SnO₂ nanosheets and (b) galvanostatic charge/discharge curves of SnO₂ nanosheet-based LIB anodes at a current density of 100 mA g⁻¹.^[27]

Reproduced (adapted) with permission from Ref. [27]. Copyright 2017, Elsevier and Techna Group.

4.3.5 3D hollow nanostructures

Beyond the 0D, 1D, and 2D SnO₂ materials introduced above, porous 3D morphologies were fabricated in recent years. Among them, hollow and porous nano- and microspheres,^[29, 31] as well as 3D ordered macroporous structures,^[68-69] were synthesized and proposed to possess structural flexibility to counteract fast pulverization of the anode by volume changes induced upon cycling. A promising synthetic route was presented by Li *et al.*, who used negatively charged carbonaceous microspheres (CMSs) prepared through a hydrothermal method that electrostatically bound Sn⁴⁺ ions on their surface.^[29] After calcination in air with simultaneous template removal, hollow dumbbell-shaped microspheres of several micrometers were obtained (Figure 10).

Electrochemical measurements reveal a very high and reversible lithium-ion storage capability of the material of about 1000 mAh g⁻¹ in the second discharge cycle (≈ 1750 mAh g⁻¹ in the first discharge cycle) that is maintained after 100 cycles, with about 600 mAh g⁻¹ at a rate of 500 mA g⁻¹ and still above 500 mAh g⁻¹ with an applied rate of 1 A g⁻¹. The capability of the hollow spherical structures to effectively buffer volume changes and to allow high rate applications is reflected by galvanostatic charge/discharge measurements, with rates of up to

1600 mA g⁻¹ and a resulting capacity of over 500 mAh g⁻¹, which returns to 695 mAh g⁻¹ if the rate is decreased to the initial value of 100 mA g⁻¹.^[29]

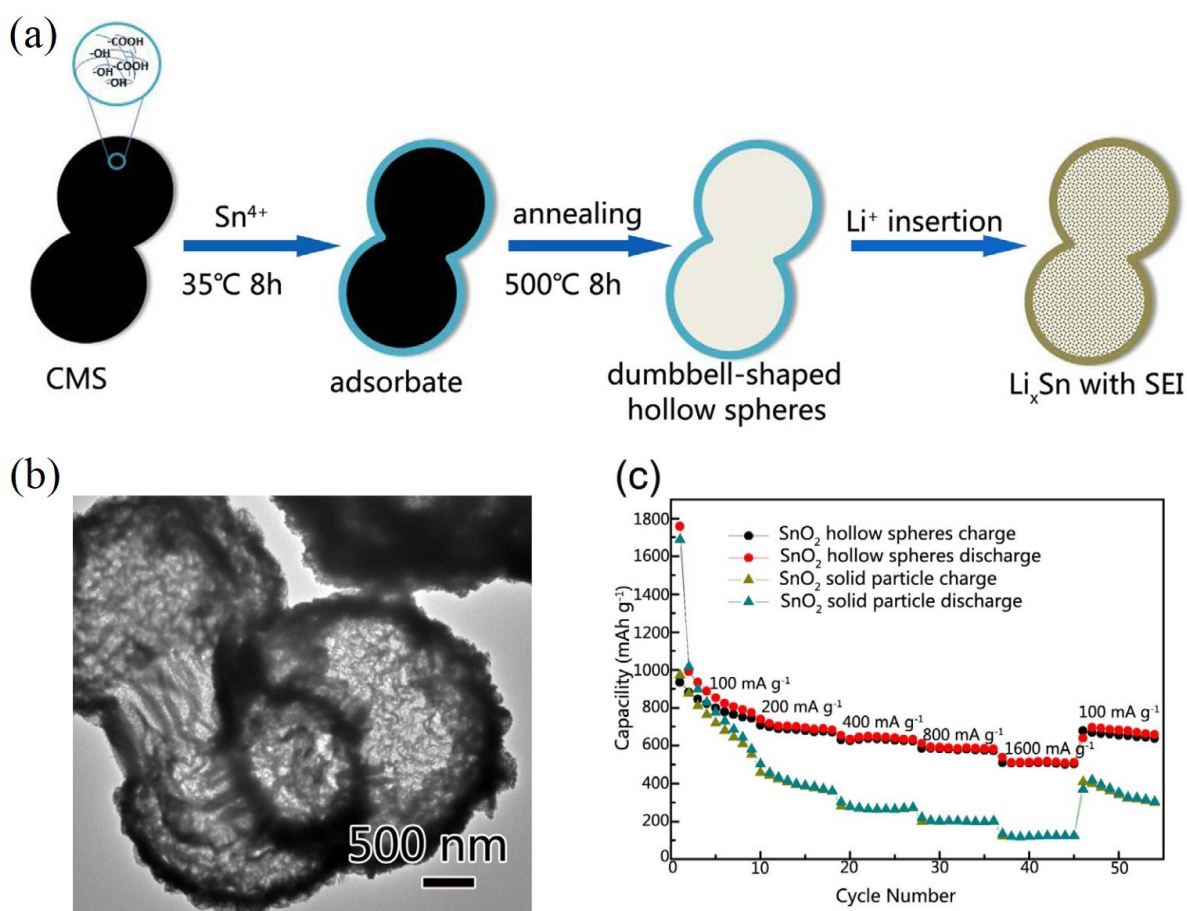


Figure 10 (a) Schematic representation of the synthesis of dumbbell-shaped hollow spheres. (b) TEM image and (c) galvanostatic charge/discharge curves at varying rates (100–1600 mA g⁻¹).^[29]

Reproduced (adapted) with permission from Ref. [29]. Copyright 2018, Elsevier.

Another way to obtain large hollow SnO₂ structures with rodlike shapes was developed by Wang *et al.*^[70] In their synthetic approach, a genetically modified microbial *Escherichia coli* template binds a Sn²⁺ precursor on its surface through electrostatic interactions. Subsequent calcination results in the formation of about 400 × 600 nm rodlike hierarchical SnO₂ structures composed of smaller nanosheets and particles. However, the electrochemical performance of the prepared anodes is moderate, with an initial discharge capacity of about 975 mAh g⁻¹ and a capacity retention fading to 194 mAh g⁻¹ (≈20% of the initial value) after 50 cycles at a rate of 200 mA g⁻¹.

4.4 Doped SnO₂ LIB Anodes

Element doping is a known approach to optimize the electrochemical performance of SnO₂-based electrodes. Doping can lead to a greatly increased electronic conductivity, which is beneficial for the electrode performance.

Pure SnO₂ is a wide band gap semiconductor, with an optical band gap of 3.6 eV at room temperature. It exhibits an intrinsic n-type conductivity due to the presence of shallow donor levels located at 0.46 eV below the conduction band, which is attributed to ionized defects (e.g., unintentional hydrogen atom doping), according to computational studies by Singh *et al.* and more recently by Villamagua *et al.*^[71-72] Fluorine doping is reported to increase the conductivity up to about 5×10^3 S cm⁻¹ by substituting O²⁻ in the crystal structure, and thereby creating shallow donors that enhance the n-type conductivity significantly.^[73]

Due to better synthetic control than that with fluorine doping, p-type doping with Group III atoms (In, Ga, and Al)^[72] or n-type doping with Group V atoms (Sb doping),^[74-75] which creates shallow levels, was thoroughly explored in recent years. In addition to increasing conductivity, transition-metal doping is reported to decrease large volume changes upon lithiation/delithiation.^[76-79]

In recent years, a variety of transitionmetal dopants for SnO₂ were proposed in the literature; these can be divided into two groups: redox-inactive and -active elements that can undergo conversion/alloying reactions with lithium ions in the potential range applicable for SnO₂-based anodes.^[80] Niobium,^[81] titanium,^[82] zirconium,^[80] palladium,^[83] and tungsten^[84] can be assigned to the first group. Doping with these transition-metal ions does not result in an observable gain in capacity because the lithiation/delithiation curves of SnO₂ anode materials remain unchanged, without additional redox features from the doping elements in the respective potential window. However, doped tin oxides show a significantly increased cyclability and rate capability.^[80] The beneficial effect on the cycling performance provided by

both redox-active and inactive transition-metal doping in conversion-type anodes (ZnO, SnO₂) was initially attributed to the decreased crystal size observed upon doping; thus limiting the aggregation of primary nanoparticles and enabling a reversible lithium alloy formation.^[85] Recent investigations suggest that the improved performance of doped tin oxides results from an increase in the conductivity of the active material caused by an additional charge percolation pathway provided by the transition-metal (dopant) ion network in the SnO₂ structure, as well as through an increase in the intrinsic conductivity through newly generated surface oxygen vacancies.^[83-85] The degree of conversion reaction versus side reactions, such as particle aggregation, is thereby correlated with the reaction kinetics, which depend strongly on the electron-transfer properties and local current density.^[83-84]

Apart from increased conductivity, a catalytic effect of transition-metal ions on decomposition of the Li₂O phase is discussed; this further promotes a reversible conversion reaction.^[83] In the context of widely applied SnO₂/graphene composites, transition-metal doping (W-doped SnO₂) has also been shown to reduce the charge-transfer resistance between active material particles and graphene through an increased interaction at the interface.^[84]

Redox-active dopants include manganese,^[80, 86] iron,^[80, 86-88] antimony,^[74, 89-95] cobalt,^[5, 76, 78-80, 86, 96] nickel,^[80] copper,^[80] zinc,^[79-80, 97] and molybdenum^[77]. In addition to the effect of redox-inactive dopants discussed above, their corresponding metal oxides can, in principle, undergo a conversion reaction with lithium over the applied potential range of the anode, resulting in a theoretical gain in capacity (see also section 4.5.4).^[80] However, the increased capacity does not necessarily translate into an increased energy density of a full-cell assembly because dopants (e.g., Cu) can cause a voltage hysteresis; thus lowering the total storable energy.^[80]

Moreover, other dopants or multidoping strategies have been reported, for example, Mg,^[79] Al,^[98] In,^[99] F,^[78, 100-103] N,^[104] P,^[105-106] S/F,^[107] Co/F,^[78] and Co/N^[76].

Among others, cobalt is an interesting redox-active dopant because Co-doped SnO₂ shows a volume buffering effect that is attributed to a reduced and maintained small SnO₂ primary particle size upon cycling. Furthermore, Co-doped SnO₂ demonstrates a measurable gain in capacity versus undoped SnO₂, with a decreased voltage hysteresis and increased coulombic efficiency.

Nithyadharseni *et al.* compared Co-, Mg-, and Zn-doped SnO₂ nanoparticles.^[79] The compounds were prepared through sol-gel synthesis with ethylene glycol, dimethyl ether, and citric acid. They found that cobalt doping led to a superior electrochemical performance.

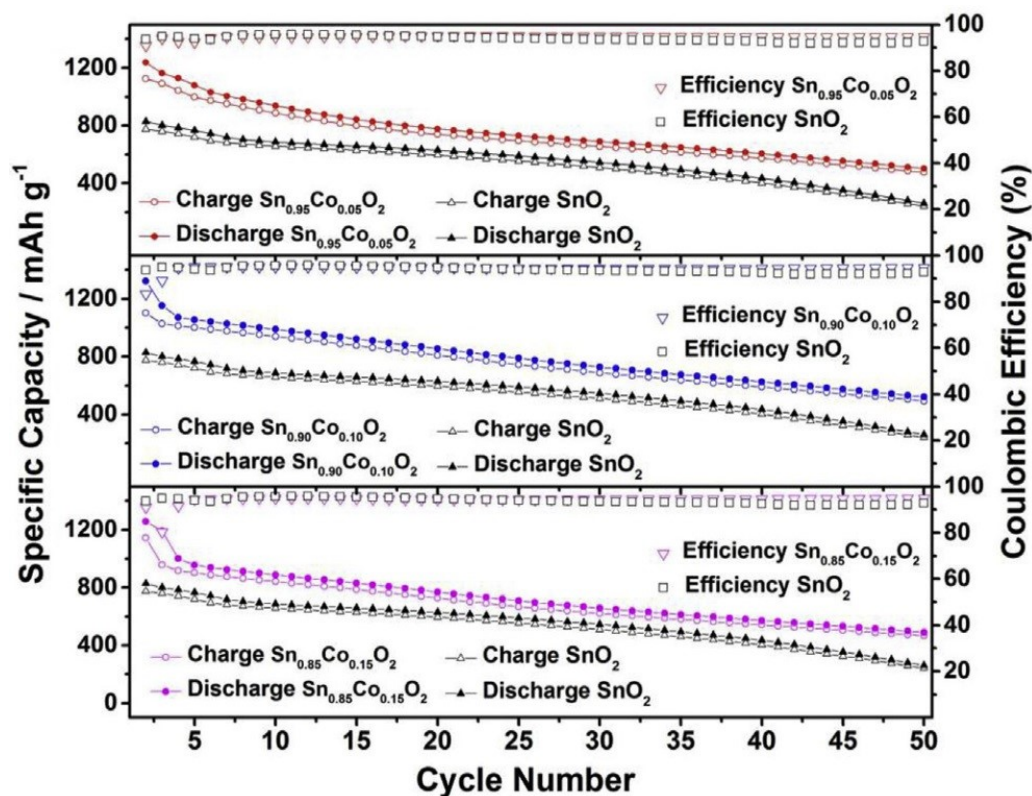


Figure 11 Galvanostatic cycling of Co-doped SnO₂-based anodes. Charge/ discharge curves shown for 5, 10, and 15 at% doped SnO₂ with cycle number.^[5]

Reproduced with permission from Ref. [5]. Copyright 2018, Elsevier Ltd.

The Co-doped electrodes deliver a specific capacity of 573 mAh g⁻¹, compared with 330 mAh g⁻¹ for the undoped sample, after 50 cycles at 60 mA g⁻¹. They attributed this to structural stability and Co-Sn intermetallic interactions. Lebke *et al.* reported similar results

and confirmed that, in their case, Co doping was also superior to that of Nb-, Ti-, Zr-, Fe-, Cu-, Zn-, Mn-, and Ni-doped materials.^[80]

Not only does the nature of the dopant, but also the doping ratio, strongly influence the electrochemical performance, as studied by Ma *et al.*, who compared pure SnO₂ with Co-doped SnO₂ with cobalt concentrations of 5, 10, and 15%.^[5] They found that the particle size decreased with increasing dopant concentration. A dopant ratio of 10% (Sn_{0.90}Co_{0.10}O₂) provided the best cycling stability of four investigated materials. After 50 cycles at 0.1 A g⁻¹, a specific capacity of 493 mAh g⁻¹ was obtained for the Sn_{0.90}Co_{0.10}O₂ sample, compared with 242, 464, and 476 mAh g⁻¹ for SnO₂, Sn_{0.85}Co_{0.15}O₂, and Sn_{0.95}Co_{0.05}O₂, respectively (Figure 11).

Moreover, Ma *et al.* also demonstrated that the electrochemical performance of Sn_{0.9}Co_{0.10}O₂ could be further enhanced by carbon coating.^[5] The influence of carbon and its derivatives on the electrochemical performance of SnO₂/C composites is reviewed in more detail in section 4.5. Very promising results regarding the incorporation of transition metals into SnO₂ were also reported by Wang *et al.*^[88]

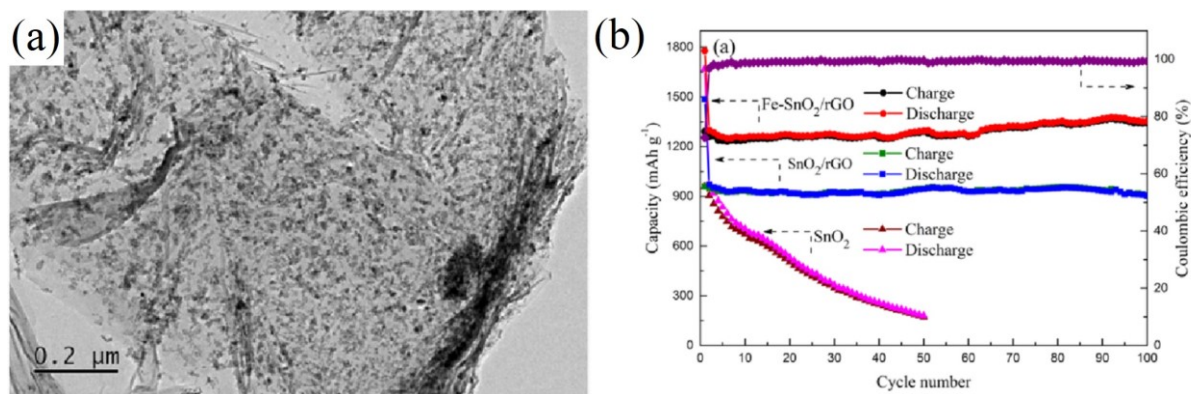


Figure 12 a) TEM image of the Fe@SnO₂/rGO composite and b) cycling performance of bare SnO₂, SnO₂/rGO, and Fe@SnO₂/rGO electrodes at 0.1 A g⁻¹ and the coulombic efficiency of the Fe@SnO₂/rGO electrode.^[88]

Reproduced (adapted) with permission from Ref. [88]. Copyright 2018, Elsevier.

The authors compared the electrochemical performance of an Fe-doped SnO₂/reduced graphene oxide (rGO) nanocomposite with undoped SnO₂/rGO and pristine SnO₂ nanoparticles; all of them synthesized through a wet chemical approach. TEM measurements showed that the 6–8 nm small SnO₂ and Fe@SnO₂ nanoparticles were highly dispersed (Figure 12) over the rGO sheets; this is beneficial for buffering volume changes upon cycling (see section 4.5.3), and hence, influences the cycling performance: the bare SnO₂ electrode reached only 172 mAh g⁻¹ after 60 cycles at 0.1 A g⁻¹ compared with 905 mAh g⁻¹ for the rGO composite after 100 cycles (Figure 12). The Fe@SnO₂/rGO nanocomposite even retained a capacity of 1353 mAh g⁻¹ after 100 cycles. The performance improvement is attributed to iron doping because it leads to better electrical conductivity and encourages the conversion reaction. Consequently, the rate performance of the Fe@SnO₂/rGO nanocomposite is also superior to that of the undoped analogue.^[88]

4.5 SnO₂-Based Composite LIB Anodes

The use of SnO₂ together with a carbonaceous material has positive effects on the electrochemical performance.^[5] The carbonaceous support can buffer volume changes that occur during the alloying/dealloying processes, suppress pulverization and agglomeration of the electrode material, and enhance the overall electrical conductivity in the material.^[37, 39] SnO₂/carbon composites are synthesized either from SnO₂ active material together with a molecular organic carbon precursor or from preformed carbon allotrope based precursors. Beyond the use of carbon, various metal-based components, especially transition-metal chalcogenides, were investigated for the fabrication of composite anodes with SnO₂ for superior electrochemical performance.

4.5.1 Amorphous carbon (SnO₂/C composites)

There are different synthetic routes to obtain an amorphous carbon layer coated on SnO₂ as an active electrode material. One approach is to use both SnO₂ and carbonaceous precursors to form SnO₂ and the carbon layer in situ.^[32, 47, 108-111] A further synthetic route utilizes preformed 3D carbon structures present during SnO₂ synthesis.^[112] A third possible strategy is to synthesize SnO₂ first and subsequently treat it with a carbon precursor.^[33-37, 39, 113-116] This is especially helpful for retaining the morphology of SnO₂ compounds with exceptional structures.

Zhou *et al.*, for example, used the last approach to preserve the “sub-microbox” structure of SnO₂.^[34] They used N-doped carbon, instead of pure carbon, which was supposed to further enhance the conductivity and electrochemical performance. The sub-microboxes were prepared by means of a multistep synthetic strategy in which Fe₂O₃ sub-microcubes served as templates to be covered with SnO₂ particles in an in situ hydrothermal process. The resulting core-shell structure was then covered with a smooth layer of polydopamine, which was converted into N-doped carbon by annealing at 500 °C under nitrogen. Finally, the Fe₂O₃ core

was removed by etching with oxalic acid. The resulting SnO₂/N-doped carbon (SnO₂/NC) sub-microboxes have an average size of 400 nm constructed from nanoparticles with sizes of 4 – 5 nm. Zhou *et al.* could show that SnO₂/NC displayed a better cycling performance and rate capability than that of uncoated SnO₂ sub-microboxes. After 100 cycles at 0.5 A g⁻¹, capacities of 491 and 75 mAh g⁻¹ were obtained for the NC-coated and “pure” SnO₂ sub-microboxes, respectively (Figure 13).

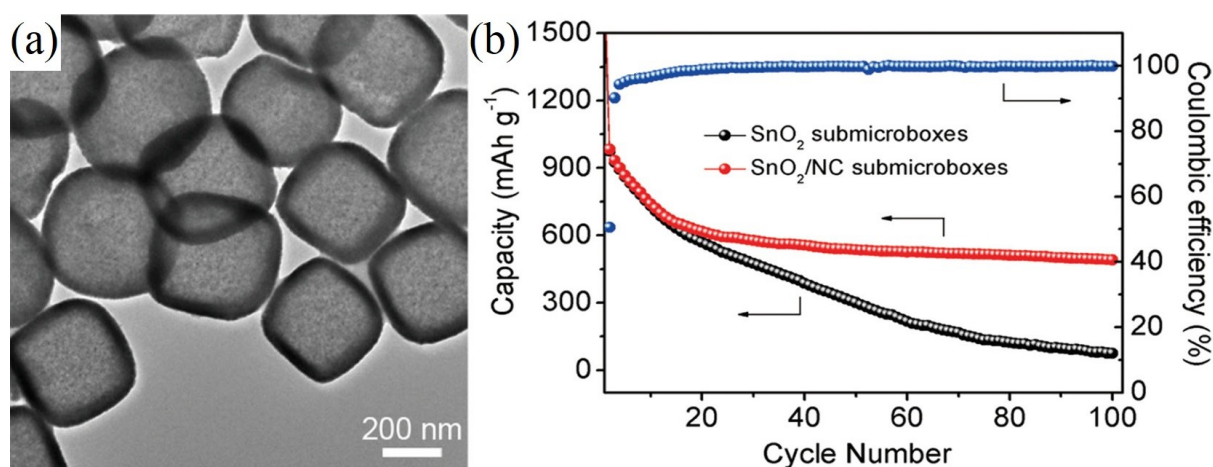


Figure 13 (a) TEM image of SnO₂/NC sub-microboxes and (b) their cycling performance at 0.5 A g⁻¹ compared to SnO₂ sub-microboxes.^[34]

Reproduced (adapted) with permission from Ref. [34]. Copyright 2018, Wiley-VCH.

The authors attributed the superior electrochemical performance of the SnO₂/NC sub-microboxes to the large specific surface area and pore volume, small particle size, and increased conductivity supplied by the NC.

4.5.2 CNTs (SnO₂/C composites)

CNTs are an important example of 1D nanostructured carbon support materials. The use of CNTs together with SnO₂ can add attractive features. The CNTs can improve the electrical conductivity, buffer volume changes during alloying/dealloying with Li ions, and enable fast electron-transfer pathways.^[40-42] The first step in the synthesis of SnO₂/CNT composites is often a harsh treatment of pristine CNTs with strong acids or strong oxidizing agents. This

creates functional groups on the CNTs that can be used to anchor SnO₂ particles.^[42, 117] Such treatment leads, however, to structural damage and decreased electrical conductivity.^[42]

Ma *et al.* reported a synthesis without the oxidation of CNTs.^[42] They used glucose as a mediating agent during hydrothermal synthesis to assist in the in-situ formation of 7 nm SnO₂ particles and serve as a carbon source. The glucose-assisted SnO₂/CNT composites exhibited a superior cycling performance. After 150 cycles at 1 A g⁻¹, a specific capacity of around 900 mAh g⁻¹ was retained, compared with around 450 mAh g⁻¹ for the unmediated SnO₂/CNT composite. Pure SnO₂ exhibits even lower values. The glucose-assisted SnO₂/CNT composites also showed a superior cycling performance at different C rates; this was also attributed to the unique structure and, consequently, enhanced electrical conductivity.^[42]

Cheng *et al.* reported that the Sn-C bond content played a crucial role.^[41] They synthesized SnO₂/CNT composites through a hydrothermal approach by using commercial functionalized multiwalled CNTs followed by an annealing step at different temperatures. The Sn-C fraction strongly depends on this step. The composite annealed at 500 °C exhibited the best cycling and rate performance, compared with those of composites heated at 400 and 600 °C. The first compound demonstrates a capacity of around 600 mAh g⁻¹ after 400 cycles at 0.2 A g⁻¹, whereas the other two have capacities of only 323 and 211 mAh g⁻¹, respectively, after 200 cycles. The authors attributed the promising electrochemical performance to the interplay of the particle size; conductivity; and, most importantly, favorable Sn-C bonding in the SnO₂/CNT composite.

4.5.3 Graphene (SnO₂/C composites)

Graphene is an important 2D carbonaceous support material with exceptional properties, such as very good electrical conductivity, large surface area, high theoretical capacity of 744 mAh g⁻¹, and excellent mechanical properties. The last of these, for example, can help to

avoid aggregation of SnO₂ particles and buffer volume changes during alloying/dealloying with Li ions; thus leading to better cycling stability (Figure 14).^[48, 118-120]

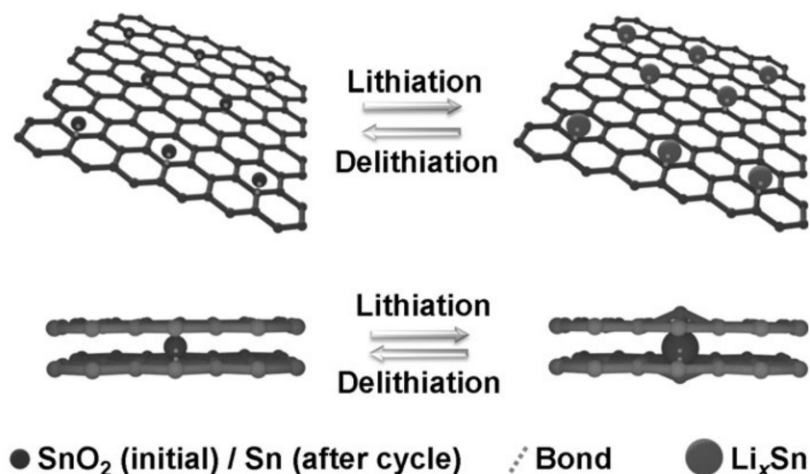


Figure 14 Schematic illustration of lithiation/delithiation processes in a SnO₂ nanocrystal/graphene composite.^[120]

Reproduced (adapted) with permission from Ref. [120]. Copyright 2014, Wiley-VCH.

SnO₂/graphene composites can be obtained by simply mixing SnO₂ with graphene or graphene oxide (GO) or through an in situ method, which is more common.^[50, 121] For the latter, graphene or GO is treated with a tin precursor (e.g., SnCl₄ or SnSO₄) to form SnO₂ particles attached to the graphene or GO surface. In particular, functional groups such as epoxide, carbonyl, or hydroxyl, which can be found on the GO surface, are attractive anchor points for the tin precursors.^[49, 118, 122] If GO has not been reduced to graphene during the synthesis, there are two popular options: the use of a strong reducing agent (e.g., hydrazine) or heating the sample under a reducing or inert atmosphere, for example, H₂ or N₂. The obtained graphene/rGO has a superior conductivity to that of GO.^[49-50, 123-125] Zhang *et al.* showed that this had a positive effect on the electrochemical performance of SnO₂/graphene composites.^[49]

They used a pH-dependent, one-pot hydrothermal method to grow SnO₂ nanoparticles (2 – 5 nm) in situ onto the surface of graphene sheets. The SnO₂/rGO nanocomposite delivers a specific capacity of 942 mAh g⁻¹ after 80 cycles at 100 mA g⁻¹, compared with 827 and

142 mAh g⁻¹ for SnO₂/GO and pristine SnO₂ particles, respectively. The SnO₂/rGO nanocomposite also exhibits a superior rate capability.^[49]

However, SnO₂ particles can aggregate on graphene sheets during cyclic lithiation/delithiation reactions, which could lead to a loss in capacity.^[122] Carbon coating of SnO₂ particles can avoid the formation of such agglomerates, as discussed previously herein. Hence, the use of both carbon coating and graphene as a support is reported to be advantageous for the electrochemical performance.

For example, Zhang *et al.* presented a porous carbon (PC)-coated SnO₂ graphene (rGO/PC/SnO₂) nanocomposite with an improved rate performance and cycling stability to that of an uncoated reference composite.^[122] The SnO₂ nanoparticles are formed in situ on the GO sheets through a solvothermal approach, with a size of around 4 nm. The additionally added glucose served both as a soft template and as a carbon-coating source. The rGO/PC/SnO₂ nanocomposite exhibits a capacity of 1468 mAh g⁻¹ after 150 cycles at 0.1C, relative to 200 mAh g⁻¹ for the uncoated sample. The rate performance of the coated nanocomposite is also superior. The authors argued that this excellent performance was caused by the small particle size, good conductivity, large electrolyte–active material interface, and mechanical stabilization of the nanocomposite.

Importantly, not only SnO₂, but also graphene sheets, can suffer from some kind of aggregation. Graphene sheets tend to restack due to π – π interactions, which implies an inferior compensation of the volume changes of SnO₂ and, as a consequence, a reduced electrochemical performance.^[2, 48] Fabrication of 3D structures and/or the introduction of a buffering layer are reported to prevent the restacking of individual graphene sheets, which has positive effects on the electrochemical performance.^[48, 126] The 3D graphene structures, such as graphene foams, aerogels, or skeletons, can have an increased surface area and more voids to host and/or encapsulate SnO₂ particles. The latter can be beneficial to alleviate volume changes; hence

increasing the structural stability and electrochemical performance of SnO₂/graphene composites.^[126-128]

Liu *et al.*, for example, used a spray-drying approach to prepare a SnO₂/skeleton-structured 3D network of graphene sheets.^[126] Their composite exhibits a specific capacity of 1140 mAh g⁻¹ after 120 cycles, relative to 121 mAh g⁻¹ after 50 cycles for pristine SnO₂ (at 100 mA g⁻¹). They attributed the improved electrochemical performance to the skeleton-like 3D structure, which could buffer the volume changes of SnO₂ and was beneficial for electrolyte transport and the diffusion of lithium ions. Another strategy to improve the performance of SnO₂-based anode materials is to use doped SnO₂ nanoparticles and graphene as a support material.^[74, 82, 84, 88, 90, 96-97, 101-103]

Zoller *et al.* demonstrated that the electrochemical performance of Sb-doped SnO₂ (ATO)/rGO composite was superior to that of SnO₂/rGO and unsupported ATO particles. The composites and pure ATO were synthesized through a microwave-assisted solvothermal approach, which led to SnO₂ and ATO particles of around 3–4 nm in size.

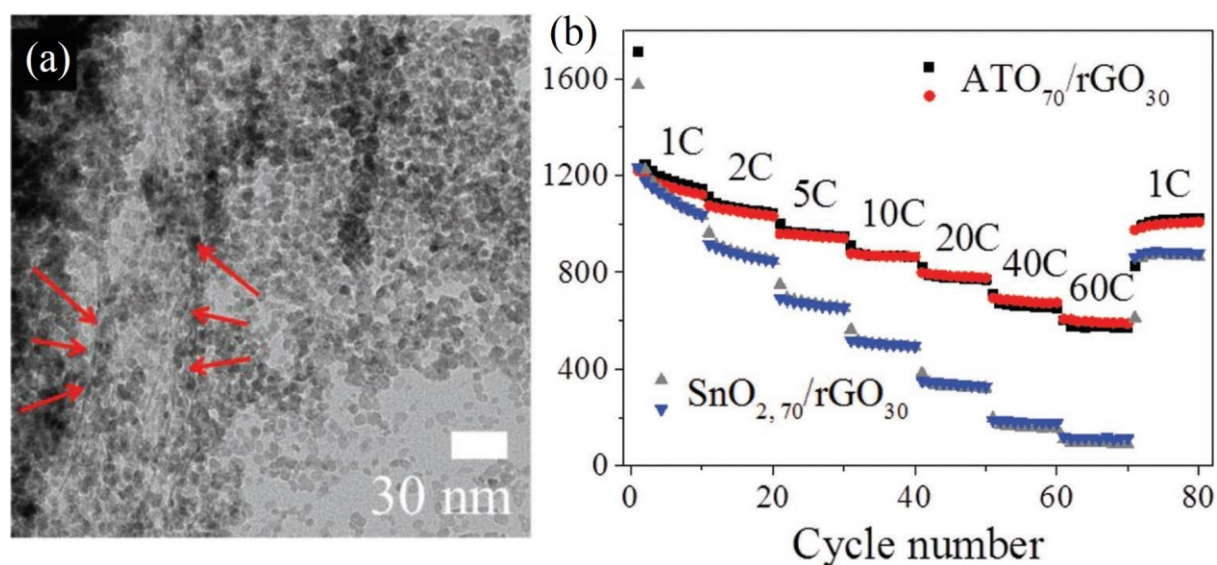


Figure 15 (a) HR-TEM image of Sb:SnO₂ nanoparticles on rGO sheets. (b) Specific capacity of galvanostatic charge/discharge measurements at C rates up to 60C.^[74]

Reproduced with permission from Ref. [74]. Copyright 2018, WileyVCH.

The superior electrochemical performance of the ATO/rGO composite, relative to those of SnO₂/rGO and pure ATO, was especially demonstrated in performance tests at high C rates of up to 60C (Figure 15).^[74]

Additionally, graphene can be functionalized and doped with nitrogen^[17, 129] and/or sulfur,^[130] which can further enhance the electrochemical rate performance of the SnO₂/graphene composites, as demonstrated in the recent work by Wu *et al.*^[130] The authors showed that SnO₂ quantum dots anchored on sulfur-doped rGO (S-rGO) outperformed the analogous undoped rGO composite in terms of rate capability and cycling stability; this was attributed to sulfur doping of graphene resulting in an improved structural stability and better charge and ion conduction at the electrode interface.

4.5.4 SnO₂/non-carbonaceous composites

Much research has been conducted in the field of composite materials of SnO₂ together with metal oxides and sulfides, such as CoS,^[131] SnS,^[132-133] SnS₂,^[134-135] MoS₂,^[136-138] CoO,^[139] Co₃O₄,^[140] CuO,^[141-142] Fe₂O₃,^[143-146] MnO₂,^[147] Mn₂O₃,^[148-149] MoO₃,^[150] NiO,^[151-152] WO₃,^[153-154] TiO₂,^[155-158] Li₄Ti₅O₁₂ (LTO),^[159] VO₂,^[160] SiO₂,^[161-164] or ZnO^[165].

Additionally, SnO₂/C₃N₄^[166] and SnO₂/titanium carbide nanosheets (MXene)^[167] are among reported hybrid materials. The SnO₂ composites are often additionally supported by carbonaceous matrices. In general, the improved electrochemical performance of these composites compared with the phase-pure counterparts is attributed to synergistic effects between the components. In the case of SnO₂/metal sulfide (M_xS_y; M=Sn, Mo) composites, the individual compounds have different band gap energies that enable the formation of heterojunctions.^[134-135, 137, 168]

As mentioned in section 4.4, SnO₂ is a wide band gap (3.8 eV) n-type semiconductor, whereas SnS is a narrow-band-gap (1.3 eV) p-type semiconductor, for example.^[132-133] A p-n heterojunction forms at the interface between SnO₂ and the metal sulfide. This entails holes

diffusing from the metal sulfide to SnO₂ and electrons diffusing in the opposing direction; thereby leading to the formation of a depletion region and the formation of an internal electric field. This enhances charge-transfer kinetics through increased carrier mobilities and thereby eventually results in a higher conductivity. [132-133, 169]

In this context, Ye *et al.* demonstrated that SnO₂/SnS NC composite showed a superior electrochemical performance to those of pure SnS, SnO₂, and SnO₂/NC, reaching values of 550, 300, 200, and 50 mAh g⁻¹, respectively, after 100 cycles at 0.1 A g⁻¹ (Figure 16). [132] The authors also demonstrated an improved rate performance for the SnO₂/SnS/NC nanocomposite; thus underlining the beneficial effect of the formation of the SnO₂/SnS heterojunction on the conductivity of the active material.

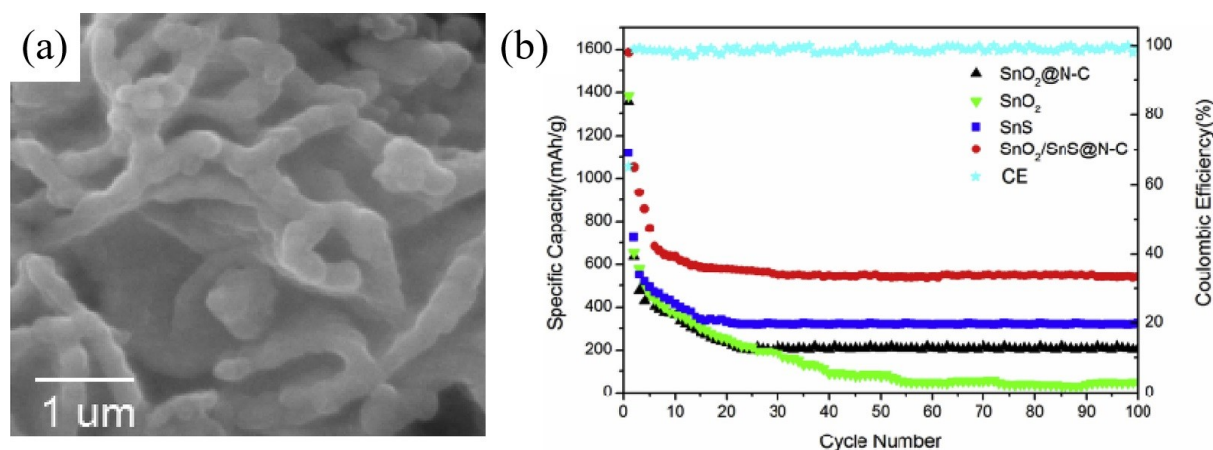


Figure 16 (a) SEM image of the SnO₂/SnS/NC nanocomposite and (b) its cycling performance compared with those of SnS, SnO₂, and SnO₂/NC. [132]

Reproduced (adapted) with permission from Ref. [132]. Copyright 2018, Elsevier B.V.

However, the improved electrochemical performance of SnO₂/metal oxide (M_xO_y; M=Co, Cu, Fe, Mn, Mo, Ni, W, etc.) hybrids compared with that of SnO₂ is associated with sequential lithiation at different potentials of SnO₂ and M_xO_y. [142-143, 146, 150, 152, 154] Consequently, if the SnO₂ nanoparticles are reduced, at the same time, the M_xO_y particles are practically electrochemically inactive and can buffer volume changes and prevent newly formed Sn

particles from aggregating.^[146] Additionally, it was reported that, upon cycling, in situ generated metal nanoparticles from the M_xO_y phase catalytically decomposed the formed Li₂O matrix, which increased the overall capacity and cycling stability.^[139-140, 142-143, 149, 152, 154]

Notably, titanium oxides in SnO₂/M_xO_y composites are “zero” or low-strain materials that display negligible volume changes upon lithiation/delithiation, with the downside of a low specific capacity. Titanium oxides can therefore be used to preserve the nanostructure of SnO₂ by physical confinement and anchoring.^[157-158, 170]

The class of 2D metal carbides and nitrides known as MXene has gained considerable attention for composite formation in recent years.^[171-173] The synergistic effect in SnO₂/MXene anodes is based, on one hand, on the very good electronic conductivity and enhanced lithium-ion transport ability of the layered MXene structures, together with their mechanical flexibility, which is important for buffering the volume changes of SnO₂. On the other hand, SnO₂ prevents the MXene sheets from restacking, and thus, improves the cyclability remarkably.^[167, 174]

This was, for example, successfully demonstrated by Liu *et al.*^[167] They compared the cycling performance of a SnO₂ nanowire/Ti₃C₂(MXene) nanosheet composite, SnO₂ nanowires, and Ti₃C₂ (MXene) nanosheets (Figure 17), and obtained values of 530, 31, and 139 mAh g⁻¹, respectively, after 500 cycles at 1 A g⁻¹. The rate performance measurements also confirmed the improved electrochemical performance of the SnO₂ nanowire/MXene composite.

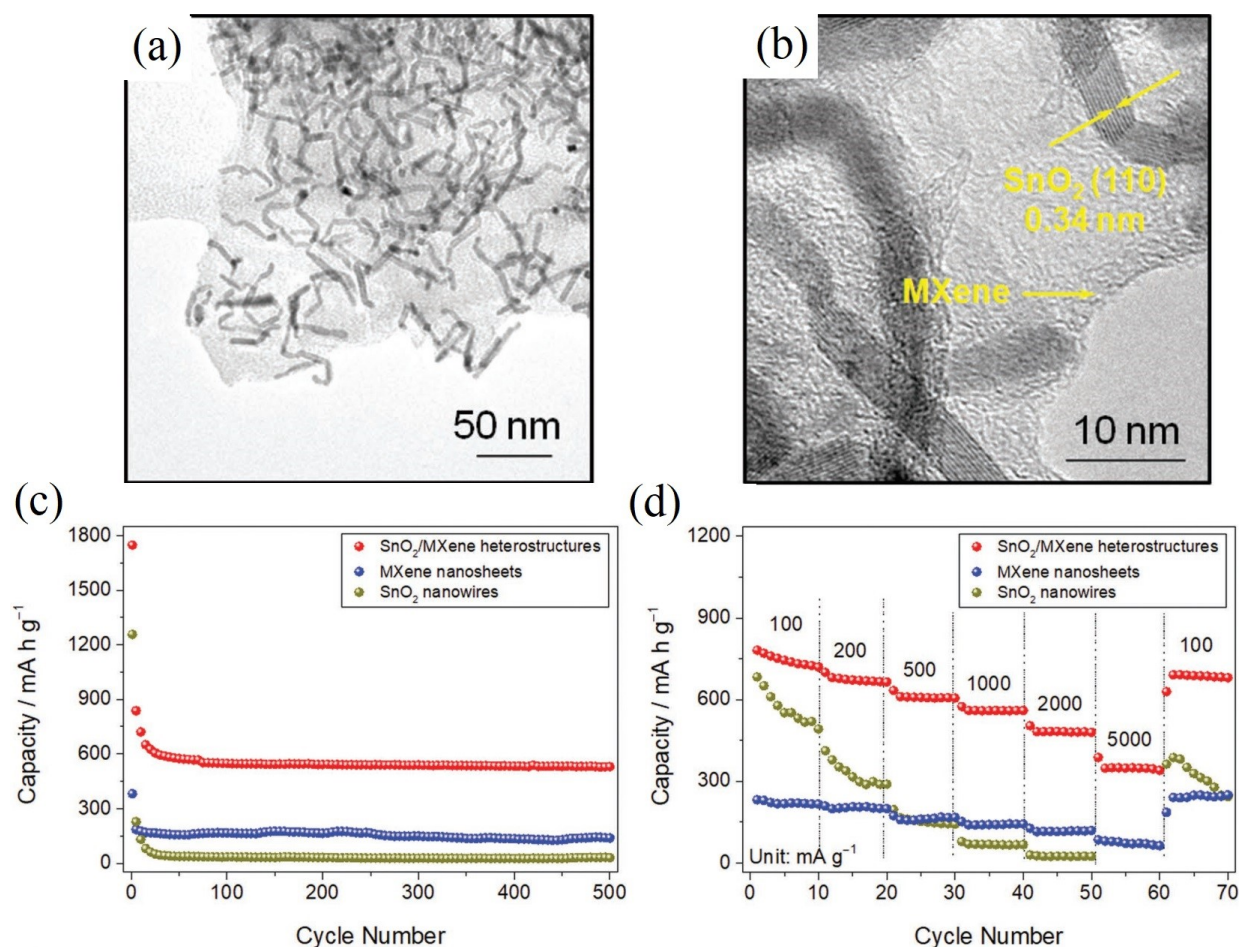


Figure 17 (a) High-magnification TEM and (b) HRTEM images of a SnO₂ nanowire/Ti₃C₂(MXene nanosheet) nanocomposite. (c) Cycling performance at 1 A g⁻¹ and (d) rate capability at different current densities of this composite, in comparison with the phase-pure counterparts.^[167]

Reproduced (adapted) with permission from Ref. [167]. Copyright 2018, Wiley-VCH.

A further example of a SnO₂/non-carbonaceous composite was presented by Idota *et al.*, who embedded redox-active Sn^{II} centers into an amorphous glass-forming matrix of -(M-O)-elements composed of B^{III}, P^V, and Al^{III}, resulting in an amorphous SnM_xO_y composite.^[4] A reversible capacity of >600 mAh g⁻¹ was reported at a charge/discharge current of 48 mA g⁻¹, with a capacity retention of >90% after 100 cycles in a full-cell configuration with a LiCoO₂ (LCO) cathode.

4.6 Full LIB Cell Performance with SnO₂-Based Anodes

Because SnO₂-based materials exhibit very promising results in half-cells (meaning with Na or Li metal foil as the cathode), there is growing interest in testing these materials in full cells to evaluate their possible application in LIBs. Mismatching charge/discharge potentials and kinetics of corresponding anode–cathode materials may result in low performance and/ or fast degradation of the active material.^[175]

Table 1 Overview of lithium ion full cell battery capacities with SnO₂ based anodes

Anode	Cathode	Capacity [mAh g ⁻¹] (Cycle#), Potential window [V]	Current density [A g ⁻¹]	Lit.
SnO ₂ / N,S co-doped graphene	LiCoO ₂ (LCO)	356.4 (100) 1.2 - 3.9	0.1	[176]
S/F doped SnO ₂ /GO	Li[Ni _{0.6} Co _{0.2} Mn _{0.2}]O ₂ (NCM)	~25 ^[a]	0.01	[107]
SnO ₂ /C/ graphene	LiCoO ₂ (LCO)	345.8 (90) 1.2 - 4.2	0.1	[177]
SnSe/SnO ₂ /graphene	LiCoO ₂ (LCO)	312 (50) 1.0 - 3.8	0.1	[168]
SnO ₂ -Fe ₂ O ₃ -C	Li[Ni _{0.6} Co _{0.2} Mn _{0.2}]O ₂ (NCM)	~490 (20) 1.8 - 4.2	0.1	[143]
Zn doped SnO ₂ /rGO	LiFePO ₄ (LFP)	Can light a green/red LED		[97]
SnO ₂ /3D rGO	LiCoO ₂ (LCO)	~300 (100) 1.8 - 4.2	~0.12 (0.2C)	[178]
Pre-treated- SnO ₂ ^[b]	Li _{0.995} V _{0.005} Ni _{0.5} Mn _{1.5} O ₄ (LVNMO)	~475 (50) 3.7 - 4.7	0.1	[62]
SnO ₂ /NC/ TiO ₂	LiFePO ₄ (LFP)	135 50 2.0 - 4.0	0.1	[158]

[a] original electrode area-based value: 2.7 mA h cm⁻² (10)

[b] pre-treatment of anode by two full discharge/charge cycles for anode in order to eliminate irreversible capacity loss (ICL) in full cell

Table 1 presents an overview of performance data for full-cell assemblies employing SnO₂-based anodes and the most commonly used lithium cobalt oxide-based cathode materials.

Wu *et al.* reported a composite consisting of hollow SnO₂ nanospheres, NC, and rGO sheets.[177] This unique structure enabled an encouraging electrochemical performance, also on the full-cell level, with commercial LCO as the cathode material (Figure 18). The full cells were investigated over a potential range of 1.2–4.2 V. After 90 cycles at 0.1 A g⁻¹, a discharge capacity of 346 mAh g⁻¹ (based on the weight of the anode) was reported; this equaled a capacity retention of approximately 67%.

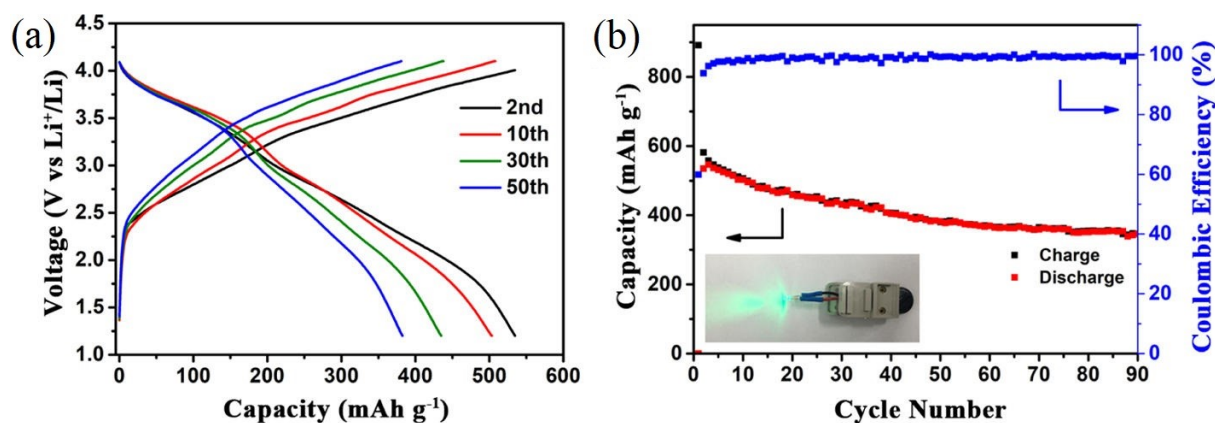


Figure 18 Full-cell LIBs with SnO₂/C/graphene composite as an anode and commercial LCO as a cathode (based on anode mass). (a) Discharge/charge curves, (b) cycling performance at 0.1 A g⁻¹; inset: a light-emitting diode (LED) powered by such a full cell.^[177]

Reproduced (adapted) with permission from Ref. [177]. Copyright 2018, American Chemical Society

4.7 SnO₂-Based Anodes for NIBs and KIBs

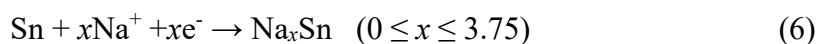
4.7.1 SnO₂-based NIB anodes

Since the first successful demonstration of SnO₂ as a promising anode material in LIBs, there has been growing interest in the use of tin-based anode materials in NIBs and KIBs. The sodiation reactions of SnO₂ are similar to those of lithiation and can be described by Equations (5) and (6), resulting in a total theoretical specific capacity of 1398 mAh g⁻¹.^[3]

Conversion:



Alloying/De-alloying:



The larger ionic diameters of Na⁺ and K⁺ (K⁺ > Na⁺ > Li⁺; 1.38 Å > 1.02 Å > 0.76 Å, respectively), however, aggravate problems caused by volume changes upon charge/discharge, and result in a decreased cycling performance compared with that of Li⁺.^[3, 177, 179-180]

To tackle these problems, strategies successfully employed for SnO₂-based anodes in LIBs, such as nanosizing, 3D structuring, or the introduction of carbonaceous support materials, were also suggested to improve the electrochemical performance in KIBs and NIBs.^[3, 179-181] The use of SnO₂ together with rGO is an example of this development. Jo *et al.* synthesized a SnO₂/rGO composite that exhibited an improved electrochemical performance to that of bare SnO₂ anodes.^[180] In their approach, SnO₂ particles were first solvothermally prepared and then attached to the rGO sheets through a layer-by-layer self-assembly process (Figure 19).

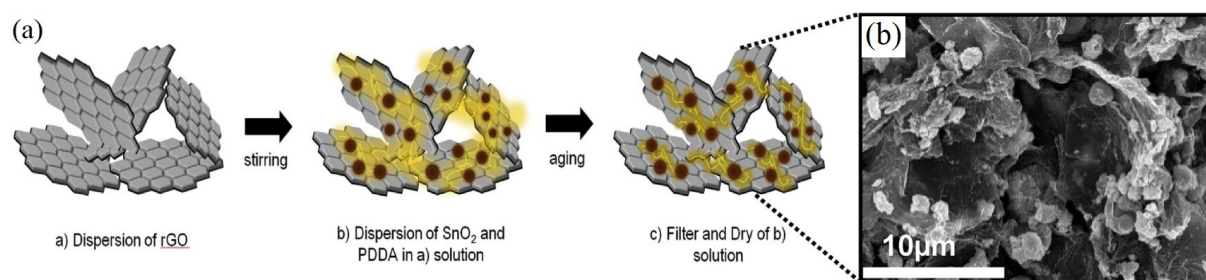


Figure 19 (a) Schematic illustration of the synthetic process for the SnO₂-nanoparticle/rGO composite and (b) a SEM image of the product.^[180]

Reproduced (adapted) with permission from Ref. [180]. Copyright 2017, Elsevier.

Cycling tests at 0.1 A g⁻¹ revealed a capacity of 492 mAh g⁻¹ (capacity retention: 80.2% relative to that of the first charging cycle) for the composite and 194 mAh g⁻¹ (42.5% retention of the initial charge capacity) for SnO₂ after 100 cycles. The rate performance of the SnO₂/rGO composite could also be significantly increased from about 250 to 425 mAh g⁻¹ at 2.4 A g⁻¹ compared with that of bare SnO₂.^[180]

For the construction of a high energy density sodium ion full cell, they further paired the SnO₂-nanoparticle/rGO anode with a C-NaCrO₂ cathode. The resulting NaCrO₂//SnO₂/rGO composite full cells showed an excellent cycling stability at a rate of 0.5C (55 mA g⁻¹), with a capacity retention of 84% after 300 cycles and high rate capability tested up to 10C (87 mAh g⁻¹ based on the cathode mass at 1.1 A g⁻¹).^[180]

A further example of a sodium-ion full-cell assembly was reported by Lee *et al.*^[178] In their work, a SnO₂/3D graphene composite prepared through a hydrothermal approach was paired with self-produced Na₃V₂(PO₄)₃ (NVP) serving as a cathode. The anode material was preactivated before the first cycle to avoid alkaline ion consumption during SEI formation. In the case of the SnO₂/3D graphene-NVP full cells, a specific capacity of 71 mAh g⁻¹ (based on the weight of the anode) was reached after 100 cycles at a rate of 0.05C.

A further increase in performance was achieved by Wang *et al.*, who used a layer-by-layer assembly technique with a porphyrin derivative as an interfacial linker to homogeneously attach SnO₂ crystals about 5 nm in size onto N and S codoped graphene.^[176] By combining it with a NVP/C cathode, a remarkable full-cell capacity of 108.2 mAh g⁻¹ was measured after 100 cycles at a rate of 0.1 A g⁻¹.

Table 2 gives a brief overview of recently published sodium ion full-cell battery performance data.

Table 2 Overview of sodium ion full cell battery capacities with SnO₂-based anodes

Anode	Cathode	Capacity [mAh g ⁻¹] (Cycle#), Potential window [V]	Current density [A g ⁻¹]	Lit.
SnO ₂ / N,S co-doped graphene	Na ₃ V ₂ (PO ₄) ₃ /C (NVP/C)	108.2 (100), 1.0 - 3.9	0.1	[176]
SnO ₂ /3D rGO	Na ₃ V ₂ (PO ₄) ₃ (NVP)	71 (100), 2.5 - 3.8	0.055 (0.5C)	[178]
SnO ₂ /rGO	NaCrO ₂	92 (300), 1.5 - 3.4	0.055 (0.5C)	[180]

4.7.2 SnO₂-based KIB anodes

Inspired by a study on K-Sn alloying and intercalation by Sultana *et al.*,^[182] Wang *et al.* published an in situ TEM and diffraction study on the potassiation of Sn nanoparticles in KIBs.^[183] They observed a high volume expansion of about 197% after an uptake of only one equivalent of K, with the formation of a KSn phase identified by electron diffraction, accompanied by the reversible formation of nanopores and finally pulverization of the active material.^[183] However, in a follow-up study by Ji *et al.*, on dual-ion batteries, with Sn foil as the anode, a higher potassium uptake could be observed by means of ex situ XRD measurements, with the formation of a K₂Sn phase as a final alloying product.^[184]

Large volume changes induced by the potassiation of metallic Sn and accompanying capacity fading caused by electrode pulverization constitute significant challenges for its application as an anode material in KIBs. However, it has been demonstrated that the use of SnO₂-based electrodes, instead of Sn, can significantly mitigate these effects. Similar to lithiation processes, the K₂O matrix formed in the conversion reactions and surrounding the newly formed Sn (nano) particles can buffer volume changes upon alloying and suppress aggregation.^[185]

The positive influence of the K₂O matrix formed around Sn nanoparticles on the structural integrity of the tin oxide based anodes for KIBs, in contrast to metallic Sn-based electrodes, was demonstrated, for example, by Shimizu *et al.* (Figure 20).^[186] They precipitated SnCl₂ precursor, with subsequent thermal oxidation, to obtain a 10 nm sized flowerlike morphology composed of SnO₂ sheets of about 100 nm as primary building blocks. The resulting electrodes exhibit a rather limited potassium storage capability of about 25 mAh g⁻¹ at a rate of 0.025 A g⁻¹, but demonstrate stability over 50 cycles.^[186]

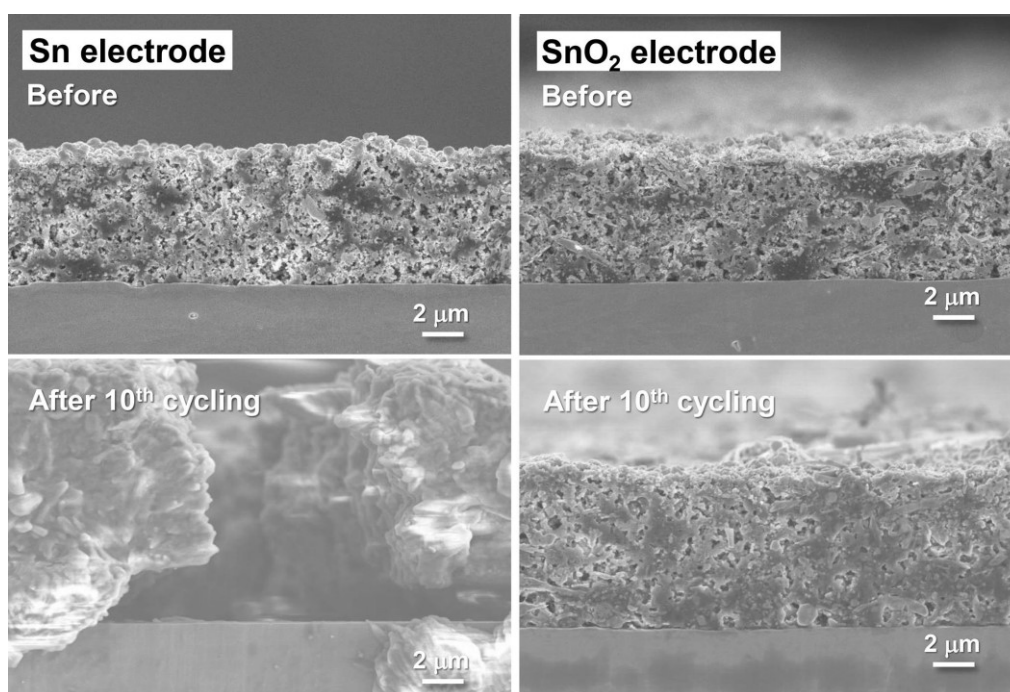


Figure 20 (Cross-sectional field-emission (FE) SEM images of Sn-based anodes in KIB half-cells before and after the 10th cycle under a constant current density of 25 mA g⁻¹).^[186]

Reproduced (adapted) with permission from Ref. [186]. Copyright 2018, The American Chemical Society.

Huang *et al.* recently investigated the potassium-storage capability of SnO₂-carbon nanofibers synthesized by means of electrospinning of a precursor solution containing SnCl₂/polyacrylonitrile (PAN)/polymethylmethacrylate (PMMA), with a subsequent pyrolysis step, to obtain fibers with a diameter of about 490 nm and several micrometers in length.^[181] The focus of their work was on enhancing electrode conductivity by the addition of graphene to the electrospinning process and a synergistic effect on the K⁺ storage behavior among the SnO₂, rGO, and carbon constituents. As a result, the capacity could be increased from about 170 (SnO₂/C) to 250 mAh g⁻¹ (SnO₂/rGO/C) upon cycling at a rate of 0.1 A g⁻¹.^[181]

In a follow-up paper by Huang *et al.*, P doping of SnO₂/rGO/C by phosphoric acid was reported, with the aim of further increasing the electrochemical performance.^[179] The electrospinning process of a GO/(H₃PO₄)/SnCl₄/PVP-containing precursor solution yielded nanofibers of about 150 (non-P-doped) and 120 nm in diameter (P-doped) and micrometers in length. The cycling performance at a rate of 0.1 A g⁻¹ could be increased from about 206 (undoped material) to 285 mAh g⁻¹ (P-doped), both determined for the 60th cycle.

The authors hypothesize that modification with H₃PO₄ had several beneficial effects on the K⁺ diffusion kinetics. These include the formation of a beneficial mesoporous structure, an increase in conductivity, and a widening of the interlayer spacing of rGO, which is reflected in a reversible capacity of 200 mAh g⁻¹ at a high rate of 1 A g⁻¹.^[179]

The best performing SnO₂ anode for KIBs so far, to the best of our knowledge, was recently published by Suo *et al.*, who prepared a binder-free SnO₂-nanosheet/stainless-steel mesh (SSM) anode through solvothermal synthesis with a SnCl₂ precursor in the presence of the mesh (Figure 21).^[185]

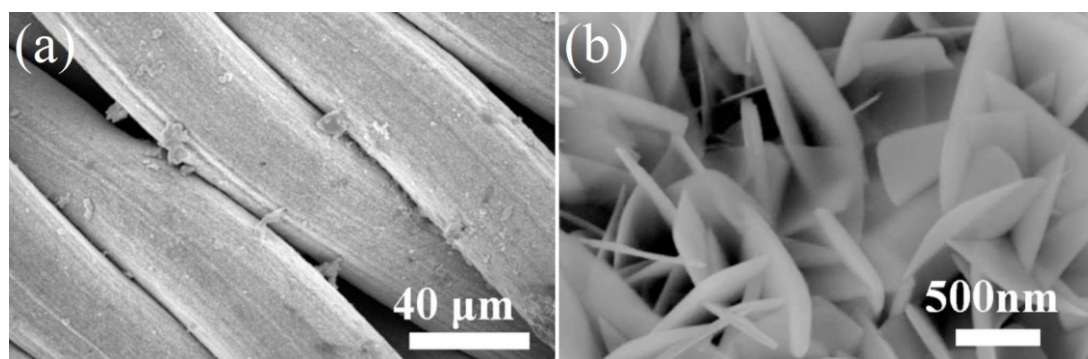


Figure 21 SEM images of (b) SnO₂ nanosheets synthesized on a SSM electrode (a).^[185]

Reproduced (adapted) with permission from Ref. [185]. Copyright 2018, Elsevier.

An initial discharge capacity of 603 mAh g⁻¹ was determined for this material, which stabilized within 5 cycles at a reversible capacity of about 450 mAh g⁻¹. Within 100 cycles, a moderate decrease in capacity to 339 mAh g⁻¹ was observed. The prepared anode material also showed a good rate capability of 125 mAh g⁻¹ at 1 A g⁻¹.

Table 3 presents an overview of SnO₂-based anode materials for application in KIBs tested in half-cell configurations.

Table 3 Overview of electrochemical storage properties of SnO₂ based potassium ion battery anodes (half-cell measurements).

Anode	Capacity [mAh g ⁻¹] (Cycle#), Potential window [V]	Current density [A g ⁻¹]	Lit.
SnO ₂ -carbon nanofibers (SC) (~490 nm Ø)	~170 (60), 0 – 2.5	0.1	[181]
SnO ₂ -rGO-carbon nanofibers (SGC) (~490 nm Ø)	~250 (60), 0 – 2.5	0.1	[181]
SnO ₂ - rGO-carbon (SGC) nanofibers (~150 nm Ø)	206 (60), 0.001 – 3.0	0.1	[179]
Phosphoric acid doped SnO ₂ -rGO-carbon (P-SGC) nanofibers (~120nm Ø)	285 (60), 0.001 – 3.0	0.1	[179]
SnO ₂ nanosheets on Stainless steel mesh (SSM) (binder-free)	351 (100), 0.02 – 2.6	0.05	[185]

4.8 Summary and Outlook

The alloying of alkali ions with tin results in a high theoretical volumetric and gravimetric charge capacity, which is accompanied by volume changes of up to 200^[183]–250 %^[8] (for K⁺ and Li⁺, respectively). Large volume changes pose a major challenge for the mechanical and structural integrity of the electrode upon cycling.^[8, 183] To address this problem, much effort was dedicated to fabricate diverse 0D–3D SnO₂ nanostructures.

Based on an analysis of the most recent developments, herein, we aimed to elucidate the relationship between the nanostructure, synthetic route employed (resulting phase), and the electrochemical performance of phase-pure SnO₂. It can be concluded that the optimum size of SnO₂ nanocrystals, with respect to reversible capacity and cyclability, strongly depends on the exact nature (crystallinity and dominating crystal facets determined by the synthetic conditions) and spatial distribution of nanosized Sn and its surrounding amorphous Li₂O matrix formed during the initial conversion reaction.

From the performance data of recently published articles with differing SnO₂ nanomorphologies and crystallite sizes, we conclude that particles with a size smaller than 10 nm may yield anodes with a high ion-storage capacity and reversibility,^[22] which, however, cannot effectively be enhanced by nanostructuring. As another means to improve the electrochemical performance of SnO₂ anodes, doping with either redox-active or -inactive atoms was explored by many research groups. We conclude that the increase in electrochemical performance (capacity and rate) observed is associated with an increase in conductivity (known for Sb)^[75] induced by a modification of the band structure of the wide band semiconductor SnO₂. Additionally, among a variety of investigated transition metals, cobalt is very promising because Co-doped SnO₂ was also reported to show a volume buffering effect, which might additionally increase its cyclability.^[5] On the electrode level, carbon composite formation in the form of SnO₂/(doped)graphene, SnO₂/CNT, SnO₂/amorphous carbon, and/or their

combination was discussed as a very efficient strategy to improve the anode performance, in terms of storage capacity and cyclability. Graphene-type carbon (undoped rGO^[74] or doped with N,^[17, 129] S,^[130, 187] or P^[179]), with a high surface area and high conductivity, is often used as a support for the homogeneous attachment of nanosized SnO₂-based active materials. Together with a thin layer of amorphous carbon obtained through the pyrolysis of organic molecules in the precursor mixture, this results in a highly conductive, flexible, and porous matrix.^[49-50, 74] The best performing composite anodes with transition-metal-doped nanostructured SnO₂ showed a remarkable reversible capacity of over 1200 mAh g⁻¹ (after 100 cycles at 0.1 A g⁻¹),^[167] which greatly outperformed that of standard graphite anodes (e.g., ≈226 mAh g⁻¹ cycled at 0.5C for 100 cycles with a loading of 10.1 mg cm⁻²)^[188] in classical LIBs by more than a factor of five.

However, regarding the future commercialization of SnO₂-based anodes, two objectives need to be addressed. First, high-capacity and rate-capable anodes, with mass loadings in the range of 10 mg cm⁻²,^[189] need to be realized. Second, and most important, for practical applications is the combination with a suitable high-rate-capable, high-voltage cathode material to obtain full cells with equal or increased energy density to that of classical LIBs employing only carbonaceous anodes.

Future work could include the combination of SnO₂-based anodes with high-voltage cathodes, exceeding the stability window of conventional carbonate electrolytes (EC, ethyl methyl carbonate, diethyl carbonate, etc.), which would require the use of respective additives or ionic-liquid-based electrolytes.^[190] From the perspective of increased operational safety, which is already increased at the anode side by the replacement of graphitic carbon with SnO₂, a solid electrolyte that allows for a high-voltage window (e.g., NASICON-type or LiGe₂(PO₄)₃-type)^[190] would be beneficial. The high rate capability and increased gravimetric capacity, relative to that of graphite electrodes, paired with increased operational safety renders SnO₂-

based anodes interesting for applications in future energy-storage devices in the industrial and automotive sector.

NIBs with SnO₂-based anodes have gained considerable attention in recent years, with the first published examples of full cells. Knowledge transfer from the design of LIBs resulted in the fabrication of full cells with reversible capacities of up to about 108 mAh g⁻¹ after 100 cycles at 0.1C.^[176] It can be expected that research into SnO₂-based anodes for NIBs will intensify due to the general attractiveness of NIBs, such as low cost, high abundance of sodium, low toxicity, and increased safety due to a lack of dendrite formation.

Although research into KIBs with SnO₂-based anodes is very new, rapid progress has been made due to knowledge transfer (synthesis of active materials, anode architecture, and methodology) from LIBs and NIBs with SnO₂-based anodes. However, the processes taking place during reversible potassiation/depotassiation of tin and occurring intermediate phases^[3] still have to be clarified, although the first publications have identified possible K-Sn alloys.^[183, 186] Fabricated KIB half-cells have shown a capacity of up to 351 mAh g⁻¹ for a pure, binder-free SnO₂ nanosheet anode,^[185] and results for the first full cells are expected in the near future.

4.9 References

- [1] S. Chen Jun, W. Lou Xiong, *Small* **2013**, 9, 1877.
- [2] Y. Deng, C. Fang, G. Chen, *J. Power Sources* **2016**, 304, 81.
- [3] B. Huang, Z. Pan, X. Su, L. An, *J. Power Sources* **2018**, 395, 41.
- [4] Y. Idota, T. Kubota, A. Matsufuji, Y. Maekawa, T. Miyasaka, *Science* **1997**, 276, 1395.
- [5] Y. Ma, Y. Ma, U. Ulissi, Y. Ji, C. Streb, D. Bresser, S. Passerini, *Electrochim. Acta* **2018**, 277, 100.
- [6] R. Hu, D. Chen, G. Waller, Y. Ouyang, Y. Chen, B. Zhao, B. Rainwater, C. Yang, M. Zhu, M. Liu, *Energ. Environ. Sci.* **2016**, 9, 595.
- [7] I. A. Courtney, J. Dahn, *J. Electrochem. Soc.* **1997**, 144, 2045.
- [8] J. Y. Huang, L. Zhong, C. M. Wang, J. P. Sullivan, W. Xu, L. Q. Zhang, S. X. Mao, N. S. Hudak, X. H. Liu, A. Subramanian, H. Fan, L. Qi, A. Kushima, J. Li, *Science* **2010**, 330, 1515.
- [9] C.-M. Wang, W. Xu, J. Liu, J.-G. Zhang, L. V. Saraf, B. W. Arey, D. Choi, Z.-G. Yang, J. Xiao, S. Thevuthasan, D. R. Baer, *Nano Lett.* **2011**, 11, 1874.
- [10] C. J. Pelliccione, E. V. Timofeeva, C. U. Segre, *J. Phys. Chem. C* **2016**, 120, 5331.
- [11] I. Sandu, T. Brousse, D. M. Schleich, M. Danot, *J. Solid State Chem.* **2004**, 177, 4332.
- [12] A. Nie, L.-Y. Gan, Y. Cheng, H. Asayesh-Ardakani, Q. Li, C. Dong, R. Tao, F. Mashayek, H.-T. Wang, U. Schwingenschlögl, R. F. Klie, R. S. Yassar, *ACS Nano* **2013**, 7, 6203.
- [13] Y. Cheng, A. Nie, L.-Y. Gan, Q. Zhang, U. Schwingenschlögl, *J. Mater. Chem. A* **2015**, 3, 19483.
- [14] G. Ferraresi, C. Villevieille, I. Czekaj, M. Horisberger, P. Novák, M. El Kazzi, *ACS Appl. Mater. Inter.* **2018**, 10, 8712.
- [15] H.-J. Ahn, H.-C. Choi, K.-W. Park, S.-B. Kim, Y.-E. Sung, *J. Phys. Chem. B* **2004**, 108, 9815.
- [16] K. Zhao, L. Zhang, R. Xia, Y. Dong, W. Xu, C. Niu, L. He, M. Yan, L. Qu, L. Mai, *Small* **2016**, 12, 588.
- [17] X. Zhou, L.-J. Wan, Y.-G. Guo, *Adv. Mater.* **2013**, 25, 2152.
- [18] X. W. Lou, Y. Wang, C. Yuan, J. Y. Lee, L. A. Archer, *Adv. Mater.* **2006**, 18, 2325.
- [19] C. Kim, M. Noh, M. Choi, J. Cho, B. Park, *Chem. Mater.* **2005**, 17, 3297.

- [20] R. Hu, H. Zhang, Z. Lu, J. Liu, M. Zeng, L. Yang, B. Yuan, M. Zhu, *Nano Energy* **2018**, 45, 255.
- [21] L. Yin, S. Chai, F. Wang, J. Huang, J. Li, C. Liu, X. Kong, *Ceram. Int.* **2016**, 42, 9433.
- [22] D. Jiang, C. Wang, L. Sun, X. Xu, B. Wu, X. Chen, *Chem. Lett.* **2017**, 46, 1639.
- [23] D. F. Zhang, L. D. Sun, J. L. Yin, C. H. Yan, *Adv. Mater.* **2003**, 15, 1022.
- [24] S. H. Lee, Y.-R. Jo, Y. Noh, B.-J. Kim, W. B. Kim, *J. Power Sources* **2017**, 367, 1.
- [25] S. H. Lee, W. B. Kim, *J. Power Sources* **2016**, 307, 38.
- [26] J. Wang, N. Du, H. Zhang, J. Yu, D. Yang, *J. Phys. Chem. C* **2011**, 115, 11302.
- [27] D. Narsimulu, S. Vinoth, E. S. Srinadhu, N. Satyanarayana, *Ceram. Int.* **2018**, 44, 201.
- [28] C. Wang, Y. Zhou, M. Ge, X. Xu, Z. Zhang, J. Z. Jiang, *J. Am. Chem. Soc.* **2010**, 132, 46.
- [29] H. Li, Q. Su, J. Kang, M. Huang, M. Feng, H. Feng, P. Huang, G. Du, *Mater. Lett.* **2018**, 217, 276.
- [30] Z. Wen, F. Zheng, K. Liu, *Mater. Lett.* **2012**, 68, 469.
- [31] W. Weng, J. Lin, Y. Du, X. Ge, X. Zhou, J. Bao, *J. Mater. Chem. A* **2018**, 6, 10168
- [32] J. Qin, N. Zhao, C. Shi, E. Liu, F. He, L. Ma, Q. Li, J. Li, C. He, *J. Mater. Chem. A* **2017**, 5, 10946.
- [33] Q. Liu, Y. Dou, B. Ruan, Z. Sun, S.-L. Chou, S. X. Dou, *Chem.,-Eur. J.* **2016**, 22, 5853.
- [34] X. Zhou, L. Yu, X. W. D. Lou, *Adv. Energy Mater.* **2016**, 6, 1600451.
- [35] D. Pham-Cong, J. S. Park, J. H. Kim, J. Kim, P. V. Braun, J. H. Choi, S. J. Kim, S. Y. Jeong, C. R. Cho, *Carbon* **2017**, 111, 28.
- [36] J. S. Chen, Y. L. Cheah, Y. T. Chen, N. Jayaprakash, S. Madhavi, Y. H. Yang, X. W. Lou, *J. Phys. Chem. C* **2009**, 113, 20504.
- [37] J. Read, D. Foster, J. Wolfenstine, W. Behl, *J. Power Sources* **2001**, 96, 277.
- [38] R. Jin, Y. Meng, G. Li, *Appl. Surf. Sci.* **2017**, 423, 476.
- [39] X. Zhou, L. Yu, X. W. Lou, *Nanoscale* **2016**, 8, 8384.
- [40] S. H. Kim, J. Y. Lee, Y. S. Yoon, *J. Alloys Compd.* **2018**, 742, 542.
- [41] Y. Cheng, J. Huang, H. Qi, L. Cao, X. Luo, J. Li, Z. Xu, J. Yang, *Nanoscale* **2017**, 9, 18681.
- [42] C. Ma, W. Zhang, Y.-S. He, Q. Gong, H. Che, Z.-F. Ma, *Nanoscale* **2016**, 8, 4121.

- [43] A. Gupta, S. R. Dhakate, P. Gurunathan, K. Ramesha, *Appl. Nanosci.* **2017**, 7, 449.
- [44] Q. Han, F. Wang, Z. Wang, Z. Yi, Z. Na, X. Wang, L. Wang, *Ionics* **2018**, 24, 1049.
- [45] M. Liu, Y. Liu, Y. Zhang, Y. Li, P. Zhang, Y. Yan, T. Liu, *Sci. Rep.* **2016**, 6, 31496.
- [46] H. Zhang, L. Li, Z. Li, W. Zhong, H. Liao, Z. Li, *Appl. Surf. Sci.* **2018**, 442, 65.
- [47] J. Liang, X.-Y. Yu, H. Zhou, H. B. Wu, S. Ding, X. W. Lou, *Angew. Chem. Int. Ed.* **2014**, 53, 12803.
- [48] X. Liu, T. Ma, L. Sun, Y. Xu, J. Zhang, N. Pinna, *ChemSusChem* **2018**, 11, 1321.
- [49] H. Zhang, L. Gao, S. Yang, *RSC Adv.* **2015**, 5, 43798.
- [50] X. Hu, G. Zeng, J. Chen, C. Lu, Z. Wen, *J. Mater. Chem. A* **2017**, 5, 4535.
- [51] F. Yakuphanoglu, *J. Alloys Compd.* **2009**, 470, 55.
- [52] J. Xie, N. Imanishi, A. Hirano, Y. Takeda, O. Yamamoto, X. B. Zhao, G. S. Cao, *Solid State Ionics* **2010**, 181, 1611.
- [53] H. Ying, W.-Q. Han, *Adv. Sci.* **2017**, 4, 1700298.
- [54] F. Hernandez-Ramirez, A. Tarancon, O. Casals, E. Pellicer, J. Rodriguez, A. Romano-Rodriguez, J. R. Morante, S. Barth, S. Mathur, *Phys. Rev. B* **2007**, 76.
- [55] I. A. Courtney, W. R. McKinnon, J. R. Dahn, *J. Electrochem. Soc.* **1999**, 146, 59.
- [56] M. Usman Hameed, S. Ullah Dar, S. Ali, S. Liu, R. Akram, Z. Wu, I. S. Butler, *Physica E* **2017**, 91, 119.
- [57] Y. K. Liu, C. L. Zheng, W. Z. Wang, C. R. Yin, G. H. Wang, *Adv. Mater.* **2001**, 13, 1883.
- [58] B. Cheng, J. M. Russell, Shi, L. Zhang, E. T. Samulski, *J. Am. Chem. Soc.* **2004**, 126, 5972.
- [59] G. Xi, J. Ye, *Inorg. Chem.* **2010**, 49, 2302.
- [60] Z. Jiao, D. Chen, Y. Jiang, H. Zhang, X. Ling, H. Zhuang, L. Su, H. Cao, M. Hou, B. Zhao, *J. Mater. Res.* **2014**, 29, 609.
- [61] X. Han, X. Han, L. Sun, Q. Liu, W. Xu, L. Li, P. Wang, C. Wang, *CrystEngComm* **2015**, 17, 1754.
- [62] P. Sennu, V. Aravindan, Y.-S. Lee, *Chem. Eng. J.* **2017**, 324, 26.
- [63] S. Wu, M. Wang, C. Li, Y. Zhu, H. Wang, *Mater. Chem. Phys.* **2014**, 147, 184.
- [64] C. Han, B. Zhang, K. Zhao, J. Meng, Q. He, P. He, W. Yang, Q. Li, L. Mai, *Chem. Commun.* **2017**, 53, 9542.
- [65] J. S. Chen, X. W. Lou, *Mater. Today* **2012**, 15, 246.

- [66] J. S. Chen, M. F. Ng, H. B. Wu, L. Zhang, X. W. Lou, *CrystEngComm* **2012**, 14, 5133.
- [67] Y. Masuda, K. Kato, *J. Cryst. Growth* **2009**, 311, 593.
- [68] J. C. Lytle, H. Yan, N. S. Ergang, W. H. Smyrl, A. Stein, *J. Mater. Chem.* **2004**, 14, 1616.
- [69] Z. Li, Y. Tan, X. Huang, W. Zhang, Y. Gao, B. Tang, *Ceram. Int.* **2016**, 42, 18887.
- [70] M. Wang, H. Ping, H. Xie, B. Chen, M. Yan, W. Fang, Z. Fu, *RSC Adv.* **2016**, 6, 81809.
- [71] A. K. Singh, A. Janotti, M. Scheffler, C. G. Van de Walle, *Phys. Rev. Lett.* **2008**, 101, 055502.
- [72] L. Villamagua, A. Stashans, M. Carini, F. Maldonado, *AIP Adv.* **2016**, 6, 115217.
- [73] B. Russo, G. Z. J. A. P. A. Cao, *Appl. Phys. A-Mater.* **2008**, 90, 311.
- [74] F. Zoller, K. Peters, P. M. Zehetmaier, P. Zeller, M. Döblinger, T. Bein, Z. Sofer, D. Fattakhova-Rohlfing, *Adv. Funct. Mater.* **2018**, 28, 1706529.
- [75] V. Skoromets, H. Němec, J. Kopeček, P. Kužel, K. Peters, D. Fattakhova-Rohlfing, A. Vetushka, M. Müller, K. Ganzerová, A. Fejfar, *J. Phys. Chem. C* **2015**, 119, 19485.
- [76] N. Wan, X. Lu, Y. Wang, W. Zhang, Y. Bai, Y.-S. Hu, S. Dai, *Sci. Rep.* **2016**, 6, 18978.
- [77] X. Wang, Z. Li, Z. Zhang, Q. Li, E. Guo, C. Wang, L. Yin, *Nanoscale* **2015**, 7, 3604.
- [78] D. Pan, N. Wan, Y. Ren, W. Zhang, X. Lu, Y. Wang, Y.-S. Hu, Y. Bai, *ACS Appl. Mater. Inter.* **2017**, 9, 9747.
- [79] P. Nithyadharseni, K. P. Abhilash, S. Petnikota, M. R. Anilkumar, R. Jose, K. I. Ozoemena, R. Vijayaraghavan, P. Kulkarni, G. Balakrishna, B. V. R. Chowdari, S. Adams, M. V. Reddy, *Electrochim. Acta* **2017**, 247, 358.
- [80] M. Lübke, D. Ning, C. F. Armer, D. Howard, D. J. L. Brett, Z. Liu, J. A. Darr, *Electrochim. Acta* **2017**, 242, 400.
- [81] S. Zhang, J. Zhang, G. Cao, Q. Wang, J. Hu, P. Zhang, G. Shao, *J. Alloys Compd.* **2018**, 735, 2401.
- [82] C. Ba, L. Shi, Z. Wang, G. Chen, S. Wang, Y. Zhao, M. Zhang, S. Yuan, *Res. Chem. Intermed.* **2017**, 43, 5857.
- [83] P. Zhao, W. Yue, X. Yuan, H. Bao, *Electrochim. Acta* **2017**, 225, 322.

- [84] S. Wang, L. Shi, G. Chen, C. Ba, Z. Wang, J. Zhu, Y. Zhao, M. Zhang, S. Yuan, *ACS Appl. Mater. Inter.* **2017**, 9, 17163.
- [85] D. Bresser, S. Passerini, B. Scrosati, *Energy Environ. Sci.* **2016**, 9, 3348.
- [86] Y. Ma, Y. Ma, G. Giuli, T. Diemant, R. J. Behm, D. Geiger, U. Kaiser, U. Ulissi, S. Passerini, D. Bresser, *Sustainable Energy Fuels* **2018**, 2, 2601.
- [87] F. Mueller, D. Bresser, V. S. K. Chakravadhanula, S. Passerini, *J. Power Sources* **2015**, 299, 398.
- [88] J. Wang, L. Wang, S. Zhang, S. Liang, X. Liang, H. Huang, W. Zhou, J. Guo, *J. Alloys Compd.* **2018**, 748, 1013.
- [89] Y. Wang, I. Djerdj, B. Smarsly, M. Antonietti, *Chem. Mater.* **2009**, 21, 3202.
- [90] X. Zhao, J. Zhang, J. Zhang, C. Gong, X. Gu, Z. Ma, J. Zhou, L. Yu, Z. Zhang, *J. Power Sources* **2015**, 294, 223.
- [91] Y. S. Kim, W. B. Kim, Y. L. Joo, *J. Mater. Chem. A* **2014**, 2, 8323.
- [92] G.-H. An, D.-Y. Lee, Y.-J. Lee, H.-J. Ahn, *ACS Appl. Mater. Inter.* **2016**, 8, 30264.
- [93] Y. Wang, T. Chen, *Electrochim. Acta* **2009**, 54, 3510.
- [94] O. Cevher, U. Tocoglu, H. Akbulut, *Int. J. Hydrogen Energ.* **2014**, 39, 21429.
- [95] J. Cui, S. Yao, J.-Q. Huang, L. Qin, W. G. Chong, Z. Sadighi, J. Huang, Z. Wang, J.-K. Kim, *Energy Storage Mater.* **2017**, 9, 85.
- [96] X. Zhang, X. Huang, X. Zhang, L. Xia, B. Zhong, T. Zhang, G. Wen, *Electrochim. Acta* **2016**, 222, 518.
- [97] P. Dou, Z. Cao, C. Wang, J. Zheng, X. Xu, *Chem. Eng. J.* **2017**, 320, 405.
- [98] C. Wei, G. Zhang, Y. Bai, D. Yan, C. Yu, N. Wan, W. Zhang, *Solid State Ionics* **2015**, 272, 133.
- [99] Y. Liu, A. Palmieri, J. He, Y. Meng, N. Beauregard, S. L. Suib, W. E. Mustain, *Sci. Rep.* **2016**, 6, 25860.
- [100] H.-W. Ha, K. Kim, M. d. Borniol, T. Toupance, *J. Solid State Chem.* **2006**, 179, 702.
- [101] D. Cui, Z. Zheng, X. Peng, T. Li, T. Sun, L. Yuan, *J. Power Sources* **2017**, 362, 20.
- [102] J. Sun, L. Xiao, S. Jiang, G. Li, Y. Huang, J. Geng, *Chem. Mater.* **2015**, 27, 4594.
- [103] P. Shahnawaz, S. Jinhua, Q. Siqu, X. Linhong, Y. Shouke, G. Jianxin, *Nanotechnology* **2017**, 28, 395404.
- [104] L. P. Wang, Y. Leconte, Z. Feng, C. Wei, Y. Zhao, Q. Ma, W. Xu, S. Bourrioux, P. Azais, M. Srinivasan, Z. J. Xu, *Adv. Mater.* **2017**, 29, 1603286.

- [105] Y. Yang, X. Zhao, H.-E. Wang, M. Li, C. Hao, M. Ji, S. Ren, G. Cao, *J. Mater. Chem. A* **2018**, 6, 3479.
- [106] X. Liu, D. Teng, T. Li, Y. Yu, X. Shao, X. Yang, *J. Power Sources* **2014**, 272, 614.
- [107] Y. Luo, D. Yuan, M.-S. Balogun, H. Yang, W. Qiu, J. Liu, P. Liu, Y. Tong, *J. Mater. Chem. A* **2016**, 4, 13431.
- [108] H. Zhou, M. A. Naeem, P. Lv, J. Zhang, Z. Pang, L. Luo, Y. Cai, X. Xia, Q. Wei, *J. Alloys Compd.* **2017**, 711, 414.
- [109] Q. Tian, P. Chen, Z. Zhang, L. Yang, *Carbon* **2017**, 118, 634.
- [110] L. Li, H. Zhang, Z. Li, W. Zhong, H. Liao, Z. Li, *RSC Adv.* **2017**, 7, 34442.
- [111] Y. Cheng, Q. Li, C. Wang, L. Sun, Z. Yi, L. Wang, *Small* **2017**, 13, 1701993.
- [112] Z. Wang, M. A. Fierke, A. Stein, *J. Electrochem. Soc.* **2008**, 155, A658.
- [113] X. Ao, J. Jiang, Y. Ruan, Z. Li, Y. Zhang, J. Sun, C. Wang, *J. Power Sources* **2017**, 359, 340.
- [114] M.-S. Wang, M. Lei, Z.-Q. Wang, X. Zhao, J. Xu, W. Yang, Y. Huang, X. Li, *J. Power Sources* **2016**, 309, 238.
- [115] L. Zu, Q. Su, F. Zhu, B. Chen, H. Lu, C. Peng, T. He, G. Du, P. He, K. Chen, S. Yang, J. Yang, H. Peng, *Adv. Mater.* **2017**, 29, 1701494.
- [116] L. Zhang, G. Zhang, H. B. Wu, L. Yu, X. W. Lou, *Adv. Mater.* **2013**, 25, 2589.
- [117] C. Xu, J. Sun, L. Gao, *J. Phys. Chem. C* **2009**, 113, 20509.
- [118] S. Zuo, D. Li, Z. Wu, Y. Sun, Q. Lu, F. Wang, R. Zhuo, D. Yan, J. Wang, P. Yan, *Electrochim. Acta* **2018**, 264, 61.
- [119] H. Xu, J. Chen, D. Wang, Z. Sun, P. Zhang, Y. Zhang, X. Guo, *Carbon* **2017**, 124, 565.
- [120] F. Ye, B. Zhao, R. Ran, Z. Shao, *Chem.–Eur. J.* **2014**, 20, 4055.
- [121] S.-M. Paek, E. Yoo, I. Honma, *Nano Lett.* **2009**, 9, 72.
- [122] Q. Zhang, Q. Gao, W. Qian, H. Zhang, Y. Tan, W. Tian, Z. Li, H. Xiao, *J. Mater. Chem. A* **2017**, 5, 19136.
- [123] S.-K. Park, S.-H. Yu, N. Pinna, S. Woo, B. Jang, Y.-H. Chung, Y.-H. Cho, Y.-E. Sung, Y. Piao, *J. Mater. Chem.* **2012**, 22, 2520.
- [124] C. Zhu, Z. Chen, S. Zhu, Y. Li, H. Pan, X. Meng, M. Imtiaz, D. Zhang, *Sci. Rep.* **2017**, 7, 3276.
- [125] S. Shi, T. Deng, M. Zhang, G. Yang, *Electrochim. Acta* **2017**, 246, 1104.

- [126] D. Liu, Z. Kong, X. Liu, A. Fu, Y. Wang, Y.-G. Guo, P. Guo, H. Li, X. S. Zhao, *ACS Appl. Mater. Inter.* **2018**, 10, 2515.
- [127] R. Tian, Y. Zhang, Z. Chen, H. Duan, B. Xu, Y. Guo, H. Kang, H. Li, H. Liu, *Sci. Rep.* **2016**, 6, 19195.
- [128] L. Fan, X. Li, B. Yan, X. Li, D. Xiong, D. Li, H. Xu, X. Zhang, X. Sun, *Appl. Energy* **2016**, 175, 529.
- [129] X. Zhou, S. Chen, J. Yang, T. Bai, Y. Ren, H. Tian, *ACS Appl. Mater. Inter.* **2017**, 9, 14309.
- [130] K. Wu, B. Shi, L. Qi, Y. Mi, B. Zhao, C. Yang, Q. Wang, H. Tang, J. Lu, W. Liu, H. Zhou, *Electrochim. Acta* **2018**, 291, 24.
- [131] X. Zhang, Y. Sun, H. Li, J. Guo, X. Zhang, *Ceram. Int.* **2018**, 44, 5569.
- [132] H. Ye, H. Li, F. Jiang, J. Yin, H. Zhu, *Electrochim. Acta* **2018**, 266, 170.
- [133] B. Zhao, H. Zhuang, Y. Yang, Y. Wang, H. Tao, Z. Wang, J. Jiang, Z. Chen, S. Huang, Y. Jiang, *Electrochim. Acta* **2019**, 300, 253.
- [134] L. Yin, S. Chai, J. Huang, X. Kong, L. Pan, *Electrochim. Acta* **2017**, 238, 168.
- [135] H. Li, B. Zhang, X. Wang, J. Zhang, T. An, Z. Ding, W. Yu, H. Tong, *Front. Chem.* **2019**, 7.
- [136] Z. Chen, D. Yin, M. Zhang, *Small* **2018**, 14, 1703818.
- [137] M. Li, Q. Deng, J. Wang, K. Jiang, Z. Hu, J. Chu, *Nanoscale* **2018**, 10, 741.
- [138] H. Zhou, X. Xia, P. Lv, J. Zhang, Z. Pang, D. Li, Y. Cai, Q. Wei, *Part. Part. Syst. Char.* **2017**, 34, 1700295.
- [139] J. H. Choi, G. D. Park, D. S. Jung, Y. C. Kang, *Chem. Eng. J.* **2019**, 369, 726.
- [140] G. D. Park, J.-K. Lee, Y. Chan Kang, *J. Mater. Chem. A* **2017**, 5, 25319.
- [141] J. Y. Cheong, C. Kim, J.-W. Jung, K. R. Yoon, I.-D. Kim, *J. Power Sources* **2018**, 373, 11.
- [142] X. Zhu, H. Shi, J. Yin, H. Zhu, Y. Zhou, Y. Tang, P. Wu, T. Lu, *RSC Adv.* **2014**, 4, 34417.
- [143] J. Choi, W.-S. Kim, S.-H. Hong, *Nanoscale* **2018**, 10, 4370.
- [144] N. Kijima, H. Yomono, T. Manabe, J. Akimoto, K. Igarashi, *Chem. Lett.* **2017**, 46, 886.
- [145] K. Lee, S. Shin, T. Degen, W. Lee, Y. S. Yoon, *Nano Energy* **2017**, 32, 397.
- [146] W. Zeng, F. Zheng, R. Li, Y. Zhan, Y. Li, J. Liu, *Nanoscale* **2012**, 4, 2760.

- [147] Y. Wang, W. Guo, Y. Yang, Y. Yu, Q. Li, D. Wang, F. Zhang, *Electrochim. Acta* **2018**, 262, 1.
- [148] J. Bai, B. Xi, Z. Feng, J. Zhang, J. Feng, S. Xiong, *ACS Omega* **2017**, 2, 6415.
- [149] S. Yuan, D.-l. Ma, S. Wang, Y. Liu, X. Yang, Z. Cao, *Mater. Lett.* **2015**, 145, 104.
- [150] X.-Y. Xue, Z.-H. Chen, L.-L. Xing, S. Yuan, Y.-J. Chen, *Chem. Commun.* **2011**, 47, 5205.
- [151] Z. Wang, J. Mu, Y. Li, J. Chen, L. Zhang, D. Li, P. Zhao, *J. Alloys Compd.* **2017**, 695, 2909.
- [152] L.-L. Xing, C.-X. Cui, B. He, Y.-X. Nie, P. Deng, X.-Y. Xue, *Mater. Lett.* **2013**, 96, 158.
- [153] H. Huang, X. Ju, H. Li, B. Qu, T. Wang, *J. Alloys Compd.* **2018**, 744, 375.
- [154] X.-Y. Xue, B. He, S. Yuan, L.-L. Xing, Z.-H. Chen, C.-h. Ma, *Nanotechnology* **2011**, 22, 395702.
- [155] Q. Tian, L. Li, J. Chen, L. Yang, S.-i. Hirano, *J. Power Sources* **2018**, 376, 1.
- [156] Q. Tian, Y. Mao, X. Zhang, L. Yang, *Appl. Surf. Sci.* **2018**, 447, 408.
- [157] H. Chen, Y. Lu, H. Zhu, Y. Guo, R. Hu, R. Khatoon, L. Chen, Y.-J. Zeng, L. Jiao, J. Leng, J. Lu, *Electrochim. Acta* **2019**, 310, 203.
- [158] D. Wei, S. Zhong, H. Zhang, X. Zhang, C. Zhu, J. Duan, L. Li, Z. Chen, P. Liu, G. Zhang, H. Duan, *Electrochim. Acta* **2018**, 290, 312.
- [159] M. Ding, H. Liu, J. Zhu, X. Zhao, L. Pang, Y. Qin, L. Deng, *Appl. Surf. Sci.* **2018**, 448, 389.
- [160] W. Guo, Y. Wang, Q. Li, D. Wang, F. Zhang, Y. Yang, Y. Yu, *ACS Appl. Mater. Inter.* **2018**, 10, 14993.
- [161] X. Liu, Y. Han, J. Zeng, H. Yang, K. Zhou, D. Pan, *J. Mater. Sci.-Mater. El.* **2018**, 29, 5710.
- [162] X. Xu, H. Zhang, Y. Chen, N. Li, Y. Li, L. Liu, *J. Alloys Compd.* **2016**, 677, 237.
- [163] J. Zhang, L. B. Chen, C. C. Li, T. H. Wang, *Appl. Phys. Lett.* **2008**, 93, 264102.
- [164] H. He, W. Fu, H. Wang, H. Wang, C. Jin, H. J. Fan, Z. Liu, *Nano Energy* **2017**, 34, 449.
- [165] Y. Zhao, X. Li, L. Dong, B. Yan, H. Shan, D. Li, X. Sun, *Int. J. Hydrogen Energ.* **2015**, 40, 14338.
- [166] V. Vo, X. D. Nguyen Thi, Y.-S. Jin, G. Ly Thi, T. T. Nguyen, T. Q. Duong, S.-J. Kim, *Chem. Phys. Lett.* **2017**, 674, 42.

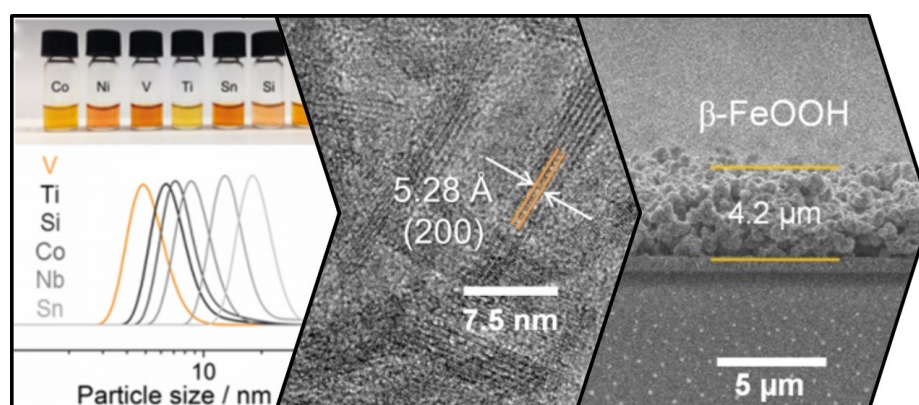
- [167] Y. T. Liu, P. Zhang, N. Sun, B. Anasori, Q. Z. Zhu, H. Liu, Y. Gogotsi, B. Xu, *Adv. Mater.* **2018**, 0, 1707334.
- [168] K. Chen, X. Wang, G. Wang, B. Wang, X. Liu, J. Bai, H. Wang, *Chem. Eng. J.* **2018**, 347, 552.
- [169] Y. Zheng, T. Zhou, C. Zhang, J. Mao, H. Liu, Z. Guo, *Angew. Chem. Int. Ed.* **2016**, 55, 3408.
- [170] Y. Zhou, J. Lei, X. Jin, J. Ni, S. Zhang, K. Du, Z. Wang, *ChemistrySelect* **2018**, 3, 12712.
- [171] J. Yang, W. Bao, P. Jaumaux, S. Zhang, C. Wang, G. Wang, *Adv. Mater. Interfaces* **2019**, 6, 1802004.
- [172] X. Tang, X. Guo, W. Wu, G. Wang, *Adv. Energy Mater.* **2018**, 8, 1801897.
- [173] J. Pang, R. G. Mendes, A. Bachmatiuk, L. Zhao, H. Q. Ta, T. Gemming, H. Liu, Z. Liu, M. H. Rummeli, *Chem. Soc. Rev.* **2019**, 48, 72.
- [174] J. Xiong, L. Pan, H. Wang, F. Du, Y. Chen, J. Yang, C. Zhang, *Electrochim. Acta* **2018**, 268, 503.
- [175] M.-S. Balogun, W. Qiu, Y. Luo, H. Meng, W. Mai, A. Onasanya, T. K. Olaniyi, Y. J. N. R. Tong, *Nano Res.* **2016**, 9, 2823.
- [176] H.-g. Wang, Q. Wu, Y. Wang, X. Wang, L. Wu, S. Song, H. Zhang, *Adv. Energy Mater.* **2019**, 9, 1802993.
- [177] Q. Wu, Q. Shao, Q. Li, Q. Duan, Y. Li, H.-g. Wang, *ACS Appl. Mater. Inter.* **2018**, 10, 15642.
- [178] J.-I. Lee, J. Song, Y. Cha, S. Fu, C. Zhu, X. Li, Y. Lin, M.-K. Song, *Nano Res.* **2017**, 10, 4398.
- [179] Z. Huang, Z. Chen, S. Ding, C. Chen, M. Zhang, *Nanotechnology* **2018**, 29, 375702.
- [180] C.-H. Jo, J.-H. Jo, S.-T. Myung, *J. Alloys Compd.* **2018**, 731, 339.
- [181] Z. Huang, Z. Chen, S. Ding, C. Chen, M. Zhang, *Mater. Lett.* **2018**, 219, 19.
- [182] I. Sultana, T. Ramireddy, M. M. Rahman, Y. Chen, A. M. Glushenkov, *Chem. Commun.* **2016**, 52, 9279.
- [183] Q. Wang, X. Zhao, C. Ni, H. Tian, J. Li, Z. Zhang, S. X. Mao, J. Wang, Y. Xu, *The J. Phys. Chem. C* **2017**, 121, 12652.
- [184] B. Ji, F. Zhang, X. Song, Y. Tang, *Adv. Mater.* **2017**, 29, 1700519.
- [185] G. Suo, D. Li, L. Feng, X. Hou, Y. Yang, W. Wang, *J. Electroanal. Chem.* **2019**, 833, 113.

- [186] M. Shimizu, R. Yatsuzuka, T. Koya, T. Yamakami, S. Arai, *ACS Appl. Energy Mater.* **2018**, 1, 6865.
- [187] J. Li, Y. Wang, J. Wu, H. Zhao, H. Liu, *J. Alloys Compd.* **2018**, 731, 864.
- [188] J. Ma, J. Sung, J. Hong, S. Chae, N. Kim, S.-H. Choi, G. Nam, Y. Son, S. Y. Kim, M. Ko, J. Cho, *Nat. Commun.* **2019**, 10, 475.
- [189] M. Singh, J. Kaiser, H. Hahn, *J. Electrochem. Soc.* **2015**, 162, A1196.
- [190] S. Chen, K. Wen, J. Fan, Y. Bando, D. Golberg, *J. Mater. Chem. A* **2018**, 6, 11631.

5. Nonagglomerated Iron Oxyhydroxide Akaganeite Nanocrystals Incorporating Extraordinary High Amounts of Different Dopants

This chapter is based on the following publication:

Fominykh K.,* Böhm, D.,* Zhang S., Folger A., Döblinger M., Bein, T. Scheu C. and Fattakhova-Rohlfing, D., Chem. Mater., **2017**, *29*, 7223–7233 (* the authors contributed equally to the work)



The TOC graphic shows the high dispersibility of transition metal doped β -FeOOH nanoparticles with hydrodynamic radii around 10 nm. The elongated shape of differently doped nanocrystals is further revealed by high resolution transmission electron microscopy with a scanning electron microscopy cross-sectional image depicting the formation of dense films of nanoparticles with thicknesses over 4 μ m which are employed as anodes in photoelectrochemical water splitting.

Reprinted (adapted) with permission from: Fominykh K., Böhm, D., Zhang S., Folger A., Döblinger M., Bein, T. Scheu C. and Fattakhova-Rohlfing, D., Chem. Mater., **2017**, *29*, 7223–7233. Copyright (2017) American Chemical Society.

5.1 Introduction

Nanostructured iron oxides and oxyhydroxides are intensively investigated materials for different areas of technology because of their semiconducting properties, in combination with abundance, stability, and low toxicity.^[1-8] Akaganeite (β -FeOOH) is one of the iron oxyhydroxide polymorphs that is widely used in electrocatalysis, pigments, and ion-exchange applications.^[7, 9-10] Its crystal structure has a monoclinic symmetry and forms a tunnel matrix of double chains of edge-sharing Fe(III)O₃(OH)₃ octahedra. The channels are usually occupied by Cl⁻ ions or other halogenides that were found to be essential for the stabilization of the tunnel structure and, therefore, the formation of β -FeOOH.^[11-14] Because of the intrinsically elongated tunnel-type structure, akaganeite particles preferentially adopt a rodlike shape.^[1, 15-16] The thermal stability of akaganeite is rather low, and, hence, it can be easily converted to the more stable hematite (α -Fe₂O₃).^[1, 15, 17-19]

An interesting feature of this transformation is that the morphology of the parent akaganeite structure is retained in the resulting hematite.^[1, 17, 20] This fact was exploited by several groups to fabricate anisotropically shaped nanostructured hematite photoanodes exhibiting good performance for photoelectrochemical (PEC) water oxidation.^[1, 6, 8, 15, 18, 21-23]

The most common method to produce akaganeite structures is the hydrolysis of aqueous FeCl₃ solutions at low pH upon heating to 70 - 100 °C.^[4, 12, 24-26] This process is generally very fast, resulting in rather large particles of up to 500 nm in size.^[12, 25]

To obtain smaller particles, other wet chemical routes such as coprecipitation, microemulsion, surfactant mediation, and solvothermal syntheses were applied to effectively reduce the crystal dimensions.^[4, 7, 14-15, 26-27] In this way, particles with morphologies different from the preferred rodlike shape were also obtained, including stars and spheres.^[4, 26, 28] The microemulsion technique was shown to be the most suitable for fabricating very small nanoparticles of only a few nanometers in size.^[26] Although significant progress has been achieved in controlling the

dimensions and shape of the akaganeite nanomorphologies, the dispersibility of the reported nanoparticles still remains a serious issue, as the particles obtained by different methods are typically strongly agglomerated.^[26-28]

Besides nanoscaling, several groups have pursued the development of synthesis strategies that give access to doped akaganeite nanostructures.^[15, 24-25, 28] Doping with different elements is an efficient tool to tune the physicochemical properties of akaganeite and the resulting hematite. Doping of akaganeite with Co(II), Ti(IV), Si(IV) was reported using hydrolysis of aqueous precursor solutions at room temperature, but the maximum doping level was rather low, reaching only ≈ 4 at%.^[24-25, 28]

In the present study, we report the fabrication of very small crystalline and dispersible nonagglomerated akaganeite nanoparticles with varying rodlike shapes, using a novel solvothermal microwave reaction in tert-butanol. The developed method enables incorporation of Co(II), Ni(II), V(III), Ti(IV), Sn(IV), Si(IV), and Nb(V) into the β -FeOOH crystal lattice at very high concentrations reaching more than 20 at%. The maximum doping levels of the nanocrystals are influenced by the nature of the incorporated ions. Furthermore, the particles are suitable for the preparation of porous doped hematite films, which are of interest for applications in photoelectrochemical devices.

5.2 Results and Discussion

Nanocrystals of akaganeite (β -FeOOH) were synthesized via a microwave-assisted solvothermal reaction in *t*-BuOH. The formation of the β -FeOOH phase is strongly dependent on the choice of the Fe precursor (Figure S1 in the Supporting Information). Since halogen ions are necessary to stabilize the tunnel structure of the akaganeite phase, it was formed only when iron chloride ($\text{FeCl}_3 \cdot 6\text{H}_2\text{O}$) was used as a precursor.^[25] The corresponding XRD analysis in Figure S1a in the Supporting Information shows a single-phase β -FeOOH pattern.^[29] For the synthesis of doped nanocrystals, Co(II), Ni(II), V(III), Ti(IV), Sn(IV), Si(IV), and Nb(V) were added to the reaction mixture in different ratios. Later in the text, we use the term “dopant” for these additives, while noting that the levels of their incorporation are many orders of magnitude higher than those encountered in classical semiconductor physics. To approach a reactivity that is at least similar to that of FeCl_3 , the dopant ions were introduced as nitrate or chloride salts in the reaction mixtures, with the exception of Ti(IV), where the highly reactive TiCl_4 was replaced by titanium butoxide.

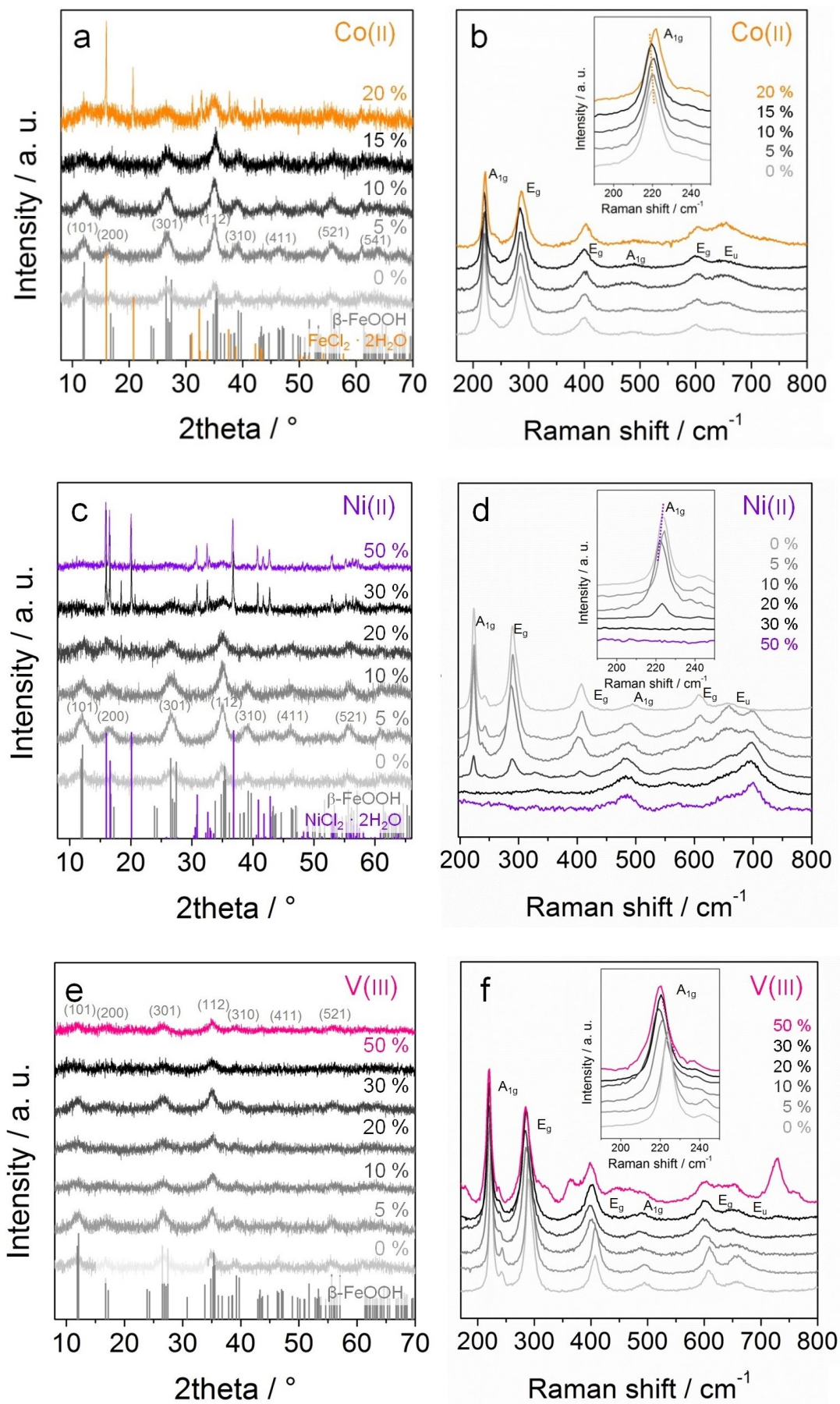
The phase purity of the doped akaganeite materials was investigated by XRD and Raman spectroscopy. The β -FeOOH phase was found to be very sensitive to the Raman laser beam. Laser with a standard intensity ($\lambda = 633 \text{ nm}$, 10 mW) causes a phase transformation of akaganeite to the thermodynamically more stable hematite during the measurement (see the time dependent Raman study in Figure S2 in the Supporting Information), as was also reported by other groups.^[30-31]

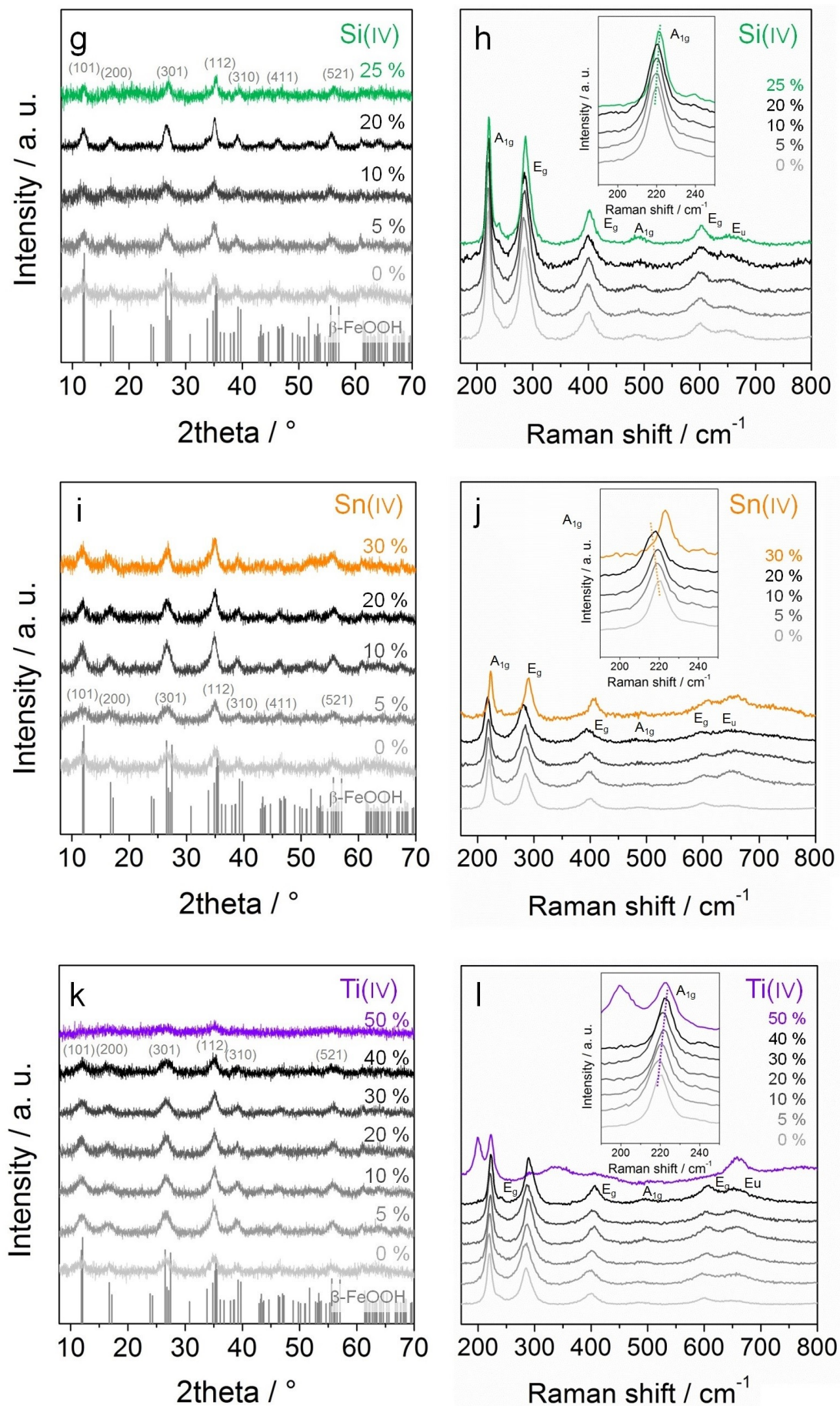
However, the Raman spectra of akaganeite can be acquired only with strongly reduced laser intensity, resulting in low signal level and broadening of Raman bands. Low-intensity Raman spectra of akaganeite doped with Ni(II), V(III) and Sn(IV) ions (Figure S3 in the Supporting Information) indicate the formation of a β -FeOOH phase with crystallinity that decreases with increasing doping ion concentration; however, the further interpretation is ambiguous, because

of a poorly defined shape of broadened Raman bands. Therefore, Raman spectra acquired with high laser intensity (Figures 1b, d, f, h, j, l, and n) are discussed in the following in more detail. Despite the phase transformation, these spectra can be used to see the signatures of secondary phases, because of their high sensitivity to both crystalline and amorphous compounds. In combination with the XRD data, detection of a phase-pure hematite Raman spectrum can be interpreted as an indication of the phase purity of the parent akaganeite sample.

The structure and morphology of β -FeOOH doped with different ions is described in greater detail in the following. The doped samples are labeled as AX , where A is the dopant element and X is the nominal doping concentration (in at%) added to the reaction solution (for example, Sn10 for β -FeOOH doped with 10 at% Sn). The nominal dopant concentration is given, although the incorporated content might be slightly lower, as discussed below.

The addition of $\text{Co}(\text{NO}_3)_2$ to the reaction mixture leads to the formation of a phase structurally similar to β -FeOOH. XRD patterns of Co5-Co15 powders (Figure 1a) show a phase-pure akaganeite structure. In the corresponding Raman spectra, only the hematite bands are visible, which we attribute to the material change induced by the laser beam irradiation, as mentioned above.^[30-31] Furthermore, the peaks in the Raman spectra of Co5-Co15 particles are slightly shifted, compared to that of undoped akaganeite (for instance, the A_{1g} mode at 221 cm^{-1} shifts to 219 cm^{-1}) (see inset in Figure 1b), indicating the successful incorporation of Co(II) ions into the β -FeOOH lattice. Further increase in Co doping over 15 at% leads to the formation of an additional $\text{FeCl}_2 \cdot 2\text{H}_2\text{O}$ phase that is visible in the XRD patterns, as well as in the Raman spectra.





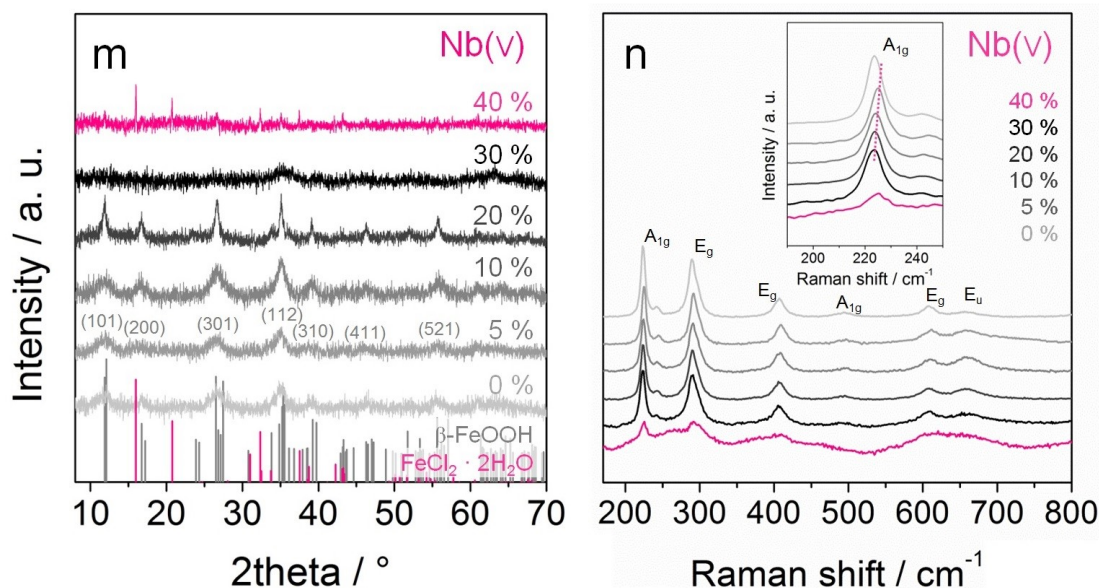


Figure 1 XRD analysis and Raman spectroscopy of doped β -FeOOH nanocrystals. XRD patterns of (a) Co0-Co20, (c) Ni0-Ni50, (e) V0-V50, (g) Si0-Si25, (i) Sn0-Sn30, (k) Ti0-Ti50, and (m) Nb0-Nb40. [Legend of diffraction patterns: β -FeOOH, ICDD File Card No. 01-074-2567 (gray) (monoclinic symmetry, $a = 10.594 \text{ \AA}$, $b = 3.019 \text{ \AA}$, $c = 10.299 \text{ \AA}$, $\alpha = \gamma = 90^\circ$, $\beta = 91.02^\circ$); $\text{FeCl}_2 \cdot 2\text{H}_2\text{O}$, ICDD File Card No. 01-072-0268 (orange and pink); and $\text{NiCl}_2 \cdot 2\text{H}_2\text{O}$, ICDD File Card No. 01-072-0044 (purple).] Raman spectra of (b) Co0-Co20, (d) Ni0-Ni50, (f) V0-V50, (h) Si0-Si25, (j) Sn0-Sn30, (l) Ti0-Ti50, and (n) Nb0-Nb40. The bands at 221 cm^{-1} (A_{1g}), 237 cm^{-1} (E_g), 284 cm^{-1} (E_g), 398 cm^{-1} (E_g), 489 cm^{-1} (A_{1g}), 601 cm^{-1} (E_g), and 649 cm^{-1} (E_u) correspond to hematite.^[30-31] The band at 654 cm^{-1} is assigned to the water vibration mode in $\text{FeCl}_2 \cdot 2\text{H}_2\text{O}$.^[32] The bands at 333 cm^{-1} (E_g), 484 cm^{-1} (T_{2g}), 573 cm^{-1} (T_{2g}), 661 cm^{-1} (E_g), and 701 cm^{-1} (A_{1g}) are characteristic for NiFe_2O_4 .^[33] The bands at 200 , 223 , 337 , and 658 cm^{-1} are assigned to FeTiO_3 .^[34] The numbers in the sample codes (given as a suffix) indicate the respective dopant amounts (in at%).

Similar incorporation of Ni into β -FeOOH is observed when $\text{Ni}(\text{NO}_3)_2$ is added to the reaction mixture. Although only the β -FeOOH phase is observed in XRD patterns (Figure 1c) for up to 20 at% Ni, the Raman spectra (Figure 1d) reveal that a nickel ferrite (NiFe_2O_4)^[33] impurity is formed already at low Ni contents of 5 and 10 at%. However, the hematite bands are still dominating, which indicates that mainly akaganeite was formed in the reaction. The shift of the Raman spectrum to lower wavenumbers from sample Ni0 to sample Ni10 suggests successful incorporation of Ni(II) into the β -FeOOH lattice (inset in Figure 1d). In the spectrum of Ni20, the intensity of the hematite signals is significantly reduced and nickel ferrite is the dominating phase. The absence of the respective nickel ferrite signal in the XRD patterns points to an amorphous character of this phase, which agrees well with literature reports on the crystallization behavior of transition-metal ferrites.^[35-38] At even higher concentrations,

increasing amounts of nonreacted NiCl_2 are detected in the XRD patterns, while presumably amorphous nickel ferrite is observed in the Raman spectra. We attribute the existence of nickel ferrite and nickel chloride impurities in Ni(II)-doped samples and iron chloride impurities in Co(II)-doped samples to the lower oxidation state and the larger ionic radii of dopant ions, compared to Fe(III) in akaganeite, with a mismatch of 14% and 7% for Co(II) and Ni(II), respectively.

Trivalent vanadium was examined as another possible dopant for $\beta\text{-FeOOH}$. XRD patterns of V(III)-doped samples show only the akaganeite structure without formation of other phases for V concentrations of up to 50 at% (Figure 1e). The Raman spectra reveal phase-pure hematite structures for V5-V20 with a shift to lower wavenumbers, suggesting a successful incorporation (Figure 1f).

However, for higher V levels of 30 at% and above, the Raman spectra detect the formation of an additional iron vanadate (FeVO_4) impurity phase that is presumably amorphous, as follows from the absence of corresponding signals in the XRD patterns.^[39-41] Therefore, the maximum doping concentration of V(III) without phase separation is 20 at%, although $\beta\text{-FeOOH}$ is still formed to a large extent, even for high V contents in the range of 30-50 at% and a shift of the Raman signals is observed for up to 30 at%, indicating successful incorporation.

Incorporation of tetravalent Ti, Sn, and Si ions into $\beta\text{-FeOOH}$ is particularly interesting, with regard to the properties of the resulting hematite, for which doping with these elements was shown to greatly improve its photoanode performance in solar water splitting.^[22, 42-47]

Si(IV) and Sn(IV) exhibit similar behavior as dopant elements in the akaganeite structure. For Si0-Si25 and Sn0-Sn30, only the akaganeite phase is present in the XRD patterns (Figures 1g, i), and only the hematite phase is detected in the Raman spectra without phase separation (Figures 1h, j).

XRD patterns of the nanocrystals synthesized in the presence of Ti(IV) (samples Ti5-Ti50) show exclusively reflections of akaganeite (Figure 1k). The Raman spectra in Figure 1l indicate the presence of the hematite structure for Ti5-Ti40, with a continuous shift of the hematite bands to higher wavenumbers for increasing Ti concentration. For a Ti content exceeding 40 at%, the hematite bands vanish almost completely and bands presumably due to amorphous FeTiO_3 arise in the Raman spectra.^[34, 48]

XRD measurements of nanocrystals containing Nb(V) show the presence of only the akaganeite phase for Nb contents of up to 30 at% (Figure 1m). Furthermore, the Raman spectra exhibit a consistent shift of the hematite bands to higher wavenumbers with increasing Nb content, pointing to the successful incorporation of Nb(V) into the $\beta\text{-FeOOH}$ structure (Figure 1n). For even-higher Nb contents (the Nb40 sample), however, the presence of $\text{FeCl}_2 \cdot 2\text{H}_2\text{O}$ and a significantly reduced intensity of the hematite bands are detected in the XRD patterns and in the Raman spectra, respectively.

A remarkable feature of the nanosized akaganeite particles is their excellent dispersibility without agglomeration. Even dried powders can be redispersed in water and water/ethanol ($\text{H}_2\text{O}/\text{EtOH}$) mixtures after the addition of very small amounts of acetic acid in the microliter range (see the Experimental Section for the details). An image of selected particle dispersions with different dopants is shown in the inset in Figure 4a, shown later in this work. The perfect dispersibility of the crystals is demonstrated by DLS measurements (Figure 4a). The DLS data reveal effective particle sizes in the range of 5 - 18 nm, which demonstrates that the type of incorporated dopant affects the apparent size (when keeping the initial precursor concentration constant, e.g., 5 at% of dopant). Note that the size determination with DLS was carried out under the assumption that the particles are spherical. To obtain more detailed information on particle morphology, we also investigated the nanoparticles with HRTEM, HAADF, and ABF-STEM, as shown in Figure 2.

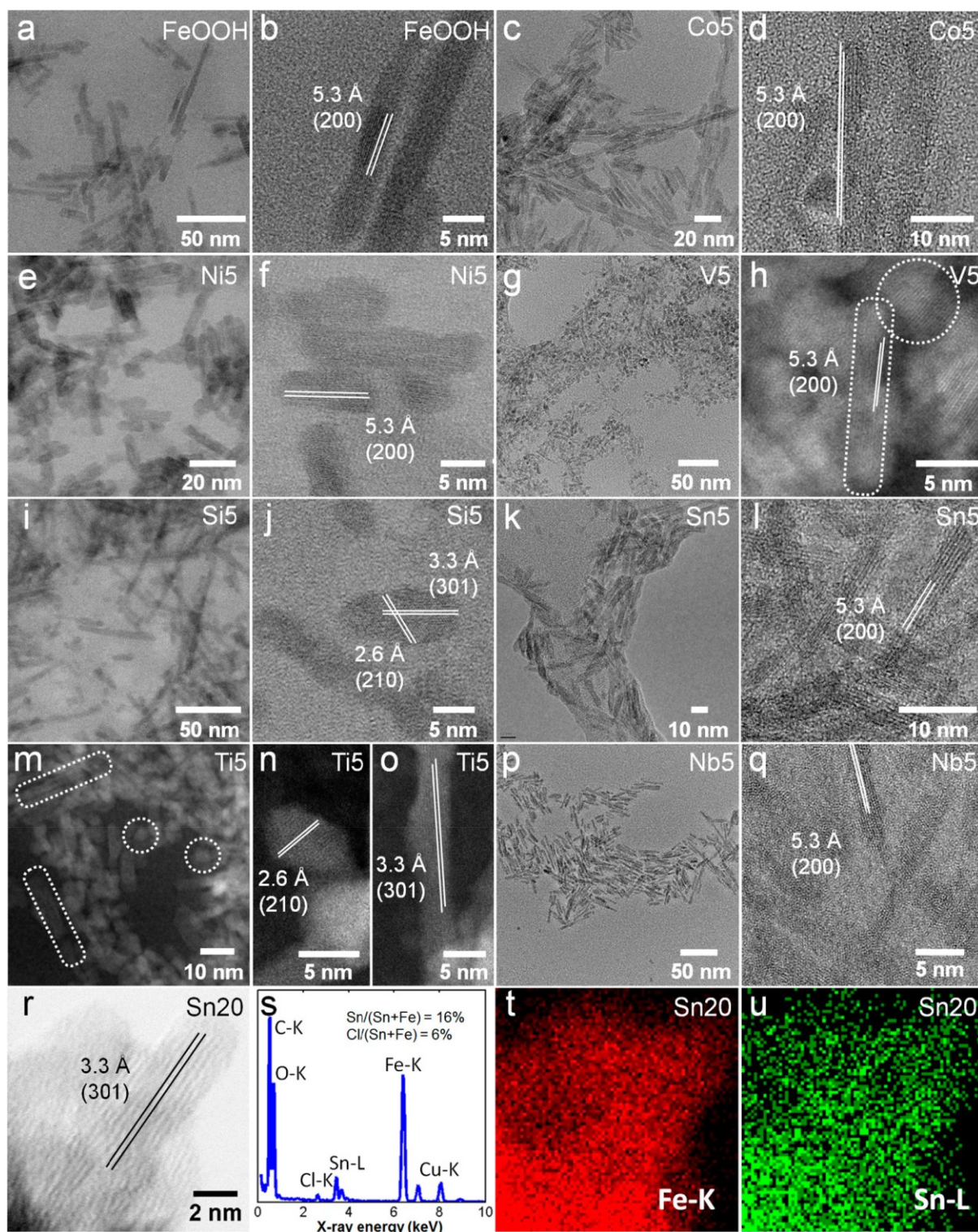


Figure 2 TEM, HRTEM, ABF-STEM, and HAADF-STEM images of either several or a few nanoparticles of (a, b) undoped β -FeOOH, (c, d) doped Co5, (e, f) doped Ni5, (g, h) doped V5, (i, j) doped Si5, and (k, l) doped Sn5 nanocrystals. The other figures show (m) a large number of Ti5 nanoparticles, (n) a single near spherical Ti5 nanoparticle, (o) a single Ti5 nanorod, (p) a large number of Nb5, (q) a few single Nb5 nanocrystals, and (r) a few single elongated Sn20 nanocrystals, respectively. Panel (s) shows the EDS spectrum of Sn20 from the area identified in panel (r) (note that Cu and C stem from the TEM grid), and panels (t) and (u) show the EDS integration maps of the Fe K peak and the Sn L peak, respectively.

According to the HRTEM, HAADF, and ABF-STEM images shown in Figure 2, the morphology of all doped and undoped particles is mostly anisotropic, consisting of nanorods with a width of ≈ 4 nm and varying lengths. Depending on the dopant, the length ranges from ≈ 4 nm, resulting in an almost-spherical shape, to 90 nm, giving the highest aspect ratio. Undoped FeOOH particles shown in Figures 2a and b exhibit a variation in length, mostly between 10 nm and 50 nm. Co5 particles are shown in Figures 2c and d.

The crystals exhibit a rodlike shape with a length of ≈ 20 nm, comprising the major part of the sample. However, a few 90 nm long rods with the same width are also observed. The major portion of the Ni5 particles is 10-20 nm long, which is shorter than the Co5 particles (see Figures 2e and f).

Incorporation of V(III) into β -FeOOH has a stronger impact on the particle morphology. TEM and HAADF-STEM images of V5 in Figures 2g and h reveal that mostly short nanorods with a small aspect ratio of ≈ 1 are formed. In contrast, Si(IV)-doped Si5 particles exhibit a high aspect ratio, with the major portion of the particles being ≈ 50 nm long and 4 nm wide (Figure 2i). Figure 2j shows some of the few smaller Si5 particles, having an almost spherical morphology. Sn5 particles (Figures 2k and 2l) exhibit a rodlike shape 4 nm in width and 15 - 50 nm in length.

The homogeneity of Sn doping into β -FeOOH is verified by EDS acquired in STEM mode, as shown in Figures 2r-u. The nominal Sn20 nanoparticles, having the highest dopant level applied to ultimately create Sn-doped hematite nanostructures, are evaluated to have $16 \text{ at}\% \pm 1.5 \text{ at}\%$ Sn incorporation, which is only slightly lower than the nominal value (see Figure 2s). The incorporation of Ti(IV) has a strong impact on particle morphology, even at low concentrations. The HAADF-STEM images of Ti5 particles in Figures 2m-o show a mixture of large- and small-aspect ratio nanorods (the latter appearing almost spherical). The fraction of nanocrystals with elongated shape is higher than for the V(III)-doped sample. Figures 2n

and o show single particles with different shapes and widths of ≈ 5 nm. The TEM images of Nb5 in Figures 2p and q demonstrate a uniform anisotropic crystal morphology with rod lengths in the range of 10-30 nm. For all of the doped samples, lattice fringes of either the monoclinic (200) or (301) planes are observed parallel to the long axis of the particles, in agreement with the β -FeOOH phase, which has a preferred growth direction parallel to the monoclinic [010] orientation.

There is no apparent correlation between the type of dopants and the nanoparticle morphology. In most cases, an elongated nanorod-like shape was observed. This type of particle morphology was often reported for akaganeite and other iron oxyhydroxides.^[4, 15-16, 25, 27] However, the particle lengths described in the literature are mostly in the range of 100-500 nm, which is much larger than the dimensions observed in the present study. The maximum doping level is dependent on different factors, among which the nature of the dopants, their ionic radii, and the charge are expected to play major roles. Generally, the ions with the same or slightly smaller size than Fe(III) in the akaganeite structure are not expected to cause much lattice strain and should be incorporated more favorably than larger ions. The ionic radii of the different elements investigated in this work are listed in Table 1.

Furthermore, the charge of incorporated ions can influence the maximum doping level. An excess of positive charge induced by ions with an oxidation state higher than +3 can be easily balanced by incorporated Cl^- or OH^- ions in the akaganeite structure, as was discussed by different groups.^[21, 28] In contrast, lower valence ions would reduce the total charge that should be compensated by the uptake of counter cations, which is, however, less preferential.^[49] Thus, despite having the same ionic radius of 83 pm, the maximum doping concentration of Sn(IV) exceeds that of Ni(II), which is in agreement with the preferential incorporation of ions with oxidation states higher than +3.

The main results of the structural and morphological analyses are summarized in Table 1.

Table 1 Precursors and Ionic Parameters of Fe(III) and Dopant Element with Maximum Doping Concentrations and Morphology of Doped β -FeOOH Nanoparticles

Dopant	Ionic radius ^a (pm)	Precursor	Maximum doping concentration ^b (XRD at% / Raman at%)
Fe(III)	78.5	FeCl ₃ ·6H ₂ O	15/15
Co(II)	88.5	Co(NO ₃) ₂ ·6H ₂ O	20/10
Ni(II)	83	Ni(NO ₃) ₂ ·6H ₂ O	50/30
V(III)	78	VCl ₃	50/40
Ti(IV)	74.5	Ti(OBu) ₄	30/20
Sn(IV)	83	SnCl ₄ ·5H ₂ O	25/25
Si(IV)	54	SiCl ₄	30/30
Nb(V)	78	NbCl ₅	

[a] Crystal ionic radii for 6-fold (octahedral) coordinated ions (in high spin state, if applicable).^[50]

[b] Determined as a maximum dopant concentration at which predominantly akaganeite phase was detected.

The higher valence ions Si(IV), Ti(IV), Sn(IV), and Nb(V) are incorporated to a greater extent than Co(II), Ni(II), and V(III). Noticeably, doping contents reported in the literature for bulk akaganeite (≈ 4 at%) are much lower than the values obtained with our synthesis route.^[15, 24-25, 28, 51] Therefore, we can hypothesize that an ultrasmall crystallite size can play an important role in the formation of unusual compositions in mixed oxides and an increased solubility of the dopants.^[24, 42, 51] Several groups have previously described the formation of thermodynamically less stable phases that only exist on the nanoscale.^[52-54]

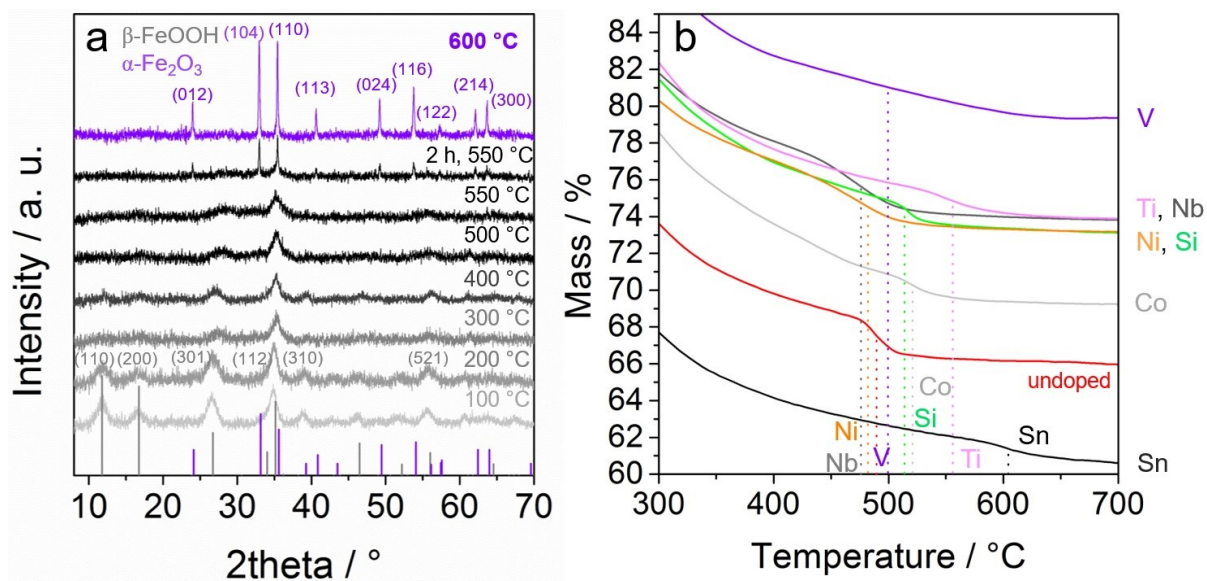


Figure 3 (a) XRD heating study of undoped β -FeOOH particles with a step size of 100 °C below 500 and 50 °C above 500 °C, respectively, and a dwell time of 30 min for each step up to 550 °C. (b) TGA curves of undoped and doped β -FeOOH samples in the range of 300-700 °C with a heating rate of 10 °C min⁻¹. The nominal doping concentration for all doped samples is 10 at%.

Upon thermal treatment in air, the nanocrystals undergo a phase transformation from the monoclinic akaganeite to the hexagonal hematite structure. Phase transformation temperatures reported in the literature are mostly in the range of 300 °C.^[17-18, 21] In contrast to literature findings, the results of the XRD analysis, TGA analysis and DSC (Figure 3) point to an increased thermal stability of the nanosized β -FeOOH crystals that undergo phase transformation to α -Fe₂O₃ at a much higher temperature of \approx 500 °C. Although experimentally obtained transformation temperatures are strongly dependent on the analysis parameters (mass, atmosphere, and heating rate) and are therefore not directly comparable to literature-stated values using altered analysis parameters, the obtained difference of the transformation temperature to the literature values is rather significant and cannot solely be explained by the difference in measurement conditions.

Despite the fact that the phase transformation temperature of the akaganeite nanocrystals is higher, the mechanism involved seems to be unaffected by the nanoscaling. According to the literature for macroscopic sized crystals, the tunnel structure continuously releases water and

Cl⁻ ions and transforms to hematite in a narrow temperature window without the detectable formation of an intermediate amorphous phase, while, upon further increases in temperature, crystalline hematite with large domain size is formed.^[21]

Similar conclusions can be drawn from the in situ XRD heating study on the undoped nanocrystals obtained in this work (Figure 3a). Up to 200 °C, no visible change in the akaganeite structure is observed. Above 200 °C, a shift of the (112) main reflection, accompanied by a generally decreased intensity of other diffraction peaks, is observed, which can be attributed to a significant loss of structural bound water, stabilizing Cl⁻ ions and a reduction of surface hydroxyl groups caused by the formation of an intermediate strained β -FeOOH phase, as reported recently by Park *et al.* and indicated by TGA (Figure S7).^[55] At higher temperatures between 300 °C and 500 °C, the (112) reflection becomes very pronounced while the (101), (200), and (521) reflections gradually lose intensity. Furthermore, (301) and (521) shift to higher angles with increasing temperature, indicating the formation of intermediate phases. For instance, the (112) akaganeite reflection shifts from 34.0° to 35.4°, which is the hematite (110) peak position. At 550 °C, the hematite (110) peak appears with low intensity. After 2 h of heating at the same temperature, the hematite pattern becomes more pronounced; however, the broad signal at $2\theta = 35^\circ$ indicates the presence of an intermediate mixed phase. At 600 °C, the transition to hematite is complete, showing only hematite signals with a large crystalline domain size of 50 nm.

The phase transformation temperature of nanosized akaganeite to hematite is significantly influenced by introducing dopant elements, as follows from the TGA and DSC analyses (see Figure 3b and Figure S7 in the Supporting Information). For instance, nanocrystals containing 10 at% of Nb(V) undergo the transformation already at ≈ 470 °C, while Ti(IV) doping leads to a much higher transformation temperature of ≈ 550 °C. The V(III)-containing sample shows a mass loss in a very broad temperature range between 400 °C and 600 °C. The thermally

induced phase transformation provides a facile way to fabricate doped hematite structures from the akaganeite nanocrystals.

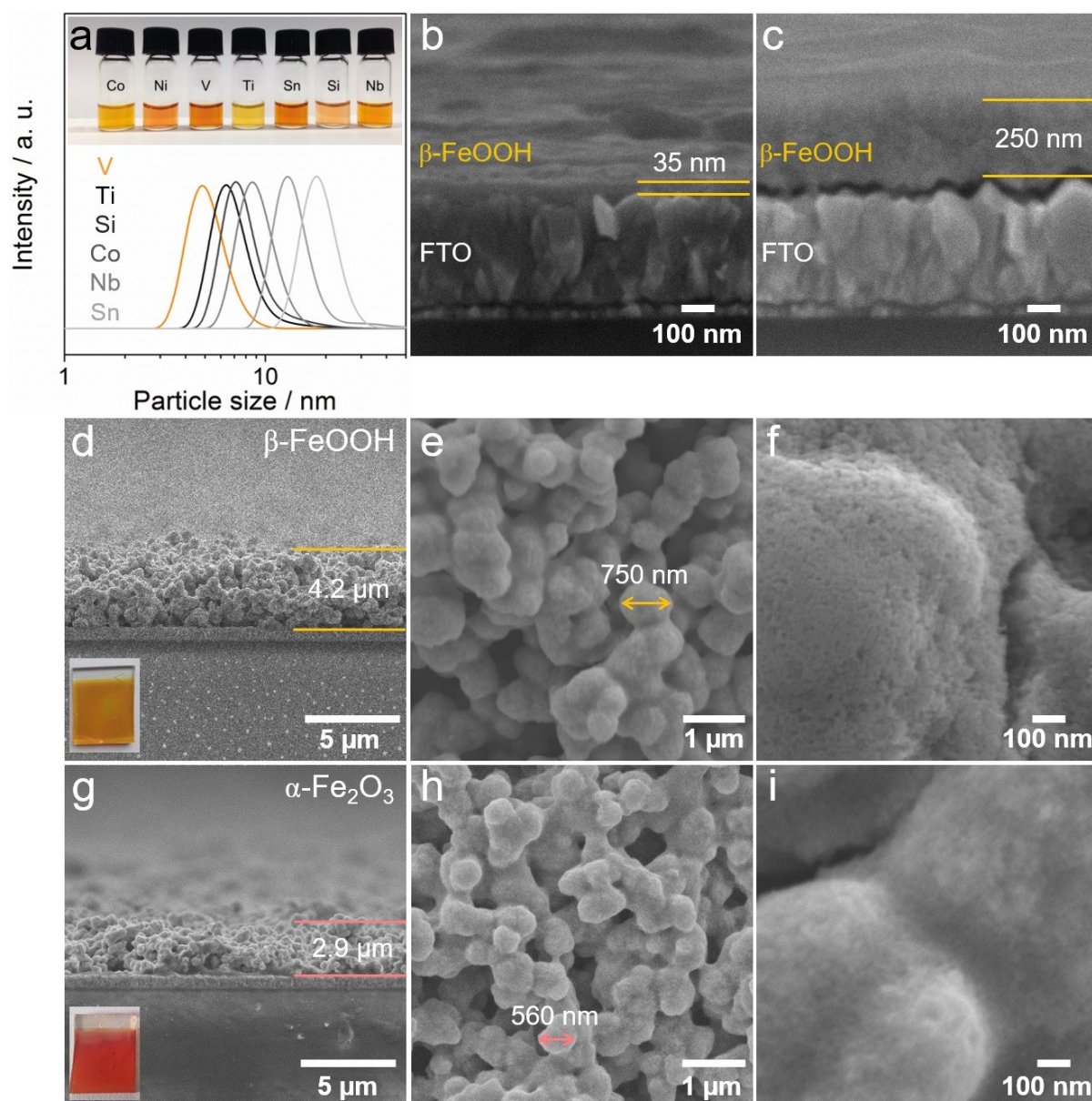


Figure 4 Dispersibility of doped β -FeOOH crystals and preparation of films. (a) DLS curves of dispersions containing different dopants (the color code of the dopants is consistent with the curves) (inset shows a photograph of doped β -FeOOH nanoparticle dispersions in water (concentration = 2 mg mL^{-1}); the dispersions are denoted with the respective dopant). Side-view SEM images of β -FeOOH thin films prepared via spin coating: (b) 2 mg mL^{-1} and (c) 10 mg mL^{-1} nanoparticle dispersions on FTO substrates. SEM images of a β -FeOOH film grown in situ during the microwave reaction. (d, e, f) Different magnifications of the as-prepared β -FeOOH film. (g, h, i) Different magnifications of the film after annealing at $600 \text{ }^\circ\text{C}$ and phase transformation to α -Fe₂O₃.

Excellent dispersibility makes the β -FeOOH nanoparticles suitable starting materials for the fabrication of homogeneous thin hematite films by coating the colloidal dispersions on

different substrates, followed by heating in air (Method 1) (see Figures 4b and 4c). The film thickness can be varied between 35 nm and 250 nm by applying different particle concentrations between 2-10 mg mL⁻¹, respectively.

The thickness is homogeneous over a large area, as shown in Figures S6a and b in the Supporting Information. Furthermore, akaganeite thick films can be grown in situ on FTO substrates directly during the microwave reactions (Method 2). The SEM images in Figures 4d-f show such a β -FeOOH film at different magnifications. The film exhibits a disordered macroporous morphology that consists of interconnected akaganeite spheres with a film thickness of $\approx 4 \mu\text{m}$ (see the SEM cross-section in Figure 4d). The average size of the spheres is relatively large (ca. 750 nm).

However, the XRD-based domain size is still in the range of a few nanometers (Figure S9d in the Supporting Information), indicating that the small akaganeite nanocrystals act as building blocks for the macrospheres. The high-resolution SEM image reveals a high textural porosity with features $\approx 10 \text{ nm}$ in size, which may indicate the formation of an underlying mesoporous structure (see Figure 4f).

The different dopants have no significant influence on the morphology and thickness of the films, showing similar porous structures for all samples. An interesting feature of this in situ process is the possibility to fabricate thick stable films. By increasing the reaction time to 2.5 h, even 30 μm thick films could be obtained (Figure S9 in the Supporting Information).

Calcination of the above akaganeite films at 600 °C results in the formation of hematite layers. The insets in Figures 4d and g show photographs of the nonheated and heated films with the typical dark yellow akaganeite and bright red hematite color, respectively. The corresponding SEM images in Figures 4g-i demonstrate that the initial overall film morphology and the mesoporous structure of the spheres remain preserved during the heating process. However, the spheres shrink to $\approx 560 \text{ nm}$, leading to a reduction of total film thickness by $\approx 20\%$.

Generally, all of the films prepared from dispersions (Method 1) or in situ (Method 2) during the synthesis are very homogeneous, showing a complete coverage over a large area, as demonstrated in the SEM overview images in Figures S6 and S9. The XRD-based domain size of hematite films prepared by calcination of the in-situ method can be estimated to be ≈ 45 nm, according to the Debye-Scherrer equation (Figure S9).

The incorporation of various doping elements into the β -FeOOH nanoparticles not only strongly affects their morphology and crystal structure but also introduces novel functional properties, which can be used for a design of novel akaganeite-based materials for different applications. As an example for the impact of doping, we investigated the performance of hematite layers prepared from Sn-doped akaganeite nanoparticles with different doping levels in photoelectrochemical water splitting reactions. The hematite films obtained after calcination of akaganeite films prepared in situ were subjected to CV measurements while being illuminated with a blue LED. Note that the hematite films obtained at 600 °C show low photoelectrochemical activity. We attribute this observation primarily to the small domain size and, consequently, the large number of grain boundaries present where recombination can occur. Because of the increased phase transformation temperature of the nanosized akaganeite, a higher temperature would be necessary to obtain highly photoactive hematite layers, which requires a large size of the crystalline domains (temperatures of ≈ 800 °C are reported in the literature to yield hematite with the maximum performance).^[1, 56-57]

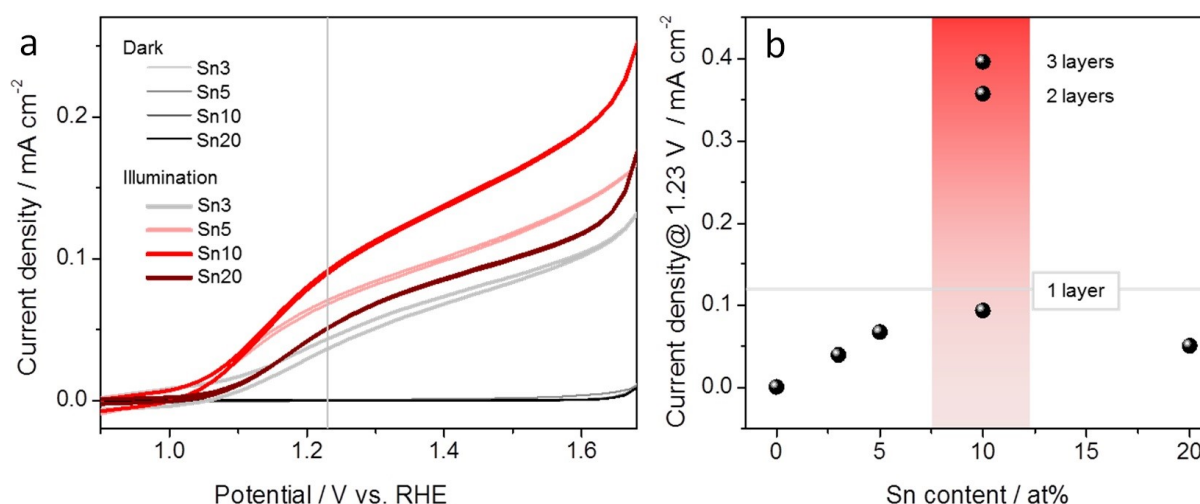


Figure 5 **Photoelectrochemical performance of undoped hematite films prepared in situ and Sn(IV)-doped hematite films.** (a) CV curves for single layers containing 0 at% Sn (black), 3 at% Sn (gray), 5 at% Sn (light red), 10 at% Sn (red), and 20 at% Sn (brownish red), respectively, under illumination with a blue LED (intensity = $9.16 \times 10^{16} \text{ cm}^{-2} \text{ s}^{-1}$); corresponding dark CV curves are shown in light gray, gray, dark gray, and black, respectively. (b) Photocurrent densities for the different Sn-containing films at 1.23 V vs. RHE.

However, introducing only 3 at% Sn(IV) ions into the hematite lattice significantly increases the photocurrent density from $6.04 \times 10^{-4} \text{ mA cm}^{-2}$ for the undoped hematite to 0.04 mA cm^{-2} for 3 at% Sn content to reach a maximum of 0.09 mA cm^{-2} at 1.23 V vs. RHE for 10 at% Sn content (Figures 5a and b). A further increase in Sn content to 20 at% reduces the photocurrent density to 0.05 mA cm^{-2} at 1.23 V vs. RHE (Figure 5a), in good agreement with reported observations.^[58-59] To increase the amount of PEC active material, multiple layers of hematite were prepared by placing a calcined Sn10 film into the reaction mixture, allowing for a new FeOOH film to grow on top of the first layer that was calcined again at 600 °C. This procedure was repeated to obtain the desired number of layers. The presence of a second layer already led to a remarkable increase in photocurrent density, reaching 0.34 mA cm^{-2} at 1.23 V vs. RHE. The photocurrent was further enhanced to 0.39 mA cm^{-2} by applying a third layer (Figure 5b).

5.3 Conclusion

The microwave-assisted synthesis in *t*-BuOH enables the fabrication of nonagglomerated crystalline β -FeOOH akaganeite nanoparticles. The remarkable feature of the obtained nanoparticles is their very small size (≈ 4 nm in width and up to 90 nm in length, the smallest reported so far), and the possible incorporation of different dopant ions at very high concentrations of up to 20 at%. We attribute the increased solubility of the dopants to the kinetic control of the reaction, together with the extremely small crystal size, which can stabilize the unusual chemical compositions while retaining the akaganeite structure.

The dopant incorporation is influenced by the oxidation state of the dopants, showing a higher uptake level for high valence state ions such as Ti(IV), Si(IV), and Sn(IV). The dopants have a strong impact on the size and morphology of the β -FeOOH nanocrystals, ranging from low-aspect-ratio (almost spherical) to high-aspect-ratio nanorods, depending on the nature and concentration of the incorporated ions. Furthermore, the dopants significantly affect the crystalline structure and the physicochemical properties of the nanosized akaganeite crystals, such as the phase transformation temperature to α -Fe₂O₃.

Because of their excellent dispersibility, doped and undoped nanoparticles can be used for film fabrication, whereby film thicknesses can be controlled from several nanometers, for films prepared from particle dispersions, to several micrometers, for films grown in situ during solvothermal reactions. An attractive feature of the doped β -FeOOH nanoparticles is the possibility to introduce novel functional properties to akaganeite, as well as to hematite structures derived from it, as demonstrated for Sn-doped hematite layers serving as photoanodes for photoelectrochemical water splitting. The tunable chemical and functional properties of the doped akaganeite nanoparticles make them excellent candidates for a wide range of applications, as well as versatile building blocks for the fabrication of doped hematite nanomorphologies.

5.4 Experimental

Synthesis of Doped Iron Oxyhydroxide Nanoparticles

Iron(III) chloride hexahydrate ($\text{FeCl}_3 \cdot 6\text{H}_2\text{O}$) (Sigma-Aldrich, ACS reagent, 97% purity), cobalt(II) nitrate hexahydrate ($\text{Co}(\text{NO}_3)_2 \cdot 6\text{H}_2\text{O}$) (Sigma-Aldrich, $\geq 98\%$ purity), nickel(II) nitrate hexahydrate ($\text{Ni}(\text{NO}_3)_2 \cdot 6\text{H}_2\text{O}$) (Sigma-Aldrich, purum, $\geq 97\%$ purity), vanadium(III) chloride (VCl_3) (Aldrich, 97% purity), titanium(IV) butoxide ($\text{Ti}(\text{O}i\text{Bu})_4$) (Sigma-Aldrich, reagent grade, 97% purity), tin(IV) chloride pentahydrate ($\text{SnCl}_4 \cdot 5\text{H}_2\text{O}$) (Sigma-Aldrich, 98% purity), silicon(IV) chloride (SiCl_4) (Aldrich, 99% purity), niobium(V) chloride (NbCl_5) (Alfa Aesar, 99% purity) were used as received. *tert*-butanol (*t*-BuOH) was purchased from Sigma-Aldrich (puriss. p.a., ACS reagent, $\geq 99.7\%$), dried over a 4 Å molecular sieve at 28 °C and filtered prior to use. For the solvothermal microwave-assisted synthesis of metal (*M*)-doped β -FeOOH nanoparticles (where *M* = Co, Ni, V, Ti, Sn, Si, Nb), $\text{FeCl}_3 \cdot 6\text{H}_2\text{O}$ was mixed with the dopant precursor in the desired molar composition, while the total amount of the metal precursors was kept at a constant value of 0.6 mmol. The dopant concentration (c_M) was calculated using the equation

$$c_M = \frac{n_M}{0.6 \text{ mmol}} \quad (1)$$

with n_M being the molar amount of the metal dopant precursor. As an example, for the synthesis of $\text{Sn}_{0.2}\text{Fe}_{0.8}\text{OOH}$ nanocrystals, 129.7 mg (0.48 mmol) of $\text{FeCl}_3 \cdot 6\text{H}_2\text{O}$ was mixed with 42.1 mg (0.12 mmol) of $\text{SnCl}_4 \cdot 5\text{H}_2\text{O}$. The solid mixtures were added to 14 mL of *tert*-butanol in a microwave Teflon vessel, forming a suspension that was yellow to rusty-red in color, depending on the dopant, then placed into a ceramic microwave reactor and hermetically sealed. The reactions were carried out under vigorous stirring at 80 °C for 1 h with the microwave radiation power limited to 120 W and 14 mL of H_2O in the reference vessel resulting in uniform brown, red, or yellow dispersions of nanoparticles. The as-prepared particles were dried in air by evaporating the solvent at 80 °C on a hot plate, resulting in

M/ β -FeOOH nanopowders that exhibit various particle shapes and sizes. Dispersions of the M/ β -FeOOH nanoparticles were prepared in water or water/ethanol mixtures with the addition of acetic acid.

In a typical dispersion procedure, 1 mg of the dried powder was covered with 500 μ L water (Millipore) and 20 μ L of acetic acid was added to the turbid mixture. After 10 min of stirring, colloidal dispersions with a metal oxide concentration of 2 mg mL⁻¹ were obtained.

Characterization

Wide-angle X-ray diffraction (XRD) analysis was carried out in transmission mode using a STOE STADI P diffractometer with Cu K α 1 radiation ($\lambda = 1.54060 \text{ \AA}$) and a Ge(111) single-crystal monochromator that was equipped with a DECTRIS solid-state strip detector (Mythen 1K). Powder XRD patterns of the samples were collected with an omega-2theta scan in the 2θ range from 5° to 70° with a step size of 1° and a fixed counting time of 90 s per step and a resolution of 0.05°. The size of the crystalline domains was calculated from the XRD patterns for the (301) reflection, using the Scherrer equation. Raman spectroscopy was carried out using a LabRAM HR UV-vis (HORIBA JOBIN YVON) system, a Raman microscope (OLYMPUS, Model BX41) with a liquid-N₂-cooled Symphony CCD detection system and a He-Ne laser ($\lambda = 633 \text{ nm}$). The resulting spectral resolution of the measurements was 1.2 cm⁻¹, which was achieved with a 100 μ m confocal pinhole aperture and a 600 gr mm⁻¹ grating as dispersive element. For spectra recorded with high laser power (10 mW laser and filter, with an optical density of 0.6), an Olympus MPLAN objective lens (numerical aperture 0.75) with a 50X magnification, and acquisition times of 50 s per spectrum with 6 accumulations were used. The acquisition of spectra with reduced laser intensity (optical density of the filter = 2.0) was done using an Olympus MPLAN objective lens with a 10-fold magnification (numerical aperture = 0.25) and integration times of 60 s with 421 accumulations. High-resolution transmission electron microscopy (HRTEM) images were taken using a FEI Titan 80-300 microscope that

was operated at 300 kV. High-angle annular dark field (HAADF) and annular bright field (ABF) scanning TEM (STEM) images were taken using a FEI Titan Themis microscope with aberration correction of the probe-forming lenses operated at 120 kV or 300 kV. Energy-dispersive X-ray spectroscopy (EDS) was performed using a SuperX windowless, four quadrant silicon drift detector with a solid angle of 0.7 sr. TEM specimens were prepared by dispersing the colloid of akaganeite nanoparticles in ethanol on a holey carbon coated copper grid and drying in air. Hydrocarbon contaminants were removed by plasma cleaning for 15 s at 50 mW and, in some cases, large-area illumination in the TEM for 40 min. Dynamic light scattering (DLS) measurements were performed on a MALVERN Zetasizer-Nano instrument equipped with a 4 mW He-Ne laser ($\lambda = 633$ nm) and an avalanche photodiode detector. Secondary electron images were obtained with a JEOL JSM-6500F scanning electron microscopy (SEM) system that was equipped with a field emission gun operated at 5 kV and a FEI Helios NanoLab G3 UC SEM equipped with a Schottky thermal field emitter operated at 3 kV (20 kV for EDS), ELSTAR in-lens BSE/SE detector and an silicon drift detector (SDD) (OXFORD INSTRUMENTS, Model X-Max^N). The films were prepared on Si substrates and glued onto a brass sample holder with silver lacquer. Thermogravimetric analysis (TGA) and differential scanning calorimetry (DSC) of the samples was performed on a NETZSCH Model STA 440 C TG/DSC system (using a heating rate of 10 K min⁻¹ in a stream of synthetic air of ≈ 25 mL min⁻¹).

Film Preparation

For film preparation, fluorine-doped tin oxide (FTO) coated glass (TEC 15 Pilkington TEC glass, 2.5 × 1.5 cm) was used as a conductive substrate. Prior to use, the FTO was washed by sequential sonication for 15 min each in detergent (1 mL Extran in 50 mL Millipore water), water (Millipore), and ethanol (absolute) and dried in a N₂ stream. The films on the FTO substrates were prepared by deposition of the dispersed preformed akaganeite nanoparticles

(Method 1), as well as in situ in the microwave synthesis (Method 2). Thin films (Method 1) were prepared by deposition of the dispersed akaganeite nanoparticles by spin coating on the FTO substrates. For the spin coating method, 40 μL of akaganeite dispersion was deposited on a masked FTO substrate exposing an area of 2.25 cm^2 and spun at 1000 rpm for 30 s. The films prepared in this way were subsequently dried at 80 $^\circ\text{C}$ in a laboratory oven resulting in films 35 - 250 nm thick. Photoelectrodes (Method 2) were prepared in situ by placing the FTO substrates into a specially designed sample holder that allows for magnetic stirring during the microwave reaction, while keeping the substrates covered in solution. The $\beta\text{-FeOOH}$ films grown in this way were $\approx 3 \mu\text{m}$ thick, exhibiting a porous structure. After the synthesis, the nonconductive side of the FTO, as well as 1 cm of the conductive side was cleaned with 1 M hydrochloric acid (HCl), leaving a coated area of ca. 1.5 $\text{cm} \times 1.5 \text{ cm}$. To produce metal-doped hematite films, the electrodes were subsequently heated to 600 $^\circ\text{C}$ in air in a laboratory oven with a heating ramp of 3.33 $^\circ\text{C min}^{-1}$ and a dwell time of 30 min. The film growth procedure was repeated 2 or 3 times to obtain double or triple hematite layers, respectively. To introduce a Co(II) co-catalyst, the calcined films were subjected to a surface treatment with a 50 mM aqueous solution of $\text{Co}(\text{NO}_3)_2$. The films were dipped into the solution for 30 s, rinsed in deionized water, and dried in air.

Photoelectrochemical Measurements

Hematite photoelectrodes (obtained from FeOOH films fabricated in situ) were masked with a Teflon-coated glass fiber adhesive tape, leaving a circular area of 0.785 cm^2 exposed to a 0.1 M NaOH aqueous electrolyte. All electrochemical measurements were performed in a quartz cell, using a METROHM Autolab PGSTAT302N potentiostat/galvanostat with a FRA32 M impedance analyzer connected to a Ag/AgCl/KCl (sat.) reference electrode (+0.197 V vs. NHE) and a Pt mesh counter electrode. Potentials versus the reversible hydrogen electrode

(E_{RHE}) were calculated from those measured at pH=13 versus the Ag/AgCl electrode $E_{\text{Ag/AgCl}}$, according to the relation:

$$E_{\text{RHE}} = E_{\text{Ag/AgCl}} + 0.197 + 0.059 \text{ pH}$$

The light intensity was measured inside the cells using a 4 mm² photodiode that had been calibrated against a certified Fraunhofer ISE silicon reference cell equipped with a KG5 filter. The currents were obtained using cyclic voltammetry (CV) in darkness or under illumination, with a scan rate of 20 mV s⁻¹. Illumination was incident through the substrate, provided by a high-powered light-emitting diode (LED) (THORLABS, 455 nm).

5.5 Supporting Information

Following Supporting Information is associated with this publication: Influence of different iron precursors and the reaction conditions on the formation of akaganeite; time-resolved Raman investigation of the β -FeOOH powder; SEM images of β -FeOOH films prepared by spin-coating from H₂O/EtOH nanoparticle dispersions; TGA and DSC curves of the doped β -FeOOH powders; SEM images of thick β -FeOOH films grown in situ during the microwave reaction before and after annealing in air.

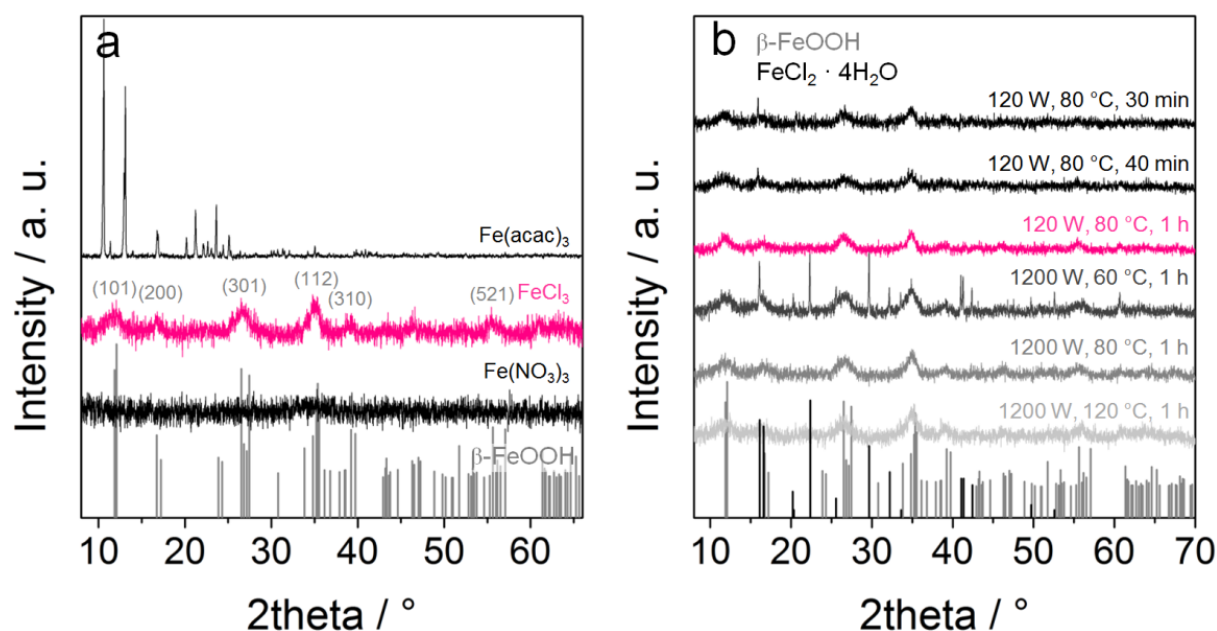


Figure S1 Influence of different iron precursors and the reaction conditions on the formation of akaganeite. (a) XRD patterns of powders obtained at the same reaction conditions using Fe(NO₃)₃, Fe(acac)₃ (black) and FeCl₃ (pink) as precursors. (b) XRD patterns of samples obtained using FeCl₂ · 6H₂O at different reaction conditions. The numbers indicate the microwave power in W, temperature in °C and reaction time in hours or minutes. β -FeOOH pattern ICDD card number 01-074-2567 (grey lines). FeCl₂ · 4H₂O pattern ICDD card number 00-016-0123 (black lines).

The Fe compounds Fe(NO₃)₃, Fe(acac)₃ and FeCl₃ were investigated as precursors for the akaganeite synthesis. The XRD patterns in Figure S1a show the formation of β -FeOOH only in case of FeCl₃. Iron nitrate results in an amorphous phase and Fe(acac)₃ did not react at the relatively low temperature of 120 °C, probably because the solubility of iron acetylacetonate

in *tert*-butanol is rather low. The sharp reflections in the XRD pattern correspond to the precursor signals. Figure S1b shows XRD patterns of selected powders obtained at different reaction conditions. The initial synthesis was performed at 1200 W microwave power, 120 °C for 1 h and resulted in phase-pure 8 nm sized β -FeOOH particles (calculated from the (301) peak using the Scherrer equation). To obtain smaller crystals, the reaction temperature was reduced to 80 °C, resulting in particle sizes of around 5 nm. The further decreased temperature of 60 °C was too low to obtain phase-pure akaganeite, as a second phase corresponding to $\text{FeCl}_2 \cdot 4\text{H}_2\text{O}$ is visible in the XRD pattern (Figure S1b, black reference pattern). Further reactions were carried out at 80 °C with reduced microwave radiation power. The smallest particle dimensions of around 5 nm were obtained upon heating with 120 W for 1 h (Figure S1b, pink). Further decrease in the reaction time to 40 min and 30 min again resulted in a mixture of β -FeOOH and $\text{FeCl}_2 \cdot 4\text{H}_2\text{O}$. The reaction conditions 120 W, 80 °C and 1 h were therefore applied in all following reactions.

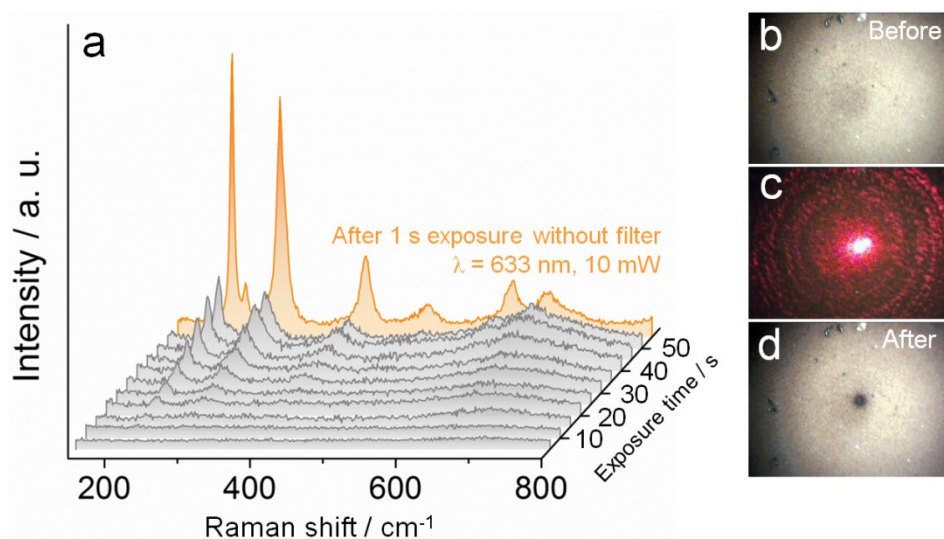


Figure S2 Time-resolved Raman investigation of the undoped β -FeOOH powder. (a) Raman spectra recorded every 5 min with a filter (optical density of 0.6) to reduce the intensity of the laser beam (grey). The orange spectrum was taken after exposure of the sample to the laser with full intensity for 1 s. Micrographs of the sample with a 10-fold magnification (b) before, (c) during and (d) after the Raman measurement, showing a dark spot caused by the laser beam.

Figure S2 shows an in-situ time-resolved Raman study of the undoped β -FeOOH. The spectra were taken with a time step of 5 min using an intensity-reducing laser filter (Figure S2a) with an optical density of 0.6. The signals at 221 cm^{-1} (A_{1g}), 237 cm^{-1} (E_g), 284 cm^{-1} (E_g), 398 cm^{-1} (E_g), 489 cm^{-1} (A_{1g}), 601 cm^{-1} (E_g) and 649 cm^{-1} (E_u) can be assigned to hematite (α -Fe₂O₃) bands. Noticeably, neither β -FeOOH nor any other phases are visible below 10 min irradiation. The hematite spectrum starts to appear after 15 min and becomes gradually more pronounced with extended exposure time. To compare, the unfiltered laser beam immediately leads to the formation of hematite (Figure S2a, orange line). Corresponding micrographs recorded before and after the Raman measurement in Figure S2b – d show a dark spot occurring at the position where the laser beam was focused. This additionally confirms the structural change.

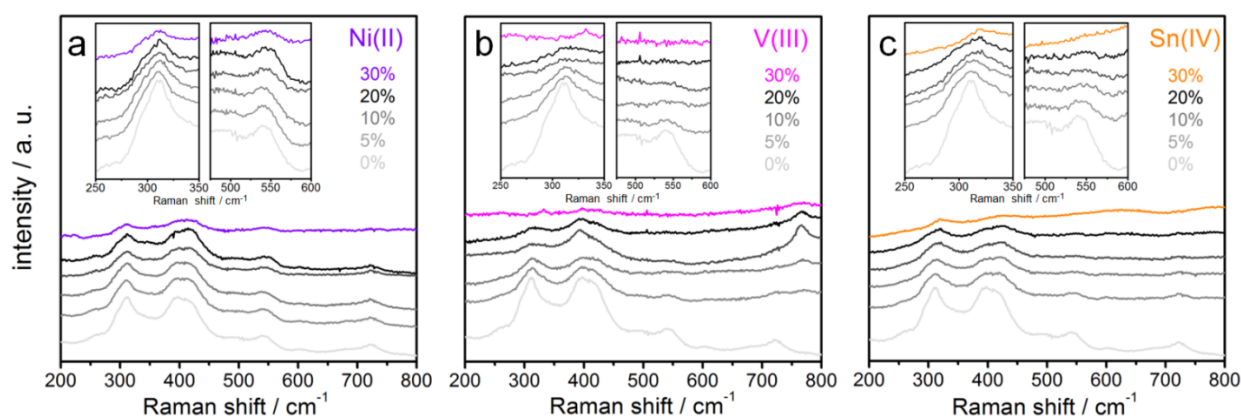


Figure S3 Low laser intensity (filter with optical density 2.0) Raman spectra of undoped (a) Ni(II) doped (b) V(III) doped and (c) Sn(IV) doped akaganeite nanocrystals.

Figure S3 shows Raman spectra of β -FeOOH with selected doping elements ((a) Ni, (b) V and (c) Sn) with oxidation states +II to +IV in various concentrations acquired by low laser intensity (filter with optical density 2.0) to avoid heat induced phase transformation to the hematite phase. The Raman spectra confirm the formation of akaganeite phase in the microwave assisted solvothermal synthesis, indicated by the presence of the phase specific bands at 310 cm^{-1} and 390 cm^{-1} as well as by the absence of the hematite specific bands at 223 cm^{-1} and 289 cm^{-1} . Higher doping concentration reduces the crystallinity in the shown cases, indicated by a relative

loss in the signal intensity of the specific bands and causes the formation of side products above the solubility limit of the respective doping elements in the β -FeOOH structure. An analysis of the shift of the akaganeite specific Raman bands in dependence of the doping ion concentration is not possible due to broad peaks in general and a low signal level caused by the reduced laser intensity.

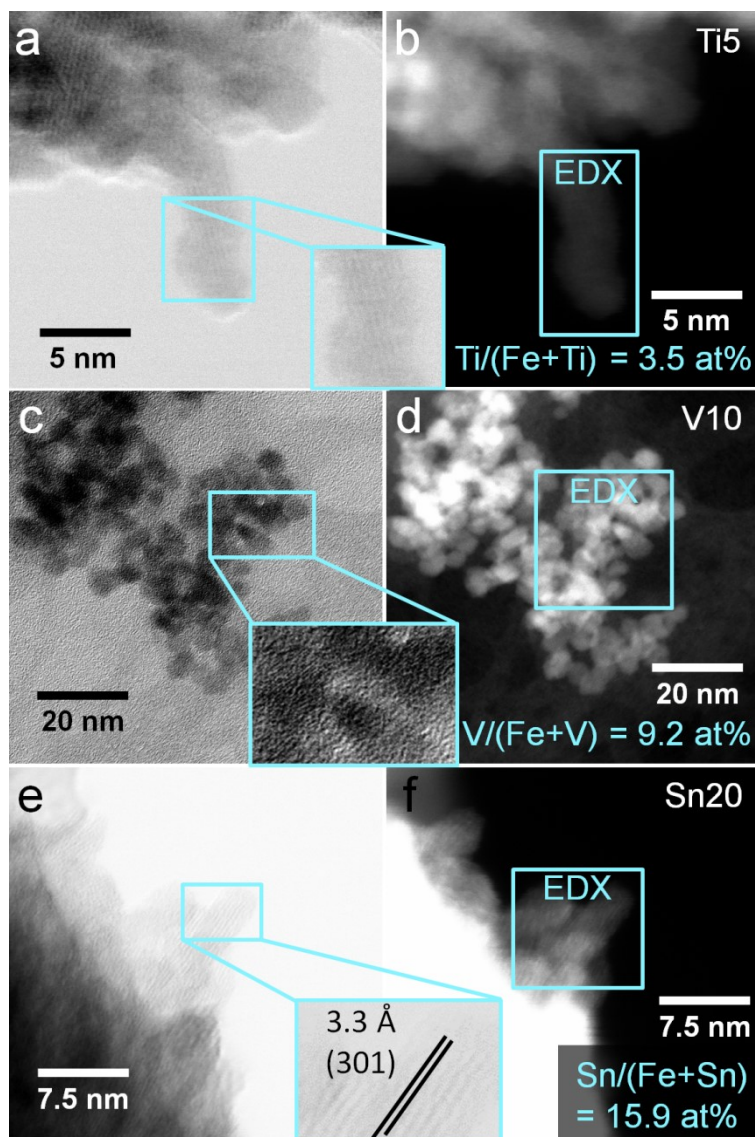
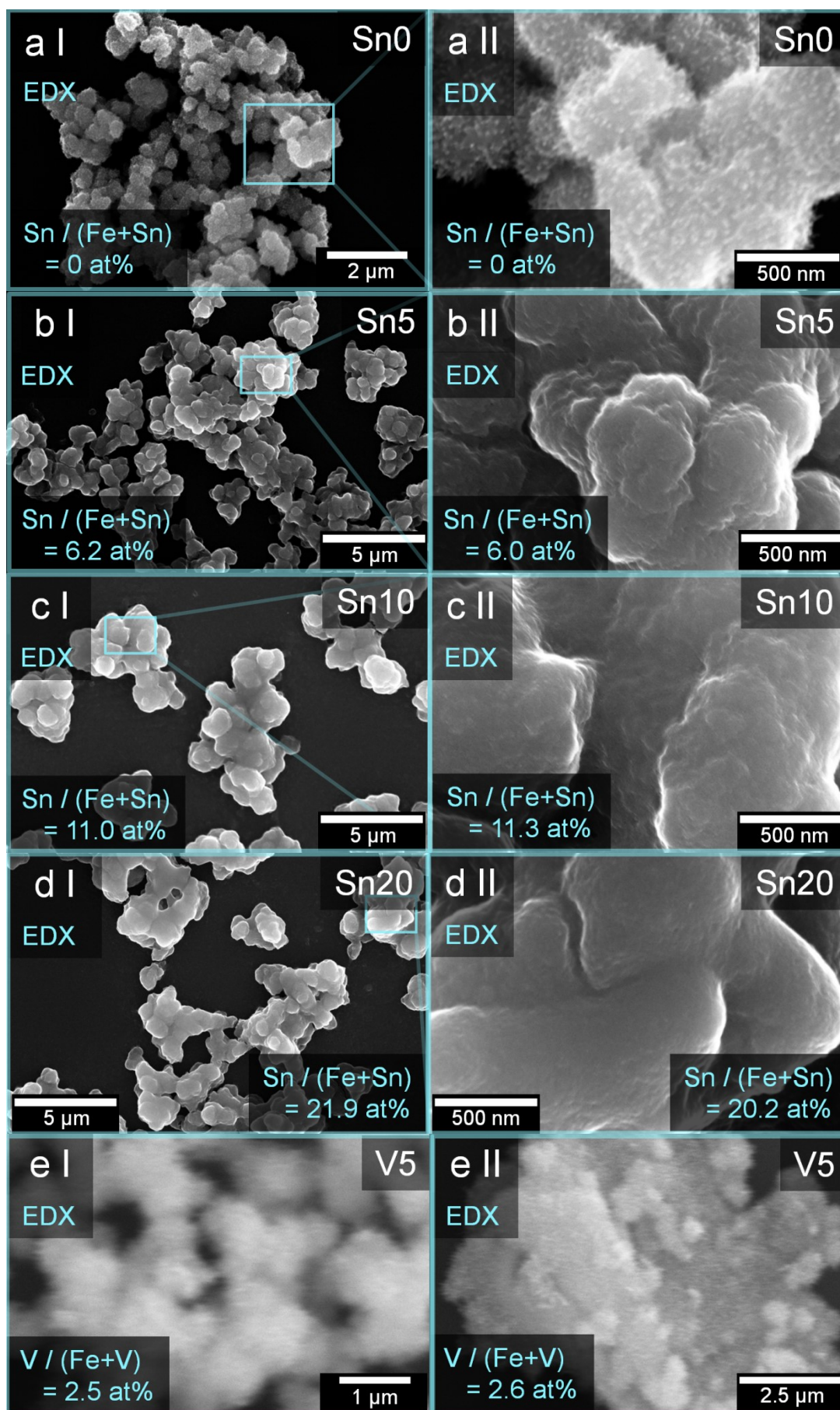


Figure S4 TEM micrographs of (a, b) 5 at% Ti (IV), (c, d) 10 at% V(III) and (e, f) 20 at% Sn(IV) doped β -FeOOH with corresponding EDX quantification of doping ion concentrations in the nanocrystals.



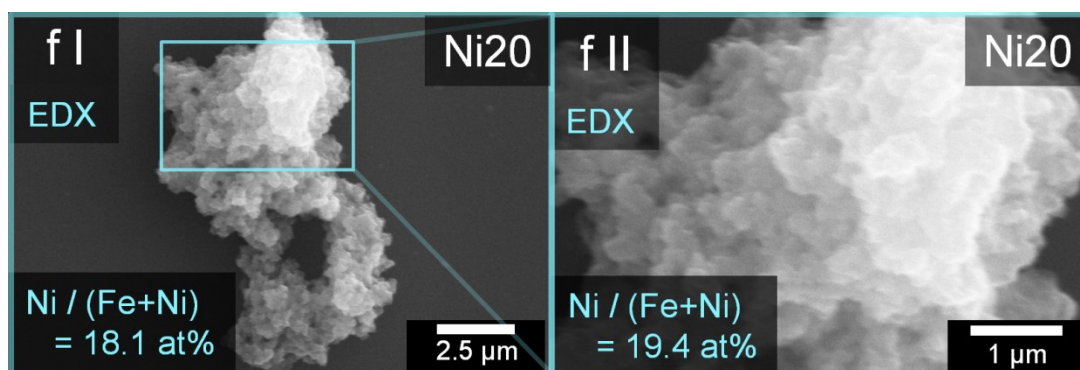


Figure S5 SEM micrographs of (a) undoped, (b,c,d) 5, 10, 20 at% Sn(IV) doped (e) 5 at% V(III) and (f) 20 at% Ni(II) β -FeOOH with corresponding EDX quantification of doping ion concentrations on the microscale.

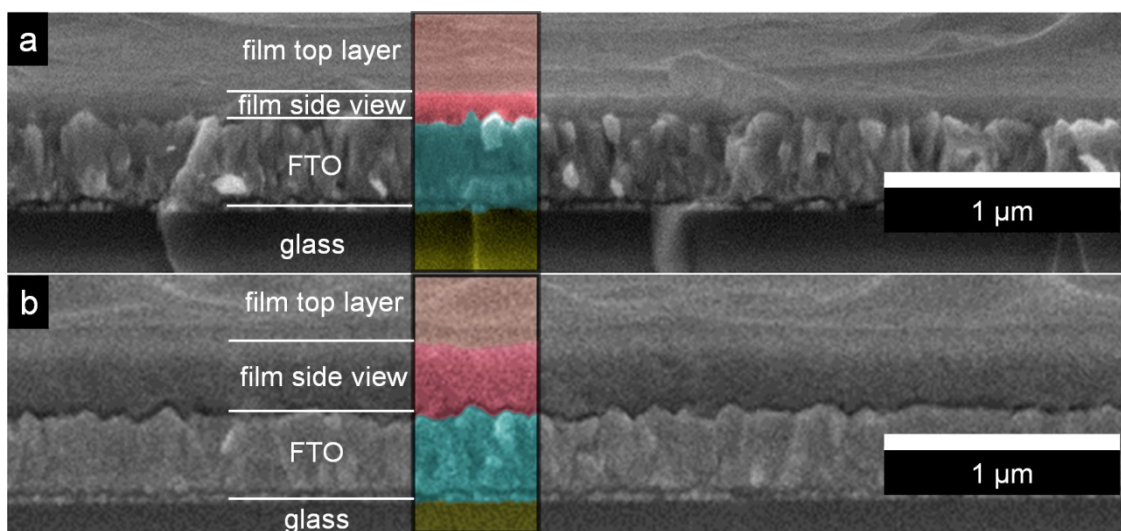


Figure S6 SEM images of β -FeOOH films prepared by spin-coating from H₂O/EtOH nanoparticle dispersions with the concentrations of (a) 2 mg mL⁻¹ and (b) 10 mg mL⁻¹ on FTO substrate.

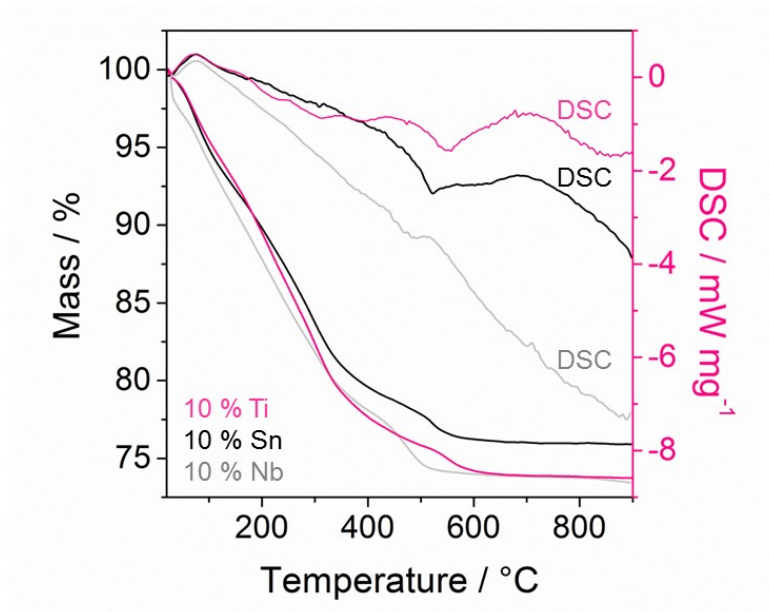


Figure S7 TGA and DSC curves of the samples Ti10 (pink), Sn10 (black) and Nb10 (grey).

Thermogravimetric analysis (TGA) and differential scanning calorimetry (DSC) curves of the samples Ti10, Sn10 and Nb10 in Figure S7 show several processes that are accompanied by changes in mass. The endothermic process with the mass loss of around 5 % at 100 °C corresponds to evaporation of adsorbed water and is visible for all samples that are stored in air. In the range between 100 and 400 °C all organic species such as *tert*-butoxide residues are burned off as well as structural bound water and stabilizing chloride ions with the greatest mass loss of around 20 %. The exothermic events with only minor mass losses of 2 – 3 % between 480 and 600 °C are caused by the phase transformation into hematite, as is supported by the XRD results.

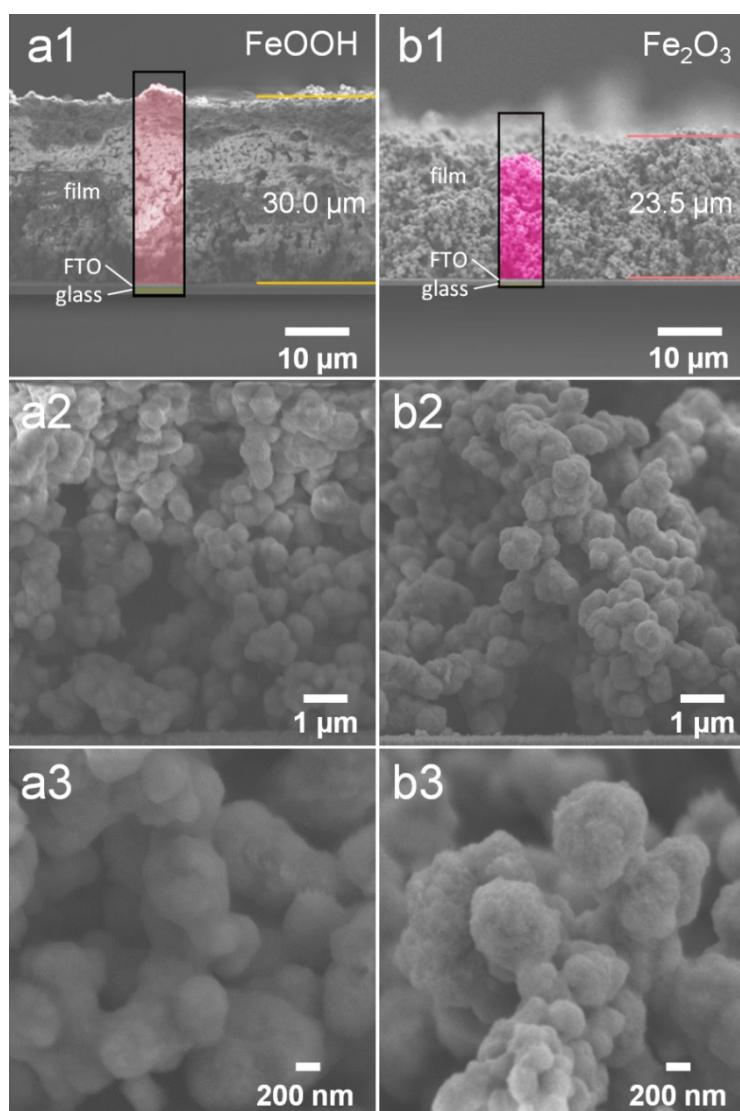


Figure S8 SEM images of a thick β -FeOOH film grown in situ for 2.5 h on FTO substrate during the microwave reaction. (a1, a2, a3) Different magnifications of the as-prepared β -FeOOH film. (b1, b2, b3) Different magnifications of the film after annealing at 600 °C and phase transformation to α -Fe₂O₃.

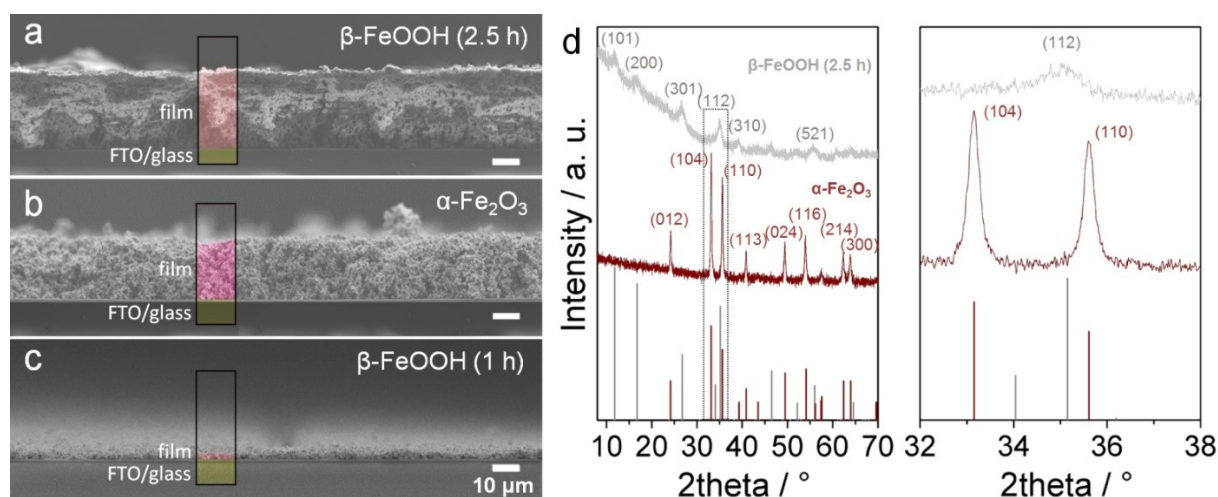


Figure S9 SEM images of as-prepared β -FeOOH films grown in situ on FTO during the microwave reaction with a reaction time of (a) 2.5 h and (c) 1 h. (b) SEM image of the film grown in situ for 2.5 h on FTO after annealing at 600 °C and phase transformation to α -Fe₂O₃. The scale bars correspond to a length of 10 μ m. Powder XRD patterns (material scratched from substrate) of as-prepared β -FeOOH films grown in situ during the microwave reaction with a reaction time of 2.5 h (d, grey curve) and XRD pattern of corresponding film (material scratched from substrate) after annealing at 600 °C (d, dark-red curve). Corresponding reflections (akaganeite (112), hematite (104)) in insets (d) used for estimation of crystalline domain size according to the Debye-Scherrer equation.

In Figure S9, SEM cross section micrographs of in situ prepared akaganeite films by microwave assisted synthesis reveal a homogenous coverage of the substrate over the whole image of $\approx 250 \mu\text{m}$. The XRD-based domain size of the in situ prepared akaganeite films is estimated to be $\approx 9 \text{ nm}$ according to the Debye-Scherrer equation (Figure S9a, d), indicating that the small akaganeite nanocrystals act as building blocks for larger macro-spheres visible in SEM. The XRD-based domain size of thermally transformed akaganeite films to hematite at 600 °C (Figure S9b, d) can be estimated to be about 45 nm according to the Debye-Scherrer equation.

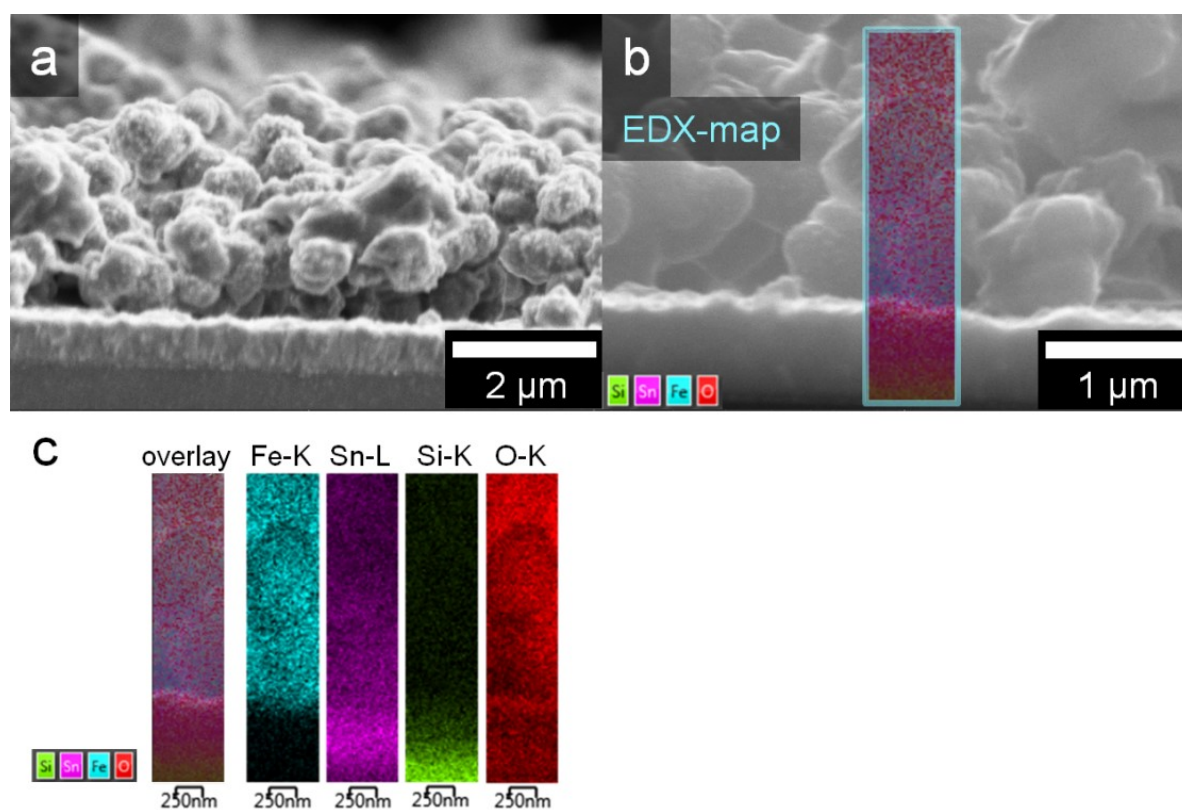


Figure S10 (a, b) SEM cross section micrograph and (b, c) EDX elemental distribution maps of a 10 at% Sn doped α - Fe_2O_3 film on FTO substrate prepared by thermal transformation (600°C) of a β - FeOOH film grown in situ during microwave reaction (1 h).

A SEM cross section micrograph (Figure S10a, b) of a 10 at% Sn doped α - Fe_2O_3 film on FTO substrate prepared by thermal transformation (600°C) of a β - FeOOH film grown in situ during microwave reaction (1 h) was further investigated by EDX to map the Sn atom distribution across the film depth. The quantitative elemental mapping images in Figure S10 c show a homogenous Fe atom distribution in the investigated film depth of $\approx 1.5 \mu\text{m}$ from the FTO substrates upwards. The Sn atom concentration in the FTO substrate can be clearly distinguished from the 10 at% Sn doping in the overlying α - Fe_2O_3 film and shows a rather homogenous distribution throughout the measured mapping area. Heating of the akaganeite film on the FTO substrate at 600°C does not seem to promote a significant Sn atom migration from the substrate into the β - FeOOH film, as no clear gradient in the Sn atom distribution is visible.

5.6 References

- [1] J. Y. Kim, G. Magesh, D. H. Youn, J. W. Jang, J. Kubota, K. Domen, J. S. Lee, *Sci. Rep.* **2013**, 3, 2681.
- [2] M. Mohapatra, S. Anand, *Int. J. Eng. Sci. Technol.* **2010**, 2, 127.
- [3] H.-J. Song, L. Liu, X.-H. Jia, C. Min, *J. Nanopart. Res.* **2012**, 14, 1290.
- [4] X. Wang, X. Chen, L. Gao, H. Zheng, M. Ji, C. Tang, T. Shen, Z. Zhang, *J. Mater. Chem.* **2004**, 14, 905.
- [5] L. Yu, L. P. Wang, S. Xi, P. Yang, Y. Du, M. Srinivasan, Z. J. Xu, *Chem. Mater.* **2015**, 27, 5340.
- [6] Q. Yu, X. Meng, T. Wang, P. Li, J. Ye, *Adv. Funct. Mater.* **2015**, 25, 2686.
- [7] X. Zhang, Y. Du, *RSC Adv.* **2016**, 6, 17504.
- [8] X. Zong, S. Thaweesak, H. Xu, Z. Xing, J. Zou, G. M. Lu, L. Wang, *Phys. Chem. Chem. Phys.* **2013**, 15, 12314.
- [9] W. D. Chemelewski, H. C. Lee, J. F. Lin, A. J. Bard, C. B. Mullins, *J. Am. Chem. Soc.* **2014**, 136, 2843.
- [10] M. Zou, W. Wen, J. Li, Y. Lin, H. Lai, Z. Huang, *J. Energy Chem.* **2014**, 23, 513.
- [11] R. Chitrakar, S. Tezuka, A. Sonoda, K. Sakane, T. Hirotsu, *Ind. Eng. Chem. Res.* **2009**, 48, 2107.
- [12] D. Carroll, W. R. Richmond, *Am. Mineral.* **2008**, 93, 1641.
- [13] C. Luna, M. Ilyn, V. Vega, V. M. Prida, J. González, R. Mendoza-Reséndez, *J. Phys. Chem. C* **2014**, 118, 21128.
- [14] R. Parameshwari, P. Priyadarshini, G. Chandrasekaran, *Am. J. Mater. Sci.* **2011**, 1, 18.
- [15] Y. Song, B. H. Bac, Y.-B. Lee, M. H. Kim, I. M. Kang, *CrystEngComm* **2011**, 13, 287.
- [16] C. Wei, X. Wang, Z. Nan, Z. Tan, *J. Chem. Eng. Data* **2010**, 55, 366.
- [17] F. N. Sayed, V. Polshettiwar, *Sci. Rep.* **2015**, 5, 9733.
- [18] V. Klimas, K. Mažeika, V. Pakštas, E. Spudulis, A. Jagminas, *J. Fluorine Chem.* **2015**, 173, 55.
- [19] Y. Piao, J. Kim, H. B. Na, D. Kim, J. S. Baek, M. K. Ko, J. H. Lee, M. Shokouhimehr, T. Hyeon, *Nat. Mater.* **2008**, 7, 242.
- [20] A. M. Xavier, F. F. Ferreira, F. L. Souza, *RSC Adv.* **2014**, 4, 17753.
- [21] J. E. Post, P. J. Heaney, R. B. Von Dreele, C. J. Hanson, *Am. Mineral.* **2003**, 88, 782.
- [22] P. Liao, J. A. Keith, E. A. Carter, *J. Am. Chem. Soc.* **2012**, 134, 13296.

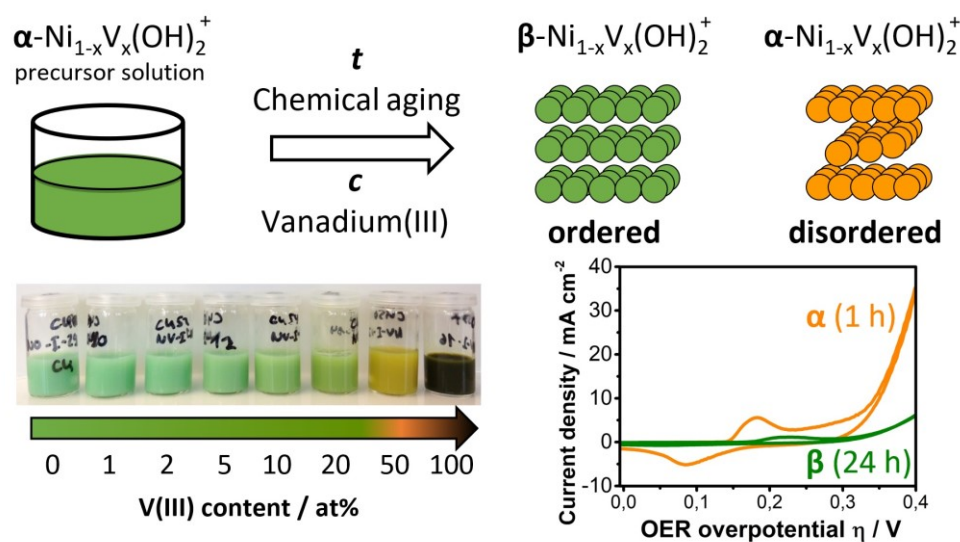
- [23] M. Žic, M. Ristić, S. Musić, *Mater. Chem. Phys.* **2010**, 120, 160.
- [24] N. G. Holm, *GFF* **2010**, 107, 297.
- [25] T. Ishikawa, T. Motoki, R. Katoh, A. Yasukawa, K. Kandori, T. Nakayama, F. Yuse, *J. Colloid Interf. Sci.* **2002**, 250, 74.
- [26] L. Xiaojuan, Y. Yuxiang, L. Xiangnong, Z. Hui, Y. Haiping, Z. Zheyu, C. Yaru, *Russ. J. Inorg. Chem.* **2014**, 53, 367.
- [27] W. R. Richmond, J. M. Cowley, G. M. Parkinson, M. Saunders, *CrystEngComm* **2006**, 8, 36.
- [28] R. M. Cornell, *Z. Pflanzenernahr. Bodenkd.* **1991**, 155, 449.
- [29] S. H. Kilcoyne, J. L. Lawrence, *Z. Kristallogr.* **1999**, 214, 666.
- [30] D. L. A. de Faria, S. Venâncio Silva, M. T. de Oliveira, *J. Raman Spectrosc.* **1997**, 28, 873.
- [31] A. M. Jubb, H. C. Allen, *ACS Appl. Mater. Interfaces* **2010**, 2, 2804.
- [32] L. Graf, *Solid State Commun.* **1978**, 27, 1361.
- [33] G. Dixit, J. P. Singh, R. C. Srivastava, H. M. Agrawal, R. J. Chaudhary, *Adv. Mat. Lett.* **2012**, 3, 21.
- [34] A. T. Raghavender, N. Hoa Hong, K. Joon Lee, M.-H. Jung, Z. Skoko, M. Vasilevskiy, M. F. Cerqueira, A. P. Samantilleke, *J. Magn. Magn. Mater.* **2013**, 331, 129.
- [35] S. Joshi, M. Kumar, S. Chhoker, G. Srivastava, M. Jewariya, V. N. Singh, *J. Mol. Struct.* **2014**, 1076, 55.
- [36] R. S. Melo, F. C. Silva, K. R. M. Moura, A. S. de Menezes, F. S. M. Sinfrônio, *J. Magn. Magn. Mater.* **2015**, 381, 109.
- [37] C. Dong, G. Wang, D. Guo, C. Jiang, D. Xue, *Nanoscale Res. Lett.* **2013**, 8, 196.
- [38] M. C. Wang, H. J. Lin, T. S. Yang, *J. Alloys Compd.* **2009**, 473, 394.
- [39] A.-M. Zhang, K. Liu, J.-T. Ji, C.-Z. He, Y. Tian, F. Jin, Q.-M. Zhang, *Chin. Phys. B* **2015**, 24, 126301.
- [40] A. Dixit, G. Lawes, *J. Phys. Condens. Mat.* **2009**, 21, 456003.
- [41] H. S. Oliveira, L. C. Oliveira, M. C. Pereira, J. D. Ardisson, P. P. Souza, P. O. Patrício, F. C. Moura, *New J. Chem.* **2015**, 39, 3051.
- [42] A. Annamalai, P. S. Shinde, T. H. Jeon, H. H. Lee, H. G. Kim, W. Choi, J. S. Jang, *Sol. Energ. Mat. Sol. C.* **2016**, 144, 247.
- [43] M. H. Lee, J. H. Park, H. S. Han, H. J. Song, I. S. Cho, J. H. Noh, K. S. Hong, *Int. J. Hydrogen Energ.* **2014**, 39, 17501.

- [44] A. G. Tamirat, W.-N. Su, A. A. Dubale, H.-M. Chen, B.-J. Hwang, *J. Mater. Chem. A* **2015**, 3, 5949.
- [45] L. Wang, C.-Y. Lee, P. Schmuki, *Electrochem. Commun.* **2013**, 30, 21.
- [46] N. Mirbagheri, D. Wang, C. Peng, J. Wang, Q. Huang, C. Fan, E. E. Ferapontova, *ACS Catal.* **2014**, 4, 2006.
- [47] Y. Hou, F. Zuo, A. Dagg, P. Feng, *Angew. Chem. Int. Ed.* **2013**, 52, 1248.
- [48] S. Petit, S. T. A. G. Melissen, L. Duclaux, M. T. Sougrati, T. Le Bahers, P. Sautet, D. Dambournet, O. Borkiewicz, C. Laberty-Robert, O. Durupthy, *J. Phys. Chem. C* **2016**, 120, 24521.
- [49] P. A. Kozin, J.-F. Boily, *J. Phys. Chem. C* **2013**, 117, 6409.
- [50] R. Shannon, *Acta Crystallogr. A* **1976**, 32, 751.
- [51] A. E. Tufo, K. E. García, C. A. Barrero, E. E. Sileo, *Hyperfine Interact.* **2013**, 224, 239.
- [52] K. Fominykh, *ACS Nano* **2015**, 9, 5180.
- [53] J. A. Bau, E. J. Lubber, J. M. Buriak, *ACS Appl. Mater. Inter.* **2015**, 7, 19755.
- [54] R. B. Soriano, J. Wu, M. G. Kanatzidis, *J. Am. Chem. Soc.* **2015**, 137, 9937.
- [55] G. Park, Y.-I. Kim, Y. H. Kim, M. Park, K. Y. Jang, H. Song, K. M. Nam, *Nanoscale* **2017**, 9, 4751.
- [56] K. Sivula, R. Zboril, F. Le Formal, R. Robert, A. Weidenkaff, J. Tucek, J. Frydrych, M. Grätzel, *J. Am. Chem. Soc.* **2010**, 132, 7436.
- [57] Y. Ling, G. Wang, D. A. Wheeler, J. Z. Zhang, Y. Li, *Nano Lett.* **2011**, 11, 2119.
- [58] H. K. Dunn, J. M. Feckl, A. Müller, D. Fattakhova-Rohlfing, S. G. Morehead, J. Roos, L. M. Peter, C. Scheu, T. Bein, *Phys. Chem. Chem. Phys.* **2014**, 16, 24610.
- [59] S. Li, J. Cai, Y. Mei, Y. Ren, G. Qin, *Int. J. Photoenergy* **2014**, 2014, 6.

6. V(III) Doped Nickel Oxide-Based Nanocatalysts for Electrochemical Water Splitting: Influence of Phase Composition and Doping on the Electrocatalytic Activity

This chapter is based on the following manuscript:

Böhm, D., Beetz, M., Kutz, C., Zhang, S., Scheu, C., Bein T., and Fattakhova-Rohlfing, D.



ToC image: Schematic illustration of the effect of vanadium (III) doping and chemical aging duration on the phase transformation of $\alpha\text{-Ni}(\text{OH})_2$ to well-stacked $\beta\text{-Ni}(\text{OH})_2$ or remaining V(III) containing disordered α -phase. An evaluation as oxygen evolution reaction catalysts revealed a strong influence of the chemical aging process and related crystallinity with the electrocatalytic activity.

6.1 Introduction

Hydrogen generated by energy from renewable sources is regarded as a potential clean energy carrier and storage medium for the future energy and mobility sector.^[1-2] In addition, the generated “green” hydrogen can further be used as process feedstock to lower the environmental impact in industry and generate valuable chemicals.^[3-4] Alkaline electrolysis has been in commercial use for decades and employs nickel-based electrocatalysts that exhibit some of the highest activity within the 3d metal group, in addition to their relatively low cost and great abundance in contrast to noble metal catalysts such as RuO₂ and IrO₂.^[5-6]

Oxygen evolution reaction (OER) catalysts on the anode side are thereby required to promote the kinetically more demanding half-reaction of the overall water splitting reaction involving four proton-coupled electron transfer reactions and an O-O bond formation step.^[7] In the recent years diverse nickel-based OER catalyst such as Ni-transition metal (TM) layered-double hydroxides^[8-10], Ni-TM-phosphides (Ni-TM-P)^[11-12] and micro- and nanostructured nickel-TM-oxide and -hydroxides^[13-14] gained considerable attention due to their high catalytic activity and stability under alkaline OER conditions.^[15] The outstanding performance of these catalysts is attributed to synergistic effects of nickel and neighboring transition metals as well as a result of nanosizing and -structuring leading to a significantly increased catalytic surface area or an increased share of exposed highly active crystal facets or coordination unsaturated edge-structures.^[15] Among the transition metals investigated for doping nickel-based materials to date, iron was first reported in 1987 by D. Corrigan to influence the OER activity of nickel oxide anodes.^[16] Since then Ni-Fe based catalyst were intensively investigated due to their high performance, although the exact mechanism behind the extraordinary decrease in the OER overpotential (η_{OER}) as well as the structure and identity of the catalytically active site were still unclear. This has been attributed to the numerous difficulties arising from the complex structure-activity relationship in the nickel hydroxide structure.^[8]

Recent studies revealed that even trace concentrations of transition metal ions, down to the parts per billion level in the electrolyte, have a tremendous effect on the OER activity of pure undoped Ni(OH)₂ anodes, which otherwise exhibit a low OER activity and rather high OER overpotential.^[17-18] In-situ X-ray absorption spectroscopy analysis of Ni-Fe oxides together with density functional theory (DFT) calculations in the group of Bell have indicated that iron and not nickel is the active site for the catalytic reaction in the mixed-metal oxide films.^[18-19] However, the fact that pure iron (oxy)hydroxide films do not show a reasonable OER activity and that the performance of mixed NiFe catalysts reaches a maximum activity for ≈ 25 at% Fe level indicates that a surrounding NiOOH matrix is required for the dopant active sites.^[19] It could be further shown by X-ray absorption spectroscopy and with cyclic voltammetry (CV) data that an initially present α -Ni(OH)₂ phase with nickel in oxidation state +II is transformed to a structurally similar Ni³⁺-containing γ -NiOOH phase at elevated potential, representing an initial active phase for OER, which is in accordance with the phase transition model of Ni(OH)₂ first proposed by Bode *et al.* and extended by Mellisop *et al.*^[19-21]

These findings highlight the importance of the initial Ni(OH)₂ phase as a second important factor determining the electrochemical properties of Ni-based catalysts, whose final structure can strongly vary depending on the synthesis conditions and chemical or electrochemical post-treatments. The α -Ni(OH)₂ phase is a layered brucite-type structure composed of Ni²⁺ ions bound to six octahedrally coordinated OH⁻ anions (each hydroxide being bonded to three nickel ions), with water molecules between the parallel layers.^[19] It is further known that several forms of structural disorder exist, including stacking defects, different degrees of hydration and the incorporation of foreign anions resulting in a turbostratic structure.^[22] An interesting and electrochemically relevant reaction for the nickel hydroxide is known as chemical aging, in which α -Ni(OH)₂ converts to a well-ordered β -Ni(OH)₂ phase with parallel-stacked layers accompanied by a removal of interlayer H₂O. Depending on the pH value, this process can

proceed via either a dissolution/precipitation mechanism comparable to Ostwald-ripening, or a “zipper” model displacing interlayer H₂O molecules with hydroxide as the “teeth” on a nickel backbone.^[23] Among other transition metal ions, doping with trivalent Al³⁺ was shown to significantly affect the stacking of Ni(OH)₂ layers during the aging process and thereby to stabilize the α -phase.^[24-25]

In a recent work by Fan *et al.* the synthesis of highly OER active monolayers of vanadium (III) doped Ni(OH)₂ layered double hydroxide (LDH) of the α -Ni(OH)₂ phase was demonstrated, even outperforming similarly synthesized NiFe(OH)₂ LDH. The effect of V-doping on the catalytic activity and the complex nature of active sites in Ni(OH)₂-based OER catalysts are however not yet fully understood.^[8]

To investigate the structure-activity relationship of V(III) doped Ni(OH)₂, we have synthesized nanosized Ni_{1-x}V_x(OH)₂ with different degrees of V-doping to address the following questions: (i) whether the doping element vanadium is incorporated in the crystal structure and how it affects the morphology at the nanoscale; (ii) how V-doping influences the phase transformation of α - to β -Ni(OH)₂ phase during the chemical aging process (iii) how the altered phases and nanostructures of doped Ni(OH)₂ correlate with the catalyst performance towards the oxygen evolution reaction. Since small particle sizes below 10 nm^[26-28] and a high degree of disorder^[29-30] within the structure of nickel hydroxide are reported to positively influence the catalytic activity of the material as shown for recent examples of highly OER active nanostructured α -Ni(OH)₂^[31-33], we have modified a rapid aqueous oxidation method introduced by Sutto for the synthesis of various metal hydroxide nanoparticles^[34] to obtain nanosized undoped and V-doped α -Ni(OH)₂.

6.2 Results and Discussion

Figure 1 depicts the synthesis approach used for the fabrication of pure and vanadium doped α - and β -Ni(OH)₂ polymorphs. Rapid oxidation of the aqueous Ni(II) / V(III) solution and quenching with MeOH under optimized reaction conditions (see supplementary information Figure S1-4) leads to the co-precipitation of an α -Ni_{1-x}V_x(OH)₂⁺Cl⁻ product whose color gradually shifts from turquoise and green to yellow for increased V(III) concentrations (Figure 1b). The transformation to the β -Ni(OH)₂ phase could be achieved by stirring the aqueous reaction product under ambient conditions, as revealed by X-ray diffractograms (XRD) (Figure 2a). Reaction products stirred and aged for up to 1 h (Figure 2a black curve) display broad reflections correlated with the α -Ni(OH)₂ phase (see zoom insets in Figure 2a for details), which gradually transforms to the β -phase with broad reflections visible after 3 h aging time (dark grey curve). The proposed models for this phase transition known as chemical aging are the ripening and zipper models, whereby the latter one is assumed to dominate at the given reaction conditions in deionized (DI) water.^[23] The different broadening of the 100 and 101 reflex is thereby associated with a β -phase Ni(OH)₂ structure with defects in the layer stacking^[30, 35], which increases in order by visibly sharpened reflections upon extended aging periods of 24 h (brownish curve) and 2 weeks (orange curve).

To effectively discriminate between α and/or β -phase Ni(OH)₂ we have used Raman spectroscopy, which is very sensitive towards structural variation induced by the degree of hydration, crystallinity or impurities in form of doping elements. Differently aged products (Figure 2b) indicate the presence of a Ni(OH)₂ phase by the strongly visible lattice vibrational mode at 450 cm⁻¹ associated with both the α - (lattice mode) and β -phase (A_{1g} mode)^[22]. With increasing aging duration the α -phase associated 2nd order lattice vibrational mode at 1075 cm⁻¹^[22] is reduced and not further visible in the spectra of the 24 h aged sample. In parallel with ongoing aging periods an increased intensity for the β -phase associated E_g mode is shown

at $\approx 315\text{ cm}^{-1}$ as well as for the vibrational mode at 3581 cm^{-1} associated with surface OH, lattice/bulk OH and layer H_2O .^[22] According to the Raman spectra and X-ray diffractograms, for up to 1 h aging, the pure $\alpha\text{-Ni}(\text{OH})_2$ is formed, which slowly undergoes a phase transition to $\beta\text{-Ni}(\text{OH})_2$ by chemical aging in DI water within $\approx 24\text{ h}$, with an intermediate product associated with an interstratified α/β -phase $\text{Ni}(\text{OH})_2$ structure after 3 h aging.^[23] The emerging β -phase $\text{Ni}(\text{OH})_2$ structure for the 3 h aged samples thereby exhibits strong structural defects shown by respective XRD line broadening and the presence of α and β -phase related Raman bands, which are associated with a disordered stacking sequence.^[23]

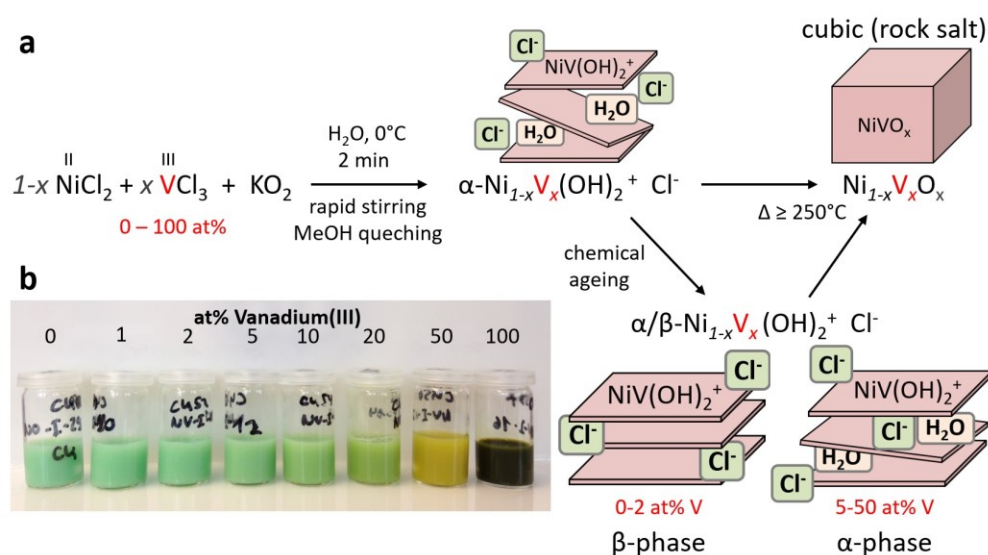
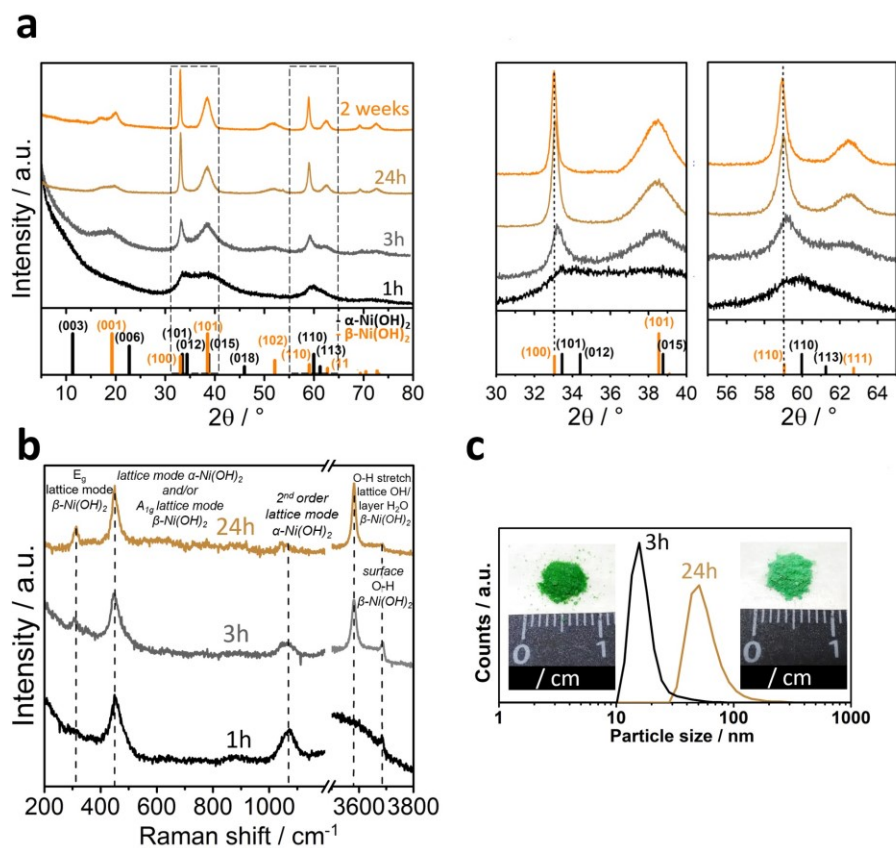


Figure 1 Schematic illustration of products prepared by the $\alpha/\beta\text{-Ni}_{1-x}\text{V}_x(\text{OH})_2^+ \text{Cl}^-$ synthesis route. (a) Schematic illustration of rapid co-precipitation by KO_2 , phase transformation by chemical aging and calcination of $\text{Ni}_x\text{V}_{1-x}(\text{OH})_2$. (b) Image of $\text{Ni}_x\text{V}_{1-x}(\text{OH})_2^+ \text{Cl}^-$ product series with $x \in [0;1]$.

Dynamic light scattering (DLS) (Figure 2c) shows no measurable signal for fresh (aged below 1 h) $\text{Ni}(\text{OH})_2$, as the product is strongly agglomerated and practically not dispersible. However, after 3 h aging in solution, nanoparticles in the range of $\approx 10\text{-}20\text{ nm}$ are detected, and for 24 h aged $\text{Ni}(\text{OH})_2$ the particle sizes increase to $\approx 80\text{ nm}$. The observed change in particle size indicates that XRD line broadening and sharpening upon aging are not solely based on stacking disorder as proposed Delmas *et al.* but may also originate from the nanosized morphology.^[30]

To the best of our knowledge, morphological changes on the nanoscale from interstratified α -Ni(OH)₂ to β -Ni(OH)₂ nanoparticles were not reported in the literature so far, although β -Ni(OH)₂ nanoparticles in the range of 10 - 25 nm were observed but not specifically characterized as an aging product of α -Ni(OH)₂.^[13] Further transformation to larger β -Ni(OH)₂ sheet-like structures with disordered stacking sequence upon chemical aging and transformation to an ordered β -Ni(OH)₂ phase are well described in the literature, including their properties as OER catalysts.^[20, 36-38] The focus in most of the recent literature is thereby on the activity of specifically synthesized α - or β -phases featuring various nanostructures^[13, 31-32, 39], however lacking a detailed investigation of the nanomorphology change during the chemical aging process and the effect of doping elements on this process. In this work, we therefore wish to address the question of how the addition of vanadium (III) ions in the synthesis influences the time-dependent phase transformation and morphological changes and to correlate these modifications with changes in OER activity.



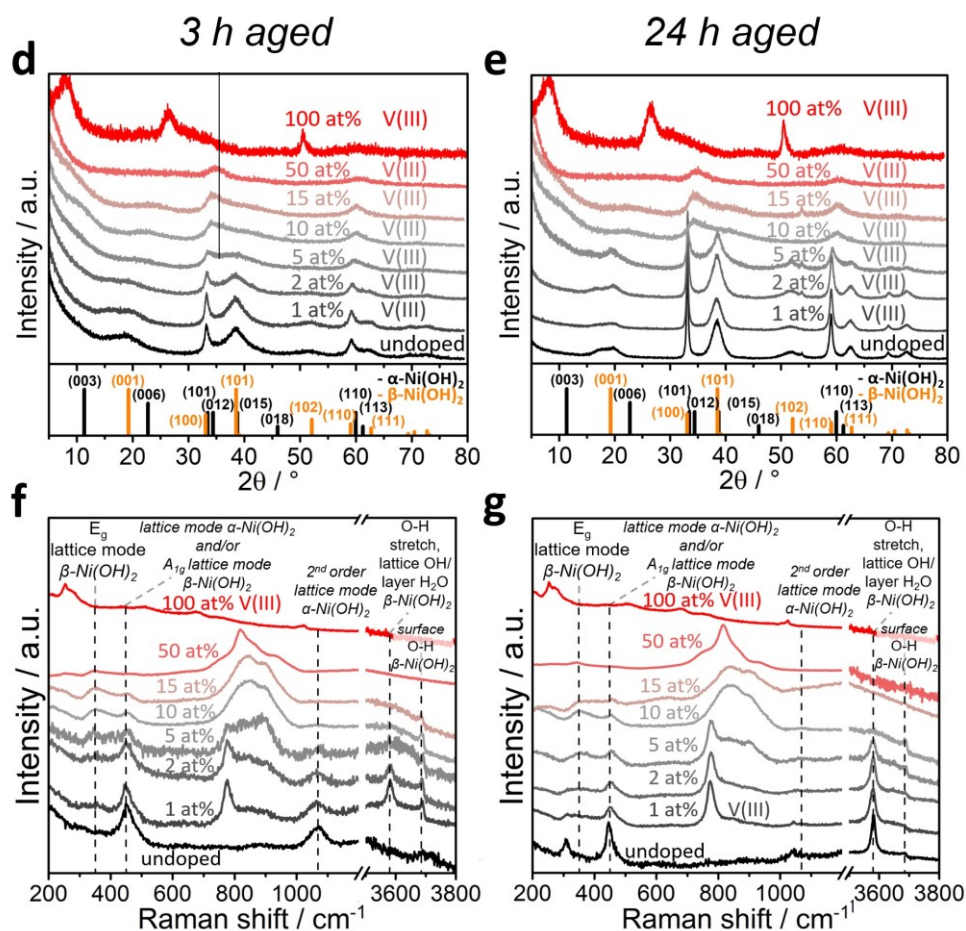


Figure 2 Structural characterization of time-dependent phase transitions of undoped and V(III)-doped Ni(OH)₂ in aqueous solution (a) X-ray diffractograms of undoped Ni(OH)₂ after 1, 3, 24 h and 2 weeks of stirring of the aqueous reaction product mixture before drying. (b) Raman spectra of undoped Ni(OH)₂ after 1, 3 and 24 h of stirring of the aqueous reaction product mixture before drying. (c) Dynamic light scattering data of a diluted sample of undoped Ni(OH)₂ after 3 and 24 h of stirring of the aqueous reaction product mixture. X-ray diffractograms of a series of V(III)-doped Ni(OH)₂ (0-100 at% V(III)) after (d) 1 h and (e) 24 h of stirring of the aqueous reaction product mixture. α -Ni(OH)₂ (Ni(OH)₂ x 0.75 H₂O) pattern: ICDD card # 00-038-0715 (rhombohedral, $a = b = 3.08$ Å, $c = 23.41$ Å, $\alpha = \beta = 90^\circ$, $\gamma = 120^\circ$). β -Ni(OH)₂ (Ni(OH)₂) pattern: ICDD card # 00-014-0117 (hexagonal, $a = b = 3.126$ Å, $c = 4.605$ Å, $\alpha = \beta = 90^\circ$, $\gamma = 120^\circ$). (e) Raman spectra of a series of V(III)-doped Ni(OH)₂ (0-100 at% V(III)) after (f) 1 h and (g) 24 h of stirring of the aqueous reaction product mixture. The bands at 450 cm⁻¹ (lattice mode) and 1070 cm⁻¹ (2nd order lattice mode) are assigned to the α -Ni(OH)₂ phase.^[22-23] Bands at 447 cm⁻¹ (A_{1g} lattice mode), 3581 cm⁻¹ (O-H stretch / lattice OH / layer H₂O mode) and 3690 cm⁻¹ (surface O-H stretch) were assigned to the β -Ni(OH)₂ phase.^[23]

The addition of 2 at% V(III) results in the formation of a product with visibly altered crystallinity, as indicated by the broadened reflections in the respective diffractogram in Figure 2d for the ≈ 3 h aged doping series as compared to the undoped material (black curve). With increasing V(III) concentration, the reflections broaden significantly, which indicates a delayed aging process with increased stacking defects and small crystallite domain sizes. A successful doping of V(III) in the Ni(OH)₂ structure by the proposed rapid co-precipitation

synthesis is indicated by a gradual shift of the 100 reflection at $\approx 34^\circ$ 2-theta and 110 reflection at $\approx 60^\circ$ 2-theta to higher angles in the concentration range of 0-50 at% V(III) due the slightly smaller ionic radius of V^{3+} ($\approx 0.64\text{\AA}$)^[40] vs. Ni^{2+} (0.69\AA)^[40].

Inductively coupled plasma – optical emission spectrometry (ICP-OES) measurements (Figure S1) of washed co-precipitation products furthermore confirmed the quantitative incorporation of vanadium ions over a range of 1-15 at%. Even for a 50 at% V(III) concentration in the precursor solution, ≈ 39 at% vanadium is incorporated in the reaction product without any visible side phase formation (as observed by XRD) (Figure 2d).

The presence of vanadium ions is visible in the Raman spectra of samples doped with as little as 1 at% V(III), with an additional band present at around $\approx 775\text{ cm}^{-1}$ attributed to a V-O vibrational mode, which was not reported in literature so far for doped $Ni(OH)_2$. With increasing vanadium content, a broad band at $\approx 845\text{ cm}^{-1}$ with a shoulder at $\approx 900\text{ cm}^{-1}$ arises. These may be attributed to vanadium oxide anions, which may form after the solubility limit of V^{3+} ions in $Ni(OH)_2$ is reached. The insertion of vanadate anions into the interlayer space was described by Park *et al.*^[41] This concentration-dependent increase of interlayer ion-associated bands is correlated with a decrease in intensity of the β -phase-associated band at 3581 cm^{-1} , suggesting a lower content of stacked $Ni(OH)_2$ sheets or β - $Ni(OH)_2$ particle size with surrounding α -phase.^[23, 26] Doping concentrations of 50 at% V(III) in the precursor solution, corresponding to ≈ 39 at% V(III) content in the product (Table S1) show one dominant band at 850 cm^{-1} , besides broadened bands at ≈ 775 and $\approx 900\text{ cm}^{-1}$. The difference in band intensities may thereby be explained by an altered amount of excitable inter- and intralayer V-O vibrations.

A chemical aging period of 24 h for the $Ni_{1-x}V_x(OH)_2$ series reveals a correlation between the V-doping concentration and the crystallization process over an intermediate nanocrystalline β -phase $Ni(OH)_2$ (3 h aged sample) with high stacking disorder to form the β -phase product (24 h

aged sample) with increased stacking order. Doping concentrations as low as 2 at% V(III) (Figure 2e) significantly delay the ordering of $\text{Ni}_{1-x}\text{V}_x(\text{OH})_2$ sheets, with concentrations from 10 at% V and higher fully preventing further crystallization as shown by matching diffractograms of 3 h vs. 24 h aged samples with respective concentrations. An inhibiting effect of V(III) ions on the β - $\text{Ni}(\text{OH})_2$ crystallization and ordering by chemical aging is also visible in the Raman spectra of the differently aged doping series. The intensity of the band corresponding to the A_{1g} lattice mode at $\approx 450\text{ cm}^{-1}$, corresponding to both α - and β - $\text{Ni}(\text{OH})_2$ ^[22], is inversely correlated to the V(III) concentration as well as the band at 3581 cm^{-1} , which is associated with an O-H stretch / lattice OH and layer H_2O mode^[22] observed for undoped β -phase $\text{Ni}(\text{OH})_2$ (Figure 2b).

Time-dependent phase transitions induced by chemical aging were investigated in more detail by electron microscopy to correlate changes of the crystal structure analyzed by XRD and Raman spectroscopy to the nanoscale morphology and local structure of the material. Figure 3a-c confirms the amorphous and agglomerated structure of up to 1 h chemically aged $\text{Ni}(\text{OH})_2$ as indicated above by XRD, Raman and DLS data. The electron diffraction pattern shows broad diffuse rings that are attributed to the presence of α -phase $\text{Ni}(\text{OH})_2$. The crystallization of small nanoparticles in the range of 2-4 nm from the surrounding turbostratic α -phase (Figure 3d) for 3 h aged $\text{Ni}(\text{OH})_2$ could be observed directly in high resolution TEM images (Figure 3e and inset) and was already proposed by DLS measurements (Figure 2c), with lattice spacings of single nanoparticles (Figure S5a) corresponding to the β -phase. In agreement with the XRD data, the electron diffraction results confirm the increase in crystallinity and transformation to well-stacked β -phase $\text{Ni}(\text{OH})_2$ for 24 h aged $\text{Ni}(\text{OH})_2$ (Figure 3i).

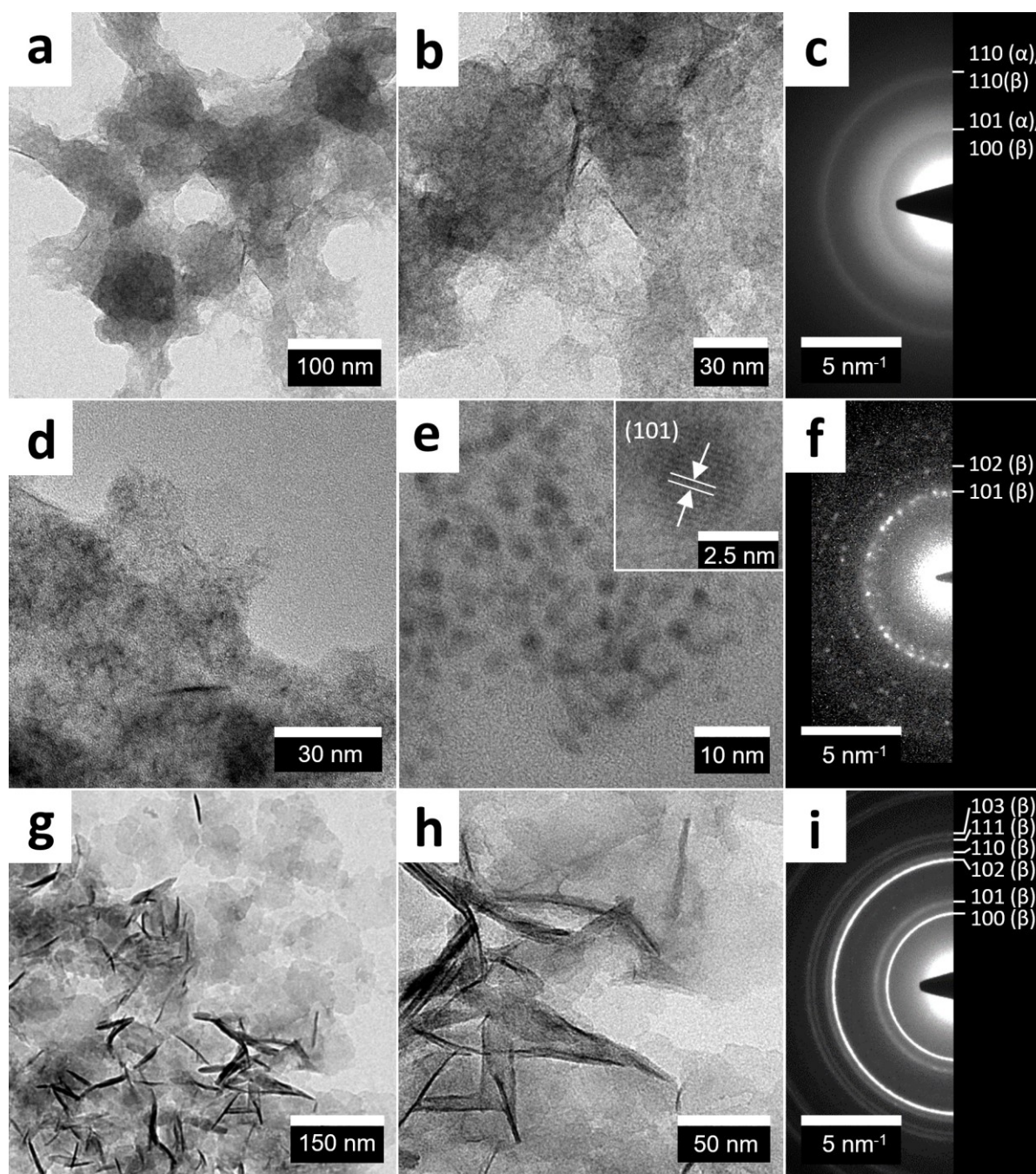


Figure 3 Structural characterization of time-dependent phase transformations by TEM of 1 h (a-c), 3 h (d-f) and 24 h (g-i) $\text{Ni}(\text{OH})_2$ aged samples. TEM images of 1h aged $\text{Ni}(\text{OH})_2$ (a, b) turbostratic phase with selected area electron diffraction pattern (c). TEM images of 3 h aged sample (d, e) with nanoparticle (e, and inset) morphology and ED pattern (f). TEM images of 24h aged $\text{Ni}(\text{OH})_2$ sample with nanosheet morphology and ED pattern (i). α - $\text{Ni}(\text{OH})_2$ ($\text{Ni}(\text{OH})_2 \cdot 0.75 \text{H}_2\text{O}$) pattern: ICDD card # 00-038-0715. β - $\text{Ni}(\text{OH})_2$ ($\text{Ni}(\text{OH})_2$) pattern: ICDD card # 00-014-0117.

The visibly sharpened β - $\text{Ni}(\text{OH})_2$ 101 reflection observed by XRD (Figure 2a) upon chemical aging suggests - besides a lower amount of defects in the layer stacking - a growth of the nanosized material along the crystallographic ac -plane that is directly observable in form of a

nanosheet-like morphology and evident in the respective electron diffraction pattern (Figure 3i).

The microstructure of doped Ni(OH)₂ was investigated for 5 at% (Figure 4) and 10 / 15 at% (Figure S6) V-containing product chemically aged for ≈3 h and 24 h, respectively. 5 at% V-doped Ni(OH)₂ aged for 3 h depicted in Figure 4a,b resembles the nanoparticle-based morphology of undoped and equally long aged hydroxide depicted in Figure 3d, e. Although the crystallinity shown by XRD (Figure 2d) is lower than that of the undoped counterpart (Figure 2a), the electron diffraction pattern (Figure 3f and Figure 4c) indicate a similar β-phase Ni(OH)₂ structure with disordered stacking sequence.

An influence on the phase transformation process becomes evident for 5 at% doped samples chemically aged for 24 h. As suggested by the X-ray diffractograms in Figure 2d, e, vanadium doping strongly inhibits the crystallization and proper Ni(OH)₂ sheet stacking, which is illustrated by a comparison of the respective electron diffraction patterns (Figure 3i and Figure 4f). According to our TEM investigations, V-doping inhibits particle growth along the crystallographic ac-plane, as only short and stacked sheet-like structures are observable by TEM (Figure 4e) in contrast to tens of nanometer long well-defined sheets (Figure 3g, h) for equally aged undoped material. Higher concentrations of 10 and 15 at% V(III) in 3 h and 24 h aged samples (Figure S6), respectively, show very similar nanostructures of particles (3 h aged) and small sheet-like fragments (24 h aged) in HR-TEM images.

ICP-OES measurements (Table S1) confirm that the V(III) contents in the Ni_{1-x}V_x(OH)₂ samples are very close to the nominal doping level of up to 15 at% V. STEM-EDX mapping measurements of 10 at% V-doped samples chemically aged for 3 h (Figure 4g-i) and 72 h (Figure 4j-l), further confirm the uniform distribution of V on the nanoscale (Figure 4i,l and Figure S7a-f), as well as the micrometer-scale (Figure S7g-i).

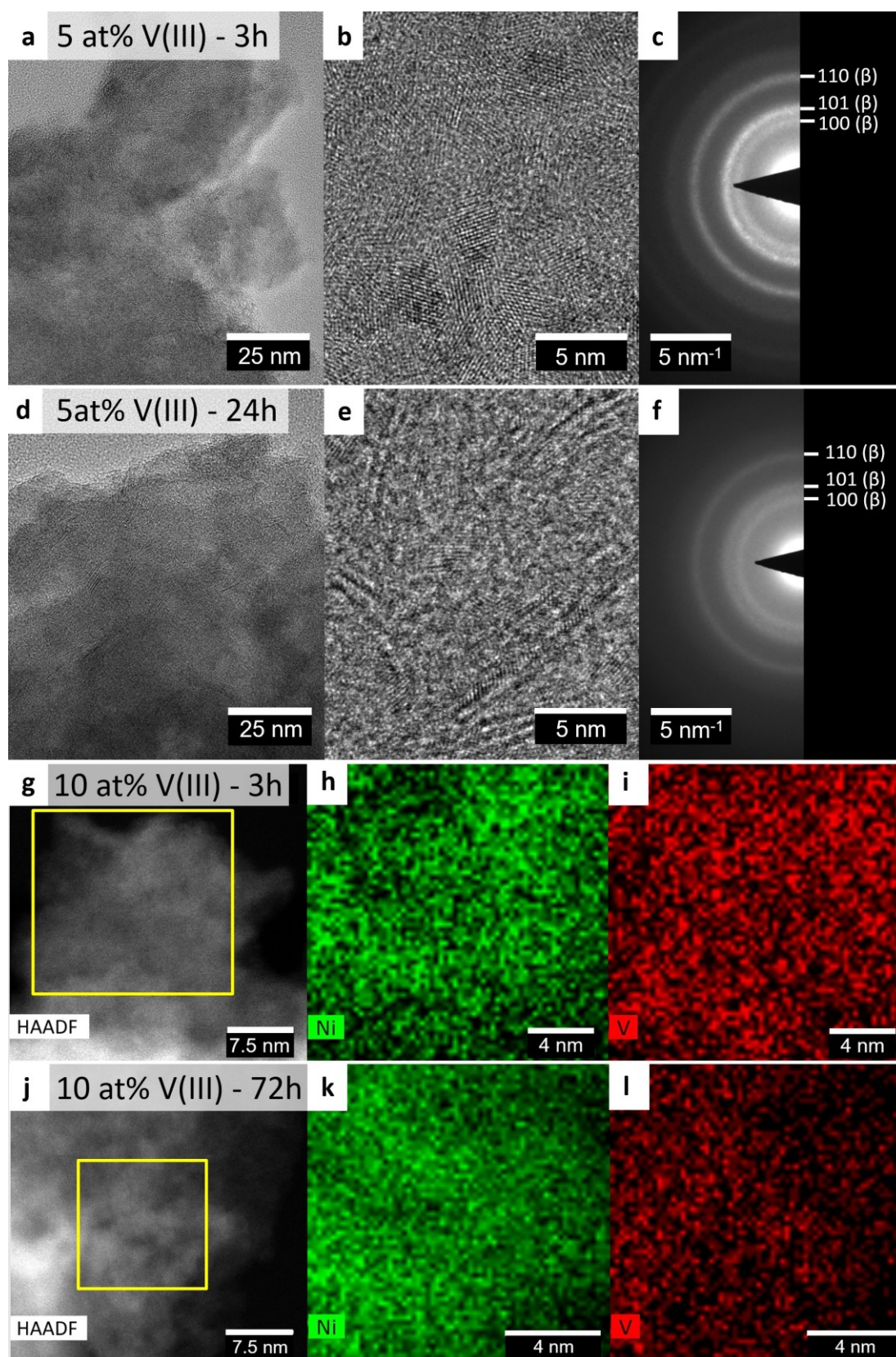


Figure 4 Structural characterization of time-dependent phase transformations of V(III) doped Ni(OH)₂ by TEM. TEM images and electron diffraction pattern of 5 at% V(III) doped Ni(OH)₂ after 3 h (a-c) and 24 h (d-f) aging time. β -Ni(OH)₂ (Ni(OH)₂) pattern: ICDD card # 00-014-0117. STEM atomic-contrast

micrographs and EDX elemental mappings of Ni and V of 10 at% V(III) doped Ni(OH)₂ after 3 h (g-i) and 72 h (j-l) aging time.

It can be concluded that the rapid co-precipitation of the Ni(II) and V(III) precursor by KO₂ in aqueous solution leads to homogeneously doped α -Ni_{1-x}V_x(OH)₂ that undergoes a transformation to β -phase nanoparticles after \approx 1 - 3 h and for low doping concentrations (up to \approx 5 at%) a further assembly/growth of nanoparticles to sheet-like β -Ni(OH)₂ particles within 24 h without a detectable segregation of V(III) dopant. Higher V(III) concentrations \geq 10 at% thereby inhibit the proper stacking required for the beta phase formation also with a 24 h aging duration.

To further investigate the influence of V(III) doping on the phase transformation upon chemical aging, electron energy loss (EELS) spectra (Figure 5 and Figure S8) were recorded. As shown in Figure 5b, Ni-L₃ and Ni-L₂ edges of α -Ni(OH)₂ (15 min) and α -Ni_{0.9}V_{0.1}(OH)₂ (72 h) are at very similar positions. In contrast, the edges of β -Ni(OH)₂ (72 h) shift towards higher energy loss. The so-called chemical shift is caused by a shift in the unoccupied states with respect to the core states (2p for L₂ and L₃ edges), which may indicate changes in the valence state and the local coordination of the present phase. For example, there is a clear peak shift of \approx 0.3 eV between α - and β -Ni(OH)₂. On the other hand, the introduction of 10 at% V(III) hardly changes the chemical shift of the α -like Ni_{0.9}V_{0.1}(OH)₂. The calculated electronegativity (dimensionless values according to the Pauling scale) values of Ni²⁺ and V³⁺ are $\chi_i = 1.367^{[42]}$ and $\chi_i = 1.545^{[42]}$, respectively. A shift of the Ni-L₃ edge due to a partial oxidation of Ni²⁺ may not be ruled out, but clearly plays a lesser role. The EELS measurement serves as further evidence for a V(III) induced inhibition of the phase transformation and stacking of turbostratic α -Ni(OH)₂ to the well stacked β -Ni(OH)₂ under given synthesis conditions.

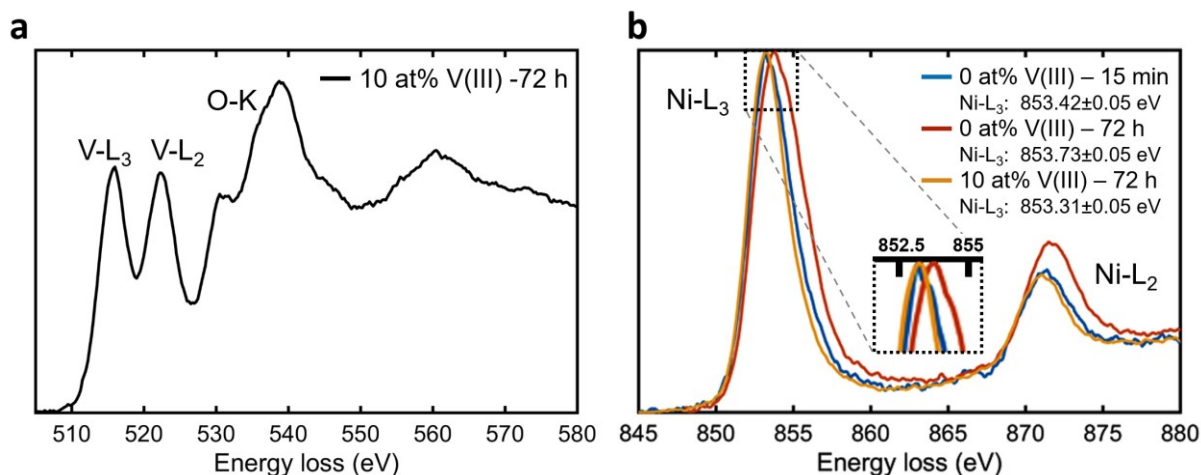


Figure 5 Structural characterization of time-dependent phase transformation of V(III) doped $\text{Ni}(\text{OH})_2$ by EELS. (a) EELS spectrum with V-L₃, V-L₂ and O-K edge of 10 at% V(III) doped $\text{Ni}(\text{OH})_2$ sample after 72 h aging. (b) Overlay of EELS spectra in energy loss region of Ni-L₃ and Ni-L₂ edge of $\text{Ni}(\text{OH})_2$ samples after 15 min (blue curve), 72 h (orange curve) aging, and 10 at% V(III) doped $\text{Ni}(\text{OH})_2$ samples after 72 h aging (yellow curve).

The electrochemical performance of chemically aged $\text{Ni}_{1-x}\text{V}_x(\text{OH})_2$ towards the oxygen evolution reaction was measured for thin film samples in a diluted KOH electrolyte (see experimental part for sample preparation and exact measurement conditions). SEM images of prepared electrodes of 1 h and 24 h aged product reveal an aggregated particle-like morphology and a smoother sheet containing (indicated by red arrows in Figure S9d) morphology, respectively.

In the cyclic voltammograms, α -phase electrodes (Figure 6a and Figure S10a) show a pronounced $\text{Ni}^{2+}/\text{Ni}^{3+}$ redox feature centered around 160 mV with respect to theoretical oxygen evolution reaction potential of 1.23 V vs. reversible hydrogen electrode (RHE) and referenced as η_{OER} . The Ni^{3+} oxidation peak located at $\eta_{\text{OER}} \approx 250$ mV in the first cycle with a marked shift to $\eta_{\text{OER}} \approx 175$ mV for later cycles is attributed to the α - γ phase transformation as proposed in the literature.^[21, 43-44] The shift of the oxidation peak to lower potentials within the first cycles is thereby assumed to result from a restructuring of the initial anodic $\text{Ni}(\text{OH})_2$ layer.^[21] Upon cycling (the 4th vs. the 20th cycle) the $\text{Ni}^{2+}/\text{Ni}^{3+}$ redox feature slightly decreases accompanied

by an increase in OER activity, which is explained by a quasi-reversible formation of the catalytically active γ -NiOOH phase, as widely accepted in the literature.^[20-21, 33]

In comparison, aged β -Ni(OH)₂ phase (Figure 6b and Figure S10b) does not show a visible reduction to Ni²⁺ during CV cycling, but a Ni³⁺ oxidation feature that is $\eta_{\text{OER}} \approx 50$ mV further positive centered at $\eta_{\text{OER}} \approx 300$ mV than for the α -phase product. During cycling this Ni²⁺/Ni³⁺ oxidation feature is analogously lowered to $\eta_{\text{OER}} \approx 225$ mV, which is ≈ 50 mV higher than for the α -phase. The oxidation peak is thereby associated with a less reversible β -Ni(OH)₂ to β -NiOOH transformation and in agreement with the structural characterization of the 24 h aged Ni(OH)₂ product.^[21, 43-44]

In terms of the OER activity, the turbostratic α -phase product (0 at% V – 1 h aged) (Figure 6e) shows, with ≈ 34.5 mA cm⁻¹, more than 4 times the activity as compared to ≈ 6.8 mA cm⁻¹ for the 24 h aged β -phase Ni(OH)₂ (0 at% V – 24 h aged) (Figure 6f), with both values being determined for the 20th CV scan cycle at an OER overpotential of 400 mV. The overpotentials required to reach an OER current density of 10 mA cm⁻² were calculated to be ≈ 340 mV and ≈ 432 mV for the 1 h and 24 h aged sample, respectively. In comparison, α -Ni(OH)₂ OER catalysts reported by Luan *et al.* exhibit an OER overpotential of 260-320 mV depending on the morphology with highest performance obtained for a nanoparticle based catalyst.^[33] A further example of an optimized OER catalyst was reported by Zhang *et al.* who synthesized an α -Ni(OH)₂-nanosheet catalyst on nickel foam substrate that showed an η_{OER} of 266 mV.^[32] The limited OER activity of our prepared catalyst samples compared to literature reports is attributed to the non-optimized electrode morphology in form of densely coated, micrometer thick (see Figure S9) and relatively poor conductive hydroxide layers deposited simply by drop-casting. Together with a non-optimized nanomorphology a comparably low electrochemically active surface area is expected which further lowers the performance.

The effect of vanadium (III) doping on the cyclic voltammograms of 1 h aged Ni(OH)₂ (Figure 6c and Figure S11a) is a significantly broadened Ni²⁺/Ni³⁺ oxidation feature beginning around $\eta_{OER}=150$ mV and ranging up to the OER potential depending on the doping concentration. The low potential part of the feature thereby indicates the presence of α -Ni(OH)₂, which undergoes the α - γ phase transformation.^[21, 43-44] The broadening of the oxidation peak enhanced for higher doping concentrations is further regarded to result from a restructuring of the initial anodic Ni(OH)₂ layer that is still observable after 20 scan cycles, as opposed to the undoped α -phase product where this process is completed within the first 2-3 scan cycles (see Figure 6a). The OER activity of the 1 h aged sample shows a maximum of ≈ 38.1 mA cm⁻¹ for 1 at% V-doped sample (Figure 6e and Table S2) and a decrease directly correlated to the doping ion concentration.

In comparison, 24 h chemically aged Ni_{1-x}V_x(OH)₂ shows a lower and anodically shifted Ni²⁺/Ni³⁺ redox feature as observed for equally aged undoped Ni(OH)₂, indicating a β -Ni(OH)₂ to β -NiOOH transformation for doping concentrations below 10 at% V(III). Higher doping concentrations lead to a cathodic shift of the oxidation feature onset by ≈ 50 mV, which we attribute to a partial contribution by a α - γ phase transformation (Figure 6d and Figure S11b). According to the voltammograms it can be concluded that 24 h aged Ni(OH)₂ doped with ≥ 10 at% V(III) shows characteristics of a α/β -Ni(OH)₂ mixed or interstratified phase.

The OER activity (Figure 6f and Table S3) exhibits a maximum at a V(III) concentration of 5 at%, which results in an approximately doubled (≈ 14.6 vs. ≈ 6.8 mA cm⁻¹ at $\eta_{OER}=400$ mV, 20th scan cycle) catalytic performance for the doped sample.

The discrepancy between the V(III) ion concentrations of catalytically most efficient 1 h and 24 h aged samples indicates that the structure/morphology of Ni(OH)₂ modified by the doping is the reason for the altered OER activity, which is in agreement with literature reports on the electrocatalytic activity of different Ni(OH)₂ phases^[21, 32] and active center sites.^[33]

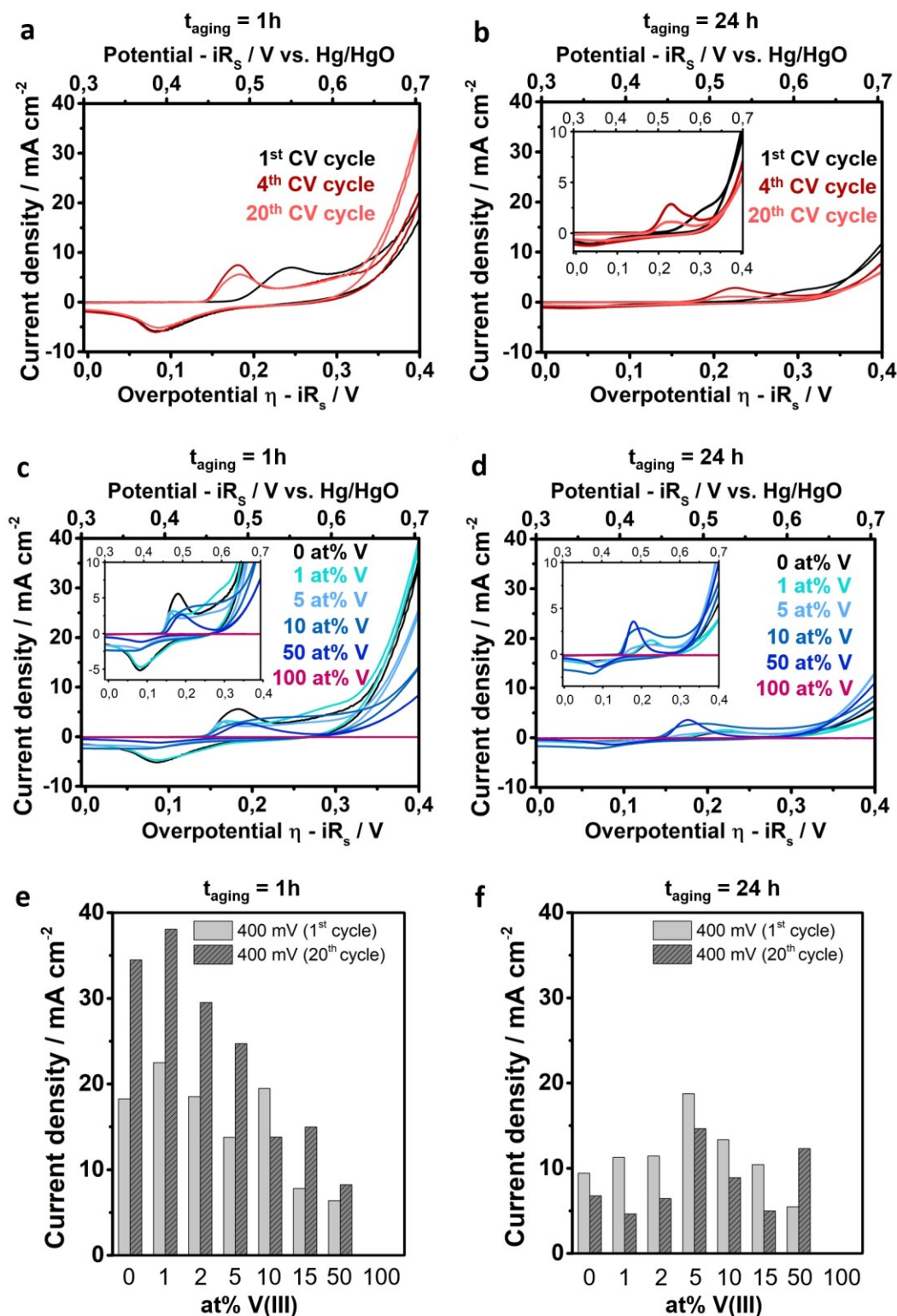


Figure 6 Electrochemical characterization of chemically aged and V(III) doped Ni(OH)₂. Cyclic voltammograms (1st, 4th and 20th scan cycle) of 1 h (a) and 24 h (b) aged undoped Ni(OH)₂. (c) Cyclic voltammograms (20th scan cycle each) of 1 h (c) and 24 h (d) aged 0, 1, 5, 10 and 50 at% V(III) containing Ni(OH)₂ (nominal doping concentration) and 100 at% V(III) based sample. Plot of OER activities of V(III) containing Ni(OH)₂ at an overpotential of 400 mV for the 1st and 20th CV scan cycle for 1 h (e) and 24 h (f) chemically aged samples.

With a series of V(III) doping concentrations, the phase transformation from hydroxide to the rock-salt $\text{Ni}_{1-x}\text{V}_x\text{O}$ structure upon calcination was investigated. For the 1 h aged $\text{Ni}(\text{OH})_2$ sample with α -phase structure a transition temperature of $\approx 275^\circ\text{C}$ was measured by thermogravimetric analysis with differential scanning calorimetry (Figure S12a). For the undoped $\text{Ni}(\text{OH})_2$ a calcination temperature of 250°C was applied to obtain a nanosized product that can be assigned to the NiO rock salt phase with a further growth of crystalline domain sizes at higher calcination temperatures of up to 450°C (Figure S12b). In comparison, for the 24 h aged β -phase $\text{Ni}(\text{OH})_2$ product an increased phase transition temperature of close to 300°C was measured (Figure S12c).

As the applied temperature range of $250\text{-}300^\circ\text{C}$ is below or very close to literature reported nickel hydroxide-oxide phase transition temperatures of $\approx 285^\circ\text{C}$ ^[45] for α - $\text{Ni}(\text{OH})_2$ and $\approx 315\text{-}325^\circ\text{C}$ ^[45-46] for β - $\text{Ni}(\text{OH})_2$, presumably a distorted nanosized NiO rock salt phase with residual water content is formed as reported in literature for similarly low calcination temperatures and indicated by a the broad NiO 111 and 200 reflex.^[47]

XRD patterns of 300°C and 250°C calcined samples of 1 h aged $\text{Ni}_{1-x}\text{V}_x\text{OH}$ (Figure 7a and Figure S13b, respectively) reveal an inhibited growth of crystalline domains with increasing V(III) content, based on significantly broadened peaks and thermogravimetric analysis (Figure S13a). The phase transition temperature of 1 h aged $\text{Ni}_{0.9}\text{V}_{0.1}\text{O}$ is increased by $\approx +50^\circ\text{C}$ versus the equally prepared undoped α - $\text{Ni}(\text{OH})_2$.

The hydroxide to rock salt $\text{Ni}_{1-x}\text{V}_x\text{O}$ transformation (Figure S13a) is regarded to originate from a different degree of stacking disorder and interlayer H_2O in the hydroxide phase caused by vanadium doping. Even at higher calcination temperatures of up to 450°C , V(III) doping levels of 10 at% significantly decrease the crystalline domain size as indicated by respective peak broadening (Figure S13c).

Possible ways to tune the crystallinity are therefore altering the calcination temperature (Figure 7b, c) or the doping level

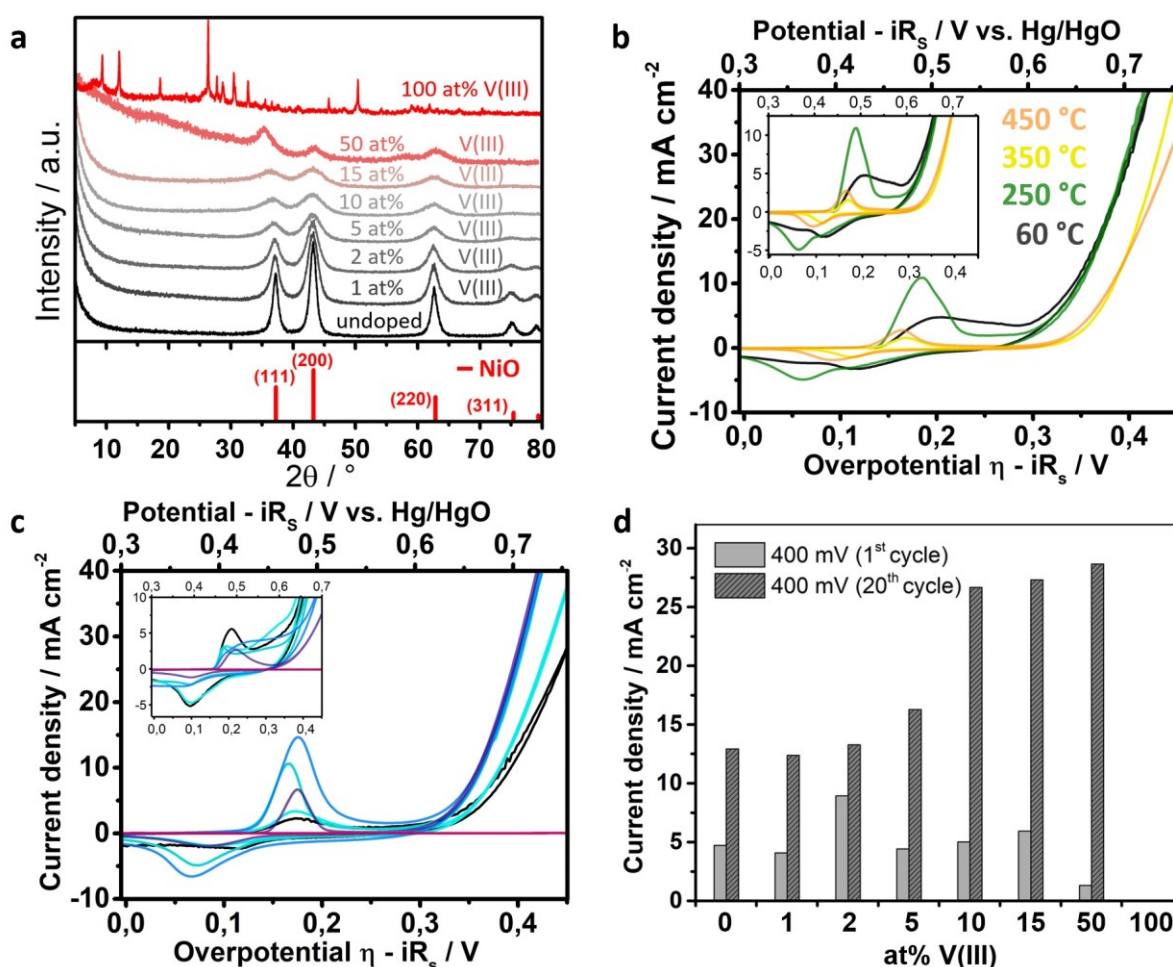


Figure 7 Characterization of structure and electrochemical activity of V(III)-doped $\text{Ni}(\text{OH})_2$ after calcination. (a) X-ray diffractogram of $300\text{ }^\circ\text{C}$ calcined V(III) doped $\text{Ni}(\text{OH})_2$ (0-50 at% V(III) black and greyscale). (b) Cyclic voltammetry (20th scan cycle each) of 1 h aged $60\text{ }^\circ\text{C}$ dried (black), and heated at $250\text{ }^\circ\text{C}$ (green), $350\text{ }^\circ\text{C}$ (yellow) and $450\text{ }^\circ\text{C}$ (orange) $\text{Ni}_{0.9}\text{V}_{0.1}\text{O}_x$. (c) Cyclic voltammetry (20th scan cycle each) of $300\text{ }^\circ\text{C}$ calcined $\text{Ni}(\text{OH})_2$ with doping concentrations ranging from 0 (black), 5 (light turquoise), 10 (turquoise), 15 (blue), 50 (dark-violet) and 100 at% (violet) V(III). (d) Plot of OER activities of V(III) containing (0-100 at% V), $300\text{ }^\circ\text{C}$ calcined $\text{Ni}(\text{OH})_2$ at an overpotential of 400 mV for the 1st and 20th CV scan cycle.

Calculated crystalline domain sizes of the rock salt structure according to Scherrer's equation derived from XRD signal broadening reveal a continuous decrease from $\approx 4.5\text{ nm}$ for undoped down to $\approx 2\text{ nm}$ for 10 at% V-doped samples calcined at $250\text{ }^\circ\text{C}$ (Figure S13d, black data points). Analogously, samples calcined at $300\text{ }^\circ\text{C}$ show domain sizes ranging from $\approx 8.5\text{ nm}$ for undoped NiO down to $\approx 2.5\text{ nm}$ for 15 at% V(III) doped $\text{Ni}_{1-x}\text{V}_x\text{O}$ (Figure S13d, red data points). Along with the decrease of crystallinity due to doping ions, an increase of the lattice

parameter from $\approx 4.185 \text{ \AA}$ (undoped – 300 °C calcined) to $\approx 4.205 \text{ \AA}$ ($\geq 10 \text{ at\%}$ – 300 °C calcined) determined from fitted reflection centers of X-ray diffractograms can be observed (Figure S13e and Table S4). Calculated lattice parameters linearly rise between 0 and 2 at% V, leveling off at 5 at% and reaching a maximum for 10 at% doping. The lattice parameters are larger than for rock salt NiO (4.178 \AA , ICDD #01-071-1179) and are associated with a NiO_x phase containing hydroxyl group residues not fully transformed to the stoichiometric NiO rock salt phase within that temperature range.^[48] Increased V(III)-ion doping that was shown to reduce the crystalline domain size is therefore regarded to lead to increased amounts of hydroxyl group residues enlarging the resulting crystallographic unit cell upon calcination at moderate temperatures of 300 °C. This hypothesis is supported by the formation of a hydrated NiO_x phase with even larger lattice parameters ranging from 4.27 - 4.30 Å (depending on the doping level) for a decreased calcination temperature of 250 °C (Figure S13e and Table S5).

Strikingly, even for high V(III) precursor concentrations of 50 at% resulting in a doping level of $\approx 39 \text{ at\%}$ (Table S1) no additional phases originating from V₂O₃, VO₂ or V₂O₅ can be observed at calcination temperatures of up to 300 °C. At even higher calcination temperatures of 450 °C for a Ni_{0.9}V_{0.1}OH_x sample no phase separation could be detected (Figure S13c). The high solvation limit of V(III) in the NiO_x phase, significantly exceeding the proposed limit of 5-10 at% V(III) by Park *et al.*, may be attributed to a stabilization effect for nanoscale phases, as described by Fominykh *et al.* for Fe- and Co-doped NiO.^[14, 49] Above the solubility limit, vanadium ions are not further incorporated into the Ni(OH)₂ lattice and result in a colored supernatant after washing of the synthesis product that is discarded.

Electrodes calcined at 250 °C (Figure S14) and 300 °C were investigated regarding their electrocatalytic activity with focus on the influence of their doping level. Calcination of 1 h aged α -Ni(OH)₂ Ni_{0.9}V_{0.1}O_x product to 250 °C leads to a significant increase of the Ni²⁺/Ni³⁺

redox feature with an accompanied shift of the oxidation feature from $\eta_{OER} \approx 200$ mV to $\eta_{OER} \approx 175$ mV.

The activity of the 250 °C calcined sample determined after 15 scan cycles thereby remained comparable to that of the hydroxide-based sample (Figure 7b) with a Tafel slope even outperforming both the unheated α - and β -phase product (Figure S15).

The cyclic voltammogram of V(III) doped $\text{Ni}_{1-x}\text{V}_x\text{OH}$ calcined at 300 °C shows a strong increase of the $\text{Ni}^{2+}/\text{Ni}^{3+}$ redox feature for up to 10 at% doped samples, which is attributed to the decreased crystallite domain size and thus increased accessible active sites. An even higher V(III) content leads to a reduction of the redox feature, as the doping ion is shown to be redox inactive in the scanned potential range (see 100 at% V in Figure 7c).

Concerning the electrocatalytic activity for the oxygen evolution reaction, samples with 10 - 50 at% V(III) content show the best performance with up to ≈ 27.5 mA cm⁻² among the 300 °C calcined samples (Figure 7d). The discussed effects of V-doping on the $\text{Ni}(\text{OH})_2$ to NiO phase transition and resulting crystallite domain sizes upon calcination thereby explain the high catalytic activity of nanosized nickel-vanadium-oxide based OER catalysts upon calcination at temperatures up to 300 °C. For even higher calcination temperatures of 350 and 450 °C, a decrease in intensity of the $\text{Ni}^{2+}/\text{Ni}^{3+}$ redox feature is observed with a further shift of the oxidation feature to $\eta_{OER} \approx 150$ mV accompanied by a significant decline of catalytic activity (Figure 7b).

6.3 Conclusion

Employing in-depth structural characterization, we have demonstrated that the rapid co-precipitation of nickel (II) and vanadium (III) chloride by potassium superoxide under cooling is a suitable synthesis approach for obtaining homogeneously doped α -Ni(OH)₂. Chemical aging by stirring of the reaction product in DI water - a known route for the conversion of α - to β - phase^[23, 50] - is strongly inhibited by V(III) ions. Samples from 5 at% V(III) and higher thereby show a delayed transformation to a Ni(OH)₂ β -phase product with stacking disorder within 24 h, with samples of 10 at% V-content and higher structurally resembling the initial turbostratic α -phase. Foreign ion incorporation in the α - or β -phase Ni(OH)₂ has been reported for a variety of transition metal ions, and results for most in a slightly distorted Ni(OH)₂ structure^[24-25, 35] as also shown in this work. We attribute the inhibiting effect on the phase transition to the presence of vanadium ions in the structure that prevent the formation of larger Ni(OH)₂ nanosheets. These sheet-like structures can stack for low doping concentrations (<5 at%) according to proposed models^[20, 23] and form β -Ni(OH)₂ with a higher (doped samples) or lower (undoped samples) content of stacking defects.

Regarding the electrochemical activity towards the oxygen evolution reaction, it could be shown that a very low V-doping content of 1 at% can enhance the activity of α -phase related 1 h aged Ni(OH)₂ by ≈ 10 % to ≈ 37.5 mA cm⁻² ($\eta_{OER}=400$ mV). The catalytic performance of chemically aged product resembling the β -phase Ni(OH)₂ on the other hand is generally lower by a factor of ≈ 3 (≈ 7.5 mA cm⁻² for undoped, 24 h aged Ni(OH)₂), but can be doubled to ≈ 15 mA cm⁻² by 5 at % V-doping. We attribute this minor enhancement for the 1 h short aged product to the fact that already the undoped product resembles the highly disordered α -phase, which is reported to be electrocatalytically more active than the ordered β -phase.^[32-33, 39] The increase in activity for the V-doped and chemically aged samples is more pronounced due to the difference in crystallinity and phase. For these samples, a higher V(III) content effectively

prevents a transformation to the ordered and stacked β -phase $\text{Ni}(\text{OH})_2$. Vanadium doping in this synthesis procedure is therefore regarded to enhance the OER activity indirectly by its influence on the crystallization upon chemical aging.

Further evidence for this hypothesis is obtained by the analysis of calcined $\text{Ni}_{1-x}\text{V}_x(\text{OH})_2$. Again, V-doping can be directly correlated to a decreased crystallization or crystalline domain growth of $\text{Ni}_{1-x}\text{V}_x\text{O}$ in the cubic rock-salt structure. Here, even higher doping concentrations of up to 50 at% enhance the OER activity of given samples from $\approx 12 \text{ mA cm}^{-2}$ to $\approx 27.5 \text{ mA cm}^{-2}$ although the pure vanadium oxide was shown to be redox inactive in the applied potential range.

6.4 Experimental

Synthesis of (vanadium-doped) nickel-hydroxide polymorphs

The synthesis of undoped and vanadium doped nickel-hydroxide polymorphs is based on a rapid aqueous oxidation method introduced by Sutto^[34].

For the synthesis of different nickel-hydroxide polymorphs per reaction 1.125 mmol nickel (II) chloride (SIGMA-ALDRICH, 98%) was dissolved in 7.5 mL bidistilled water (Millipore Q grade) to obtain a 0.15 M solution which was stirred for 1 h in air at room temperature. For vanadium doped Ni(OH)₂ samples vanadium(III)chloride (SIGMA-ALDRICH, 97%) was added to the solution to obtain a final concentration of 1, 2, 5, 10, 15, 50 at% vanadium and further stirred for 1 h for complete intermixing. Subsequently the precursor solution was cooled with an ice bath and 2.25 mmol potassium superoxide powder (KO₂, ABCR, 96.5% purity) was slowly added to the solution within 15 seconds under continuous stirring and quenched after 2 minutes by addition of 3.75 mL of precooled methanol (analytical grade). Amorphous α -Ni(OH)₂ was obtained as a powder after washing and evaporation of the solvent on a hot plate at 60 °C for 30 minutes and further drying in a laboratory oven in air at 60 °C for 16 hours. Ultrasmall β -Ni(OH)₂ nanoparticles were obtained as a powder in the same way, while the stirring time after the washing step was prolonged to 3 hours. After a stirring time of 24 hours, plate-like β -Ni(OH)₂ nanoparticles were obtained in the above-described way. During that stirring period, a color change from dark to light turquoise could be observed. The product was not obtained as a powder after evaporation of the solvent, but as a film on the glass slide. It had a brighter color compared to the α -Ni(OH)₂ powder after the film was scraped off and homogenized in a mortar.

Synthesis of (vanadium-doped) nickel-oxide powder

Dried samples obtained from the synthesis of undoped and vanadium doped Nickel-hydroxide were heated in a laboratory oven (NABERTHERM, model N15/65SHA) at 250 °C and 300 °C in air with a ramp time of 2 h and a dwell time of 2 h.

(V-doped) Ni(OH)₂ and NiO electrode preparation

Thin films of the catalytic layer were prepared by drop-casting a diluted dispersion of the wet pellet of nickel hydroxide onto FTO (fluorine-doped tin oxide, TEC15 substrates, DYESOL, Australia) or on quartz crystal microbalance (QCM) substrates. FTO substrates were cleaned with an aqueous solution of alkaline cleaner Extran (MERCK MILLIPORE), bidistilled H₂O and acetone. To enhance the hydrophilic properties of the surface, substrates were oxygen plasma-cleaned (Femto oxygen plasma surface cleaner, DIENER ELECTRONIC) prior to the drop-casting procedure. A Teflon-coated glass fiber tape leaving an exposed area of 0.159 cm² was used for masking. To precisely determine the mass loadings of equally prepared FTO electrodes, 0.5-inch Au-coated QCM sensors (KVG 10 MHz QCM device with gold electrode, Quartz Crystal Technology GmbH) were acetone cleaned, equally prepared and drop-casted with the catalysts according to the method employed for the FTO substrates. Dispersions with a concentration of $\approx 2 \text{ mg mL}^{-1}$ were prepared by mixing 0.2 mL stock solution (wet pellet after last washing step in 3.5 mL H₂O) with 2.8 mL MilliQ H₂O. To reach a mass loading of 50 - 200 $\mu\text{g cm}^{-2}$, 4 μL of the dispersion were deposited 1-4 times on a masked (0.159 cm²) substrate, intermediate-dried on a hot plate at 50 °C, and completely dried for 16 h at 60 °C in a laboratory oven. (V-doped) nickel-oxide electrodes were fabricated by calcination of substrates at temperatures of 250 °C and 300 °C with a heating ramp of 2 h and a dwell time of 2 h.

Physico-chemical characterization

Wide angle X-ray diffraction analysis was carried out in transmission mode using a STOE STADI P diffractometer with Cu $K_{\alpha 1}$ radiation ($\lambda = 1.54060 \text{ \AA}$) and a Ge(111) single crystal monochromator equipped with a DECTRIS solid state strip detector Mythen 1K. Powder XRD patterns of the samples were collected with an omega-2theta scan in the 2θ range from 5° to 90° with a step size of 1° and fixed integration time of 25 - 35 seconds per step and a resolution of 0.05° . The size of crystalline domains of β -Ni(OH)₂ nanoparticles was calculated from line broadening of the 101 reflection with Scherrer's equation and XRD reference pattern for the β -Ni(OH)₂ phase (ICDD card number 00-014-0117: hexagonal, $a = b = 3.126 \text{ \AA}$, $c = 4.605 \text{ \AA}$, $\alpha = \beta = 90^\circ$, $\gamma = 120^\circ$).

Raman spectroscopy was carried out using a LabRAM HR UV-Vis (HORIBA JOBIN YVON) Raman microscope (OLYMPUS BX41) with a SYMPHONY CCD detection system and a He-Ne laser ($\lambda = 633 \text{ nm}$). Spectra were recorded using a lens with a 10-fold magnification in the range from 100 cm^{-1} to 1000 cm^{-1} with filters of OD 0.3 - 0.6. Spectrum accumulation mode was used with integrating 600 times 30 sec per spectrum. The data acquisition was carried out with LabSpec software.

Transmission electron microscopy (TEM) specimens were prepared from nanoparticles in a 1:1 (v/v) ratio of water to ethanol solution and deposited on a carbon-film coated copper grid and dried in air. High resolution TEM, scanning TEM (STEM) images as well as electron diffraction patterns were recorded using two FEI Titan Themis microscopes with aberration correction of the probe-forming lenses operated at 120 kV or 300 kV. Energy dispersive X-ray spectroscopy (EDX) was performed using a SuperX windowless, four quadrant Silicon drift detector with a solid angle of 0.7 sr. Electron energy loss spectra (EELS) were acquired by a Gatan Quantum ERS spectrometer, collecting electrons scattered up to 35 mrad. Dual EELS

acquisition enabled a reliable determination of the edge onset of Ni-L₃. Multivariate statistical analysis^[51] was performed on the spectrum imaging datasets to reduce the noise.

SEM images were obtained with an FEI Helios Nanolab G3 UC scanning electron microscope equipped with a field emission gun operated at 3-5 kV. Specimens were prepared from nanoparticles in a 1:1 (v/v) ratio of water to ethanol solution and deposited on FTO or Si substrates that were glued onto a stainless-steel sample holder with silver lacquer. EDX measurements were performed at an operating voltage of 20 kV with a X-Max^N Silicon Drift Detector with 80 mm² detector area (OXFORD INSTRUMENTS) and AZTec acquisition software (OXFORD INSTRUMENTS).

Electrochemical characterization

For electrode preparation, dispersions with a concentration of around 2 mg mL⁻¹ were produced by mixing 0.2 mL stock solution (wet pellet in 3.5 mL H₂O) with 2.8 mL MilliQ H₂O, stirred for 10 minutes at 500 rpm and sonicated for \approx 30 minutes. To reach a mass loading of 50 μ g cm⁻², 4 μ L dispersion was deposited on a plasma-cleaned FTO substrate or Au-coated QCM sensors (14 mm, 5 and 10 MHz AT-cut Cr/Au crystals from KVG QUARTZ CRYSTAL TECHNOLOGY GMBH and QUARTZ PRO AB) before drying on a hot plate at 50 °C. Electrodes were masked with PTFE tape to leave a circular electrode area of 0.196 cm² (FTO) and 0.126 cm² (Au-QCM sensors) respectively. The frequency of uncoated and coated QCM sensor crystals was determined with a QCM200 5 MHz measurement system (STANFORD RESEARCH SYSTEMS INC.) and an openQCM 5/10 MHz measurement system (NOVAETECH SRL). Deposited mass loadings on QCM chips were calculated according to the Sauerbrey equation^[52] from determined frequency differences Δf , an overlapping electrode area A of 0.196 cm² and a sensitivity factor C_f of 56.6 Hz μ g⁻¹ cm² and 4.4 Hz μ g⁻¹ cm² for a 1-inch 5 and 0.55-inch 10 MHz AT-cut crystals respectively.

All electrochemical measurements at room temperature were carried out in a 3-electrode setup with quartz cell filled with 15 mL 0.5 M KOH (SIGMA-ALDRICH, volumetric solution) as electrolyte, using an PGSTAT302N potentiostat/galvanostat (METROHM AUTOLAB B.V.) equipped with a FRA32 M impedance analyzer connected to a Hg/HgO (0.5M KOH) reference electrode. To convert all potentials measured against Hg/HgO (0.5 M KOH) reference electrode and to ensure stability of the potential before and after every measurement session, the potential was measured against a reversible hydrogen electrode (RHE, HydroFlex, GASKATEL Gesellschaft für Gassysteme durch Katalyse und Elektrochemie mbH) stored in 0.5 M KOH and that was in turn verified by a self-constructed Pt-wire/H₂(≈1 atm) electrode. The potential was determined to be 0.925 V, which is in accordance with literature stated values.^[17]

The electrochemical activity of catalyst on FTO and QCM substrates was measured by *iR*-drop corrected linear sweep voltammetry (LSV) in a potential window of 1.1 - 1.7 V vs. RHE and 1.0 - 1.65 V vs. RHE respectively in 20 scan cycles with a scan rate of 10 mV s⁻¹. Impedance spectroscopy data at 1.0 V vs. RHE were recorded prior to each measurement to determine the corresponding electrolyte resistance (95 %) from the high frequency region. Nickel hydroxide mass-based catalyst activity was either directly calculated with the measured QCM determined mass loadings or calculated from the coating volume (3 - 15 μl) of a dispersion of known concentration (2 mg ml⁻¹). Current densities were determined from the mean value of capacity current corrected (mean current in potential region 1.0 - 1.23 V vs. RHE) anodic and cathodic scans of the respective LSV cycle.

6.5 Supporting Information

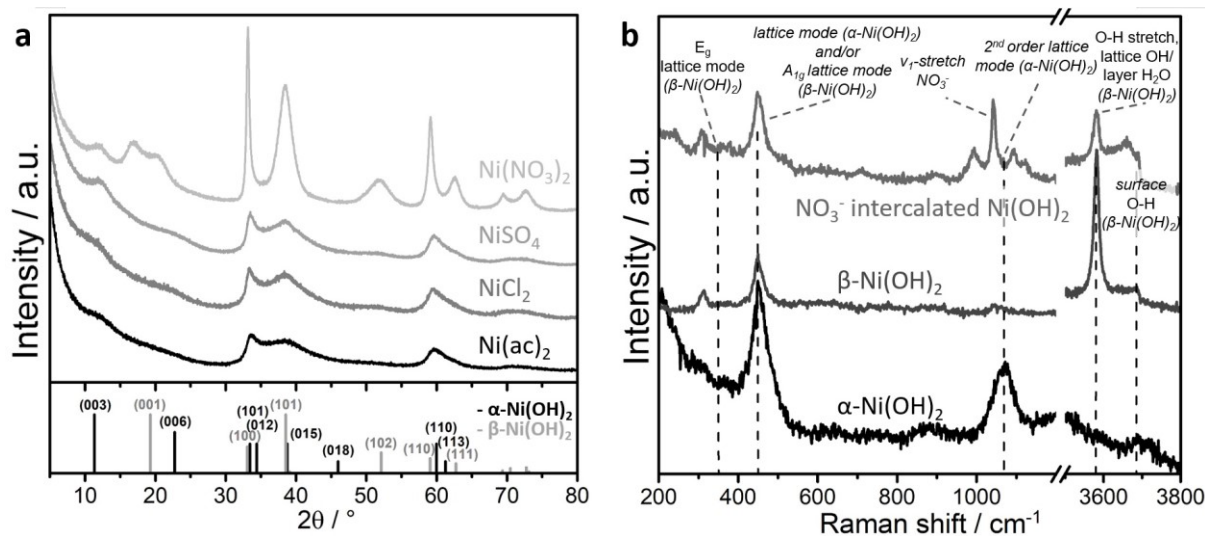


Figure S1 X-ray diffractograms (a) of nanocatalyst prepared by rapid precipitation method with different Ni(II)-precursors and Raman spectra (b) of nitrate anion intercalated $\text{Ni}(\text{OH})_2$. $\alpha\text{-Ni}(\text{OH})_2$ ($\text{Ni}(\text{OH})_2 \times 0.75 \text{H}_2\text{O}$) pattern: ICDD card number 00-038-0715 (rhombohedral, $a = b = 3.08 \text{ \AA}$, $c = 23.41 \text{ \AA}$, $\alpha = \beta = 90^\circ$, $\gamma = 120^\circ$). $\beta\text{-Ni}(\text{OH})_2$ ($\text{Ni}(\text{OH})_2$) pattern: ICDD card number 00-014-0117 (hexagonal, $a = b = 3.126$, $c = 4.605$, $\alpha = \beta = 90^\circ$, $\gamma = 120^\circ$). The bands at 450 cm^{-1} (lattice mode) and 1070 cm^{-1} (2nd order lattice mode) were assigned to the $\alpha\text{-Ni}(\text{OH})_2$ phase.^[22-23] Bands at 447 cm^{-1} (A_{1g} lattice mode), 3581 cm^{-1} (O-H stretch / lattice OH / layer H_2O mode) and 3690 cm^{-1} (surface O-H stretch) were assigned to the $\beta\text{-Ni}(\text{OH})_2$ phase.^[23]

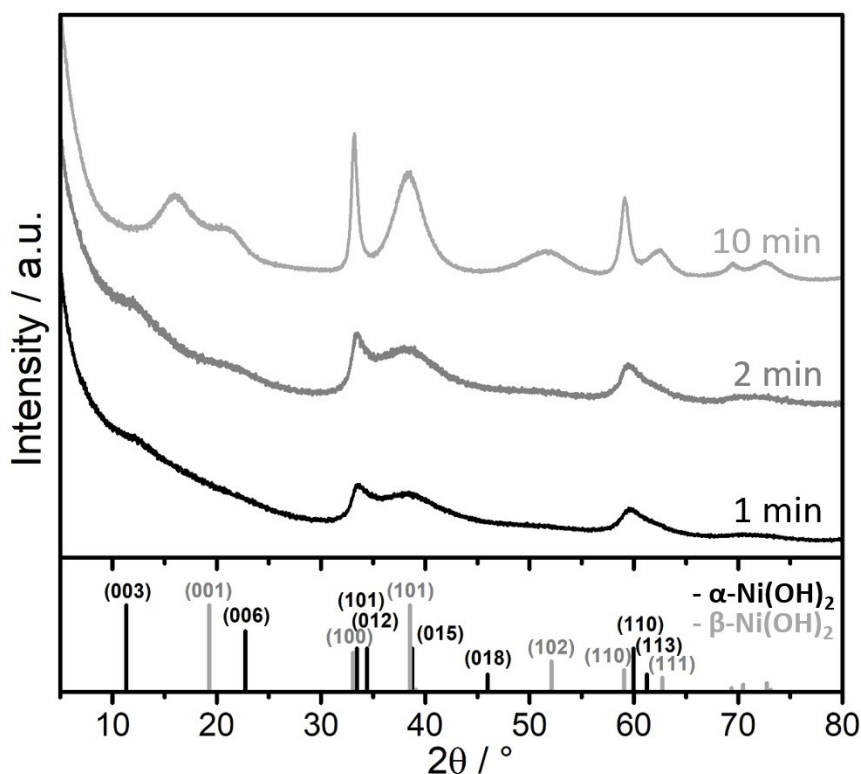


Figure S2 X-ray diffractograms of $\text{Ni}(\text{OH})_2$ products obtained by the rapid precipitation method with KO_2 with variation of reaction time before quenching. Synthesis performed at room temperature. $\alpha\text{-Ni}(\text{OH})_2$ ($\text{Ni}(\text{OH})_2 \times 0.75 \text{H}_2\text{O}$) pattern: ICDD card number 00-038-0715 (rhombohedral, $a = b = 3.08 \text{ \AA}$, $c = 23.41 \text{ \AA}$, $\alpha = \beta = 90^\circ$, $\gamma = 120^\circ$). $\beta\text{-Ni}(\text{OH})_2$ ($\text{Ni}(\text{OH})_2$) pattern: ICDD card number 00-014-0117 (hexagonal, $a = b = 3.126 \text{ \AA}$, $c = 4.605 \text{ \AA}$, $\alpha = \beta = 90^\circ$, $\gamma = 120^\circ$).

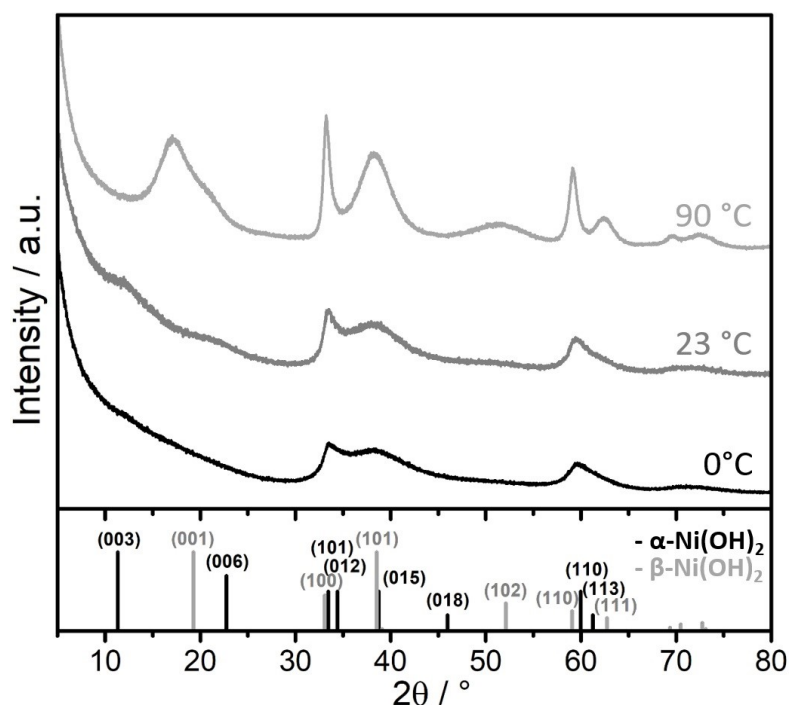


Figure S3 X-ray diffractograms of Ni(OH)_2 products obtained by rapid precipitation method with KO_2 with variation of synthesis temperature. Synthesis performed with 2 min reaction time before quenching. $\alpha\text{-Ni(OH)}_2$ ($\text{Ni(OH)}_2 \times 0.75 \text{H}_2\text{O}$) pattern: ICDD card number 00-038-0715 (rhombohedral, $a = b = 3.08 \text{ \AA}$, $c = 23.41 \text{ \AA}$, $\alpha = \beta = 90^\circ$, $\gamma = 120^\circ$). $\beta\text{-Ni(OH)}_2$ (Ni(OH)_2) pattern: ICDD card number 00-014-0117 (hexagonal, $a = b = 3.126 \text{ \AA}$, $c = 4.605 \text{ \AA}$, $\alpha = \beta = 90^\circ$, $\gamma = 120^\circ$).

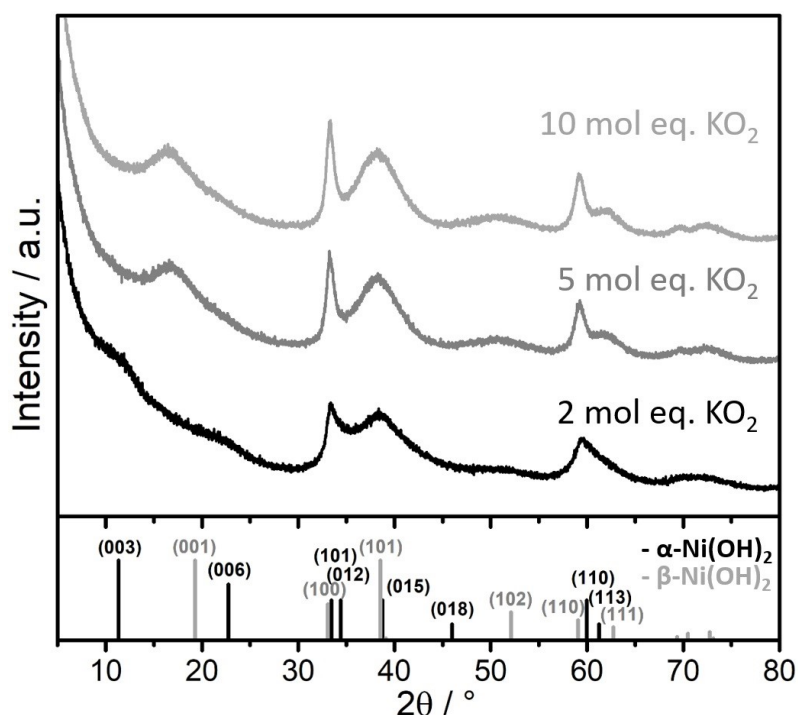


Figure S4 X-ray diffractograms of Ni(OH)_2 products obtained by rapid precipitation method with varied amounts of KO_2 . Synthesis was performed with 2 min reaction time before quenching each at 0°C . $\alpha\text{-Ni(OH)}_2$ ($\text{Ni(OH)}_2 \times 0.75 \text{H}_2\text{O}$) pattern: ICDD card number 00-038-0715 (rhombohedral, $a = b = 3.08 \text{ \AA}$, $c = 23.41 \text{ \AA}$, $\alpha = \beta = 90^\circ$, $\gamma = 120^\circ$). $\beta\text{-Ni(OH)}_2$ (Ni(OH)_2) pattern: ICDD card number 00-014-0117 (hexagonal, $a = b = 3.126 \text{ \AA}$, $c = 4.605 \text{ \AA}$, $\alpha = \beta = 90^\circ$, $\gamma = 120^\circ$).

Table S1 Elemental analysis via inductively coupled plasma optical emission spectrometry (ICP-OES) of V(III)-doped $\text{Ni}_{1-x}\text{V}_x(\text{OH})_2 \text{Cl}$

doping element	precursor	doping level / at%	ICP-OES / at%
pure $\text{Ni}(\text{OH})_2$	NiCl_2	0	N/A
V(III)	$\text{NiCl}_2 + \text{VCl}_3$	1	1.0
V(III)	$\text{NiCl}_2 + \text{VCl}_3$	2	2.1
V(III)	$\text{NiCl}_2 + \text{VCl}_3$	5	4.9
V(III)	$\text{NiCl}_2 + \text{VCl}_3$	10	9.7
V(III)	$\text{NiCl}_2 + \text{VCl}_3$	15	15.4
V(III)	$\text{NiCl}_2 + \text{VCl}_3$	50	38.6
pure vanadium compound	VCl_3	100	N/A

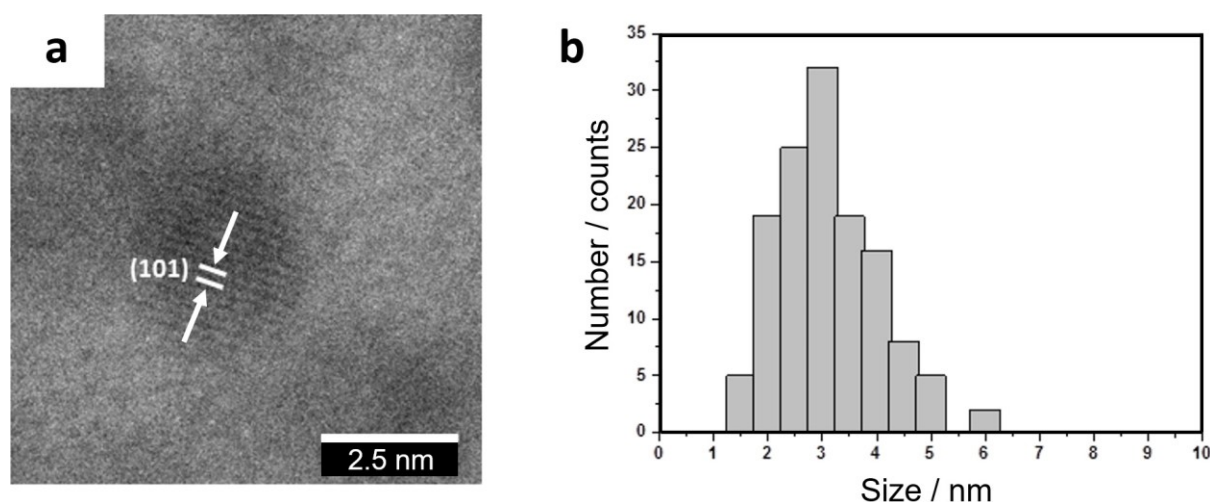


Figure S5 (a) Transmission electron micrograph of single $\beta\text{-Ni}(\text{OH})_2$ nanoparticle. (b) Size distribution determined from particles imaged by TEM. Indexing of d-spacings of $\beta\text{-Ni}(\text{OH})_2$ nanoparticle according to $\beta\text{-Ni}(\text{OH})_2$ pattern: ICDD card number 00-014-0117 (hexagonal, $a = b = 3.126 \text{ \AA}$, $c = 4.605 \text{ \AA}$, $\alpha = \beta = 90^\circ$, $\gamma = 120^\circ$).

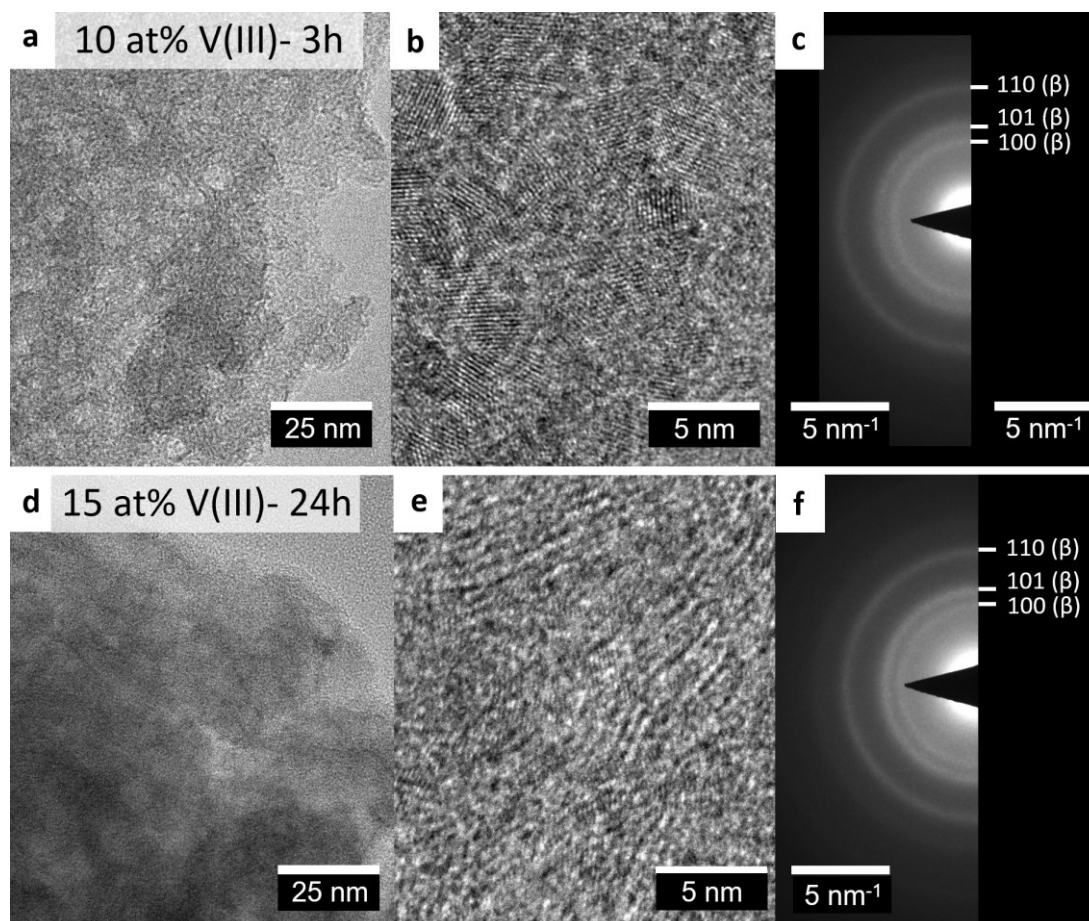


Figure S6 Structural characterization of time-dependent phase transformations of V(III) doped $\text{Ni}(\text{OH})_2$ by transmission electron microscopy. TEM images and electron diffraction pattern of 10 at% V(III) doped $\text{Ni}(\text{OH})_2$ after 3 h (a-c) and 15 at% V(III) doped $\text{Ni}(\text{OH})_2$ after 24 h (d-f) aging time. β - $\text{Ni}(\text{OH})_2$ ($\text{Ni}(\text{OH})_2$) pattern: ICDD card number 00-014-0117 (hexagonal, $a = b = 3.126 \text{ \AA}$, $c = 4.605 \text{ \AA}$, $\alpha = \beta = 90^\circ$, $\gamma = 120^\circ$)

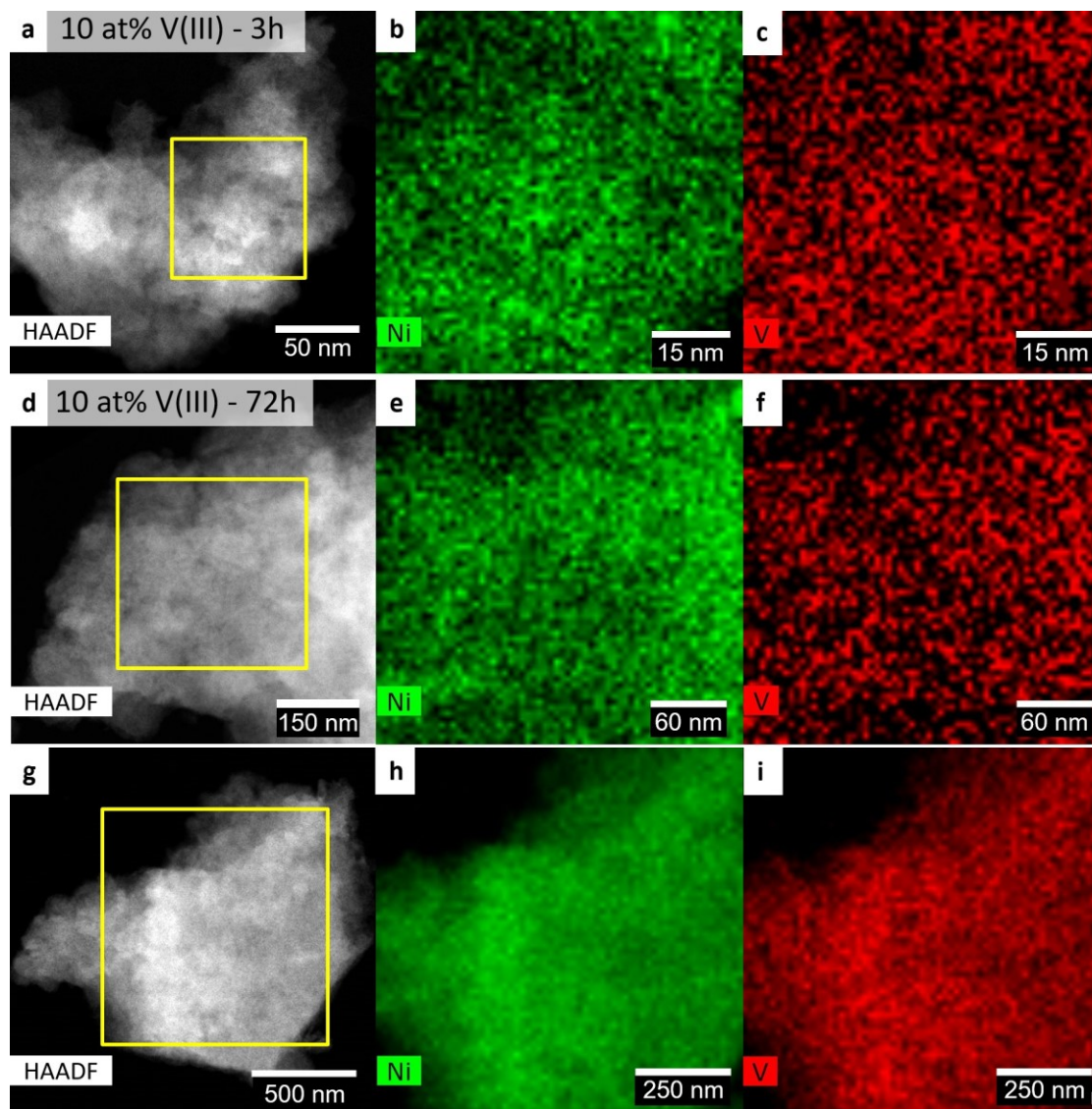


Figure S7 STEM-EDX and energy-dispersive X-ray spectroscopy mapping of V(III) doped Ni(OH)₂ at different length scales. STEM-EDX mappings of 3 h aged 10 at% V(III) doped sample (a-c). STEM-EDX mappings of 72 h aged 10 at% V(III) doped, at medium (d-f) and lower (g-i) magnification.

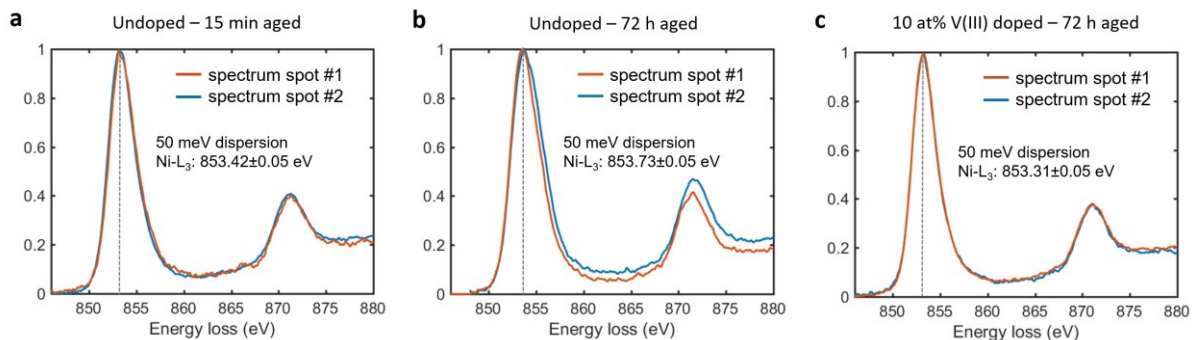


Figure S8 Characterization of the electronic structure of nickel in aged and V(III)-doped samples by electron energy loss spectroscopy. EELS spectra with 50 meV dispersion of (a) undoped 15 min, (b) undoped 72 h and (c) 10 at% V(III) 72 h aged Ni(OH)₂ samples.

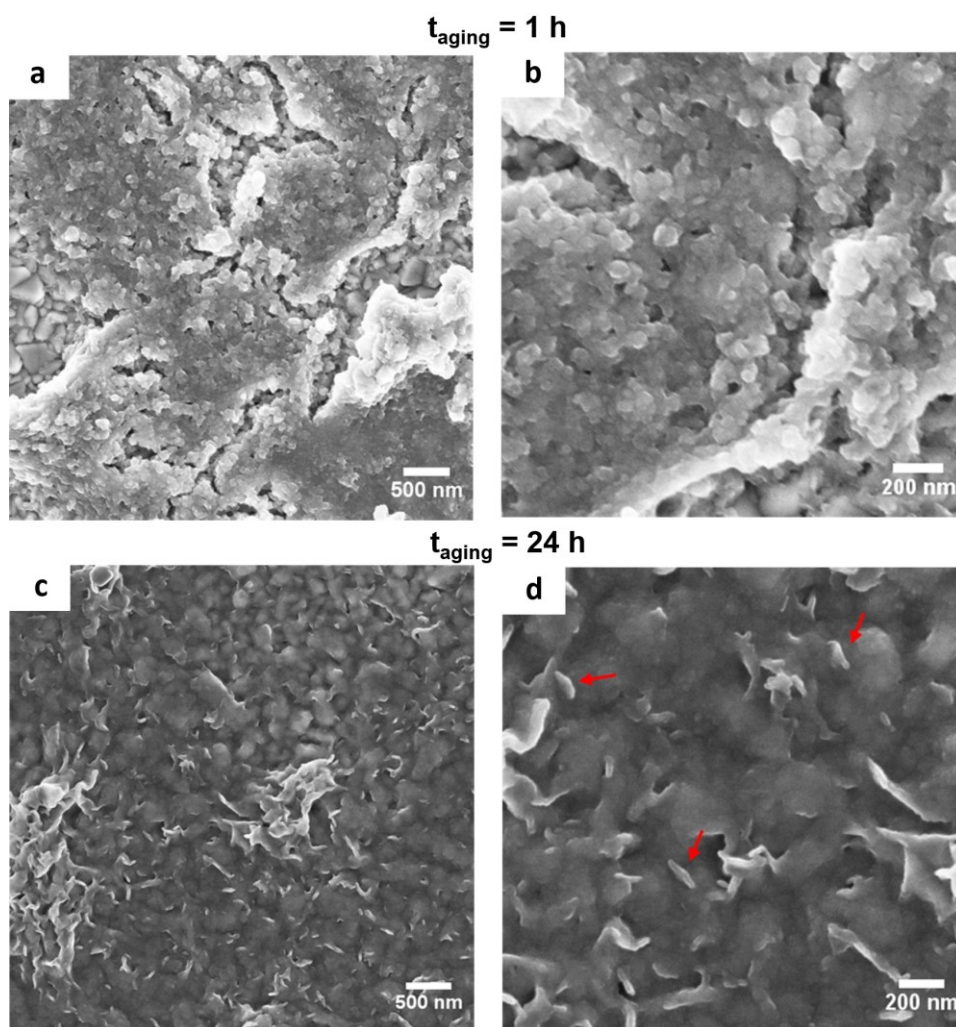


Figure S9 Scanning electron micrographs of Ni(OH)₂ based electrodes for electrochemical characterization. (a-d) Top-view of 1 h (a, b) and 24 h (c, d) aged undoped Ni(OH)₂ drop-cast on an FTO substrate with loadings of $\sim 50 \mu\text{g cm}^{-2}$.

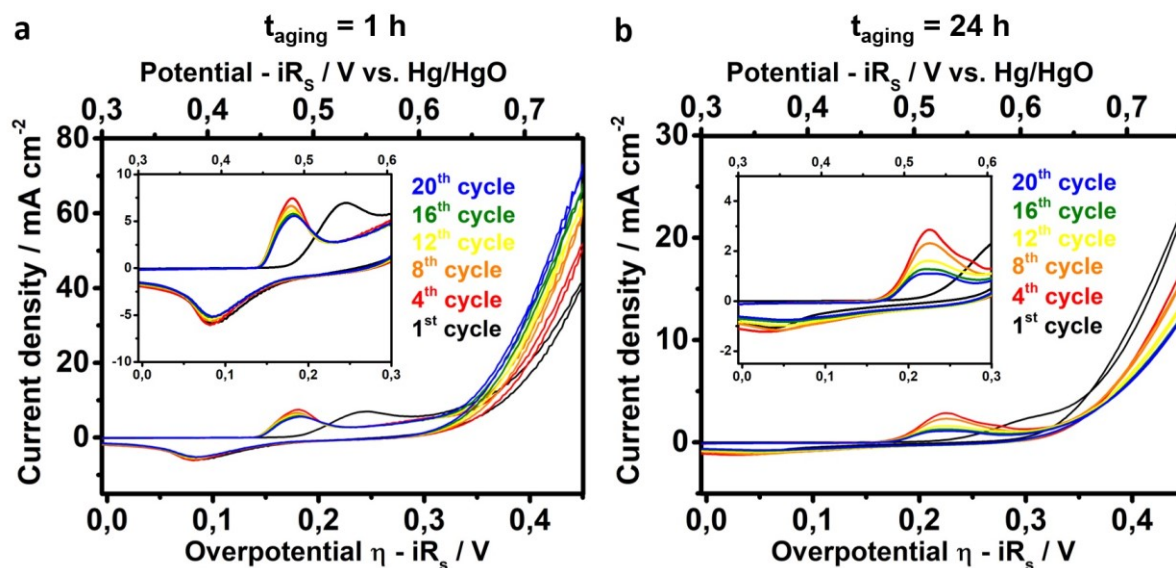


Figure S10 Electrochemical characterization of chemically aged $\text{Ni}(\text{OH})_2$. Cyclic voltammograms (1st, 4th, 8th, 12th, 16th and 20th scan cycle) of 1 h (a) and 24 h (b) aged undoped $\text{Ni}(\text{OH})_2$.

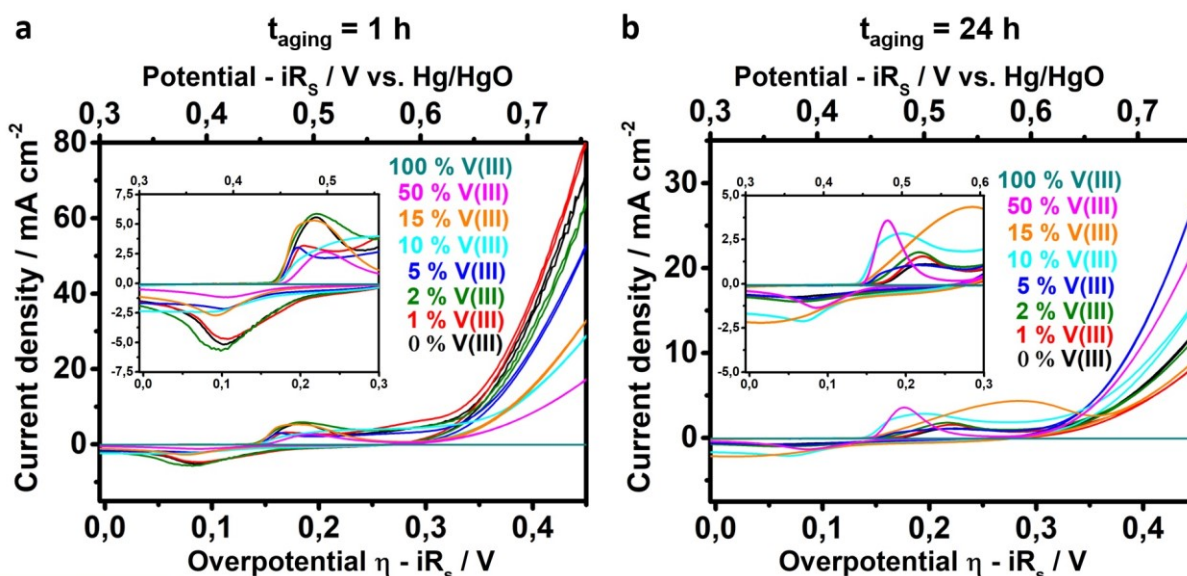


Figure S11 Electrochemical characterization of chemically aged and V(III) doped $\text{Ni}(\text{OH})_2$. Cyclic voltammograms (20th scan cycle) of 1 h (a) and 24 h (b) aged 0, 1, 2, 5, 10, 15, 50 and 100 at% V(III) containing $\text{Ni}(\text{OH})_2$.

Table S2 Results obtained from the electrochemical characterization of 1 h chemically aged $\text{Ni}_{1-x}\text{V}_x(\text{OH})_2$ obtained in the 20th cycle

V(III) content / at%	mass loading (determined) / $\mu\text{g cm}^{-2}$	E_a / η in mV	E_c / η in mV	Redox potential E_{red} / η in mV	η at 10 mA cm^{-2} / mV	current density j at $\eta = 350$ mV / mA cm^{-2}	current density j at $\eta = 400$ mV / mA cm^{-2}
0	N/A ^a	184	84	134	344	10.91	34.48
1	N/A ^a	169	88	128.5	335	12.64	38.05
2	N/A ^a	184	82	133	350	9.59	29.53
5	N/A ^a	163	84	123.5	357	7.90	24.74
10	60.8	N/A ^b	N/A ^b	N/A ^b	379	5.59	13.81
15	70.7	177	77	127	379	4.44	14.98
50	35.6	N/A ^b	N/A ^b	N/A ^b	411	2.95	8.24
100	24.7	N/A ^b	N/A ^b	N/A ^b	> 900	0.01	0.01

^a No mass loading could be determined. ^b No value listed due to a broad and undefined peak.

Table S3 Results obtained from the electrochemical characterization of 24 h chemically aged $\text{Ni}_{1-x}\text{V}_x(\text{OH})_2$ obtained in the 20th cycle

V(III) content / at%	mass loading (determined) / $\mu\text{g cm}^{-2}$	E_a / η in mV	E_c / η in mV	Redox potential E_{red} / η in mV	η at 10 mA cm^{-2} / mV	current density j at $\eta = 350$ mV / mA cm^{-2}	current density j at $\eta = 400$ mV / mA cm^{-2}
0	72.7	221	49	135	433	2.48	6.78
1	72.7	220	54	137	459	1.77	4.64
2	71.7	216	62	139	438	2.46	6.45
5	66.8	218	77	148	389	4.59	14.64
10	N/A ^a	191	68	130	411	3.39	8.91
15	85.9	284	15	150	458	2.23	5.01
50	21.7	176	86	131	396	3.96	12.31
100	19.7	N/A ^b	N/A ^b	N/A ^b	> 900	0.01	0.01

^a No mass loading could be determined. ^b No value listed due to a broad and undefined peak.

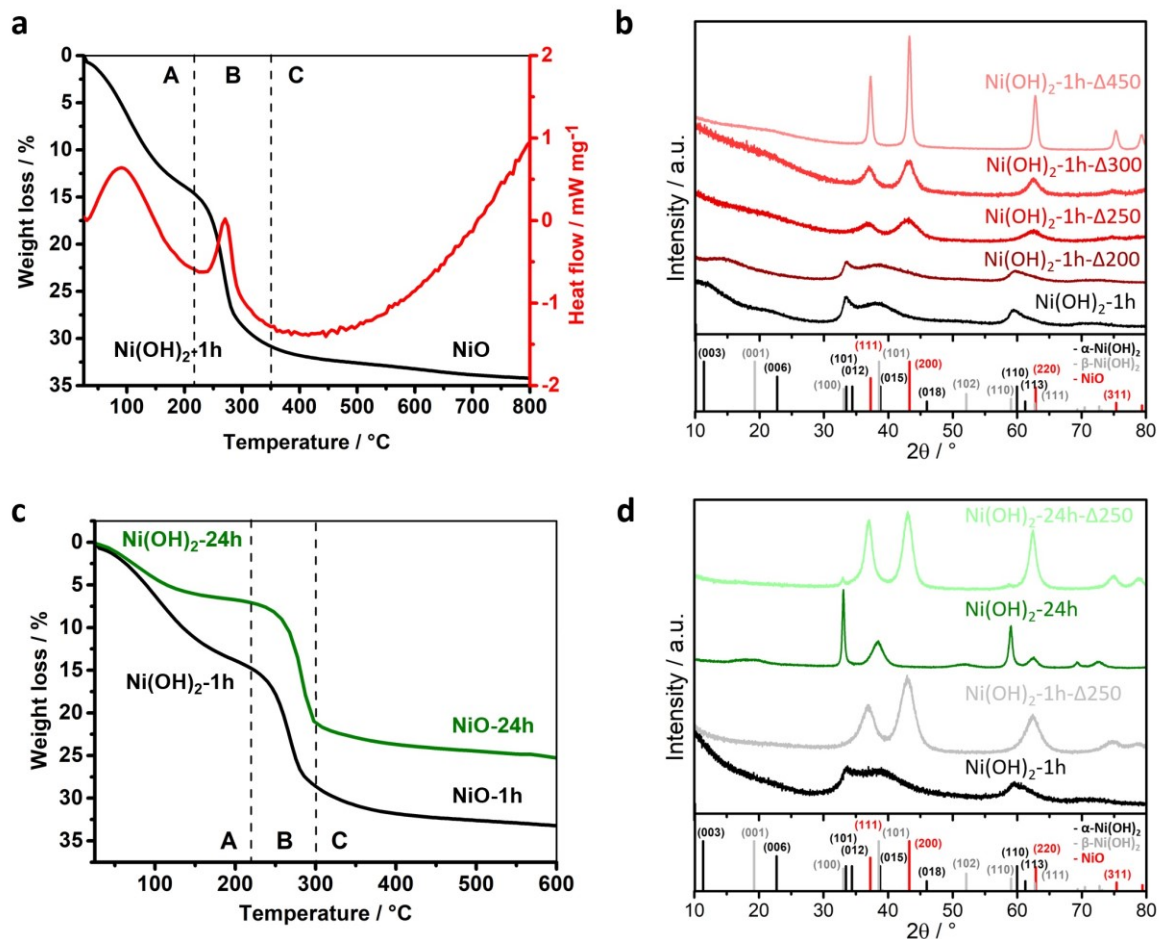


Figure S12 Structural characterization of aged Ni(OH)_2 upon calcination. (a) Thermogravimetric analysis (black curve) and differential scanning calorimetry (red curve) of 1 h aged Ni(OH)_2 sample. (b) X-ray diffractogram of 200 – 450 $^\circ\text{C}$ (red curves) calcined 1 h aged Ni(OH)_2 sample. (c) TGA of 1 h (black curve) and 24 h (green curve) aged Ni(OH)_2 samples. (d) XRD of calcined 1 h aged (black and grey curve) and 24 h aged (dark and light green curve) Ni(OH)_2 . $\alpha\text{-Ni(OH)}_2$ ($\text{Ni(OH)}_2 \times 0.75 \text{H}_2\text{O}$) pattern: ICDD card number 00-038-0715 (rhombohedral, $a = b = 3.08 \text{ \AA}$, $c = 23.41 \text{ \AA}$, $\alpha = \beta = 90^\circ$, $\gamma = 120^\circ$). $\beta\text{-Ni(OH)}_2$ (Ni(OH)_2) pattern: ICDD card number 00-014-0117 (hexagonal, $a = b = 3.126 \text{ \AA}$, $c = 4.605 \text{ \AA}$, $\alpha = \beta = 90^\circ$, $\gamma = 120^\circ$). NiO pattern: ICDD card number 01-071-1179 (cubic, $a = b = c = 4.178 \text{ \AA}$, $\alpha = \beta = \gamma = 90^\circ$).

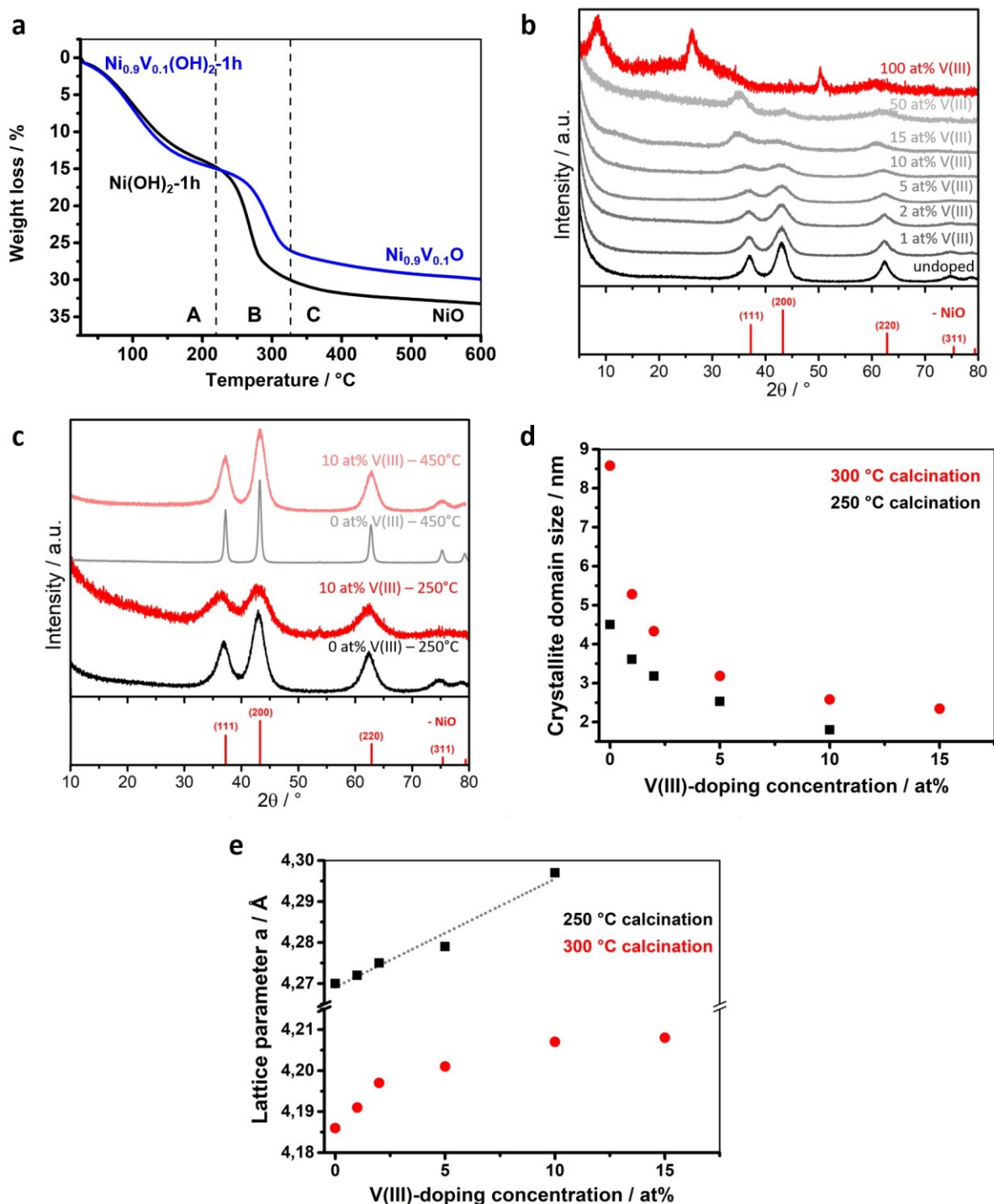


Figure S13 Structural characterization of calcined $\text{Ni}_{1-x}\text{V}_x(\text{OH})_2$. (a) Thermogravimetric analysis of 1 h chemically aged undoped and 10 at% V(III) containing $\text{Ni}(\text{OH})_2$. (b) X-ray diffractograms of V(III) doped (0-100 at% V(III) - greyscale and red curves) $\text{Ni}(\text{OH})_2$ calcined at 250 °C. (c) XRD of undoped and $\text{Ni}_{0.9}\text{V}_{0.1}(\text{OH})_2$ calcined at 250 °C (black, red curve) and 450 °C (grey, light red curve). NiO pattern: ICDD card number 01-071-1179 (cubic, $a = b = c = 4.178 \text{ \AA}$, $\alpha = \beta = \gamma = 90^\circ$) (d) Crystallite domain sizes of 250 °C (black) and 300 °C (red) calcined $\text{Ni}_{1-x}\text{V}_x(\text{OH})_2$ derived from XRD line broadening according to Scherrer's equation. Graphical representation of data listed in Table S4 and S5. (e) Lattice parameter a of 250 °C (black) and 300 °C (red) calcined $\text{Ni}_{1-x}\text{V}_x(\text{OH})_2$ calculated from the position (Gaussian fitted center of broadened reflection) of the NiO phase (200) reflection. Linear regression for 0-10 at% V(III) (dashed grey line) added for 250 °C calcined sample series. Graphical representation of data listed in Table S4 and S5.

Table S4 Calculated particle/domain sizes and lattice parameter a (NiO phase) based on the broadening of the 200 reflection in $\text{Ni}_{1-x}\text{V}_x\text{O}$ after calcination at 250 °C according to the Scherrer equation

V(III) content / at%	particle size / nm	Position / ° 2θ	lattice parameter a / Å
0	8.6	43.197	4.186
1	5.3	43.147	4.191
2	4.3	43.098	4.197
5	3.2	43.056	4.201
10	2.6	42.995	4.207
15	2.3	42.993	4.208

Table S5 Calculated particle/domain sizes and lattice parameter a (NiO phase) based on the broadening of the 200 reflection in $\text{Ni}_{1-x}\text{V}_x\text{O}$ after calcination at 300 °C according to the Scherrer equation

V(III) content / at%	particle size / nm	position / ° 2θ	lattice parameter a / Å
0	4.5	43.010	4.270
1	3.6	42.961	4.272
2	3.2	42.913	4.275
5	2.5	42.834	4.279
10	1.8	42.504	4.297

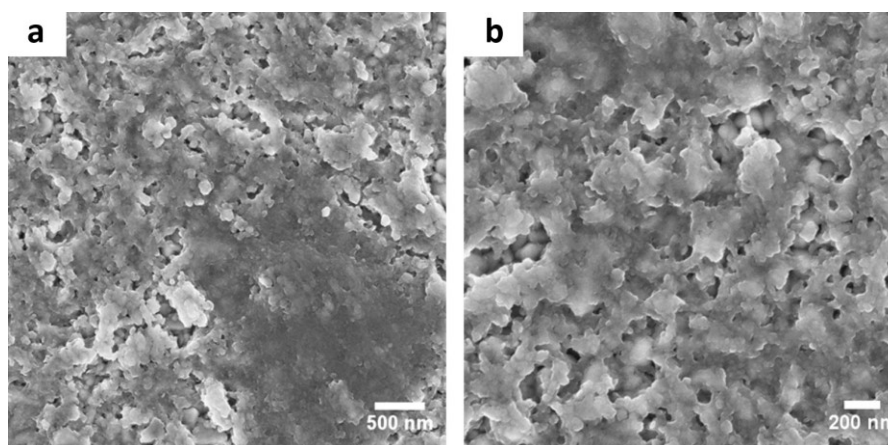


Figure S14 Scanning electron micrographs of NiO-based electrodes for electrochemical characterization. (a, b) Top-view of 1 h aged undoped $\text{Ni}(\text{OH})_2$ dropcasted on an FTO substrate and calcined at 250 °C with loadings of $\sim 50 \mu\text{g cm}^{-2}$.

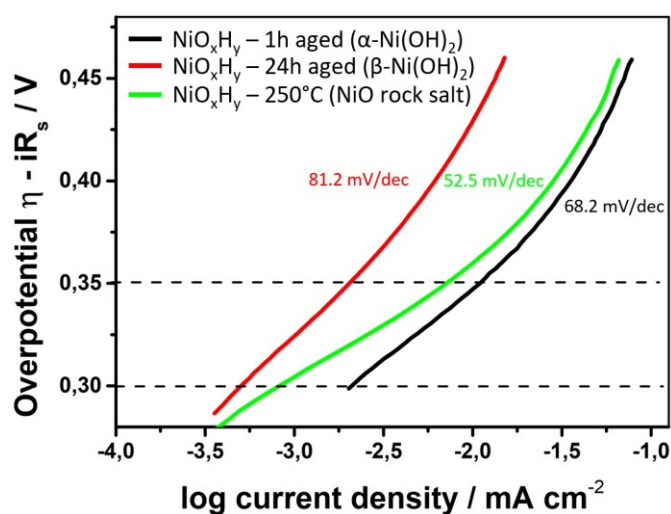


Figure S15 Tafel plot of chemically aged and calcined nickel hydroxide phases. Tafel plot of NiO_xH_y 1 h aged (black), 24 h aged (red) and 250 °C calcined (green) product.

6.6 References

- [1] D. Parra, L. Valverde, F. J. Pino, M. K. Patel, *Renew. Sust. Energ. Rev.* **2019**, 101, 279.
- [2] A. Boretta, *Int. J. Hydrogen Energ.* **2013**, 38, 1806.
- [3] D. Kushnir, T. Hansen, V. Vogl, M. Åhman, *J. Clean. Prod.* **2020**, 242, 118185.
- [4] A. M. Bazzanella, F. Ausfelder, DECHEMA Gesellschaft für Chemische Technik und Biotechnologie e.V., **2017**. (ISBN 978-3-89746-196-2)
- [5] R. Subbaraman, D. Tripkovic, K.-C. Chang, D. Strmcnik, A. P. Paulikas, P. Hirunsit, M. Chan, J. Greeley, V. Stamenkovic, N. M. Markovic, *Nat. Mater.* **2012**, 11, 550.
- [6] B. Steen, G. Borg, *Ecol. Econ.* **2002**, 42, 401.
- [7] C. Hu, L. Zhang, J. Gong, *Energ. Environ. Sci.* **2019**, 12, 2620.
- [8] K. Fan, H. Chen, Y. Ji, H. Huang, P. M. Claesson, Q. Daniel, B. Philippe, H. Rensmo, F. Li, Y. Luo, L. Sun, *Nat. Commun.* **2016**, 7, 11981.
- [9] W. Ma, R. Ma, C. Wang, J. Liang, X. Liu, K. Zhou, T. Sasaki, *ACS Nano* **2015**, 9, 1977.
- [10] Z. Cai, X. Bu, P. Wang, J. C. Ho, J. Yang, X. Wang, *J. Mater. Chem. A* **2019**, 7, 5069.
- [11] B. You, N. Jiang, M. Sheng, M. W. Bhushan, Y. Sun, *ACS Catal.* **2016**, 6, 714.
- [12] M. Ledendecker, S. Krick Calderón, C. Papp, H.-P. Steinrück, M. Antonietti, M. Shalom, *Angew. Chem. Int. Ed.* **2015**, 54, 12361.
- [13] M. Gao, W. Sheng, Z. Zhuang, Q. Fang, S. Gu, J. Jiang, Y. Yan, *J. Am. Chem. Soc.* **2014**, 136, 7077.
- [14] K. Fominykh, P. Chernev, I. Zaharieva, J. Sicklinger, G. Stefanic, M. Döblinger, A. Müller, A. Pokharel, S. Böcklein, C. Scheu, T. Bein, D. Fattakhova-Rohlfing, *ACS Nano* **2015**, 9, 5180.
- [15] V. Vij, S. Sultan, A. M. Harzandi, A. Meena, J. N. Tiwari, W.-G. Lee, T. Yoon, K. S. Kim, *ACS Catal.* **2017**, 7, 7196.
- [16] D. A. Corrigan, *J. Electrochem. Soc.* **1987**, 134, 377.
- [17] L. Trotochaud, S. L. Young, J. K. Ranney, S. W. Boettcher, *J. Am. Chem. Soc.* **2014**, 136, 6744.
- [18] S. Klaus, Y. Cai, M. W. Louie, L. Trotochaud, A. T. Bell, *J. Phys. Chem. C* **2015**, 119, 7243.

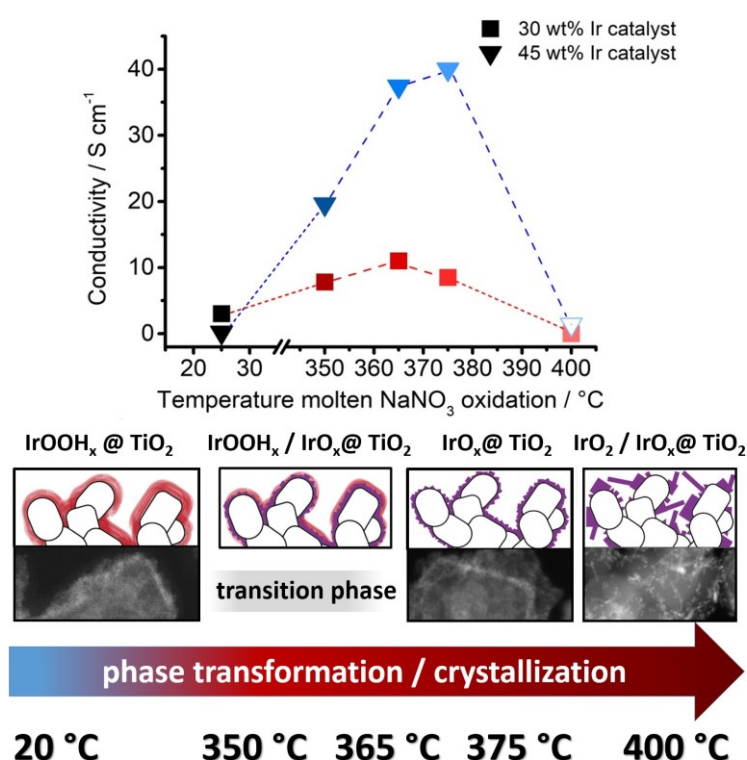
- [19] D. Friebel, M. W. Louie, M. Bajdich, K. E. Sanwald, Y. Cai, A. M. Wise, M.-J. Cheng, D. Sokaras, T.-C. Weng, R. Alonso-Mori, R. C. Davis, J. R. Bargar, J. K. Nørskov, A. Nilsson, A. T. Bell, *J. Am. Chem. Soc.* **2015**, 137, 1305.
- [20] H. Bode, K. Dehmelt, J. Witte, *Electrochim. Acta* **1966**, 11, 1079.
- [21] S. R. Mellso, A. Gardiner, B. Johannessen, A. T. Marshall, *Electrochim. Acta* **2015**, 168, 356.
- [22] D. S. Hall, D. J. Lockwood, S. Poirier, C. Bock, B. R. MacDougall, *J. Phys. Chem. A* **2012**, 116, 6771.
- [23] D. S. Hall, D. J. Lockwood, S. Poirier, C. Bock, B. R. MacDougall, *ACS Appl. Mater. Inter.* **2014**, 6, 3141.
- [24] H. Chen, J. M. Wang, T. Pan, Y. L. Zhao, J. Q. Zhang, C. N. Cao, *J. Power Sources* **2005**, 143, 243.
- [25] Y. L. Zhao, J. M. Wang, H. Chen, T. Pan, J. Q. Zhang, C. N. Cao, *Int. J. Hydrogen Energ.* **2004**, 29, 889.
- [26] R. Wang, J. Lang, Y. Liu, Z. Lin, X. Yan, *NPG Asia Mater.* **2015**, 7, e183.
- [27] K. Fominykh, J. M. Feckl, J. Sicklinger, M. Döblinger, S. Böcklein, J. Ziegler, L. Peter, J. Rathousky, E.-W. Scheidt, T. Bein, D. Fattakhova-Rohlfing, *Adv. Funct. Mater.* **2014**, 24, 3123.
- [28] T. Reier, M. Oezaslan, P. Strasser, *ACS Catal.* **2012**, 2, 1765.
- [29] C. Tessier, P. H. Haumesser, P. Bernard, C. Delmas, *J. Electrochem. Soc.* **1999**, 146, 2059.
- [30] C. Delmas, C. Tessier, *J. Mater. Chem.* **1997**, 7, 1439.
- [31] L. Xu, Y.-S. Ding, C.-H. Chen, L. Zhao, C. Rimkus, R. Joesten, S. L. Suib, *Chem. Mater.* **2008**, 20, 308.
- [32] Q. Zhang, C. Zhang, J. Liang, P. Yin, Y. Tian, *ACS Sustain. Chem. Eng.* **2017**, 5, 3808.
- [33] C. Luan, G. Liu, Y. Liu, L. Yu, Y. Wang, Y. Xiao, H. Qiao, X. Dai, X. Zhang, *ACS Nano* **2018**, 12, 3875.
- [34] T. E. Sutto, *Inorg. Chem.* **2014**, 53, 4570.
- [35] C. Tessier, L. Guerlou-Demourgues, C. Faure, M. t. Basterreix, G. Nabias, C. Delmas, *Solid State Ionics* **2000**, 133, 11.
- [36] M. C. Bernard, P. Bernard, M. Keddou, S. Senyari, H. Takenouti, *Electrochim. Acta* **1996**, 41, 91.
- [37] G. W. D. Briggs, G. W. Stott, W. F. K. Wynne-Jones, *Electrochim. Acta* **1962**, 7, 249.

-
- [38] W. Visscher, E. Barendrecht, *J. Electroanal. Chem.* **1983**, 154, 69.
- [39] S. C. Jung, S. L. Sim, Y. W. Soon, C. M. Lim, P. Hing, J. R. Jennings, *Nanotechnology* **2016**, 27, 275401.
- [40] R. Shannon, *Acta Crystallogr. A* **1976**, 32, 751.
- [41] H. W. Park, J. S. Chae, S.-M. Park, K.-B. Kim, K. C. Roh, *Met. Mater. Int.* **2013**, 19, 887.
- [42] K. Li, D. Xue, *J. Phys. Chem. A* **2006**, 110, 11332.
- [43] M. E. G. Lyons, R. L. Doyle, I. Godwin, M. O'Brien, L. Russell, *J. Electrochem. Soc.* **2012**, 159, H932.
- [44] B. S. Yeo, A. T. Bell, *J. Phys. Chem. C* **2012**, 116, 8394.
- [45] X. Liang, J. Xiao, Y. Gou, B. Chen, *J. Mater. Res.* **2011**, 26, 3091.
- [46] Z.-H. Liang, Y.-J. Zhu, X.-L. Hu, *J. Phys. Chem. B* **2004**, 108, 3488.
- [47] T. Sato, T. Nakamura, F. Ozawa, *J. Appl. Chem. Biotechn.* **1975**, 25, 583.
- [48] W. Xing, F. Li, Z.-f. Yan, G. Q. Lu, *J. Power Sources* **2004**, 134, 324.
- [49] H. W. Park, B.-K. Na, B. W. Cho, S.-M. Park, K. C. Roh, *Phys. Chem. Chem. Phys.* **2013**, 15, 17626.
- [50] S. Le Bihan, M. Figlarz, *J. Cryst. Growth* **1972**, 13-14, 458.
- [51] S. Zhang, C. Scheu, *Microscopy* **2017**, 67, i133.
- [52] G. Sauerbrey, *Z. Phys.* **1959**, 155, 206.

7. Core-shell titania/iridium oxide nanoarchitectures with ultrathin Ir shells are highly efficient OER catalysts for massively scalable PEM electrolysis

This chapter is based on the following publication: (submitted)

Böhm, D., Beetz M., Gebauer, C., Bein T., and Fattakhova-Rohlfing, D.



ToC graphic illustrating a high surface area TiO₂ homogeneously coated with a thin layer of amorphous IrOOH_x that exhibits a limited conductivity and catalytic stability. Upon oxidation in molten salt a layer of interconnected IrO_x nanoparticles is formed which significantly increases the conductivity and stability and thereby results in the formation of an OER catalyst with low Ir density for large-scale PEM electrolysis.

7.1 Introduction

The awareness of the global warming potential of green-house gases emitted on a large scale by the combustion of carbon based fossil energy carriers has led to enormous investments in renewable energy sources in the last decades.^[1] Related to the generation and transmission of sustainable electrical energy, mainly intermittent in nature, is its storage which is required to mitigate power fluctuations.^[2] Among different possibilities, conversion of electrical energy to hydrogen as fuel via electrolysis of water is one of the most economically feasible and sustainable energy storage technologies. Besides the long-established alkaline (KOH-based) and high temperature solid oxide electrolyte electrolyzers, proton exchange membrane (PEM)-electrolyzers enjoy an upswing in the industrial and research interest as prospective conversion technique for decentralized electrical renewable energy generators with high output fluctuations. The key advantages of PEM electrolyzers are their high efficiency, high applicable current density, capability for intermittent operation, high hydrogen output pressure and compact size.^[3] However, high investment costs mainly governed by the Nafion® (PEM) membrane, Ti-sinter and the platinum group metals (PGM) Pt (cathode) and Ir (anode)^[4] used as hydrogen evolution (HER) and oxygen evolution reaction (OER) catalysts, respectively, still limit their widespread application.

Besides economic factors, large-scale deployment of these electrolyzers is hindered by the scarce PGM catalysts.^[5] Especially iridium, which is employed as an OER catalyst and being mined only as a platinum by-product,^[6] is in the focus of attention with a projected required 40-fold reduction^[5] in its utilization.

However, up to date iridium and especially its oxide are still the best compromise of a corrosion-stable and active catalyst material applicable under the harsh oxidizing and acidic environment of a PEM anode.^[7]

The main challenge to be addressed is therefore the reduction of the iridium mass loading on the anode by increasing the mass-based electrocatalytic activity (determined in $A\text{ g}_{\text{Ir}}^{-1}$) while maintaining or even increasing the long-term corrosion stability.^[5]

To accomplish this task, several partly complementary approaches were suggested in the literature for Ir-based OER catalysts.

As one of the means to increase the electrocatalytic and Ir mass-based activity of catalysts, stabilization of the highly active but less stable^[8] hydrous IrO_x phase,^[9] as well as the preparation of transition metal or fluorine doped ternary^[10-15] or quaternary^[16-18] oxide catalysts have been investigated. Another widespread approach to increase the atom-efficiency of Ir-based catalysts is an increase of their electrochemically active surface area, achieved either via nanostructuring,^[19-25] preparation of thin films^[26] or porous material^[27-29], or via a nanoparticle synthesis approach^[30].

Finally, the dispersion of the active material on corrosion-stable supports is a strategy explored and already commercialized in recent years. This approach increases the noble metal mass-based activity and furthermore leads to the formation of a catalyst with low volumetric Ir density (packing density) favorable for the preparation of thick and stable electrode layers in PEM electrolyzers with reduced areal Ir-loading.^[5, 31-32]

For applications in the current PEM electrolyzer designs the catalysts layer has to be electrically conducting, which ideally implies electrical conductivity also for the support material to provide continuous charge transport pathways to the current collectors and to minimize ohmic losses. The search for electrically conducting support materials for Ir-based catalysts has been intensive, with reported examples including transparent conductive oxides (TCO) such as antimony doped SnO_2 (ATO)^[21, 31, 33-35], indium tin oxide (ITO)^[36-37] and fluorine doped tin oxide (FTO)^[35] or recently investigated carbidic materials such as NbC, TiC, WC^[38] or TaC^[38-39] which allow for maximum Ir dispersions and shows record OER activities

due to the provided conductivity. However, none of the materials demonstrated so far offers sufficient long-term stability under harsh OER conditions (large positive overpotentials and acidic pH values), which is another essential requirement for the PEM catalysts.^[31, 40] So far, TiO₂ is the only truly oxidation-stable support material known, and it has been used in chlorine-alkali electrolysis for years as dimensionally stable electrode material (DSA®)^[41]. In recent years TiO₂ was also investigated regarding its use in acidic OER, with favorable particle-support interactions improving the electrocatalytic activity^[42-45] for diverse nano-morphologies^[44, 46] and high surface area TiO₂ structures^[44-45]. In addition, advances in the maximum possible iridium dispersion and thus reduced loading were made by introducing conductivity in the n-type semiconductor TiO₂ by doping^[47-50], oxynitride formation^[51], hydrogenation^[52] or by direct formation of substoichiometric conductive Magnéli phases^[53].

Undoped, practically non-conductive TiO₂ requires a charge percolation pathway established by interconnected highly conductive IrO₂ domains, with a lower reported threshold for unconstrained OER of $\approx 1.0 \times 10^{-3} \text{ S cm}^{-1}$.^[54] For a random TiO₂/IrO₂ distribution resulting from intermixing of Ti/Ir precursors, a minimum Ir content of 25 – 30 wt% Ir^[54-55] for mesoporous structures and $\approx 55 \text{ wt}\%$ Ir^[45, 56] for random structures built from nanoparticles were reported to be required for efficient OER.

For industrial applications with current densities of several A cm⁻², the conductivity within the catalyst layer becomes a decisive factor due to the corresponding voltage loss.^[57] To obtain a TiO₂-supported catalyst with a macroscopic conductivity of several S cm⁻¹ and at the same time reduced noble metal loading, a homogeneous distribution and interconnectivity of the nanosized Ir-oxide phase has to be realized. Due to the lack of truly homogeneous coating processes for TiO₂ nanostructures with IrO₂ nanoparticle layers, the state-of-the-art commercially available TiO₂-supported IrO₂ catalysts still have Ir contents of 75 wt%.^[57-58]

Here, we report the generation of a novel highly active TiO₂ supported IrO₂ nanoparticle catalyst with only 30 wt% Ir, based on a controlled iridium oxidation process for the formation of a layer of interconnected IrO₂ nanoparticles. Commercially available high surface area Aeroxide P25® titania (EVONIK INDUSTRIES) is employed as a corrosion-resistant catalyst support that is coated with a thin homogeneous layer of amorphous IrOOH_x. To increase the corrosion resistance of the hydrous iridium oxide, calcination in air is a valid approach that results in the formation of rutile IrO₂ phase at ≈ 400 °C.^[59-61] However, this approach suffers from a rather non-uniform growth of nanoparticles that leads to the formation of larger IrO₂ crystals together with isolated nanoparticles on the non-conductive TiO₂, hence interrupting charge percolation pathways.

By applying a precisely controllable oxidation of the material in molten NaNO₃, a phase transformation and crystallization of uniform IrO₂ nanoparticles from the amorphous IrOOH_x layer can be achieved. Optimizing the synthesis conditions leads to a continuous layer of interconnected IrO₂ nanoparticles, resulting in a highly active TiO₂-supported IrO₂ nanoparticle catalyst with significantly increased conductivity and stability. The proposed synthesis pathway thereby allows for a facile preparation and tuneability of the catalyst nanomorphology and surface area (via selection of the respective TiO₂ support), Ir-loading (via the thickness of the applied IrOOH_x layer) and activity, crystallinity and conductivity (controlled by the parameters of the molten salt oxidation). This novel strategy enables the preparation of Ir-based oxide-supported OER catalysts with optimized iridium dispersion and low Ir-volume density, which are required for the preparation of PEM-electrolyzer anodes with significantly reduced Ir content.

7.2 Results and Discussion

Structural characterization of P25 TiO₂ / IrOOH_x before and after oxidation

Two batches of commercially available IrOOH_x coated TiO₂ (Aeroxide®P25, EVONIK INDUSTRIES) catalyst were obtained from HERAEUS Deutschland GmbH & Co. KG with nominal Ir metal contents of 30 and 45 wt% Ir, respectively, which are designated as “non-heated” catalysts. In a facile and industrially scalable molten salt oxidation in NaNO₃, the IrOOH_x coated TiO₂ is oxidized at temperatures of 350, 365, 375 and 400 °C. In the following work, the products obtained by the oxidation of the 30 and 45 wt% Ir containing catalysts are color-coded in the respective plots as shades of red and blue, respectively. Details about the preparation and oxidation procedure are given in the Experimental Section.

X-ray diffraction analysis (Figure 1a) of the non-heated 30 wt% Ir containing IrOOH_x/TiO₂ catalyst (black line) shows reflections with high intensity at the position related to TiO₂ anatase phase (red reference pattern) and less intensive reflections related to rutile TiO₂ (orange reference pattern) identical to the recorded reference pattern of P25 TiO₂ (grey curve). In addition to the P25 TiO₂ reference, the pattern of the IrOOH_x coated catalyst shows a very broad increase in intensity centered around $\approx 33^\circ 2\theta$ ranging from the TiO₂ rutile 110 to the 101 reflection. This broad feature is associated with the amorphous or “hydrous” IrOOH_x phase.^[62] Identical reflections are also observed for the 45 wt% Ir coated IrOOH_x/TiO₂ catalyst (Figure S1a) with a significantly increased intensity centered around $\approx 33^\circ 2\theta$ ranging from the TiO₂ rutile 110 up to rutile 101 reflection and representing an increased amount of amorphous Ir-phase besides the highly crystalline P25 TiO₂.

The Raman spectrum shown in Figure 1b further confirms the presence of the major TiO₂ anatase phase for the 30 wt% Ir coated catalyst with a visible B_{1g} band at $\approx 400\text{ cm}^{-1}$, a A_{1g}/B_{2g} band at $\approx 520\text{ cm}^{-1}$ and the E_g band at $\approx 640\text{ cm}^{-1}$.^[63] Indication for the presence of an additional amorphous Ir-phase is given by the low slope between the TiO₂ anatase A_{1g}/B_{1g} and E_g bands,

as the IrO₂ E_g band is located at 561 cm⁻¹.^[64-65] Similar Raman spectra for the 45 wt% Ir containing catalyst are shown in Figure S1b, although the bands of the TiO₂ anatase phase are even broader with a slightly increased intensity in the region of the IrO₂ E_g band at ≈560 cm⁻¹. The reduced signal of the TiO₂ phase can be explained by the homogeneous IrOOH_x or IrO₂ coating, respectively, which significantly decreases the observable Raman scattering of the underlying TiO₂.

For both Ir coating contents of 30 and 45 wt% (Figure 1b and Figure S1b), a gradual and relative increase in intensity at ≈560 cm⁻¹ can be observed with increasing oxidation temperature in molten NaNO₃.^[64-65]

Reaction products obtained at oxidation temperatures of 350 – 375 °C indicate crystallization of the IrOOH_x phase to form an IrO_x phase that is not fully crystalline and distinct from the tetragonal IrO₂ phase.^[62, 66-67] This intermediate phase with small IrO_x nanoparticles of about 1 – 2 nm is described in the literature for the molten salt or “Adams fusion” synthesis from Ir-precursors in the temperature range of around 350 °C. It only shows one broad bump of intensity around 35° 2θ in the X-ray diffractograms (Figure 1a and Figure S1).^[45, 56, 68] The broad diffraction peak thereby cannot be assigned to the 101 rutile IrO₂ lattice plane or any other Ir phase but rather represents a pair distribution function originating from an amorphous or disordered IrO_x phase with a reported Ir-O atomic distance of ≈2.03 Å determined from EXAFS measurements.^[66-67]

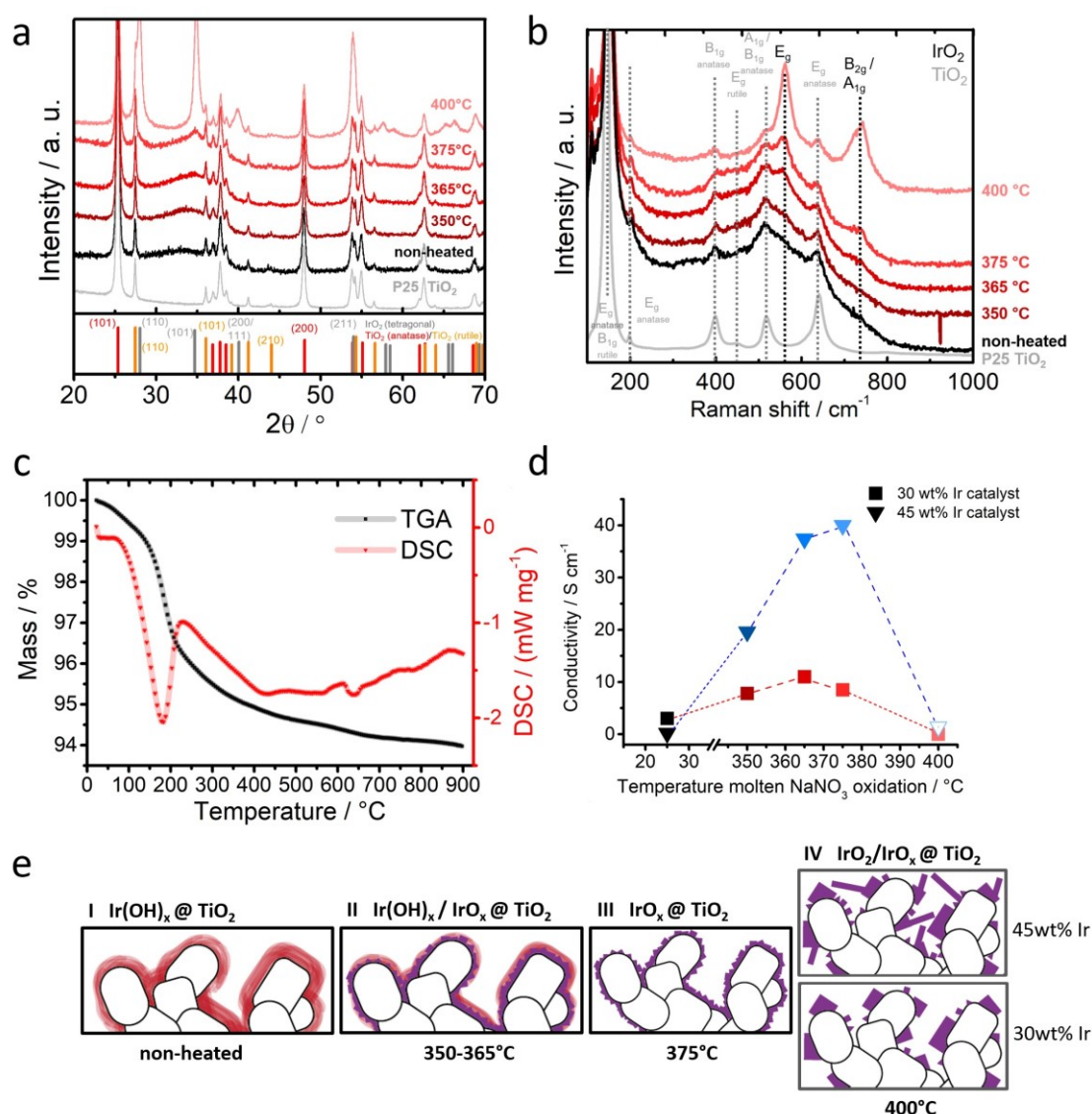


Figure 1 Physico-chemical characterization of high surface area TiO_2 (P25) supported IrOOH_x , IrO_x and IrO_2 with a total loading of 30 wt% Ir after oxidation at various temperatures, with scheme of Ir coating nanostructure. (a) X-ray diffraction patterns and (b) Raman spectra of IrOOH_x coated P25 TiO_2 before (black curve) and after oxidation in molten NaNO_3 at temperatures between 350 - 400°C (dark-red to light red curves). IrO_2 pattern: ICDD card number 00-015-0870 (grey) (tetragonal symmetry, $a = b = 4.4983 \text{ \AA}$, $c = 3.1544 \text{ \AA}$, $\alpha = \beta = \gamma = 90^\circ$). TiO_2 (anatase) (ICDD card number 00-004-0477, tetragonal symmetry, $a = b = 3.783 \text{ \AA}$, $c = 9.510 \text{ \AA}$, $\alpha = \beta = \gamma = 90^\circ$) and TiO_2 (rutile) (ICDD card number 00-004-0551, tetragonal symmetry, $a = b = 4.594 \text{ \AA}$, $c = 2.958 \text{ \AA}$, $\alpha = \beta = \gamma = 90^\circ$). Raman bands at 561 cm^{-1} (E_g) and close bands at 728 cm^{-1} (B_{2g}) and at 752 cm^{-1} (A_{1g}) correspond to the tetragonal iridium oxide phase.^[64-65] Raman bands at 144 cm^{-1} (E_g), 197 cm^{-1} (E_g), 399 cm^{-1} (B_{1g}), 519 cm^{-1} (A_{1g}/B_{1g}) and 639 cm^{-1} (E_g) correspond to anatase TiO_2 and bands at 143 cm^{-1} (B_{1g}) and 447 cm^{-1} (E_g) were assigned to rutile TiO_2 .^[63] (c) Thermogravimetric analysis with differential scanning calorimetry. (d) Specific conductivities of non-heated and oxidized catalyst powder samples of 30 (red squares) and 45 wt% Ir (blue triangles) coated P25 TiO_2 catalyst. (e) Schematic representation of $\text{TiO}_2/\text{IrOOH}_x$ catalyst nanostructure formation after oxidation at various temperatures for low (30 wt%) and high (45 wt%) Ir loading.

Oxidation at 400 °C leads, for both Ir loadings, to a significant increase in crystallinity indicated by the formation of the rutile IrO_2 phase with average domain sizes of $\approx 18 \text{ nm}$ and

≈ 27 nm for the 30 and 45 wt% containing TiO₂ supported catalyst, respectively (calculated from the 101 reflection broadening with the Scherrer equation).^[69]

The significantly enhanced crystallization at 400 °C - exceeding the expected influence of the sole temperature difference compared to an oxidation at 375 °C - is attributed to a decomposition of the NaNO₃ melt starting at that temperature. According to literature, thermal decomposition of NaNO₃ consists of three successive or concurrent reactions and processes that include a nitrate to nitrite plus oxygen reaction as well as thermal evaporation. The decomposition temperature of NaNO₃ thereby depends on the exact reaction parameters (heating rate, atmosphere, crucible etc.) with reported values ranging from 380 °C to 450 °C and above.^[70-72] The low boiling point of NaNO₃ of $T_b=380$ °C and the partial decomposition of NO₃⁻ to NO₂ + ½ O₂ + e⁻ thereby lead to strong oxidizing conditions in contrast to the lower O₂ partial pressure present in molten NaNO₃ at lower temperatures, resulting in a limited particle growth.^[70-72]

The Raman spectrum for 45 wt% Ir coated TiO₂ (IrOOH_x oxidized at 400 °C) (Figure S1b) does not even show distinct reflections as the bands are further broadened. This can be explained by the complete coverage of the TiO₂ by IrO₂ on the one hand, and by the very low signal intensities resulting from a significantly increased optical absorption of the sample on the other hand.

The phase transformation of amorphous 30 wt% Ir containing IrOOH_x/TiO₂ to IrO₂/TiO₂ was further investigated by thermogravimetric analysis (TGA) and differential scanning calorimetry (DSC) shown in Figure 1c, and is in accordance with results obtained by Cruz *et al.*^[62] In the first temperature range up to ≈ 150 °C the IrOOH_x phase is physically dehydrated which accounts for ≈ 1 wt% of the sample. In the second temperature regime from 150 – 240 °C, further crystal-bound water and hydroxyl groups are removed from the amorphous IrOOH_x phase and a disordered IrO_x phase is formed. This electrochemically active phase gradually

increases in crystallinity up to ≈ 400 °C in the third temperature regime to finally form the rutile IrO_2 phase, which is in agreement with literature reports.^[59] Temperatures above 400 °C lead to a further crystallization and growth of initially formed small and defect rich IrO_2 domains to stoichiometric bulk IrO_2 , which is reflected by a minor mass loss below 1 wt% in the range up to 900 °C.

A key factor for the application of the oxidized $\text{IrOOH}_x/\text{TiO}_2$ catalyst in PEM electrolyzers is its conductivity, which was measured with compressed powder pellets with a 4-point probe conductivity and Hall-effect measurement device. Based on the observed trends in the conductivity with the calcination temperature shown in Figure 1d for 30 wt% (shades of red) and 45 wt% (shades of blue) Ir containing catalyst, together with the results of electron microscopy, X-ray diffraction and Raman spectroscopy we have proposed a crystallization mechanism schematically depicted in Figure 1e, which will be addressed in more detail below. For the 30 wt% $\text{IrOOH}_x/\text{TiO}_2$ catalyst a conductivity of $\approx 3.0 \text{ S cm}^{-1}$ (Figure 1d, black square and Figure 1e, step I) for the non-heated material is high when compared to literature values of up to $1.5 \times 10^{-2} \text{ S cm}^{-1}$ reported for electro-flocculated 2 nm sized IrO_x particles.^[73] However, the conductivity of hydrous iridium oxide is significantly influenced by the morphology, degree of hydration and the oxidation state of iridium. This leads to a broad scatter of reported conductivity values ranging from $10^{-6} \text{ S cm}^{-1}$ for IrO_x nanoparticles with Ir in oxidation state +III up to an apparent conductivity of $8.1 \times 10^{-1} \text{ S cm}^{-1}$ for an ATO supported IrO_x nanoparticle catalyst with a conductivity of $1.8 \times 10^{-2} \text{ S cm}^{-1}$ determined for the ATO support only, which indicates an even higher conductivity of the IrO_x nanoparticle phase.^[59, 73-74] The high conductivity value measured for the 30 wt% Ir containing sample is attributed to the presence of a very thin hydrated IrOOH_x layer (as shown by electron microscopy in following sections) on the TiO_2 support and a possible beneficial (hydrous)metal-support interaction leading to an increased conductivity.^[42-43]

Thicker IrOOH_x layers formed in the case of non-heated 45 wt% Ir containing IrOOH_x/TiO₂ catalyst exhibit a slightly lower conductivity reaching 0.2 S cm⁻¹ (Figure 1d, black triangle and Figure 1e, step I), which might be explained by a lower degree of hydration or reduced (hydrous)metal-support interaction.

Upon oxidation and the associated increase in crystallinity, the conductivity significantly increases to reach a maximum of 11 S cm⁻¹ at 365 °C for the 30 wt% Ir catalyst and 40 S cm⁻¹ at 375 °C for the 45 wt% Ir containing catalyst (Figure 1d and Figure 1e, step II and III), which agrees well with a reported conductivity of ≈ 26 S cm⁻¹ for a layer of about 2 – 3 nm IrO₂ nanoparticles.^[75] The values are of the same order of magnitude as an industrial IrO₂/TiO₂ reference catalyst^[57-58] with 75 wt% Ir content, with a determined conductivity of 73.1 S cm⁻¹ under the same measurements conditions. The higher absolute conductivity as well as the higher temperature optimum for the 45 wt% Ir containing catalyst compared to the 30 wt% Ir containing sample can be explained by the possible formation of larger IrO₂ nanocrystals from the precursor IrOOH_x phase as depicted in Figure 1e, step III. For both Ir loadings an interconnected layer of highly conductive IrO₂ nanoparticles on top of the non-conductive TiO₂ support is formed in this step, albeit at slightly different temperatures.

Above the temperature optimum, the further growth of IrO₂ particles via Ostwald ripening, consuming surrounding IrOOH_x and smaller IrO_x crystals, results in the formation of larger isolated IrO₂ crystals. The formation of isolated crystals significantly lowers the overall conductivity due to missing charge percolation pathways as depicted in Figure 1e, step IV. The higher amount of IrOOH_x precursor phase in the 45 wt% Ir containing samples allows for the formation of larger IrO₂ crystals that still enable charge percolation and are not fully isolated in the case of 400 °C oxidized samples. Hence, a reasonable conductivity of 1.4 S cm⁻¹ is retained for the 45 wt% sample as compared to a significant loss in conductivity with 4.9×10^{-4} S cm⁻¹ for the 30 wt% Ir containing catalyst.

The proposed scheme in Figure 1e is supported by structural characterization by scanning electron microscopy shown in Figure 2 and Figure S2-3 for the 30 and 45 wt% Ir containing catalyst samples. The morphology of the non-heated 30 wt% Ir containing $\text{IrOOH}_x/\text{TiO}_2$ exactly matches that of the uncoated P25 TiO_2 structure. The latter is composed of aggregates and larger agglomerates of about 20 – 30 nm primary TiO_2 crystals (Figure 2a,c), which are mainly composed of anatase phase with a minor contribution of rutile TiO_2 (Figure 1a). To assess the coverage of the TiO_2 substrate by the iridium phase, all sample areas were imaged once by scanning with a secondary electron (SE) sensitive detector (Figure 1a,c,e,g,i,k) for morphological contrast and further imaged with a detector sensitive towards backscattered electrons (BSE) for enhanced material contrast (Figure 1b,d,f,h,j,l).

From the comparison of the backscattered electron-based SEM images depicted in Figure 2b,d with the morphology shown in Figure 2a,c and the respective diffractogram (Figure 1a, black curve), a homogeneous coverage of the TiO_2 nanostructure with a thin amorphous IrOOH_x phase is suggested. From the scanning electron microscopy images shown in Figure S2 and Figure 1e-h it can also be concluded that oxidation at 350 °C, 365 °C and up to 375 °C in molten NaNO_3 does not alter the morphology of the Ir coated catalyst or affects the homogeneous coverage of the TiO_2 by the formed IrO_x nanoparticle (Figure 1a,b) layer.

At an oxidation temperature of 400 °C the morphology of the P25 TiO_2 is still maintained (Figure 2i,k) but the $\text{IrO}_x/\text{IrO}_2$ nanoparticle phase (Figure 1a,b) visibly forms larger aggregates and crystals of several tens of nanometers, as shown by the light spots in the backscattered electron-based SEM images (Figure 2j,l), which were already indicated by the respective XRD patterns (Figure 1a and Figure S1).

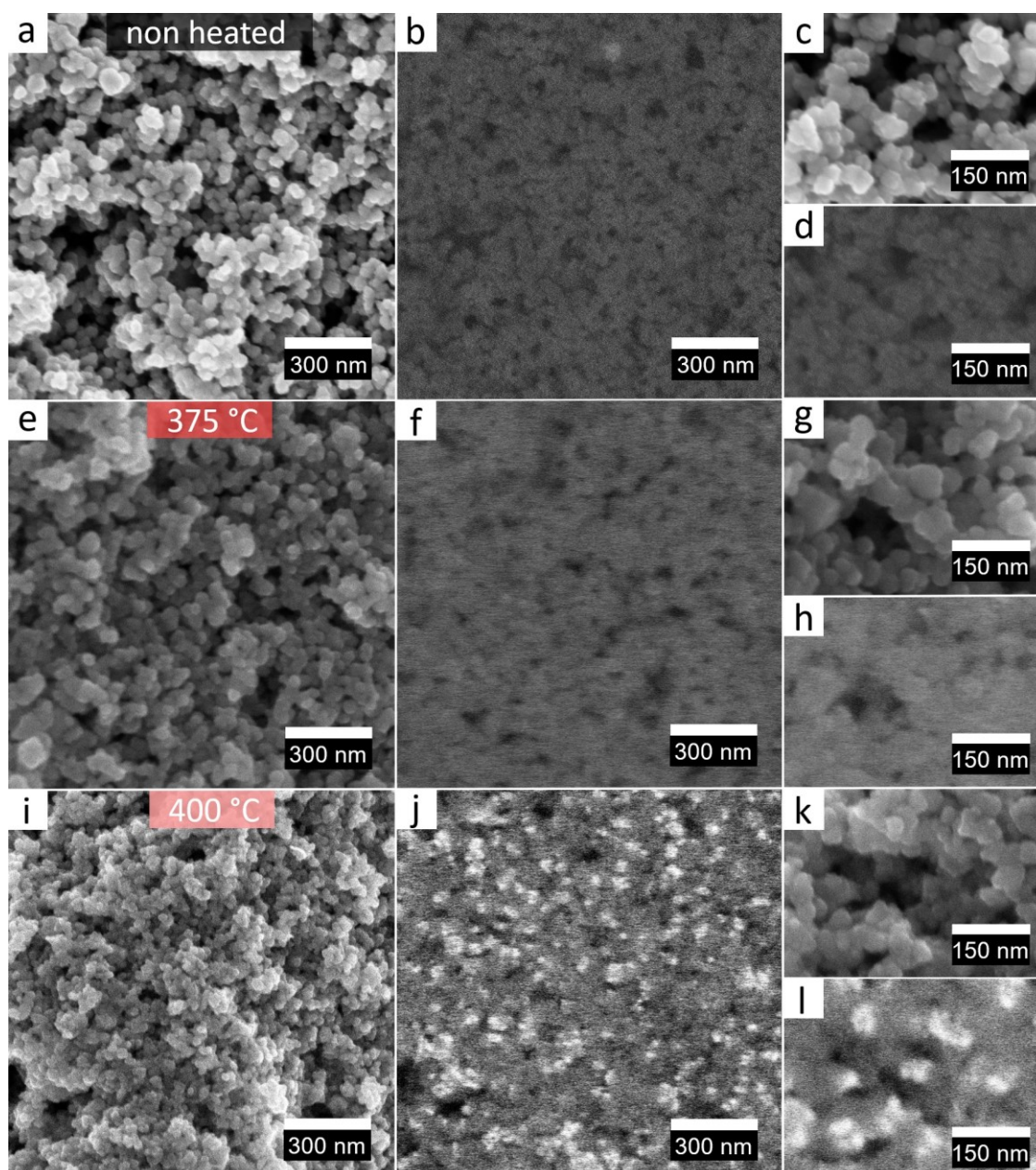


Figure 2 SEM images of IrO_x and IrO_2 nanoparticles on P25 TiO_2 with 30 wt% Ir content. Variation in oxidation temperature of IrOOH_x -coated P25 TiO_2 from non-heated (a-d) over 375 °C (e-h), 400 °C (i-l) in NaNO_3 . All sample areas were imaged once by recording with a secondary electron sensitive detector (a,c,e,g,i,k) for morphological contrast and further imaged with a detector sensitive towards backscattered electrons for enhanced material contrast (b,d,f,h,j,l).

The 45 wt% Ir containing $\text{IrOOH}_x/\text{TiO}_2$ catalyst series also exhibits the morphology of the unloaded P25 TiO_2 up to an oxidation temperature of 375 °C (Figure S3a,c,e,g,i,k,m,o), although a slightly rounded shape and increased thickness of the particles (Figure S3a,c) indicate a smooth coverage by the IrOOH_x phase (Figure S1a,b). In contrast to the 30 wt% Ir containing catalyst sample series, the homogeneity of the coverage with the Ir active phase for

the 45 wt% Ir catalyst series seems to be slightly reduced, as small intensity variations across the scan area in the respective backscattered electron based SEM images are visible (Figure S3b,d,f,h,j,l,n,p). In addition, for 45 wt% Ir catalyst samples the formation of a continuous IrOOH_x and IrO_x/IrO₂ particle layers at temperatures of up to 375 °C can directly be observed in the high-resolution BSE-based SEM images (Figure S3d,h,l,p) by lighter rims around the TiO₂ nanocrystals.

Oxidation at 400 °C leads to a significantly altered morphology, being composed of the underlying P25 TiO₂ structure with needle-like and particle-like nanostructures on the surface (Figure S3q,s). A comparison with the acquired backscattered electron-based SEM images further confirms the formation of IrO_x/IrO₂ (Figure S1a,b) needle-like structures shown as brighter features on the underlying TiO₂ structure (Figure S3r,t).

To investigate the phase transformation of amorphous IrOOH_x to IrO_x nanoparticles and the coverage of the TiO₂ nanocrystals at the local scale, high resolution scanning transmission electron microscopy (STEM) and energy dispersive X-ray spectroscopy (EDX) were performed.

Figure 3a-d shows the larger agglomerated P25 TiO₂ nanocrystals with a dimension of about 20 – 30 nm that are homogeneously coated with a 1 – 2 nm thin amorphous IrOOH_x phase, visible as a bright diffuse rim around the titania. The electron diffraction pattern (Figure 3d) only shows a diffuse ring that cannot be associated with metallic Ir or a IrO₂ phase, but which agrees well with the X-ray diffraction pattern (Figure 1a) and can be assigned to the amorphous or “hydrous” IrOOH_x phase.^[62]

The visualization of thin amorphous IrOOH_x layers is possible only under low-dose imaging conditions with short acquisition times, otherwise an electron beam-induced crystallization with the formation of 1 – 2 nm sized particles can be observed after only seconds of illumination (Figure S4).

Upon oxidation in molten NaNO_3 at $365\text{ }^\circ\text{C}$, the continuous amorphous layer of the 30 wt% Ir containing catalyst partially crystallizes with the formation of 1 – 2 nm small IrO_x particles embedded in a surrounding amorphous IrOOH_x phase, as observed in high resolution STEM images (Figure S5b,c,d) and high resolution TEM images (Figure S5a). At a slightly higher oxidation temperature of $375\text{ }^\circ\text{C}$ the crystallinity of the IrO_x layer increases but the layer continuity remains preserved. The corresponding STEM images show that the TiO_2 crystal facets (Figure 3e,f) are covered by an interconnected layer of about 2 nm sized IrO_x nanocrystals (Figure 3g,h).

The further increase in oxidation temperature to $400\text{ }^\circ\text{C}$ dramatically alters the catalyst morphology, as already indicated by the XRD, SEM and conductivity measurements discussed above. STEM images and EDX mapping of $\text{IrOOH}_x/\text{TiO}_2$ samples oxidized at $400\text{ }^\circ\text{C}$ show that the P25 TiO_2 support remains unaltered, but now the titania crystals are covered by isolated and aggregated 1 – 2 nm sized particles as well as longer rod-like crystals (Figure 3i-k,m). According to the electron diffraction pattern depicted in Figure 3l, the nanoparticles and rod-like crystals can both be assigned to the rutile IrO_2 phase. The formation of larger rod-like IrO_2 crystals resulting from a preferential growth along the [001] and [112] directions of the rutile unit cell was described by Abbott *et al.* for IrO_2 synthesized by the Adams fusion method at temperatures above $500\text{ }^\circ\text{C}$, and explained by a thermodynamically favorable formation of 110 surface terminations.^[67]

STEM imaging of the 45 wt% Ir containing TiO_2 supported sample series shown in Figure S6 features a similar microstructural evolution of the IrOOH_x phase upon oxidation in NaNO_3 .

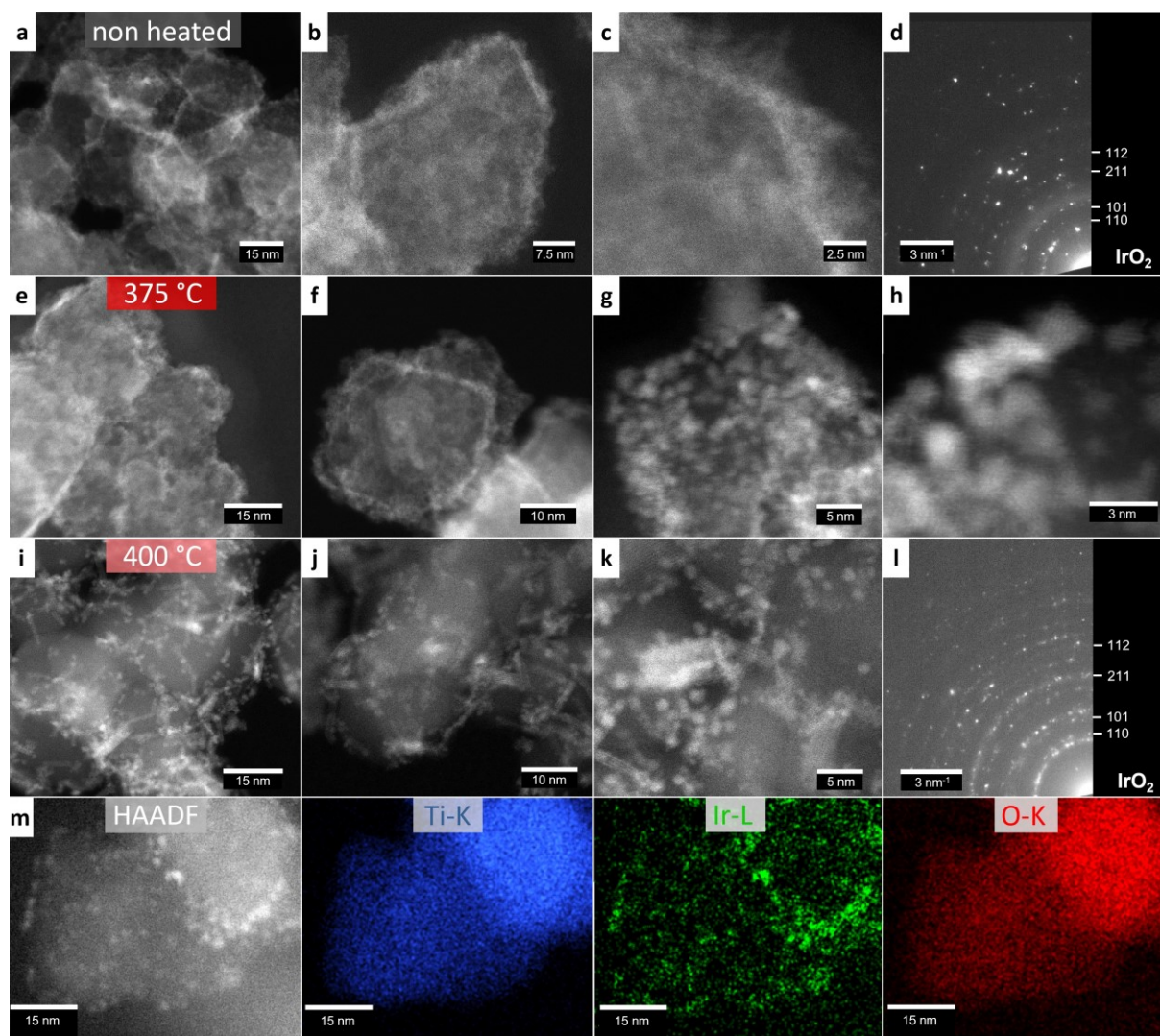


Figure 3 TEM images of IrOOH_x and IrO_2 nanoparticles on P25 TiO_2 with 30 wt% Ir content. Variation in oxidation temperature of IrOOH_x coated P25 TiO_2 from non-heated (a-d) over 375 °C (e-h) to 400 °C (i-m) in NaNO_3 . Phase identification and assignment of lattice planes in electron diffraction pattern (d,l) according to literature values. IrO_2 pattern: ICDD card number 00-015-0870 (grey) (tetragonal symmetry, $a = b = 4.4983 \text{ \AA}$, $c = 3.1544 \text{ \AA}$, $\alpha = \beta = \gamma = 90^\circ$). (m) STEM/EDX elemental mapping of aggregated IrO_2 nanoparticles on P25 TiO_2 nanocrystals after oxidation at 400 °C.

The non-heated $\text{IrOOH}_x/\text{TiO}_2$ sample (Figure S6a-c) displays a rather homogeneous coating with a 5-10 nm thick amorphous Ir-containing phase as indicated by EDX mapping (Figure S6e) and electron diffraction patterns, and which only shows diffraction spots related to TiO_2 anatase and rutile phase (Figure S6d). The microstructure of the 45 wt% catalyst oxidized at 375 °C appears very similar to the lower-loaded counterpart with 1 – 2 nm IrO_x mostly interconnected particles attached to the surface of the TiO_2 crystals (Figure S6f-h). The particles are homogeneously distributed on the TiO_2 as shown by EDX mapping (Figure S6j)

and consist of an intermediate phase IrO_x and rutile IrO_2 as shown by the electron diffraction pattern (Figure S6i). Finally, an oxidizing temperature of 400 °C leads to the formation of IrO_2 nanorods and aggregates of small particles sized about 1 – 2 nm, similar to those observed for the 30 wt% loaded catalyst. However, the length of the nanorods significantly exceeds that of the lower-loaded sample with dimensions of up to about 100×10 nm (Figure S6k), which is also in agreement with the larger average crystalline domain size of ≈ 27 nm determined from XRD line broadening. Although the homogeneity of the Ir distribution is lowered as shown by EDX mapping (Figure S6o), the larger rod-like structures still seem to connect isolated particle aggregates on the non-conductive TiO_2 (Figure S6k-n) in contrast to the 400 °C oxidized 30 wt% Ir containing catalyst.

The results shown by electron microscopy therefore support the structural model shown in Figure 1e with implications on the conductivity as shown in Figure 1d. Further evidence for the homogeneous coverage of the P25 TiO_2 support with an IrOOH_x phase and the evolution of the accessible surface area by increasing temperature in the NaNO_3 oxidation is given by nitrogen sorption measurements shown in the Supplementary Information Figure S7-9. The Brunauer-Emmett-Teller (BET) surface area of P25 TiO_2 increases after IrOOH_x coverage (30 wt% Ir catalyst) and oxidation at 365 °C from $62 \text{ m}^2 \text{ g}^{-1}$ (Figure S7) to $78 \text{ m}^2 \text{ g}^{-1}$ (Figure S8a). A further reduction of the amorphous IrOOH_x content and formation of IrO_x nanoparticles at 375 °C leads to an increased surface area of $119 \text{ m}^2 \text{ g}^{-1}$ (Figure 8b), which is again significantly reduced to $76 \text{ m}^2 \text{ g}^{-1}$ by the formation of larger IrO_2 crystals upon oxidation at 400 °C (Figure S8c).

The BET surface area of the oxidized 45 wt% Ir coated catalyst shows a similar trend with a significant increase upon IrO_x nanoparticle formation with $109 - 101 \text{ m}^2 \text{ g}^{-1}$ (350 and 365 °C, respectively) and a maximum of $119 \text{ m}^2 \text{ g}^{-1}$ shown at 375 °C. Oxidation at 400 °C significantly reduces the BET area to $38 \text{ m}^2 \text{ g}^{-1}$, which is even below the value for the uncoated P25 TiO_2 .

This can be explained by a coverage of TiO₂ surface by larger IrO₂ crystals with reduced surface area that exceeds the average domain size of the TiO₂ as shown by XRD (Figure S1a) and STEM imaging (Figure S6k-o).

Electrochemical characterization of P25 / IrOOH_x

To investigate the redox activity of the differently oxidized TiO₂ supported Ir-phases, cyclic voltammograms were recorded over a broad potential range between the hydrogen evolution reaction (HER) and OER onset potentials (0.05 – 1.52 V vs. RHE) before each rotating disc electrode activity measurement (Figure 4a). Besides the OER onset above about 1.45 V vs. RHE, the non-heated 30 wt% Ir containing IrOOH_x/TiO₂ sample shows a broad peak centered around 0.8 V vs. RHE attributed to the Ir(III)/Ir(IV) redox reaction in acidic environment.^[76-77] This feature is reduced in intensity for the IrO_x/TiO₂ sample oxidized at 375 °C and not further detectable for the IrO₂/TiO₂ sample prepared at 400 °C (Figure 4a). The presence and reduction of the Ir(III)/Ir(IV) redox feature upon oxidation is even more pronounced in the cyclic voltammograms of the 45 wt% Ir sample series (Figure S10a) due to the increased thickness of the initial amorphous IrOOH_x layer with bulk redox activity.^[59]

To assess the OER onset potential (defined at 1 mA cm⁻²) and catalytic activity under controlled reaction parameters (see Experimental section for details) rotating disc electrode measurements with repeated cyclic voltammetry were performed as shown in Figure 4bc and Figure S11ab for the 30 wt% Ir containing sample series. The non-heated IrOOH_x/TiO₂ catalyst sample exhibits an onset potential of only 202 mV which is in the expected range of a highly OER active hydrous Ir-oxide.^[21, 78]

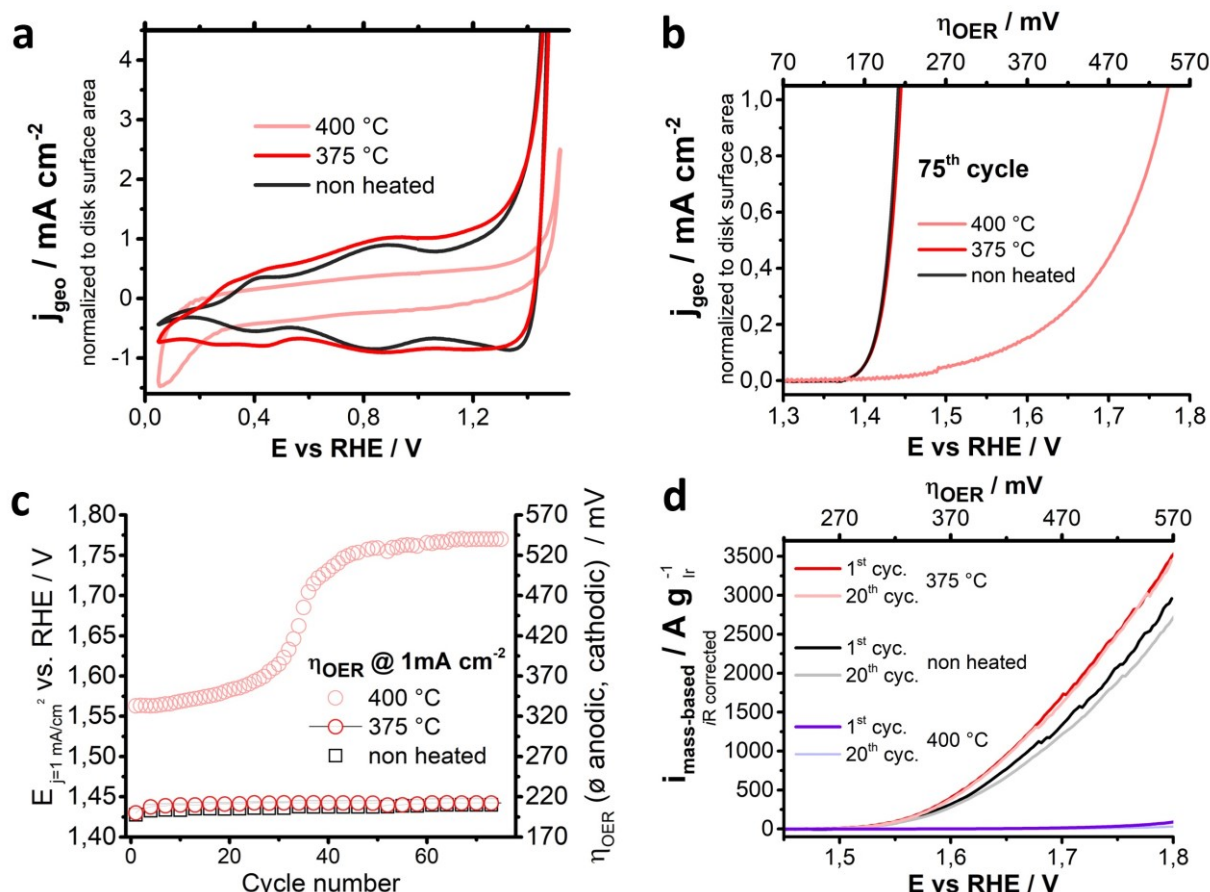


Figure 4 Electrochemical characterization of IrOOH_x and IrO_2 nanoparticles on P25 TiO_2 with 30 wt% Ir content. (a) Cyclic voltammogram between 0.05-1.50 V vs. reversible hydrogen reference electrode (RHE) of IrOOH_x coated TiO_2 before (black curve) and after oxidation at 375 °C (dark red curve) and 400 °C (light red curve) with a scan rate of 50 mV s^{-1} . (b) 75th scan cycle of rotating disc electrode measurements for non-heated $\text{IrOOH}_x/\text{TiO}_2$ catalyst (black curve) and 375 °C (red curve) and 400 °C (light red curve) oxidized catalyst. (c) Extracted overpotentials (η_{OER}) of RDE measurements for each cycle required to reach a current density of 1 mA cm^{-2} . (d) Iridium mass based OER activities for $\text{IrOOH}_x/\text{TiO}_2$ based catalysts determined by cyclic voltammetry measurements (1st and 20th cycle each) of respective catalyst samples (15 μg_{Ir} abs.) on fluorine doped tin oxide substrates.

Interestingly, with the oxidation in molten NaNO_3 the onset potential remains low at 204 mV (365 °C) – 206 mV (375 °C) compared to 252 mV determined for the more crystalline $\text{IrO}_2/\text{TiO}_2$ reference catalyst under same measurements conditions (Figure S12a-c). The low onset potential values compare well with the best catalysts reported in the literature, in spite of the relatively low surface area and insulating character of the P25 substrate used in our work. Thus, a similar low onset potential of 200 mV was reported by Hu *et al.* for a supported catalyst with a comparable Ir loading but evidently more beneficial electrically conducting Nb-doped TiO_2 (NTO) support with a higher surface area ($\approx 83 \text{ m}^2 \text{ g}^{-1}$).^[49] Apparently, a conductive NTO

support, even with a homogeneous IrO₂ coverage, does not necessarily translate into a lower onset potential as shown by Hufnagel *et al.* for an 8 wt% Ir coated catalyst with an $\eta_{OER}=250$ mV.^[48] In contrast to the samples oxidized at lower temperatures, oxidation of 30 wt% Ir containing catalyst at 400 °C leads to a significantly increased onset potential of initially 328 mV (5th RDE cycle) that rises from the 30th cycle up to 532 mV after 75 cycles due to its limited conductivity (Figure 4b,c).

The 45 wt% Ir sample series exhibits a slightly higher onset potential of 211 mV for the non-heated IrOOH_x/TiO₂ catalyst that also remains low upon oxidation with values of 214 mV (365 °C) – 208 mV (375 °C) (Figure S10b). Samples oxidized at 400 °C still exhibit a relatively low onset potential of 231 mV after 75 RDE scan cycles, which can be explained by the retained conductivity compared to the similarly oxidized 30 wt% Ir sample (Figure S10 and Figure 1).

To assess the electrocatalytic activity of the oxidized IrOOH_x/TiO₂ and the IrO₂/TiO₂ reference catalyst, cyclic voltammetry in a potential window up to 1.8 V vs. RHE was conducted on fluorine doped tin oxide substrates at room temperature with results presented in Figure 4d, S10, S11 and Figure S13. Figure 4d shows a visibly increased activity of the 375 °C oxidized sample compared to the non-heated 30 wt% Ir containing IrOOH_x/TiO₂ with increasing overpotential, which can be explained by the significantly higher conductivity of the oxidized sample and thus a reduced ohmic resistance at high current densities. The contrasting example is given by the 400 °C oxidized sample (Figure 4d), showing only a low OER activity due to its limited conductivity (Figure 1).

The 45 wt% sample series shows an even higher spread in OER activity (Figure S10) with increasing overpotential, which is in agreement with the larger change in conductivity upon oxidation (Figure 1). Due to the retained conductivity, the 400 °C oxidized sample thereby still shows a moderate OER activity compared to the 30 wt% Ir sample.

Absolute OER activities normalized to the iridium mass are very similar for the 30 and 45 wt% Ir containing IrOOH_x/TiO₂ catalysts oxidized at 375 °C, which is regarded to be the optimum synthesis temperature resulting in maximized conductivity and activity for the 30 wt% sample series (Figure S13). In the low overpotential range of 300 mV, the 375 °C oxidized 30 and 45 wt% IrOOH_x/TiO₂ catalysts exhibit an Ir-based OER current of about 62 and 71 A g_{Ir}⁻¹ after the 10th cycle, respectively, which is about 8 times higher than the measured 8 A g_{Ir}⁻¹ of the 75 wt% Ir containing IrO₂/TiO₂ reference catalyst under the same conditions. At an elevated overpotential of 420 mV, the 30 and 45 wt% Ir coated catalysts show a coinciding activity of about 1048 and 1047 A g_{Ir}⁻¹, respectively, which is still 3 times higher than the measured 345 A g_{Ir}⁻¹ of the reference catalyst.

Comparison to literature shows a similar high activity of our prepared catalysts to a very high surface area (245 m² g⁻¹) 40 mol% Ir (≅ 56 wt% Ir) containing IrO₂/TiO₂ catalyst prepared by Oakton *et al.*, which delivers 70 A g⁻¹ at an overpotential of 287 mV.^[45] However, the reported conductivity of the randomly mixed oxide of 0.26 S cm⁻¹ is expected to limit the performance in the high overpotential range that is typically used for the operation of an electrolyzer. Compared to the highly active catalyst reported by Hu *et al.* with 548 A g_{Ir}⁻¹ at an overpotential of 362 mV (26 wt% Ir containing Nb-doped TiO₂ supported IrO₂ nanoparticle catalyst), our 30 wt% Ir containing IrOOH_x/TiO₂ catalyst oxidized at 375 °C shows a slightly lower mass-based activity of 487 A g_{Ir}⁻¹ determined at the same overpotential.^[49]

Although the supported catalysts presented here do not surpass the best performing NTO supported IrO₂ nanoparticle catalyst, they combine required key properties of an OER catalyst that can effectively reduce the Ir-loading in the anode layer of an actual PEM electrolyzer such as high conductivity, high iridium dispersion and resulting low Ir-density with a high catalytic activity.^[5, 57]

Keeping these factors in perspective, P25 titania with its moderately high surface area and low powder density of $0.1 - 0.18 \text{ g cm}^{-3}$ (according to product specification, EVONIK INDUSTRIES, 2019), therefore presents a suitable corrosion-resistant and commercially available support material for the synthesis of novel highly active OER catalysts with low Ir-density. Neglecting the influence of the 1–2 nm thin coating layer on the TiO_2 mass, the 30 wt% Ir containing $\text{IrOOH}_x/\text{TiO}_2$ catalyst series exhibits a calculated Ir density as low as $0.046 - 0.083 \text{ g}_{\text{Ir}} \text{ cm}^{-3}$. According to Bernt *et al.*, these iridium density values would already allow for a reduction of the iridium loading on the anode at a scale sufficient for establishing large scale PEM electrolysis without limitations by the abundance of the scarce noble metal.^[5, 57]

The 45 wt% Ir containing P25 TiO_2 supported catalyst series with calculated Ir densities ranging between $0.095 - 0.17 \text{ g}_{\text{Ir}} \text{ cm}^{-3}$ are above the aforementioned target of $\approx 0.05 \text{ g}_{\text{Ir}} \text{ cm}^{-3}$ [5] (derived from a targeted Ir utilization of $0.01 \text{ g}_{\text{Ir}} \text{ kW}^{-1}$) but still represent a major advancement towards the reduction of the noble metal content when comparing to the experimentally determined Ir density (bulk powder density) of $\approx 1.5 \text{ g}_{\text{Ir}} \text{ cm}^{-3}$ [31] for the industrial $\text{IrO}_2/\text{TiO}_2$ reference catalyst with 75 wt% Ir loading.

A further important requirement for the use of the $\text{IrO}_x, \text{IrO}_2/\text{P25 TiO}_2$ as catalyst in electrolyzers is their stability under OER conditions. This aspect was initially investigated by means of chronopotentiometry measurements over 2 h that were conducted at a moderate current density of 10 mA cm^{-2} as depicted in Figure 5a for the 30 wt% Ir containing catalyst. Non-heated (black curve) as well as $350 \text{ }^\circ\text{C}$ oxidized $\text{IrOOH}_x/\text{TiO}_2$ catalyst (dark red curve) thereby show the characteristic potential evolution of metallic or hydrous IrO_x with a decrease in the potential over an activation period of about 30 min and a slight increase of the potential over the remaining measurement period. However, the curve of the $350 \text{ }^\circ\text{C}$ oxidized sample is shifted about 10 mV to higher potentials indicating a slightly decreased activity.

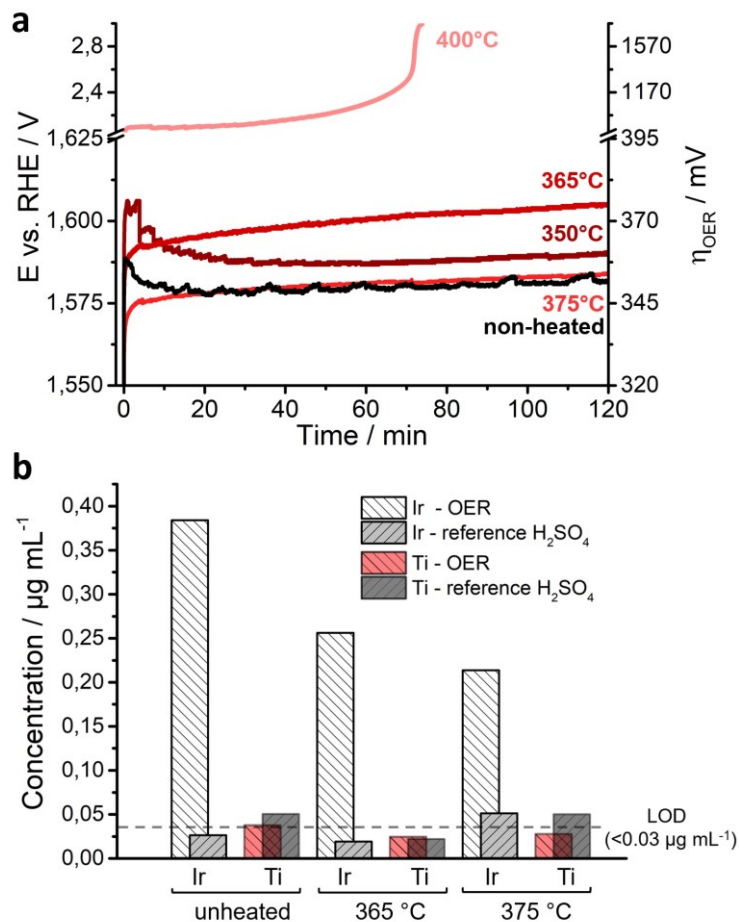


Figure 5 Stability and activity measurements by chronopotentiometry and detection of dissolved iridium by ICP-OES of 30 wt% Ir containing TiO_2 supported catalyst. Chronopotentiometry measurements (a) at $j = 10 \text{ mA cm}^{-2}$ over 120 min. ICP-OES measurements of dissolved Ir and Ti during 24 h of chronopotentiometry at $j = 10 \text{ mA cm}^{-2}$ (white and red bars; declining dash) or storage in the acidic electrolyte without applied potential (grey bars; rising dash) for non-heated, 365 °C and 375 °C oxidized catalyst.

Increasing the oxidation temperature to 365 °C leads to a dehydration of the IrOOH_x phase and formation of IrO_x particles, which already resemble the oxide in its potential course over time but with a reduced activity attributed to mass transfer limitations caused by dehydration as proposed by Geiger *et al.*^[59] As shown by RDE and cyclic voltammetry (Figure 4b,d and S11c), oxidation at 375 °C results in an optimum in catalytic activity reflected by a potential curve decreased by about 21 mV compared to the 365 °C sample and coinciding with the non-heated $\text{IrOOH}_x/\text{TiO}_2$ at a potential of 1.58 V vs. RHE after 2 h. The drastic reduction in conductivity and formation of rather isolated rutile IrO_2 crystals upon oxidation at 400 °C leads

to significantly decreased OER activity, reflected by a required potential of 2.1 V vs. RHE in the chronopotentiometry with a complete loss of activity after 75 min.

The higher-loaded 45 wt% Ir containing catalyst series exhibits a similar trend shown in Figure S14a, although the potential curve of the 350 °C oxidized IrOOH_x/TiO₂ already resembles that of an Ir oxide. Oxidation at 400 °C again leads to a significant reduction of the OER activity reflected by an initial potential of 1.72 V vs. RHE that constantly rises to over 2.8 V vs. RHE within the measurement period. The chronopotentiometry results are in accordance with the RDE and CV data and confirm the formation of a highly active amorphous oxidic iridium phase in the temperature range of 365 – 375 °C that exhibits a similar OER activity as the initial hydrous IrOOH_x and which is stable under OER conditions over the measurement period.

According to literature, oxidation (e.g., thermal annealing) of hydrous iridium oxide films (HIROF) is a known and well-investigated technique to enhance the corrosion stability under OER conditions, required for a stable operation as PEM anode catalyst.^[59-61]

To quantify the stability of the oxidized IrOOH_x/TiO₂ catalysts, inductively coupled plasma optical emission spectroscopy (ICP-OES) of dissolved iridium in the electrolyte was performed after 24 h of electrolysis (Figure 5b and Figure S14). The Ir concentration is shown to be inversely correlated to the oxidation temperature starting with 38 μg_{Ir} mL⁻¹ in 24 h for the non-heated 30 wt% Ir containing hydrous oxide and significantly declining to 26 μg_{Ir} mL⁻¹ for the 365 °C oxidized sample down to 21 μg_{Ir} mL⁻¹ for IrOOH_x oxidized at 375 °C.

These findings are at first sight in contrast to literature reports about the stability and activity of hydrous iridium oxide and a suggested compromise by tuning the crystallinity with the annealing temperature.^[7, 59] In general, thermal annealing was shown to decrease the activity with increasing temperature for several iridium based systems, which is explained by a change

in the oxide stoichiometry, a lower amount of accessible active sites and mass transfer limitations due to dehydration in the lower temperature regime. [27, 30, 55, 61, 79]

For our oxidized IrOOH_x/TiO₂ catalysts a reduction of the electrochemical surface area (ECSA) was indeed shown by cyclic voltammetry (Figure 4, S12), but it was also accompanied by a significant increase in the catalyst surface area (factor of about 2) as revealed by sorption analysis (Figures S7-9). These findings can be explained by the transition of a bulk to a surface redox active catalyst and do not necessarily imply a lower activity if the surface to bulk ratio of iridium active phase is high enough.^[80]

Based on the data presented in this work, we therefore conclude that for the thin intermediate IrO_x phase no trade-off exists between catalytic activity and stability with respect to the hydrous IrOOH_x, which further outlines the advantage of the proposed synthesis method in addition to the established positive effects of the increased conductivity and enhanced morphology.

7.3 Conclusion

In this work, the facile synthesis of a novel highly active and industrially applicable IrO₂ nanoparticle based P25 TiO₂ supported OER catalyst for PEM electrolysis is presented. Commercially available IrOOH_x / P25 TiO₂ OER catalyst with nominal homogeneous loadings of 30 and 45 wt% Ir were used a precursor phase. By employing oxidation in molten NaNO₃, the moderately conductive IrOOH_x phase (3 and 0.2 S cm⁻¹ for 30 and 45 wt% Ir containing catalyst, respectively) could be transformed to small intergrown IrO_x/IrO₂ nanoparticles on the non-conductive TiO₂. This way, the conductivity of the TiO₂-supported catalysts reached values as high as 11 and 40 S cm⁻¹ for the 30 and 45 wt% Ir containing catalyst, respectively, at the temperature optimum for oxidation of 375 °C. In-depth structural characterization shows that a higher oxidation temperature of 400 °C leads to further particle growth consuming surrounding IrOOH_x and IrO_x particles, which causes the formation of isolated or poorly interconnected rod-like IrO₂ particles of about 10 and up to 100 nm length for the 30 and 45 wt% Ir catalysts, respectively.

Electrochemical characterization revealed an Ir mass-based OER activity exceeding an industrial IrO₂/TiO₂ reference catalyst with 75 wt% Ir by a factor of 3 and 8 in the moderate and low overpotential regimes of 420 and 300 mV, respectively. The 30 wt% Ir containing IrOOH_x/P25 TiO₂ catalyst oxidized at 375 °C in molten NaNO₃ thereby delivers 62 A g_{Ir}⁻¹ at η_{OER} =300 mV and 572 A g_{Ir}⁻¹ at η_{OER} =380 mV, which is in the range of best performing IrO₂ nanoparticle OER catalysts with Nb-doped TiO₂ support.

Intermediate term chronopotentiometry measurements over 24 h and ICP-OES measurements of dissolved Ir in the electrolyte further confirm a significantly increased stability of the IrOOH_x/TiO₂ catalyst upon oxidation in molten salt at the temperature optimum of 375 °C.

Overall, our synthesis approach enables the fabrication of a novel supported OER catalyst with greatly reduced Ir-density of 0.046 – 0.083 g_{Ir} cm⁻³ (30 wt% Ir catalyst) through the

homogeneously coated P25 TiO₂ nanostructure and retained catalytic activity, which allows a significant reduction of the noble metal content in anodes of PEM electrolyzers and thereby enables their large scale application. Importantly, the general findings of our work are not limited to the P25 TiO₂ support, but rather demonstrate that the controlled crystallization of amorphous IrOOH_x to a crystalline but continuous IrO₂ layer enables the significant reduction in Ir loading by maintaining high catalytic activity and stability. Provided the required wetting can be ensured, our novel approach is universally applicable to any type of support, and it can be expected that even further reduction of the iridium density with enhanced OER activity could be achieved by the use of more advanced oxidic support morphologies such as microparticles with inverse opal structure recently demonstrated by our group, or highly conductive and corrosion-stable TiON phases obtained by Bele *et al.*^[31, 51]

7.4 Experimental

P25 TiO₂/IrOOH_x precursor phase

Two batches of commercially available IrOOH_x coated TiO₂ (Aeroxide®P25, EVONIK INDUSTRIES AG) catalyst were obtained from HERAEUS Deutschland GmbH & Co. KG with nominal Ir metal contents of ≈30 and 45 wt% Ir, respectively. The catalyst provided consists of a fine, non-agglomerated powder and used as received for further experiments.

Synthesis of P25 TiO₂ supported IrO_x and IrO₂ nanoparticles

The synthesis of IrO_x and IrO₂ nanoparticles supported by P25 TiO₂ from an amorphous IrOOH_x precursor phase is based on the well-known molten salt oxidation route in NaNO₃, initially introduced in 1923 by Adams and Shriner for the preparation of platinum oxide nanoparticles and described by Oakton *et al.* for the preparation of a TiO₂/IrO₂ OER catalyst from a mixture of molecular precursors.^[45, 81] The process was adapted to transform a thin amorphous IrOOH_x layer on the TiO₂ substrate to IrO_x nanoparticles.

30 or 45 wt% Ir TiO₂/IrOOH_x powder and NaNO₃ (VWR, ≥ 99.9%) were mixed in a mass ratio of 1:12 with an addition of 24 mass equivalents of deionized H₂O. In a typical reaction 500 mg of TiO₂/IrOOH_x catalyst were added to 6.0 g of NaNO₃ with the addition of 12 mL H₂O. The reaction mixture was stirred and sonicated 3 times for 20 min for a complete dissolution and intermixing of the precursors. In a following step the reaction mixture was dried in glass dishes by evaporation on a hot plate at 95 °C to obtain a greyish/white product that was transferred to a ceramic calcination tray and placed in a laboratory oven (NABERTHERM, model N15/65SHA). All reactions were first heated to 150 °C for 2 h (3 °C min⁻¹ heating ramp) in air to remove residual water in the reaction mixture. Depending on the targeted crystallinity of the IrO_x, the product was further heated to a temperature between 350 and 400 °C for 1 h (3 °C min⁻¹ heating ramp) in air. The resulting P25 TiO₂/IrO_x was encapsulated in the NaNO₃ melt after cool down and isolated by 4 consecutive washing steps with DI H₂O and

centrifugation. To obtain a fine powder, the product was finally freeze-dried using an ALPHA 1-4 machine (MARTIN CHRIST GEFRIERTROCKNUNGSANLAGEN GMBH).

Physico-chemical characterization

Wide angle X-ray diffraction (XRD) analysis was carried out in transmission mode using a STOE STADI P diffractometer with Cu $K_{\alpha 1}$ radiation ($\lambda = 1.54060 \text{ \AA}$) and a Ge(111) single crystal monochromator equipped with a DECTRIS solid state strip detector Mythen 1K. Powder XRD patterns of the samples were collected with an omega-2theta scan in the 2θ range from 5° to 90° with a step size of 1° and fixed integration time of 25 – 35 seconds per step and a resolution of 0.05° . The size of crystalline domains of IrO_2 , TiO_2 (anatase phase) and TiO_2 (rutile phase) nanoparticles were calculated with Scherrer's Equation from line broadening of the 101, 101 and 110 reflections, respectively. Reflection positions were compared to XRD reference patterns for the IrO_2 phase (ICDD card #00-015-0870, tetragonal symmetry, $a = b = 4.4983 \text{ \AA}$, $c = 3.1544 \text{ \AA}$, $\alpha = \beta = \gamma = 90^\circ$), TiO_2 (anatase) (ICDD card #00-004-0477, tetragonal symmetry, $a = b = 3.783 \text{ \AA}$, $c = 9.510 \text{ \AA}$, $\alpha = \beta = \gamma = 90^\circ$) and TiO_2 (rutile) (ICDD card #00-004-0551, tetragonal symmetry, $a = b = 4.594 \text{ \AA}$, $c = 2.958 \text{ \AA}$, $\alpha = \beta = \gamma = 90^\circ$).

Raman spectroscopy was carried out using a LabRAM HR UV-Vis (HORIBA JOBIN YVON) Raman Microscope (OLYMPUS BX41) with a SYMPHONY CCD detection system and a He-Ne laser ($\lambda = 633 \text{ nm}$). Spectra were recorded using a lens with a 10-fold magnification in the range from 100 cm^{-1} to 1000 cm^{-1} with filters of OD 0.3 - 0.6. Spectrum accumulation mode was used with integration times of 30 sec per spectrum and 600 cycles. The data acquisition was carried out with LabSpec software.

HRTEM, HAADF-STEM images were recorded using a FEI Titan Themis 80 – 300 microscope with aberration correction of the probe-forming lenses operated at 120 kV or 300 kV, respectively. Energy dispersive X-ray spectroscopy (EDX) was performed using a SuperX windowless, four quadrant Silicon drift detector with a solid angle of 0.7 sr. TEM

specimens were prepared from nanoparticles in a 1:1 (v/v) ratio of water to ethanol and deposited on a carbon-film coated copper grid and dried in air.

Scanning electron microscopy (SEM) images were recorded with a FEI Helios Nanolab G3 UC scanning electron microscope equipped with a field emission gun operated at 3 – 5 kV. Specimens were prepared from powders in a 1:1 (v/v) ratio of water to ethanol and deposited on FTO or Si substrates that were glued onto a stainless-steel sample holder with silver lacquer. EDX measurements were performed at an operating voltage of 20 kV with a X-Max^N Silicon Drift Detector with 80 mm² detector area (OXFORD INSTRUMENTS) and AZTec acquisition software (OXFORD INSTRUMENTS).

For the analysis of the porosity, samples were degassed for 12 h at 120 °C under vacuum. Nitrogen sorption measurements were performed on a QUANTACHROME Autosorb-1 instrument at the boiling point of liquid nitrogen (77 K). The specific surface area was determined with the Brunauer-Emmett-Teller (BET) method at $p/p_0 = 0.05-0.2$. The pore size distribution was calculated using a non-local DFT adsorption and equilibrium model for silica with cylindrical pores.

Conductivity measurements of P25 TiO₂ supported IrOOH_x and the IrO₂/TiO₂ reference catalyst (Elyst Ir75, UMICORE) were carried out on a HMS 3000 apparatus (ECOPIA) in the Van-der-Pauw geometry (5 mm separation of electrodes). Powder samples were measured as pellets that were compressed for 10 min at 150 kg cm⁻². Due to restrictions on sample volume conductivity measurements of TiO₂/IrO₂ (45 wt% Ir, 400 °C oxidation) were conducted on an in-house constructed dc-conductivity measurements cell on loosely compressed powders by recording $I-V$ curves between -5 to +5 V with an AUTOLAB 302N potentiostat/galvanostat (METROHM AUTOLAB B.V.).

Thermogravimetric analysis (TGA) and differential scanning calorimetry (DSC) of the samples was performed on a NETZSCH STA 440 C TG/DSC (heating rate of 10 K min^{-1} in a stream of synthetic air of about 25 mL min^{-1}).

Stability measurements of the IrOOH_x , IrO_x and IrO_2 coated TiO_2 electrodes with an absolute loading of $400 \mu\text{g}_{\text{catalyst}}$ were performed by analyzing electrolyte ($0.5 \text{ M H}_2\text{SO}_4$) aliquots (1.0 mL of 20.0 mL total volume) by inductively coupled plasma optical emission spectrometry after chronopotentiometry measurements over 24 h at a current density of 6.67 mA cm^{-2} (10 mA absolute). Reference samples were stored in electrolyte under the same conditions for 24 h without applying a potential. All samples were stored/washed in electrolyte (which was discarded) for 5 min prior to each measurement to detect only potential/current induced dissolution related to electrolysis and avoid detection of dissolved ions from initial contact with the acidic electrolyte.

Electrochemical characterization

All electrochemical measurements at room temperature were carried out in a 3-electrode setup with quartz cells filled with $20 \text{ mL } 0.5 \text{ M H}_2\text{SO}_4$ (SIGMA-ALDRICH, Titripur® volumetric standard) as electrolyte using an PGSTAT302N potentiostat/galvanostat (METROHM AUTOLAB B.V.) equipped with a FRA32 M impedance analyzer connected to a Hydroflex reversible hydrogen electrode (GASKATEL Gesellschaft für Gassysteme durch Katalyse und Elektrochemie mbH) or $\text{Hg/HgSO}_4/\text{K}_2\text{SO}_4(\text{sat.})$ (REF601, RADIOMETER ANALYTICAL-HACH COMPANY) for cyclic voltammetry and chronopotentiometry measurements, respectively.

The electrochemical activity of the catalysts on FTO substrates was measured by *iR*-drop corrected linear sweep voltammetry (LSV) in a potential window of $1.0 - 1.8 \text{ V}$ vs. RHE in 20 scan cycles with a scan rate of 20 mV s^{-1} . Impedance spectroscopy data at 0.5 V vs. RHE was recorded prior to each measurement to determine the corresponding electrolyte resistance

(95 %) from the high frequency region (R_s determined from semi-circle or linear fit). The iridium mass-based catalyst activity in $A\text{ gr}_{\text{Ir}}^{-1}$ was calculated from the coating volume (3 – 15 μl) of a dispersion of known concentration ($2\text{ mg}_{\text{catalyst}}\text{ ml}^{-1}$) to deposit $15\text{ }\mu\text{g}_{\text{Ir}}$ on each electrode on a masked area of 0.196 cm^2 . The coating volume for the 30 and 45 wt% Ir (nominal loading values) containing $\text{IrOOH}_x/\text{TiO}_2$ catalysts were calculated according to Ir content measured by SEM/EDX of 28 and 52 wt% respectively from the obtained batches. The difference of the local Ir loading to the stated nominal values obtained by elemental analysis can be explained by a certain inhomogeneity resulting from the industrial-type kilogram scale synthesis method of the catalyst. Current densities were determined from the mean value of capacity current corrected (mean current in potential region 1.0 – 1.23 V vs. RHE) anodic and cathodic scans of the respective LSV cycle.

Stability measurements of electrodes were performed with an $\text{Hg}/\text{HgSO}_4/\text{K}_2\text{SO}_4(\text{sat.})$ reference electrode. Potentials versus the reversible hydrogen electrode E_{RHE} were calculated by measuring the open circuit potential of the $\text{Hg}/\text{HgSO}_4/\text{K}_2\text{SO}_4(\text{sat.})$ reference electrode against a Hydroflex reversible hydrogen electrode (GASKATEL Gesellschaft für Gassysteme durch Katalyse und Elektrochemie mbH) before and after each chronopotentiometry measurement and by shifting the measured potential accordingly.

Rotating disk electrode (RDE) measurements were conducted with a MSR Electrode rotator with mirror finished polished 5 mm diameter glassy carbon disc insets (PINE RESEARCH INSTRUMENTATION) connected to an Autolab PGSTAT302N potentiostat/galvanostat equipped with a FRA32 M impedance analyzer (METROHM AUTOLAB B.V.) and a double-walled glass cell with Luggin-capillary for the reference electrode compartment. Electrolyte temperature of $60.0\pm 0.1\text{ }^\circ\text{C}$ was maintained by a KISS 104A circulation thermostat (PETER HUBER KÄLTEMASCHINENBAU AG) and monitored with an immersed K-element temperature sensor. The Nernst potential for water oxidation was kept constant by continuous

O₂ (AIR LIQUIDE, AlphaGaz® 2 N5 purity) purging of the electrolyte (0.5 M H₂SO₄, SIGMA-ALDRICH, Titripur® volumetric standard). Catalyst loadings of 50 μg_{Ir} cm⁻² (10 μg_{Ir} absolute) were drop-casted on cleaned glassy carbon discs and dried at 60 °C before applying 10 μL of a 1:100 dilution of a Nafion® perfluorinated resin solution (SIGMA-ALDRICH, 5 wt% in lower aliphatic alcohols and water (15 - 20% water) in a H₂O/*i*PrOH mixture (1:1 v/v). The electrolyte resistance was determined before and after each RDE measurement in the high frequency region of recorded impedance spectra at 0.5 V vs. RHE. Due to low current densities reached in the measurement protocol and repeatedly low electrolyte resistance values around 5 – 10 Ω, an *iR* drop correction of the recorded data was not performed. The applied measurement protocol consisted of 75 LSV cycles starting from 1.0 V vs. Hydroflex RHE (GASKATEL Gesellschaft für Gassysteme durch Katalyse und Elektrochemie mbH). The upper vertex potential was defined to be at a current density of $j = 1 \text{ mA cm}^{-2}$ ($i_{\text{abs}} = 0.2 \text{ mA}$, $A = 0.196 \text{ cm}^2$). Reported current densities were determined from the mean value of capacity current (mean value in potential region 1.0 – 1.23 V vs. RHE) corrected anodic and cathode scan for a given overpotential η_{OER} of the respective scan cycle.

Additional cyclic voltammetry measurements over the potential range of 0.05 – 1.52 V vs. RHE were performed during RDE measurements to identify redox features and compare the electrocatalytically active surface area of catalyst samples. Three cyclic voltammograms were therefore recorded prior to each RDE measurement (as described above), after 50 and after 75 RDE LSV cycles.

7.5 Supporting Information

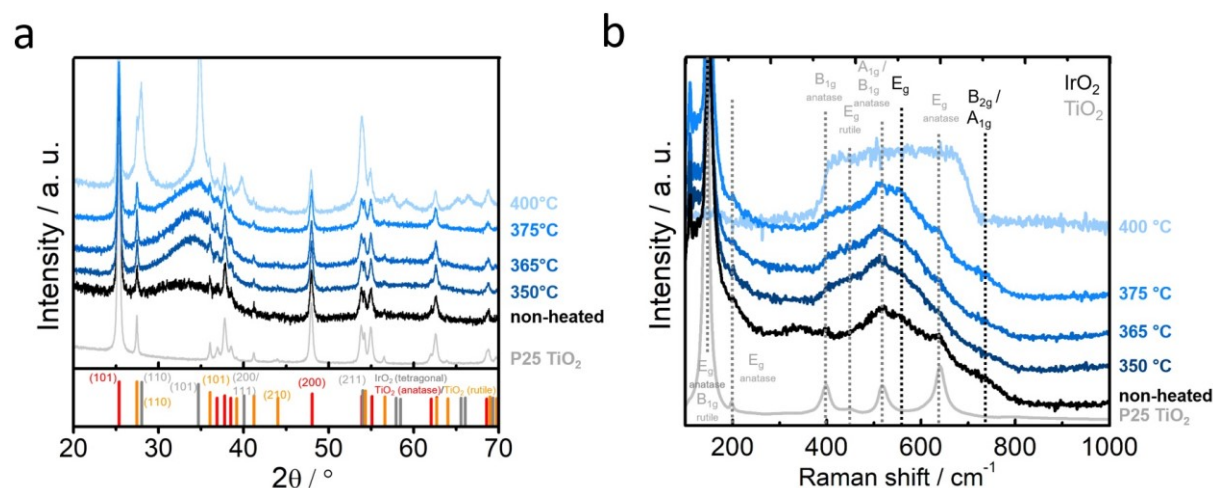


Figure S1 X-ray diffraction analysis (a) and Raman spectroscopy (b) of IrO_x and IrO_2 nanoparticles on P25 TiO_2 with 45 wt% Ir content. Variation in oxidation temperature of IrOOH_x coated P25 TiO_2 (black curve) from 350–400 °C (blue shaded curves) in NaNO_3 . Uncoated Aeroxide P25 TiO_2 included as reference (grey curve). TiO_2 (anatase) pattern: ICDD card number 00-004-0477 (red) (tetragonal symmetry, $a = b = 3.783$ Å, $c = 9.51$ Å, $\alpha = \beta = \gamma = 90^\circ$). TiO_2 (rutile) pattern: ICDD card number 00-004-0551 (orange) (tetragonal symmetry, $a = b = 4.594$ Å, $c = 2.958$ Å, $\alpha = \beta = \gamma = 90^\circ$). IrO_2 pattern: ICDD card number 00-015-0870 (grey) (tetragonal symmetry, $a = b = 4.4983$ Å, $c = 3.1544$ Å, $\alpha = \beta = \gamma = 90^\circ$). The Raman band at 561 cm^{-1} (E_g) and the close bands at 728 cm^{-1} (B_{2g}) and at 752 cm^{-1} (A_{1g}) correspond to the tetragonal iridium oxide phase.^[64-65] The Raman bands at 147 cm^{-1} (E_g), 198 cm^{-1} (E_g), 398 cm^{-1} (B_{1g}), 515 cm^{-1} (A_{1g} , B_{1g}) and 640 cm^{-1} (E_g) are attributed to TiO_2 anatase phase whereas bands at 144 cm^{-1} (B_{1g}) and 448 cm^{-1} (E_g) are assigned to TiO_2 rutile phase.^[63]

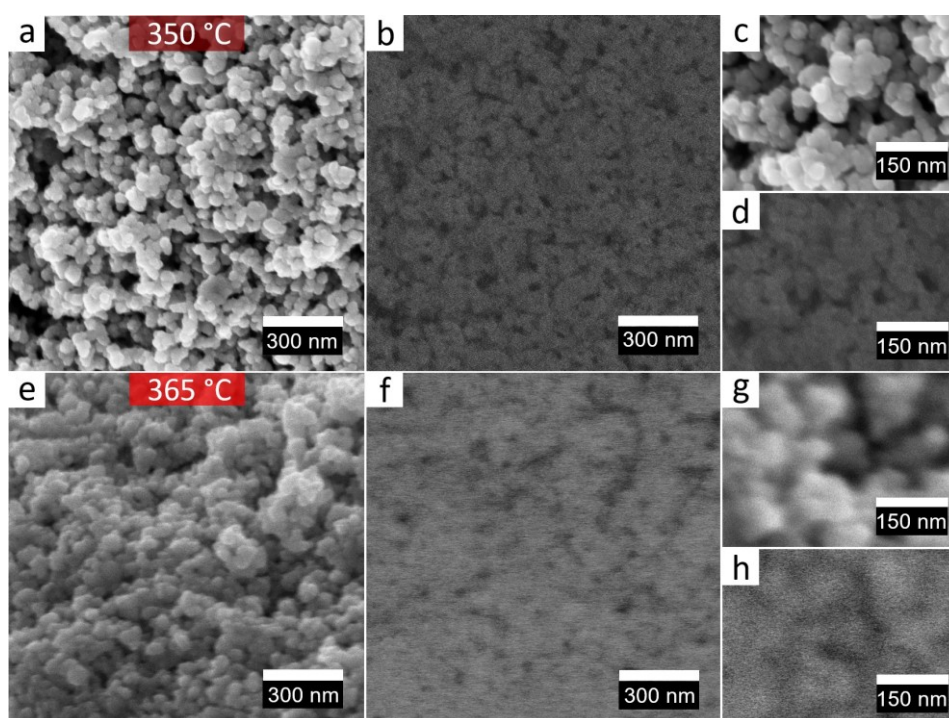


Figure S2 SEM images of IrO_x nanoparticles on P25 TiO_2 with 30 wt% Ir content. Applied oxidation temperature of IrOOH_x coated P25 TiO_2 of 350 °C (a-d) and 365 °C (e-h) in NaNO_3 .

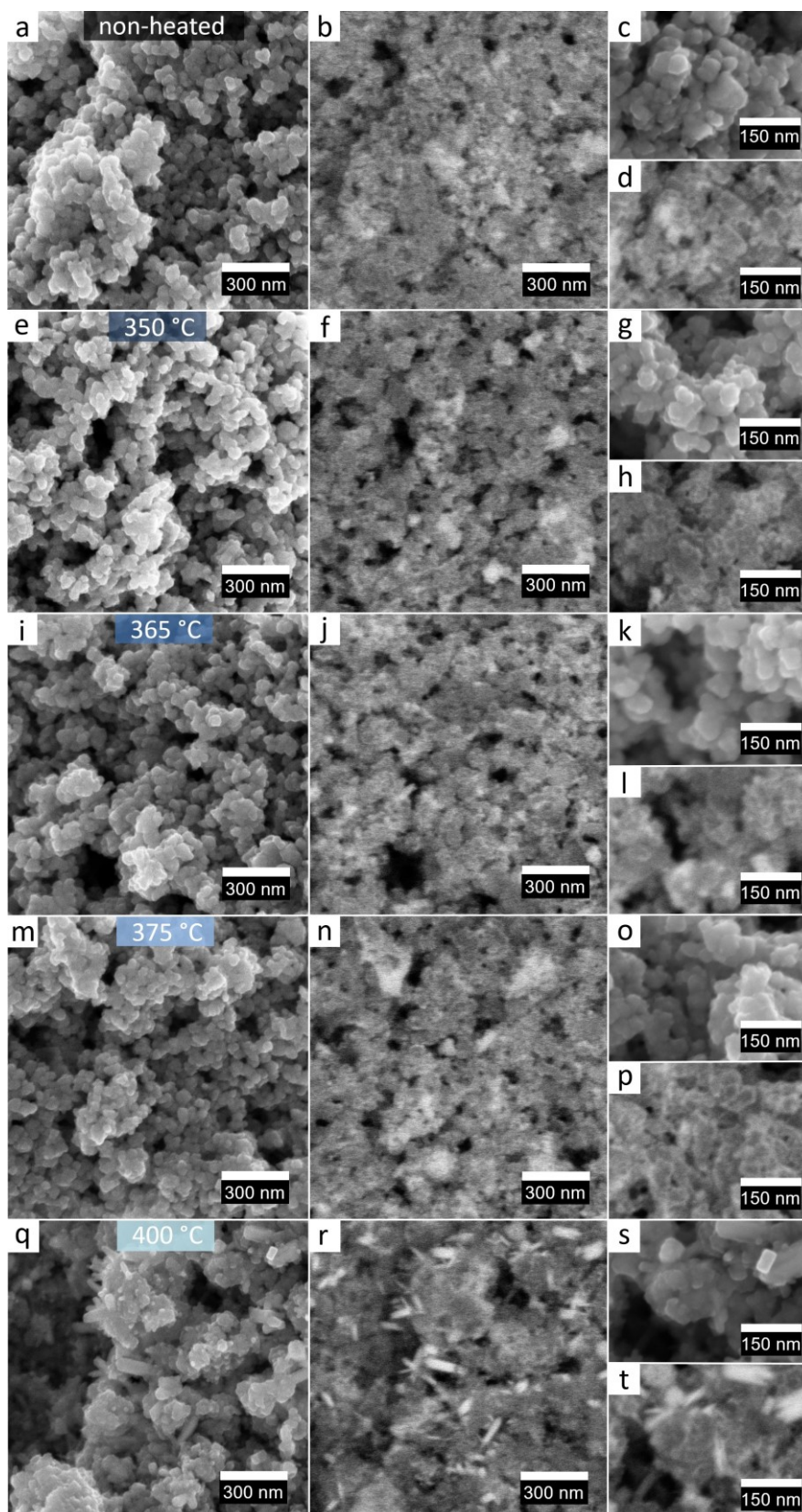


Figure S3 SEM images of IrO_x and IrO₂ nanoparticles on P25 TiO₂ with 45 wt% Ir content. Variation in oxidation temperature of IrOOH_x coated P25 TiO₂ from nonheated (a-d) over 350 °C (e-h), 365 °C (i-l), 375 °C (m-p) to 400 °C (q-t) in NaNO₃. All sample areas were imaged once by recording with a secondary electron detector (a,c,e,g,i,k,m,o,q,s) for morphological contrast and imaged further with a detector sensitive towards backscattered electrons for enhanced material contrast (b,d,f,h,j,l,n,p,r,t).

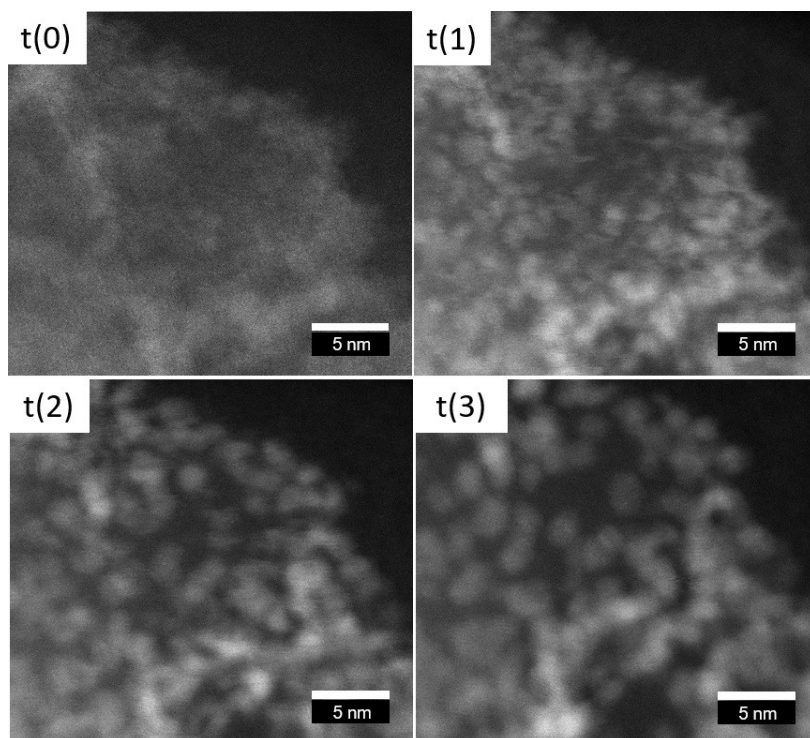


Figure S4 STEM image series (t(0)-(t(3))) of electron beam induced crystallization of the amorphous IrOOH_x layer on P25 TiO_2 (t(0)). t(0) indicating low dose image taken at time point 0 without preceding illumination of the sample area. t(1)-t(3) representing consecutive time points (~10 seconds interval) of image acquisition and accompanied sample illumination.

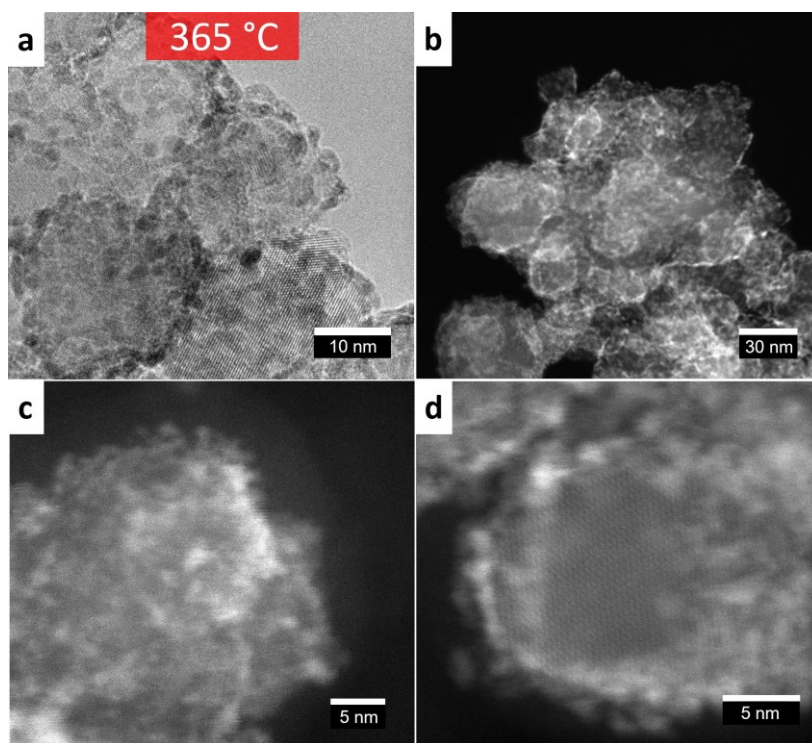


Figure S5 TEM (a) and STEM (b-d) images of IrO_x nanoparticles on P25 TiO_2 with 30 wt% Ir content. Oxidation temperature of IrOOH_x coated P25 TiO_2 was 365 °C (a-d) in NaNO_3 .

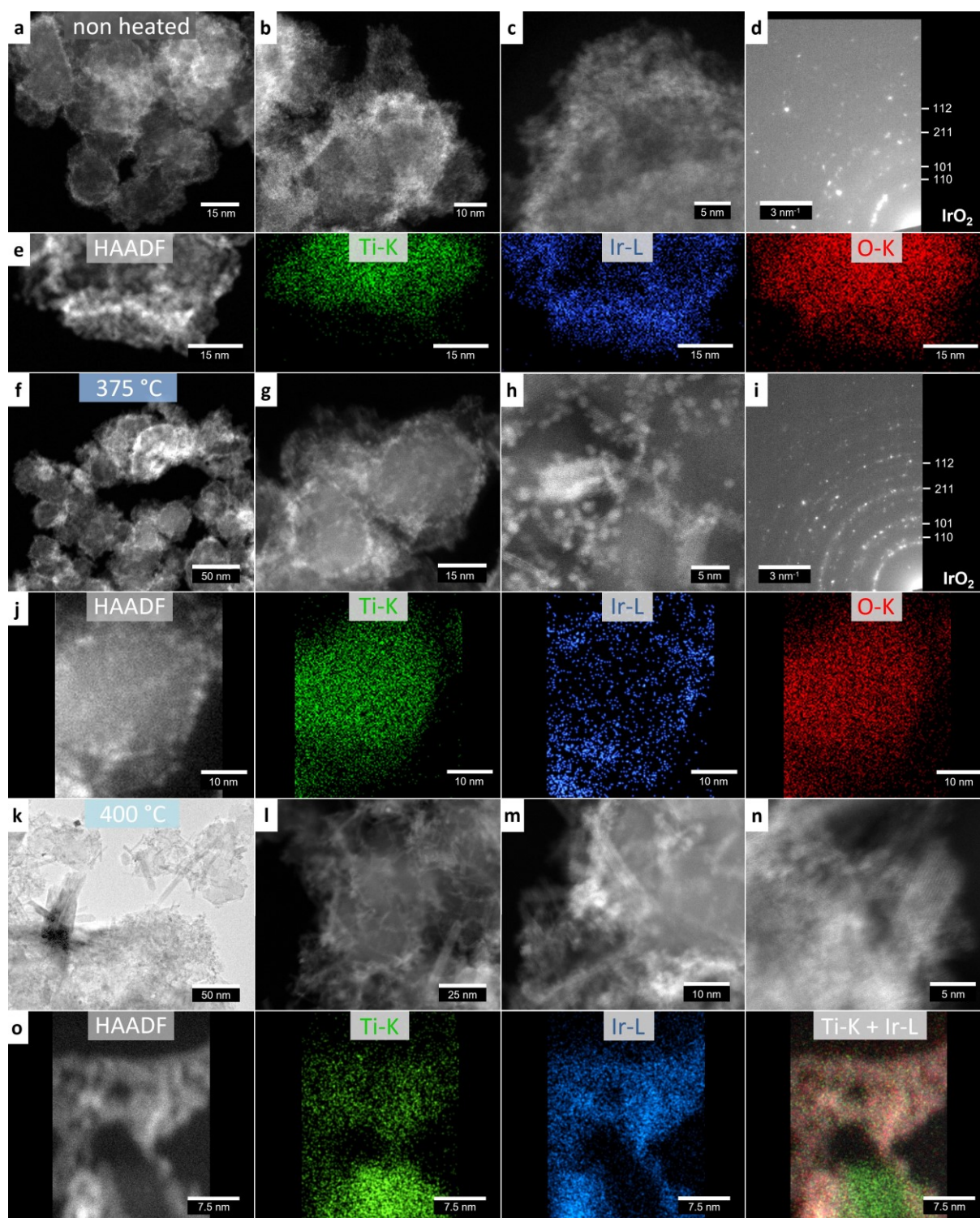


Figure S6 TEM images of IrOOH_x and IrO_2 nanoparticles on P25 TiO_2 with 45 wt% Ir content. Variation in oxidation temperature of IrOOH_x coated P25 TiO_2 from nonheated (a-e) over 375 °C (f-j) to 400 °C (k-o) in NaNO_3 . Phase identification and assignment of lattice planes in electron diffraction patterns (d,i) according to literature values. IrO_2 pattern: ICDD card number 00-015-0870 (grey) (tetragonal symmetry, $a = b = 4.4983 \text{ \AA}$, $c = 3.1544 \text{ \AA}$, $\alpha = \beta = \gamma = 90^\circ$). (e,j,o) STEM/EDX elemental mapping of iridium distribution on P25 TiO_2 nanocrystals after applying different oxidation temperatures.

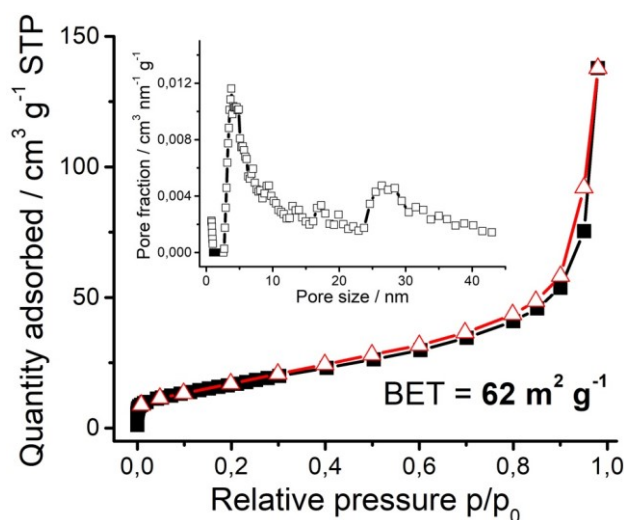


Figure S7 Nitrogen sorption isotherm of P25 TiO₂ (Aeroxide®P25, EVONIK INDUSTRIES) catalyst support with Brunauer-Emmett-Teller (BET) area and pore size distribution (non-local DFT model) as inset. BET surface area was in the range of product specification of 35-65 m² g⁻¹ (EVONIK INDUSTRIES, 2019) and literature report by Raj and Viswanathan of 56 m² g⁻¹.^[82]

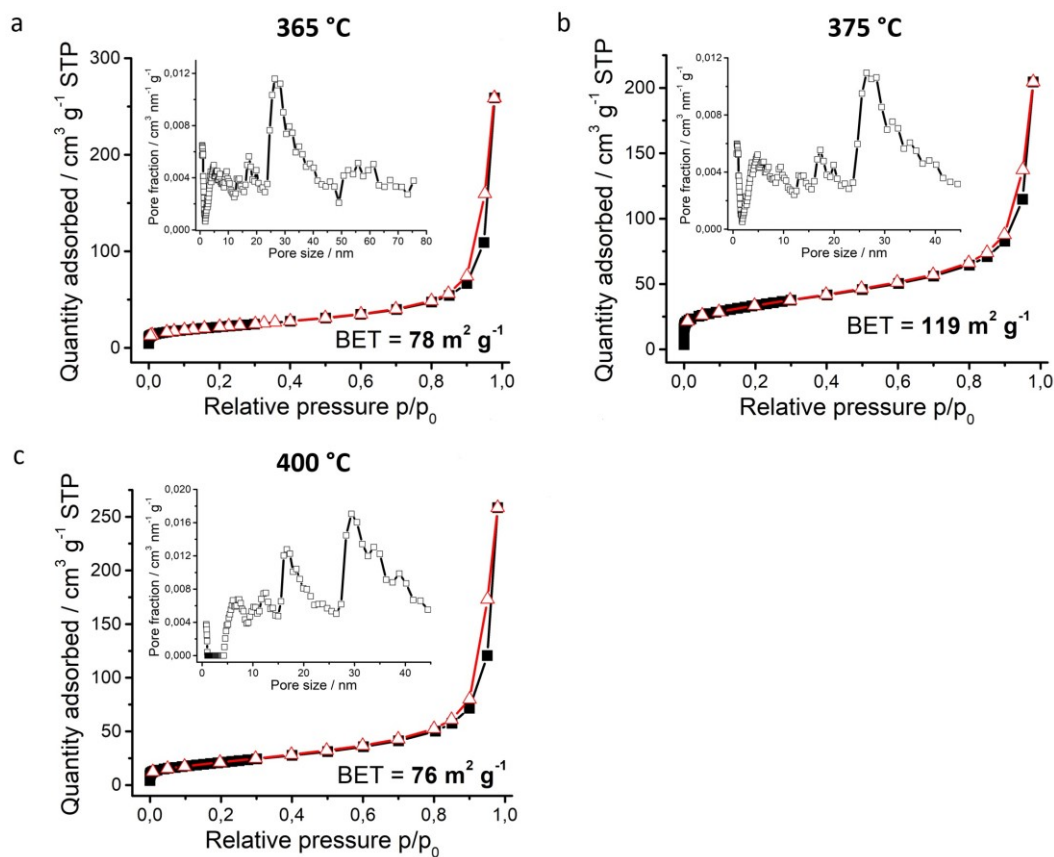


Figure S8 Nitrogen sorption isotherms of IrO_x and IrO₂ nanoparticles on P25 TiO₂ with 30 wt% Ir content. Variation in oxidation temperature (a: 365 °C, b: 375 °C, c: 400 °C) of IrOOH_x coated P25 TiO₂ catalyst with Brunauer-Emmett-Teller (BET) area and pore size distributions (non-local DFT model) as inset.

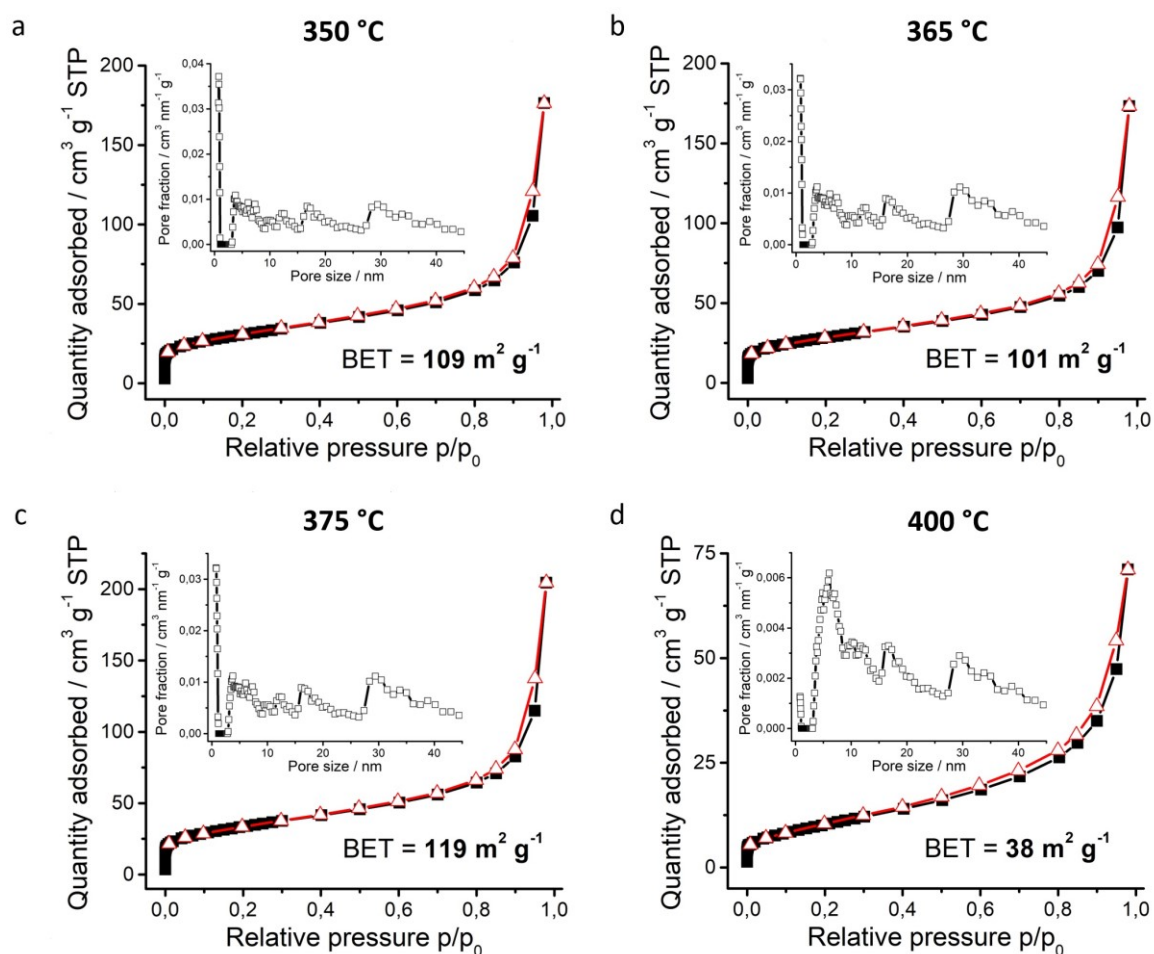


Figure S9 Nitrogen sorption isotherms of IrO_x and IrO₂ nanoparticles on P25 TiO₂ with 45 wt% Ir content. Variation in oxidation temperature (a: 350 °C, b: 365 °C, c: 375 °C, d: 400 °C) of IrOOH_x coated P25 TiO₂ catalyst with Brunauer-Emmett-Teller (BET) area and pore size distributions (non-local DFT model) as inset.

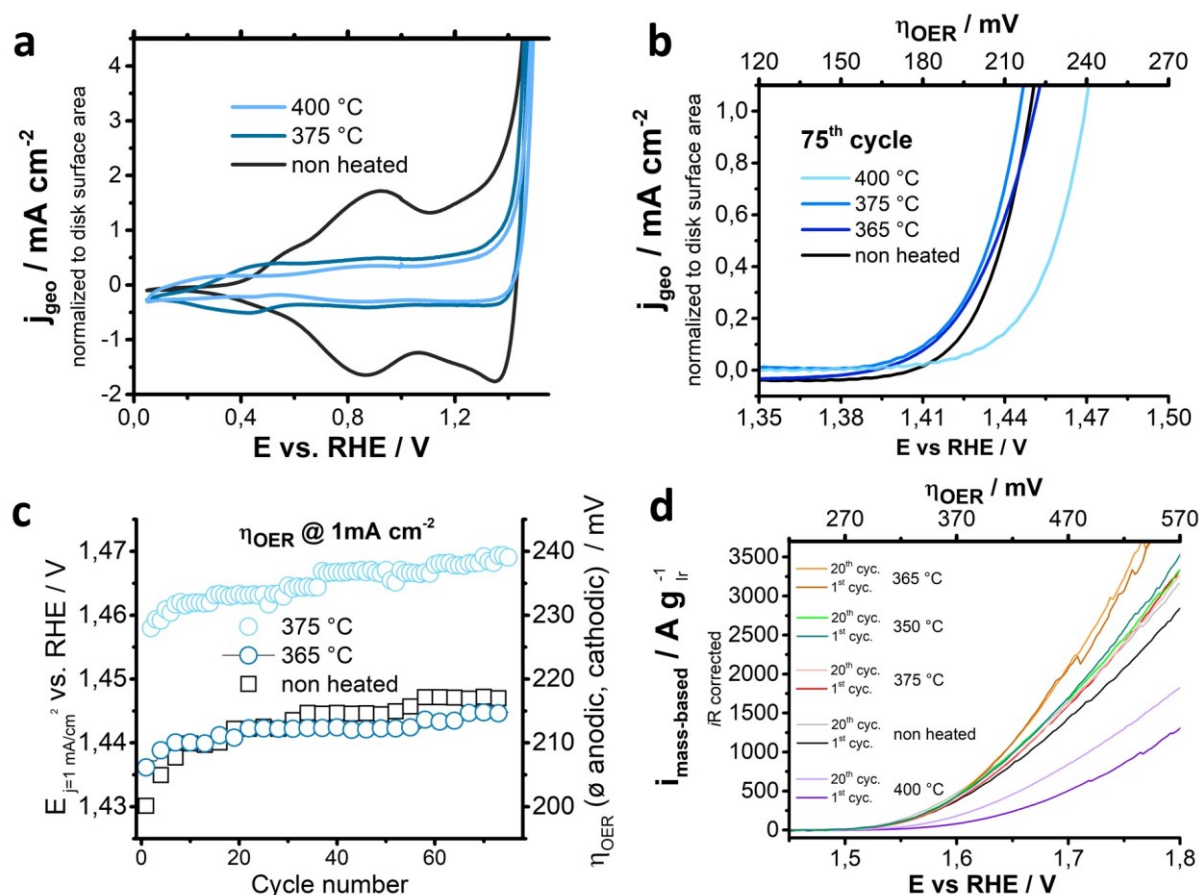


Figure S10 Electrochemical characterization of IrOOH_x and IrO_2 nanoparticles on P25 TiO_2 with 45 wt% Ir content. (a) Cyclic voltammograms between 0.05 - 1.50 V vs. reversible hydrogen reference electrode (RHE) of IrOOH_x coated TiO_2 before (black curve) and after oxidation at 375 °C (dark blue curve) and 400 °C (light blue curve) with a scan rate of 50 mV s^{-1} . (b) 75th scan cycle of rotating disc electrode measurements for differently oxidized (non-heated, 365 °C, 375 °C and 400 °C) $\text{IrOOH}_x/\text{TiO}_2$ catalysts. (c) Extracted overpotentials (η_{OER}) for each cycle required to reach a current density of 1 mA cm^{-2} . (d) Iridium mass based OER activities for $\text{IrOOH}_x/\text{TiO}_2$ based catalysts determined by cyclic voltammetry measurements of catalyst samples (15 μg_{Ir} abs.) on fluorine doped tin oxide substrates.

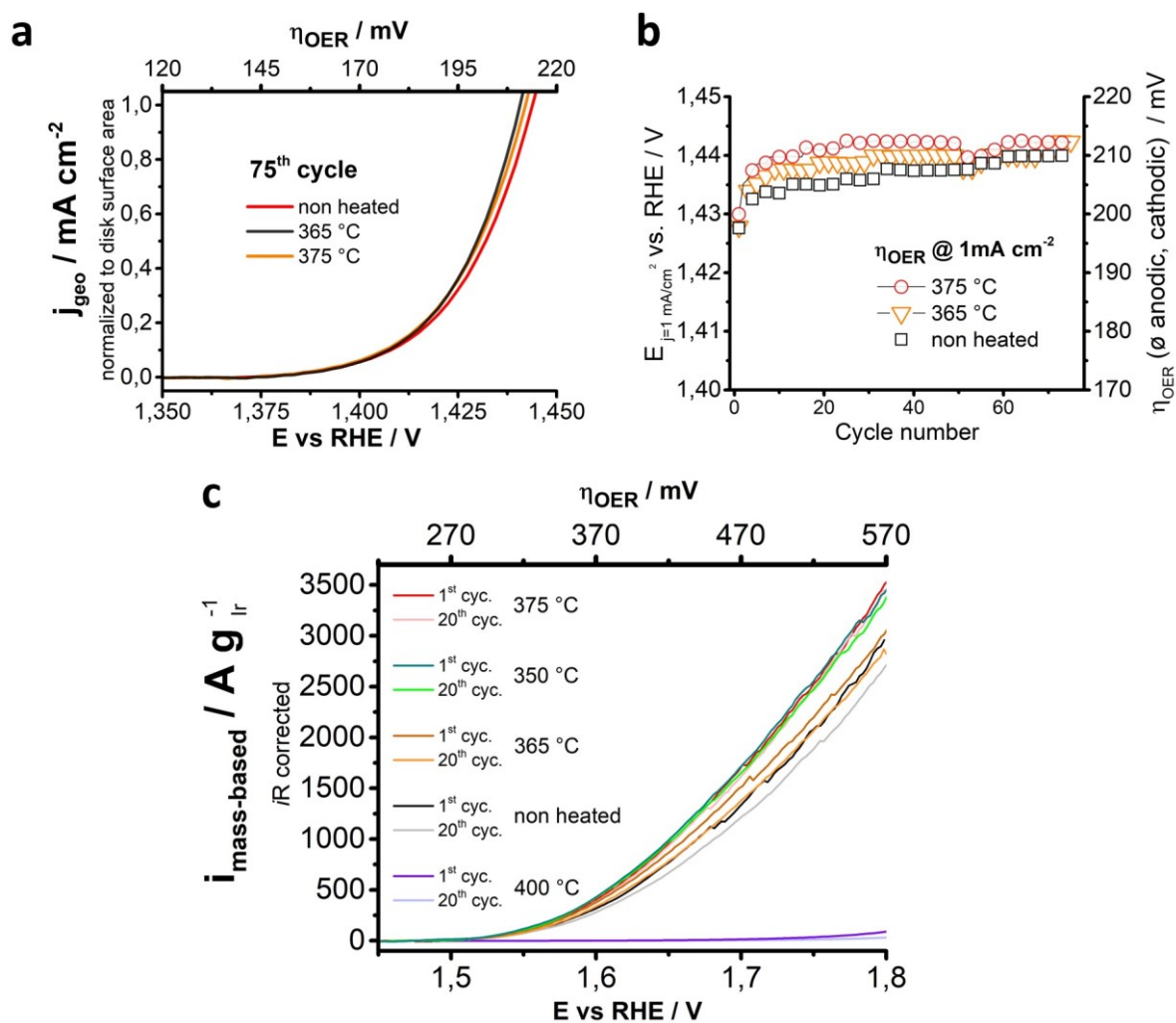


Figure S11 Electrochemical characterization of IrOOH_x and IrO_2 nanoparticles on P25 TiO_2 with 30 wt% Ir content. (a) 75th scan cycle of rotating disc electrode measurements for differently oxidized (non-heated, 365 °C and 375 °C) $\text{IrOOH}_x/\text{TiO}_2$ catalysts. (b) Extracted overpotentials (η_{OER}) for each cycle required to reach a current density of 1 mA cm^{-2} . (c) Iridium mass based OER activities for $\text{IrOOH}_x/\text{TiO}_2$ based catalysts determined by cyclic voltammetry measurements of catalyst samples ($15 \mu\text{g}_{\text{Ir}}$ abs.) on fluorine doped tin oxide substrates.

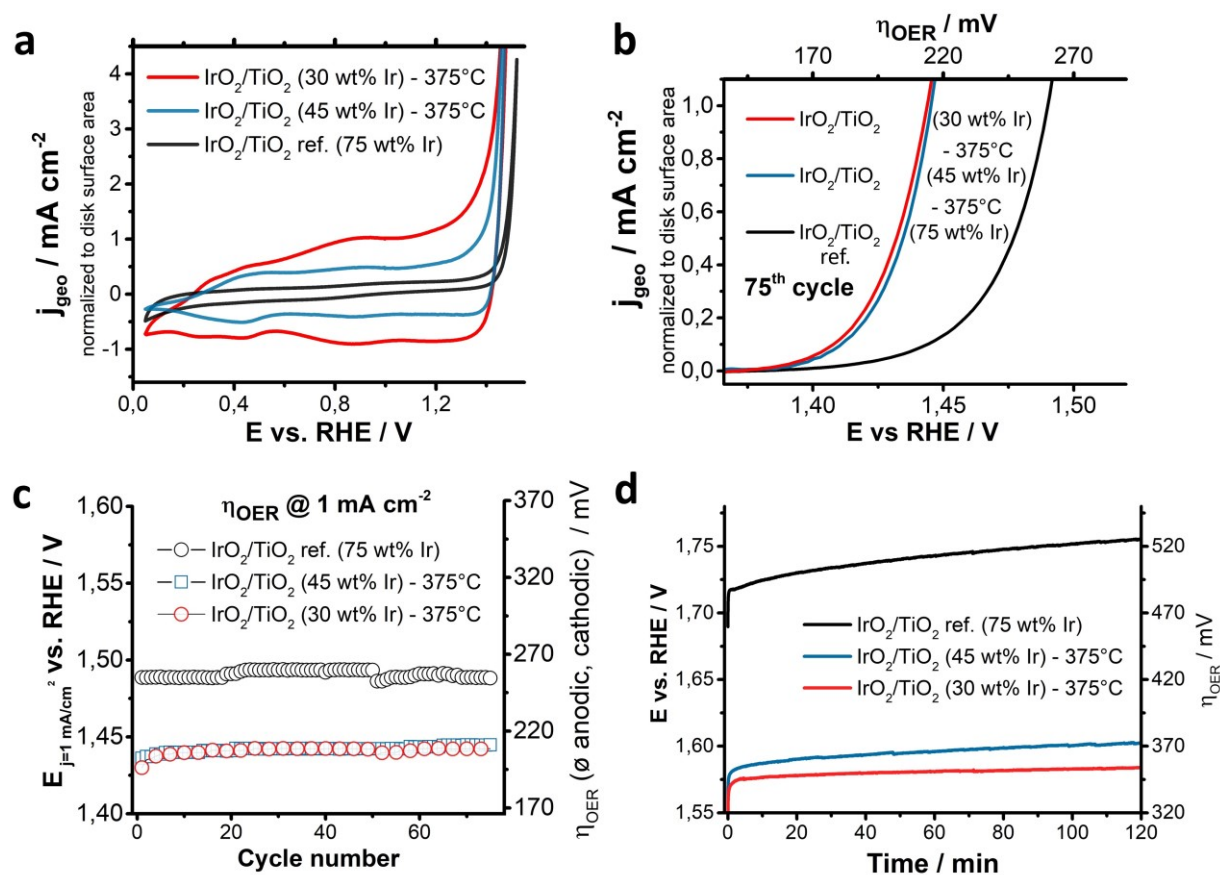


Figure S12 Electrochemical characterization $\text{IrOOH}_x/\text{TiO}_2$ catalysts oxidized at 375 °C with 30 and 45 wt% Ir content versus an $\text{IrO}_2/\text{TiO}_2$ reference catalyst with 75 wt% Ir loading. (a) Cyclic voltammograms between 0.05 - 1.50 V vs. reversible hydrogen reference electrode (RHE) of $\text{IrO}_2/\text{TiO}_2$ reference catalyst (black curve) and $\text{IrOOH}_x/\text{TiO}_2$ catalysts (30 and 45 wt% Ir) oxidized at 375 °C (red and blue curve, respectively) with a scan rate of 50 mV s^{-1} . (b) 75th scan cycle of rotating disc electrode measurements for reference catalyst and 375 °C oxidized $\text{IrOOH}_x/\text{TiO}_2$ catalysts. (c) Extracted overpotentials (η_{OER}) for each cycle required to reach a current density of 1 mA cm^{-2} . (d) Chronopotentiometry measurements at $j = 10 \text{ mA cm}^{-2}$ over 120 min.

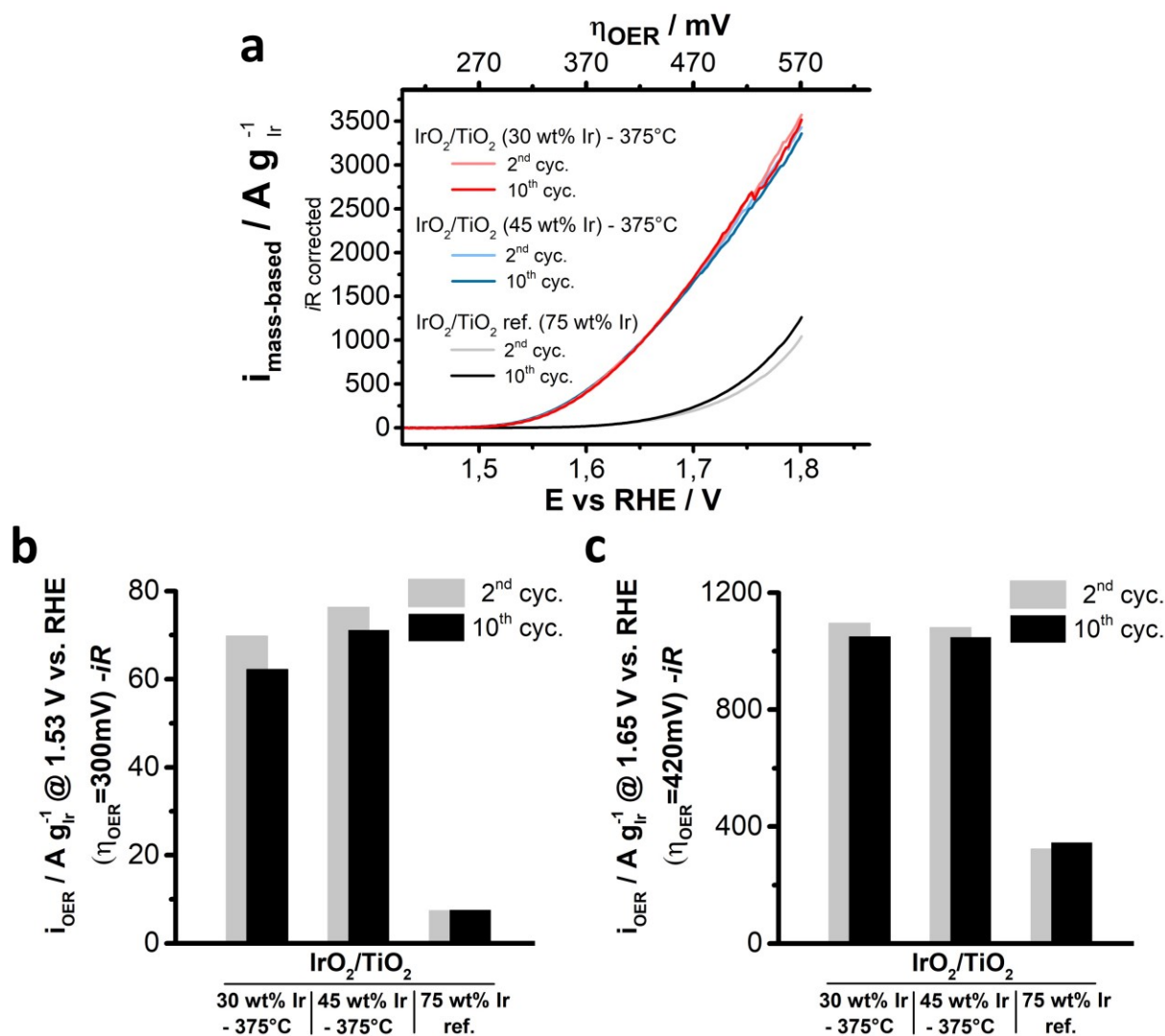


Figure S13 Comparison of OER activity of 375 °C oxidized $\text{IrOOH}_x/\text{TiO}_2$ with $\text{IrO}_2/\text{TiO}_2$ reference catalyst. (a) Cyclic voltammetry measurements (2nd and 10th scan cycle each) with respective Ir mass-based OER activities of $\text{IrO}_2/\text{TiO}_2$ reference catalyst and $\text{IrOOH}_x/\text{TiO}_2$ catalysts oxidized at 375 °C. Values determined by measurements of catalyst samples (15 μg_{Ir} abs.) on fluorine doped tin oxide substrates. Extracted Ir mass-based OER activities at an overpotential (η_{OER}) of (b) 300 mV and (c) 420 mV for the 2nd and 10th scan cycle.

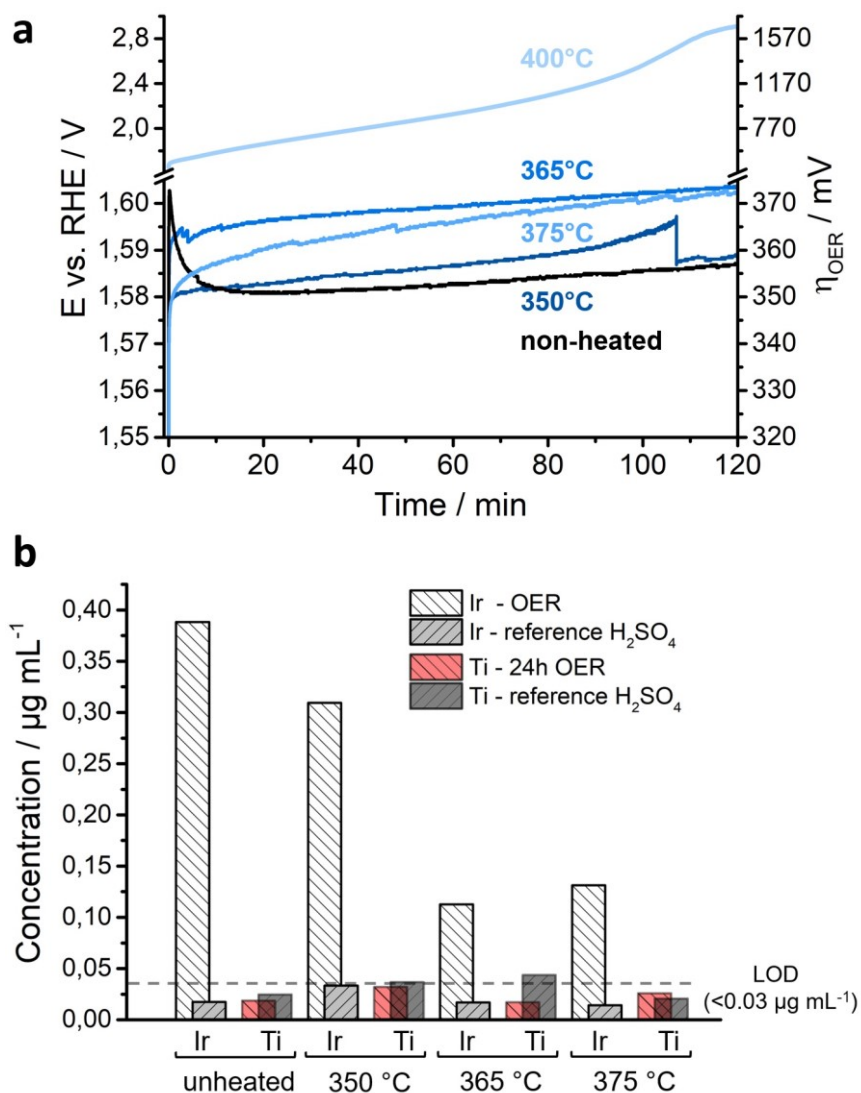


Figure S14 Stability and activity measurements by chronopotentiometry and detection of dissolved iridium by ICP-OES of 45 wt% Ir containing TiO_2 supported catalysts oxidized at different temperatures. Chronopotentiometry measurements (a) at $j = 10 \text{ mA cm}^{-2}$ over 120 min. (b) ICP-OES measurements of dissolved Ir and Ti during 24 h of chronopotentiometry at $j = 10 \text{ mA cm}^{-2}$ (white and red bars; declining dash) or storage in the acidic electrolyte without applied potential (grey bars; rising dash) for catalysts unheated and oxidized at 350 °C, 365 °C and 375 °C in NaNO_3 .

7.6 References

- [1] S. Oberthür, C. Roche Kelly, *Int. Spect.* **2008**, 43, 35.
- [2] S. Inage, *WIREs Energy Environ.* **2015**, 4, 115.
- [3] F. Barbir, *Sol. Energy* **2005**, 78, 661.
- [4] K. E. Ayers, C. Capuano, E. B. Anderson, *ECS Transactions* **2012**, 41, 15.
- [5] M. Bernt, A. Hartig-Weiß, M. F. Tovini, H. A. El-Sayed, C. Schramm, J. Schröter, C. Gebauer, H. A. Gasteiger, *Chem.-Ing.-Tech.* **2020**, 92, 31.
- [6] C. Hagelüken, in *Competition and Conflicts on Resource Use. Natural Resource Management and Policy*, Vol. 46 (Eds: S. Hartard, W. Liebert), Springer International Publishing, Cham **2015**, Ch. 8.
- [7] N. Danilovic, R. Subbaraman, K.-C. Chang, S. H. Chang, Y. J. Kang, J. Snyder, A. P. Paulikas, D. Strmcnik, Y.-T. Kim, D. Myers, V. R. Stamenkovic, N. M. Markovic, *J. Phys. Chem. Lett.* **2014**, 5, 2474.
- [8] S. Cherevko, S. Geiger, O. Kasian, A. Mingers, K. J. J. Mayrhofer, *J. Electroanal. Chem.* **2016**, 774, 102.
- [9] P.-Y. Liu, C.-C. Hsu, M.-C. Chuang, *J. Mater. Chem. A* **2017**, 5, 2959.
- [10] S. Xu, Y. Liu, J. Tong, W. Hu, Q. Xia, *Russ. J. Electrochem.* **2016**, 52, 1021.
- [11] H. N. Nong, L. Gan, E. Willinger, D. Teschner, P. Strasser, *Chem. Sci.* **2014**, 5, 2955.
- [12] R. G. González-Huerta, G. Ramos-Sánchez, P. B. Balbuena, *J. Power Sources* **2014**, 268, 69.
- [13] M. Tariq, W. Q. Zaman, W. Sun, Z. Zhou, Y. Wu, L.-m. Cao, J. Yang, *ACS Sustain. Chem. Eng.* **2018**, 6, 4854.
- [14] K. Sardar, S. C. Ball, J. D. B. Sharman, D. Thompsett, J. M. Fisher, R. A. P. Smith, P. K. Biswas, M. R. Lees, R. J. Kashtiban, J. Sloan, R. I. Walton, *Chem. Mater.* **2012**, 24, 4192.
- [15] A. Zlotorowicz, F. Seland, S. Sunde, *ECS Transactions* **2013**, 50, 71.
- [16] J. L. Corona-Guinto, L. Cardoño-García, D. C. Martínez-Casillas, J. M. Sandoval-Pineda, P. Tamayo-Meza, R. Silva-Casarin, R. G. González-Huerta, *Int. J. Hydrogen Energ.* **2013**, 38, 12667.
- [17] K. Kadakia, M. K. Datta, O. I. Velikokhatnyi, P. H. Jampani, P. N. Kumta, *Int. J. Hydrogen Energ.* **2014**, 39, 664.

- [18] K. S. Kadakia, P. H. Jampani, O. I. Velikokhatnyi, M. K. Datta, P. Patel, S. J. Chung, S. K. Park, J. A. Poston, A. Manivannan, P. N. Kumta, *Mater. Sci. Eng. B* **2016**, 212, 101.
- [19] S. M. Alia, S. Shulda, C. Ngo, S. Pylypenko, B. S. Pivovarov, *ACS Catal.* **2018**, 8, 2111.
- [20] G. Li, H. Yu, D. Yang, J. Chi, X. Wang, S. Sun, Z. Shao, B. Yi, *J. Power Sources* **2016**, 325, 15.
- [21] H.-S. Oh, H. N. Nong, T. Reier, M. Gliech, P. Strasser, *Chem. Sci.* **2015**, 6, 3321.
- [22] S. Kim, M. Cho, Y. Lee, *J. Electrochem. Soc.* **2017**, 164, B3029.
- [23] D. Takimoto, K. Fukuda, S. Miyasaka, T. Ishida, Y. Ayato, D. Mochizuki, W. Shimizu, W. Sugimoto, *Electrocatalysis* **2017**, 8, 144.
- [24] C. Zhao, E. Yifeng, F. Louzhen, *Microchim. Acta* **2012**, 178, 107.
- [25] C. Wang, Y. Sui, G. Xiao, X. Yang, Y. Wei, G. Zou, B. Zou, *J. Mater. Chem. A* **2015**, 3, 19669.
- [26] E. Slavcheva, I. Radev, S. Bliznakov, G. Topalov, P. Andreev, E. Budevski, *Electrochim. Acta* **2007**, 52, 3889.
- [27] M. Bernicke, E. Ortel, T. Reier, A. Bergmann, J. Ferreira de Araujo, P. Strasser, R. Kraehnert, *ChemSusChem* **2015**, 8, 1908.
- [28] E. Ortel, T. Reier, P. Strasser, R. Kraehnert, *Chem. Mater.* **2011**, 23, 3201.
- [29] G. Li, H. Yu, X. Wang, D. Yang, Y. Li, Z. Shao, B. Yi, *J. Power Sources* **2014**, 249, 175.
- [30] S. Siracusano, N. Van Dijk, E. Payne-Johnson, V. Baglio, A. S. Aricò, *Appl. Catal. B-Environ.* **2015**, 164, 488.
- [31] D. Böhm, M. Beetz, M. Schuster, K. Peters, A. G. Hufnagel, M. Döblinger, B. Böller, T. Bein, D. Fattakhova-Rohlfing, *Adv. Funct. Mater.* **2020**, 30, 1906670.
- [32] K. E. Ayers, J. N. Renner, N. Danilovic, J. X. Wang, Y. Zhang, R. Maric, H. Yu, *Catal. Today* **2016**, 262, 121.
- [33] H. N. Nong, H. S. Oh, T. Reier, E. Willinger, M. G. Willinger, V. Petkov, D. Teschner, P. Strasser, *Angew. Chem. Int. Edit.* **2015**, 127, 3018.
- [34] V. K. Puthiyapura, M. Mamlouk, S. Pasupathi, B. G. Pollet, K. Scott, *J. Power Sources* **2014**, 269, 451.
- [35] H.-S. Oh, H. N. Nong, P. Strasser, *Adv. Funct. Mater.* **2015**, 25, 1074.
- [36] V. K. Puthiyapura, S. Pasupathi, H. Su, X. Liu, B. Pollet, K. Scott, *Int. J. Hydrogen Energ.* **2014**, 39, 1905.

- [37] M. Yagi, E. Tomita, S. Sakita, T. Kuwabara, K. Nagai, , *J. Phys. Chem. B* **2005**, 109, 21489.
- [38] F. Karimi, B. A. Peppley, *Electrochim. Acta* **2017**, 246, 654.
- [39] J. Polonský, P. Mazúr, M. Paidar, E. Christensen, K. Bouzek, *Int. J. Hydrogen Energ.* **2014**, 39, 3072.
- [40] S. Geiger, O. Kasian, A. M. Mingers, K. J. J. Mayrhofer, S. Cherevko, *Sci. Rep.* **2017**, 7, 4595.
- [41] S. Trasatti, *Electrochim. Acta* **2000**, 45, 2377.
- [42] T. Reier, I. Weidinger, P. Hildebrandt, R. Kraehnert, P. Strasser, *ECS Transactions* **2013**, 58, 39.
- [43] T. Reier, D. Teschner, T. Lunkenbein, A. Bergmann, S. Selve, R. Kraehnert, R. Schlögl, P. Strasser, *J. Electrochem. Soc.* **2014**, 161, F876.
- [44] P. Mazúr, J. Polonský, M. Paidar, K. Bouzek, *Int. J. Hydrogen Energ.* **2012**, 37, 12081.
- [45] E. Oakton, D. Lebedev, M. Povia, D. F. Abbott, E. Fabbri, A. Fedorov, M. Nachtegaal, C. Copéret, T. J. Schmidt, *ACS Catal.* **2017**, 7, 2346.
- [46] H. Yoo, K. Oh, Y. R. Lee, K. H. Row, G. Lee, J. Choi, *Int. J. Hydrogen Energ.* **2017**, 42, 6657.
- [47] C. Hao, H. Lv, Q. Zhao, B. Li, C. Zhang, C. Mi, Y. Song, J. Ma, *Int. J. Hydrogen Energ.* **2017**, 42, 9384.
- [48] A. G. Hufnagel, S. Häringer, M. Beetz, B. Böller, D. Fattakhova-Rohlfing, T. Bein, *Nanoscale* **2019**, 11, 14285.
- [49] W. Hu, S. Chen, Q. Xia, *Int. J. Hydrogen Energ.* **2014**, 39, 6967.
- [50] H. Xu, NREL project #PD103 **2015**.
- [51] M. Bele, K. Stojanovski, P. Jovanovič, L. Moriau, G. Koderman Podboršek, J. Moškon, P. Umek, M. Sluban, G. Dražič, N. Hodnik, M. Gaberšček, *ChemCatChem* **2019**, 11, 5038.
- [52] Z.-X. Lu, Y. Shi, C.-F. Yan, C.-Q. Guo, Z.-D. Wang, *Int. J. Hydrogen Energ.* **2017**, 42, 3572.
- [53] S. Siracusano, V. Baglio, C. D'Urso, V. Antonucci, A. S. Aricò, *Electrochim. Acta* **2009**, 54, 6292.
- [54] D. Bernsmeier, M. Bernicke, R. Schmack, R. Sachse, B. Paul, A. Bergmann, P. Strasser, E. Ortel, R. Kraehnert, *ChemSusChem* **2018**, 11, 2367.

- [55] M. Bernicke, D. Bernsmeier, B. Paul, R. Schmack, A. Bergmann, P. Strasser, E. Ortel, R. Kraehnert, *J. Catal.* **2019**, 376, 209.
- [56] E. Oakton, D. Lebedev, A. Fedorov, F. Krumeich, J. Tillier, O. Sereda, T. J. Schmidt, C. Copéret, *New J. Chem.* **2016**, 40, 1834.
- [57] M. Bernt, H. A. Gasteiger, *J. Electrochem. Soc.* **2016**, 163, F3179.
- [58] Lopez, M.; Schleuning, A.; Biberbach, P. (Umicore AG) U.S. 7,976,989B2, **2004**.
- [59] S. Geiger, O. Kasian, B. R. Shrestha, A. M. Mingers, K. J. J. Mayrhofer, S. Cherevko, *J. Electrochem. Soc.* **2016**, 163, F3132.
- [60] M. Vuković, *J. Appl. Electrochem.* **1990**, 20, 969.
- [61] M. Vuković, *J. Appl. Electrochem.* **1987**, 17, 737.
- [62] J. C. Cruz, V. Baglio, S. Siracusano, R. Ornelas, L. Ortiz-Frade, L. G. Arriaga, V. Antonucci, A. S. Aricò, *J. Nanopart. Res.* **2011**, 13, 1639.
- [63] U. Balachandran, N. G. Eror, *J. Solid State Chem.* **1982**, 42, 276.
- [64] A. V. Korotcov, Y. S. Huang, K. K. Tiong, D. S. Tsai, *J. Raman Spectrosc.* **2007**, 38, 737.
- [65] Y. S. Huang, S. S. Lin, C. R. Huang, M. C. Lee, T. E. Dann, F. Z. Chien, *Solid State Commun.* **1989**, 70, 517.
- [66] M. Povia, D. F. Abbott, J. Herranz, A. Heinritz, D. Lebedev, B.-J. Kim, E. Fabbri, A. Patru, J. Kohlbrecher, R. Schäublin, M. Nachttegaal, C. Copéret, T. J. Schmidt, *Energy Environ. Sci.* **2019**, 12, 3038.
- [67] D. F. Abbott, D. Lebedev, K. Waltar, M. Povia, M. Nachttegaal, E. Fabbri, C. Copéret, T. J. Schmidt, *Chem. Mater.* **2016**, 28, 6591.
- [68] C. Felix, B. J. Bladergroen, V. Linkov, B. G. Pollet, S. Pasupathi, *Catalysts* **2019**, 9, 318.
- [69] A. L. Patterson, *Phys. Rev.* **1939**, 56, 978.
- [70] P. Gimenez, S. Fereres, *Enrgy. Proced.* **2015**, 69, 654.
- [71] H. Yoshio, U. Taizo, A. Osami, *B. Chem. Soc. Jpn.* **1981**, 54, 1385.
- [72] M. R. Guire, M. Z. Hu, Y. Gogotsi, S. W. Lu, *Ceramic Nanomaterials and Nanotechnology II: Proceedings of the symposium held at the 105th Annual Meeting of The American Ceramic Society, April 27-30, in Nashville, Tennessee, Ceram. Trans.*, Wiley, **2004**.
- [73] K.-F. Chow, T. M. Carducci, R. W. Murray, *J. Am. Chem. Soc.* **2014**, 136, 3385.
- [74] H. Ohno, S. Nohara, K. Kakinuma, M. Uchida, H. Uchida, *Catalysts* **2019**, 9, 74.

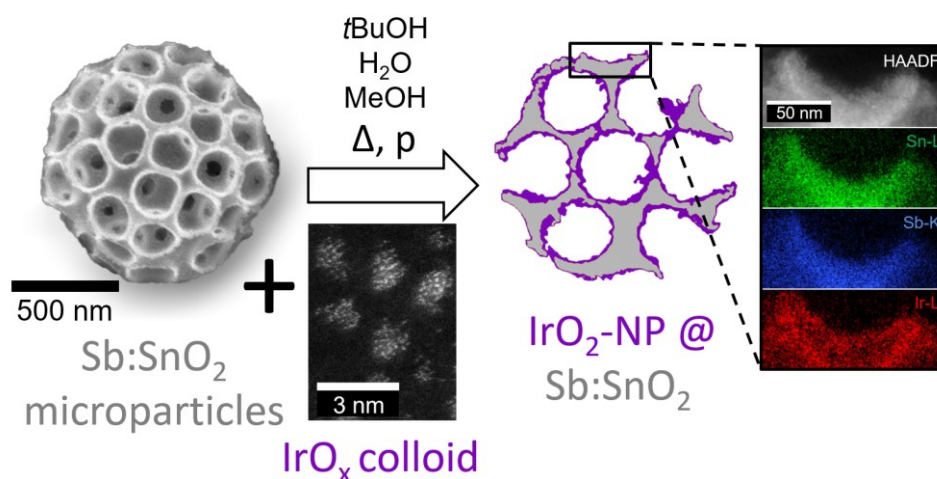
-
- [75] J. Lim, D. Park, S. S. Jeon, C. W. Roh, J. Choi, D. Yoon, M. Park, H. Jung, H. Lee, *Adv. Funct. Mater.* **2018**, 28, 1704796.
- [76] L. Ouattara, S. Fierro, O. Frey, M. Koudelka, C. Comninellis, *J. Appl. Electrochem.* **2009**, 39, 1361.
- [77] J. Juodkazytė, B. Šebeka, I. Valsiunas, K. Juodkazis, *Electroanal.* **2005**, 17, 947.
- [78] F. Godínez-Salomón, L. Albiter, S. M. Alia, B. S. Pivovar, L. E. Camacho-Forero, P. B. Balbuena, R. Mendoza-Cruz, M. J. Arellano-Jimenez, C. P. Rhodes, *ACS Catal.* **2018**, 8, 10498.
- [79] W. Xu, G. M. Haarberg, S. Sunde, F. Seland, A. P. Ratvik, E. Zimmerman, T. Shimamune, J. Gustavsson, T. Åkre, *J. Electrochem. Soc.* **2017**, 164, F895.
- [80] A. Minguzzi, O. Lugaresi, E. Achilli, C. Locatelli, A. Vertova, P. Ghigna, S. Rondinini, *Chem. Sci.* **2014**, 5, 3591.
- [81] R. Adams, R. L. Shriner, *J. Am. Chem. Soc.* **1923**, 45, 2171.
- [82] K. Raj, B. Viswanathan, *Indian J. Chem. A* **2009**, 48, 1378.

8. Efficient OER Catalyst with Low Ir Volume Density Obtained by Homogeneous Deposition of Iridium Oxide Nanoparticles on Macroporous Antimony-Doped Tin Oxide Support

This chapter is based on the following publication:

Böhm, D., Beetz M., Schuster M., Peters K., Hufnagel A. G., Döblinger M., Böller B., Bein T., and Fattakhova-Rohlfing, D., *Adv. Funct. Mater.* **2019**, 1906670

A cover image (*Adv. Funct. Mater.*, Vol. 30, No.1/2020) associated with this publication can be found in the following section 8.1.

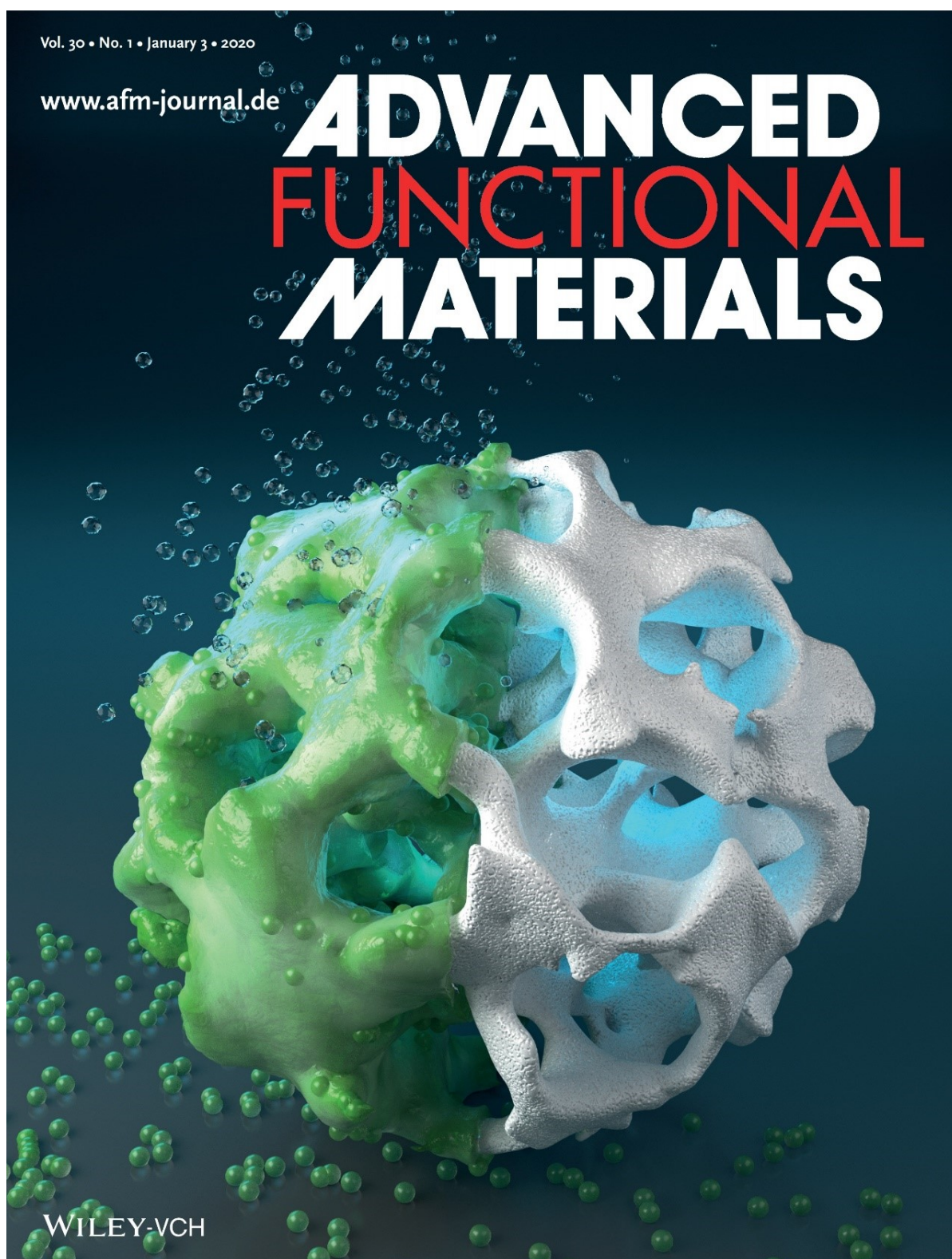


ToC image illustrates the solvothermal loading of an open porous antimony doped tin oxide microparticle employed as catalyst support with a thin layer of catalytic highly active IrO₂ nanoparticles in the range of 2 nm. The scheme shows the independent control of the microparticle porosity, doping level as well as of the IrO_x precursor-to-support ratio which allows for the synthesis of optimized supported OER catalyst with high catalytic activity for the oxygen evolution reaction.

Reprinted with permission from: Böhm, D., Beetz M., Schuster M., Peters K., Hufnagel A. G., Döblinger M., Böller B., Bein T., and Fattakhova-Rohlfing, D., *Adv. Funct. Mater.* 2019, 1906670.

8.1 Cover image

Artwork created by Hohmann C. (e-conversion cluster of excellence) (2019)



Reprinted with permission from: Böhm, D., Beetz M., Schuster M., Peters K., Hufnagel A. G., Döblinger M., Böller B., Bein T., and Fattakhova-Rohlfing, D., *Adv. Funct. Mater.* **2019**, 1906670. © 2020 WILEY-VCH Verlag GmbH & Co. KGaA, Weinheim.

8.2 Introduction

Generation of hydrogen via the electrolysis of water is considered one of important pillars of a future sustainable economy. In this way, the renewably generated electricity is converted into hydrogen that can be stored and used when required, either in a fuel cell or to replace petrochemically produced hydrogen as a process feedstock.^[1-2]

Relatively recent but already advanced proton exchange membrane (PEM) electrolysis technology enjoys an upswing in the industrial and research interest due to its compact design enabling high efficiency, high applicable current density and intermittent operation capability, which makes it an excellent match for decentralized renewable generators with high output fluctuations.^[3] However, the large scale application of PEM electrolysis is currently limited by the high cost of its components and in particular iridium used to catalyze the oxygen evolution reaction (OER) process.^[4-5]

In spite of intensive research on different classes of OER catalysts, iridium oxide remains the only material demonstrating sufficient long-term catalytic activity without stability fading.^[6] This is however achieved by a high Ir loading in the electrode assemblies of about 1.5–3 mg_{Ir} cm⁻² in the state of the art PEM cells.^[7-9] Taking into account the cost, scarcity and total availability of Ir, at least a 10-fold decrease in the Ir loading is required.^[10] At the same time, a certain thickness of the catalyst layer of several μm is needed to enable its integration in the cells without the shortcuts in their functionality.^[7]

In fact, it is not only the decreased loading but the drastic decrease in the Ir volumetric packing density in the electrode assembly with the simultaneous increase in the OER activity that should be targeted to make PEM technology economically feasible for the large-scale hydrogen generation. Due to a high economic impact of PEM electrolysis, considerable efforts have been made to improve the performance of Ir-based catalysts.

Nanostructuring, and in particular inverse opal morphology with its high void volume were demonstrated to be beneficial for decreasing the catalyst loading in membrane based electrolyzers as has been recently reported by Park *et al.*^[11] and by Faustini *et al.*^[12] for IrO₂ or RuIrO₂ catalysts, respectively. The critical point in the fabrication of nanostructured Ir-based catalysts is however the simultaneous optimization of the nanomorphology and the catalytic activity, which is strongly influenced even by the subtle changes in phase composition and is sensitive to the fabrication method.

Another established approach is a dispersion of the Ir-based OER catalyst on a nanostructured support, which potentially results in a much larger active surface area for a given amount of catalyst than could be achieved by a solid compact structure.^[13-18] TiO₂-supported IrO₂ has been used for years as dimensionally stable electrodes (DSA) in chlorine-alkali electrolysis^[19] and in the state of the art PEM electrolysis.^[7, 9, 20] The major advantages brought by the commercially available supported catalysts are however more an improved mechanical stability and simple processability of the catalyst layers rather than the decrease in Ir loading. Significant efforts have been made therefore to optimize the morphology of supports by using materials with high surface area, high electric conductivity and high oxidation stability such as mesoporous transparent conductive oxides (TCO). Mesoporous antimony doped tin oxide (ATO),^[13, 21] indium tin oxide (ITO),^[21] fluorine-doped tin oxide (FTO), and niobium doped titania (NTO)^[18,22] coated with a thin iridium active phase have been reported to show the high electrocatalytic activity with a substantially decreased iridium loading.

Still, in spite of the progress achieved, the rather small pore size and compact structure of the mesoporous materials put constraints on the homogeneous dispersion of iridium layers and the volumetric density as well as on the gas transport at high current densities. Therefore, a combination of conductivity provided by TCOs with a low volumetric density of macroporous supports can be expected to enable a further decrease in the Ir loading per membrane area on a

scale required for large scale application of the PEM technology.^[7] The challenges in the development of supported catalysts are the synthesis of an ideally conductive, corrosion-stable support with the optimized morphology, as well as its conformal coating with a very thin layer of catalyst in a simple and scalable way.

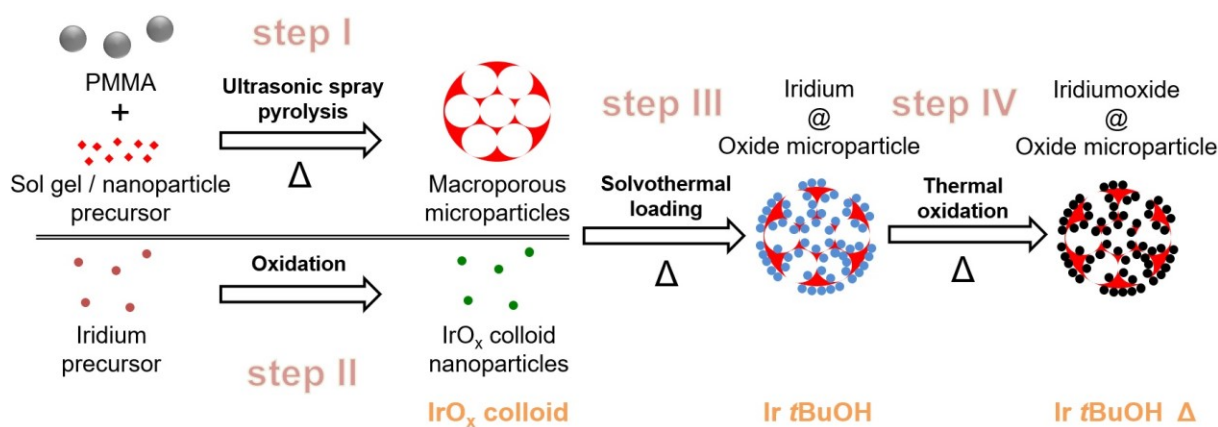
We present a scalable approach to prepare a dimensionally stable OER catalyst with a very low Ir volumetric loading density but very high OER activity. In contrast to previous work on supported catalysts and Ir-based OER catalysts, our multistep synthesis approach allows for an independent optimization of all single components to result in a highly active and stable catalyst. With the introduced synthesis concept the composition (by choice of the transition metal precursor), morphology (by the size of porogen), and conductivity (by the doping level) of the oxidic support, as well as the iridium loading (by the ratio of Ir precursor to oxidic support) and the active phase (by the oxidation procedure applied on the Ir@oxidic-support) can be tuned individually to enable the development of highly active OER catalysts with high Ir-volume dispersion for future PEM-electrolysis.

8.3 Results and Discussion

Scheme 1 depicts the synthesis workflow starting from the ultrasonic spray pyrolysis of electrically conducting macroporous antimony-doped tin oxide (Sb:SnO₂ or ATO) microparticles templated by poly(methyl methacrylate) (PMMA) (Step I), and an iridium chloride precursor that is oxidized in an aqueous environment to form hydrous IrO_x colloid nanoparticles (Step II). A solvothermal reaction in *tert*-butanol/methanol/H₂O as a key step leads to a reduction of the IrO_x colloid nanoparticles at the oxide microparticle surface (Step III) to form a homogeneous layer of metallic nanoparticles (referred to as Ir *t*BuOH) of comparable size (≈ 2 nm). The resulting ATO microparticle-supported Ir nanoparticle product is referred to as SG₂₈₀Δ-Ir-YX, with “SG” abbreviated for sol–gel derived product, subscript (“280” or “120”) representing the PMMA bead diameter (in nm) used for the synthesis of inverse opal microparticles, “Δ” indicating thermally cured ATO scaffold particles, “Ir” indicating an Ir nanoparticle loaded product obtained by a solvothermal synthesis and “Y” = 1/2, 1, 2, 3, 4 being a multiplier of the iridium amount “X” on the ATO scaffold theoretically yielding a ≈ 15 wt% Ir content in the composite catalyst (see the Experimental Section and Table S1, Supporting Information, for further details). Thermal oxidation in air (Step IV) leads to the formation of ATO microparticle-supported IrO₂ nanoparticles referred to as SG₂₈₀Δ-IrO₂-YX which represents IrO₂ nanoparticles supported on ATO scaffold particles originating from the thermal oxidation in air.

In addition to the catalyst described above, particles with a smaller macropore size were prepared using 120 nm PMMA beads for the ATO microparticle synthesis. The samples are assigned as SG₁₂₀Δ-Ir-YX and SG₁₂₀Δ-IrO₂-YX for supported catalysts before and after thermal oxidation, respectively. As two series of the catalysts show very similar materials properties, mainly the characterization of particles with a larger pore size is shown in the paper, with

characterization results of the smaller pore size catalyst series being shown in the Supporting Information.



Scheme 1 Synthesis of ATO microparticle-supported IrO_2 oxygen evolution reaction catalyst. Step I: Synthesis of macroporous oxide microparticles (red) by ultrasonic spray pyrolysis. Step II: Synthesis of IrO_x colloid nanoparticles (green) used for catalyst loading. Step III: Solvothermal loading of oxidic support by reduction of IrO_x to metallic Ir (blue) on the microparticle surface (assigned as “Ir tBuOH”). Step IV: Thermal oxidation of Ir-loaded ATO microparticles leads to the formation of IrO_2 nanoparticles (black, assigned as Ir tBuOH Δ) resulting in the final ATO-supported IrO_2 -based OER catalyst.

Macroporous ATO microparticles depicted in Figure 1 were synthesized using an ultrasonic spray pyrolysis (USP) approach (Scheme 1, Step I, also see Scheme S1 in the Supporting Information and the Experimental Section for further details).^[23] PMMA with bead sizes of ≈ 120 and ≈ 280 nm were used as templates to form ordered macroporous^[24]

ATO particles either from sol gel derived precursor (in the following referred to as $\text{SG}_{120\Delta}$ and $\text{SG}_{280\Delta}$ for 120 and 280 nm PMMA templated particles, respectively) or from presynthesized ATO nanoparticles^[25] (referred to as $\text{NP}_{120\Delta}$). Resulting powders before (SG_{120} , SG_{280} , and NP_{120}) and after thermal curing ($\text{SG}_{120\Delta}$, $\text{SG}_{280\Delta}$, and $\text{NP}_{120\Delta}$ with “ Δ ” representing an additional heating step in air after the spray pyrolysis reaction) for the removal of residual carbon as well as undoped reference ($\text{SG}_{280\Delta}$ w/o Sb) were analyzed by X-ray diffraction and Raman spectroscopy (see Figure S1a,c in the Supporting Information) confirming the exclusive formation of the SnO_2 cassiterite phase for undoped and ≈ 4 at% (sol–gel based) and ≈ 5 at% (nanoparticles based) Sb-doped samples. X-ray photoelectron spectroscopy (XPS) (see Figure S3 in the Supporting Information) and energy dispersive X-ray (EDX) analysis (value

noted in Figure 1a) point to a Sb doping concentration of 4.3 at% for the SG₂₈₀Δ samples, which is in a good agreement with the Sb content of 4.8 at% in the precursor solution.

n-Type doping by antimony is known to increase the conductivity of stoichiometric SnO₂ significantly, with the highest values reported for an Sb-doping level of about 5 at%.^[25] Dc measurements for densely compressed pellets return a high specific conductivity of 3.6 S cm⁻¹ for the Sb-doped (SG₂₈₀Δ) SnO₂ microparticle samples, which is an increase by a factor of $\approx 10^4$ compared to a respective undoped sample SG₂₈₀Δ (3.8×10^{-4} S cm⁻¹).

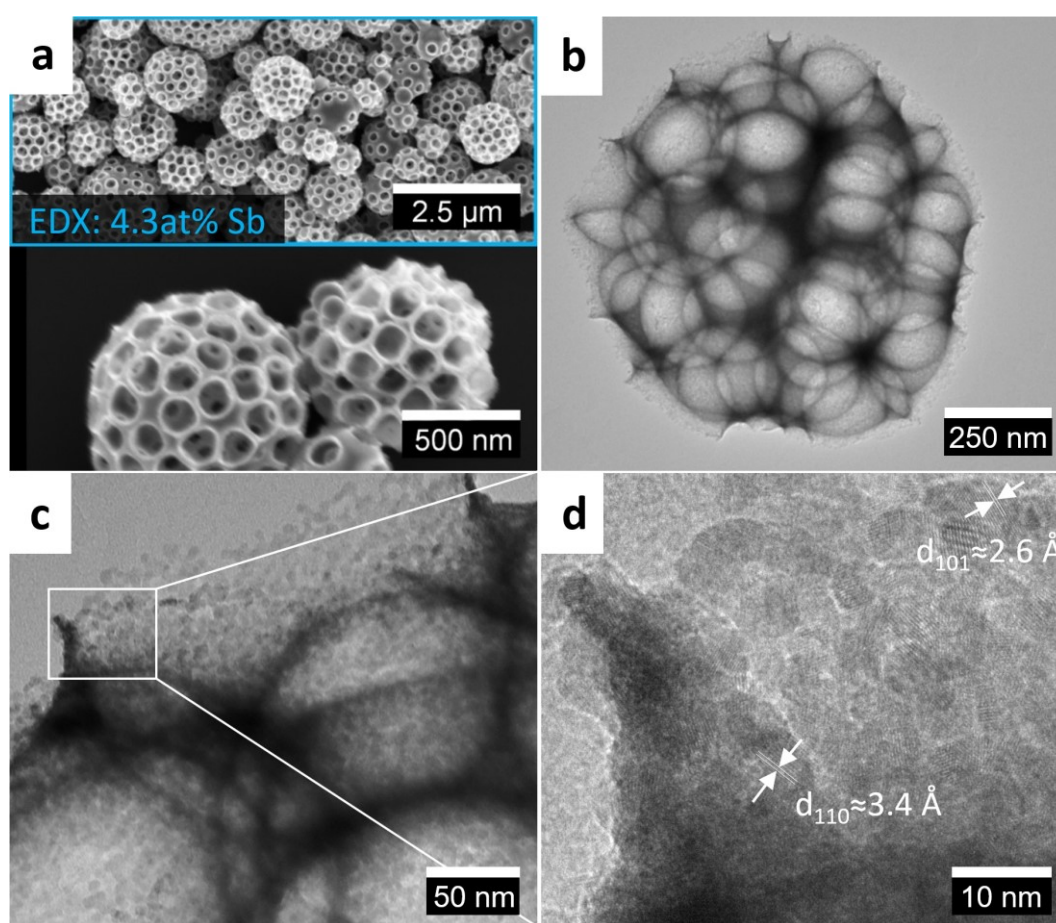


Figure 22 (a–c) Electron microscopy images of macroporous antimony-doped tin oxide microparticles templated with 280 nm PMMA beads (SG₂₈₀Δ). d) Lattice spacings indexed for individual ATO crystallites determined by intensity profiles of crystallites and correlated to *d*-spacings and orientation according to ICDD card number 00-041-1445 (SnO₂, tetragonal symmetry, $a = b = 4.7382(4)$ Å, $c = 3.1871(1)$ Å, $\alpha = \beta = \gamma = 90^\circ$).

Scanning electron microscopy (SEM) and transmission electron microscopy (TEM) images reveal the formation of ATO microparticles with a mean diameter of 850 nm and inverse opal

morphology with an outer pore opening diameter of 150 – 190 nm (mean $\text{\O}172$ nm, $N = 191$) (Figure 1a,b) and a mean inner pore diameter determined from high resolution (HR)-TEM images of ≈ 232 nm indicating a shrinkage of the initial pores obtained by the 280 nm PMMA beads by $\approx 17\%$ during the spray pyrolysis reaction.

The pore size of the inverse opal ATO microparticles can be easily tuned by the size of the PMMA beads, as shown in Figures S4 and S5 (Supporting Information) for sol–gel and nanoparticle based ATO microparticles templated with 120 nm PMMA beads. 120 nm PMMA porogen templating thereby results in the formation of pore opening diameters of 55 – 75 nm (mean $\text{\O}65$ nm, $N = 137$) on the outer microparticle surface and mean inner pore diameter of ≈ 83 nm as shown by electron microscopy translating to a pore shrinkage of $\approx 30\%$ during the pyrolysis reaction.

According to X-ray diffraction (XRD) and high resolution TEM images, the scaffold is composed of ≈ 5 nm nanocrystals (Figure 1d and Figure S1, Supporting Information). Nitrogen sorption measurements (Figure S6, Supporting Information) correspond to mainly macroporous adsorbent with minor contribution of microporosity originating from textural porosity of interconnected small crystalline domains. A Brunauer–Emmett–Teller surface area of 54 and 52 $\text{m}^2 \text{g}^{-1}$ was determined for 120 and 280 nm PMMA templated ATO microparticles, respectively. Direct evidence of macropores of about 70 nm for sample $\text{SG}_{120}\Delta$ is given by the pore size distribution shown in inset of Figure S6a (Supporting Information), which is in a good agreement with the pore size quantification by SEM and TEM (see Figure S4 in the Supporting Information). The pore size distribution of $\text{SG}_{280}\Delta$ does not show any porosity beyond a minor amount of micropores which can be explained by a detection limitation of the nitrogen sorption technique with regard to larger macropores ($\gtrsim 80$ nm) as present in 280 nm PMMA templated microparticles.

However, the visibly open porosity observed by SEM and TEM (Figure 1) in combination with the BET surface area strongly suggest interconnected macropores also for the 280 nm PMMA templated ATO microparticles.

For the synthesis of a highly OER active iridium phase we have introduced a facile synthesis method for ultrasmall colloidal IrO_x particles (Scheme 1, Step II), which was used as an Ir precursor phase for the solvothermal loading of the oxidic scaffold. The procedure employs the rapid oxidation of an Ir(III)Cl₃ precursor in aqueous solution with KO₂, which was inspired by a synthesis introduced by Sutto for the fabrication of ultrasmall metal oxide nanoparticles.^[26]

The as-prepared IrO_x colloid (Figure 2e,f and Figure S7a, Supporting Information) consists of approximately spherical particles with a mean diameter of ≈2.4 nm as shown by scanning transmission electron microscope (STEM). The electron diffraction pattern (Figure 2f) of the particles only shows a diffuse ring that does not correspond to a distinct crystallographic plane but represents a mean Ir–O atomic distance in this poorly crystalline hydrated material.^[27] The hydrous IrO_x particles are also easily reduced and crystallize in the electron beam evidenced by a visible growth and aggregation of nanoparticles with extended illumination periods (see Figure S8 in the Supporting Information).

Hydrous IrO_x colloids display a remarkable electrocatalytic performance but a rather limited long-term stability which requires an additional thermal treatment for the transformation to a stable active IrO₂ phase.^[28,29] To obtain a more stable unsupported nanosized IrO₂ reference catalyst the precursor colloid was therefore oxidized in air at a moderate temperature of 375 °C to avoid significant particle growth and sintering. Powder X-ray diffraction patterns of the IrO_x colloid sample (Figure 2a) show a broad peak centered around 33° 2θ that is shifted to 35° 2θ upon heating.

According to the XRD line broadening and peak positions, the as-prepared as well as the heated IrO_x colloid is composed of a nanosized iridium oxide phase presumably differing in the degree

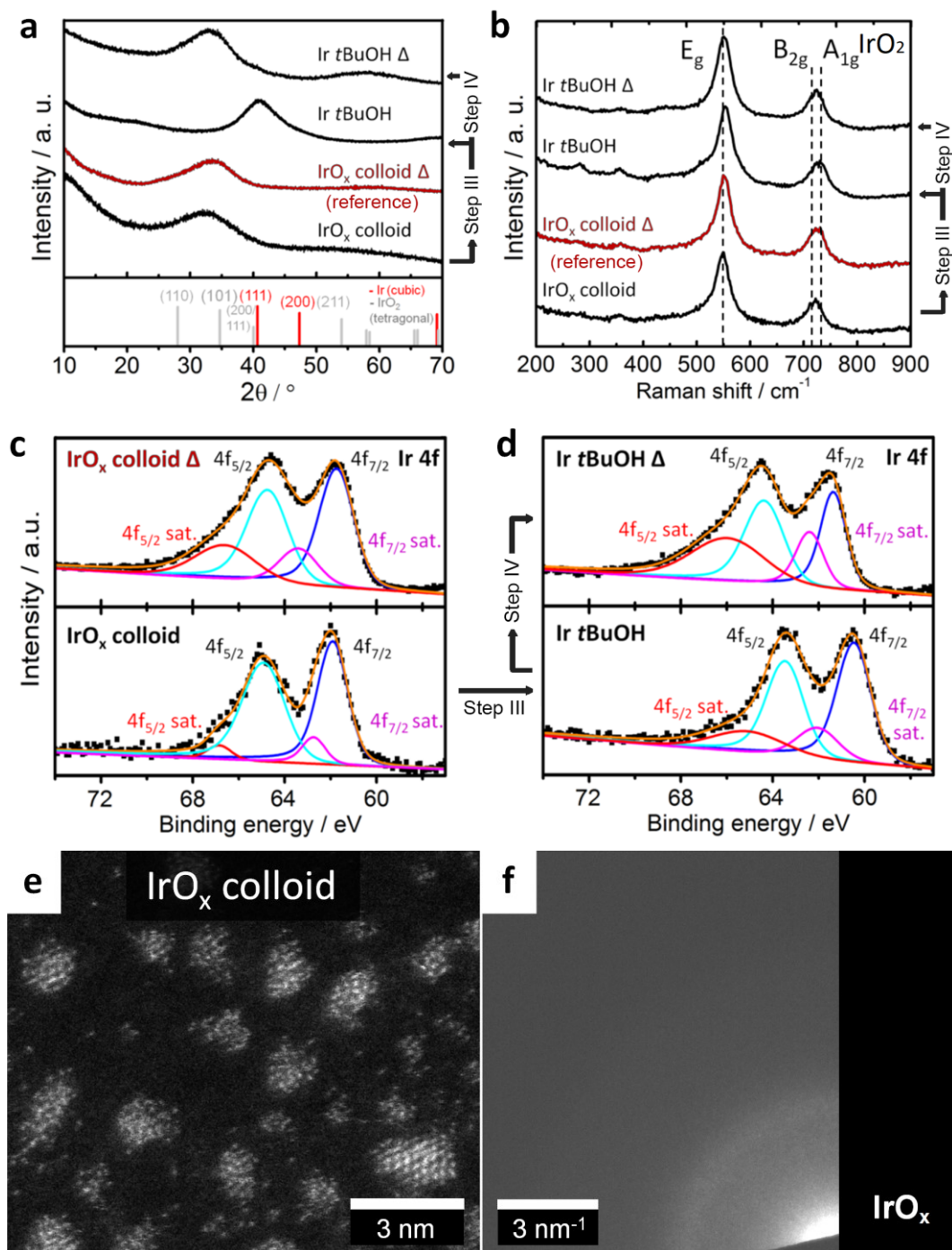
of crystallinity and present crystal water causing a slight peak shift.^[27] After calcination, aggregated nanoparticles (Figure 2g and Figure S7b, Supporting Information) with a mean particle size of ≈ 3.0 nm are observed with an electron diffraction pattern (Figure 2h) displaying diffraction rings mainly associated with the tetragonal IrO₂ phase. The increase in crystallinity accompanied by only negligible particle growth can directly be observed by STEM and is furthermore indicated by XRD (Figure 2a). The tetragonal iridium oxide phase of the IrO_x colloid before and after calcination is further confirmed by Raman spectroscopy (Figure 2b) displaying the characteristic E_g band around 560 cm⁻¹ and a broad peak around 740 cm⁻¹, which is presumably formed by an overlapping B_{2g} and A_{1g} band at 728 and 752 cm⁻¹, respectively.^[30-31]

For the preparation of the IrO₂/ATO composite catalyst a solvothermal reaction of the precursor IrO_x colloid in presence of the porous ATO microparticles scaffold is introduced as integral part of this work to homogeneously coat the accessible surface of a porous support with iridium nanoparticles (Scheme 1, Step III).

To obtain an unsupported reference catalyst the solvothermal reaction is simply performed without the presence of the oxidic support. The solvothermal treatment of the IrO_x colloid in *tert*-butanol/MeOH/H₂O (with or without the presence of oxidic support material in the reaction) leads to a reduction and formation of metallic iridium nanoparticles, whereby unsupported Ir nanoparticles are referred to as “Ir *t*BuOH” in the following.

The reduction process is indicated by the broad diffraction peak centered at around 41° 2θ corresponding to the cubic Ir phase and the absence of any peaks related to the tetragonal IrO₂ phase or hydrous IrO_x (Figure 2a and Figure S9a, Supporting Information). HR-TEM and STEM images reveal the formation of crystalline uniform nanoparticles (Ir *t*BuOH; Figure 2i,j and Figure S7c, Supporting Information) with an average diameter of ≈ 2.8 nm. The electron

diffraction pattern (Figure 2j) indicates the presence of metallic iridium (cubic phase), which is in agreement with the X-ray diffraction (Figure 2a).



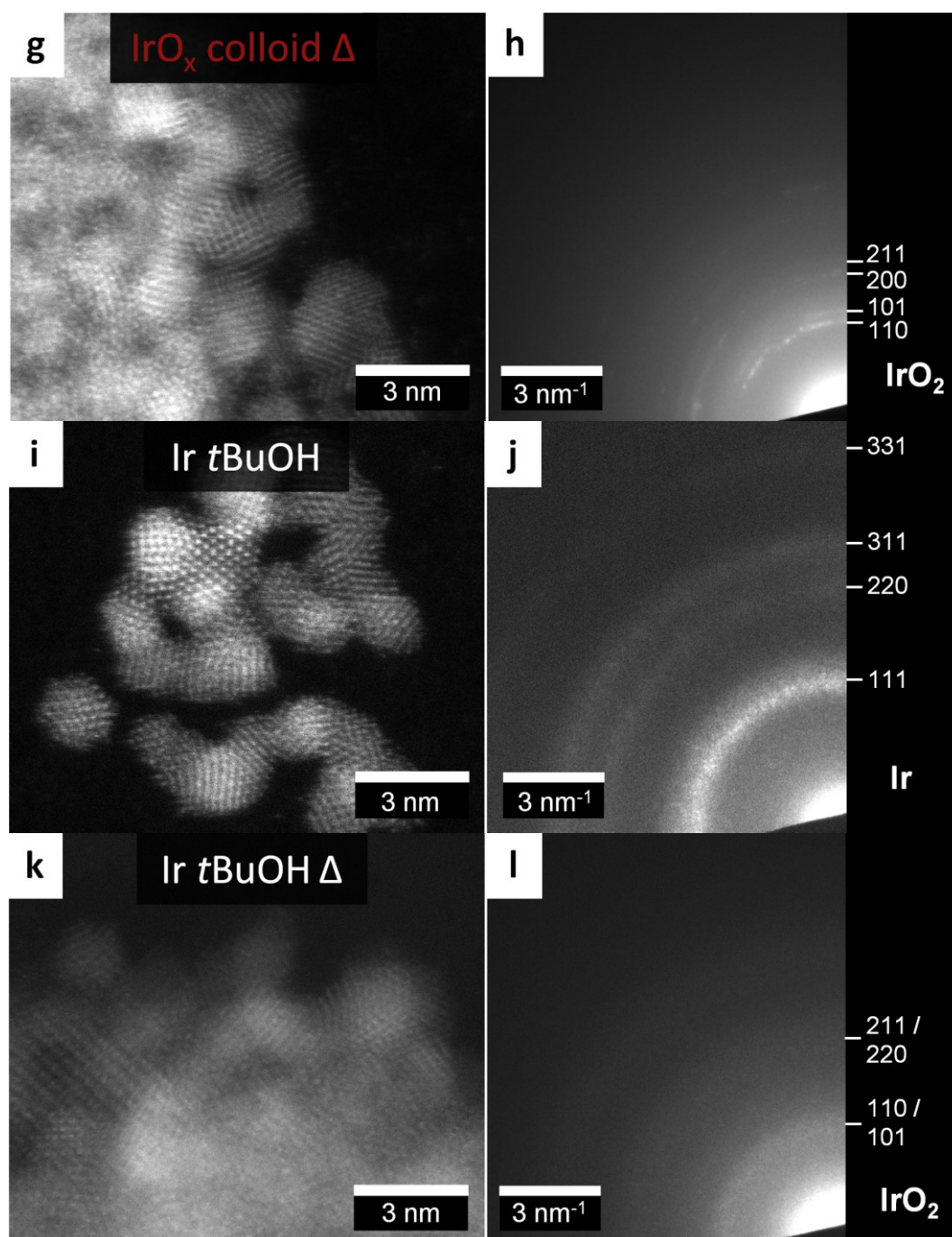


Figure 23 Structural and spectroscopic characterization of iridium and iridium oxide nanoparticles. a) X-ray diffraction pattern of IrO_x colloid before (IrO_x colloid) and after thermal oxidation (IrO_x colloid Δ , red curve) and metallic iridium nanoparticles (Ir tBuOH) and IrO_2 nanoparticles ($\text{Ir tBuOH}\Delta$). Ir pattern: ICDD card number 00-006-0598 (red) (cubic symmetry, $a = b = c = 3.8394 \text{ \AA}$, $\alpha = \beta = \gamma = 90^\circ$). IrO_2 pattern: ICDD card number 00-015-0870 (gray) (tetragonal symmetry, $a = b = 4.4983 \text{ \AA}$, $c = 3.1544 \text{ \AA}$, $\alpha = \beta = \gamma = 90^\circ$). b) Raman spectra of Ir/ IrO_2 nanoparticles with reference band at 561 cm^{-1} (E_g) and close bands at 728 cm^{-1} (B_{2g}) and at 752 cm^{-1} (A_{1g}) correspond to the tetragonal iridium oxide phase.^[30,31] XPS spectra of c) IrO_x colloid before and after thermal oxidation and d) iridium nanoparticles (Ir tBuOH) and IrO_2 nanoparticles ($\text{Ir tBuOH}\Delta$). An Ir $4f_{7/2}$ core electron binding energy of 60.8 eV was assigned to metallic Ir(0) and an Ir $4f_{7/2}$ binding energy of 61.9 eV was assigned to Ir(IV) O_2 .^[32] e,g,i,k) Scanning transmission electron microscopy data and f,h,j,l) electron diffraction (ED) patterns of respective Ir/ IrO_2 samples. Phase identification and assignment of lattice planes in ED pattern according to literature values.

The XRD pattern of particles after calcination at 375 °C in air (Ir *t*BuOH Δ) shows a broad peak around 33° 2 θ , indicating the presence of a nanosized iridium oxide phase (Figure 2a and Figure S9b, Supporting Information). During thermal treatment the metallic nanoparticles undergo a transformation to the tetragonal IrO₂ phase (Ir *t*BuOH Δ ; Figure 2k,l) as confirmed by electron microscopy with broad diffraction rings visible in Figure 2l, which matches well with the X-ray diffraction data.

This process is accompanied only by a minor particle growth to a mean diameter of \approx 3.2 nm (Figure 2k). The presence of an iridium oxide phase is further confirmed by Raman spectroscopy (Figure 2b) for the calcined metallic Ir nanoparticles (Ir *t*BuOH Δ) sample. However, the Raman spectrum of metallic Ir nanoparticles after solvothermal reduction (Ir *t*BuOH) also displays the characteristic bands of the oxide phase at 560 and around 740 cm⁻¹, which can be explained by an oxide- or hydroxide-terminated nanoparticle surface, which is detected by Raman spectroscopy but not by XRD.

To further investigate and distinguish the electronic properties of the synthesized iridium and iridium oxide phases and to derive the oxidation states of the iridium present, XPS (Figure 2c,d) was conducted. Fitting of the Ir 4f_{7/2} peak in the XPS spectrum of hydrous iridium oxide colloid (IrO_x colloid) returned a binding energy of 61.9 eV versus 62.1 eV for the calcined sample (IrO_x colloid Δ). Although an oxidation state of +IV can be assigned to iridium in both nanoparticle samples in accordance to literature values,^[32] subtle differences in the XPS spectra of both oxide species can be observed.

By comparison, the ratio between the Ir 4f_{5/2} and Ir 4f_{7/2} peak is higher in the calcined sample, and we observe a visibly increased peak area and a shifted position of the Ir 4f_{7/2} and Ir 4f_{5/2} satellite peaks. The subtle changes in the XPS spectra in combination with the observed small shift in the XRD pattern (Figure 2a) are attributed to an increase in crystallinity with an accompanying loss of crystal-bound water which slightly alters the chemical surrounding of

the Ir atoms in the hydrous oxide nanoparticles. Solvothermal reduction of the IrO_x colloid nanoparticles in *tert*-butanol/MeOH/H₂O causes a shift of the Ir 4f_{7/2} binding energy to 60.6 eV (Ir *t*BuOH in Figure 2d) which is assigned to Ir(0)^[32] and is in agreement with the corresponding X-ray diffraction (Figure 2a). Upon thermal oxidation the Ir 4f_{7/2} peak shifts again to higher binding energies (61.3 eV) and is therefore assigned to the oxide phase (Ir (+IV)).^[32] However, the Ir 4f spectrum of the final IrO₂ nanoparticles differs from the spectra of the IrO_x colloid samples shown in Figure 2c. A significantly increased signal intensity, a further shift of the Ir 4f_{7/2} and Ir 4f_{5/2} satellite peaks and a slightly increased Ir 4f_{5/2} to Ir 4f_{7/2} ratio are observed. This indicates the formation of a nanoparticle oxide phase, as shown by the diffraction data, with a slightly altered chemical surrounding of the Ir atoms in contrast to the initial hydrous oxide phase.

The results can be interpreted as a slightly altered local structure of the oxide phase differing in the degree of crystallinity and the number of defects caused by altered change in the Ir/O ratio over the course of the multistep synthesis. These structural differences not distinguishable in the powder X-ray diffraction data can have a significant impact on the OER activity and stability of the Ir-active phase (see section on electrochemical characterization).

The crucial step in the synthesis of highly active oxide supported catalysts is the homogeneous coating of a complex support morphology with a thin compact layer of iridium nanoparticles. Simple infiltration of the oxidic support with IrO_x colloid results in a very poor support coverage, with the majority of colloidal nanoparticles remaining in the dispersion. We found, however, that the solvothermal treatment of this mixture in *tert*-butanol/methanol/H₂O (step III) leads to a reduction of IrO_x colloid to metallic Ir nanoparticles of similar size, conformally precipitating on the surface of porous ATO particles. The resulting composite catalyst is termed as SG₂₈₀Δ-Ir-YX, with Y = 1/2, 1, 2, 3, 4 as a multiplier of the iridium amount declared as “X” which corresponds to an amount of precursor for a theoretical loading of

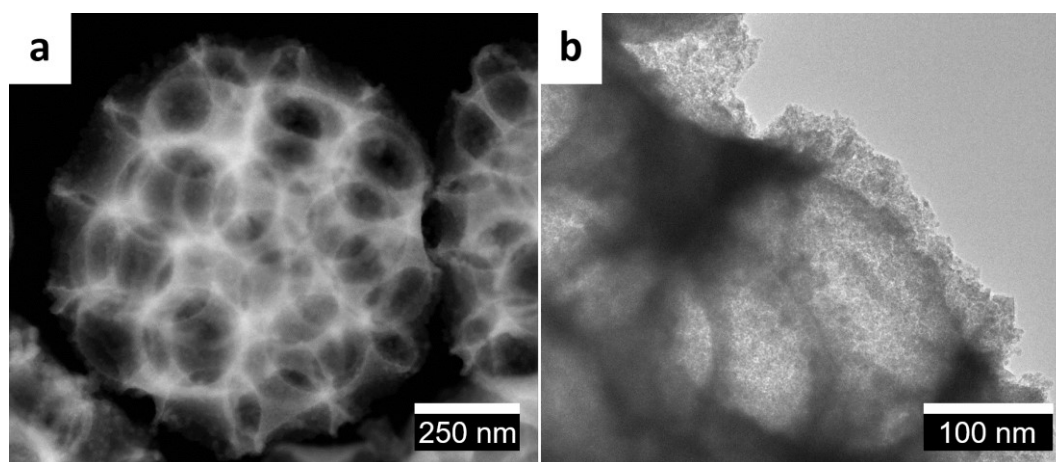
15 wt% Ir in the supported catalyst. The subscript represents the diameter of the templating porogen PMMA with 280 nm. Analogous results presented in the Supporting Information on ATO microparticles templated by 120 nm PMMA beads demonstrate a successful homogeneous coating of complex porous substrates also with decreased pore size (Figures S10a,c, S11, S12a,b,e,f, and S13 and Table S1, Supporting Information).

The diffractograms of Ir-loaded ATO microparticles templated by 280 nm PMMA beads (Figure S10b, Supporting Information) exhibit peaks associated with the cassiterite (ATO) phase and an additional peak corresponding to the Ir 111 reflection that increases in intensity with the amount of IrO_x colloid added to the solvothermal synthesis, although its maximum intensity is lower than for the SG₁₂₀Δ based samples (Figure S10a, Supporting Information).

As was shown above for the unsupported Ir nanoparticles, thermal oxidation of Ir-loaded ATO microparticles at 375 °C in air (Scheme 1, Step IV) leads to a transformation of metallic Ir particles to a nanosized tetragonal IrO₂ phase. Raman spectra of IrO₂-loaded as well as Ir-loaded ATO microparticles (Figure S11, Supporting Information) show two broad peaks around 550 and 740 cm⁻¹ corresponding to the E_g band and the overlapping B_{2g}/A_{1g} band of IrO₂.^[30,31] The absence of any signal from the underlying ATO indicates a complete coverage of the surface with Ir/IrO₂ particles. As indicated by scanning electron microscopy and EDX, Ir- (Figure S12a–d, Supporting Information) and IrO₂ (Figure S12e–h, Supporting Information) nanoparticle-coated ATO microparticles after solvothermal loading do not show a visible difference in shape or morphology as compared to the parent microparticle support (Figure 1 and Figure S4, Supporting Information). Also, the presence of chloride ions in the solvothermal reaction introduced by the IrCl₃ precursor has no significant impact on the microparticle phase (Figure S1b, Supporting Information), composition (Figure S2e, Supporting Information) or conductivity (Figure S2e,f, Supporting Information). EDX (Figure S12a,c,e,g, Supporting Information) confirms the presence of iridium, which is

homogeneously distributed on the microparticle scale. The loading of ATO microparticles with iridium nanoparticles and the oxidation state of the active Ir phase were also investigated by XPS (Figure S14, Supporting Information), which confirms the formation of a metallic Ir phase (Figure S14a, Supporting Information) upon solvothermal treatment in the presence of ATO microparticles as shown for unsupported nanoparticles (Figure 2d) which underwent the same synthesis procedure.

Calcination also leads to the formation of the respective oxide phase (Figure S14a, Supporting Information and Figure 2d). Table S1 (Supporting Information) summarizes the theoretical and experimentally determined Ir fractions in the ATO microparticle-supported Ir and IrO₂ nanoparticle materials. The measured values deviate only slightly from the theoretical ones with the exception of the highly Ir-loaded sample ATO-SG₂₈₀/IrO₂-4X. The reason for the smaller loading capacity of the large-pore ATO microparticles at high iridium amounts (“4X” sample with theoretical loading of 43 wt% Ir) compared to the ATO-SG₁₂₀/IrO₂ series is expected to be caused by the slightly smaller surface area available for particle adhesion. In summary, a near quantitative adsorption of the supplied iridium on the ATO scaffold could be realized for a broad range (7 to ≈40 wt% Ir) of ATO/Ir ratios by our solvothermal loading method.



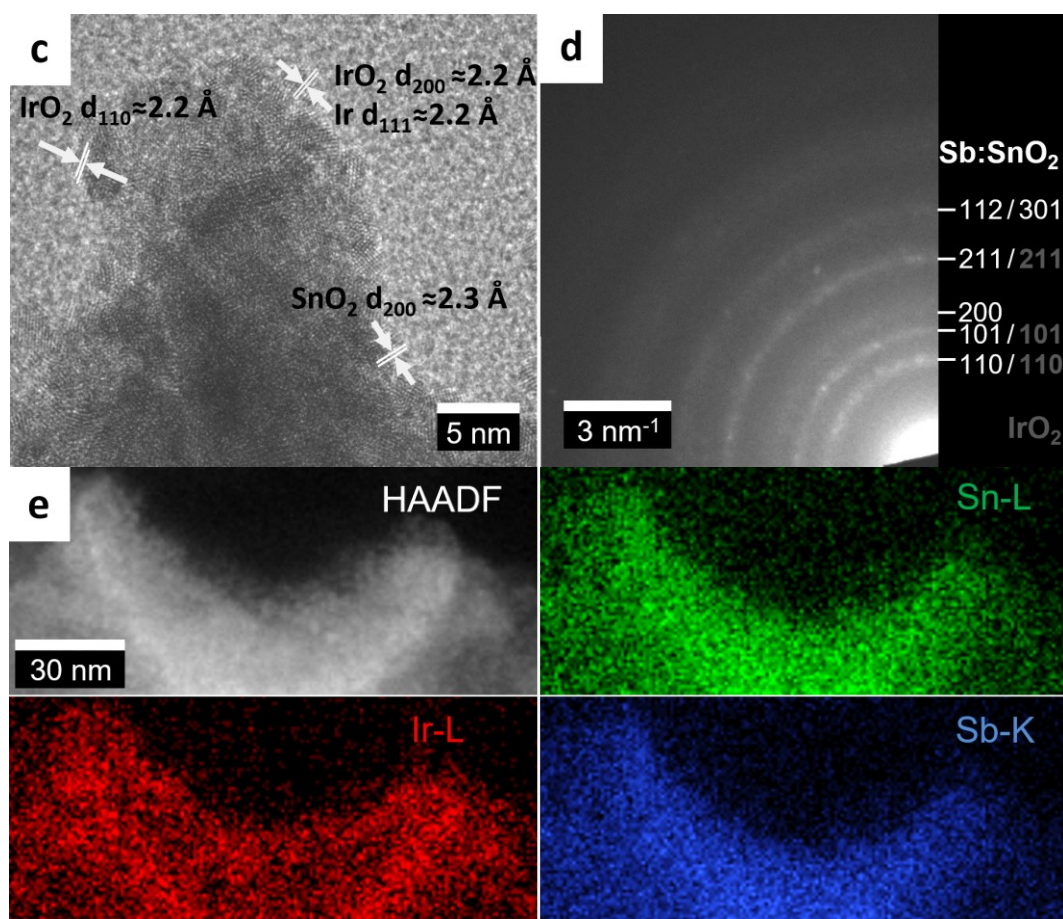


Figure 24 Transmission electron micrographs and EDX mapping of IrO₂ nanoparticles supported on macroporous ATO microparticles templated with 280 nm PMMA beads. a–c) Electron micrographs, d) electron diffraction pattern, and e) STEM/EDX elemental mapping of an outer pore. ATO microparticles with IrO₂ loadings of 25 wt% Ir (ATO-SG₂₈₀Δ-IrO₂-2X). Phase identification and assignment of lattice spacings in d) electron diffraction pattern and c) high resolution TEM image according to literature values. SnO₂ (cassiterite) pattern: ICDD card number 00-041-1445 IrO₂ pattern: ICDD card number 00-015-0870

For a more detailed analysis of the spatial IrO₂ distribution on the macroporous ATO microparticles, high resolution transmission electron microscopy with energy-dispersive X-ray spectroscopy analysis and elemental distribution mapping was performed as shown in Figure 3. The overview images (Figure 3a,b) of the microparticles show that the morphology and pore structure of the unloaded particles has been maintained. The lattice spacings derived from electron diffraction patterns of individual ATO/IrO₂ particles (Figure 3d) indicate the exclusive presence of the cassiterite (ATO) and tetragonal IrO₂ phase.

The deposition of a thin layer of IrO₂ nanoparticles on the inner ATO surface is shown by the lattice fringes visible in the high resolution TEM images, which can be assigned to the

cassiterite and IrO₂ phase for individual nanocrystals (Figure 3c). Furthermore, the inner pore diameter of IrO₂- loaded 280 nm PMMA-templated particles could be quantified to ≈ 216 nm (\emptyset inner pore diameter, $N = 14$) according to HR-TEM images as shown in Figure 3 versus ≈ 71 nm (\emptyset inner pore diameter, $N = 6$) for 120 nm PMMA templated microparticles (Figure S13b, Supporting Information). As the inner pore diameter of unloaded ATO microparticles is ≈ 232 nm (\emptyset inner pore diameter, $N = 27$) and ≈ 83 nm (\emptyset inner pore diameter, $N = 13$, Supporting Information) for SG₂₈₀ Δ and SG₁₂₀ Δ , respectively, a mean thickness of the IrO₂ nanoparticle catalyst coating of ≈ 16 nm (ATO-SG₁₂₀ Δ -IrO₂-2X) and ≈ 12 nm (ATO-SG₁₂₀ Δ -IrO₂-2X) can be calculated.

The reduction of the mean pore diameter is caused by a layer of nanocrystals of about 3 nm diameter (see Figure 2) that can be identified in the HR-TEM images of both samples (Figure 3c and Figure S13c, Supporting Information), which is in good agreement with the crystallite domain size derived from X-ray diffraction data (Figure 2a) The active material layer on the ATO microparticle surface is therefore built up from an average of two to three IrO₂ nanoparticles for ≈ 25 wt% Ir loaded microparticles. EDX elemental mappings of outer ATO pores was performed (Figure 3e and Figure S13e, Supporting Information) for Ir coated ATO with both pore sizes. For both samples a colocalization of the Sn-L, Sb-L, and Ir-L signal was observed. As the Ir-L signal extends beyond the areas of high tin and antimony concentration, we infer a homogeneous coating of the ATO surface with IrO₂.

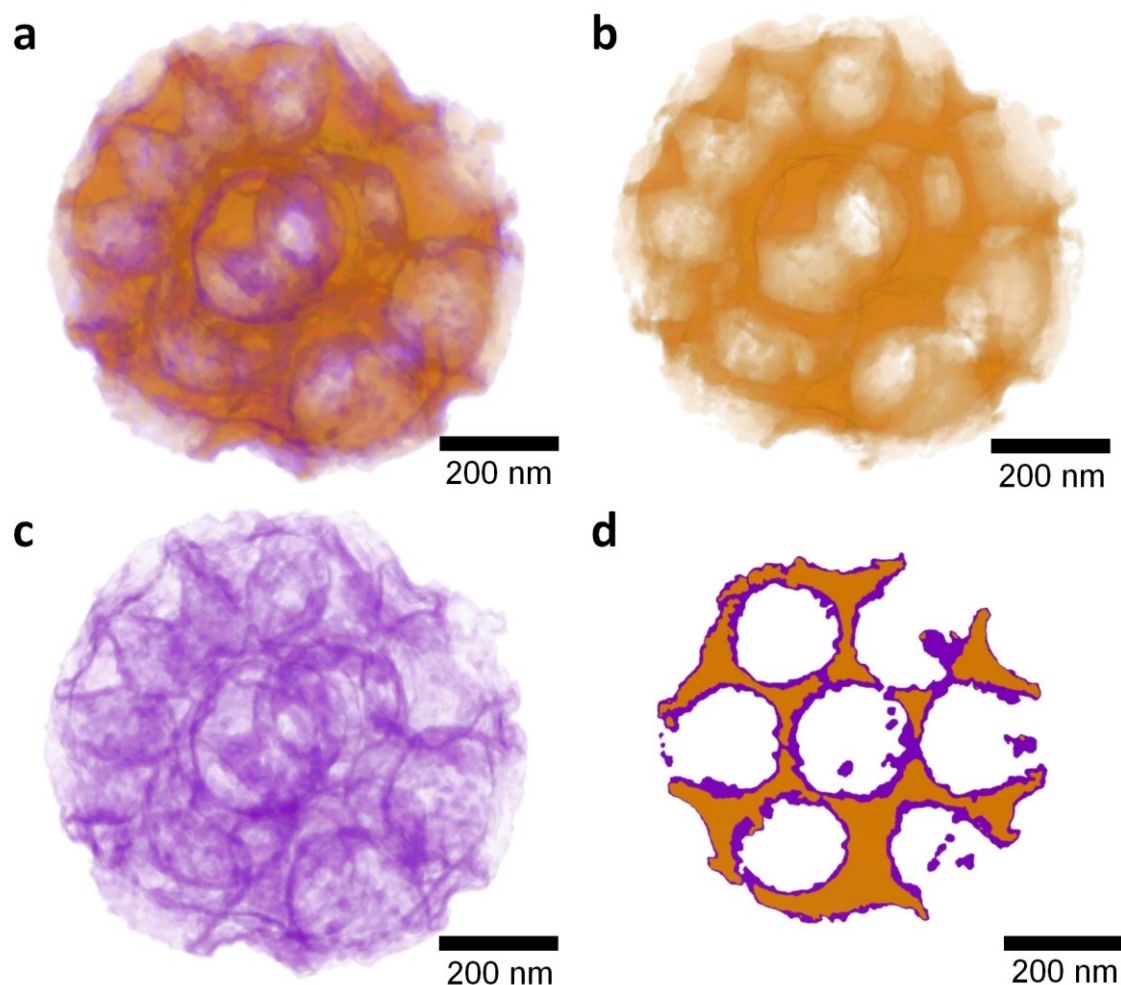


Figure 25 STEM-based tomography with 3D intensity volume reconstruction of IrO_2 nanoparticles supported on macroporous ATO microparticles templated by 280 nm PMMA (≈ 25 wt% Ir). a) Total (ATO and IrO_2) 3D intensity volume derived from particle reprojection. b) Extracted ATO 3D intensity volume from a complete particle. c) Extracted IrO_2 3D intensity volume from a complete particle. d) Extracted cross section of an IrO_2 -coated ATO microparticle from the 3D intensity volume.

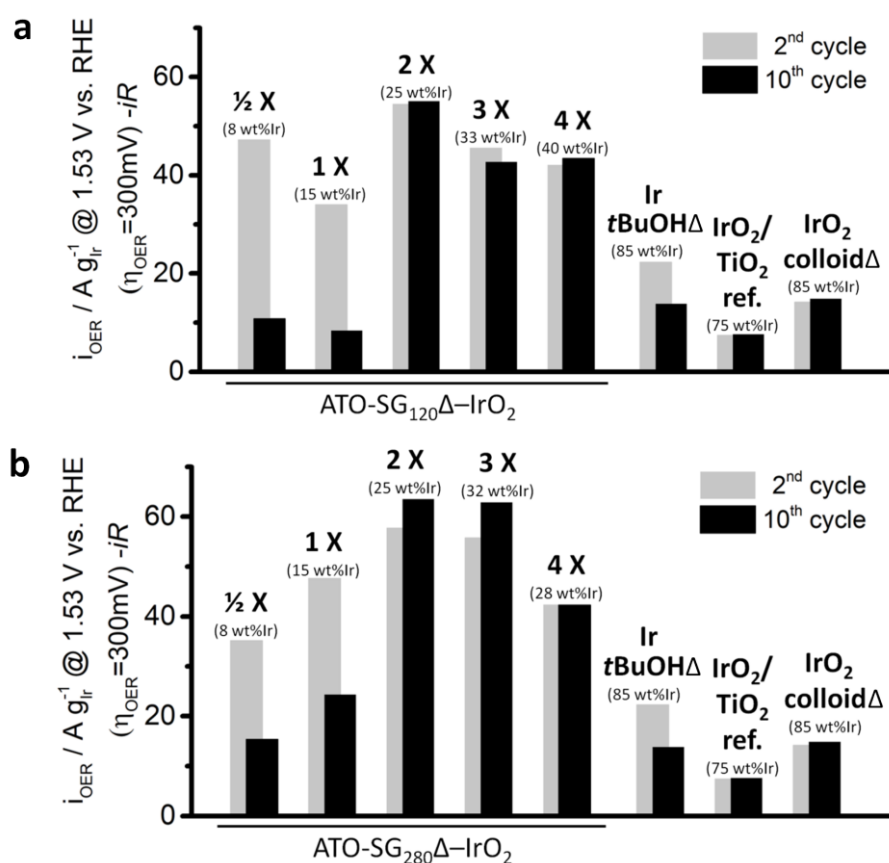
The distribution and interconnection of ATO, IrO_2 and void volume within this composite catalyst is of critical importance for the OER activity and its possible application in membrane based electrolyzers and was therefore studied by the 3D reconstruction of a representative, fully processed particle by means of STEM tomography (see the Experimental Section and Figure S15–S18, Supporting Information). The reconstruction for a 280 nm PMMA templated ATO-based particle is shown in Figure 4.

Due to the higher electron scattering efficiency of high-atomic-number atoms (Z-contrast), a strong contrast between Sn and Ir is observed in high-angle annular dark-field (HAADF)

imaging. The employed tomography algorithms were used to render a discrete 3D reconstruction, in which the volume occupied by ATO and IrO₂ is represented by orange and violet colors, respectively. Figure 4a shows the combined 3D intensity volume of ATO and IrO₂ reconstructed from a series of HAADF-STEM images recorded at different tilt angles. Figure 4b,c shows the extracted 3D intensity volume of the ATO scaffold and the loaded IrO₂ nanoparticle layer, respectively. The 3D intensity volume of IrO₂ (Figure 4c) closely follows the geometry of the ATO scaffold (Figure 4b). A calculated particle cross-section, shown in Figure 4d, confirms the homogeneous coverage of the total internal pore surface with IrO₂. The porosity and the volume dispersion of iridium could also be extracted from the 3D particle reconstruction. For the specific SG₂₈₀Δ-IrO₂-2X particle with ≈25 wt% iridium, a void volume of 84.4% including ATO as void and 59.7% excluding ATO as void was determined (Figure S18, Supporting Information).

To calculate the volume dispersion of iridium in a catalyst film composed of ATO microparticle-supported IrO₂ nanoparticles expected in a membrane-electrode assembly of a PEM electrolyzer, the porosity of individual microparticles as well as the packing density of the microparticles have to be taken into account. The void volume present in a catalyst film of spherical microparticles can be approximated by a random closed packing model^[33] to reach 34 vol% for the experimentally determined particle size distribution (for further details and calculation, see Figure S19 in the Supporting Information). This results in an iridium volume fraction of 10.3 vol% in a catalyst film composed of SG₂₈₀Δ-IrO₂-2X particles with ≈25 wt% iridium loading. The resulting Ir density of ≈0.08 g_{Ir} cm⁻³ of bulk catalyst powder is much lower than the ≈1.5 g_{Ir} cm⁻³ determined for a commercial IrO₂/TiO₂ reference catalyst. Thus, when employed in a PEM electrolyzer cell, a supported catalyst synthesized by the introduced procedure enables the preparation of a continuous, porous anode catalyst layer with a significantly lowered Ir loading than possible with commercial catalysts.

Electrochemical characterization was performed to assess the performance of macroporous ATO microparticle-supported iridium oxide nanoparticles as an oxygen evolution reaction catalyst in acidic media. For the experiments shown in Figure 5a,b (120 and 280 nm PMMA-templated ATO microparticles, respectively), thin films of the catalyst particles dropcasted onto Au-coated quartz crystal microbalance (QCM) sensors were used as working electrodes. The amount of iridium on the QCM chips was obtained from the absolute mass deposited onto the sensors and the iridium fraction determined by EDX measurements of the catalyst film (for Ir fractions of ATO supported catalysts see Table S1 in the Supporting Information). The morphology of thin films of unsupported IrO₂ nanoparticle reference catalysts “IrO_x colloid Δ ” and “Ir *t*BuOH Δ ” were investigated by SEM together with their unheated precursor phases “IrO_x colloid” and “Ir *t*BuOH” as shown in Figure S20 (Supporting Information).



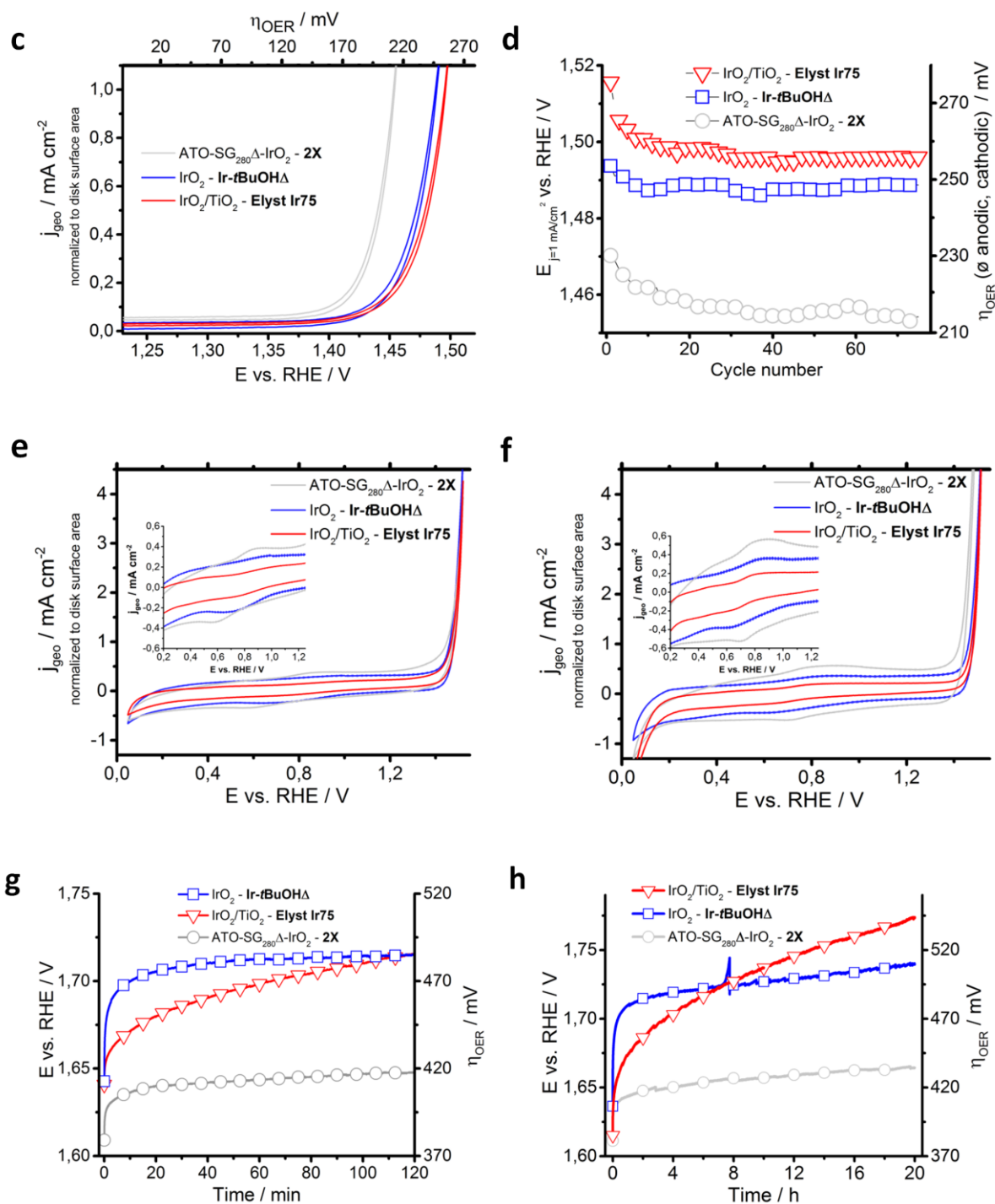


Figure 26 Electrochemical characterization of IrO_2 nanoparticles supported on macroporous ATO microparticles. Iridium mass-based catalytic activity of IrO_2 nanoparticle-loaded microparticles templated by a) 120 nm ($\text{ATO-SG}_{120\Delta}\text{-IrO}_2$) and b) 280 nm ($\text{ATO-SG}_{280\Delta}\text{-IrO}_2$) PMMA for $\eta_{\text{OER}} = 300$ mV. c–f) Rotating disc electrode (RDE) measurements of IrO_2 nanoparticles ($\text{Ir-tBuOH}\Delta$, blue), 25 wt% Ir loaded ATO ($\text{ATO-SG}_{280\Delta}\text{-IrO}_2\text{-2X}$, gray) and commercial TiO_2 -supported IrO_2 with 75 wt% Ir loading ($\text{IrO}_2/\text{TiO}_2\text{-Elyst Ir75}$, red). c) 75th scan cycle of RDE measurement with scan rate of 5 mV s^{-1} . d) Extracted overpotentials (η_{OER}) for each cycle required for 1 mA cm^{-2} . Cyclic voltammograms e) before and f) after 75 RDE cycles at a scan rate of 50 mV s^{-1} . Chronopotentiometry measurements at g) $j = 10 \text{ mA cm}^{-2}$ over 120 min and h) 20 h on FTO substrates with catalyst loading of $15 \mu\text{g}$.

Ir-mass based OER currents for an overpotential of 300 mV for 120 and 280 nm PMMA-templated ATO based catalysts in Figure 5a,b, respectively, show a similar maximum in activity for the 2X samples (55 A g⁻¹ for ATO-SG₁₂₀Δ-IrO₂-2X and 63.5 A g⁻¹ for ATO-SG₂₈₀Δ-IrO₂-2X after 10 CV cycles, respectively) that correspond to a Ir loading of ≈25 wt%. The slightly higher performance of the 280 nm PMMA templated supported catalyst is thereby attributed to a better dispersion of the IrO₂ nanoparticles on the internal surface of the porous microparticle. Higher Ir loadings of up to 40 wt% do not further increase the noble metal mass-based OER activity but rather resulted in a decrease.

On the other hand, low Ir loadings of up to 15 wt% Ir for ATO-SG₁₂₀Δ-IrO₂-1X and ATO-SG₂₈₀Δ-1X exhibit activities of only 8.4 and 24.3 A g⁻¹, respectively. Compared to the unsupported IrO₂ nanoparticle (Ir *t*BuOHΔ) reference catalyst from the same synthesis, a 4- and 4.6-fold increase versus the most active ATO-SG₁₂₀Δ-IrO₂-2X and ATO-SG₂₈₀Δ-2X sample could be observed.

A comparable difference is observed for unsupported calcined IrO₂ from the colloid synthesis (IrO₂ colloidΔ). The best-performing ATO-supported samples with ≈25 wt% Ir have a 7.3-fold (ATO-SG₁₂₀Δ-IrO₂-2X) and 8.4-fold (ATO-SG₂₈₀Δ-2X) higher Ir mass-based activity at η_{OER} = 300 mV than an industrial TiO₂-supported IrO₂ catalyst composed of IrO₂ nanocrystals with domain sizes of ≈4 nm (according to XRD analysis) on a nanocrystalline TiO₂ scaffold (Figure S21, Supporting Information) with a stated Ir loading of 75 wt% (Elyst Ir75, Umicore, Germany).^[34]

The significantly higher mass-based activity of the IrO₂/ATO versus the IrO₂/TiO₂ supported reference catalyst may at first be explained by an optimized dispersion of IrO₂ nanoparticles on the surface of the macroporous ATO resulting in a high catalytically accessible surface area. A further beneficial effect of the open macroporous morphology is an optimized mass transport through the catalyst layer enabling high current densities (Figure S22e,f, Supporting

Information) without a limitation through pore clogging by evolving oxygen, which is a possible scenario for a micro- or mesoporous structure composed of aggregated nanoparticles. IrO₂ nanoparticles oxidized at a temperature of 375 °C show a similar size of crystalline domains of tetragonal IrO₂ phase ($\approx 2\text{--}3$ nm) as the reference catalyst (≈ 4 nm), but a lower crystallinity (Figure 2a and Figure S21, Supporting Information). According to Geiger *et al.*, Ir(O_x) heated at ≈ 375 °C is not fully crystalline but at the upper temperature range of an intermediate phase between the amorphous IrO_x and thermal IrO₂ with an increased intrinsic activity compared to the thermal oxide phase at the expense of a lower conductivity.^[35]

For comparison with the literature, the best performing ATO supported Ir-based catalyst reported to our knowledge are high surface area (≈ 260 m² g⁻¹) mesoporous-ATO supported core-shell IrNi_x@IrO_x nanoparticles prepared by Nong *et al.*, which were obtained by electrochemical leaching of respective supported IrNi_x nanoparticles. The composite catalyst with a loading of ≈ 19 wt% Ir exhibits an OER activity of ≈ 90 A g_{Ir}⁻¹ at an overpotential of 280 mV.^[14] The reported 30% higher initial activity of this catalyst as compared to our best performing sample is however obtained for a more compact structure, with a high volumetric Ir performance density disadvantageous for the application in PEM electrolyzers.

Besides ATO supported catalysts, recently a nanostructured porous NTO with remarkably high conductivity of ≈ 440 S cm⁻¹ was introduced by Hufnagel *et al.* to support a ≈ 1 nm thin IrO₂ coating based on atomic layer deposition. The thin film catalyst with a low Ir-loading of ≈ 8 wt% thereby showed an onset potential of ≈ 250 mV and an OER activity of ≈ 654 A g_{Ir}⁻¹ at an overpotential of 460 mV, as compared to an onset potential of ≈ 215 mV and an activity of over 3200 A g_{Ir}⁻¹ for our catalyst at a slightly lower overpotential of 420 mV.^[36] The best performing IrO₂ catalyst supported by mesoporous NTO with a surface area of ≈ 83 m² g⁻¹ was reported by Hu *et al.*, with an onset potential as low as 200 mV for a 33 wt% Ir loaded catalyst. The maximum OER activity of ≈ 548 A g_{Ir}⁻¹ at an overpotential of 362 mV was thereby

measured for a 26 wt% Ir containing catalyst with an increased overpotential of 270 mV.^[18] In comparison, our catalyst shows a significantly higher mass based activity of $\approx 1100 \text{ A gr}^{-1}$ at a slightly higher overpotential of 380 mV.

The decreased activity of our introduced ATO-supported samples with low loading (8 and 15 wt% Ir) is attributed to an incomplete layer of IrO₂ nanoparticles on the porous ATO microparticle, whereas a complete layer is formed at 25 wt% Ir. As the conductivity of the ATO scaffold ($\approx 3.6 \text{ S cm}^{-1}$, Figure S2, Supporting Information) is lower than that of a layer of IrO₂ nanoparticles of similar particle size ($\approx 26 \text{ S cm}^{-1}$),^[37] the absence of a continuous conducting pathway through the IrO₂ layer limits the performance.

For the case of a the poor conductive TiO₂ support, Bernsmeier *et al.* have correlated catalyst conductivity for different Ir contents with the OER activity. They have demonstrated that the high performance values can be reached only for Ir loadings exceeding $\approx 25 \text{ wt}\%$ Ir, while below this threshold value practically no activity was observed. Furthermore, a minimum in the electrical conductivity of $\approx 1.0 \times 10^{-3} \text{ S cm}^{-1}$ in the catalyst films is suggested to eliminate negative effects of slow electron transport on the catalytic performance.^[38] The conductivity of the ATO scaffold used in our work exceeds this conductivity limit (as opposed to TiO₂), which explains the considerably high OER performance of our composite catalysts even at low Ir contents of 8 wt% and 15 wt%.

To further investigate the slightly reduced performance of low Ir loaded (<25 wt% Ir) catalyst, the trend in the conductivity of loosely compressed powders of IrO₂/ATO catalyst with varying Ir content as well as the IrO₂/TiO₂ reference catalyst were measured (Figure S22 and Table S2, Supporting Information). The conductivity of the ATO/IrO₂ composite catalyst is rather low for low Ir loadings of 8 and 15 wt% Ir (1.00×10^{-6} and $1.79 \times 10^{-5} \text{ S cm}^{-1}$, respectively). The electrocatalytic activity of the samples is however very high, with the values equaling or even exceeding those of the commercial IrO₂/TiO₂ reference catalyst with much higher Ir loading

(75 wt%) and much higher conductivity. The conductivity of the ATO/IrO₂ composite powders rises to $1.16 \times 10^{-2} \text{ S cm}^{-1}$ for the 25 wt% Ir sample (SG₁₂₀Δ-IrO₂-2X). Higher iridium contents of 33 and 40 wt% further increase the conductivity up to a value of 0.88 S cm^{-1} .

In comparison, a value of 4.42 S cm^{-1} was determined for the commercial IrO₂/TiO₂ reference catalyst with 75 wt% Ir under same measurement conditions. Due to the low compressive force applied by the in house constructed dc-conductivity measurement setup (Figure S23, Supporting Information) and thus limited contact between particles across the powder-pellet thickness, the absolute values are expected to be significantly underestimated. However, the measurements performed in similar conditions enable to estimate a trend among the equally prepared samples series (Table S2, Supporting Information).

As can be seen from the measured values, for the samples with Ir loading beyond 25 wt% (percolation threshold) the conductivity mainly depends on the Ir content, showing nearly linear dependence on the Ir loading. However, for the samples with very low Ir loadings below 25 wt% the conductivity of the support becomes a decisive factor, providing for a high electrocatalytic activity even without a direct contact between the IrO₂ nanoparticles. In total, there is no a linear correlation between the electrical conductivity and the electrocatalytic activity, as the commercial IrO₂/TiO₂ reference catalyst featuring the highest conductivity shows the lowest electrocatalytic activity among the investigated series.

The effect of limited conductivity in the low-iridium-loading samples (1/2X and 1X with 8 and 15 wt% Ir, respectively) becomes pronounced at higher current densities as shown in Figure S22 (Supporting Information). However, at low overpotentials of $\eta_{OER} < 380 \text{ mV}$, even samples with low Ir loading possess an Ir mass-based activity comparable to the industrial TiO₂-supported reference despite a significantly reduced Ir content. To investigate OER kinetics, rotating disc electrode (RDE) measurements of selected catalyst samples were performed under controlled reaction conditions (1600 rpm, 60 °C, O₂- purged electrolyte). The

TiO₂-supported IrO₂ reference (Elyst Ir75) exhibits an overpotential of 258 mV, Ir *t*BuOHΔ requires a slightly lower overpotential of 250 mV and the ATO microparticle-supported IrO₂ nanoparticles require only an overpotential of 215 mV to reach an OER current of 1 mA cm⁻² in the 75th scan cycle (Figure 5c,d and for more details, see Figure S24 in the Supporting Information). The RDE performance data thus confirm the synthesis of highly OER-active IrO₂ nanoparticles by the multistep synthesis introduced in this work and furthermore emphasize the importance of a nanostructured conductive support that can enhance the catalytic activity due to a high volume dispersion of the active iridium oxide nanoparticle phase.

To investigate possible electrochemical side reactions, cyclic voltammograms of ATO-supported IrO₂ were recorded over a broad potential range between the hydrogen evolution reaction (HER) and OER onset potentials (0.05 – 1.52 V vs. RHE) before and after each RDE activity measurement (Figure 5e,f, respectively). For all samples a very broad redox peak centered around 0.8 V versus RHE attributed to the Ir(III)/Ir(IV) redox reaction^[39,40] can be observed with increasing intensities in the order TiO₂/IrO₂ reference < Ir *t*BuOHΔ < ATO-SG₂₈₀Δ-IrO₂-2X. After the RDE activity measurements, the intensity of the aforementioned feature has notably increased for all samples (for more details, see Figures S24 and S25 in the Supporting Information). We assign this increase to a redox surface activation of the crystalline (thermal) iridium oxide in the first few cycles^[41] with the formation of a highly catalytically active surface hydroxide layer.^[42] This results in an increase in OER activity as seen by a decline of the required overpotentials during the early CV cycles in Figure 5d or by a shift of the CV curves shown in Figure S24 (Supporting Information).

Finally, the short (Figure 5g: 120 min) and intermediate term (Figure 5h: 20 h) corrosion behavior of the IrO₂ nanoparticle-based supported catalyst was investigated by chronopotentiometry measurements at a current density of 10 mA cm⁻². Unsupported IrO₂ nanoparticles (Ir *t*BuOHΔ) display a required potential of 1.72 V versus RHE remaining

constant over the measurement period. For ATO-supported particles (ATO-SG₂₈₀Δ-IrO₂-2X) the potential is lower by ≈ 70 mV at 1.65 V versus RHE. The TiO₂-supported reference catalyst (Elyst Ir75) shows a slight increase in the potential over the measurement period up to 1.72 V versus RHE after 120 min, matching that of unsupported IrO₂ nanoparticles.

However, intermediate term measurements show the same trend for unsupported as well as ATO-supported IrO₂ nanoparticles, with only a slight increase in potential to 1.74 and 1.66 V versus RHE after 20 h, respectively. In contrast to the catalyst particles with the conducting ATO support, the potential of TiO₂-supported IrO₂ reference catalyst constantly rises with time and reaches the highest measured end potential with 1.77 V versus RHE after 20 h in the chronopotentiometric measurement, which indicates a lower activity and stability as compared to the IrO₂ nanoparticle catalysts introduced in this work.

Small differences in the absolute potential obtained by the 120 min versus 20 h measurement period indicated by an offset of the $V-t$ curves are thereby attributed to slightly varying amounts of catalyst coated onto the FTO substrate. Deviations of the slope of the curves as visible for the TiO₂/IrO₂ reference however may originate from a slightly altered catalyst dissolution during the two different experiments, as manifested by a detachment of active material from the electrode. Electron microscopy of catalyst samples after OER measurements (Figure S26, Supporting Information) further confirms a rather stable iridium content in the electrodes for a chronopotentiometric current density of 10 mA cm⁻² (20 h) and 100 mA cm⁻² (1.5 h), amounting to 24 and 23 wt% Ir, respectively, for the ATO-SG₂₈₀Δ-IrO₂-2X sample with an initial Ir-loading of 25 wt%.

Contrarily, analysis of the antimony content indicates a leaching process during the OER at the applied potentials shown by a reduction from initially ≈ 4.3 at% Sb (Figure 1a) to below 3 at% Sb after the OER experiments (Figure S26, Supporting Information).

The stability of ATO as a catalyst support for proton exchange membrane fuel cells has been discussed in the literature.^[43-45] Surface segregation of antimony caused by the preparation method^[43] or by potential cycling^[45] were discussed to lead to Sb-dissolution in an acidic environment. This results in a reduced conductivity of the surface of the obtained core-shell structure that can directly affect the electrocatalytic performance of attached catalyst nanoparticles.^[45]

Geiger *et al.* recently investigated the corrosion stability of tin-oxide based catalysts (ATO, ITO, FTO) in acidic media and under applied potentials.^[46] They could show that these materials (dopants and SnO₂ host structure) possess a critical dissolution rate under cathodic potential. But also the anodic potential range for the thermodynamic stability of ATO is reported to be limited to theoretically 1.1 V versus RHE with measured critical Sb- and related Sn-dissolution upon anodic polarization,^[46] rendering the material inappropriate for an industrial long-term application at high potentials and current densities.

For an adoption of this model system for industrial use a more oxidation stable conductive oxide support such as fluorine-doped tin oxide (corrosion stable up to 2.7 V vs. RHE)^[46] or niobium-doped TiO₂ may therefore be employed. The overall high Ir mass-based activity of the synthesized iridium oxide catalyst is attributed to the small size of the spherical IrO₂ nanoparticles obtained by the synthesis approach and the low-temperature calcination that is known to result in an increased fraction of high-surface-energy crystal facets and defects which are associated with high OER activity.^[47]

However, the key factor for increased OER activity is the high Ir volume dispersion resulting from the homogeneous coating of nanoparticles onto the surface of the ordered porous conducting support. Catalysts prepared by the introduced multistep synthesis procedure provide two complementary current transmission pathways from the electrode contact to the reaction interface and thereby limit the series resistance and ensure electrical contact to

nanoparticles of the catalytically active phase. The comparably small mass-specific charge for the corresponding redox feature of the IrO₂/TiO₂ reference is attributed to a higher degree of crystallinity and slightly larger crystalline domain sizes of the thermal oxide resulting in a comparably low redox-active surface area with iridium being stable in the +IV oxidation state. The unsupported IrO₂ nanoparticles (Ir *t*BuOHΔ) as well as the ATO-supported nanoparticles (ATO-SG₂₈₀Δ-IrO₂-2X) oxidized at a low temperature possess small crystalline domains (Figures 2 and 3) and a moderate degree of crystallinity (as shown in Figure 2a and Figure S10, Supporting Information), therefore exhibiting an increased redox-active surface. For the well-dispersed IrO₂ nanoparticles on the porous ATO scaffold the accessible redox-active surface area is further increased as indicated by the increased mass-specific charge (Figure 5e,f).

8.4 Conclusion

This work introduces a multistep synthesis procedure for the homogeneous decoration of complex porous Sb-doped SnO₂ structures as an example for a conductive oxidic OER catalyst support for iridium nanoparticles in the range of 2 – 3 nm.

Detailed structural characterization of the synthesized inverse opal macroporous ATO-microparticle/Ir(O₂) model catalyst system thereby shows how to independently tune the morphology, porosity, and conductivity of an oxide support material through the ultrasonic spray pyrolysis of a sol–gel or nanoparticle precursor. Furthermore, the ATO/IrO₂ catalyst was thoroughly investigated by high-resolution (S)TEM imaging, which allowed for a detailed analysis of the catalyst particle distribution within the porous 3D structure by means of STEM tomography.

An approximation of the iridium volume dispersion in a thin film of porous microparticles returns a roughly 18 times lower iridium volume density than for a TiO₂-supported reference catalyst; this would allow for the fabrication of PEM electrolyzer anodes with strongly reduced Ir loading and retention of the film thickness required for electrolyzer operation. The ATO-microparticle/IrO₂ catalyst with 25 wt% Ir furthermore shows improved OER activity and stability compared to similarly prepared pure IrO₂ nanoparticles, presumably due to the homogeneous dispersion and stabilization of the small IrO₂ particles on the ATO surface.

The model catalyst system shown here significantly outperformed an industrial TiO₂-supported IrO₂ catalyst in Ir mass-based OER activity, underlining the advantage of a suitable oxide support morphology and a homogeneous distribution of the active material on a conductive support. On the other hand, even lower iridium loadings (≤ 15 wt% Ir) on the macroporous microparticle scaffold result in considerably lower catalytic performance, suggesting a major current transport pathway through the iridium oxide nanoparticle layer which is lacking in samples with a very low Ir-loading in which the nanoparticles do not form a continuous layer.

This emphasizes the need for a highly conductive support to effectively contact isolated catalyst nanoparticles. Overall, this study shows that combining iridium oxide nanoparticles with a suitable conductive and rationally designed porous oxide promises to be a suitable approach toward highly active anodes for PEM electrolyzers with drastically reduced iridium loading and increased long term stability.

8.5 Experimental

Synthesis of Macroporous ATO Microparticles (Oxidic Catalyst Support) by Spray Drying

The synthesis of macroporous ATO microparticles by USP is based on the USP synthesis of macroporous silica particles with polymer bead templating initially proposed by Iskandar *et al.*^[48] and later modified by Hieda *et al.*^[23] to obtain macroporous (Sb-doped) SnO₂ microparticles. For the synthesis of sol–gel based macroporous antimony doped tin-oxide microparticles, first antimony (III) acetate (224 μmol/67 mg, SIGMA-ALDRICH, 99.99% trace metals basis) was dissolved in ethanol (4 mL) by stirring for 1 h. The antimony solution was slowly added to 1.14 g (4.376 mmol) tin (IV) chloride (SIGMA-ALDRICH, 98% purity) under constant stirring. Possibly precipitated solids were dissolved by further stirring and by using an ultrasonic bath for 5 min. Finally, an aqueous PMMA bead colloid (120 or 280 nm, respectively) was added to the precursor solution to obtain a final polymer bead content of 5.85 wt% and a total metal–salt concentration of 180×10^{-3} M. The synthesis of PMMA beads with mean diameters of 280 and 120 nm was conducted according to the emulsion polymerization route described elsewhere resulting in an aqueous colloidal solution^[49,50] (see the Supporting Information for further details). The in-house constructed spray pyrolysis setup consists of a T-shaped high-temperature polypropylene discharge pipe system (OSTENDORF KUNSTOFFE) that connects the carrier gas flow (laboratory pressured air) at a flow rate of ≈ 60 L h⁻¹ to a 45 cm long quartz tube (25 mm diameter) placed in a single zone tube furnace (EUROTHERM 2404 temperature controller) with a temperature set point of 615 °C (609 °C oven temperature). The lower part of the pipe system including the precursor solution was sealed with a thin three-layer polyethylene cling film (TOPPITS) versus a water filled beaker with a 1.7 MHz FULOON 24V DC (700 mA, max. 400 mL aerosol h⁻¹) household ultrasonic nebulizer (SHENZHEN KULETONG TECHNOLOGY CO LTD) placed inside. Aerosol

collection was achieved with an in-house constructed filter system with polytetrafluoroethylene (PTFE) inset (50 mm diameter RCT-BIOFIL-PX-SU, 0.65 μm pore size, 60 μm thickness, REICHELT CHEMIETECHNIK GMBH + CO). The obtained ATO powder was calcined at 450 $^{\circ}\text{C}$ in air for 5 h with a heating rate of 1.4 $^{\circ}\text{C min}^{-1}$ to finish thermal curing and remove residual carbon traces. The spray pyrolysis of porous ATO based on a presynthesized ATO nanoparticle precursor followed the synthesis of nanoparticle-based titanium oxide microparticles proposed by Iskander *et al.*^[51] Highly conducting, 4.5 at% Sb-doped tin oxide nanoparticles with a size of about 3 nm were solvothermally synthesized in *tert*-butanol according to literature.^[25] ATO nanoparticle (3–4 nm) powder (200 mg) was dispersed in a mixture of ethanol (2.8 mL) and hydrochloric acid (37 wt%, 0.16 mL) by stirring for 2 h. The dispersion was mixed with an aqueous PMMA bead colloid (120 nm mean diameter) to obtain a 2 wt% dispersion of ATO/PMMA. After 15 min sonication and further stirring for 2 h, the spray drying was performed according to the synthesis of sol–gel based ATO particles with a furnace temperature of 500 $^{\circ}\text{C}$. The obtained product was further processed according to the method used for the sol–gel based microparticles.

Synthesis of Colloidal IrO_x Catalyst Nanoparticles (Ir Active Phase Precursor)

The synthesis of an iridium oxide nanoparticle colloid is based on an aqueous oxidation method introduced by Sutto^[26] with a further solvothermal treatment in *tert*-butanol introduced by Szeifert *et al.*^[52] For the synthesis of an iridium oxide nanoparticle colloid per reaction 0.075 mmol (30.09 mg) iridium (III) chloride hydrate (SIGMA-ALDRICH, 99% reaction grade) were dissolved in 4 mL bidistilled water (Millipore Q grade) and stirred for 1 h in air at room temperature. Subsequently the precursor solution was cooled with an ice bath and 0.5 mmol (35.5 mg) potassium superoxide powder (KO_2 , ABCR, 96.5% purity) was slowly added to the cooled solution within 1 min under continuous stirring and quenched after 1 min by addition of 2.5 mL of precooled methanol (analytical grade). For the synthesis of ATO

supported IrO_x catalyst or the synthesis of unsupported Ir catalyst the obtained yellow-green IrO_x nanoparticle colloid was either used after 30 min stirring time or further stirred overnight which resulted in the formation of a blue IrO_x colloid.

Conformal Coating of Oxidic Support (ATO Microparticles) with Ir Nanoparticles by Solvothermal Reduction in *t*BuOH

The solvothermal treatment of synthesized IrO_x colloid was performed in glass-lined stainless-steel autoclaves (Parr Series 4760 FH, PARR INSTRUMENT COMPANY). For the synthesis of unsupported Ir catalyst nanoparticles, per autoclave reaction 37.5–300 μmol previously prepared IrO_x colloid were added to 90 mL of prewarmed (60 °C) *tert*-butanol (GRÜSSING GMBH, 99% purity). An additional amount of water and methanol at a volume ratio of 2:1 were added to obtain a final volume of 180 mL. The solvothermal loading of macroporous ATO scaffold (0.49 mmol, 75 mg) microparticles with iridium nanoparticles was achieved by the reduction of iridium oxide colloid nanoparticles in the presence of dispersed scaffold microparticles during the solvothermal reaction in *tert*-butanol. Sealed autoclaves with internal temperature and pressure sensor were heated to 175 °C for 12 h with a temperature controlled (HEJU LTR2500, JUCHHEIM GMBH & CO. KG) ceramic heating mantle (KJT 950W) and kept under constant stirring. The reaction product was washed by centrifugation (7197 rcf, 15 min) with bidistilled water (Millipore Q grade, 18 MΩ). The product was redispersed in a few mL bidistilled H₂O and freeze-dried using an ALPHA 1-4 machine (MARTIN CHRIST GEFRIERTROCKNUNGSANLAGEN GMBH). Obtained powders of Ir nanoparticle loaded ATO scaffolds were characterized, used for the preparation of electrodes and further electrochemical measurements or calcined to obtain IrO_x nanoparticle coated porous ATO scaffold. Calcination of Ir nanoparticles and Ir-NP@porous-ATO-microparticles (solvothermally treated IrO_x colloid) was performed in a NABERTHERM laboratory oven

(model N15/65SHA) at 375 °C in air with a heating rate of 1.94 °C min⁻¹ and a dwell time of 1 h.

Physicochemical Characterization

Wide-angle X-ray diffraction analysis was carried out in transmission mode using a STOE STADI P diffractometer with Cu-K_{α1} radiation ($\lambda = 1.54060 \text{ \AA}$) and a Ge(111) single crystal monochromator equipped with a DECTRIS solid state strip detector Mythen 1K. Powder XRD patterns of the samples were collected with an omega-2theta scan in the 2θ range from 5° to 90° with a step size of 1° and fixed integration time of 25 – 35 s per step and a resolution of 0.05°. The size of the crystalline domains was calculated from the XRD patterns for the Ir 111 (ICDD#00-006-0598), IrO₂ 112 (ICDD#00-015-0870), and SnO₂ 110 (ICDD#00-041-1445) reflection, respectively, using the Scherrer equation. Raman spectroscopy was carried out using a LabRAM HR UV–Vis (HORIBA JOBIN YVON) Raman Microscope (OLYMPUS BX41) with a SYMPHONY CCD detection system and a He–Ne laser ($\lambda = 633 \text{ nm}$). Spectra were recorded using a lens with a 10-fold magnification in the range from 100 to 1000 cm⁻¹ with filters of *OD* 0.3–0.6. Spectrum accumulation mode was used with integration times of 30 s per spectrum and 600 cycles. The data acquisition was carried out with LabSpec software. HR-TEM and HAADF-STEM images as well as electron diffraction patterns were recorded using a FEI Titan Themis 80-300 transmission electron microscope with aberration correction of the probe-forming lenses operated at 120 kV or 300 kV, respectively. EDX was performed using a SuperX windowless, four quadrant Silicon drift detector with a solid angle of 0.7 sr. TEM specimens were prepared by dispersing IrO_x colloids, catalyst nanoparticles, or Ir loaded ATO microparticles respectively in a 1:1 (v:v) ratio of water to ethanol and depositing them on a carbon-film coated copper grid, followed by drying in air. HAADF-STEM tilt series of 29 images for TEM tomography were recorded in 5° steps from -70° to +70°. For a reconstruction of the 3D intensity volume and a presentation of different phases of Ir and ATO, respectively,

a masked simultaneous iterative reconstruction technique (SIRT) with further refinement by a discrete algebraic reconstruction technique (DART) were employed (see the Supporting Information for further details). SEM images were obtained with a FEI Helios Nanolab G3 UC scanning electron microscope equipped with a field emission gun operated at 3 – 5 kV. SEM specimens were prepared by dispersing dried catalyst nanoparticles, microparticles, and composites in a (1:1 v/v) water to ethanol ratio on FTO or Si substrates that were glued onto a stainless-steel sample holder with silver lacquer. EDX measurements were performed at an operating voltage of 20 kV with a X-Max^N Silicon Drift Detector with 80 mm² detector area (OXFORD INSTRUMENTS) and AZTec acquisition software (OXFORD INSTRUMENTS). For the analysis of the porosity of the samples, the calcined samples were degassed for 12 h at 120 °C under vacuum. Nitrogen sorption measurements were performed on a QUANTACHROME Autosorb-1 instrument at the boiling point of liquid nitrogen (77 K). The specific surface area was determined with the Brunauer–Emmett–Teller (BET) method at $p/p_0 = 0.05-0.2$. The pore size distribution was calculated using a nonlocal DFT equilibrium model for silica with cylindrical pores. XPS analysis was conducted with the non-monochromated Mg-K α radiation of a VSW TA10 X-ray source and a VSW HA100 hemispherical analyzer. For the XPS measurements the nanoparticles were drop-casted on silicon substrates in air before the transfer to the UHV chamber. Peaks were fitted using a convolution of a Doniach–Šunjić-function^[53] and a Gaussian function with linear background subtraction. If possible, the carbon 1s peak was calibrated to 284.8 eV to compensate for charging effects. An Ir 4f_{7/2} core electron binding energy of 60.8 eV was assigned to metallic Ir(0) and an Ir 4f_{7/2} binding energy of 61.9 eV was assigned to Ir(IV)O₂.^[32] Conductivity measurements of macroporous ATO microparticles were carried out on an HMS 3000 apparatus (ECOPIA) in the Van der Pauw geometry (5 mm separation of electrodes). Powder samples were measured in form of pellets that were compressed for 10 min at 150 kg cm⁻².

Conductivity measurements of ATO/IrO₂ and commercial TiO₂ supported reference catalyst were conducted due to restrictions on sample volume on an in-house constructed dc-conductivity measurements cell on loosely compressed powders by recording $I-V$ curves between -5 to +5 V by an AUTOLAB 302N.

Electrochemical Characterization

Unsupported IrO_x, IrO₂ nanoparticles and ATO supported IrO₂ nanoparticles were dispersed in 1:1 (v/v) H₂O to isopropanol and drop-casted onto conducting FTO glass or Au-coated QCM sensors (14 mm, 5 and 10 MHz AT-cut Cr/ Au crystals from KVG QUARTZ CRYSTAL TECHNOLOGY GMBH and QUARTZ PRO AB). Electrodes were masked with PTFE tape to leave a circular electrode area of 0.196 and 0.126 cm², respectively. Prior to each measurement, the samples were either dried at 60 °C or calcined at 375 °C in air. The frequency of uncoated and coated QCM sensor crystals was determined with a QCM200 5 MHz measurement system (STANFORD RESEARCH SYSTEMS INC.) and an openQCM 5/10 MHz measurement system (NOVAETECH SRL). Deposited mass loadings on QCM chips were calculated according to the Sauerbrey equation^[54] from determined frequency differences Δf , an overlapping electrode area A of 0.196 cm² and a sensitivity factor C_f of 56.6 and 4.4 Hz μg^{-1} cm² for 5 and 10 MHz AT-cut crystals, respectively. All electrochemical measurements at room temperature were carried out in a three-electrode setup with a quartz cell filled with 20 mL 0.5 M H₂SO₄ (SIGMA-ALDRICH, Titripur volumetric standard) as electrolyte using an PGSTAT302N potentiostat/galvanostat (METROHM AUTOLAB B.V.) equipped with a FRA32 M impedance analyzer connected to a Hydroflex reversible hydrogen electrode (GASKATEL Gesellschaft für Gassysteme durch Katalyse und Elektrochemie mbH) or Hg/HgSO₄/K₂SO₄ (sat.) (REF601, RADIOMETER ANALYTICALHACH COMPANY) for cyclic voltammetry and chronopotentiometry measurements, respectively. The electrochemical activity of catalysts on FTO and QCM substrates was measured by iR -drop

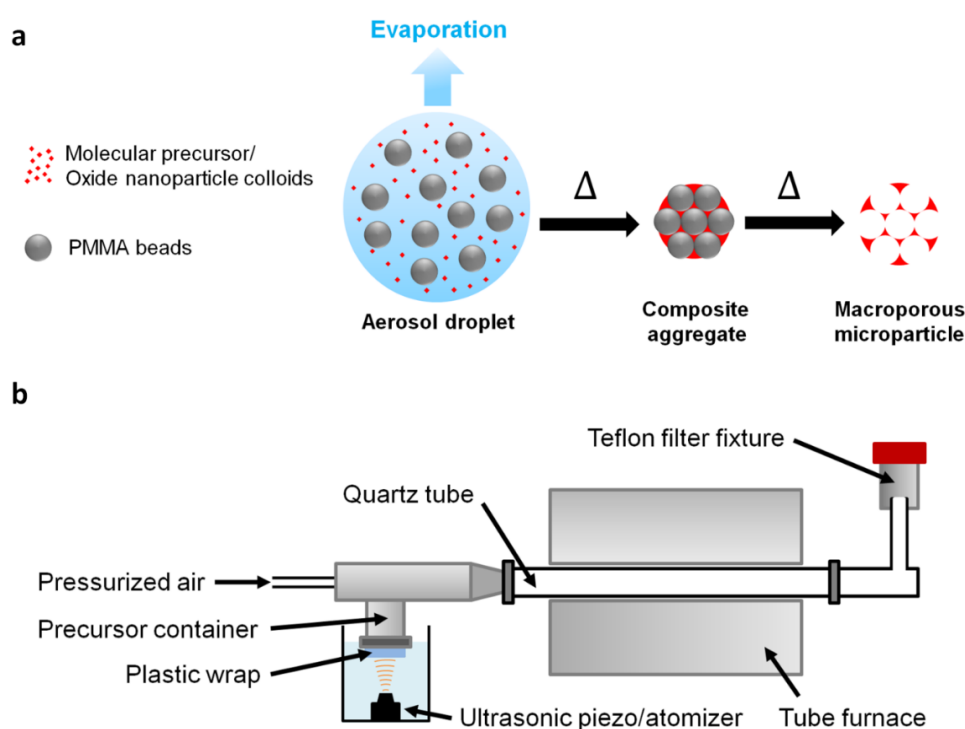
corrected linear sweep voltammetry (LSV) in a potential window of 1.0 – 1.8 V versus RHE and 1.0 – 1.65 V versus RHE, respectively, in 10 scan cycles with a scan rate of 10 mV s⁻¹. Impedance spectroscopy data at 0.5 V versus RHE was recorded prior to each measurement to determine the corresponding electrolyte resistance (95%) from the high frequency region. Iridium mass-based catalyst activity was either directly calculated with measured QCM determined mass loadings or calculated from the coating volume (3 – 15 μL) of a dispersion of known concentration (2 mg mL⁻¹) in combination with the Ir ratio in ATO/Ir(O₂) catalysts determined by SEM/EDX (mean value of at least three independent measurements). Current densities were determined from the mean value of capacity current-corrected (mean current in the potential region 1.0 – 1.23 V vs. RHE) anodic and cathodic scans of the respective LSV cycle. Stability measurements of electrodes (active material corresponding to 15 μg_{Ir} (76 μg_{Ir} cm⁻²) deposited on FTO glass substrates) were performed with an Hg/HgSO₄/K₂SO₄(sat.) reference electrode at room temperature under constant stirring of the electrolyte. Potentials versus the reversible hydrogen electrode E_{RHE} were calculated by measuring the open circuit potential of the Hg/HgSO₄/K₂SO₄(sat.) reference electrode against a Hydroflex RHE (GASKATEL Gesellschaft für Gassysteme durch Katalyse und Elektrochemie mbH) before and after each chronopotentiometry measurement and by shifting the measured potential accordingly. RDE measurements were conducted with an MSR Electrode rotator with mirror finished polished 5 mm diameter glassy carbon disc insets (PINE RESEARCH INSTRUMENTATION) connected to an Autolab PGSTAT302N potentiostat/galvanostat equipped with a FRA32 M impedance analyzer (METROHM AUTOLAB B.V.) and an in-house constructed glass/silicone cell with Luggin-capillary for the reference electrode compartment. Electrolyte temperature of 60 °C was maintained by an oil bath with external stirrer and monitored with an immersed silicone coated K-element temperature sensor. The Nernst potential for water oxidation was kept constant by continuous

O₂ (AIR LIQUIDE, AlphaGaz2 N5 purity) purging of the electrolyte (0.5 M H₂SO₄, SIGMAALDRICH, Titripur volumetric standard). Catalyst loadings of 50 μg_{Ir} cm⁻² (10 μg_{Ir} per disc) were drop-casted on cleaned glassy carbon discs and dried at 60 °C before applying 10 μL of a 1:100 dilution of a Nafion perfluorinated resin solution (SIGMA-ALDRICH, 5 wt% in lower aliphatic alcohols and water (15 – 20% water)) in a H₂O/*i*PrOH mixture (1:1 v/v). The electrolyte resistance was determined before and after each RDE measurement in the high frequency region of recorded impedance spectra at 0.5 V versus RHE. Due to low current densities reached in the measurement protocol and repeatedly low electrolyte resistance values around 5 Ω, an *iR* drop correction of the recorded data was not performed. The applied measurement protocol consisted of 75 LSV cycles starting from 1.0 V versus RHE. The upper vertex potential was defined to be at a current density of $j = 1 \text{ mA cm}^{-2}$ ($i_{\text{abs}} = 0.2 \text{ mA}$, $A = 0.196 \text{ cm}^2$). Reported current densities were determined from the mean value of capacity current (mean value in potential region 1.0–1.23 V vs. RHE) corrected anodic and cathode scans for a given overpotential η_{OER} of the respective scan cycle. Extracted overpotentials η_{OER} for each cycle required to reach an OER current of 1 mA cm⁻² were corrected for the capacitive current and calculated as a mean of anodic and cathodic scan. Additional cyclic voltammetry measurements over the potential range of 0.05 – 1.52 V versus RHE were performed during RDE measurements to identify redox active features and to compare the electrocatalytically active surface area of catalyst samples. 3 cyclic voltammograms at a scan rate of 50 mV s⁻¹ were therefore recorded prior to each RDE measurement (as described above), after 50 and after 75 RDE LSV cycles.

8.6 Supporting Information

I. Synthesis of macroporous Sb:SnO₂ (ATO) microparticles as catalyst support

Following Scheme S1 depicts the concept and synthesis scheme of ultrasonic spray pyrolysis (USP) of macroporous oxide microparticles employed for the fabrication of inverse opal Sb-doped SnO₂ microparticles.



Scheme S1 Concept and synthesis scheme of ultrasonic spray pyrolysis (USP) of macroporous oxide microparticles. (a) Concept of atomization of an aqueous PMMA / precursor (molecular or oxide nanoparticle) mixture with subsequent solvent evaporation and template pyrolysis in temperature gradient to form macroporous oxide microparticles. (b) Schematic representation of USP setup with ultrasonic atomizer, T-shaped polypropylene tube system, tube furnace and teflon filter system for generated aerosol particles.

The ultrasonic probe operated at 1.7 MHz in the USP setup generated aerosol droplets with a sizes of about 2.5 μm estimated from the synthesis parameters and based on ultrasonic nebulization theories.^[55] Obtained powders of the spray-drying process were analyzed by X-ray diffraction, as shown in Figure S1a. Diffraction patterns of the particles (NP₁₂₀, SG₁₂₀ and SG₂₈₀) prepared by USP as well as pre-synthesized ATO nanoparticles show broad reflections at positions in agreement with the cassiterite (SnO₂) structure with crystalline domain sizes of

3 - 5 nm for NP₁₂₀ and 4-5 nm for SG₁₂₀/SG₂₈₀ particles, respectively, according to Scherrer's equation. Due to the similar crystal structure of ATO and the undoped SnO₂ cassiterite phase, the low Sb doping concentration of ~4 at% Sb and the line broadening, a small peak shift caused by changed unit cell parameters cannot be observed. The Sb doped microparticles (SG₂₈₀Δ) thereby display a very similar diffraction pattern (Figure S1b) to that of undoped SnO₂ sol-gel based microparticles (SG₂₈₀Δ w/o Sb) without any side phase visible indicating a successful incorporation of Sb ions into the cassiterite host structure. Precursor ATO nanoparticles from a solvothermal synthesis in *tert*-butanol exhibit an increased line broadening indicating a domain size of about 3 nm (acc. to Scherrer's equation) which corresponds to the size of individual nanocrystals according to literature.^[25] Diffraction patterns of porous microparticles thermally cured at 450 °C (NP₁₂₀Δ, SG₁₂₀Δ, SG₂₈₀Δ) appear unchanged in peak positions or line broadening, indicating no growth of crystalline domains upon heating. Besides the marked peaks, attributable to a slightly distorted cassiterite phase, no side phases are visible in the diffraction data.

The phase purity of synthesized porous microparticles was further investigated by Raman spectroscopy, which, unlike X-ray diffraction, is sensitive towards amorphous phases. Raman spectra of ATO particles (SG₁₂₀Δ /SG₂₈₀Δ) generally match the spectrum of undoped SnO₂ (SG₂₈₀Δ w/o Sb) particles plotted in Figure S1c. Characteristic bands at 630 cm⁻¹ (A_{1g}) and 775 cm⁻¹ (B_{2g}) of the cassiterite phase are located at the positions reported in the literature,^[56-58] whereas the E_g band (477 cm⁻¹) is blue-shifted by ~25 cm⁻¹ and 50 cm⁻¹ for all sol-gel microparticles. The band at 333 cm⁻¹ (S1) visible in the spectrum of ATO precursor nanoparticles can be attributed to a disorder-activated vibrational mode of the nanosized ATO phase.^[58]

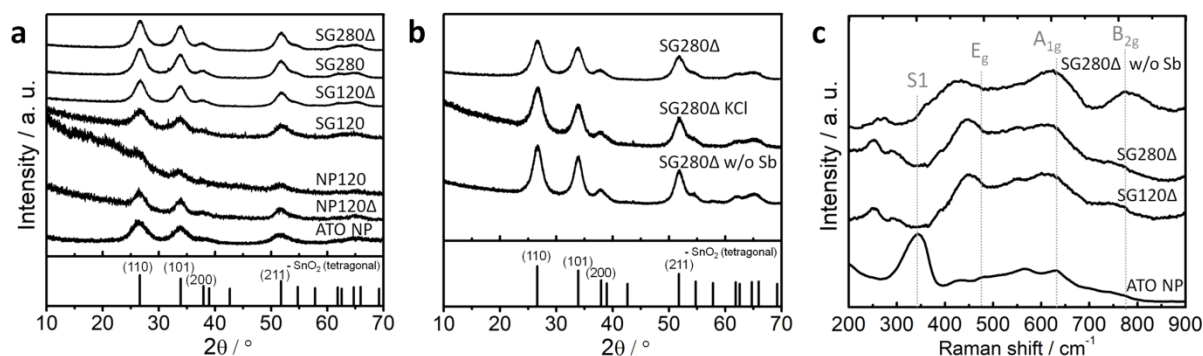


Figure S1 X-ray diffraction pattern and Raman spectra of sol-gel (SG) and nanoparticle (NP) based SnO_2/ATO microparticles with chloride post-treatment. (a) XRD patterns of microparticle precursor nanoparticles (ATO NP), nanoparticle (NP_{120}) and sol-gel derived ATO microparticles before (SG_{120} , SG_{280}) and after thermal curing ($\text{SG}_{120\Delta}$, $\text{SG}_{280\Delta}$). (b) XRD patterns of thermally cured undoped ($\text{SG}_{280\Delta}$ w/o Sb) and Sb doped ($\text{SG}_{280\Delta}$) ATO microparticles and with subsequent solvothermal reaction in presence of KCl ($\text{SG}_{280\Delta}$ KCl; High chloride concentration control; 12 mmol KCl, 0.84 mmol ATO. SnO_2 (cassiterite) pattern ICDD card number 00-041-1445 (black) (tetragonal symmetry, $a = b = 4.7382(4)$ Å, $c = 3.1871(1)$ Å, $\alpha = \beta = \gamma = 90^\circ$). (c) Raman spectra of precursor nanoparticles (ATO NP) and sol-gel derived thermally cured ATO microparticles ($\text{SG}_{120\Delta}$, $\text{SG}_{280\Delta}$) and undoped SnO_2 microparticles ($\text{SG}_{280\Delta}$ w/o Sb). The bands at 630 cm^{-1} (A_{1g}), 477 cm^{-1} (E_g), 775 cm^{-1} (B_{2g}) correspond to the cassiterite (SnO_2) phase.^[56-58] The band at 333 cm^{-1} (S1) can be attributed to a nanosized ATO phase.^[56]

To determine the conductivity of the synthesized ATO phase present in the porous particles, pellets of the respective samples were prepared by hydraulic pressing. On these, 4-point dc measurements in the Van-der-Pauw geometry were performed. Figure S2a and b show SEM images of pressed pellet surfaces of doped ($\text{SG}_{280\Delta}$) and undoped ($\text{SG}_{280\Delta}$ w/o Sb) microparticles that reveal (Figure S2b and d) a complete collapse of the porous structure of the microparticles upon compression at ~ 14.7 MPa required for pellet formation. Comparison of the dc-conductivities measured for $\text{SG}_{280\Delta}$ (3.6 S cm^{-1}) and $\text{SG}_{280\Delta}$ w/o Sb ($3.8 \times 10^{-4}\text{ S cm}^{-1}$) shows that the addition of Sb in the USP synthesis results in the formation of a highly conductive ATO phase. The specific conductivity of single intact ATO microparticles on the microscale is expected to be even higher due to missing grain boundaries and cracks present in the pellets which lower the macroscopic measurable conductivity^[25, 59]. The measured conductivity value of $\sim 3.4 \times 10^{-2}\text{ S cm}^{-1}$ for solvothermally treated ATO microparticles in presence of a high KCl salt concentration (Figure S2e,f) shows that even high salt concentrations do not lead to a loss in conductivity during the solvothermal reaction. This experiment should show that low concentrations of chloride originating from the IrCl_3 precursor

introduced in the solvothermal reaction by the addition of the IrO_x colloid do not negatively affect the conductivity of the scaffold. The measurements should further indicate that the final ATO supported IrO_2 catalyst possesses a considerable conductivity (beneficial for the electrochemical activity) originating from the ATO scaffold and not only from the IrO_2 shell. The decreased absolute value of the chloride treated sample ($\text{SG}_{280\Delta}$ KCl) vs. the non-treated ATO sample ($\text{SG}_{280\Delta}$) is mainly attributed to the differences in the quality of prepared pellets as shown in by SEM images (Figure S2e,f) and not attributed to an altered intrinsic conductivity of the material. Images of the chloride treated sample show a rather inhomogeneous surface with cracks opposed to the rather crack-free surface of the Sb-doped (Figure S2a, b) and undoped (Figure S2c,d) SnO_2 pellets.

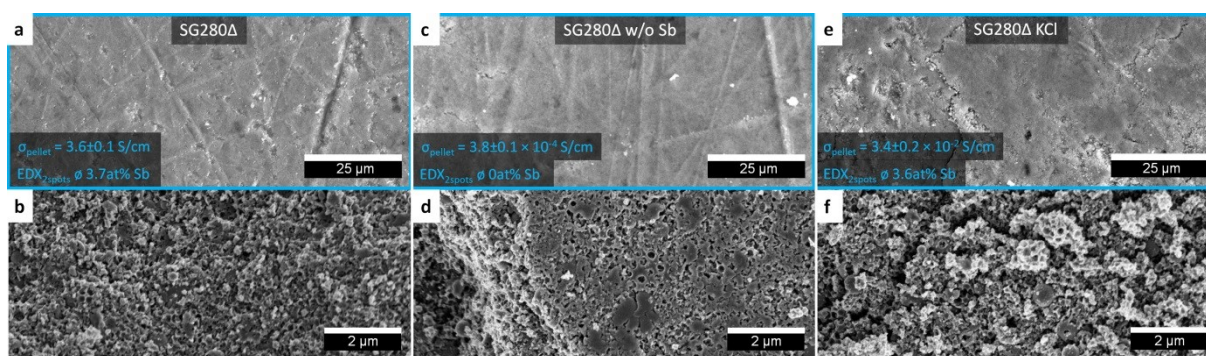


Figure S2 SEM micrographs of SnO_2 and ATO based pellets after conductivity measurements. SEM images with energy dispersive X-ray analysis (a, c, e) of ATO ($\text{SG}_{280\Delta}$; a, b), SnO_2 (c, d; $\text{SG}_{280\Delta}$ w/o Sb) and ATO with KCl high salt (12 mmol KCl, 0.84 mmol ATO) solvothermal post-treatment (e, f; $\text{SG}_{280\Delta}$ KCl).

Antimony doping was qualitatively confirmed by X-ray photoelectron spectroscopy (see following Figure S3) in thermally cured 280 nm PMMA templated sol-gel based ATO microparticles. $\text{Sn } 3d_{3/2}$ (495.2 eV) and $\text{Sb } 3d_{3/2}$ (540.3 eV) were fitted using a convolution of a Doniach-Šunjić-function and a Gaussian function with linear background subtraction to confirm the presence of Sn (Figure S3a) and Sb (Figure S3b).

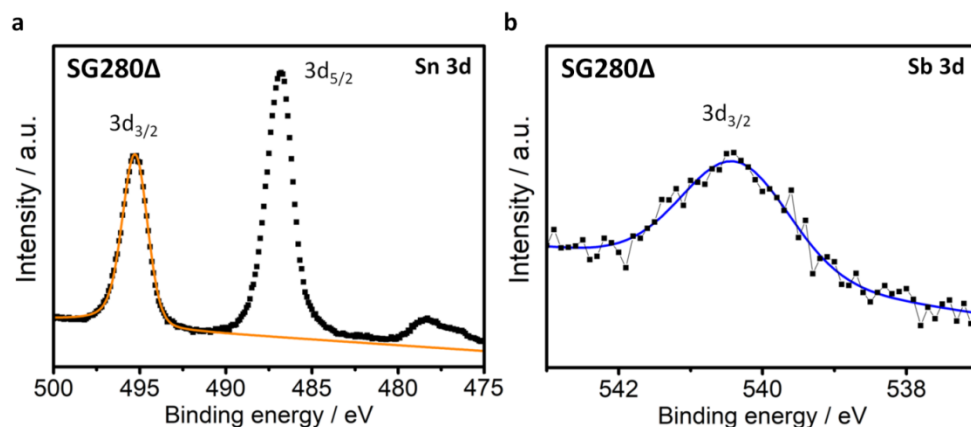


Figure S3 X-ray photoelectron spectroscopy (XPS) spectra of 280 nm PMMA templated sol-gel based ATO microparticles from ultrasonic spray pyrolysis after thermal curing. Sn 3d_{3/2} (495.2 eV) and Sb 3d_{3/2} (540.3 eV) fitted using a convolution of a Doniach-Šunjić-function and a Gaussian function with linear background subtraction confirming presence of Sn and Sb.^[32, 53]

Scanning electron microscopy images of sol-gel (Figure S4a) and ATO nanoparticle based microparticles (Figure S5) templated by 120 nm PMMA beads confirm the inverse opal morphology. Quantification of the particle size for templated sol-gel based ATO particles after thermal curing (SG₁₂₀Δ) returned a mean diameter of ~790 nm (N=1138). SEM images at higher magnifications reveal an open porous structure on the particle outer surface with connections to underlying pores. Quantification of the outer pore size (diameter) returns 55-75 nm (Ø 65 nm, N=137). Quantification of sol-gel based ATO particles templated by 280 nm PMMA beads (manuscript Figure 1a) returned a mean diameter of 850 nm (N=1161) with uniform pore sizes of 150-190 nm (Ø 172 nm, N=191). A more detailed investigation of the microstructure, crystallite size and phase was performed by high resolution transmission electron microscopy. TEM images depicted in Figure 1b-d and Figure S4b-d for SG₂₈₀Δ and SG₁₂₀Δ, respectively, confirm the existence of an accessible open porous structure. Furthermore, the pore sizes for 120 and 280 nm PMMA templated particles was quantified to be ~83 nm (Ø inner pore diameter, N=13) and ~232 nm (Ø inner pore diameter, N=27) according to HR-TEM images as shown in Figure S4c,d and Figure 1c,d respectively, which is in good agreement with the pore sizes determined by SEM. Thus, during the pyrolysis reaction, pore shrinkage by ~30 % for SG₁₂₀Δ and ~17 % for SG₂₈₀Δ, respectively takes place.

The TEM images shown in Figure S4c,d and Figure 1c, d respectively, show nanocrystals of about ~3-4 nm that act as building blocks for the porous microparticle structure independent of the templating bead size. The existence of small interconnected ATO crystals is in agreement with the line broadening observed in XRD patterns (Figure S1a and b), the shift of the E_g band in Raman spectroscopy (Figure S1c) and the textural porosity observed in the nitrogen sorption isotherms (Figure S6), which is thought to be caused by small voids between the nanocrystals. The images were further used to confirm the cassiterite parent phase of the present ATO nanocrystals on the local scale by determining the lattice spacings of individual nanocrystals as indicated in Figure 1d. Energy dispersive X-ray (EDX) analysis points to a Sb doping concentration of 4.2 at% for the $SG_{120}\Delta$ (value noted in Figure S4a) and 4.3 at% for $SG_{280}\Delta$ (Figure 1a) respectively, which is in good agreement with the Sb content of 4.8 at% in the precursor solution. EDX value stated derived as a mean value of at least three independent EDX measurements recorded at different magnifications.

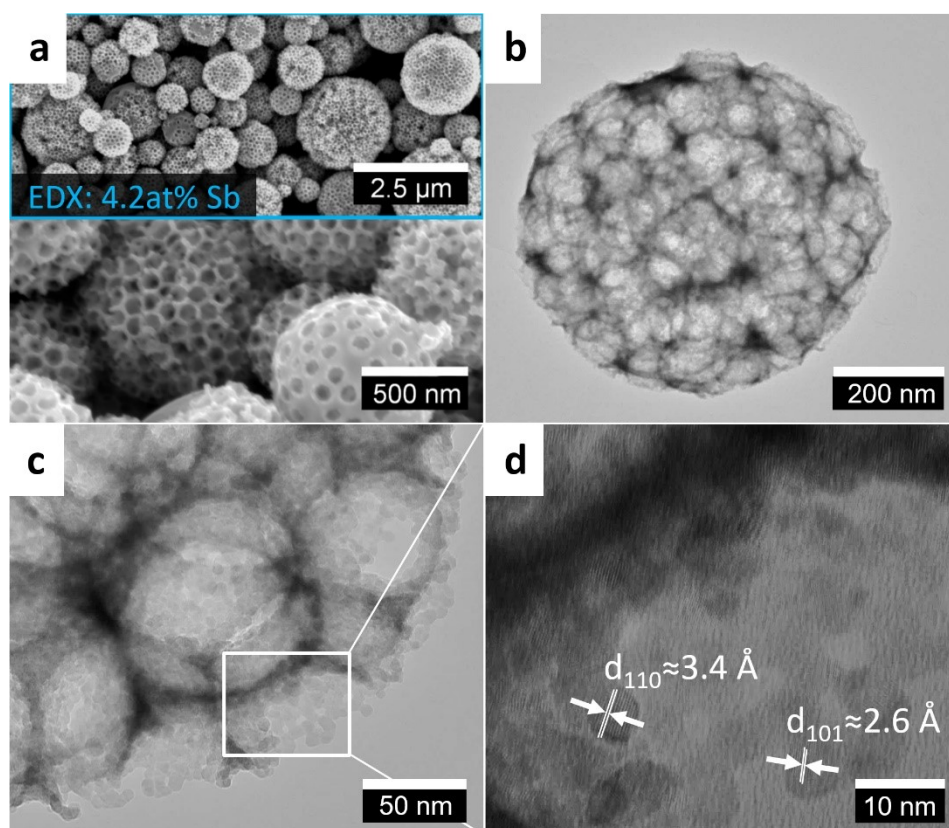


Figure S4 Scanning and transmission electron micrographs of ATO sol-gel based porous microparticles templated by 120 nm PMMA beads. (a) Overview of ATO microparticle (ATO-SG₁₂₀Δ) morphology with energy dispersive X-ray analysis. Sb at% derived from multi-spot EDX measurements. TEM image of single microparticle (b), magnification of porous structure (c) and high-resolution image with individual ATO nanocrystal building blocks of sol-gel based ATO microparticles templated with 120 nm PMMA beads (SG₁₂₀Δ).

Besides the sol-gel based approach, pre-synthesized ATO nanoparticles with an Sb doping level of ~5 at% were used in a USP synthesis. The resulting porous microparticles NP₁₂₀Δ, shown in Figure S5, show a comparable morphology to the SG₁₂₀Δ particles with slightly increased pore wall thickness (Figure S5b) and a Sb content of 5.9 at%, determined from EDX measurements.

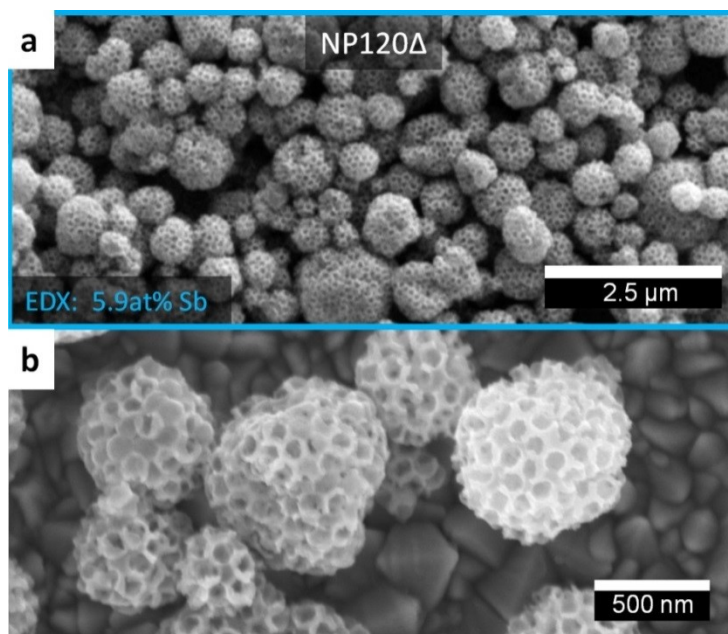


Figure S5 Scanning electron micrographs of ATO nanoparticle based porous microparticles. (a) Overview with energy dispersive X-ray analysis and (b) single microparticles in high magnification of porous nanoparticle based ATO microparticles templated with 120 nm PMMA beads (NP₁₂₀Δ).

To check the accessibility and interconnectivity of the macropores of the microparticles nitrogen sorption isotherms as shown in Figure S6 were recorded. Both samples (SG₁₂₀Δ and SG₂₈₀Δ as well as undoped SG₂₈₀Δ w/o Sb) show a type III sorption isotherm with minor contribution of a type I isotherm, corresponding to a mainly macroporous or non-porous adsorbent with minor contribution of microporosity originating from textural porosity of interconnected small crystalline domains as indicated by the diffraction pattern (Figure S1a, b) and by the high-resolution TEM image (Figure 1d and Figure S4d). A Brunauer-Emmett-Teller surface area of 54 and 52 m² g⁻¹ was determined for 120 and 280 nm PMMA templated microparticles respectively. Direct evidence of small macropores of about 70 nm for sample SG₁₂₀Δ is given by the pore size distribution shown in inset of Figure S6a which is in good agreement with the pore size quantification by SEM and TEM. The pore size distribution of SG₂₈₀Δ does not show any porosity beyond a minor amount of micropores from textural porosity which is caused by limitations of the nitrogen sorption technique with respect to the detection of macropores as present in the SG₂₈₀Δ and SG₂₈₀Δ w/o Sb sample. Sorption data shown further proves that Sb doping in the sol-gel based microparticles does not lead to a

change of the porous structure as the same BET area of $54 \text{ m}^2 \text{ g}^{-1}$ is obtained for undoped particles ($\text{SG}_{280}\Delta$ w/o Sb; Figure S6c) as well as for the doped sample ($\text{SG}_{280}\Delta$; Figure S6b).

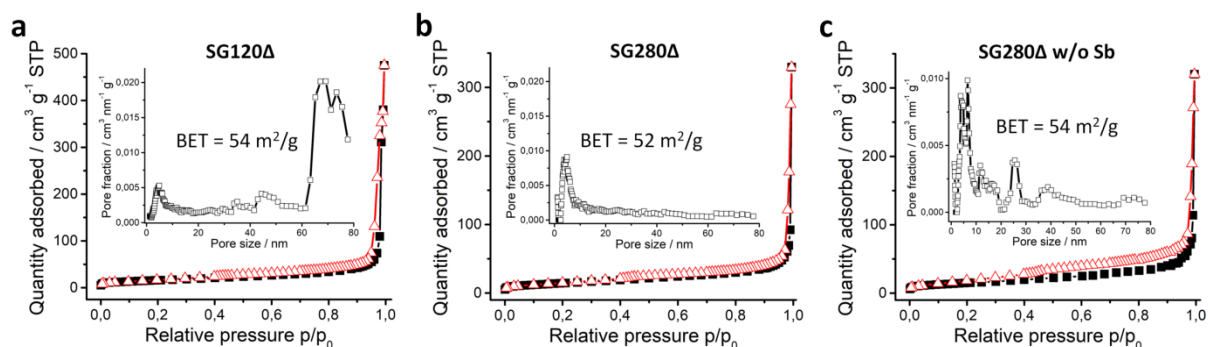


Figure S6 Nitrogen sorption isotherm of macroporous ATO and SnO_2 microparticles. (a) 120 nm ($\text{SG}_{120}\Delta$) and 280 nm ($\text{SG}_{280}\Delta$) PMMA templated macroporous ATO (a, b) and SnO_2 (c) microparticles ($\text{SG}_{280}\Delta$ w/o Sb) with Brunauer-Emmett-Teller (BET) area and pore size distributions (non-local DFT model) as inset.

II. Synthesis of dispersible Iridium(oxide) nanoparticles

Following Section II describes supporting Information for the synthesis and characterization of Ir-species involved in the introduced multi-step synthesis (Figure S7a, c and d) procedure for the homogeneous coating of porous oxide structures as well as of a IrO_2 nanoparticle reference catalyst obtained by the calcination of the IrO_x precursor (IrO_x colloid Δ , Figure S7b).

For a quantification of nanoparticle sizes HR-TEM and STEM images (Figure S7) of the different Ir-species were analyzed. Particle diameter in the main text are stated as a mean value of individual particles with number N. Size quantification of IrO_x colloid, calcined IrO_x colloid (IrO_x colloid Δ) and metallic Ir nanoparticles (Ir *t*BuOH) returned mean diameters of ~ 2.4 nm (N=145) (Figure 2e, Figure S7a), ~ 3.0 nm (N=73) (Figure 2g, Figure S7b) and ~ 3.2 nm (N=63) (Figure 2i, Figure S7c), respectively.

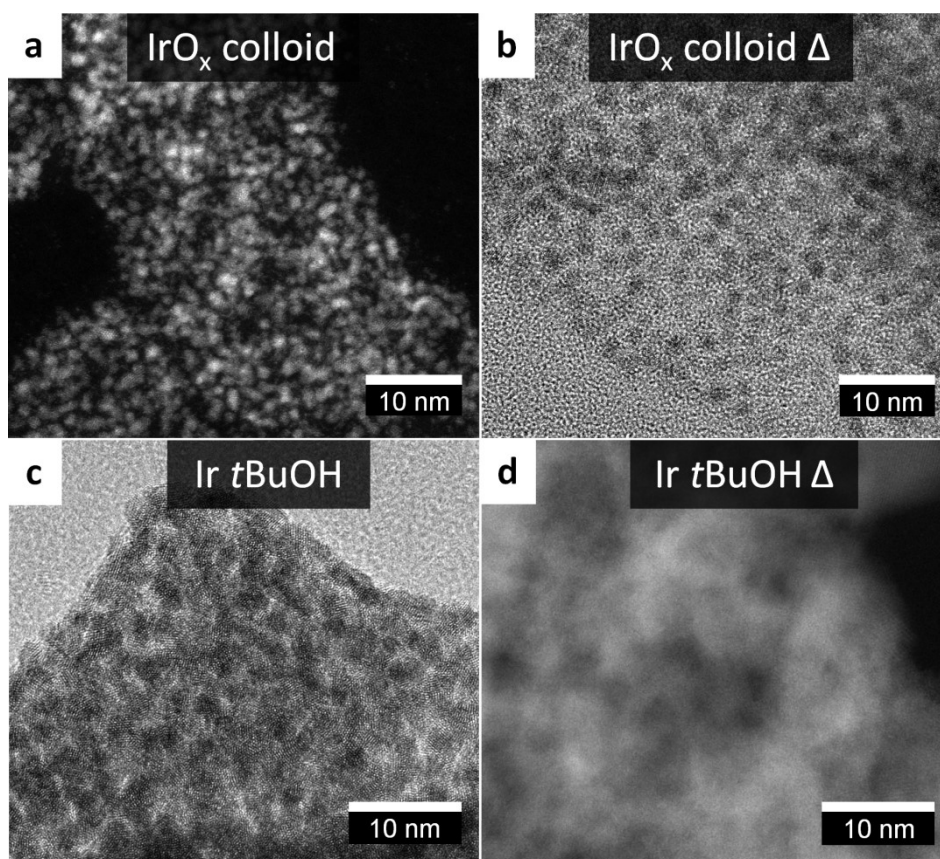


Figure S7 (Scanning) transmission electron micrographs of iridium and iridium oxide nanoparticle phases. Hydrous iridium oxide colloid before (a, IrO_x colloid) and after thermal oxidation (b, IrO_x colloidΔ). Metallic iridium nanoparticles after solvothermal treatment of IrO_x colloid before (c: Ir tBuOH) and after thermal oxidation (d: Ir tBuOHΔ) to the oxide phase.

Following Figure S8 shows an agglomerate of hydrous IrO_x colloid nanoparticles (Figure S8a) that are reduced and crystallize in the electron beam evidenced by a visible growth and aggregation of nanoparticles (Figure S8b) with an illumination period of several seconds.

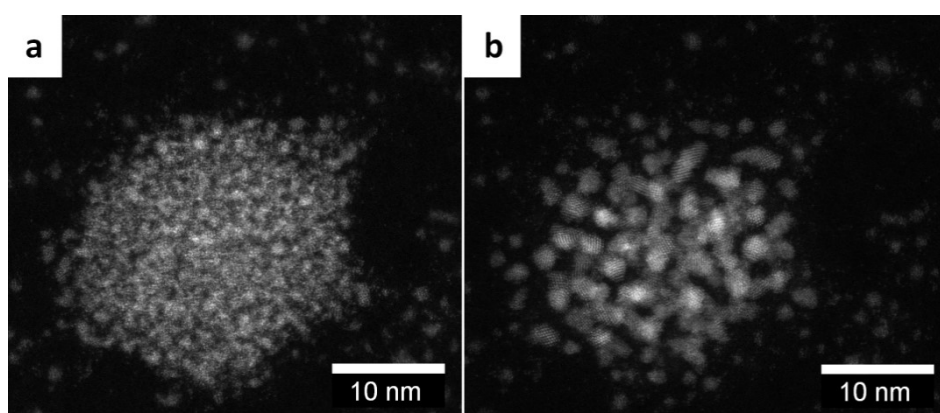


Figure S8. Scanning transmission electron microscopy depicting electron beam induced growth and crystallization of hydrous iridium oxide nanoparticles. Micrograph of hydrous IrO_x nanoparticle aggregate before (a) and after (b) extended illumination by electron beam.

The precursor IrO_x colloid nanoparticles are reduced in the crucial step of the synthesis procedure to metallic iridium nanoparticles (with or without the presence of an oxidic support) of comparable size for a range of temperatures of 150 - 200 °C and synthesis durations ranging from 12 – 24 h as indicated by the XRD line broadening in following Figure S9a. According to the Scherrer's equation, a crystallite domain size for the metallic iridium nanoparticles of ~1.3 nm is determined. A transformation to the tetragonal IrO_2 phase is observed for calcination temperatures from 175 °C and higher in (Figure S9b).

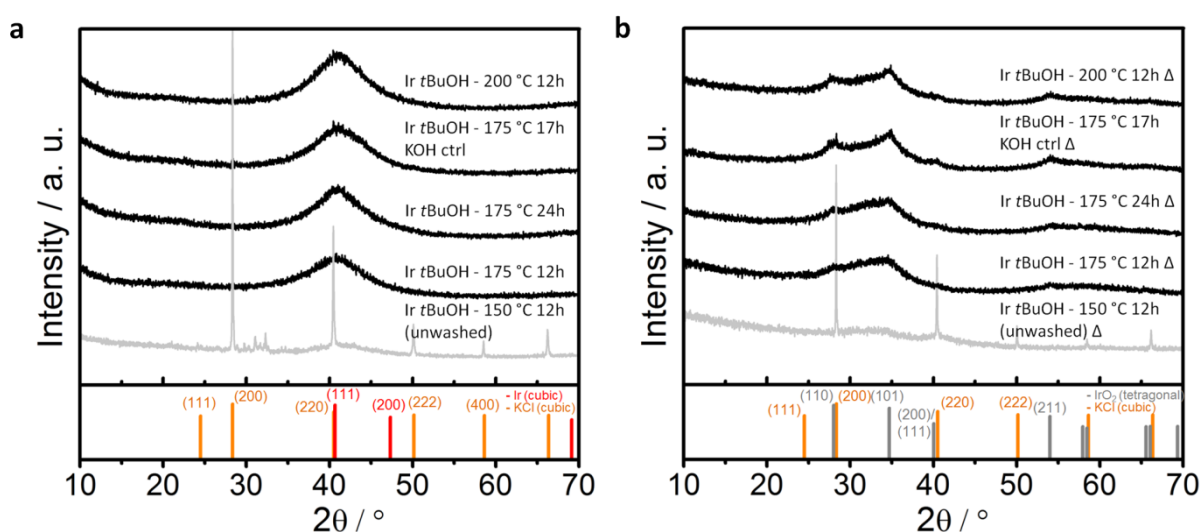


Figure S9 X-ray diffraction analysis of iridium and iridium oxide nanoparticles with parameter variation in solvothermal synthesis. XRD patterns of metallic iridium nanoparticles after solvothermal reduced IrO_x colloid nanoparticles before (a; Ir tBuOH) and after (b, Ir tBuOH Δ) thermal oxidation. Ir pattern: ICDD card number 00-006-0598 (red) (cubic symmetry, $a = b = c = 3.8394 \text{ \AA}$, $\alpha = \beta = \gamma = 90^\circ$). KCl pattern: ICDD card number 00-041-1476 (orange) (cubic symmetry, $a = b = c = 6.2917(3) \text{ \AA}$, $\alpha = \beta = \gamma = 90^\circ$). IrO_2 pattern: ICDD card number 00-015-0870 (grey) (tetragonal symmetry, $a = b = 4.4983 \text{ \AA}$, $c = 3.1544 \text{ \AA}$, $\alpha = \beta = \gamma = 90^\circ$).

III. Synthesis of ATO-microparticle supported IrO₂ nanoparticles as oxygen evolution reaction catalyst

Powder diffraction patterns of Ir-loaded 280 nm PMMA templated ATO shown in Figure S10b,d are discussed in the main text and are analogous to the results obtained for 120 nm PMMA bead templated microparticles. Diffractograms of Ir-loaded 120 nm PMMA templated ATO (Figure S11a) show broadened peaks assignable to the cassiterite (SnO₂) phase, which is also observed for unloaded microparticles (Figure S1a; SG_{120Δ}). For the Ir loaded particles an additional broad peak located at around 40 °2θ is observed, the intensity of which increases with the amount of IrO_x colloid content of the synthesis solution [$\frac{1}{2}$ -4X \cong 7-40 wt% Ir in composite catalyst]. Comparison with the pattern of Ir *t*BuOH shows that the product series (SG_{120Δ}-Ir-YX with Y = $\frac{1}{2}$ -4) is composed of coexisting ATO microparticles and metallic nanosized Ir particles.

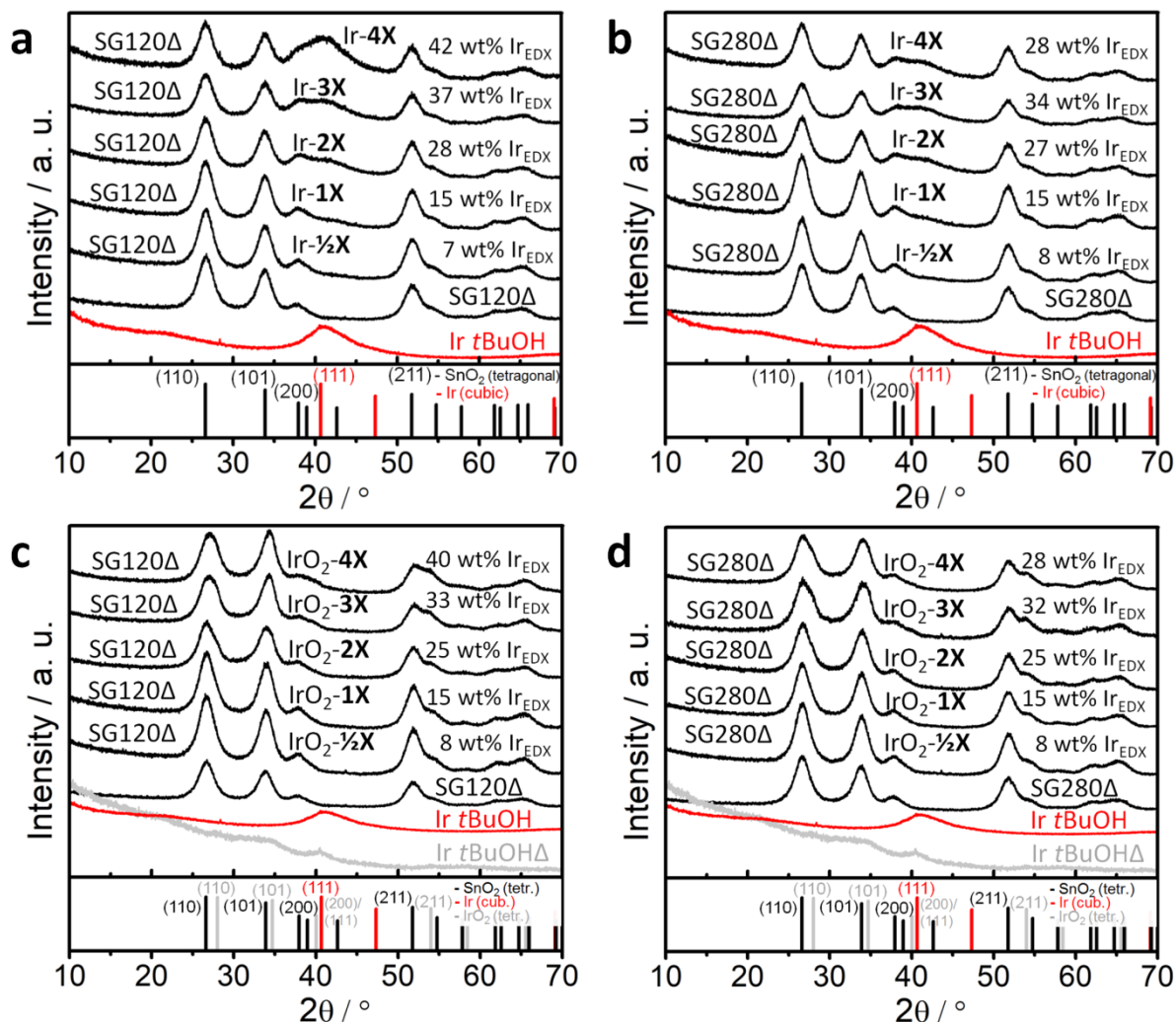


Figure S10 X-ray diffraction analysis of ATO microparticle supported iridium and iridium oxide nanoparticles. XRD pattern of (a) 120 nm PMMA and (b) 280 nm PMMA templated Ir loaded ATO microparticles with varying Ir loading of 7–42 wt% Ir (ATO-SG₁₂₀Δ-Ir- $\frac{1}{2}$ X to -4X) and 8–34 wt% Ir (ATO-SG₂₈₀Δ-Ir- $\frac{1}{2}$ X to 4X) respectively and unsupported Ir (Ir tBuOH, red) and IrO₂ (Ir tBuOHΔ, grey) nanoparticles from solvothermal reduction of IrO_x colloid nanoparticles before (Ir tBuOH, red) and after (Ir tBuOHΔ, grey) thermal oxidation as reference. (c, d) XRD pattern of thermally oxidized catalysts. SnO₂ (cassiterite) pattern: ICDD card number 00-041-1445 (black), Ir pattern: ICDD card number 00-006-0598 (red), IrO₂ pattern: ICDD card number 00-015-0870 (grey).

Thermal oxidation of 120 and 280 nm PMMA templated Ir-loaded product (Figure S10b, d) leads to the formation of a nanosized IrO₂ phase visible by the appearance of the IrO₂ 211 peak located at $\sim 54^\circ 2\theta$ (the IrO₂ 110 and 101 peak are overlapping with SnO₂ 110 and 101 and are therefore not suitable to observe the formation of a IrO₂ phase). A further indication for the phase transformation of the metallic Ir to an oxidic phase is the absence of the Ir 111 peak located at $\sim 40^\circ 2\theta$.

Raman spectra of IrO₂-loaded as well as Ir-loaded ATO microparticles (Figure S11) show two broad peaks around 550 cm⁻¹ and 740 cm⁻¹ corresponding to the E_g band and the overlapping B_{2g}/A_{1g} band of IrO₂.^[30,31] The absence of any signal from the underlying ATO indicates a complete coverage of the surface with Ir/IrO₂ particles. The spectrum of Ir coated ATO (SG₂₈₀Δ-Ir-2X) thereby shows characteristic Raman bands associated with the oxide phase which we attributed to a potential -O or -OH termination of the Ir-nanoparticles as discussed for the Raman spectrum of unsupported metallic Ir nanoparticles.

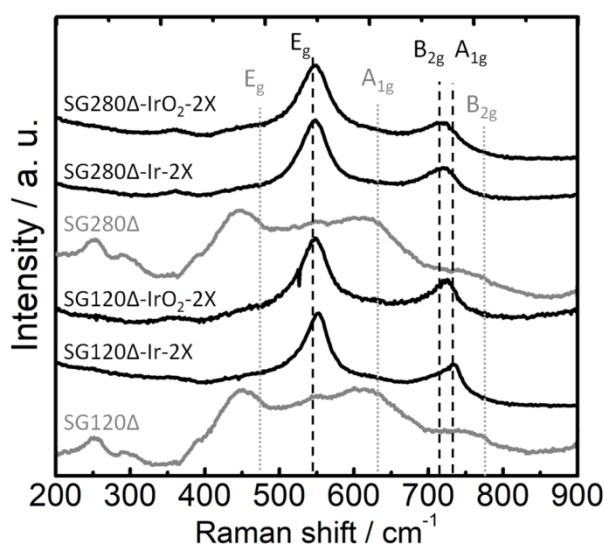


Figure S11 Raman spectra of ATO microparticle supported iridium and iridium oxide nanoparticles. Raman spectra of 120 nm (lower lines) and 280 nm (upper lines) PMMA templated ATO microparticles with loading of ~25 wt% Ir before (ATO-SG₁₂₀Δ-Ir-2X, ATO-SG₂₈₀Δ-Ir-2X) and after (ATO-SG₁₂₀Δ-IrO₂-2X, ATO-SG₂₈₀Δ-IrO₂-2X) thermal oxidation. Ir loading determined by SEM/EDX measurements of respective samples. Spectra of unloaded ATO microparticles depicted in grey. The band at 561 cm⁻¹ (E_g) and the close bands at 728 cm⁻¹ (B_{2g}) and at 752 cm⁻¹ (A_{1g}) correspond to the tetragonal iridium oxide phase.^[30] The bands at 630 cm⁻¹ (A_{1g}), 477 cm⁻¹ (E_g), 775 cm⁻¹ (B_{2g}) correspond to the cassiterite (SnO₂) phase.^[56-58]

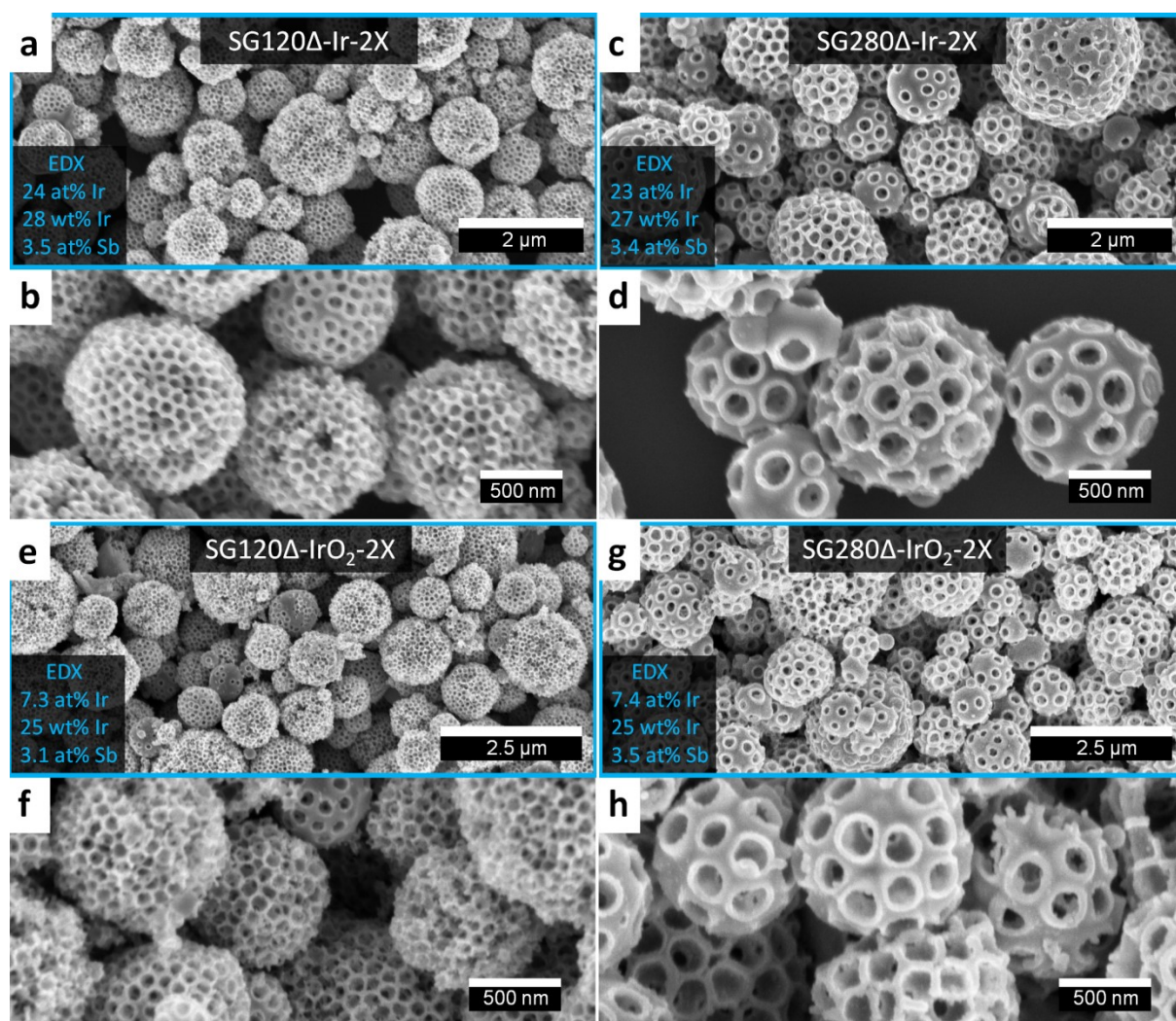


Figure S12 Scanning electron micrographs with energy dispersive X-ray analysis of ATO microparticle supported iridium and iridium oxide nanoparticles. (a, b, e, f) 120 nm PMMA bead templated ATO microparticle solvothermally loaded with Ir nanoparticles before (a, b; SG₁₂₀ Δ -Ir-2X) and after (e, f; SG₁₂₀ Δ -IrO₂-2X) thermal oxidation. (c, d, g, h) 280 nm PMMA bead templated ATO microparticle solvothermally loaded with Ir nanoparticles before (c, d; SG₂₈₀ Δ -Ir-2X) and after (g, h; SG₂₈₀ Δ -IrO₂-2X) thermal oxidation. Quantification of iridium loading (a, c, e, g) by multi spot EDX measurements (Ir, Sn, Sb as input) and theoretical stoichiometry of product. Sb at% referred to ATO support only.

Table S1 Theoretical and experimentally determined iridium fraction in ATO microparticle supported Ir and IrO₂ nanoparticles. Theoretical iridium input in solvothermal synthesis used for iridium loading of ATO microparticles expressed as a multiple (X) of single IrO_x colloid reactions (1/2-4). Experimental wt% Ir determined as average from SEM/EDX measurements in different magnifications and 5 independent sample spots. Only Sn, Sb and Ir at% used as input for quantifications in combination with theoretical sample stoichiometry (4.3 at% Sb doping).

		wt%(Ir)	wt%(Ir)	wt%(Ir)	wt%(Ir)
		theoretical,	EDX,	theoretical,	EDX,
		unheated	unheated	calcined	calcined
SG ₁₂₀ Δ-IrO ₂	4X	43	42	40	40
	3X	36	37	34	33
	2X	27	28	26	25
	1X	16	15	15	15
	1/2X	9	7	8	8
SG ₂₈₀ Δ-IrO ₂	4X	43	28	40	28
	3X	36	34	34	32
	2X	27	27	26	25
	1X	16	15	15	15
	1/2X	9	8	8	8

EDX elemental mappings of outer ATO pores was performed for 120 nm PMMA templated ATO microparticles coated with IrO₂ (~25wt% Ir acc. to EDX; see Table S1) nanoparticles according to the procedure introduced (Figure S13). Analogous results were obtained than for larger pore ATO based microparticles as discussed in the main text (Figure 3). Independent of the pore diameter a co-localization of the Sn-L, Sb-L and Ir-L signal was observed. As the Ir-L signal extends beyond the areas of high tin and antimony concentration, we infer a homogeneous coating of the ATO surface with IrO₂.

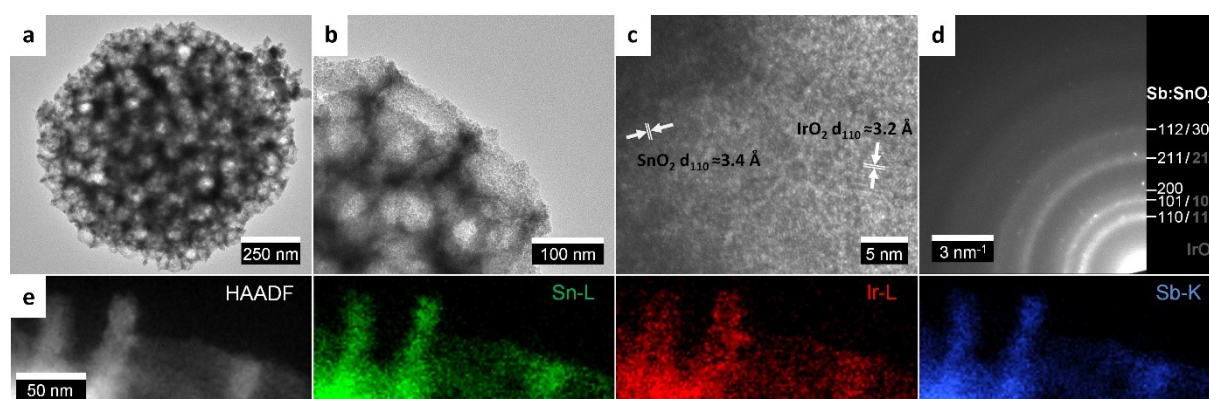


Figure S13 Transmission electron micrographs and energy-dispersive X-ray spectroscopy analysis mapping of thermally oxidized IrO_2 supported on macroporous ATO microparticles templated by 120 nm PMMA beads. Electron micrographs (SG₁₂₀: a-c), electron diffraction pattern (SG₁₂₀: d) and EDX elemental mapping of thermally oxidized 120 nm PMMA (e) IrO_2 -loaded ATO microparticles with Ir loadings of 25 wt% Ir (ATO-SG₁₂₀ Δ - IrO_2 -2X). Phase identification and assignment of lattice spacings in electron diffraction pattern (d) according to literature values. SnO_2 (cassiterite) pattern: ICDD card number 00-041-1445. IrO_2 pattern (f, l): ICDD card number 00-015-0870.

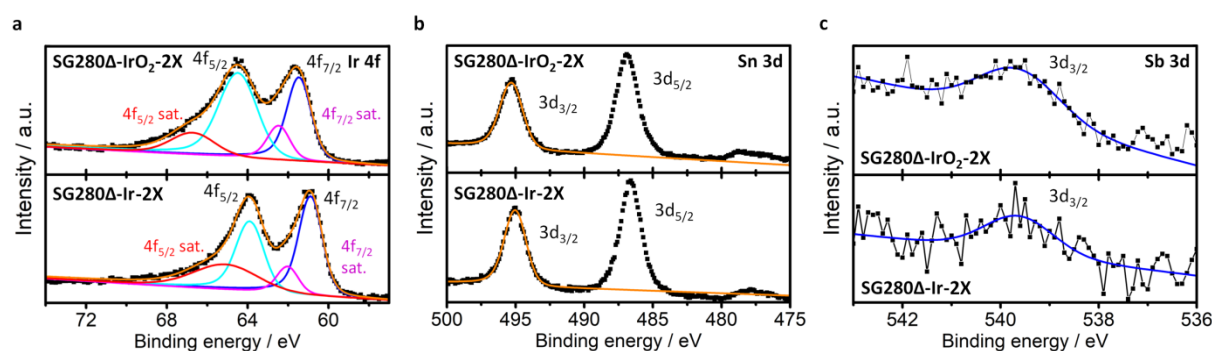


Figure S14 X-ray photoelectron spectroscopy (XPS) spectra of ATO microparticles supported iridium and iridium oxide nanoparticles. (a) Ir 4f spectra of 280 nm PMMA templated ATO microparticle supported iridium nanoparticles before (SG₂₈₀ Δ -Ir-2X) and after (SG₂₈₀ Δ - IrO_2 -2X) thermal oxidation with loading of ~25 wt% Ir. Ir loading determined by SEM/EDX measurements. Ir 4f_{7/2} peaks fitted to 60.9 eV (SG₂₈₀ Δ -Ir-2X) and 61.4 eV (SG₂₈₀ Δ - IrO_2 -2X) and assigned to metallic Ir(0) and Ir(IV) O_2 according to literature values.^[32] (b) Sn 3d spectra of respective samples confirm presence of Sn with fitted Sn 3d_{3/2} binding energies of 495.0 eV (SG₂₈₀ Δ -Ir-2X) and 495.2 eV (SG₂₈₀ Δ - IrO_2 -2X) (c) Sb 3d spectra of respective samples confirm presence of Sb with fitted Sb 3d_{3/2} binding energy of 539.6 eV (SG₂₈₀ Δ -Ir-2X and SG₂₈₀ Δ - IrO_2 -2X).

Following Figure S15 depicts a schematic representation of the STEM based tomography workflow applying a modified SIRT (Simultaneous Iterative Reconstruction Technique)^[60] and DART (Discrete Algebraic Reconstruction Technique)^[61] tomography algorithms on a particle tilt image series.

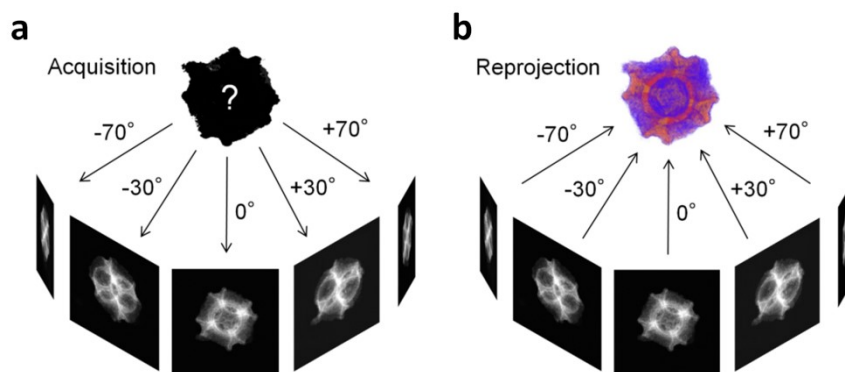


Figure S15 Schematic representation scanning transmission electron microscopy-based tomography workflow. (a) Acquisition of STEM tilt image series (b) Calculation of reprojected 3D intensity volume based on STEM tilt image series and modified SIRT (Simultaneous Iterative Reconstruction Technique)^[60] and DART (Discrete Algebraic Reconstruction Technique)^[61] tomography algorithms.

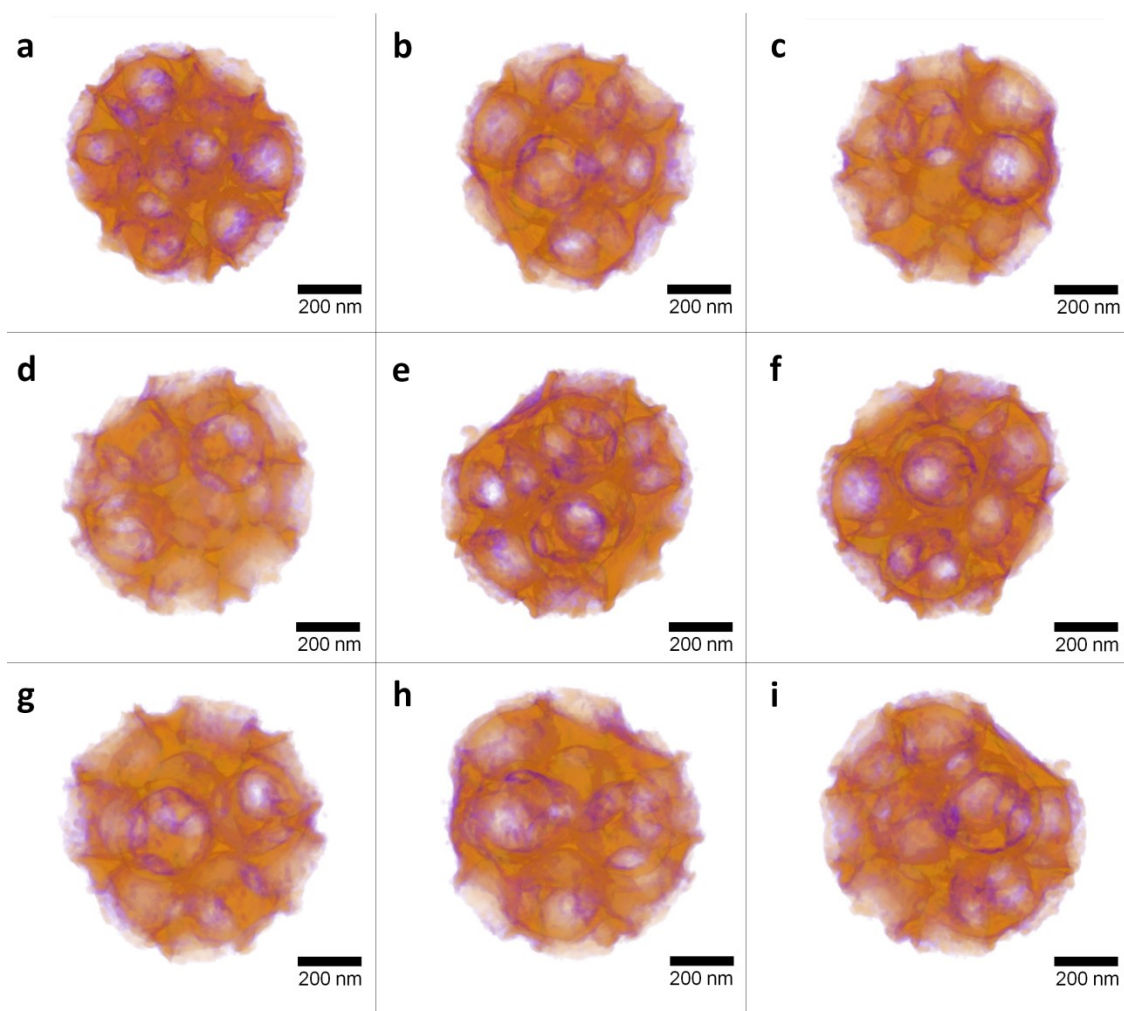


Figure S16 Scanning transmission electron microscopy-based tomography with 3D intensity volume reconstruction of thermally oxidized IrO_2 nanoparticles supported on macroporous ATO microparticles templated by 280 nm PMMA (36° rotation angle snapshots around central c-axis). (a) $0^\circ/360^\circ$ (b) $+36^\circ$ clockwise (CW) (c) $+72^\circ$ CW (d) $+108^\circ$ CW (e) $+144^\circ$ CW (f) $+180^\circ$ CW (g) $+216^\circ$ CW (h) $+252^\circ$ CW (i) $+288^\circ$ CW (j) $+324^\circ$ CW

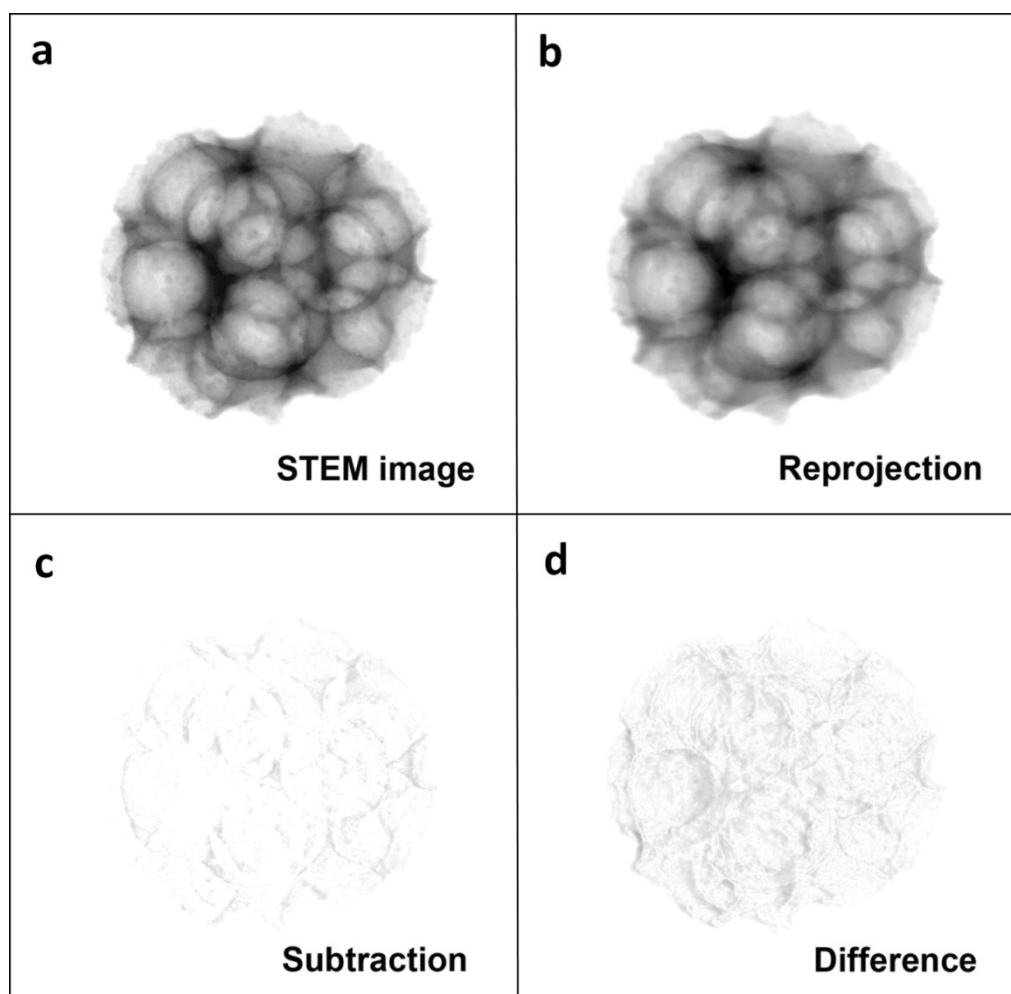


Figure S17 Quality assessment of 3D intensity volume reconstruction of thermally oxidized IrO_2 nanoparticles supported on macroporous ATO microparticles templated by 280 nm PMMA based on scanning transmission electron microscopy tomography data. (a) Acquired STEM image (0° tilt angle) (b) Calculated particle reprojection (for tilt angle of 0°) based on STEM tomography (c) Subtraction image of acquired STEM image and particle reprojection (d) Residual image intensity of acquired STEM image not contained in particle reprojection image.

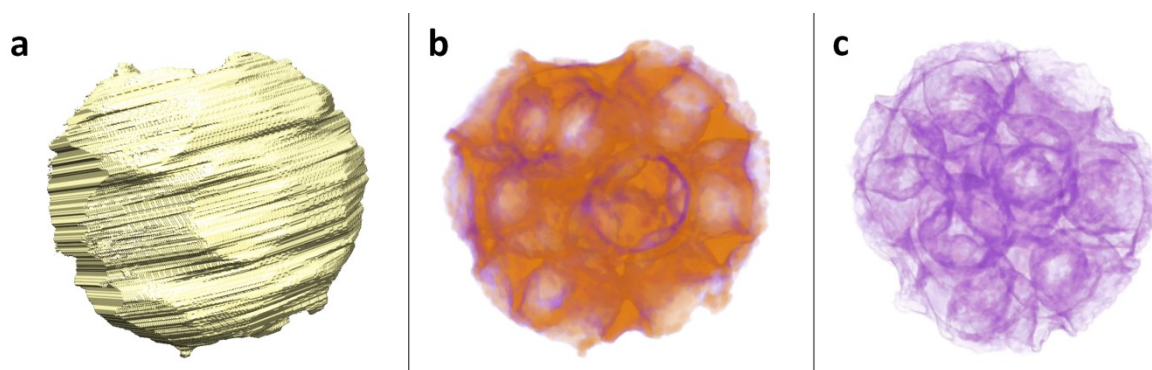


Figure S18 Representation of envelope volume of 3D intensity volume of STEM based tomography of thermally oxidized iridium nanoparticles supported on macroporous ATO microparticles templated by 280 nm PMMA. (a) Rough shape representing the „enveloped“ volume of a particle from a tilt series (-70° to $+60^\circ$) containing 27 HAADF STEM images. (b) DART-algorithm based reconstruction of ATO/IrO₂ intensity volume quantified to 40.3 vol%. (c) DART-algorithm^[61] based reconstruction of IrO₂ intensity volume quantified to 15.6 vol%. The total volume of vacuum, ATO and IrO₂ assigned voxels inside the calculated mask (a) were counted to derive the corresponding volume fractions. Derived cavity-volume may slightly be overestimated due to estimation from masking algorithm.

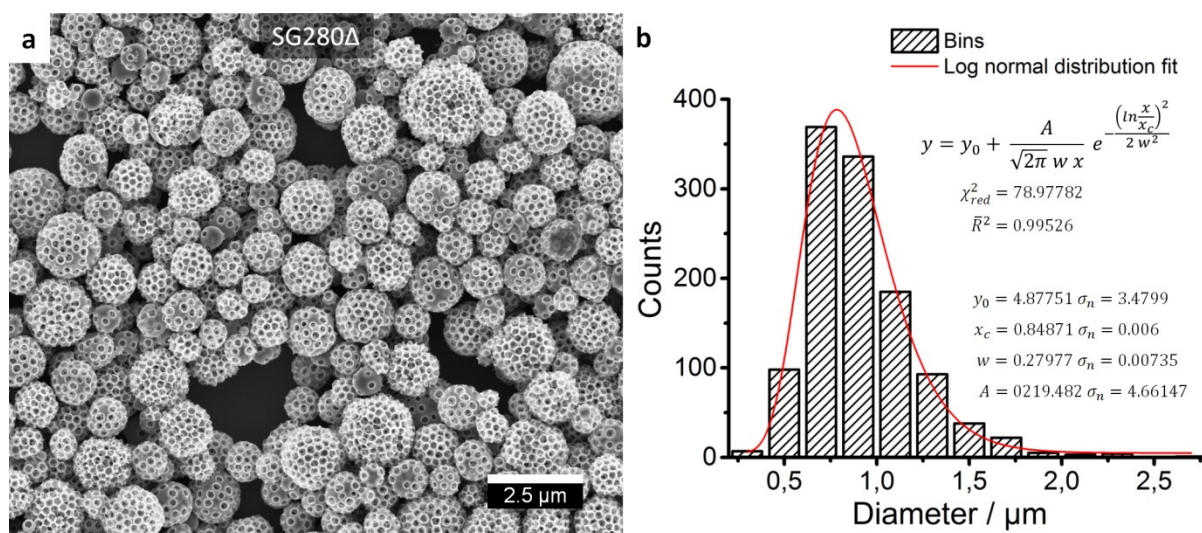


Figure S19 Scanning electron micrograph of macroporous ATO microparticles with particle size distribution. (a) Representative SEM image with overview of 280 nm PMMA templated porous ATO microparticles (SG₂₈₀Δ) for particle size quantification. (b) Log-normal function fitted to particle size distribution with stated goodness of fit values (reduced *chi*-square, adjusted *R*-square), and determined fitting parameters of Log-normal function (y_0 , x_c , w (standard deviation) with standard errors.

Log-normal distribution function fitted to experimentally determined particle size distribution by SEM shown in Figure S19b with a representative SEM image used for size quantification (Figure S19a). Calculation of the void volume in a film of randomly closed packed spheres (approximation for porous ATO microparticles) according to a model proposed by Desmond *et al.*^[33]

Log-normal function: $P(R) = \frac{A}{R} e^{-\frac{(\frac{\ln R}{\sigma} + 0.5 \sigma)^2}{2}}$

Parameters: Scale parameter $\sigma = w = 0.27977$

Constrained: $A = \frac{1}{\sqrt{2\pi\sigma^2}} = 219.482$

Polydispersity: $\delta = \sqrt{e^{\sigma^2} - 1} = 0.285334814$

Skewness: $S = (e^{\sigma^2} + 2)\sqrt{e^{\sigma^2} - 1} = 0.879235249$

Packing density (ϕ) with empirical fitting parameters (c_1, c_2):

$$\phi_{RCP} = \phi_{RCP}^* + c_1\delta + c_2S\delta^2$$

with parameters $\phi_{RCP}^* = 0.634, c_1 = 0.0658, c_2 = 0.0857$

$$\phi_{RCP} = 0.6589$$

Resulting void volume in layer of dense spheres with respective size distribution:

$$1 - \phi_{RCP} = 0.3411 \cong \mathbf{34\%}$$

IV. Electrochemical characterization of ATO-microparticle supported IrO₂ nanoparticles as oxygen evolution reaction catalyst

The morphology of dropcasted films of pure Ir-species is depicted in Figure S21 for comparison with respective supported OER catalyst. Electron micrographs of drop-casted IrO_x colloid thin films (Figure S21a-c) display a rather smooth film which is built up from primary nanoparticle aggregates of ~50 nm. Calcined IrO_x colloid (IrO_x colloidΔ) exhibits a similar but rougher morphology with smaller feature sizes down to 10-20 nm (Figure S21d-f).

Metallic Ir nanoparticles as well as the IrO₂ nanoparticles obtained by calcination form rough porous films with nanosized features (Ir *t*BuOH; Figure S21g-i and Ir *t*BuOHΔ Figure S21j-l).

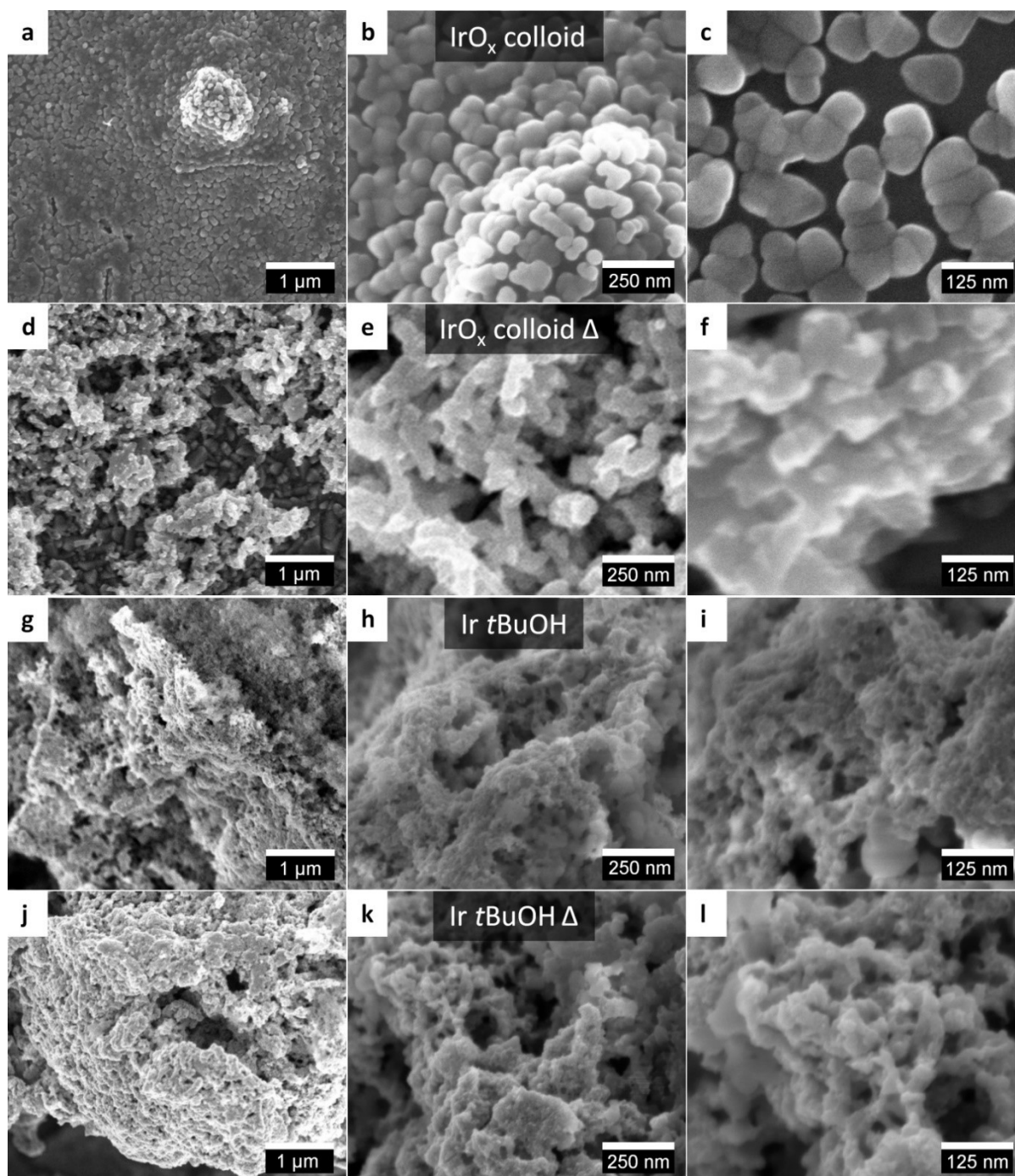


Figure S20 Scanning electron microscopy of iridium and iridium oxide nanoparticles. Micrographs of hydrous iridium oxide colloid (IrO_x colloid) before (a-c) and after (d-f; IrO_x colloid Δ) thermal treatment in different magnifications. Iridium nanoparticles obtained from solvothermal reduction of IrO_x colloid (g-i; $\text{Ir } t\text{BuOH}$) and after thermal oxidation (j-l; $\text{Ir } t\text{BuOH}\Delta$) to the oxide phase.

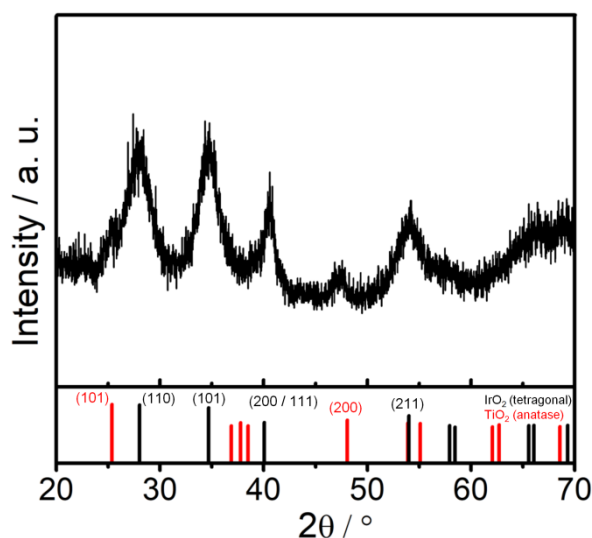


Figure S21 X-ray diffractogram of commercial reference catalyst $\text{TiO}_2/\text{IrO}_2$ (Elyst Ir75). IrO_2 pattern: ICDD card number 00-015-0870 (black) (tetragonal symmetry, $a = b = 4.4983 \text{ \AA}$, $c = 3.1544 \text{ \AA}$, $\alpha = \beta = \gamma = 90^\circ$). TiO_2 (anatase) pattern: ICDD card number 00-004-0477 (red) (tetragonal symmetry, $a = b = 3.783 \text{ \AA}$, $c = 9.510 \text{ \AA}$, $\alpha = \beta = \gamma = 90^\circ$).

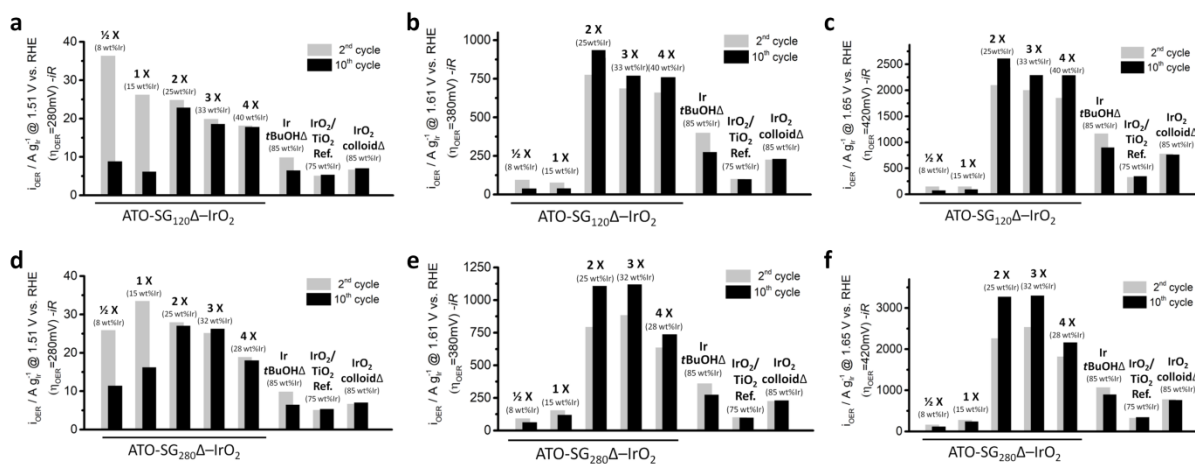


Figure S22 Iridium mass based catalytic activity of ATO microparticle supported IrO_2 nanoparticles with differing pore size. Oxygen evolution reaction (OER) currents (capacitive current corrected, i_{R} corrected) shown for best performing samples of 120 nm (a-c; $\text{ATO-SG}_{120\Delta}\text{-IrO}_2$) and 280 nm (d-f; $\text{ATO-SG}_{280\Delta}\text{-IrO}_2$) PMMA templated ATO microparticles loaded with varying amount of IrO_2 (8-40 wt% Ir for $\text{ATO-SG}_{120\Delta}\text{-IrO}_2$ and 8-32 wt% Ir for $\text{ATO-SG}_{280\Delta}\text{-IrO}_2$) (d-f) for η_{OER} of 280 mV (a, d), 380 mV (b, e) and 420 mV (c, f) from triplicates. Deposited mass determined with quartz crystal microbalance sensors with absolute iridium mass calculated from relative Ir-Sn ratio determined by SEM/EDX measurements. Unsupported IrO_2 (Ir $t\text{BuOH}\Delta$, IrO_x colloid Δ) nanoparticles and commercial TiO_2 supported IrO_2 ($\text{IrO}_2/\text{TiO}_2$ Ref.) as reference.

To assess the conductivity of ATO supported IrO_2 nanoparticle catalyst and commercial TiO_2 supported reference catalyst 2-point dc-conductivity measurements across loosely

compressed powders were conducted in an in house constructed measurement cell (see Figure S23) listed in following Table S2.



Figure S23 **In-house constructed dc-conductivity measurements cell for low sample volumes. Catalyst powder sample loosely compressed by opposing brass cylinder electrodes. Contact area of electrodes 0.126 cm².**

Due to low compressive force on the catalyst powder absolute values are significantly lower than values determined by 4-point conductivity measurement of ATO support pellets formed under high pressure. Following values should show a trend in the conductivity that correlates the iridium loading of the composite catalyst with a significant increase in conductivity.

Table S2 Conductivity trend of 120 nm PMMA templated ATO-microparticle supported IrO₂ nanoparticles and commercial TiO₂/IrO₂ reference. Measurement values derived from dc-conductivity measurement of loosely compressed powder samples.

	Conductivity / S cm ⁻¹	wt%(Ir) SEM/EDX
SG ₁₂₀ Δ-IrO ₂	½X	1.00 x 10 ⁻⁶
	1X	1.79 x 10 ⁻⁵
	2X	1.16 x 10 ⁻²
	3X	0.46
	4X	0.88
TiO ₂ /IrO ₂ commercial reference	4.42	75

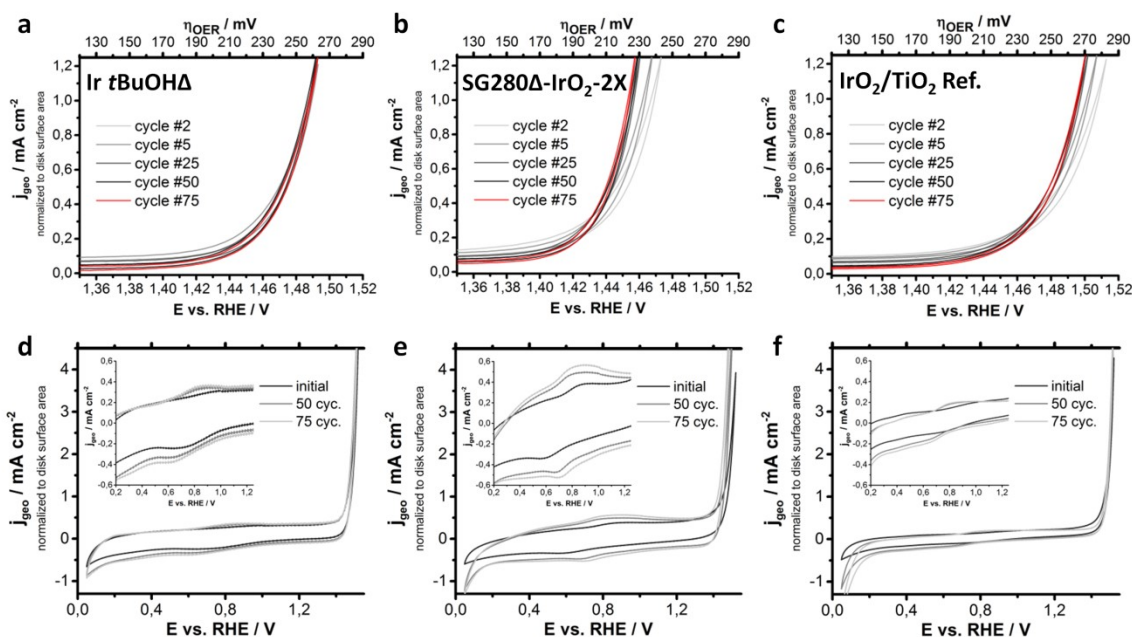


Figure S24 Rotating disc electrode (RDE) measurements of IrO₂ nanoparticles, ATO microparticle supported IrO₂ nanoparticles and IrO₂/TiO₂ reference catalyst. (a-c) Selected scan cycles (2nd, 5th, 25th, 50th, 75th) of RDE measurements conducted in O₂ purged 0.5 M H₂SO₄ electrolyte at 60 °C for 10 μg_{Ir} (50 μg_{Ir} cm⁻²) of thermally oxidized Ir nanoparticles (a; Ir-tBuOHA), 280 nm PMMA templated ATO microparticle supported IrO₂ with 25 wt% Ir loading (b; ATO-SG₂₈₀Δ-IrO₂-2X) and commercial TiO₂ supported IrO₂ with 75 wt% Ir loading (c; IrO₂/TiO₂ Ref). Potential window of RDE cycling from 1.0 V vs. RHE to $V_{vertex}@j = 1 \text{ mA cm}^{-2}$ with 5 mV s⁻¹. (d-f) Cyclic voltammograms from 0.05 - 1.52 V vs. RHE (50 mV s⁻¹) before (black), after 50 (dark grey) and after 75 RDE cycles (light grey) of respective catalyst samples. 75 RDE cycles conducted between 1.0 - 1.52 V vs. RHE to $V_{vertex}@j = 1 \text{ mA cm}^{-2}$ with 5 mV s⁻¹.

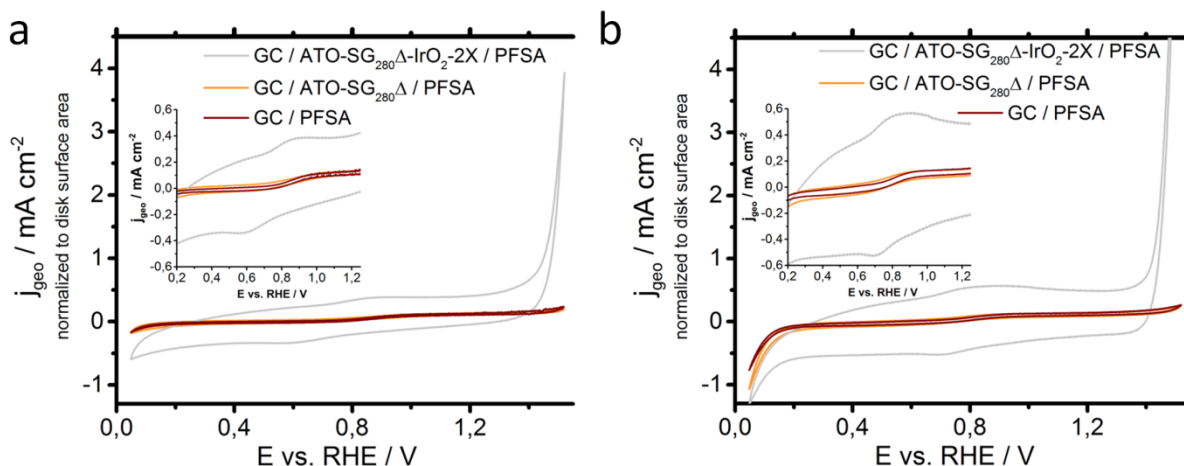


Figure S25 Cyclic voltammograms of ATO microparticle supported IrO₂ nanoparticles and glassy carbon disc substrates in rotating disc electrode setup. ATO-microparticle supported IrO₂ nanoparticles (ATO-SG₂₈₀Δ-IrO₂-2X: 50 μg_{Ir} cm⁻²), plain ATO microparticles and plain glassy carbon (GC) with Nafion® coating (PFSA) only. Cyclic voltammograms from 0.05 - 1.52 V vs. RHE (50 mV s⁻¹) before (a) and after 75 RDE cycles (b). 75 RDE cycles conducted between 1.0 - 1.52 V vs. RHE at a scan rate of 5 mV s⁻¹ in O₂ purged 0.5 M H₂SO₄ electrolyte at 60 °C.

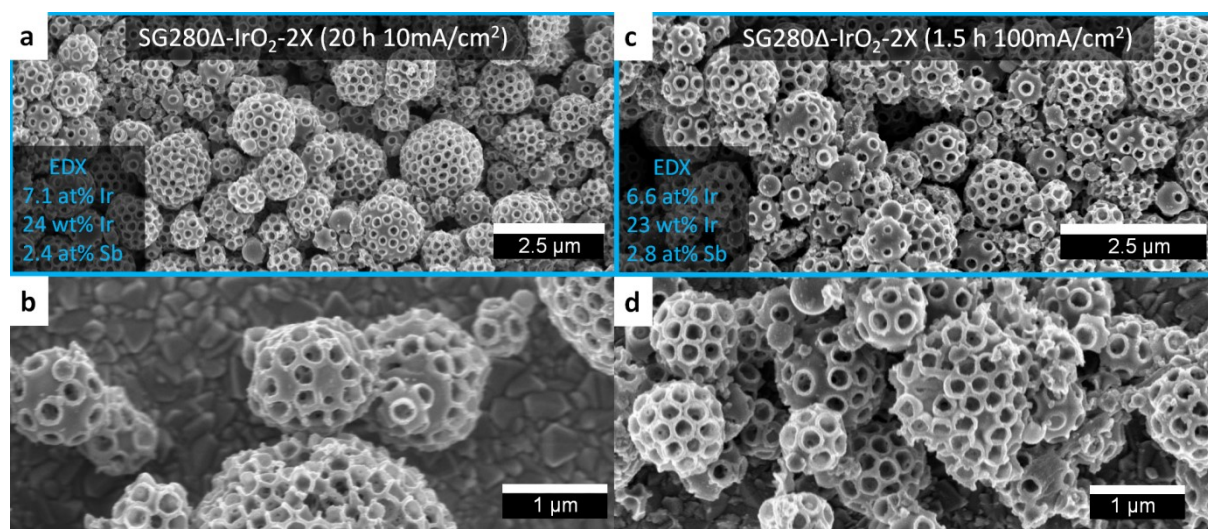


Figure S26 Scanning electron micrographs with energy dispersive X-ray analysis of ATO microparticle supported IrO₂ nanoparticles after chronopotentiometry measurements. (a, b) 280 nm PMMA bead templated ATO microparticle solvothermally loaded with Ir nanoparticles after calcination (SG₁₂₀Δ-IrO₂-2X; 25wt% Ir initially) and after chronopotentiometry at $j=10$ mA cm⁻² over 20 h in 0.5 M H₂SO₄ on FTO substrate. (c, d) 280 nm PMMA bead templated ATO microparticle solvothermally loaded with Ir nanoparticles after calcination (SG₂₈₀Δ-IrO₂-2X; 25wt% Ir initially) and after chronopotentiometry at $j=100$ mA cm⁻² over 1.5 h in 0.5 M H₂SO₄ on FTO substrate. Quantification of iridium loading (a, b) by multi-spot EDX measurements (Ir, Sn, Sb as input) and theoretical stoichiometry of product. Sb at% referred to ATO support only. EDX measurements performed on Si substrates with transferred microparticle samples.

8.7 References

- [1] S. Inage, *WIREs Energy Environ.* **2015**, 4, 115.
- [2] N. Armaroli, V. Balzani, *ChemSusChem* **2010**, 4, 21.
- [3] F. Barbir, *Sol. Energy* **2005**, 78, 661.
- [4] C. Hagelüken, in *Competition and Conflicts on Resource Use, Natural Resource Management and Policy*, Vol. 46 (Eds: S. Hartard, W. Liebert), Springer International Publishing, Cham **2015**, Ch. 3.
- [5] K. E. Ayers, C. Capuano, E. B. Anderson, *ECS Trans.* **2012**, 41, 15.
- [6] N. Danilovic, R. Subbaraman, K.-C. Chang, S. H. Chang, Y. J. Kang, J. Snyder, A. P. Paulikas, D. Strmcnik, Y.-T. Kim, D. Myers, V. R. Stamenkovic, N. M. Markovic, *J. Phys. Chem. Lett.* **2014**, 5, 2474.
- [7] M. Bernt, H. A. Gasteiger, *J. Electrochem. Soc.* **2016**, 163, F3179.
- [8] M. Carmo, D. L. Fritz, J. Mergel, D. Stolten, *Int. J. Hydrogen Energ.* **2013**, 38, 4901.
- [9] E. Oakton, D. Lebedev, M. Povia, D. F. Abbott, E. Fabbri, A. Fedorov, M. Nachtegaal, C. Copéret, T. J. Schmidt, *ACS Catal.* **2017**, 7, 2346.
- [10] U. Babic, M. Suermann, F. N. Büchi, L. Gubler, T. J. Schmidt, *J. Electrochem. Soc.* **2017**, 164, F387.
- [11] J. E. Park, S. Kim, O.-H. Kim, C.-Y. Ahn, M.-J. Kim, S. Y. Kang, T. I. Jeon, J.-G. Shim, D. W. Lee, J. H. Lee, Y.-H. Cho, Y.-E. Sung, *Nano Energy* **2019**, 58, 158.
- [12] M. Faustini, M. Giraud, D. Jones, J. Rozière, M. Dupont, T. R. Porter, S. Nowak, M. Bahri, O. Ersen, C. Sanchez, C. Boissière, C. Tard, J. Peron, *Adv. Energy Mater.* **2019**, 9, 1802136.
- [13] H.-S. Oh, H. N. Nong, T. Reier, M. Gliech, P. Strasser, *Chem. Sci.* **2015**, 6, 3321.
- [14] H. N. Nong, H. S. Oh, T. Reier, E. Willinger, M. G. Willinger, V. Petkov, D. Teschner, P. Strasser, *Angew. Chem. Int. Edit.* **2015**, 127, 3018.
- [15] H. Yoo, K. Oh, Y. R. Lee, K. H. Row, G. Lee, J. Choi, *Int. J. Hydrogen Energ.* **2017**, 42, 6657.
- [16] C. Hao, H. Lv, Q. Zhao, B. Li, C. Zhang, C. Mi, Y. Song, J. Ma, *Int. J. Hydrogen Energ.* **2017**, 42, 9384.
- [17] V. K. Puthiyapura, S. Pasupathi, H. Su, X. Liu, B. Pollet, K. Scott, *Int. J. Hydrogen Energ.* **2014**, 39, 1905.
- [18] W. Hu, S. Chen, Q. Xia, *Int. J. Hydrogen Energ.* **2014**, 39, 6967.
- [19] S. Trasatti, *Electrochim. Acta* **2000**, 45, 2377.

- [20] S. M. Alia, B. Rasimick, C. Ngo, K. C. Neyerlin, S. S. Kocha, S. Pylypenko, H. Xu, B. S. Pivovar, *J. Electrochem. Soc.* **2016**, 163, F3105.
- [21] H.-S. Oh, H. N. Nong, P. Strasser, *Adv. Funct. Mater.* **2015**, 25, 1074.
- [22] C. Hao, H. Lv, C. Mi, Y. Song, J. Ma, *ACS Sustain. Chem. Eng.* **2016**, 4, 746.
- [23] K. Hieda, T. Hyodo, Y. Shimizu, M. Egashira, *Sensor. Actuat. B-Chem.* **2008**, 133, 144.
- [24] S. Y. Lee, L. Gradon, S. Janeczko, F. Iskandar, K. Okuyama, *ACS Nano* **2010**, 4, 4717.
- [25] K. Peters, P. Zeller, G. Stefanic, V. Skoromets, H. Němec, P. Kužel, D. Fattakhova-Rohlfing, *Chem. Mater.* **2015**, 27, 1090.
- [26] T. E. Sutto, *Inorg. Chem.* **2014**, 53, 4570.
- [27] A. Minguzzi, C. Locatelli, O. Lugaresi, E. Achilli, G. Cappelletti, M. Scavini, M. Coduri, P. Masala, B. Sacchi, A. Vertova, P. Ghigna, S. Rondinini, *ACS Catal.* **2015**, 5, 5104.
- [28] S. Cherevko, S. Geiger, O. Kasian, A. Mingers, K. J. J. Mayrhofer, *J. Electroanal. Chem.* **2016**, 774, 102.
- [29] S. Cherevko, T. Reier, A. R. Zeradjanin, Z. Pawolek, P. Strasser, K. J. J. Mayrhofer, *Electrochem. Commun.* **2014**, 48, 81.
- [30] A. V. Korotcov, Y. S. Huang, K. K. Tiong, D. S. Tsai, *J. Raman Spectrosc.* **2007**, 38, 737.
- [31] Y. S. Huang, S. S. Lin, C. R. Huang, M. C. Lee, T. E. Dann, F. Z. Chien, *Solid State Commun.* **1989**, 70, 517.
- [32] S. J. Freakley, J. Ruiz-Esquius, D. J. Morgan, *Surf. Interface Anal.* **2017**, 49, 794.
- [33] K. W. Desmond, E. R. Weeks, *Phys. Rev. E* **2014**, 90, 022204.
- [34] M. Lopez, A. Schleunung, P. Biberbach (Umicore AG) *U.S. 7,976,989B2*, **2004**.
- [35] S. Geiger, O. Kasian, B. R. Shrestha, A. M. Mingers, K. J. J. Mayrhofer, S. Cherevko, *J. Electrochem. Soc.* **2016**, 163, F3132.
- [36] A. G. Hufnagel, S. Häringer, M. Beetz, B. Böller, D. Fattakhova-Rohlfing, T. Bein, *Nanoscale* **2019**, 11, 14285.
- [37] J. Lim, D. Park, S. S. Jeon, C. W. Roh, J. Choi, D. Yoon, M. Park, H. Jung, H. Lee, *Adv. Funct. Mater.* **2018**, 28, 1704796.
- [38] D. Bernsmeier, M. Bernicke, R. Schmack, R. Sachse, B. Paul, A. Bergmann, P. Strasser, E. Ortel, R. Kraehnert, *ChemSusChem* **2018**, 11, 2367.

- [39] L. Ouattara, S. Fierro, O. Frey, M. Koudelka, C. Comninellis, *J. Appl. Electrochem.* **2009**, 39, 1361.
- [40] R. Kötz, H. Neff, S. Stucki, *J. Electrochem. Soc.* **1984**, 131, 72.
- [41] S. Fierro, L. Ouattara, E. H. Calderon, C. Comninellis, *Electrochem. Commun.* **2008**, 10, 955.
- [42] D. F. Abbott, D. Lebedev, K. Waltar, M. Povia, M. Nachtegaal, E. Fabbri, C. Copéret, T. J. Schmidt, *Chem. Mater.* **2016**, 28, 6591.
- [43] E. Fabbri, A. Rabis, R. Kotz, T. J. Schmidt, *Phys. Chem. Chem. Phys.* **2014**, 16, 13672.
- [44] G. Cognard, G. Ozouf, C. Beauger, G. Berthomé, D. Riassetto, L. Dubau, R. Chattot, M. Chatenet, F. Maillard, *Appl. Catal. B-Environ.* **2017**, 201, 381.
- [45] G. Cognard, G. Ozouf, C. Beauger, L. Dubau, M. López-Haro, M. Chatenet, F. Maillard, *Electrochim. Acta* **2017**, 245, 993.
- [46] S. Geiger, O. Kasian, A. M. Mingers, K. J. J. Mayrhofer, S. Cherevko, *Sci. Rep.* **2017**, 7, 4595.
- [47] W. Xu, G. M. Haarberg, S. Sunde, F. Seland, A. P. Ratvik, E. Zimmerman, T. Shimamune, J. Gustavsson, T. Åkre, *J. Electrochem. Soc.* **2017**, 164, F895.
- [48] F. Iskandar, Mikrajuddin, K. Okuyama, *Nano Lett.* **2001**, 1, 231.
- [49] B. Mandlmeier, J. M. Szeifert, D. Fattakhova-Rohlfing, H. Amenitsch, T. Bein, *J. Am. Chem. Soc.* **2011**, 133, 17274.
- [50] B. Mandlmeier, N. K. Minar, J. M. Feckl, D. Fattakhova-Rohlfing, T. Bein, *J. Mater. Chem. A* **2014**, 2, 6504.
- [51] F. Iskandar, A. B. D. Nandiyanto, K. M. Yun, C. J. Hogan, K. Okuyama, P. Biswas, *Adv. Mater.* **2007**, 19, 1408.
- [52] J. M. Szeifert, J. M. Feckl, D. Fattakhova-Rohlfing, Y. Liu, V. Kalousek, J. Rathousky, T. Bein, *J. Am. Chem. Soc.* **2010**, 132, 12605.
- [53] S. Doniach, M. Sunjic, *J. Phys. C Solid State* **1970**, 3, 285.
- [54] G. Sauerbrey, *Z. Phys.* **1959**, 155, 206.
- [55] B. W. Mwakikunga, *CRC Cr. Rev. Sol. State* **2014**, 39, 46.
- [56] V. Müller, M. Rasp, G. Štefanić, J. Ba, S. Günther, J. Rathousky, M. Niederberger, D. Fattakhova-Rohlfing, *Chem. Mater.* **2009**, 21, 5229.
- [57] J. M. Xu, L. Li, S. Wang, H. L. Ding, Y. X. Zhang, G. H. Li, *CrystEngComm* **2013**, 15, 3296.

- [58] À. Diéguez, A. Romano-Rodríguez, A. Vilà, J. R. Morante, *J. Appl. Phys.* **2001**, 90, 1550.
- [59] V. Skoromets, H. Němec, J. Kopeček, P. Kužel, K. Peters, D. Fattakhova-Rohlfing, A. Vetushka, M. Müller, K. Ganzerová, A. Fejfar, *J. Alloy Compd.* **2015**, 119, 19485.
- [60] A. Zürner, M. Döblinger, V. Cauda, R. Wei, T. Bein, *Ultramicroscopy* **2012**, 115, 41.
- [61] K. J. Batenburg, S. Bals, J. Sijbers, C. Kübel, P. A. Midgley, J. C. Hernandez, U. Kaiser, E. R. Encina, E. A. Coronado, G. Van Tendeloo, *Ultramicroscopy* **2009**, 109, 730.

9. CONCLUSION AND OUTLOOK

In conclusion, in this thesis we reviewed the state-of-the art and advanced ceramic anode materials for possible future applications in secondary alkali metal ion battery anodes (Chapter 3), with an additional focus on nanostructured tin oxide-based anode materials for lithium ion batteries (Chapter 4). Insertion type anode materials such as lithium titanates or NaSICON-type anode materials as well as recently introduced materials such as TiO₂ bronze phase or titanium niobate are discussed. However, a further, desirable increase in the energy density of the batteries necessitates the use of high capacity anodes. Promising systems include the conversion and alloying type materials such as silicon or tin (oxide) nanostructures discussed in Chapters 3 and 4. Possible tin oxide nanostructures for high performance lithium, sodium and potassium ion batteries are reviewed concerning their capacity, rate and reversibility and related to the applied synthesis parameters, primary particle size, phase purity and composite architecture (Chapter 4).

The main experimental part of this thesis was dedicated to the synthesis of novel nanosized and nanostructured transition metal oxides (Chapter 5 - 8), which were generated using *tert*-butyl alcohol solvothermal reactions (Chapter 5 and 8) as well as an aqueous colloidal chemistry synthesis route based on rapid oxidation and condensation reactions induced by an elevation of the pH-value by KO₂ and a release of oxygen (Chapter 6 and 8). Using these reactions, dispersible ultra-small nanoparticles with unusual high doping ion concentrations could be fabricated, which were tested for their (photo)-catalytic properties as oxygen evolution reaction catalysts (Chapter 5, 6 and 8).

A microwave-assisted solvothermal reaction in *tert*-butanol was introduced to obtain a variety of transition metal (Co, Ni, V, Sn, Si, Sn, Ti) doped rod-like β -FeOOH nanoparticles

with unusual high dopant concentrations of up to 20 at%, which are not accessible by bulk synthesis methods (Chapter 5).

An aqueous rapid pH induced co-condensation reaction of vanadium (III) and nickel (II)-ions led to the formation of metastable hydroxide phases with high doping ion concentration which were employed to elucidate spontaneous time-dependent phase transformations (Chapter 6).

A further part of this thesis was dedicated to the fabrication and loading process of precisely defined macroporous oxide structures employed as support structures for nanosized noble metal oxygen evolution reaction catalyst particles (Chapter 8). The optimized highly conductive open-porous support nanomorphology, combined with the introduced homogeneous coating process for noble metal nanoparticles, led to a high-performance composite catalyst with a low iridium density of only $\approx 0.08 \text{ g}_{\text{Ir}} \text{ cm}^{-3}$ for a 25 wt% Ir containing catalyst. The introduced architecture and synthesis route could thereby guide the way for the fabrication of further supported catalysts with significantly reduced noble metal content, which could be extended beyond the electrochemical oxygen evolution reaction to various applications in heterogeneous catalysis. Future synthetic work could elucidate the influence of the catalyst support morphology and phase on the loading with transition metal (oxide) nanoparticles and the influence on the catalytic performance.

Finally, a novel and industrially scalable synthesis route for the fabrication of similar homogeneously coated composite catalyst nanostructure was introduced (Chapter 7). The process includes the precisely controllable oxidation of an amorphous transition metal oxide catalyst hydroxide phase in molten salt to obtain a continuous layer of intergrown $\approx 2 \text{ nm}$ sized particles. The resulting high surface area TiO_2 supported 30 wt% Ir loaded IrO_2 electrocatalysts thereby exhibit a high electrical conductivity of up to 11 S cm^{-1} and a mass-specific catalytic activity outperforming an industrial reference catalyst by a factor of 3 – 8 (depending on the

overpotential). Together with a low Ir density of only $0.05 - 0.08 \text{ g}_{\text{Ir}} \text{ cm}^{-3}$ this composite catalyst shows a significant potential reduction of the noble metal content regarding the application as oxygen evolution reaction catalyst in PEM electrolyzers.

It thereby allows for a large-scale application of this technology that is otherwise limited by the low natural abundance of the noble metal iridium.

In summary, this thesis presents advances regarding the application of nanostructured transition metal oxides for energy storage and conversion processes. It furthermore sheds light on the interplay of size, crystal structure and morphology regarding the physico-chemical properties of the materials and their resulting functionality. It becomes clear that an intensive feedback-loop of creative synthesis approaches with in-depth material characterization is a prerequisite for the rational synthesis and development of novel highly functional transition metal oxide nanostructures and composites.

